IRRADIATION EFFECTS ON THE MICROSTRUCTURE AND PROPERTIES OF METALS

STP 611

AMERICAN SOCIETY FOR TESTING AND MATERIALS

IRRADIATION EFFECTS ON THE MICROSTRUCTURE AND PROPERTIES OF METALS

A symposium
sponsored by ASTM Committee E-10
on Nuclear Applications
and Measurement of Radiation
AMERICAN SOCIETY FOR
TESTING AND MATERIALS
St. Louis, Mo., 4-6 May 1976

ASTM SPECIAL TECHNICAL PUBLICATION 611
F. R. Shober, symposium chairman

List price $49.00
04-611000-35

AMERICAN SOCIETY FOR TESTING AND MATERIALS
1916 Race Street, Philadelphia, Pa. 19103

Library of Congress Catalog Card Number: 76-21529

NOTE

The Society is not responsible, as a body,
for the statements and opinions
advanced in this publication.

Printed in Baltimore, Md.
November 1976

Foreword

The eighth ASTM International Symposium on Effects of Radiation on Structural Materials was held in St. Louis, Missouri, 4-6 May 1976. Committee E-10 on Nuclear Application and Measurements of Radiation Effects sponsored the symposium. F. R. Shober, Westinghouse Hanford Company, Hanford Engineering Development Laboratory, presided as symposium chairman, and J. A. Sprague, Naval Research Laboratory, served as symposium cochairman.

Related ASTM Publications

Zirconium in Nuclear Applications, STP 551 (1974), $44.50, 04-551000-35

Effects of Radiation on Substructure and Mechanical Properties of Metals and Alloys, STP 529 (1973), $49.50, 04-529000-35

Radiation Effects Information Generated on the ASTM Reference Correlation-Monitor Steels, DS 54 (1974), $9.75, 05-054000-35

A Note of Appreciation to Reviewers

This publication is made possible by the authors and, also, the unheralded efforts of the reviewers. This body of technical experts whose dedication, sacrifice of time and effort, and collective wisdom in reviewing the papers must be acknowledged. The quality level of ASTM publications is a direct function of their respected opinions. On behalf of ASTM we acknowledge with appreciation their contribution.

ASTM Committee on Publications

Editorial Staff

Jane B. Wheeler, *Managing Editor*
Helen M. Hoersch, *Associate Editor*
Ellen J. McGlinchey, *Assistant Editor*

Contents

Introduction

IRRADIATION CREEP AND STRESS RELAXATION

Effects of Prior Stress History on Irradiation-Induced Creep—G. L. WIRE 5

Analysis of In-Reactor Stress Relaxation Using Irradiation Creep Models—J. P. FOSTER 32

MECHANICAL PROPERTIES AND MICROSTRUCTURE

Dynamic Strain-Aging and Neutron Irradiation in Mild Steel—K. L. MURTY AND E. O. HALL 53

Swelling and Tensile Property Changes in Neutron-Irradiated Type 316 Stainless Steel—K. R. GARR AND A. G. PARD 72

Effect of Fast Reactor Irradiation on the Tensile Properties of 20 Percent Cold-Worked Type 316 Stainless Steel—R. L. FISH AND J. D. WATROUS 91

Mechanical Properties of Fast Reactor Fuel Cladding for Transient Analysis—C. W. HUNTER AND G. D. JOHNSON 101

Tensile Properties of Fast Reactor Irradiated Type 304 Stainless Steel—R. L. FISH AND C. W. HUNTER 119

Effects of Neutron Irradiation on Microstructure and Mechanical Properties of Nimonic PE-16—P. S. SKLAD, R. E. CLAUSING, AND E. E. BLOOM 139

Irradiation and Thermal Effects on the Tensile Properties of Inconel-718—A. L. WARD, J. M. STEICHEN, AND R. L. KNECHT 156

Tensile and Hardness Property Evaluations of Irradiated Zircaloy Cladding Under Off-Normal and Transient Conditions—L. M. LOWRY, J. S. PERRIN, AND A. A. BAUER 171

Neutron Energy Dependent Damage Functions for Tensile Properties of 20 Percent Cold-Worked Type 316 Stainless Steel—R. L. SIMONS 181

IRRADIATION SIMULATION

Swelling Simulation Studies of Type 316 Stainless Steel—J. A. ELLIS, JR., W. K. APPLEBY, AND T. LAURITZEN 195

Development and Evaluation of a Stress-Free Swelling Correlation for 20 Percent Cold-Worked Type 316 Stainless Steel—F. A. GARNER, J. J. LAIDLER, AND G. L. GUTHRIE 208

Swelling Behavior of Commercial Ferritic Alloys, EM-12 and HT-9, as Assessed by Heavy Ion Bombardment—F. A. SMIDT, JR., P. R. MALMBERG, J. A. SPRAGUE, AND J. E. WESTMORELAND 227
Observation of Defect Clusters of Columbium and Columbium Alloys *In Situ* Irradiated Under a High-Voltage Electron Microscope—N. IGATA, F. WATARI, AND H. MURAKAMI 242
Void Growth Suppression by Dislocation Impurity Atmospheres—JOHANNES WEERTMAN AND W. V. GREEN 256
Dependence of Void Swelling on the Electron Vacancy Concentration—J. S. WATKIN 271
Microstructures and Mechanisms of Ion-Simulated Irradiation-Induced Creep of Nickel—D. J. MICHEL, P. L. HENDRICK, AND A. G. PIEPER 284
Effects of Interstitial Solutes on the Microstructures of Self-Ion Irradiated Vanadium—S. C. AGARWAL, D. I. POTTER, AND A. TAYLOR 298

VOID GROWTH AND MICROSTRUCTURAL CHANGES

Swelling and Gamma-Prime Particle Stability of Ion-Bombarded Iron-Chromium-Nickel Alloys—M. L. BLEIBERG, R. BAJAJ, I. M. BARON, A. CHANG, R. W. CHICKERING, AND S. DIAMOND 315
Effect of Ion Irradiation on the Microstructure of an Iron-Nickel-Chromium Alloy—J. A. SPRAGUE, F. A. SMIDT, JR., J. E. WESTMORELAND, AND P. R. MALMBERG 337
Microstructural Changes in Ion-Irradiated Commercial Alloys—W. L. BELL, T. LAURITZEN, E. S. DARLIN, AND R. W. WARNER 353
Nickel-Ion Damage in a Precipitation-Hardened Nickel-Aluminum Alloy—L. G. KIRCHNER, F. A. SMIDT, JR., G. L. KULCINSKI, J. A. SPRAGUE, AND J. E. WESTMORELAND 370

RADIATION EMBRITTLEMENT OF PRESSURE VESSEL STEELS

Fracture Mechanics Characterization of the Trino Reactor Vessel Material—T. R. MAGER, J. DAVIDSON, AND M. GALLIANI 387
Evaluation of the Maine Yankee Reactor Beltline Materials—R. A. WULLAERT, J. W. SHECKHERD, AND R. W. SMITH 400
Evaluation of the Effect of Chemical Composition on the Irradiation Sensitivity of Reactor Vessel Weld Metal—E. C. BIEMILLER AND S. T. BYRNE 418
Annealing of Irradiation Damage in High-Copper Ferritic Steels—J. A. SPITZNAGEL, R. P. SHOGAN, AND J. H. PHILLIPS 434
Displacement Spike Annealing in Iron at Reactor Temperatures—J. R. BEELER, JR., AND M. F. BEELER 449
Neutron Displacement Damage Cross Sections for Structural Metals—D. G. DORAN AND N. J. GRAVES 463

Introduction

The ASTM Committee E-10 on Nuclear Application and Measurement of Radiation Effects sponsors, on alternate years, an international conference on the effects of irradiation to structural materials. The 1976 symposium on "Irradiation Effects on the Microstructure and Properties of Metals" was the eighth international symposium and the eleventh of a series started by Committee E-10 in 1956. The symposium serves as media for the exchange of information and data on materials used in the nuclear industry.

The symposium consisted of approximately 35 papers presented in five sessions. The topics include (1) Irradiation Creep and Stress Relaxation, (2) Mechanical Properties and Microstructures, (3) Irradiation Simulation, (4) Void Growth and Microstructural Changes, and (5) Radiation Embrittlement of Pressure Vessel Steels.

Dr. Herbert J. C. Kouts, Director of the Office of Nuclear Regulatory Research, Nuclear Regulatory Commission, presented the keynote address for the symposium. His presentation, entitled "A Review of Reactor Safety and Reactor Safety Research," reviewed the United States' total energy needs for the years 1976 through 2000 and stressed the importance of utilizing nuclear energy in order that we meet our national energy goals. Public acceptance of nuclear reactors to generate electricity will come, Dr. Kouts said, with continued demonstration of their safeness. Safety to the public is demanded in nuclear materials manufacturing facilities as well as reactor operations. Public safety is further ensured by regulations, regulations based on the results of research on materials used in reactor construction. The regulations are most often drafted exercising a large degree of conservatism. Dr. Kouts believes that nuclear reactors have already been demonstrated to be one of the safest forms of technology ever introduced. He reviewed conclusions from the Reactor Safety Study (the Rasmussen Report) and discussed current research on reactor safety. Methods, Dr. Kouts reported, are being developed for assessing the safety of nuclear power plants. Research continues in the areas of primary system integrity, fuel cycle safety, and environmental effects. He cited two reasons for continuing research. First, the estimates for margins of safety in design, construction, and operation of nuclear power, although adequate, could be improved. Second, we find that the fundamental facts of many basic areas of science and engineering are often inadequate.

The effect of neutron irradiation on load bearing structures and con-

tainer materials at elevated temperature has been a subject of extreme interest and study since the early days of water-cooled reactors. With the inclusion of LMFBR's (Liquid Metal Fast Breeder Reactors), HTGCR's (High Temperature Gas Cooled Reactors), and CTR's (Controlled Thermonuclear Reactors) as potential electrical power generators, the temperature and fluence regimes are expanded, often requiring new materials and better understanding of mechanisms which limit their use in these more adverse conditions. Irradiation-induced microstructural changes, often a function of stress and thermal gradients, can ultimately influence the time-dependent properties. The postirradiation tensile properties of materials often determine their applicability for use in reactor construction. Often of special interest to designers are the results from tests of off-normal or transient temperature conditions. Papers describing results of these kinds of tests on stainless steel and Zircaloy are published in this volume.

Particle and ion irradiation, irradiation simulation techniques, are often used to show the relative magnitudes of irradiation-induced swelling, microstructural changes, and property changes in metals. The effect is similar to that achieved by neutron irradiation, but in considerably shorter time. It continues to be a popular, less costly, and much less time consuming technique for evaluating the effect of irradiation on materials. Again, as in 1974, nearly half of the papers in the symposium were about irradiation simulation results. Irradiation simulation studies were mostly in the areas of void formation, void growth, and swelling. Mechanisms and processes are described.

One of the primary concerns about light water reactors has been its primary containment—the pressure vessel. The reliability of pressure vessel steels has been demonstrated by its utilization in PWR's and BWR's. Surveillance studies which report the irradiation-induced property changes in materials used for the construction of pressure vessels also confirm their reliability. The residual element content in weldments and pressure vessel materials has been shown to influence their susceptibility to irradiation embrittlement. Correlation of results from several studies were presented confirming this sensitivity. Further refinement is suggested for the measurement and calculation of neutron fluence to better relate damage functions with *in situ* property changes.

The members of the symposium committee were F. R. Shober, chairman; J. A. Sprague, cochairman; C. J. Baroch, J. W. Bennett, D. Kramer, and C. Z. Serpan. The symposium committee gratefully acknowledges the assistance of D. Kramer in securing a papers' review committee and directing the review meeting, and of L. E. Steele, chairman of Committee E-10, for his guidance and encouragement.

F. R. Shober
Hanford Engineering Development Laboratory, Westinghouse Hanford Company, Richland, Wash.; symposium chairman.

Irradiation Creep and Stress Relaxation

G. L. Wire[1]

Effects of Prior Stress History on Irradiation-Induced Creep

REFERENCE: Wire, G. L., **"Effects of Prior Stress History on Irradiation-Induced Creep,"** *Irradiation Effects on the Microstructure and Properties of Metals, ASTM STP 611,* American Society for Testing and Materials, 1976, pp. 5–31.

ABSTRACT: The purpose of this paper is to report the results of an experimental study to determine the effects of previous irradiation history on the fast-flux neutron irradiation creep behavior of 20 percent cold-worked Type 316 stainless steel for liquid metal fast breeder reactor (LMFBR) application. Previous irradiation creep experiments have involved monitoring the irradiation creep strain of specimens held at constant stress while irradiated at approximately constant temperature and flux. Under these conditions, the irradiation creep rates have been observed to vary with neutron exposure. Application of these "creep curve" data to design and analysis of reactor core structural materials requires some knowledge of how the creep rate at a given point in time depends upon the previous stress history.

In the present experiment, in-reactor stress relaxation tests were performed on specimens which had previously been irradiated in the stress-free condition to various exposures ranging from 0 to 4 $\times$ 10^{22} (n)/cm^2 ($E > 0.1$ MeV) at 800 and 1000°F (427 and 538°C). It was found that the creep coefficients derived from this experiment were essentially the same as that obtained from the constant-load in-reactor test when allowance was made for thermal deformations. Thus it is concluded that, for the materials and conditions studied, the irradiation creep rate is essentially independent of previous stress history. This result may be rationalized if the microstructural development during irradiation is influenced predominantly by the irradiation flux and temperature variables and only to a minor extent by the irradiation creep deformation.

The sensitivity of the experimental technique to in-reactor effects coupled with supplementary thermal control studies led to a new insight into what has been called transient irradiation creep. The results of this experiment suggest that thermal effects can account for the initially higher creep rate portion of the total in-reactor behavior observed. The thermal component was observed to recur upon reloading, giving rise to a significantly enhanced creep rate for cyclic loadings.

KEY WORDS: radiation, stainless steels, neutron irradiation, creep rate, thermal stresses, deformation, cyclic loads, stress relaxation

From an engineering viewpoint, the ultimate goal of research on irradiation-induced creep phenomena in a fast-flux reactor environment is to

[1]Hanford Engineering Development Laboratory, Westinghouse Hanford Company, Richland, Wash. 99352.

obtain the information required to predict the in-reactor creep rate of structural materials under all conditions of practical interest. These conditions include not only those of steady-state routine operation, but also transient periods as well, which range from mild upset of normal startup and shutdowns all the way to the more severe conditions attending hypothetical loss of coolant flow in the core. However, irradiation-induced creep rates are low—typically of the order of (10^{-7} in./in.)/h—so that for a description of rapid stress rate, strain rate, or high stress conditions, postirradiation testing is an appropriate method to obtain design data.

On the other hand, there are routine conditions attending reactor operation which lead to loading changes where long-term irradiation-induced creep responses will dominate. For example, plenum gas pressure buildup due to helium generation will occur continuously over the whole fuel element lifetime, producing hoop stresses which are typically well below yield stress levels. Swelling gradients across ducts lead to bending loads which vary with time.

Up to the present time, designers of fast reactors have utilized data on irradiation creep derived principally from two basic experimental approaches. The first approach consists of monitoring the deformation of actual reactor components, mainly fuel cladding. This method has the powerful advantage of completeness; that is, all possible effects, including load changes, temperature changes, chemical effects, as well as even unidentified effects, are included in the measurements. The second major source of design data relies on simulation of the anticipated loading in the reactor on tailor-made specimens of the materials of interest. As the specimens used in these experiments can be made much smaller than typical reactor components, isolation of variables such as temperature, stress, cold-work level, composition, etc. is easily accomplished. In particular, constant-stress pressurized tube experiments [*1–3*][2] have provided invaluable information on fast reactor creep phenomena. However, as these have been run at constant stress and temperature, supplemental experimentation is required to ascertain the effects of varied loading histories. The purpose of the present experiment is to establish the effects of load increase on the steady-state irradiation-induced creep rate.

It is worthwhile to anticipate several possibilities for the effect of a stress increase on the in-reactor creep rate. The solid line in Fig. 1 shows a nominal in-reactor creep curve for 20 percent cold-worked Type 316 stainless steel based on currently available biaxial constant-stress data. These data represent substantively irradiation-induced effects as the same time-temperature history outside the reactor would lead to less than 4 percent of the total effect. Irradiation-induced creep has been observed to have a linear or very close to linear dependence on the applied stress [*1–5*]

[2]The italic numbers in brackets refer to the list of references appended to this paper.

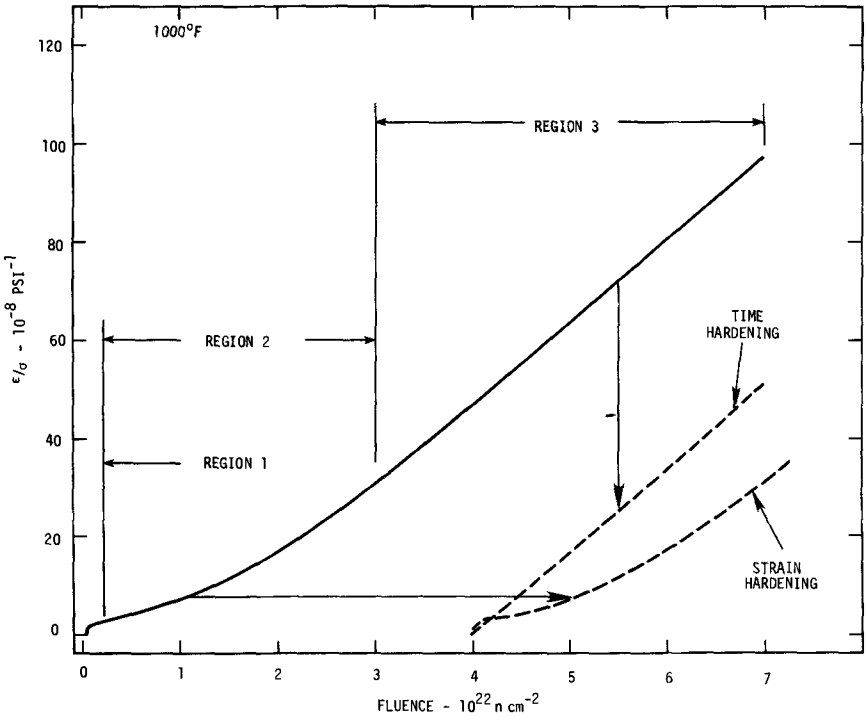

FIG. 1—*Irradiation-induced creep curve for 20 percent cold-worked Type 316 stainless steel at 1000°F (538°C). The dotted lines represent predicted creep curves for load applied at a fluence of* 4×10^{22} *n/cm*^{2} *for two hypothetical strain rules.*

so that this curve is not really specialized to a particular stress level. For discussion purposes only, we divide the curve into three segments. The first segment shows a high but rapidly decreasing strain rate, which is denoted as a "transient" region. This portion of the curve is discussed more fully later in the paper, where it is identified with thermal creep effects. Region 2 is an area of rapidly increasing strain rate, while Region 3 appears to be consistent with slowly varying creep rate or a "steady-state" creep behavior. The important fact is that there are relatively large strain rate changes from a fluence of 1.0 to 3.0 $\times$ 10^{22} (n)/cm^2 ($E > 0.1$ MeV). The pertinent question to resolve experimentally is whether this behavior will be dependent on loading history. The irradiation-induced strain rate varies by a factor of five over Region 2 and if this effect is dependent on loading history, it implies significant uncertainty in our ability to predict irradiation-induced creep behavior under different loading paths.

Several conventional ideas exist on the effect of a load increase on the

creep rate. Figure 1 illustrates two completely different predictions of the effect of a load change. The curve denoted "strain hardening" is derived by merely shifting the nominal creep curve along the time axis and is based on the premise that *only* the accumulated strain during the creep curve is responsible for changes in strain rate—albeit through changes in the dislocation structure. The second curve, denoted "time hardening," is derived by shifting the nominal curve along the strain axis and is based on the premise that structural changes induced by exposure time or fluence in the reactor determine the strain rate. It is tempting to hypothesize that one or the other of these two predictions will in fact be realized and that the effect of load changes can be predicted *entirely on the basis of constant stress creep curves* in combination with a simple rule. While concepts such as these are of great value in providing a framework to design testing programs, the philosophy of this experiment is to be alert to the possibility that the actual result may not follow either of these simple patterns.

Description of the Test

The stress-relaxation technique is the same in principle as the test devised by Manjoine [*6*] some years ago and often referred to as the "Manjoine Test." The test consists of measuring creep effects by periodically measuring the residual load and hence residual stress in a constant-strain configuration. The total strain (elastic + plastic) is constant during the test, so that measurement of the residual load or elastic strain provides a measure of the creep rate over the prescribed test condition. The method has the advantages of simplicity and compactness, which make it highly adaptable for uninstrumented tests in reactor applications. This approach has been used previously in various forms for in-reactor experiments [*4,7,8*]. In addition, the technique as utilized in this experiment enabled measurement of irradiation-induced creep rates over relatively small fluence and strain increments. This is very important because the purpose of the experiment is to measure the creep rate of previously irradiated but unstressed material and compare this with the creep rate obtained from a long-term, constant-stress loading to ascertain the effects of a stress increase. The irradiation period required for a creep-rate measurement using stress relaxation is only 2×10^{21} n/cm^2 ($E > 0.1$ MeV). Over this fluence increment, the maximum change in creep coefficient observed in pressurized tubes (Fig. 1) is $\Delta B = 1.2 \times 10^{-30}$/n/cm^2·psi, so that in effect this measurement is effectively an "instantaneous" measure of irradiation creep rate.

The specimen and stressing[3] configurations are shown in Fig. 2. The

[3]This specimen configuration was first suggested by J. E. Flinn of Argonne National Laboratory, and the author is indebted to him for sharing his unpublished work on it.

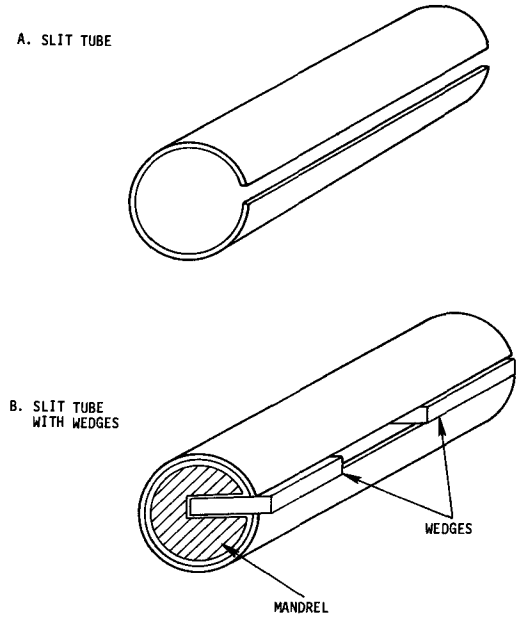

FIG. 2—*Slit tube specimen and loading wedges.*

cladding is 0.230 in. outside diameter by 0.015 in. wall thickness. The slit tube specimens were formed by using a slitting saw of 0.050 in. width on a milling machine in-cell to open the cladding as shown in Fig. 2*a*. The specimen was supported during the cutting by close-fitting mandrels both inside and out so that the tube would not be stressed during the cutting. The specimen was stressed by inserting wedges (Fig. 2*b*) into the slit. The two wedges on a given specimen were matched to within ±0.0002 in. to avoid assymetric stressing of the tube. The wedges are loosely pinned to the mandrel so that they are free to align themselves in the tube slot. The mandrel-and-wedge design allows specimen handling without actually touching the cladding and also ensures that the wedges cannot be lost in cases where the relaxation is nearly complete.

The stress distribution induced by the loading in Fig. 2 is calculated in detail in Ref *9*. The outer fiber stresses are given in terms of the clamping force F on a tube of radius

$$\sigma_\theta \approx \frac{6Fa}{l\Delta^2}(\cos\theta - 1) + \frac{F}{\Delta l} \quad \text{(tangential)} \qquad (1a)$$

$$\sigma_z = \nu\sigma_\theta \quad \text{(axial)} \qquad (1b)$$

where

F = clamping force exerted on the wedges,
l = tube length,
ν = Poisson's ratio, and
Δ = wall thickness.

In this approximate form it can be seen that the stress distribution is essentially a bending stress distribution with a bending moment which increases with the distance a ($\cos\theta - 1$) from wedge position at $\theta = 0$. The stress distribution is characterized in this report by the maximum fiber stress $\sigma_{\theta max}$ which occurs at $\theta = \pi$, on the inside of the tube

$$\sigma_{max} = \frac{8110 \text{ psi}}{\text{lb}} F \quad \text{(exact result)} \tag{2}$$

It should be noted that this somewhat complex stress distribution is not really an impediment to analysis of the test results because irradiation creep is essentially linearly dependent on stress in the temperature range and stress range used for this experiment [*1–5*]. However, a full range of stresses was included in the experiment to ensure detection of any conceivable nonlinear behavior. Equally important, having a number of otherwise identical specimens at different stress levels provided better statistics on data analysis.

The test plan for the in-reactor portion of this experiment is given in Table 1. The original matrix includes 60 specimens among two temperatures (800 and 1000°F) (427 and 538°C), three prior fluences (0 to 3.6×10^{22} n/cm^2, $E > 0.1$ MeV), and 10 specimens per condition covering a nominal stress range of $\sigma_{max} = 4$ to 50 ksi. Hence, the experiment was designed to provide information about the stress, temperature, and fluence dependence of irradiation creep after a stress increase. The chemical composition for this material is given in Ref *1*. This is the same heat of material used in pressurized tube and uniaxial experiments that provide the data for constant-stress irradiation creep rates [*1,10*], so that the results are directly comparable.

The irradiation creep coefficients are derived from measurements of the residual clamping force F which the tube exerts on its wedges. The creep induced by irradiation or thermal processes acts to relieve the residual stress distribution and to reduce the clamping force of the tube on its wedges.

The model chosen to derive the relationship between the residual clamping force and the creep coefficients is a generalized viscoelastic model as used previously by Wire and Straalsund [*4,11*]. The justification for the use of this model, as stated previously, it that it is a quite simple form; yet, it is consistent with the present experimental understanding of irradia-

TABLE 1—*Irradiation test plan.*

Specimen No.	Prior Irradiation Nominal Temperature, °F	History (unstressed) Fluence, 10^{22} n/cm^2, $E > 0.1$ MeV	Reirradiation Parameters		
			Nominal Temperature, °F	Stress Range, $\sigma_{e\max}$, ksi (at temperature)	Fluence Increments, 10^{21} n/cm^2, $E > 0.1$ MeV
1 to 10	800	3.6	800	12 to 47	1.7, 1.7
11 to 20	800	0.5	800	4 to 41	1.7, 1.7
21 to 30	...	0	800	4 to 43	1.6, 1.6
31 to 37, 39, 40, 67	1000	3.4	1000	10 to 48	2.0, 2.0
41 to 50	1000	0.5	1000	9 to 32	2.0, 2.0
51 to 60	...	0	1000	10 to 44	1.8, 1.8

tion-induced creep for this material. The essential features of the model are:

1. Creep rates are linear in the applied stress.
2. Creep is isotropic.

Whereas Refs *4* and *11* considered creep where volume changes occur, this will not be done here as no significant swelling effects are observed in this material at these fluences. The relationship between the clamping force changes and the creep coefficients in a slit tube is given in Ref *12*. The calculation is illustrated here for simple uniaxial stress relaxation. For small fluence increments over which the strain rate is essentially constant for a given stress, irradiation-induced creep at constant stress can be described as [*1–4,11*]

$$\dot{\varepsilon}_p = B\sigma\phi \quad \text{(uniaxial)} \tag{3}$$

where

ϕ = neutron flux,
σ = stress,
B = creep coefficient, and
$\dot{\varepsilon}_p$ = plastic strain rate.

For stress relaxation of an ideal Manjoine specimen, the total strain rate (elastic + plastic) is zero or

$$B\sigma\phi + \frac{\dot{\sigma}}{E} = 0 \tag{4}$$

which integrates immediately to

$$\sigma(t) = \sigma_0 e^{-EB\phi t} \quad \text{(uniaxial)} \tag{5}$$

where

σ_0 = initial stress at $5 = 0$, and
E = Young's modulus.

The "clamping force" F for the Manjoine specimen is related simply to the stress by $F = \sigma A$, so that the creep coefficient B is determined by the change in the clamping force

$$\frac{F}{F_0} = e^{-EB\phi t} \tag{6}$$

A time-varying creep coefficient $B(t)$ can be easily accommodated. In this case, Eq 6 becomes

$$\frac{F}{F_0} = e^{-E\phi\int_0^t B(t')dt'} \tag{6'}$$

The average creep coefficient

$$\bar{B} = \frac{\int_0^t B(t')dt'}{t} \tag{7}$$

can be used to characterize the relaxation, so that

$$\frac{F}{F_0} = e^{-E\bar{B}\phi t} \tag{8}$$

The present experiment consists of measurement of the average creep coefficient for each of two consecutive irradiation periods of peak fluences $\phi t = 2 \times 10^{21}$ n/cm^2 ($E > 0.1$ MeV). The simplified expression for Type 316 stainless steel slit tubes corresponding to Eq 8 for the residual clamping force and tangential stress in slit tubes is

$$\frac{F}{F_0} = \frac{\sigma}{\sigma_0} = e^{\frac{-E\bar{B}\phi t}{1.20}} \tag{9}$$

There are two terms in the complete expression because of the plane-strain nature of the deformation [*12*], but for relaxations in the range measured in this experiment the expression given is accurate to better than 0.01. The numerical factor depends on Poisson's ratio, which is taken as 0:3 for this material. For calculation of creep coefficients, the exact expression was always used.

The residual clamping force was measured by a novel mechanical device, which was designed specifically for this operation. This mechanical device provided several distinct advantages for the experiment.

1. Remote hot-cell operations were quick and easy as the only essential operations were placement of the specimen on the machine and recording the data.

2. Data readout was automatic, eliminating to a great extent the need for human judgement.

3. Overall measurement times were very short, making it possible to carry out thermal control tests with large numbers of specimens.

The operating principle of the device is shown schematically in Fig. 3*a*. The device applied a load to the slit tube at the slit and at the same time monitored displacement of loading tips which contacted the tube. The idealized relationship for the resulting force-displacement curve obtained is shown in Fig. 3*b* along with an actual curve from the experiment. For

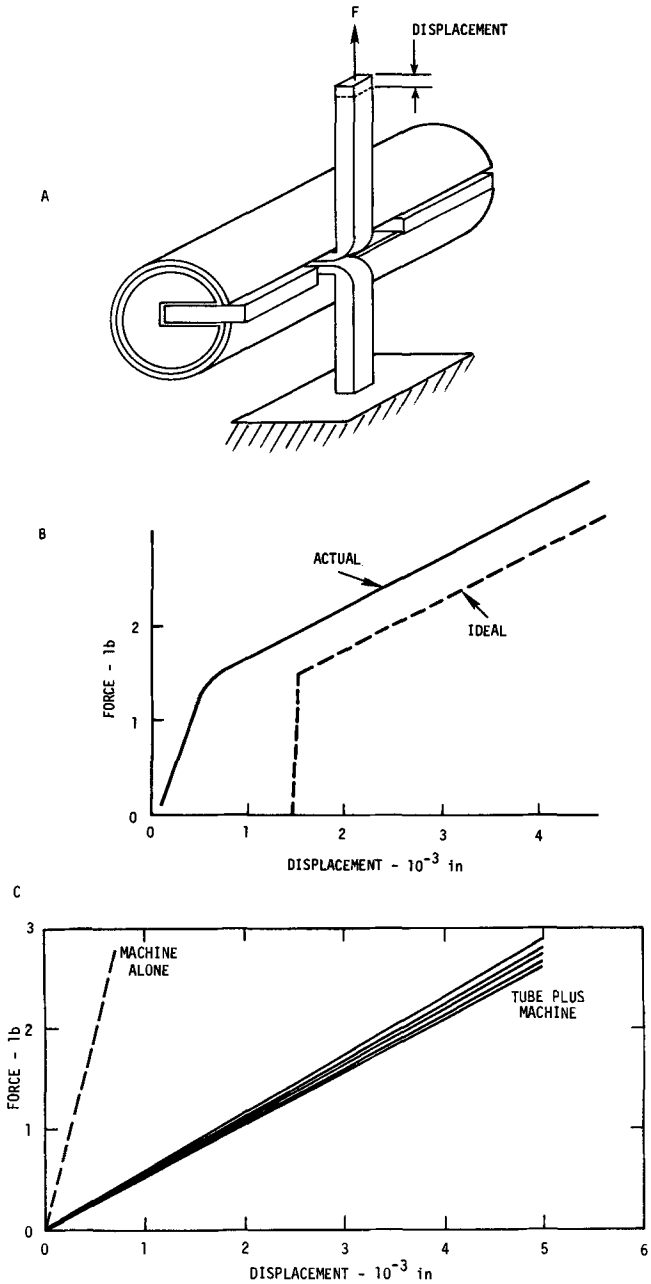

FIG. 3—*Slit tube force measurement device and typical force-displacement curves.* (c) *shows the spread in the observed compliance curve for the specimen* (*solid*) *and machine and grip compliance curve alone* (*dotted*).

forces below the clamping force, F, only small displacements per unit force due to the relatively low compliance of the loading tips on the tube and the grips themselves will occur, giving rise to the initial steep part of the curve. For forces greater than F, the tube now begins to spread open, giving rise to the high-compliance or low-slope portion of the curve. The force at the discontinuity in slope is then the clamping force.

Comparison with a typical curve obtained during this experiment (Fig. 3*b*) shows that indeed real lift-off curves with these same qualitative features can be obtained. The initial part of the curve (force less than F) is typically three times steeper than that after lift-off, and there is a fairly well-defined point where the slope changes. The dashed tangent lines in the figure illustrate the method used to obtain a unique lift-off force by extrapolation of both segments of the curve. In general, the accuracy of the clamping force measurements was ± 0.05 lb or better. For example, at a fiber stress of $\sigma_{max} = 20$ ksi, ± 0.05 lb corresponds to a ± 2 percent error in the stress measurement. This is satisfactory accuracy for the present experiment.

The development of the successful experimental apparatus required to obtain this accuracy necessitated very careful consideration of the mechanics of the loading system. The major problems which had to be overcome were

1. Elimination of frictional effects which can give discontinuities in the curve. A discontinuity of only 1×10^{-4} in. in the displacement observed can induce an uncertainty of 0.1 lb in the lift-off force.
2. Hysteresis of any elements in the load train creates curved regions so that it is difficult to define a precise lift-off force.
3. Nonuniform or erratic contact between the specimen and loading fixtures can give discontinuous curves.
4. Misalignment of the loading fixtures or changes in the line of the applied force can cause yawing of the tube and thus erroneous force readings.

The final design of the system, which is proprietary at present, was able to overcome each of these difficulties.

A valuable test of the load measurement apparatus and of the elastic stress calculations [*9*] as well was made early in the experiment in order to establish the veracity of the measurements. The test consisted of comparing the measured specimen compliance with theoretical predictions. The specimen compliance should be determined essentially by the slope of the force-displacement curve after lift-off. A series of slopes obtained from different specimens and load levels is plotted in Fig. 3*c*. The curves generally agree in slope to 5 percent, indicating both good specimen uniformity and reliable machine performance. In order to calculate the actual specimen compliance, however, the added displacement due to deformations in the load train or any warping of the cladding at the point of con-

tact must be subtracted out. The dashed line in Fig. 3*c* was obtained from a specimen which was identical to the others except that overall slit widening was prevented by slitting the cladding only in the center. The net compliance of the tube after subtracting out this contribution was observed to be 1.27×10^{-3} in./lb, while theoretical calculations give 1.38×10^{-3} in./lb for a room-temperature Young's modulus of 28×10^{6} psi. This agreement is considered satisfactory.

Experimental Data

Thermal Relaxation

A series of experiments was performed to document any relaxation due to thermal effects alone in a furnace environment. Relaxation of unirradiated specimens was monitored at temperatures in the range 700 to 1000°F (371 to 538°C). Figure 4 shows the effect of a 500 h (the length of each irradiation period for this experiment) furnace exposure on the clamping force, F, for selected temperatures. The reduction in clamping force after relaxation is plotted on the ordinate, and the initial clamping force is the abscissa. All clamping forces are as measured at room temperature, and the stress scale superimposed on the abscissa is the room-temperature maximum fiber stress. The stresses at higher temperatures are less by a factor of $E(T)/E(72°\text{F})$ (22°C), where E is Young's modulus. For several reasons, this is a convenient form for plotting and examining the data:

1. Any deviations from a linear stress dependence can easily be discerned.
2. Greater accuracy can be obtained by fitting all stress levels to a single curve.
3. The slope, S, of the curve is related to the residual clamping force ratio by $F/F_0 = S$ when the stress dependence is linear.
4. Relaxation of any systematic "built-in" stresses left over from the cold-working process should not affect the derived slope, as they should contribute a force change which is independent of the applied stress.

Built-in stresses due to cold work were present in the unirradiated tubes, as evidenced by the fact that slit opening of the tubes typically increased by 0.005 in. after cutting. No spreading was observed in the previously irradiated tubes, indicating that these residual stresses were relaxed during the previous irradiation. The possibility exists that for the unirradiated tubes these built-in stresses will contribute a small amount to the observed force changes. This is a complex subject, and work has been recently initiated at the Hanford Engineering Development Laboratory (HEDL) to quantify the effects of residual stresses in fuel cladding [*13*]. The work so far has revealed that analyzing the data in the way suggested in Item 4 of the foregoing will substantially remove the effects of systematic built-in

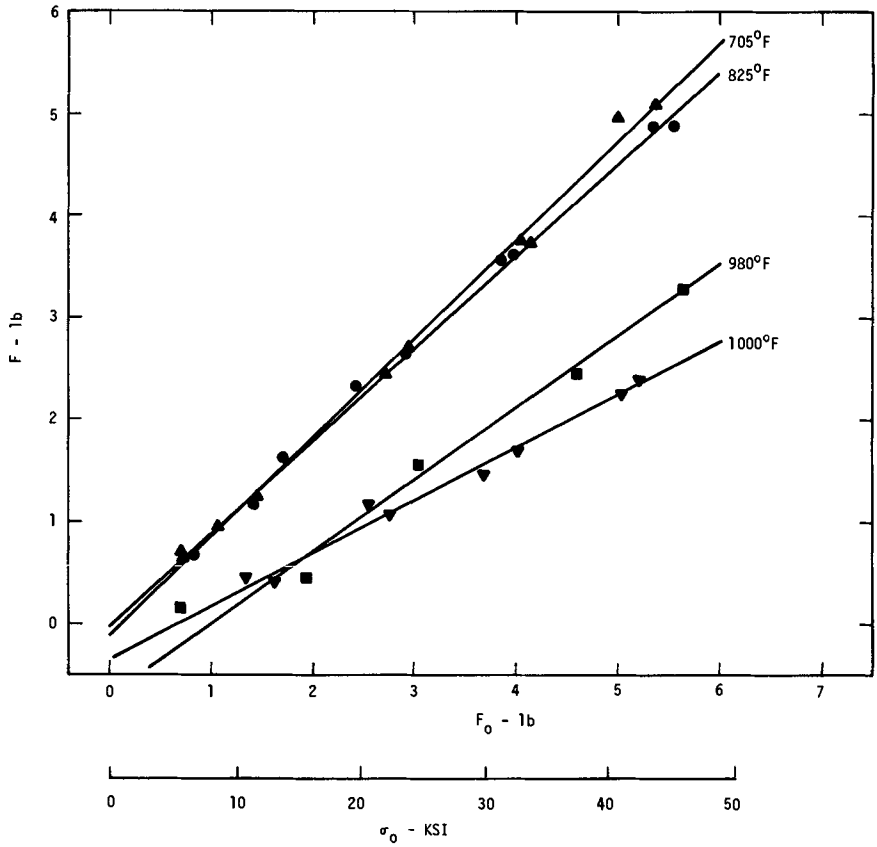

FIG. 4—*Plot of residual clamping force versus initial clamping force. Data are for 500 h thermal control tests of unirradiated 20 percent cold-worked Type 316 stainless steel.*

stresses. The intercept value of the curves in Fig. 4 is a measure of the magnitude of relaxation due to built-in stresses. At 1000°F (538°C), where the intercept is sensibly largest as the relaxation is the largest, the built-in stresses have given a relaxation $\Delta F = 0.3$ lb or an equivalent bending fiber stress change of 1200 psi.

The data in Fig. 4 show no significant nonlinear behavior. A least-squares fit to the thermal data using a power-law creep form ($\dot{\varepsilon} \alpha \sigma^n$) produced a stress exponent of $n \cong 0.85 \pm 0.15$ at 825 and 1000°F (441 and 538°C). Hence, as there is no statistically significant evidence to establish that the stress exponent is different from unity, the data were analyzed with formulas obtained from the viscoelastic approach.

The magnitudes of the thermal relaxations are given in Table 2 for both 500 and 1000-h time periods. The 1000-h values were obtained by extrap-

TABLE 2—*Summary of thermal relaxation data.*

Temperature, °F	Prior Fluence, 10^{22} n/cm², $E > 0.1$ MeV	$F(500)/F(0)$	$F(1000)/F(0)$	$F(1000)/F(500)$
705	0	0.97	0.96	0.99
825	0	0.90	0.87	0.97
900	0	0.89	0.86	0.97
980	0	0.70	0.63	0.90
1000	0	0.52	0.40	0.76
800	3.6	0.90	0.87	0.87
1000	3.4	0.70	0.62	0.89

olation of data obtained at shorter times of 500 to 800 h. The time dependence used for extrapolation was

$$\frac{F(t)}{F_0} = \frac{\sigma(t)}{\sigma_0} = 1 - bt^{1/3} \tag{10}$$

where

t = time in hours and
b = a fit constant.

Figure 5 shows that this time dependence represents the 1000°F (538°C) data quite well. At 825°F (441°C) this extrapolation is probably an overestimate at 1000 h, but the change between 500 and 1000 h is only 3 percent at this temperature.

The data obtained on thermal controls are in good agreement with results from uniaxial creep tests by Billeter and Blackburn [*14*] on the same heat of steel and cold-work level. Their results were obtained with a high-precision microwave extensometer so that it was possible to establish the detailed time dependence of these slight creep effects. Their tests showed that the effects were anelastic in nature with a linear stress dependence. Further, the time dependence of the creep they found at both 850 and 1000°F (454 and 538°C) is consistent with the $t^{1/3}$ law which was used to extrapolate the thermal control data. The exact time dependence obtained by Billeter and Blackburn is of a different form, but the $t^{1/3}$ form was found to be a satisfactory and convenient representation. We may make a quantitative comparison between the two experiments by combining Eqs 3, 7, and 9 in an appropriate form for comparison

$$\frac{F}{F_0} = e^{-\frac{E\int_0^t \dot{\epsilon}_{ss}\,dt}{1.20\sigma}} \tag{11}$$

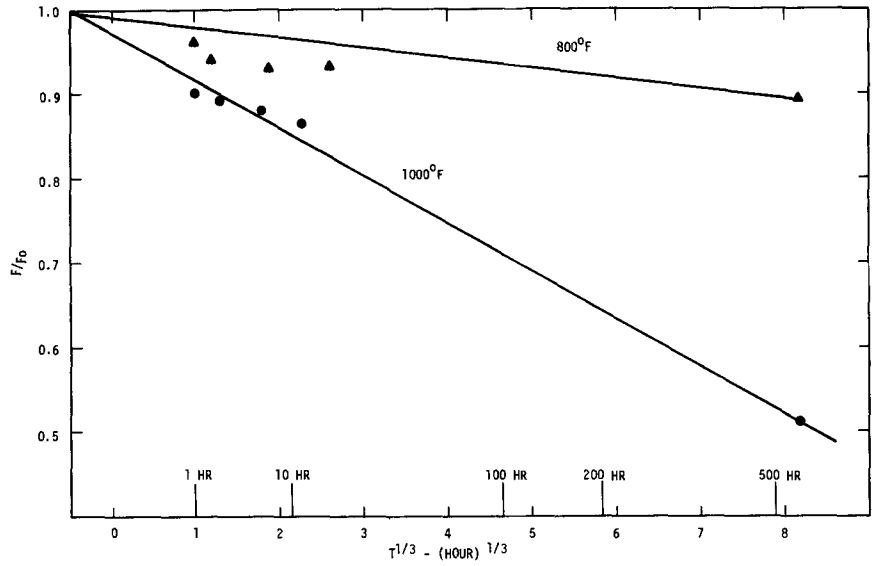

FIG. 5—*Time dependence of thermal relaxation. The 1000°F (538°C) fits the* $t^{1/3}$ *form well but the 800°F (427°C) relaxes faster.*

where $\dot{\epsilon}_u$ is the observed uniaxial strain rate. Blackburn et al obtained a strain of 1.1×10^{-4} at 20 000 psi, which leads to a prediction $F/F_0 = 0.89$. The stress relaxation at 825°F (441°C) is 0.89 so that excellent agreement is obtained, as the stress relaxation has apparently no significant temperature dependence in this stress and temperature range of 825 to 900°F (441 to 482°C). At 1000°F (538°C), Blackburn et al obtained a strain of 4.2×10^{-4} over 500 h at 20 000 psi, which leads to a predicted F/F_0 of 0.67 compared with 0.51 for the slit tube. However, the uniaxial test at 1000°F (538°C) was preceded by that at 850°F (454°C) so that part of the creep effect may have been exhausted. If the creep strain is increased by 1×10^{-4} to allow for this, the relaxation predicted is $F/F_0 = 0.60$, which is considered satisfactory agreement.

A limited number of previously irradiated specimens were available, and thermal control tests made on these are also given in Table 2. The data show that the magnitude of thermal relaxation in previously irradiated slit tubes is of the same order as that in the unirradiated material. At 825°F (441°C) they are the same to within experimental error, while at 1000°F (538°C) the previously irradiated undergo a smaller amount of relaxation. On the other hand, this difference should not be overemphasized as the relaxation at 980°F (527°C) in unirradiated tubes is nearly the same as that for those previously irradiated at 1000°F (538°C).

The fact that the thermal creep occurred in both the previously irradi-

ated as well as the unirradiated specimens is highly significant for this experiment. It shows that irradiation exposure to 3.6×10^{22} n/cm^2 ($E >$ 0.1 MeV) does not eliminate creep at the temperatures of interest. Hence, it must be anticipated that the process we have identified as thermal creep will occur during the irradiation. The process may be inhibited somewhat at 1000°F (538°C) over unirradiated tubes but is expected to occur in full amount at 800°F (427°C). Consequently, it will be necessary to account for the thermal contribution so that irradiation-induced effects may be isolated.

In-Reactor Relaxation

The observed clamping force measurements and residual stress ratios for the irradiation experiment are given in Table 3 along with the fluence and temperature data for the test. The fluence for this location in the Experimental Breeder Reactor-II (EBR-II) increments was established by the Damage Analysis Section at HEDL by analysis of dosimetry consisting of four spectral sets of foils and three iron wires. These were simultaneously irradiated with the specimens during the experiment. Temperatures were established by the use of thermal expansion monitors [*15*] which recorded the peak temperature obtained during the experiment. The accuracy for the devices in the present experiment is ±5°F.

The data in Table 3 are mostly self-explanatory. In order to put data from all the specimens on a comparative basis, the clamping forces after irradiation have been adjusted to correspond to the peak fluence within each capsule. The correction factors are fortunately very close to unity, typically 0.97 to 1.0. The procedure used is described by Wire and Straalsund [*4*]. Note that adjustments are made only to the irradiation-induced component.

The fluence-adjusted clamping force data for the in-reactor experiment are plotted in Fig. 6 for the 800°F (427°C) data and in Fig. 7 for the 1000°F (538°C) data. The data at a prior fluence of 0.5×10^{22} n/cm^2 have been omitted for clarity as they lie close to the data from zero prior fluence. The plots reveal no evidence of strong stress dependence, although there is a trend for the high-fluence data at 1000°F (538°C). Computer fits to the data were made to find the best-fit stress exponent for all the data. The stress exponents derived are plotted in Fig. 8. The average value of n for all in-reactor relaxation was 1.0. On this basis, it can be said that since all the data produced a stress exponent of unity within the 2σ limit, there is no basis for assuming a nonlinear stress dependence. On the other hand, there is a trend, which is likely to be real, for n to increase with temperature. As the largest value of n derived is still close to unity, it was not necessary to utilize nonlinear analysis at this point.

The clamping force ratios derived from least-squares fit to the in-reactor

TABLE 3—*Summary of in-reactor data.*

Specimen No.	Prior Fluence, 10^{22} n/cm^2, $E > 0.1$ MeV	First Irradiation			Second Irradiation			
		Peak Fluence			Fluence			
		Temperature, °F	Increment, 10^{21} n/cm^2	F_1/F_0	Temperature, °F	Increment, 10 n/cm	F_2/F_0	F_2/F_1
1 to 10	3.6	790	1.74	0.62	790	1.74	0.52	0.84
11 to 20	0.5	790	1.74	0.79	790	1.74	0.63	0.80
21 to 30	0	790	1.74	0.80	790	1.74	0.70	0.88
31 to 40	3.4	980	2.0	0.29	1000	2.0	0.20	0.69
41 to 50	0.5	980	2.0	0.52	1000	2.0	0.39	0.75
51 to 60	0	980	2.0	0.68	1000	2.0	0.38	0.56

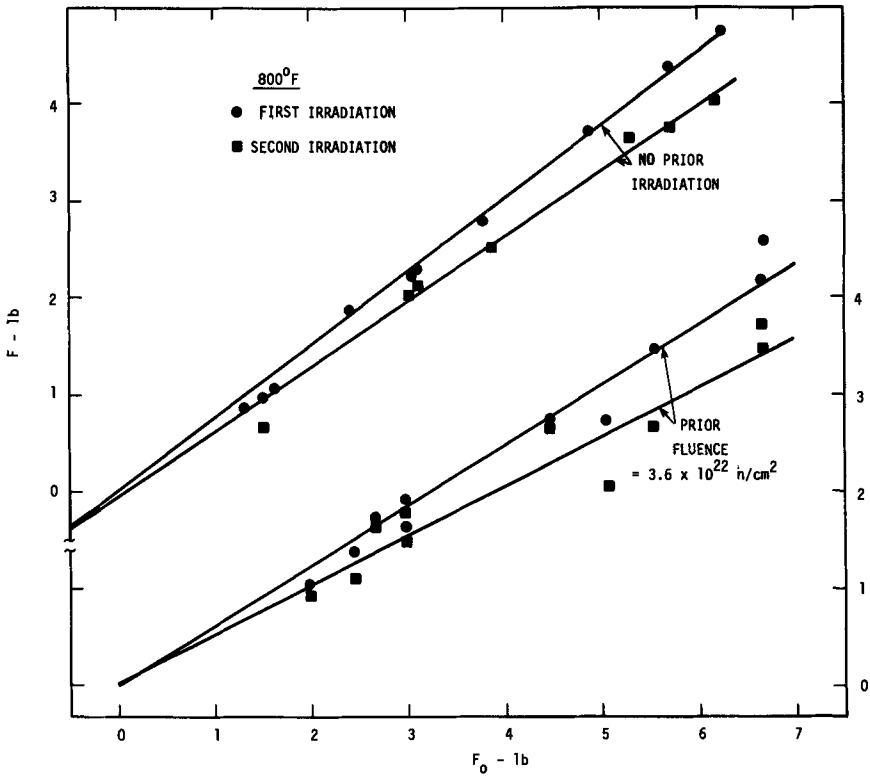

FIG. 6—*Plot of residual clamping forces after irradiation at 800°F (427°C). No significant stress dependence can be seen.*

relaxation data are summarized in Table 3. In the case of the high-fluence specimens at 800 and 1000°F (427 and 538°C), the straight-line fit was constrained to go through the origin as any "built in" stresses due to cold working would be relaxed out. The quantity F_2/F_1, which is formed by dividing the ratio F_2/F_0 by F_1/F_0, represents the percent relaxation taking place in the second irradiation. It is seen that in every case the relaxation was greater in-reactor than outside, indicating that the irradiation induced a higher creep rate. Further, the percent relaxation is greater in the first period than in the second, as would be expected because the corresponding thermal relaxation is far greater in the first time period than in the second.

Derivation of Creep Coefficients

Model Used

The model used to describe the combined effects of irradiation-induced stress relaxation and thermal relaxation is simply

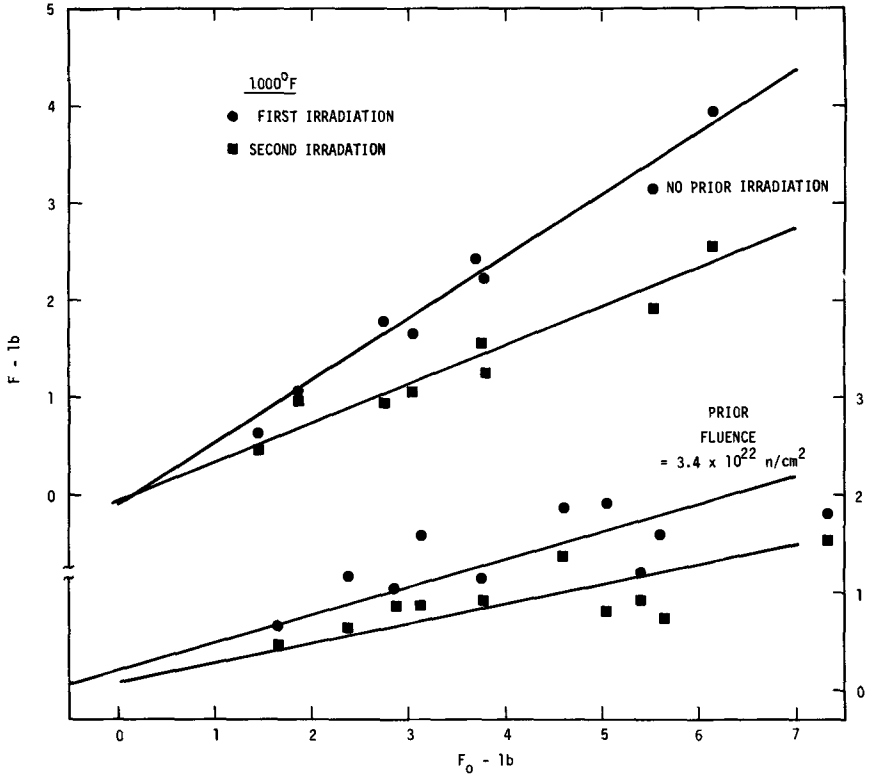

FIG. 7—*Plot of residual clamping forces after irradiation at 1000°F (538°C). The data show some stress dependence for the previously irradiated tubes.*

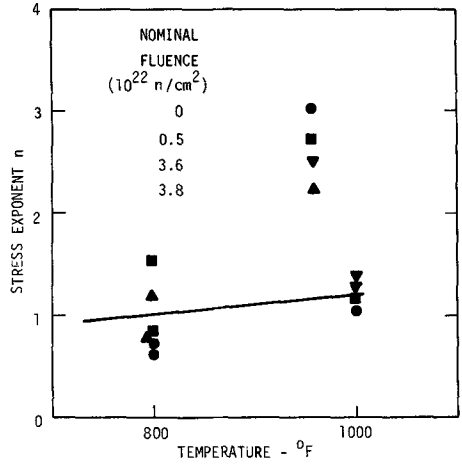

FIG. 8—*Stress exponent derived by fitting to* $\dot{\varepsilon} = A\sigma^n$. *At 800°F (427°C) the average value of* n *is 1.0 while at 1000°F (538°C)* $n \cong 1.2$.

$$\dot{\varepsilon}_T = B\sigma\phi + G(t)\sigma \quad \text{(uniaxial stress state)} \tag{12}$$

where

$G(t)$ = time dependent thermal creep coefficient appropriate at each condition,
B = irradiation creep coefficient, and
$\dot{\varepsilon}_T$ = total in-reactor strain rate.

It is implied here that $G(t)$ can be derived from thermal control experiments, on specimens at the appropriate prior fluence. This notion of thermal- and irradiation-induced effects being additive is of course not new, but it is instructive to examine what such a form requires:

1. Thermal and irradiation deformation are parallel processes, and they are independent contributions.
2. Thermal creep is not affected by irradiation exposure. Note that the thermal creep utilized is that measured outside the reactor at the nominal fluence level of interest.

It is not claimed here that these assumptions are *generally* true; however, over the parameter range in this study it is shown that this simple model does indeed give consistent results with the data.

Equation 12 can be easily integrated to yield for the uniaxial stress state

$$\begin{aligned} \frac{\sigma}{\sigma_0}\Big|_{\text{total}} &= e^{-EB\phi t - E\int_0^t G(t')dt'} \\ &= \left(\frac{\sigma}{\sigma_0}\Big|_{\text{irradiation}}\right)\left(\frac{\sigma}{\sigma_0}\Big|_{\text{thermal}}\right) \end{aligned} \tag{13}$$

where

$$\frac{\sigma}{\sigma_0}\Big|_T = \text{total relaxation,}$$

$$\frac{\sigma}{\sigma_0}\Big|_I = e^{-EB\phi t} = \text{irradiation-induced relaxation, and}$$

$$\frac{\sigma}{\sigma_0}\Big|_{\text{thermal}} = e^{-E\int_0^t G(t)dt} = \text{thermal relaxation component.}$$

The relaxation for the irradiation component is then

$$\frac{F}{F_0}\Big|_I = \frac{\sigma}{\sigma_0}\Big|_I = \frac{(\sigma/\sigma_0)_{\text{total}}}{(\sigma/\sigma_0)_{\text{thermal}}} \tag{14}$$

Equation 14 holds for the plane-strain case as well, because over this

range the relaxation function can be fit by a simple exponential as mentioned earlier.

There are conditions under which Eq 14 holds without the two restrictions; for example, if the time for thermal creep to be completed is very small compared with that for significant irradiation creep to occur. The processes are effectively parallel as they are separated in time. This would seem to be the case at 800°F (427°C), based on the time dependence shown in Fig. 5 for the thermal relaxation observed in slit tubes.

Creep Coefficients at 800°F (427°C)

This temperature is treated first, as thermal relaxation effects are smaller and more easily isolated than at 1000°F (538°C). Using Eq 14 and the thermal relaxation in Table 2, one can form $F/F_0|_I$, the irradiation-induced relaxation for each portion of the irradiation. The results are shown in Table 4, and it is seen that the irradiation-induced components for each period are in reasonable agreement with the expected average irradiation-induced relaxation $\sqrt{(F_2/F_0)_I}$. In short, the experimental results are consistent with the interpretation developed in the foregoing. The creep coefficients derived from the quantity $F_2/F_0|_{\text{irradiation}}$ via Eq 9 are listed in the same table.

At last we are ready to compare derived creep coefficients with those for constant-stress loading. This is done in Fig. 9, which shows the current best values for the creep coefficients from pressurized tubes. The agreement at low fluences (where stress history should not be a factor) to $\Delta B = (1 \times 10^{-30})/(\text{n/cm}^2 \cdot \text{psi})$ is a verification of the stress relaxation technique to obtain creep coefficients. The agreement at the high-fluence values of the creep coefficients to $\Delta B = (1.6 \times 10^{-30})/(\text{n/cm}^2 \cdot \text{psi})$ is striking—it indicates that the *stress applied over the whole irradiation of the pressurized tubes has had no significant effect on the irradiation creep rate.*

Another key point is that the fluence dependence of the creep coefficient B at this temperature provides the first direct proof that the creep coefficient is increasing with fluence at this temperature, as the dashed line in the figure is extrapolated from an overall fit to higher temperature data.

Creep Coefficients at 1000°F (538°C)

The steps cited in the foregoing have been repeated for 1000°F/(538°C), and the results are also plotted in Fig. 9. Again, quantitative agreement at the high-fluence level indicates that prolonged stressing to a fluence of 3.4×10^{22} n/cm^2 has not changed the creep coefficients from those de-

TABLE 4—*Irradiation-induced relaxation data.*

Prior Fluence, 10^{22} n/cm^2, $E > 0.1$ MeV	Nominal Temperature, °F	$\left(\frac{F_1}{F_0}\right)_t$	$\left(\frac{F_2}{F_1}\right)_t$	$\sqrt{\left(\frac{F_2}{F_0}\right)_t}$	$\left(\frac{F_2}{F_0}\right)_t$	B
3.6	800	0.69	0.86	0.77	0.60	7.4
0.5	800	0.88	0.82	0.85	0.72	4.7
0	800	0.89	0.90	0.89	0.80	3.2
3.4	1000	0.41	0.77	0.56	0.32	15.2
0.5	1000	0.74	0.84	0.79	0.63	6.2
0	1000	0.97	0.73	0.87	0.72	4.7

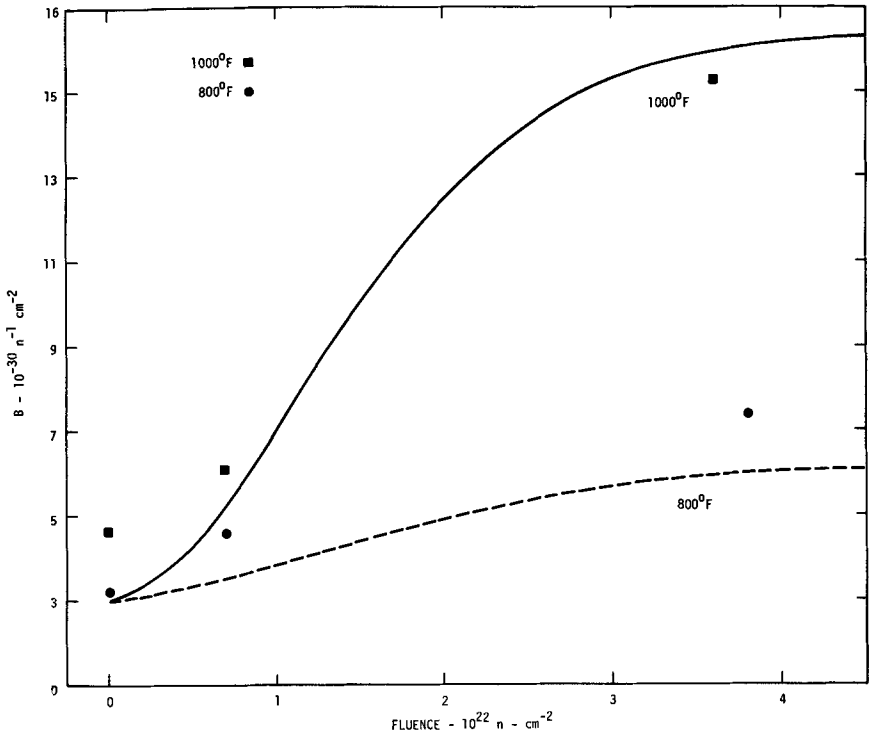

FIG. 9—*Effect of stress history on irradiation-induced creep coefficients. The creep coefficients derived from this experiment are compared with those from constant-stress pressurized tube data [solid line at 1000°F (538°C) and dashed line at 800°F (427°C)]. At 800°F (427°C), the pressurized tube curve is derived from extrapolation, higher temperature data.*

rived by a short-term load increase. Also, the fluence dependence of pressurized tube data is matched quite well by the slit tube data.

It is interesting to note that the results are not self-consistent between the two irradiation periods. This is not considered serious as there are several factors that are potentially responsible for this lower quality of self-consistency at 1000°F (538°C). First, the thermal effects are simply much larger here, so that the irradiation-induced effects are inherently more difficult to isolate. Secondly, the effects of data scatter are more serious at lower clamping forces. Finally, creep is inherently temperature dependent at these temperatures so that a temperature error of 20°F can give size to a 10 percent change in both the irradiation-induced creep rate and in the thermal creep rate as well.

Discussion of Results

The primary conclusion from this experiment is that stress history during irradiation does not change the steady-state irradiation-induced creep

rate. Rather, the creep rates are apparently influenced mainly by the irradiation temperatures and fluence. This would imply that the microstructural features associated with the applied stress, such as preferential dislocation motion producing the creep or preferential loop nucleation, are less important than other changes induced by the effects of fluence and temperature alone in the fluence range investigated in this experiment. At high fluences (1.0 to 2.0 $\times$ 10^{23} n/cm^2, $E > 0.1$ MeV) where swelling rates may become large in this material, stress-assisted swelling and swelling-enhanced creep effects may come into play [*4,16*] to change the situation.

Another significant result of this experiment is that it has shed new light on "transient" creep, that is, creep effects which occur at initiation of irradiation before the creep rate has settled down to a quasi-steady state rate. Previously, this has been described [*5,10*] by a term like

$$\varepsilon_{\text{transient}} = A(1 - e^{-\phi t/t_p})\sigma \tag{15}$$

where

A = constant representing the magnitude of the effect,
t_p = constant describing the relaxation time for the process, and
ϕ = flux

This form implies that such behavior is an irradiation-induced effect above the steady-state value. This effect was deduced, on the basis of an instrumented uniaxial experiment [*10*], to have a magnitude $A = 2.6 \times 10^{-8}$ psi at 850°F (454°C). It has been established experimentally, however, that transient effects in pressurized tubes are much smaller than predicted [*1*] from the uniaxial experiment, and hence they are difficult to quantify. This experiment is ideal for detection of these effects and has provided an entirely new concept on transient effects. During the first irradiation period of the experiment, previously unirradiated slit tubes at 800°F (427°C) showed no significant relaxation beyond the thermal relaxation and the low-fluence creep coefficient. The second irradiation period showed only the relaxation associated with the steady-state creep coefficient. At 1000°F (538°C), the net result of both irradiations also was consistent with thermal and steady-state creep. The actual $\bar{B}$ derived was 1.3×10^{-30} n/cm^2·psi larger than indicated from pressurized tubes, and, if it is assumed this is due to transient effects, the calculated value of A in Eq 15 is only 5.2×10^{-9} psi. Hence there appears to be only a small irradiation-induced transient. Instead, as furnace tests showed that thermal relaxation was observed to occur in previously irradiated tubes at approximately the same levels as in unirradiated, it is logical to conclude that thermal relaxation occurring in-reactor is the major source of "transient" behavior. The large effect observed in the previous uniaxial experiment now must be regarded as potentially misleading in view of the fact that a

large number of pressurized tubes and slit tubes do not confirm an effect of this magnitude.

The foregoing conclusions can be formulated more concretely by extending Eq 12, which described the total creep behavior. According to this experiment, the total in-reactor creep for 20 percent cold-worked Type 316 stainless steel can be described by the form

$$\dot{\varepsilon}_T = B(t,\phi)\sigma\phi + G(T,t)\sigma \qquad 800\,°\text{F}\ (427\,°\text{C}) \leqslant T < 1000\,°\text{F}\ (538\,°\text{C}) \quad (16)$$

for the uniaxial stress state. The irradiation-induced creep coefficient $B(T,\phi)$ is a function only of fluence and temperature, and not a function of past stress history. The quantity $G(T,t)$ represents the thermal creep which is mainly dependent on temperature and time and weakly dependent on fluence. Expressions for $G(T,t)$ can be derived from this experiment and that of Blackburn et al [*14*]. The application of the thermal creep portion of Eq 15 requires a knowledge of the past loading history, as the thermal component depends on the time after a stress change and will eventually saturate. This restriction can be removed by developing an expression for the thermal creep in terms of stress and strain rate. This shall be reserved for future work.

The question may be raised as to whether thermal creep effects of the relatively small magnitude observed at these low temperatures are important if they saturate and hence if they are of limited duration. Additional thermal control work done at HEDL in preparation for a continuation of this test provides a new insight. The irradiated specimens from this experiment, which had relaxed to $F_2/F_0 \leqslant 0.4$ at 1000 °F (538 °C) and $F/F_0 \leqslant 0.7$ at 800 °F (427 °C), were reloaded to levels greater or equal to the load before irradiation exposure. Relaxation was monitored in a 60-h furnace test to remove any early time portion of the thermal creep for convenience in a future irradiation experiment. It was found that the specimens exhibited relaxations as large as the relaxation observed during this time interval on the first loading. Therefore, it appears that thermal creep is not limited to a single occurrence, but can recur whenever the load level is changed. To illustrate, consider the hypothetical sequence in Fig. 10. A small misfit strain due to thermal expansion or fuel loading, etc., is imposed during reactor startup. During irradiation, both thermal creep and irradiation act to relax the stresses. After a long time the thermal relaxation becomes small compared with the irradiation-induced relaxation rate. Suppose, after significant total relaxation has occurred, that a second misfit strain is applied to raise the stress to the original level. Now thermal relaxation will recur to cause a greater relaxation rate than irradiation creep alone. The example, based on data from this experiment at 1000 °F, (538 °C), shows that thermal effects contribute nearly a third of the total relaxation of the second misfit strain. This recurrence of the

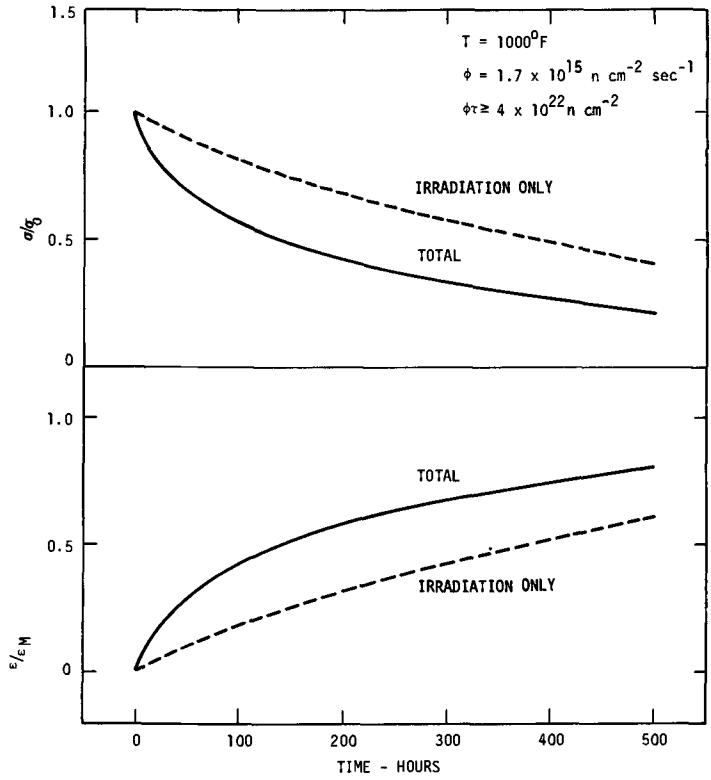

FIG. 10—*Enhancement of strain due to recurrent thermal component. The solid curves show the enhancement of relaxation rate and total plastic strain accumulated when a misfit strain* ε_m *is suddenly applied. If a misfit strain is reapplied after 500 h, the whole process will repeat.*

thermal relaxation makes it then a potentially significant contributor for a cyclic loading mechanism.

Conclusion

The experiment has shown that the irradiation-induced creep rates in 20 percent cold-worked Type 316 stainless steel are not dependent on stress history at 800 and 1000°F (427 and 538°C) to a fluence of 4×10^{22} n/cm² ($E > 0.1$ MeV). This result may be rationalized if the microstructural development during irradiation is influenced predominantly by the irradiation flux and temperature variables, and only to a minor extent by irradiation creep deformation.

Evidence was cited to show that what has been termed transient irradiation creep can be quantitatively accounted for as thermal creep. Further,

this thermal creep component was observed to be recurrent, giving rise to an additional creep mechanism for loading which changes periodically. As a result of the foregoing experimental results, an analytic description was formulated. This formulation is in only empirical form at present, but it provides a way of summarizing the sense of these experimental findings.

References

[1] Gilbert, E. R., "Dependence of Irradiation Creep on Temperature and Atom Displacements in 20% Cold Worked Type 316 Stainless Steel," International Colloquium on *Measurement of Irradiation Enhanced Creep in Nuclear Materials,* The Netherlands, 6 May 1976.

[2] Flinn, J. E., McVay, G. L., and Walters, L. C., "In Reactor Deformation of Solution Annealed Type 304L Stainless Steel," International Colloquium on Measurement of Irradiation Enhanced Creep in Nuclear Materials, Petten, The Netherlands, 6 May 1976.

[3] Gilbert, E. R. and Bates, J. F., "Creep of Cold Worked 316 Stainless Steel Pressurized Tubes," submitted to *Transactions,* American Nuclear Society, Nov. 1975.

[4] Wire, G. L. and Straalsund, J. L., "Irradiation Induced Stress Relaxation of Previously Irradiated 304 Stainless Steel in a Fast Flux Environment," submitted to *Journal of Nuclear Materials.*

[5] Mosedale, D., Lewthwaite, G. W., and Ramsay, I., *Proceedings,* British Nuclear Energy Society Conference on Irradiation Embrittlement and Creep in Fuel Cladding and Core Components, 1972, p. 239.

[6] Manoine, M. J., "Relaxation and Residual Stresses in Bent Shafts," *Bettis Technical Review, Reactor and Plant Engineering,* WAPD-BT-14, 1959.

[7] Kreyns, P. H., and Burkhart, M. W., "Radiation Enhanced Relaxation in Zircaloy-4 and Zr/2.5 Wt. % Nb/0.5 Wt. % Cu Alloys," *Journal of Nuclear Materials,* Vol. 26, 1968.

[8] Wolfe, R. A., *Transactions,* American Nuclear Society, Vol. 12, 1969, p. 589.

[9] Wire, G. L. and Straalsund, J. L., HEDL Quarterly Technical Progress Report, Oct.-Nov.-Dec. 1973, Vol. 1, *Materials Technology,* HEDL TME 73-6, Hanford Engineering Development Laboratory, Hanford, Wash., 1973.

[10] Gilbert, E. R., Kaulitz, D. C., Holmes, J. J., and Claudson, T. T., *Proceedings,* BNES Conference on Irradiation Embrittlement and Creep in Fuel Cladding and Core Components, 1972, p. 239.

[11] Wire, G. L. and Straalsund, J. L., "A Simple Method for Calculation of Steady-State Creep Rates in Non-Conservative Plastic Deformation," to be published in *Nuclear Technology.*

[12] Wire, G. L. and Straalsund, J. L., HEDL Quarterly Technical Progress Report, Jan.-Feb.-March 1974, Vol. I, *Materials Technology,* HEDL TME 74-1, Hanford Engineering Development Laboratory, Hanford, Wash., 1974.

[13] Nygren, R. E. and Straalsund, J. L., "The Effect of Residual Stresses on the Stress Relaxation Behavior of Slit Tubes," HEDL-TME 76-13, Hanford Engineering Development Laboratory, Hanford, Wash., 1976.

[14] Billeter, T. R. and Blackburn, L. D., "Design and Performance of a Microwave Strain Measuring System for Material Test," HEDL-TME 75-53, Hanford Engineering Development Laboratory, Hanford, Wash., Dec. 1975.

[15] Franklin, D. C. and Reuther, W. S., *Transactions,* American Nuclear Society, Vol. 14, No. 2, 1971, pp. 632–633.

[16] Wolfer, W. G., Ashkin, M., and Boltax, A. in *Properties of Reactor Structural Alloys After Neutron or Particle Irradiation, ASTM STP 570,* American Society for Testing and Materials, 1975, pp. 233–258.

[17] Hesketh, R. V., *Philosophical Magazine,* Vol. 8, 1963, p. 1321.

J. P. Foster[1]

Analysis of In-Reactor Stress Relaxation Using Irradiation Creep Models

REFERENCE: Foster, J. P., "**Analysis of In-Reactor Stress Relaxation Using Irradiation Creep Models,**" *Irradiation Effects on the Microstructure and Properties of Metals, ASTM STP 611,* American Society for Testing and Materials, 1976, pp. 32–50.

ABSTRACT: Irradiation creep and stress relaxation data are available from the United Kingdom for 20 percent cold-worked Type M316, 20 percent cold-worked Type FV548, and FHT Type PE-16 using pure torsion in the absence of swelling at 300°C (572°F). Irradiation creep models were used to calculate the relaxation and permanent deflection of the stress relaxation tests. Two relationships between irradiation creep and stress relaxation were assessed by comparing the measured and calculated stress relaxation and permanent deflection. The results show that for Types M316 and FV548 the stress relaxation and deflection may be calculated using irradiation creep models when the stress rate term arising from the irradiation creep model is set equal to zero. In the case of Type PE-16, the inability to calculate the stress relaxation and permanent deflection from the irradiation creep data was attributed to differences in creep behavior arising from lot-to-lot variations in alloying elements and impurity content.

A modification of Types FV548 and PE-16 irradiation creep coefficients was necessary in order to calculate the stress relaxation and deflection. The modifications in Types FV548 and PE-16 irradiation creep properties reduces the large variation in the transient or incubation parameter predicted by irradiation creep tests for Types M316, FV548, and PE-16.

KEY WORDS: radiation, mechanical properties, creep properties, creep rate, stress relaxation, plastic properties, shear properties, irradiation, neutron irradiation

Reactor core structures are subject to stresses varying with time, whereas irradiation creep tests are generally performed under constant load. In applying these constant-load test data to structures in which stress varies with time, certain assumptions must be made. The use of irradiation creep models to calculate stress relaxation assumes the existence of a mechanical equation of state between creep rate, stress, temperature, neutron flux,

[1] Westinghouse Advanced Reactors Division, Madison, Pa. 15663.

and the current creep strain. For example, an assumption must be made about the existence of a stress rate term, $\dot{\tau}^{Ic}$ (where τ is the shear stress, the superscript dot denotes a time derivative, and the superscript Ic signifies that the stress rate term originates with the irradiation creep model), arising from the irradiation creep model. Presently, the mechanical equation of state for irradiation is simply postulated, and may not be valid. The purpose of this paper is to evaluate the available irradiation creep and stress relaxation data to show that stress relaxation may be calculated from irradiation creep tests.

The United Kingdom irradiation data were selected to assess the mechanical equation of state because these data are the only available in-reactor stress relaxation [*1*][2] and creep tests [*2–4*] involving the same stress state. Furthermore, the irradiation creep tests cover completely the dose and dose rates of the stress relaxation measurements. Note that the available irradiation creep data on 20 percent cold-worked Type 316 indicate that the transient irradiation creep component is a function of the stress state. A larger transient coefficient was measured using a uniaxial stress system [*5*] than in the case of pure torsion. Since both the irradiation creep and stress relaxation tests analyzed in this paper involve pure torsion, transient irradiation creep is not subject to any uncertainty associated with stress state.

Stress Relaxation Data

The available stress relaxation measurements [*1*] were made on springs irradiated in the Dounreay Fast Reactor (DFR). Helical springs with identical geometry were cut from lengths of PFR reference size tubing manufactured for fuel pins. The cladding had an outside diameter of 5.8 mm (0.230 in.) and a thickness of 0.38 mm (15 mils). Two springs were connected in series by welding, and compressed on a mandrel. The spring-pair combinations were irradiated at 300°C (572°F) to a maximum dose of 2.80 displacements per atom (dpa). DFR irradiation creep data [*2–4*] are available in the temperature interval from 247 to 330°C (477 to 626°F) for the material spring-pair combinations irradiated (cold-worked Type M316, cold-worked Type FV548, and FHT PE-16).

Types M316 and FV548 tubing was 20 percent cold-worked, and the PE-16 tubing was fully hardened and aged. The stress relaxation specimens were only irradiated over a narrow dose interval, and Standring reports [*1*] that the measured stress relaxation is not a function of the initial stress, dose, or material pair combination. No thermal relaxation was measured with Type M316 at 280°C (536°F) out-of-reactor; therefore, the stress relaxation is due to irradiation creep. The permanent de-

[2]The italic numbers in brackets refer to the list of references appended to this paper.

flection measurements of the unloaded springs showed large differences depending on the material and applied stress. For the same initial stress, approximately the same permanent deflection was measured in the cases of Types M316 and FV548 springs. This indicates that Types M316 and FV548 have about the same irradiation creep properties. For the case of Type PE-16 springs in combination with either Type M316 or Type FV548, the PE-16 permanent deflections were smaller on the average by a factor of 2. This indicates that the irradiation creep of Types M316 and FV548 is greater than that of Type PE-16.

Standring [*1*] calculated stress relaxation by setting the irradiation creep stress rate term ($\dot{\tau}^{Ic}$) equal to zero and using the irradiation creep equation

$$\gamma/\tau = A[1 - \exp(-\phi t/B)] + C\phi t \tag{1}$$

where γ is the shear strain, τ the shear stress, ϕt the displacement damage calculated using the Half-Nelson model, and A, B, and C are material coefficients. No assessment was made of the stress rate component, $\dot{\tau}^{Ic}$. Further, recent irradiation creep measurements in DFR show that Eq 1 does not describe PE-16 [*2*]. The PE-16 data indicate either an incubation plus linear or a quadratic dose dependence. This paper extends the stress relaxation calculations just described by updating PE-16 irradiation creep, comparing the effect of including the stress rate term from the irradiation creep component on stress relaxation, and calculating the deflection in the springs due to irradiation creep.

Irradiation Creep

Irradiation creep measurements of DFR wire-wound helical springs are available on the same type, but different lots, of material that was tested in stress relaxation. References *3* and *4* show that the irradiation creep strain of Types M316 and FV548 is composed of transient and steady-state components. The irradiation creep strain γ follows a McVetty-type [*6*] representation given in Eq 1. The magnitude of the transient and steady-state components is given by the A and C constants, respectively.

The spring irradiation creep data that lie within the dose rate interval of the stress relaxation specimens were fit to Eq 1. The irradiation creep coefficients were calculated for springs that were measured and reirradiated in the same reactor position. Mosedale et al [*7*] report that the stress-reduced strains (ratio of the measured strain to the applied stress, γ/τ) are dose rate dependent. The low-flux specimens tend to exhibit less strain per dpa than the higher-flux specimens. Dose rate effects, however, are observed only for a factor of 20 variation in the dose rate. Therefore, dose rate effects would not be expected in the stress relaxation data because the dose rate variation is less than a factor of 2.

Table 1 lists the mean, minimum, and maximum values for the A and C coefficients of Eq 1 for 20 percent cold-worked Types M316 and FV548.

TABLE 1—*Irradiation creep coefficients.*

Material	McVetty Relationship $A \times 10^{10}$, $(N/m^2)^{-1}$	B^a, dpa	$C \times 10^{10}$, $(N/m^2 - dpa)^{-1}$
Cold-worked Type M316			
mean	4.5	0.27	3.3×10^{-10}
minimum	3.3	0.27	2.5
maximum	7.3	0.27	4.3
Cold-worked Type FV548			
mean	12.4	0.27	4.5
minimum	8.3	0.27	4.0
maximum	16.5	0.27	5.1

Bilinear Relationship for Type PE-16

$R \times 10^{10}$, $(N/m^2 - dpa)^{-1}$	α, dpa^{-1}	t_0, dpa
4.7	0.53	8.1

[a]Evaluated using a 20 percent cold-worked Type 316 uniaxial specimen in EBR-II [5].

The Type M316 values were derived from three different lots of material, and the Type FV548 coefficients are based on a single heat. The B coefficient in Eq 1 cannot be evaluated using the spring data because all of the measurements are in the steady-state region. Instead, the B coefficient for Types M316 and FV548 was taken to be given by the 20 percent cold-worked Type 316 uniaxial specimen [5] irradiated in the Experimental Breeder Reactor-II (EBR-II). This assumption is not critical because the calculated stress relaxation and permanent deflection were relatively insensitive to the value of B. A factor of 10 variation in B resulted in less than a 10 percent variation in the calculated permanent deflection.

The irradiation creep behavior of PE-16 [2] appears to follow an incubation plus linear dose behavior. Lewthwaite and Proctor [9] report that in the DMTR (thermal neutron spectrum) PE-16 irradiation creep strain is composed of transient and steady state (that is, linear dose dependence) components. Unpublished calculations by the author demonstrate that when the spectral-averaged displacement cross section is used as the spectral weighting function, Type M316 creeps the same in both the DFR and Dounreay Materials Test Reactor (DMTR). The DFR high-dose spring irradiation creep data for Type M316 exhibit the same irradiation creep rate as Type M316 in the DMTR. Therefore, Type PE-16 spring irradiation creep data appear to have just entered into the steady-state creep

region. The irradiation creep strain data were fit to an incubation plus linear equation [*8*]

$$\frac{\gamma}{\tau} = R\left[\phi t + \frac{1}{\alpha}\ln\left\{\frac{1 + \exp[\alpha(t_0 - \phi t)]}{1 + \exp[\alpha t_0]}\right\}\right] \tag{2}$$

where R, t_0, and α are material coefficients. The coefficients are listed in Table 1. The linear strain rate and dose intercept are given by the R and t_0 coefficients, respectively. The value of R may be an underestimate because a well-defined steady-state creep rate has not been established.

The incubation plus linear irradiation creep behavior of Type PE-16 is postulated to be related to the in-reactor precipitation of second phases. The precipitation of second phases results in densification, or shrinkage. The dimensional decrease deviates only slightly from isotropic behavior [*10*]. In a creep experiment, shrinkage contributes a negative strain component. Note that Type PE-16 is aged before being placed in-reactor, and no microstructural evidence is available to indicate the stability of the pre-aged structure. Figure 1 of Ref *2*, however, shows that the first stress-reduced strain measurement of Type PE-16 spring 395/6 [*1*] is negative. Therefore, the observed incubation effect is considered to result from similar rates of irradiation creep (that is, positive strain component) and second-phase instability (that is, negative strain component). When the microstructure is stable, the dose dependence then becomes linear. In Eq 2, the magnitude of the shrinkage is given by the t_0 parameter.

The stress-reduced irradiation creep strain versus dose behavior of Types M316, FV548, and PE-16 is shown by the dashed lines in Fig. 1. The solid lines are explained in the following. For Types FV548, M316, and PE-16, the steady-state irradiation creep rates are similar, but the strain values at a given dose are significantly different. Prior to steady-state irradiation creep, Type PE-16 has a long incubation period, whereas Type FV548 has a large positive transient irradiation creep component. The Type M316 transient irradiation creep component is smaller than that of Type FV548, and the Type M316 strain values fall intermediate between Types FV548 and PE-16.

Relationship Between Irradiation Creep and Stress Relaxation

In creep tests the load is usually constant and the specimen length increases, while in relaxation tests the specimen length is maintained constant and the stress decreases with time. Therefore, for stress relaxation

$$\gamma' + \gamma'' = \text{constant} \tag{3}$$

where γ' is the elastic shear strain and γ'' is the irradiation creep shear

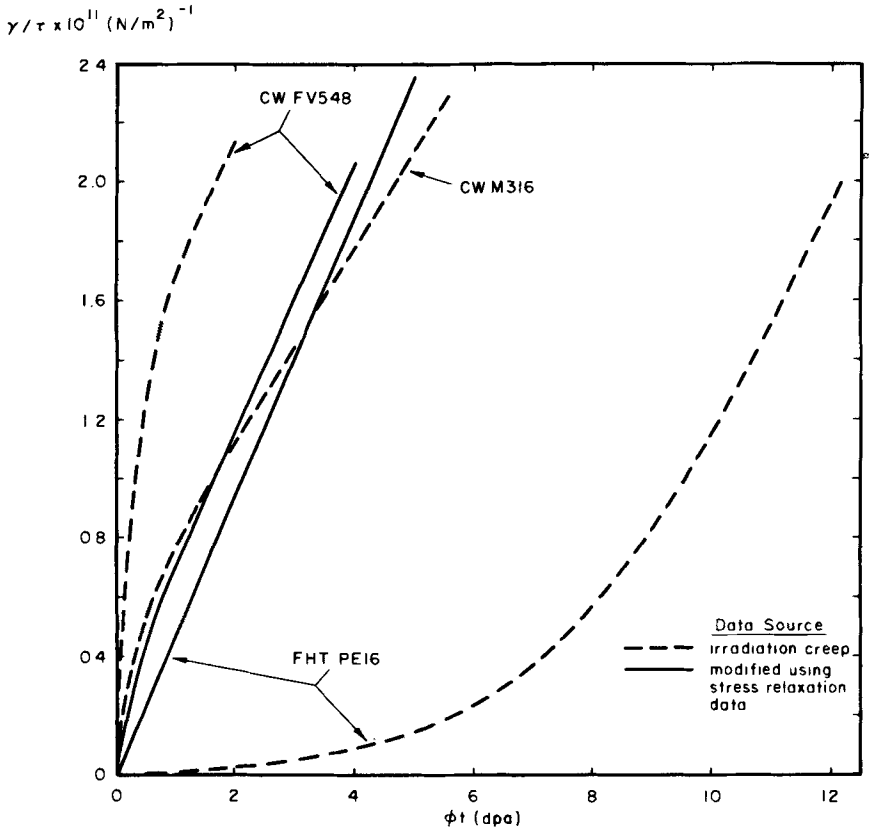

FIG. 1—*Comparison of the stress-reduced strain versus dose behavior of Types M316, FV548 and PE-16.*

strain. The shear stress is the same for two springs welded together, so Eq 3 becomes

$$\gamma_1' + \gamma_2' + \gamma_1'' + \gamma_2'' = \text{constant} \tag{4}$$

where the subscripts refer to different springs. Differentiating Eq 4 with respect to time results in

$$\dot{\gamma}_1' + \dot{\gamma}_2' + \dot{\gamma}_1'' + \dot{\gamma}_2'' = 0 \tag{5}$$

Using Eq 5, the deflection and stress relaxation equations may be derived from the irradiation creep models.

The elastic strain is

$$\gamma_i' = \frac{\tau_i}{G}, \qquad i = 1, 2 \tag{6}$$

where G is the shear modulus. Differentiating Eq 6 with respect to time yields

$$\dot{\gamma}_i' = \frac{1}{G}\dot{\tau}_i \tag{7}$$

The irradiation creep models discussed in the foregoing have different dose functions; therefore, the time derivatives of the strain will result in different strain rate functions. The McVetty relationship will be discussed first, followed by the incubation plus linear form.

McVetty Irradiation Creep Relationship for Both Springs of the Spring Pair

Differentiating Eq 1 with respect to time results in

$$\dot{\gamma}_i'' = \tau\phi\left[\frac{A_i}{B_i}e^{-\phi t/B_i} + C_i\right] + \dot{\tau}[A_i(1 - e^{-\phi t/B_i}) + C_i\phi t] \tag{8}$$

The right-hand side of Eq 8 is composed of two terms: the first depends on τ and the second depends on $\dot{\tau}$. The $\dot{\tau}$ parameter in Eq 8 results from differentiating the irradiation creep model, and thus is denoted $\dot{\tau}^{Ic}$. If $\dot{\tau}^{Ic}$ is zero, then the strain rate is given by the first term in Eq 8. However, if $\dot{\tau}^{Ic}$ is variable, then the strain rate is given by both terms of Eq 8. Currently, for reactor structural design studies, $\dot{\tau}^{Ic}$ is assumed to be zero. To assess this assumption, two cases of Eq 8 are considered: $\dot{\tau}^{Ic} = 0$ and $\dot{\tau}^{Ic} \neq 0$.

Case 1: $\dot{\tau}^{Ic} = 0$—Substituting Eq 8 with $\dot{\tau} = 0$ and Eq 7 into Eq 5 and integrating yields in closed form the stress-relaxation relation

$$\frac{\tau}{\tau_0} = \exp\left\{\frac{G_1G_2}{G_1 + G_2}\left[A_1(1 - e^{-\phi t/B_1}) + A_2(1 - e^{-\phi t/B_2}) + \phi t(C_1 + C_2)\right]\right\} \tag{9}$$

The irradiation creep strain accumulated by each spring during the relaxation test may be calculated by integrating Eq 8. Substituting Eq 9 into Eq 8 for τ results in

$$d\gamma_1'' = \tau_0\phi\left[\frac{A_1}{B_1}e^{-\phi t/B_1} + C_1\right]\exp\left\{\frac{G_1G_2}{G_1 + G_2}\left[A_1(1 - e^{-\phi t/B_1}) + A_2(1 - e^{-\phi t/B_2}) + \phi t(C_1 + C_2)\right]\right\} \tag{10}$$

Equation 10 is easily solved by numerical integration. The deflection Z is given by the relation

$$Z_i = 694.4\gamma_i \tag{11}$$

where Z_i is in units of millimetres (mm) and γ_i is in metres/metres (m/m)

Case 2: $\dot{\tau}^{lc} \neq 0$—When $\dot{\tau}$ is variable in Eq 8, the resulting differential equation is exact, and may be integrated in closed form.

The closed-form stress relaxation relation is

$$\frac{\tau}{\tau_0} = \frac{\dfrac{G_1 + G_2}{G_1G_2}}{\dfrac{G_1 + G_2}{G_1G_2} + A_1(1 - e^{-\phi t/B_2}) + \phi t(C_1 + C_2)} \tag{12}$$

Incubation Plus Linear Irradiation Creep Form for One Spring of the Spring Pair

Type PE-16 springs were irradiated in combination with Types M316 and FV548. For these spring pairs, the irradiation creep models of each spring comprising the spring pair differ. Type M316 and FV548 springs follow the McVetty irradiation creep relationship, whereas the Type PE-16 spring follows the incubation plus linear relationship. Differentiating Eq 2 with respect to time yields

$$\dot{\gamma}_i'' = \tau\left\{R_i\phi t\left[\frac{1}{1 + e^{\alpha_i(t_{0i} - \phi t)}}\right]\right\} + \dot{\tau}R_i\left[\phi t + \frac{1}{\alpha_i}\ln\left(\frac{1 + e^{\alpha_i(t_{0i} - \phi t)}}{1 + e^{\alpha_i t_{0i}}}\right)\right] \tag{13}$$

Case 1: $\dot{\tau}^{lc} = 0$—Substituting Eqs 13, 8, and 7 into Eq 5 for $\dot{\tau} = 0$, and integrating, results in the closed-form solution

$$\frac{\tau}{\tau_0} = \exp\left\{\frac{G_1G_2}{G_1 + G_2}\left[R_1\left(\phi t + \frac{1}{\alpha_1}\ln\left(\frac{1 + e^{\alpha_1(t_{01} - \phi t)}}{1 + e^{\alpha_1 t_{01}}}\right)\right)\right] + A_2(1 - e^{-\phi t/B_2}) + C_2\phi t\right\} \tag{14}$$

The Type PE-16 deflection may be calculated by numerically integrating Eq 13 with $\dot{\tau} = 0$.

Case 2: $\dot{\tau}_{Ic} \neq 0$—When $\dot{\tau}$ is variable in Eqs 8 and 13, the resulting closed-form solution is

$$\frac{\tau}{\tau_0} = \frac{\dfrac{G_1 + G_2}{G_1 G_2}}{\dfrac{G_1 + G_2}{G_1 G_2} + R\left[\phi t + \dfrac{1}{\alpha_1} \ln\left(\dfrac{1 + e^{\alpha_1 (t_{01} - \phi t)}}{1 + e^{\alpha_1 t_{01}}}\right)\right] + A_2(1 - e^{-\phi t/B_2}) + C_2 \phi t} \tag{15}$$

Results

The relaxation and permanent deflection for each spring pair were calculated using the mean, minimum, maximum, and minimum/maximum combinations of the irradiation creep coefficients listed in Table 1. The maximum calculated intervals for the stress relaxation and permanent deflection are reported in the following for each spring pair.

Type M316 Spring Pairs

The calculated values of stress relaxation and permanent deflection agree with the measured values when $\dot{\tau}^{Ic} = 0$. Figure 2 shows that the measured stress relaxation data fall within the interval calculated using the minimum and maximum irradiation creep coefficients when the $\dot{\tau}^{Ic} = 0$. When $\dot{\tau}^{Ic} \neq 0$, the data lie below the calculated stress relaxation interval. Table 2 shows that the measured deflection data fall within the interval of

TABLE 2—*Calculated deflections of the cold-worked Type M316 spring pairs.*

Specimen [*l*] No.	τ_0, MN/m^2	Displacement Damage, dpa	Deflection, mm		
				Calculated	
			Measured	$\dot{\tau}^{Ic} = 0$	$\dot{\tau}^{Ic} \neq 0$
14MM	438	2.80	2.51/2.67	1.94 to 3.73	1.02 to 1.91
13MM	564	1.75	2.97/3.58	2.07 to 4.07	1.41 to 2.19

values calculated when $\dot{\tau}^{Ic} = 0$. The deflection interval reported in Table 2 corresponds to the case of minimum/maximum irradiation creep coefficients. Note that the deflection intervals calculated with $\dot{\tau}^{Ic} \neq 0$ are about a factor of 2 less than the measured deflections. Furthermore, the interval reported in Table 2 for the $\dot{\tau}^{Ic} \neq 0$ case represents an overestimation of the

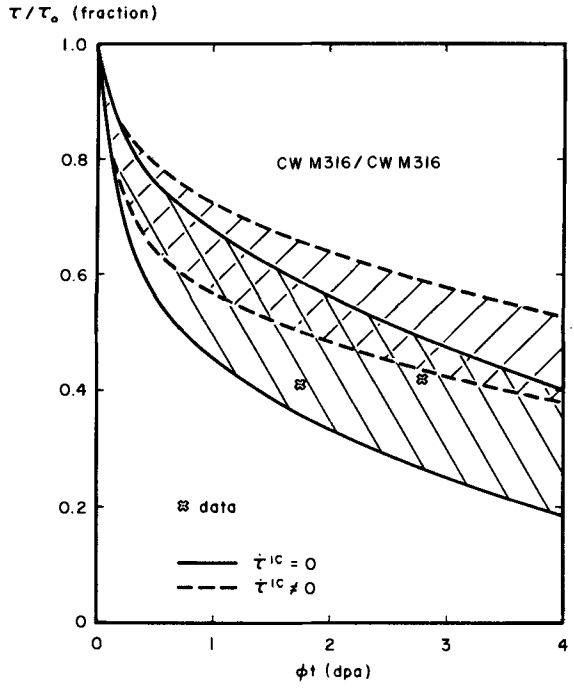

FIG. 2—*Stress relaxation of Type M316-M316 spring pairs.*

calculated deflection. Figure 2 shows that, when $\dot{\tau}^{Ic} \neq 0$, the calculated stress is higher than the measured stress. Equation 8 shows that the deflection is directly proportional to the stress. Therefore, the reported deflection interval is an overestimate because the calculated stress that is used to determine the deflection interval is greater than the measured stress.

Type FV548-M316 Spring Pairs

The calculated stress relaxation agrees with the measured values both when $\dot{\tau}^{Ic} = 0$ and when $\dot{\tau}^{Ic} \neq 0$. Figure 3 shows that when $\dot{\tau}^{Ic} = 0$ the data just fall within the interval calculated using the maximum and minimum irradiation coefficients. When $\dot{\tau}_{Ic} \neq 0$, the calculated stress relaxation interval lies slightly above the data.

Table 3 appears to indicate that the deflection measurements of Type FV548-M316 spring pairs are not in agreement with the calculations of either the $\dot{\tau}^{Ic} = 0$ or the $\dot{\tau}^{Ic} \neq 0$ cases. However, a comparison of the calculated and measured deflection values indicates that with a modification in the Type FV548 transient irradiation creep coefficient (the A-param-

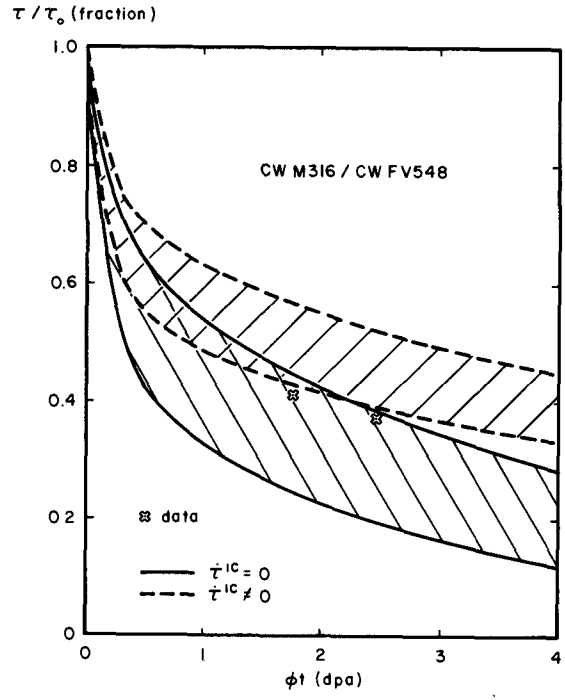

FIG. 3—*Stress relaxation of Type M316-FV548 spring pairs.*

eter) the calculated values can be made to agree with the measurements when $\dot{\tau}^{Ic} = 0$. When $\dot{\tau}^{Ic} \neq 0$, no reasonable irradiation creep coefficient modification is possible to force the calculated deflections to fit the measurements. Table 3 shows that when $\dot{\tau}^{Ic} \neq 0$ the calculated Type FV548 deflection interval is slightly less and the Type M316 deflection interval is much less than the measurements, respectively. Equation 8 shows that the calculated deflection can be increased by increasing the irradiation creep coefficients. In the case of Type M316, the irradiation creep coefficients must be increased by approximately a factor of 10 to force agreement between the calculated deflection interval for $\dot{\tau}^{Ic} = 0$ and the data. A factor of 10 increase in the irradiation creep coefficients is significantly larger than the lot-to-lot variations measured with the three different batches of material. Therefore, the measured Type M316 deflections do not agree with the $\dot{\tau}^{Ic}$ variable case. On the other hand, Table 3 shows that the calculated Types FV548 and M316 deflections are in good agreement with the data for $\dot{\tau}^{Ic} = 0$ when the Type FV548 transient coefficient is decreased by a factor of 5 less than the value measured in the irradiation creep tests (see Table 1).

TABLE 3—*Calculated deflections of the cold-worked Type M316-FV548 spring pairs.*

Specimen [*I*] No.	Spring	τ_0, MN/m^2	Displacement Damage, dpa	Deflection, mm			
					Calculated		
				Measured	$\dot{\tau}^{Ic} = 0$	$\dot{\tau}^{Ic} \neq 0$	Modified[a] Type FV548 Irradiation Creep Transient with $\dot{\tau}^{Ic} = 0$
11MV	M316	438	1.75	2.82	1.31 to 2.79	0.88 to 1.45	1.76 to 3.14
12MV	M316	438	2.46	2.64	1.47 to 3.09	0.80 to 1.55	2.02 to 3.51
11MV	FV548	438	1.75	2.31	2.93 to 4.71	1.73 to 2.31	1.88 to 2.50
12MV	FV548	438	2.46	2.79	3.21 to 5.04	1.56 to 2.38	2.22 to 3.02

[a] $A = 2.5 \times 10^{-10}$ (N/m^2)$^{-1}$ versus the Table 1 value of 12.4×10^{-10}.

Type M316-PE-16 Spring Pairs

The PE-16 stress relaxation calculations were performed only for the $\dot{\tau}^{ic} = 0$ case because of the good agreement between the data and calculations for Types M316 and FV548. The calculated stress relaxation of the Type M316-PE-16 spring pairs and the calculated Type PE-16 permanent deflection do not agree with the experimental measurements when $\dot{\tau}^{ic} = 0$. Figure 4 shows that the calculated stress relaxation is from 0 to

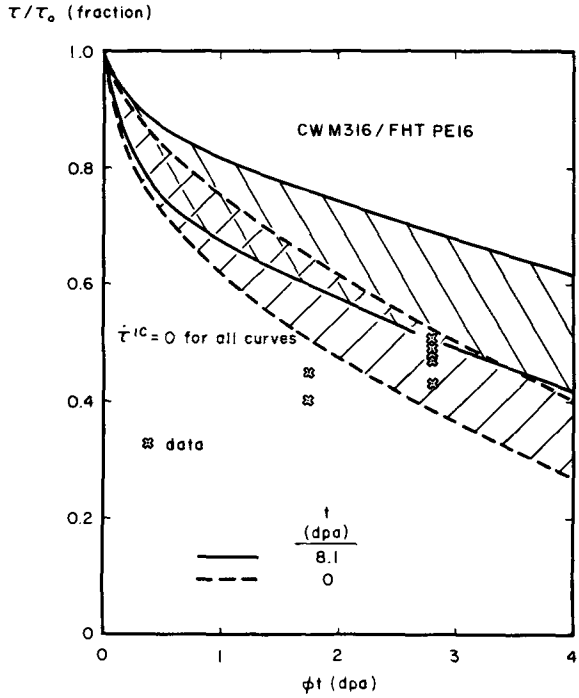

FIG. 4—*Stress relaxation of Type PE-16-M316 spring pairs.*

45 percent greater than the measurements. Table 4 shows that the calculated Type M316 deflections agree with the measurements, but that the calculated PE-16 deflections are between a factor of 10 to 30 less than the measurements. The lack of agreement between the calculated and measured PE-16 stress relaxation and deflection values is believed to be due to improperly defined PE-16 irradiation creep coefficients.

Calculations with a zero-fluence intercept (that is, $t_0 = 0$ dpa) were performed to assess the sensitivity of the calculated stress relaxation and PE-16 deflection values to t_0. Figure 4 shows that when $t_0 = 0$ the calculated stress relaxation is in reasonable agreement with the measure-

TABLE 4—*Calculated deflections for the cold-worked Type M316-FHT PE-16 spring pairs when* $\dot{\tau}^{Ic} = 0$.

Specimen [*I*] No.	Spring Type	τ_0, MN/m^2	Displacement Damage		Deflection, mm		
			dpa	dpa/s × 10^7	Measured	Calculated	
						t_0 = 1 dpa[a]	t_0 = 0 dpa[b]
03PM	M316	87	2.80	5.8	0.56	0.52 to 0.85	0.48 to 0.79
04PM	M316	263	2.80	5.8	1.70	1.58 to 2.58	1.45 to 2.40
05PM/06PM/07PM	M316	438	2.80	5.8	2.82/3.12/3.56	2.63 to 4.29	2.42 to 3.23
01PM/02PM	M316	438	1.75	3.6	2.74/3.76	2.05 to 3.53	1.95 to 3.38
03PM	PE-16	87	2.80	5.8	0.36	0.02	0.30 to 0.37
04PM	PE-16	263	2.80	5.8	1.45	0.05 to 0.06	0.90 to 1.11
05PM/06PM/07PM	PE-16	438	2.80	5.8	1.17/1.30/1.68	0.07 to 0.09	1.65 to 1.85
01PM/02PM	PE-16	438	1.75	3.6	1.17/2.44	0.04 to 0.05	1.00 to 1.18

[a]As given in Table 1.
[b]Modified fluence intercept for Type PE-16.

ments. Table 4 shows that the calculated Type M316 deflections are insensitive to the t_0 value, and that the calculated Type PE-16 deflections and stress relaxation of the spring pairs are in reasonable agreement with the measurements when $t_0 = 0$. The agreement between the measured and calculated stress relaxation and Type PE-16 deflection values could be slightly improved by increasing the steady-state irradiation creep rate. This is consistent with Type PE-16 irradiation creep data. As noted in the foregoing, the available Type PE-16 irradiation creep data probably slightly underestimate the steady-state irradiation creep rate.

Type PE-16-FV548 Spring Pairs

Figure 5 shows that the calculated stress relaxation of the Type PE-16-FV548 spring pairs agrees with the measurements. However, Table 5

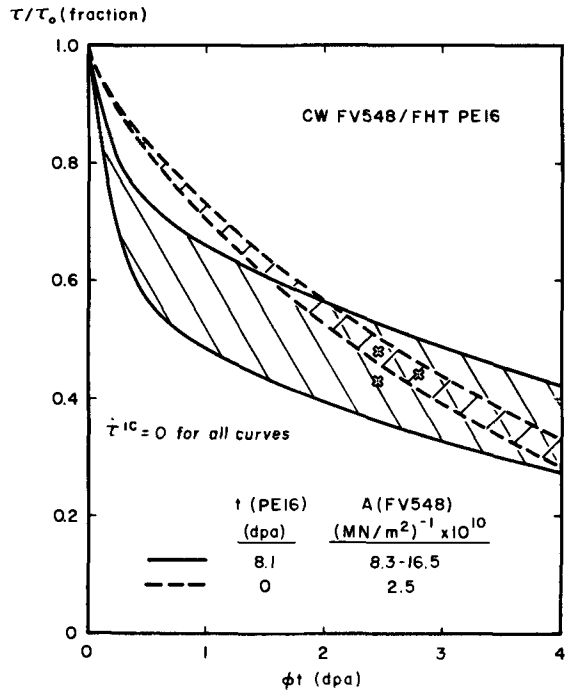

FIG. 5—*Stress relaxation of Type PE-16-FV548 spring pairs.*

shows that the calculated Type PE-16 deflection is between a factor of 20 to 50 below and that the calculated Type FV548 deflection is about 50 percent greater than the measurements, respectively. Therefore, the

TABLE 5—*Calculated deflections for the cold-worked Types FV548-FHT and PE-16 spring pairs when* $\dot{\tau}^{Ic} = 0$.

Specimen [*I*] No.	Spring Type	τ_0, MN/m^2	Displacement Damage		Deflection, mm		
			dpa	dpa/s $\times 10^7$	Measured	Calculated: Unmodified Irradiation Creep, Parameters[a]	Calculated: Modified Irradiation Creep Parameters[b]
08PV	FV548	438	2.80	5.8	2.82	4.32 to 5.79	3.00 to 3.50
09VP/10PV	FV548	438	2.46	5.1	2.79/3.33	4.11 to 5.60	2.80 to 3.27
08PV	PE-16	438	2.80	5.8	2.46	0.05 to 0.07	1.68 to 1.77
09VP/10PV	PE-16	438	2.46	5.1	1.12/2.26	0.04 to 0.06	1.51 to 1.58

[a] As given in Table 1.
[b] Modification includes for Type FV548, $A = 2.5 \times 10^{-10}\,(\mathrm{N/m^2})^{-1}$, and for Type PE-16, $t_0 =$ dpa.

agreement between the calculated and measured stress relaxation values is fortuitous because the increment of Type FV548 irradiation creep strain greater than the measurement just balances the increment of Type PE-16 irradiation creep strain smaller than the measurement.

The results discussed in the foregoing for the Type M316-PE-16 and Type M316-FV548 spring pairs showed that modifications to the Type FV548 transient and Type PE-16 fluence intercept irradiation creep coefficients are necessary in order to calculate the stress relaxation and deflection. Figure 5 shows that the calculated stress relaxation is virtually unchanged, and thus it remains in good agreement with the measurements. Table 5 shows that good agreement is obtained between the calculated and measured deflections using the modified irradiation creep coefficients. These results further support the modifications proposed for Types FV548 and PE-16 irradiation creep coefficients.

Discussion

The results of this study for Type M316 support the validity of a mechanical equation of state for in-reactor deformation. Irradiation creep models may be used to calculate stress relaxation when $\dot{\tau}^{Ic} = 0$. If $\dot{\tau}^{Ic} \neq 0$, stress relaxation cannot be calculated using irradiation creep models.

Lot-to-lot variations appear to have the largest effect on the transient irradiation creep coefficient. Mosedale et al [*7*] report that scatter is associated with the transient coefficients for different lots of Type M316. This behavior may be related to the influence of varying alloying element and impurity content on second-phase precipitation. Various authors [*10–12*] have studied the effects of precipitation at high temperatures out-of-reactor. The measured shrinkage is small, and depends on the second-phase precipitation sequence. The time-temperature-precipitation sequence is complex, and relates to the alloying element and impurity content. Therefore, the amount of shrinkage varies from lot to lot due to differences in impurity content.

Figure 1 shows that the variation in the stress-reduced strain versus dose behavior of Types FV548, M316, and PE-16 is greatly reduced when the irradiation creep coefficients are modified using the stress relaxation data. The irradiation creep tests predict substantially different behavior of the transient irradiation creep component. Adjustments were made in the Type FV548 transient and Type PE-16 incubation parameters because the irradiation creep and stress relaxation tests were performed on different lots of material. The Type M316 irradiation creep coefficients listed in Table 1 are based on the results from three different lots of material. Types FV548 and PE-16 results are limited to a single lot of material. Therefore, the irradiation creep properties listed in Table 1 probably best describe the behavior of Type M316 with respect to the lot of material

used for stress relaxation testing. The adjustments in the Type FV548 transient and the Type PE-16 incubation coefficients, respectively, are considered to reflect lot-to-lot variations in irradiation creep behavior.

Conclusions

The irradiation creep and stress relaxation data support the validity of a mechanical equation of state. The largest uncertainty in the stress relaxation calculations is considered to be associated with the use of different lots of material for the irradiation creep and stress relaxation tests. The stress relaxation and deflection of Type M316 could be calculated using the irradiation creep models when $\dot{\tau}^{Ic} = 0$, because the irradiation creep measurements were made on three lots of material. Types FV548 and PE-16 stress relaxation also could be calculated using irradiation creep models, but adjustments were necessary in the Type FV548 transient and the Type PE-16 incubation irradiation creep coefficients, respectively, because irradiation creep measurements were made on only one lot of material in each case. The adjustments probably result from lot-to-lot variations in shrinkage behavior. The modifications in Types FV548 and PE-16 irradiation creep parameters greatly reduce the variation in the strain versus dose behavior of Types M316, PE-16, and FV548.

Acknowledgments

The author would like to thank A. Biancheria and A. Boltax for their encouragement and support of this work, which was performed under contract with the Energy Research and Development Administration.

References

[1] Standring, J., European Conference on Irradiation Behavior of Fuel Cladding and Core Component Materials, *Gesellschaft für Kernforschung mbH.*, Karlsruhe, Germany, 1974, p. 151.

[2] Mosedale, D., Lewthwaite, G. W., and Ramsey, I., European Conference on Irradiation Behavior of Fuel Cladding and Core Component Materials, *Gesellschaft für Kernforschung mbH.*, Karlsruhe, Germany, 1974, p. 139.

[3] Mosedale, D. and Lewthwaite, G. W., *Creep Strength in Steel and High Temperature Alloys*, London, England, Metals Society, 1974, p. 169.

[4] Mosedale, D., Lewthwaite, G. W., and Ramsey, I., *Irradiation Embrittlement and Creep in Fuel Cladding and Core Components*, British Nuclear Energy Society, London, 1972, p. 233.

[5] Gilbert, E. R., Kaulitz, D. C., Holmes, J. J., and Claudson, T. T., *Irradiation Embrittlement and Creep in Fuel Cladding and Core Components*, British Nuclear Energy Society, London, 1973, p. 239.

[6] McVetty, P. G., *Transactions*, American Society of Mechanical Engineers, Vol. 55, 1933, p. 99.

[7] Mosedale, D., Lewthwaite, G. W., and Ramsey, I., *Physical Metallurgy of Reactor Fuel Elements*, Gloucestershire, England, Metals Society, 1975, p. 132.

[8] Jackson, R. J., Washburn, D. F., Garner, F. A., and Gilbert, E. R., *Transactions,* American Nuclear Society, Vol. 22, 1975, pp. 184–185.
[9] Lewthwaite, G. W. and Proctor, K. J., *Journal of Nuclear Materials,* Vol. 46, 1973, p. 9.
[10] Watkin, J. S., European Conference on Irradiation Behavior of Fuel Cladding and Core Component Materials, *Gesellschaft für Kernforschung mbH.* Karlsruhe, Germany, 1974, p. 69.
[11] Weiss, B. and Stickler, R., *Metallurgical Transactions,* Vol. 3, 1972, p. 851.
[12] Spitznagel, J. A. and Stickler, R., *Metallurgical Transactions,* Vol. 5, 1974, p. 1363.

Mechanical Properties and Microstructures

K. L. Murty[1] *and E. O. Hall*[2]

Dynamic Strain-Aging and Neutron Irradiation in Mild Steel

REFERENCE: Murty, K. L. and Hall, E. O., "**Dynamic Strain-Aging and Neutron Irradiation in Mild Steel,**" *Irradiation Effects on the Microstructure and Properties of Metals, ASTM STP 611,* American Society for Testing and Materials, 1976, pp. 53–71.

ABSTRACT: "Blue brittle" or dynamic strain-aging studies were carried out on mild steel in vacuum-annealed, irradiated, and irradiated decarburized conditions. The effect of neutron damage is to decrease or eliminate the concentration of free interstitial impurity elements responsible for locking the dislocations. Progressively increasing the irradiation dose from $\sim 10^{16}$ to $\sim 10^{19}$ nvt (> 1 MeV) resulted in a transition from "serrated" to "jerky" flow at and beyond $\sim 10^{17}$ nvt. The activation energies for serrated and jerky flow were determined to be the same, ~ 18 kcal/mol (75 kJ/mol), identifiable with the migration energy of carbon or nitrogen in iron. Thus neutron irradiation does not seem to affect the mechanism of dislocation locking.

Neutron irradiation was found to result in the following: (1) yield stress increases (hardening); (2) ductility decreases (embrittlement); (3) temperature of strain-aging increases; (4) temperature region of unstable flow decreases; (5) degree of locking decreases; (6) Luders bands become relatively more diffuse; (7) the transition from serrated to jerky flow results in a complex temperature dependence of yield stress and Luders strain; (8) at temperatures below unstable flow, Luders strain increases and, at the highest doses ($\sim 10^{19}$ nvt), fracture occurs during Luders extension; and (9) radiation hardening in mild steel is thermally activated.

There was no evidence of serrated flow in decarburized and irradiated decarburized material up to about 280°C (553 K). The effect of neutron damage was found to be similar to that of dry hydrogen treatment. In both cases a transition from serrated to jerky flow was observed. Both the appearance and disappearance of serrations were found to be dependent on the concentration of nitrogen in solution. These results imply that free nitrogen is primarily responsible for dynamic strain-aging in mild steel, both archive and irradiated.

KEY WORDS: radiation, neutron irradiation, ductility, embrittlement, damage, impurities, precipation hardening

[1] Senior research engineer, Lynchburg Research Center, Lynchburg, Babcock & Wilcox Company, Va. 24505.

[2] Australian Universities Commission, Canberra, Australia; formerly, professor and head, Department of Metallurgy, University of Newcastle, Newcastle, Australia.

It is well documented in the literature [*1–4*][3] that the interstitial impurities such as carbon and nitrogen play a major role in irradiation hardening and strain-aging phenomena. Earlier work by Hall [*5*] and others [*6,7*] clearly indicated that these interstitial impurities combine with irradiation-induced point defects, such as vacancies and interstitials, either individual defects or loops, to form complexes. These complexes may probably be responsible for part of the hardening [*5*]. At the same time the creation of these complexes results in reduced net concentration of interstitial atoms in solution [*7*], and thus the irradiated steel becomes non-aging at sufficiently high neutron doses [*5,6*]. Recently Murty and Hall [*8*] examined the effect of incremental neutron doses on the static strain-aging kinetics in mild steel and found that irradiation doses greater than about 10^{18} nvt render mild steel non-aging.

The stress-strain curve for mild steel at temperatures around 150 to 250°C (423 to 523 K) is serrated and most unlike the smooth curve obtained at room temperature. The accompanying increased work-hardening rate and reduced elongation constitute the so called blue-brittle behavior of mild steel. The idea that the blue-brittleness is an effect caused by strain-aging during deformation is not new [*9*], and Hall [*1*] reported one of the first systematic studies of serrated yielding. Hall distinguished between (1) "serrated yielding," with each serration produced by the propagation of a separate Luders band, and (2) "jerky flow," with plastic deformation occurring at random locations along the specimen after the initial Luders band front had traveled the gage length of the specimen.

There is substantial evidence that the dynamic strain-aging (Portevin-Le Chatelier effect) in mild steel is associated with the presence of carbon and nitrogen. The effects produced by these are additive. The effect of interstitial nitrogen seems to be more pronounced than that of carbon [*6,8*]. The temperature and strain rate at which serrations were observed were strongly dependent upon the concentration of interstitial impurities—in particular, nitrogen [*10*]. Since the effect of neutron irradiation is to reduce the concentration of free interstitial impurities, the neutron damage is expected to affect the characteristics of the dynamic strain-aging in mild steel.

A very limited amount of information on the superimposed effect of irradiation on the Portevin-Le Chatelier effect is available. Two isolated examples, one by Russell [*11*] on copper-tin and the other by Blakemore and Hall [*23*] on carburized nickel-copper alloys, may be cited on the substitutional type of locking of the dislocations. Recently, Little and Harries [*6*] reported the only study available on blue-brittle behavior of steels due to interstitial impurities. This work indicated that irradiated

[3] The italic numbers in brackets refer to the list of references appended to this paper.

($\sim 2.8 \times 10^{18}$ nvt) steels exhibit serrations of substitutional type. However, no attempt was made to investigate the incremental effect of neutron fluence on blue-brittleness.

In the present study, an attempt was made to record the characteristics of load drops not only on Luders band [*4*] but also beyond, up to necking and fracture, and to study the effect of incremental neutron doses from about 10^{16} to 10^{19} nvt (fission). The temperature dependence of various deformation characteristics such as the lower yield stress, Luders strain, and serration height and their variation with irradiation dose are documented.

Experimental

Mild steel wires of 0.001 m diameter and 0.0385 m gage length were used. The main advantage of wires is that the deformation proceeds by a single Luders band, usually nucleated in one of the grips, and the lower yield stress is thus extremely constant [*12*]. In addition, the small volume of the wire specimens reduces the decay time of γ-activity accumulated during irradiation. The material used was cold-drawn, 0.06 weight percent carbon-rimmed mild steel whose composition is given in Table 1.

TABLE 1—*Composition of steel specimens.*

Element	C	N	O	Mn	Si	S	Ni	Cr	Cu	Al	Sn	Fe
Weight %	0.05	0.004	0.012	0.39	< 0.001	0.012	0.032	0.041	0.019	0.002	0.003	remainder

The prepared specimens were annealed in vacuo for various times and temperatures depending on the desired grain size between ASTM 5 and ASTM 8.

Decarburization of the prepared specimens was carried out in a hydrogen furnace with wet hydrogen atmosphere at $\sim$ 650°C (923 K) for various times depending on the desired level of impurities. Complete decarburization (carbon < 0.001) was achieved by annealing at 650°C (923 K) for about 36 h in an atmosphere of hydrogen passed through water at 30°C (303 K) and was inferred from rounded yield in the stress-strain curve.

Vacuum-annealed and decarburized specimens were irradiated by the Australian Atomic Energy Commission in high isotopeflux Australian reactor (HIFAR), the heavy water moderated reactor at Lucas Heights. Different total neutron doses were obtained by insertion in the vertical holes—at positions close to the fuel plates for high doses and at positions away from the plates for lower doses. In all cases the time of exposure was kept essentially constant, and thus the different integrated neutron

fluxes were obtained by differing dose rates. The fission neutron fluxes were calculated from the γ-activity of ^{46}Ti wire monitors placed near the specimen cans, and four different fluences were obtained: 3.9×10^{16}, 2.8×10^{17}, 2.0×10^{18}, and 1.4×10^{19} nvt (> 1 MeV). The quoted values for the fluences are the average values, and typically the minimum and maximum values of fluxes differed by a factor of ∼ 3 over the length of the specimens.

Special precautions were taken to reduce γ-heating of the specimens, and the irradiation temperature can be taken as 80°C, the heavy-water temperature [*5*]. The irradiated specimens all became radioactive due to the relatively large capture cross section of ^{58}Fe, and thus the specimens were stored in lead coffins until the γ-activity decayed to tolerable levels.

All tension tests were carried out on a "hard" tensile machine of the type designed by Adams [*13*]. The crosshead speeds can be varied from 1.7×10^{-7} m/s to 1.0×10^{-5} m/s with seven intermediate steps. Most of the tests were carried out at a crosshead speed of 5.2×10^{-6} m/s, which corresponds to a strain rate of $\sim 1.36 \times 10^{-4}$ s^{-1}. The desired temperatures were attained by immersing the specimen and the holder assembly in an electrically heated stirred oil or salt baths, and the temperatures were controlled to ±1°C.

Results

Vacuum Annealed

A series of load-elongation curves of mild steel specimens with grain size of ASTM 7.5 annealed in vacuo is reproduced in Fig. 1. All the curves were obtained at a constant crosshead speed of 5.2×10^{-6} m/s.

At room temperature the load-elongation curve consists of a smooth Luders plateau followed by homogeneous deformation, which again is smooth with no load drops. At about 90°C (363 K), the Luders plateau is still quite smooth but the flow curve consists of random jerks. As temperature increases, "jerky" secondary Luders plateaus develop on the flow curve. At the lower critical temperature (∼ 140°C), random stress "pips" are observed on the Luders plateau while the flow curve is now "serrated" with occasional larger drops in load. The load pips on Luders band become more regular and periodic as temperature increases, and these are called "serrations." At still higher temperatures while the Luders band is serrated with increased height of the serrations, the flow curve develops random secondary bands which are in turn serrated. In addition, occasional smooth parts of the flow curve are interspersed. At about 200°C (473 K), the flow curve becomes smooth except for a few serrations during necking instability and at the very beginning of the flow curve (that is, just beyond the Luders band). Beyond 200°C (473 K) the

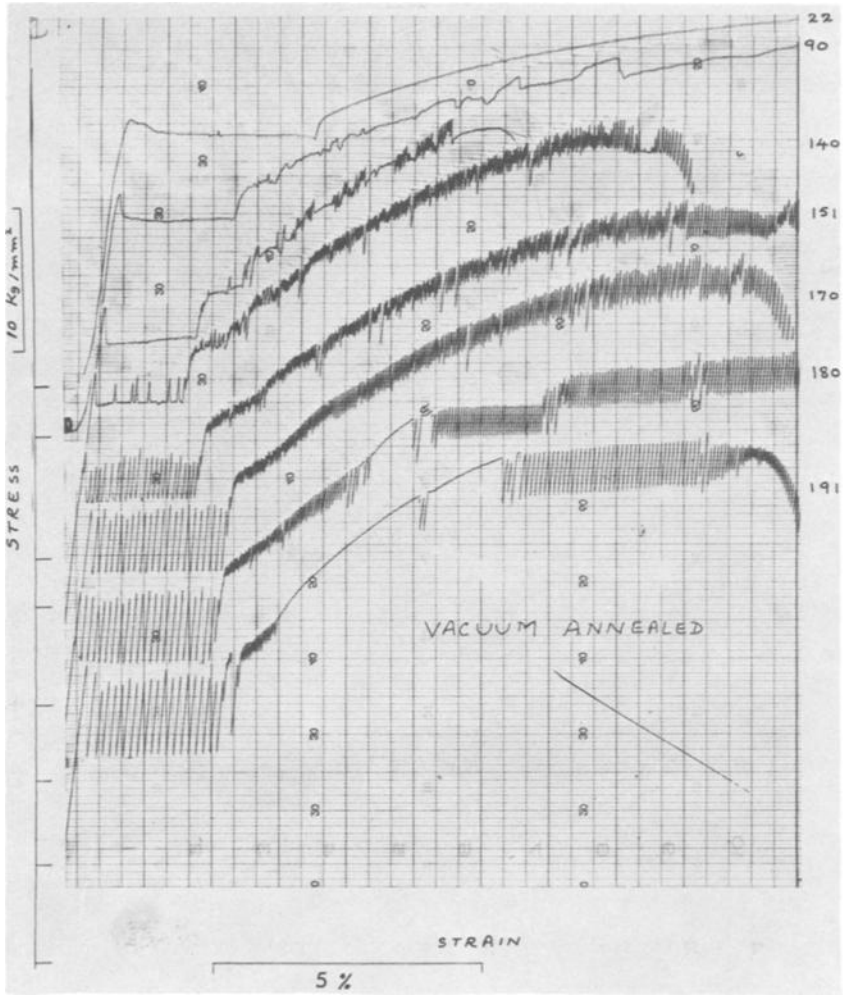

FIG. 1—*Load-elongation curves at various temperatures for vacuum-annealed specimens with grain size of ASTM 7.5.*

flow curve is essentially smooth while Luders band is serrated with decreasing magnitude of serrations. Just prior to the disappearance of all load drops from the stress-strain curve, the Luders band becomes "jerky" with a few serrations occurring in groups. Finally at about 270°C (543 K) and beyond, the stress-strain curve consists of a yield point with essentially no Luders extension.

Associated with these features is the temperature variation of Luders strain (Fig. 2). As temperature increases from ambient, Luders extension (ε_{LB}) decreases until it reaches a minimum value at approximately the

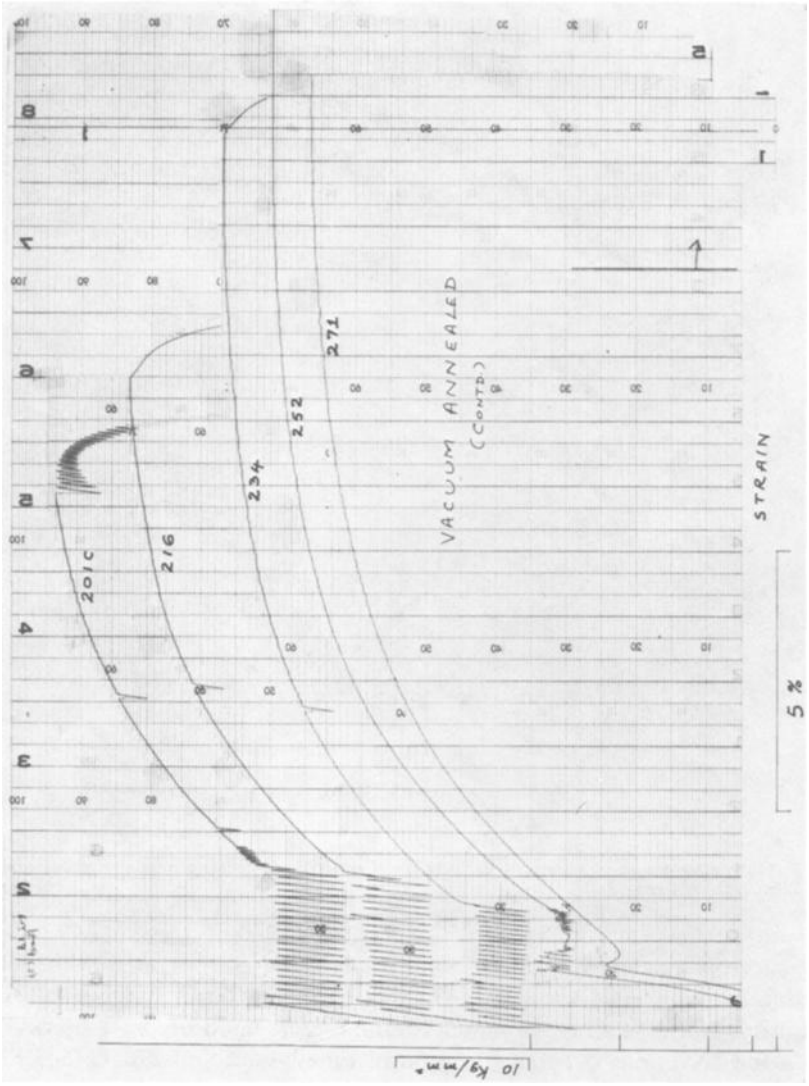

FIG. 1—(*Continued*).

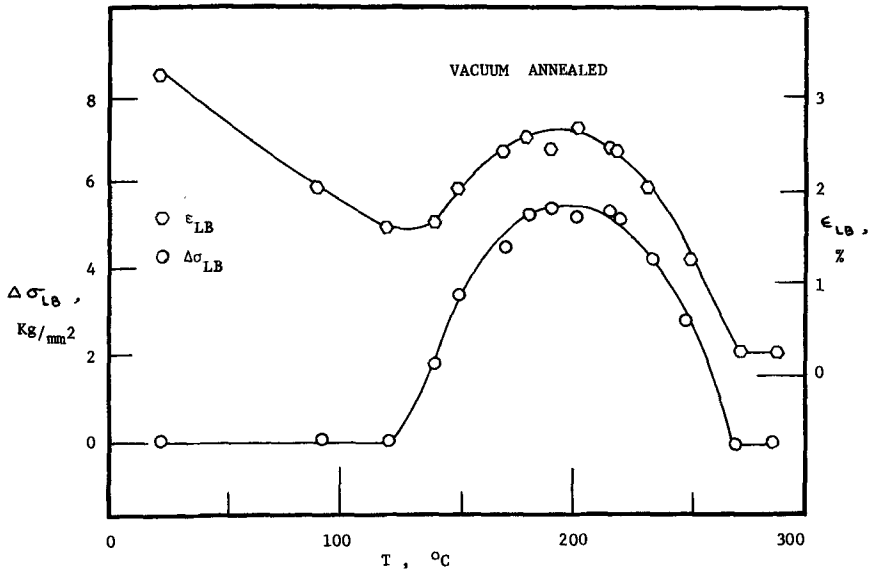

FIG. 2—*Effect of temperature on serration height* ($\Delta\sigma_{LB}$) *on the Luders band and Luders strain* (ε_{LB}) *in vacuum-annealed specimens.*

same temperature where the load "pips" first appeared on the Luders band. Beyond this, ε_{LB} increases to a maximum until about the point where the flow curve tends to become smooth and then decreases again, reaching essentially zero value at $\sim$ 270°C (543 K). Similar features exist for tests at different strain rates except for a shift to higher temperatures as strain rate increases; also, the height of the serrations decreases with the applied strain-rate [*14*]. Comparison of the room temperature and 270°C (543 K) curves indicate that at 270°C, although all serrations and jerks disappear from the curve, the rate of work hardening remains high. Similar observations were made by several investigators earlier, see, for example, Hall [*15*]. Temperature variation of total elongation indicates minima at $\sim$ 110°C (383 K) and 210°C (483 K) which correspond to the temperatures at which minimum and maximum values for ε_{LB} were noted. In the region of serrated flow, athermal yield stress (Fig. 3) (which corresponds to a peak when corrected for temperature variation of modulus) and a peak in ultimate tensile strength were observed. These results again are in line with the earlier findings.

The lower critical temperature (that is, the temperature at which the first upper yield point pips appear on the Luders band and correspondingly that at which the Luders extension first attains a minimum value) is strain-rate dependent [*4*]. The effect of the test temperature and the ap-

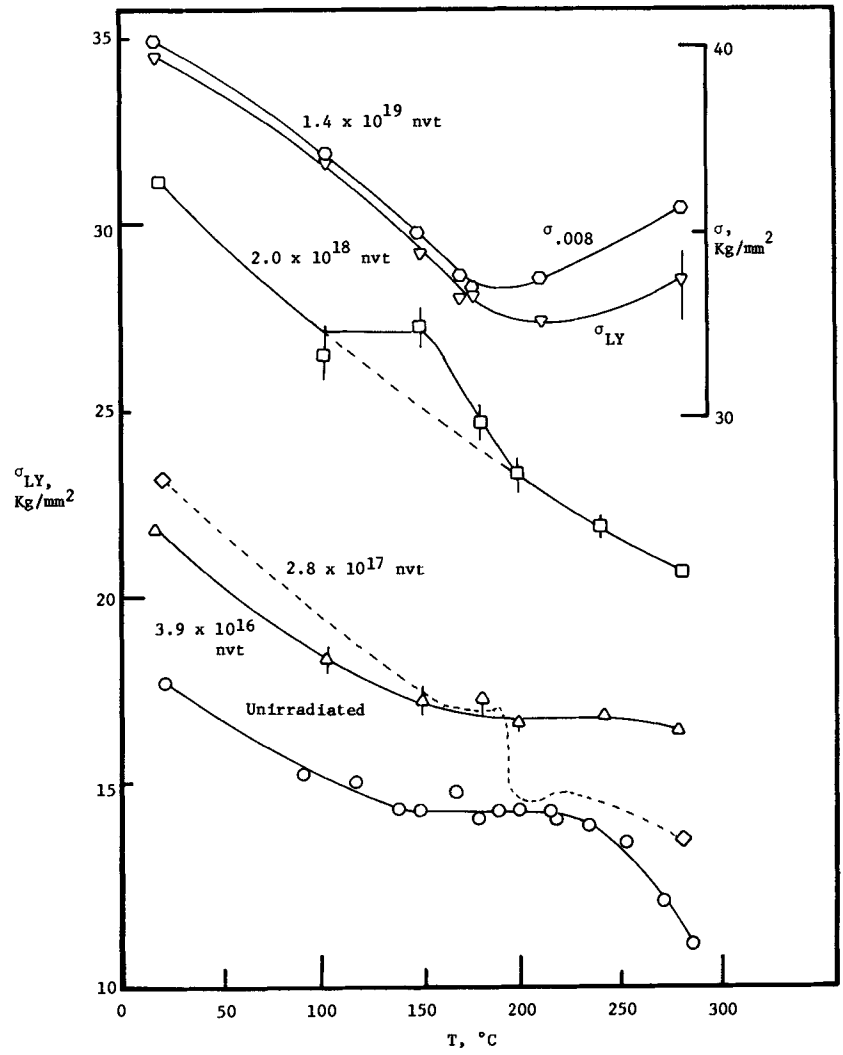

FIG. 3—*Effect of neutron dose on temperature dependence of lower yield stress.*

plied strain rate on the height of serrations on the Luders band is clearly depicted in Fig. 4, where load-elongation curves on two specimens are shown. Here the specimen was first deformed at 86°C (359 K) partway along the Luders band, load released, temperature shifted to 95.6°C (368 K), and the test continued until a few serrations appeared on the Luders band. Again the sample is unloaded and the process repeated. Thus a few specimens are enough to generate the data shown in Fig. 5,

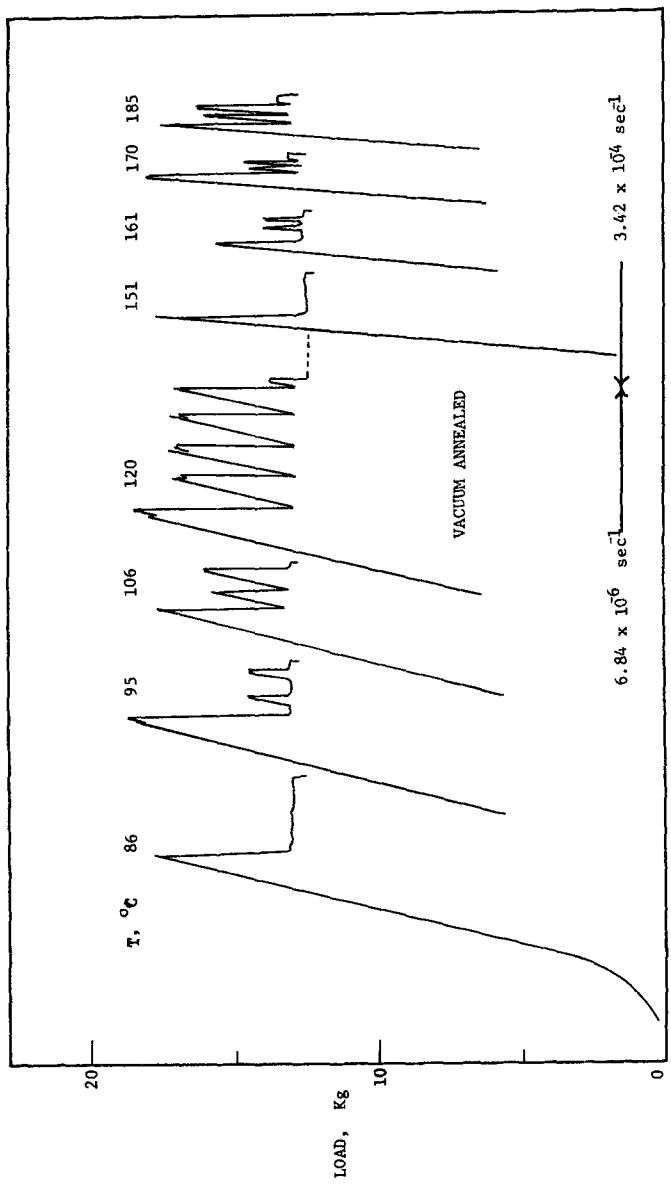

FIG. 4—*Interrupted load-time curves depicting the effect of temperature and strain rate on the height of serrations on the Luders band.*

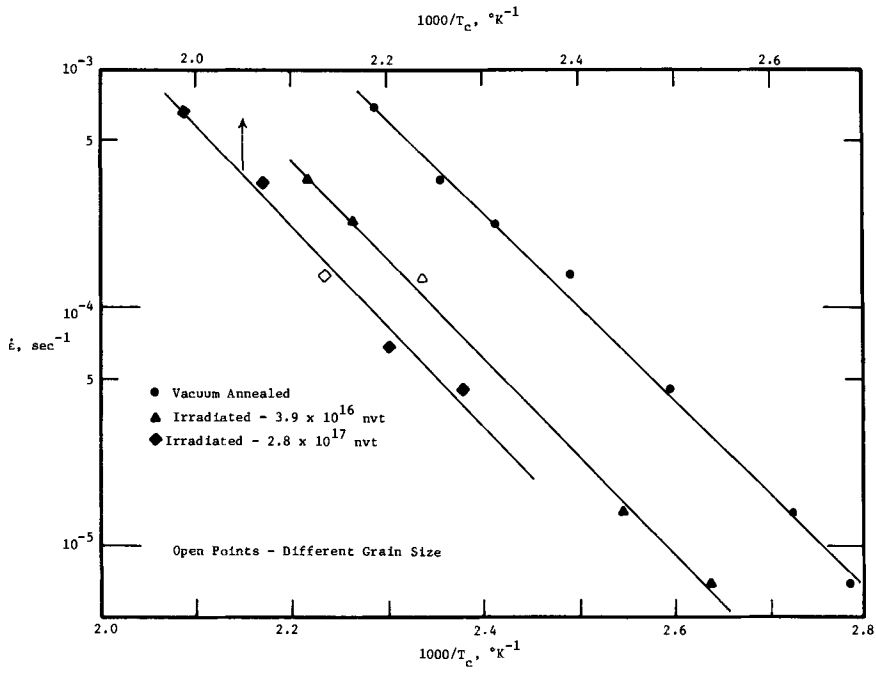

FIG. 5—*Arrhenius plots of the applied strain rate and lower critical temperature. Unfilled data points were obtained using specimens with different grain size.*

and the activation energy for serrated flow was found to be 18 kcal/mol (75 kJ/mol), which agrees with that for carbon or nitrogen diffusion.

Effect of Radiation Damage

A set of specimens irradiated to 3.9×10^{16} nvt was tested at various temperatures. Load-elongation curves of these specimens are essentially similar to those for the vacuum-annealed unirradiated specimens (Fig. 1), except that the minimum temperature at which serrations start appearing (that is, lower critical temperature) is shifted to higher values (Fig. 6). In addition, the maximum in the height of serrations ($\Delta\sigma_{LB}$) also decreases in comparison with that corresponding to the unirradiated material. Luders extension at the lower critical temperature increases while the maximum in Luders extension beyond the critical temperature remains at the same level as that in unirradiated specimen (Fig. 7). Thus the minimum in ε_{LB} at the lower critical temperature (T_c^L) in the irradiated specimen is much shallower than that in the vacuum-annealed specimen. This is indicative of the fact that the Luders band in irradiated material is relatively more diffuse, as predicted by Hall [*15*]. Another set of speci-

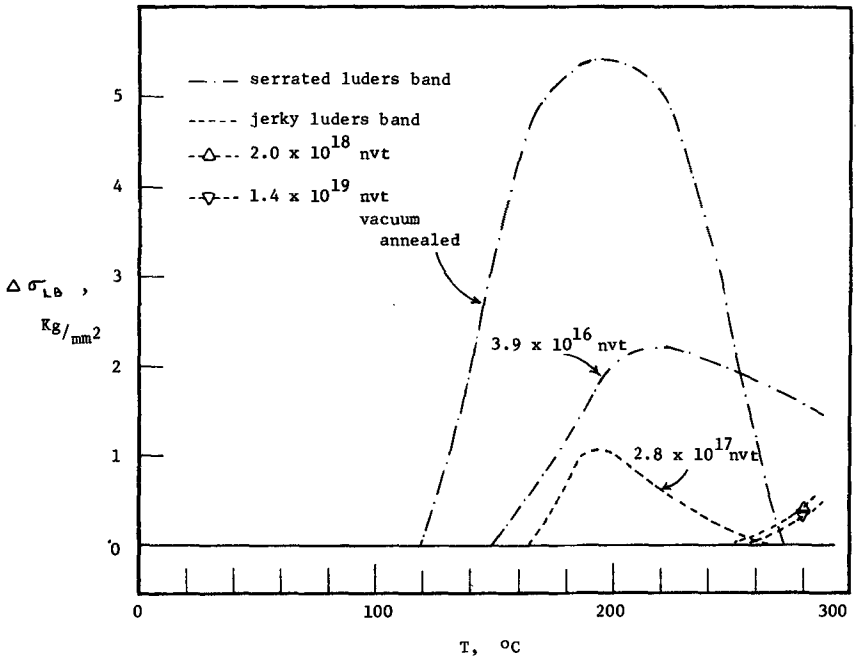

FIG. 6—*Effect of irradiation dose on temperature dependence of load drops on the Luders band* ($\Delta\sigma_{LB}$).

mens with a slightly different grain size (ASTM 5.5—10348 series) irradiated to the same dose of 3.9×10^{16} nvt is used to obtain the strain-rate dependence of the lower critical temperature (Fig. 5), and an activation energy for serrated flow of 19 kcal/mol (79.5 kJ/mol) was obtained. One datum was obtained on a specimen with a finer grain size (ASTM 7.5—10346 series) irradiated to the same level. Within the range of grain sizes employed here, no grain size dependence of the kinetics of serrated yielding was noted as reported by Hall [*4*] for unirradiated steel. Thus the neutron irradiation does not seem to affect the kinetics of serrated flow in steels at least up to about 4×10^{16} nvt.

Specimens irradiated to a higher dose of 2.8×10^{17} nvt were tested at various temperatures, and the load-elongation curves are reproduced in Fig. 8. A striking feature of this series is that the Luders band has become "jerky" in contrast to "serrated" in the former cases, although the flow curve has features identical to the unirradiated material. The jerks in the Luders band appear at a still higher temperature. In the temperature range of jerky flow, the lower yield point first stays constant and then drops suddenly to a low value at around 200°C (473 K). As temperature increases, the lower yield point returns to the "expected"

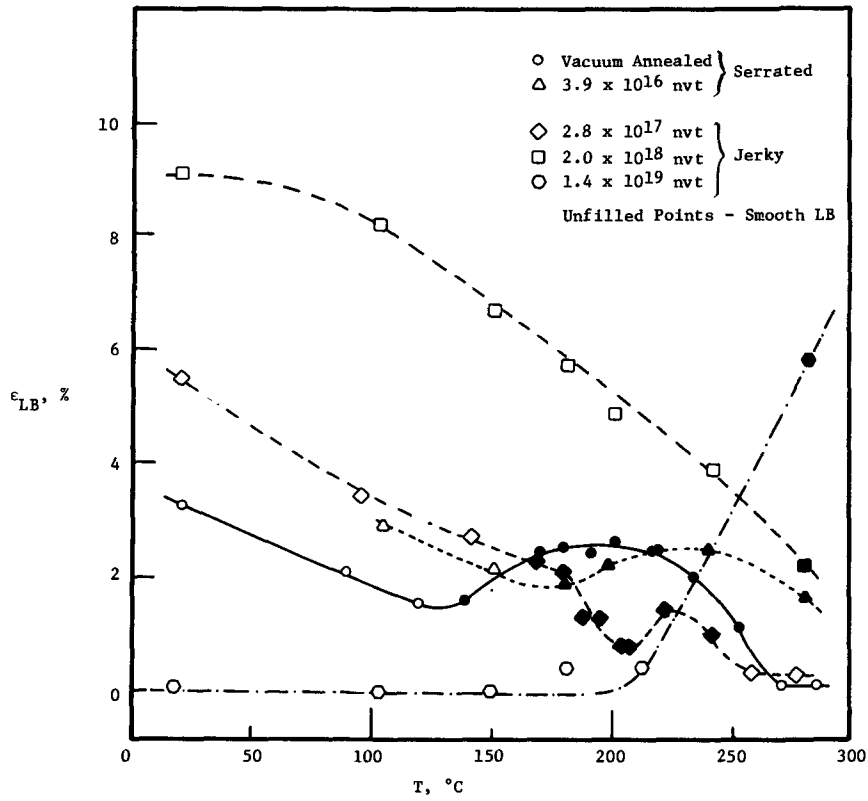

FIG. 7—*Effect of neutron irradiation and temperature on Luders strain. Filled data points indicate serrated or jerky Luders band.*

level and then decreases gradually with temperature (Fig. 3). The complex trends observed here seem to be "real." Tests were repeated at temperatures around 200°C (473 K) to establish the trend, and the sudden drop exhibited in Fig. 3 is not regarded as spurious. The case with ε_{LB} (Fig. 7) is similar. The strain rate dependence of T_c^L was found to follow an Arrhenius type of correlation, and the activation energy for jerky flow was determined to be 19 kcal/mol (79.5 kJ/mole) (Fig. 5). These data in Fig. 5 were obtained on the 10675 series with a slightly finer grain size (ASTM 7.5).

As the neutron fluence increases, the Luders band propagates quite smoothly up to about 280°C (553 K), beyond which jerky bands are noted (Fig. 9). However, the flow curve becomes jerky in a small region of temperature from ~ 179 to ~ 242°C (~ 452 to ~ 515 K). The amplitude of load drops further decreases. The Luders strain at room temperature is quite large and it decreases monotonically with temperature. Some

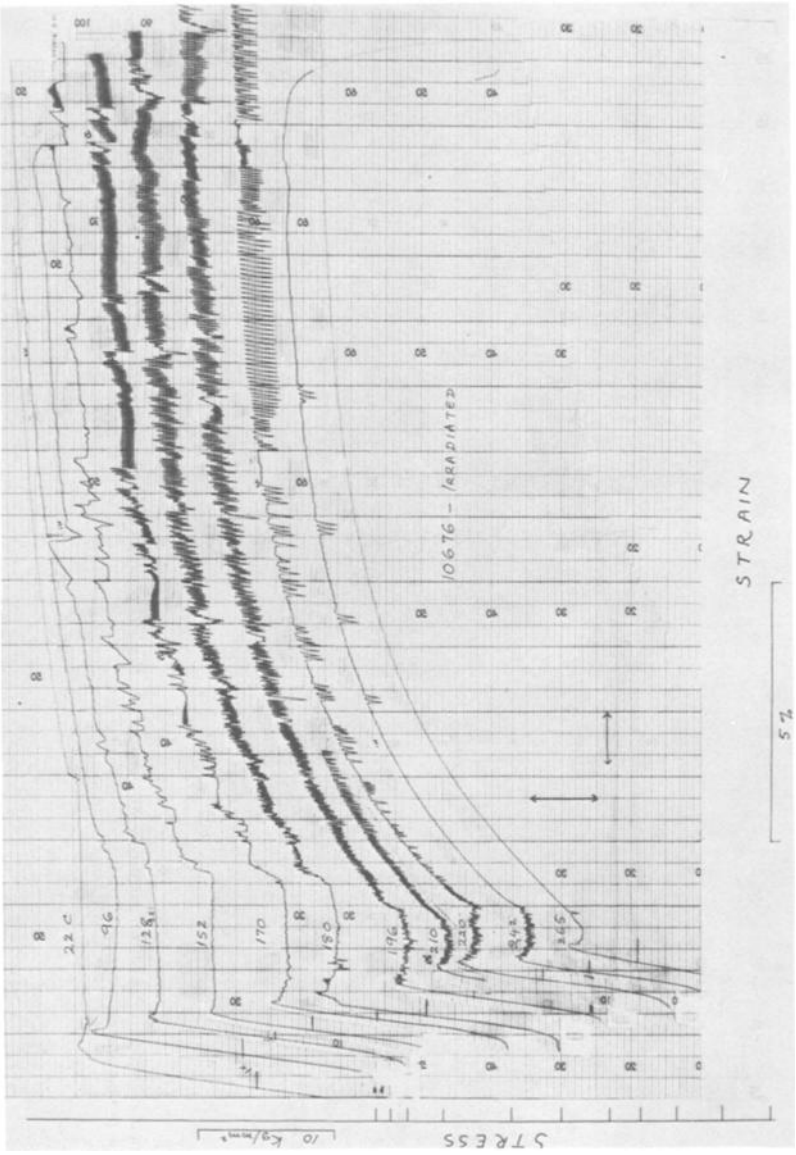

FIG. 8—*Load-elongation curves at different temperatures for irradiated steel (2.8 × 10^{17} nvt); note the jerky Luders bands.*

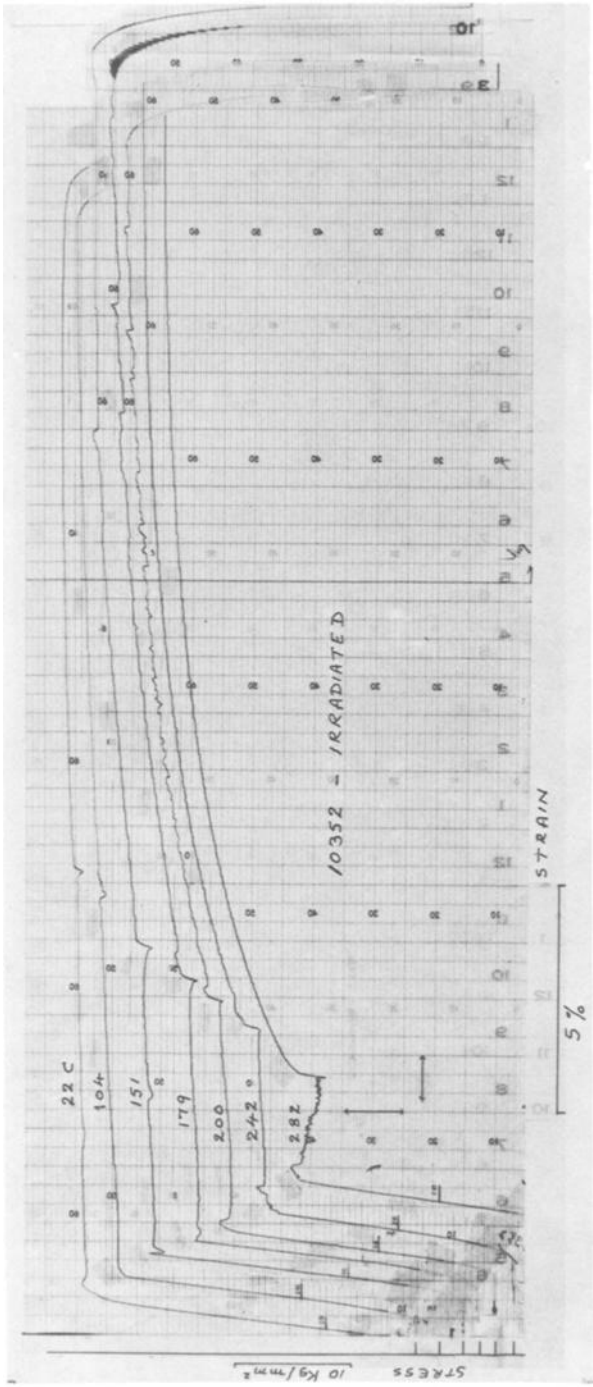

FIG. 9—*Load elongation curves at various temperatures for the 10352 series (2.0 × 10¹⁸ nvt—ASTM 6.5) specimens: Note the larger Luders extensions at low temperatures.*

curves, for example, at 179°C (452 K), indicate necking instabilities reflected as large load drops. A peak at ~ 150°C (423 K) in the lower yield stress (σ_{LY}) noted in Fig. 3 may be a spurious one since the data on the 10353 series with coarser grain size irradiated to the same dose did not indicate any such peak.

At the highest dose used in the present study, namely, 1.4×10^{19} nvt, pronounced radiation embrittlement was noted. From the data on the effect of progressive irradiation dose, it seems that specimens at temperatures to ~ 210°C (483 K) may have failed in the Luders band itself, although it cannot be inferred from the load-elongation curves per se. A Luders band with an extension of about 6 percent at 282°C (553 K) adds to such a contention. Quite often, spurious load drops and steps were observed in the load-time curves of irradiated specimens, as noted earlier by Hall [5]. Lower yield stress decreased from ambient to about 200°C (473 K) and increased slightly beyond. Such a dip in σ_{LY} was reproducible during tests on the 10358 series with coarser grain size. Since the σ_{LY} is not clearly identifiable at some temperatures, the stress at a fixed strain of 0.008 was also plotted in Fig. 3 for the highest dose.

Irradiated Decarburized Steel

There was no evidence of dynamic strain aging in decarburized and irradiated decarburized steel up to about 300°C (573 K). Neutron exposure resulted in radiation hardening and embrittlement. Stress-strain curves were all smooth with no yield point or Luders band in both the unirradiated and irradiated decarburized steel.

Analysis of Little and Harries data [6]

While Little and Harries [6] reported that jerky flow occurs in irradiated (2.5×10^{18} nvt) steels only after a finite plastic strain (ε_o), as in the case of substitutional type of locking, no such transition was observed in the present study with doses up to ~ 10^{19} nvt and temperatures to ~ 300°C (573 K). The reasons for the discrepancy are not clear; however, the Little/Harries material contained different concentrations of impurities (chromium—0.05 percent, nickel—0.11 percent, and manganese—1.22 percent). They observed that ε_0 varied with temperature through an Arrhenius type of relation, but did not analyze their data in detail. If the locking is similar to that due to substitutional type, one finds [15]

$$\dot{\varepsilon} = A\varepsilon_0^{m+\beta} e^{-Q/RT}$$

where

Q = activation energy for jerky flow;

$\varrho = \varrho_0 \varepsilon_0^{\beta}$
$C_V = \beta \varepsilon_0^{m}$
ϱ = dislocation density, and
C_V = concentration of vacancies.

Little and Harries [*6*] gathered data at four different temperatures and three strain rates. An analysis of the same yields

$$\dot{\varepsilon} = A\varepsilon_0^{5} e^{-55\,000/RT}$$

The value of 5 for $m + \beta$ is much larger than the usually observed value of 2 to 3 [*15*]. The significance of the activation energy value of $\sim$ 55 kcal/mol (230 kJ/mol) is not clear. But it is interesting to note that Tamhankar et al [*21*] obtained a value between 50 and 80 kcal/mol for serrated yielding in 10Cr-35Ni-0.39Mn-0.03C alloy ascribable to chromium or nickel diffusion [*15*] associated with Suzuki locking. Their stress-strain curves indicated smooth initial strain, and thus enhanced diffusion is probably present. A similar conclusion was reached by Barnby [*22*], who tested a similar alloy with 18Cr-11Ni in the temperature range 300 to 700°C (573 to 973 K).

Discussion and Conclusions

Present study clearly indicates that the effect of neutron irradiation is to eliminate or decrease the concentration of free interstitial impurity elements (carbon or nitrogen or both) responsible for locking of the dislocations, resulting in blue brittleness or dynamic strain-aging. Progressively increasing the irradiation dose resulted in a transition from "serrated" flow to "jerky" flow at and beyond about 10^{17} nvt. Such a transition was heralded by a complex temperature dependence of σ_{LY} (Fig. 3). Since the activation energies for serrated as well as jerky flow are essentially the same ($\sim$18 kcal/mol), the mechanism of dislocation locking may be regarded as unaffected by neutron damage. Roberts and Owen [*10*] observed jerky flow in iron-carbon alloys at low temperatures and serrated flow at high temperatures. Their results, in addition, indicated that only serrated flow occurs in martensite. They concluded that the jerky flow may be due to Snoek interaction and serrated flow due to Cottrell drag by nitrogen or carbon atoms or both. From the activation energy data alone, such a discrimination is not possible. Explicit functional dependencies of the critical strain rate and stress on the concentration of impurity atoms in solution are to be derived from the experimental data to arrive unequivocally at a conclusion as to the specific operating mechanism. Such information unfortunately cannot be extracted from the present data.

The effect of neutron fluence on the temperature dependence of σ_{LY} is recorded in Fig. 3. The effect of neutron irradiation is essentially twofold: first, it increases the yield stress (hardening), and second, it shifts the temperature of strain-aging peak to higher values. In addition, the temperature region of unstable flow decreases with irradiation. Irradiation hardening ($\Delta\sigma_y$) was found to be proportional to the cube root of the radiation dose

$$\Delta\sigma_y = \sigma_y^i - \sigma_y^0 = A(\phi t)^{1/3}$$

where σ_y^i and σ_y^0 are the room temperature yield stresses of irradiated and unirradiated material, respectively, and ϕt is the neutron fluence (> 1 MeV). A was found to decrease slightly with the grain size, implying that the fine-grain-sized material is less resistant to radiation hardening. These results confirm the earlier studies by Castagna et al [*17*] on iron-titanium alloys and by Trudeau [*18*] on 3.25 percent nickel steel, but are in conflict with Cottrell's prediction regarding the superiority of fine-grained steels to radiation embrittlement [*19*].

It is clear (Fig. 3) that radiation hardening is thermally activated at temperatures above ambient. Since thermal annealing of radiation damage is negligible below $\sim$ 300°C (573 K), the decrease in radiation hardening ($\Delta\sigma_y$) with temperature indicates that the effective stress decreases and that the irradiation-induced obstacles become increasingly transparent as temperature increases [*6*]. The pronounced decrease in $\Delta\sigma_y$ at $\sim$200°C (473 K) is due to the additional effect of the "blue brittle" region. As noted by Little and Harries, these results are in contradiction to the theoretical prediction by Arsenault [*16*] that the irradiation-induced obstacles in α-iron may be athermal. The increase in σ_{LY} at $\sim$ 280°C (553 K) in highly irradiated specimens may be due to starting of the recovery of the irradiation structure.

The effect of irradiation on the temperature variation of stress drops is depicted in Fig. 6. The primary effect is a decrease in the amplitude of load drops, and when jerky flow is noted the temperature range of unstable flow becomes quite narrow. The effect of irradiation on the temperature dependence of ε_{LB} (Fig. 7) is first to make it relatively shallow, and the transition to jerky flow results in a complex dependence. At temperatures below the unstable flow ($\lesssim$ 100°C) ($\lesssim$ 373 K), neutron irradiation results in a large increase in Luders extension. As noted earlier, the data on 10357 series (10^{19} nvt) are not conclusive, and it is quite possible that specimens tested at temperatures about 220°C (493 K) and below failed even during Luders extension.

Murty and Hall [*24*] studied the effect of nitrogen concentration on the dynamic strain-aging behavior in mild steel. Specimens treated in dry hydrogen atmosphere for times up to about 140 min at 650°C (923 K)

revealed serrated stress-strain curves essentially similar to the vacuum-annealed specimens except for a shift in T_c^L to higher temperatures and a decrease in the magnitude of load drops. Longer exposures to dry hydrogen exhibit jerky flow as in the specimens irradiated to large doses. The effect of denitriding on the temperature dependence of Luders strain is also similar to that of neutron irradiation.

The striking similarities between the effects of neutron irradiation and denitriding suggest that nitrogen is predominantly responsible for irradiation hardening, a conclusion reached earlier [*6,8*]. It clearly indicates that radiation damage manifests itself in reduced concentrations of free nitrogen due to the combination of nitrogen with irradiation-induced point defects.

We note in addition that both the appearance and the disappearance of serrations are dependent on the concentration of interstitial impurity atoms. On the other hand, Roberts and Owen [*10*] as well as Keh et al [*3*] claim that the disappearance is concentration-independent. Hirth [*20*] observes that the ending of the serrations should correlate with Cottrell or Snoek drag with inverse concentration-dependence of the strain rate; present results are in agreement with his arguments. The reason for the observations by Keh et al and Roberts and Owen may be due to the quenching of their specimens from high temperatures [*20*]. Since the concentrations of impurity atoms in solution are not known in the present study, no quantitative values for the concentration dependence of T_c^L and T_c^U are obtainable.

Acknowledgments

This work was carried out while the authors were at the University of Newcastle, Australia, and was supported by the Australian Institute of Nuclear Science and Engineering through a fellowship to one of us (KLM). We acknowledge the assistance of R. Hilditch of Australian Atomic Energy Commission and E. A. Palmer of Australian Institute of Nuclear Science and Engineering in arranging for neutron irradiation. We are grateful also to Phine Shaeff for typing the manuscript and to the supervisors at Babcock & Wilcox Company for the necessary arrangements.

References

[*1*] Hall, E. O., *Journal of the Iron and Steel Institute,* Vol. 170, 1952, p. 331.
[*2*] Brindley, B. J. and Barnby, J. T., *Acta Metallurgica,* Vol. 14, 1966, p. 1765.
[*3*] Keh, A. S., Nakada, Y., and Leslie, W. C. in *Dislocation Dynamics,* A. R. Rosenfield, Ed., McGraw-Hill, New York, 1968, p. 381.
[*4*] Blakemore, J. S. and Hall, E. O., *Journal of the Iron and Steel Institute,* Vol. 204, 1966, p. 817.

[5] Hall, E. O., *The Journal of the Australian Institute of Metals,* Vol. 7, 1962, p. 44.
[6] Little, E. A. and Harries, D. R. in *Irradiation Effects in Structural Alloys for Thermal and Fast Reactors, ASTM STP 457,* American Society for Testing and Materials, 1969, pp. 215–240.
[7] McLennan, J. E. and Hall, E. O., *The Journal of the Australian Institute of Metals,* Vol. 8, 1963, p. 191.
[8] Murty, K. L. and Hall, E. O., "Effect of Neutron Irradiation on Static Strain-Aging Kinetics in Mild Steel," paper presented at the American Nuclear Society Winter Meeting, San Francisco, Calif., 1975.
[9] Fettweis, F., *Stahl Eisen,* Vol. 39, 1919, p. 1.
[10] Roberts, M. J. and Owen, W. S., *Metallurgical Transactions,* Vol. 1, 1970, p. 3203.
[11] Russell, B., *Philosophical Magazine,* Vol. 11, 1965, p. 139.
[12] Sylwestrowicz, W. and Hall, E. O., *Proceedings of the Physical Society,* Vol. B64, 1951, p. 495.
[13] Adams, M. A., *Journal of Scientific Instruments,* Vol. 36, 1959, p. 444.
[14] Christ, B. W. and Picklesimer, M. L., *Acta Metallurgica,* Vol. 2, 1974, p. 435.
[15] Hall, E. O., *Yield Point Phenomena in Metals and Alloys,* Macmillan, London, 1970.
[16] Arsenault, R. J., *Acta Metallurgica,* Vol. 15, 1967, p. 1853.
[17] Castagna, M., Ferro, A., Ross, F. S., and Sebille, J. in *The Effects of Radiation on Structural Metals, ASTM STP 426,* American Society for Testing and Materials, 1967, pp. 3–20.
[18] Trudeau, L. P., *Journal of the Iron and Steel Institute,* Vol. 69, 1961, p. 382.
[19] Nichols, R. W. and Harries, D. R. in *Radiation Effects on Metals and Neutron Dosimetry, ASTM STP 341,* American Society for Testing and Materials, 1963, pp. 162–198.
[20] Hirth, J. P. in *Dislocation Dynamics,* A. R. Rosenfield, Ed., McGraw-Hill, New York, 1968, p. 407.
[21] Tamhankar, R., Plateau, J., and Crussard, C., *Revue de Metallurgie,* Vol. 55, 1958, p. 383.
[22] Barnby, J. T., *Journal of the Iron and Steel Institute,* Vol. 203, 1965, p. 392.
[23] Blakemore, J. S. and Hall, E. O., *Journal of Nuclear Materials,* Vol. 29, 1969, p. 238.
[24] Murty, K. L., "Yield Point Phenomena in Mild Steel—Effect of Neutron Irradiation," Final Report, Australian Institute of Nuclear Science and Engineering, 1974, unpublished.

K. R. Garr[1] *and A. G. Pard*[1]

Swelling and Tensile Property Changes in Neutron-Irradiated Type 316 Stainless Steel

REFERENCE: Garr, K. R. and Pard, A. G., "**Swelling and Tensile Property Changes in Neutron-Irradiated Type 316 Stainless Steel,**" *Irradiation Effects on the Microstructure and Properties of Metals, ASTM STP 611*, American Society for Testing and Materials, 1976, pp. 72-90.

ABSTRACT: Specimens of Type 316 stainless steel, given different thermomechanical treatments resulting in either a cold-worked or solution-annealed and aged structure, were irradiated in the Experimental Breeder Reactor-II (EBR-II) at 500 to 600 °C (932 to 1112 °F) to a fluence of 7.4×10^{26} neutrons (n)/m^2 ($E > 0.1$ MeV). Three specimen configurations were used: small sheet tension specimens, small right-circular cylinders for immersion density, and thin foils for transmission electron microscopy (TEM). TEM revealed voids in all specimens. Immersion density indicated swelling in cold-rolled specimens only after irradiation at temperatures near 600 °C (1112 °F). Considerable recovery and precipitation were observed in the cold-rolled specimens. Results of tension tests revealed an increase in strength and decrease in ductility for specimens originally in a solution-annealed and aged condition. Cold-rolled specimens exhibited a decrease in strength and a slight increase in total elongation. True stress-true plastic strain was best described by the Ludwigson equation, $\sigma = K_3\varepsilon^{n_3} \pm \exp(K_4 + n_4\varepsilon)$, in all cases. Irradiation causes a decrease in the work-hardening exponent, n_3, and strength factor, K_3. After irradiation, the values of n_3 and K_3 tended toward common values for both preirradiation treatments.

KEY WORDS: radiation, stainless steels, mechanical properties, swelling, voids, stress-strain diagrams, irradiation

High-fluence swelling and mechanical properties data for Type 316 stainless steel are needed to provide data for design equations so that extrapolations to projected liquid metal fast breeder reactor (LMFBR) goal fluence can be made with more confidence. Data obtained on Type 316 stainless steel will also be used as a basis for comparison with data on advanced and developmental alloys now being considered for use in reactors.

[1]Atomics International Division, Rockwell International Corporation, Canoga Park, Calif. 91304.

The work reported here is a continuation of the Experimental Breeder Reactor-II (EBR-II) irradiation experiment, X100, to determine the effect of the reactor environment on the tensile properties and microstructure of Type 316 stainless steel given different pre-irradiation treatments, and extends these observations to a fluence of 7.4×10^{26} neutrons (n)/m^2 ($E > 0.1$ MeV).

Experimental

Small sheet tension specimens (0.23 by 1.02 mm, with a gage length of 12.7 mm), small right-circular cylinders (3.8 mm diameter by 2.8 mm), and thin foils (3.7 mm square by 0.013 mm) of Type 316 stainless steel were irradiated in EBR-II Subassemblies X100 and X100A. The composition, specimen configuration, and preirradiation treatment designation are given in Table 1. Table 2 gives the details of the pre-irradiation treatments. These are the same alloy heats and pre-irradiation treatments as those reported earlier for Pins A and B of Subassembly X100 [*1*].[2]

Data reported here are for specimens irradiated in Pins C, D, E, or F of EBR-II Subassemblies X100 and X100A. Specimens in Pins C, E, and F received a total fluence of 8.4×10^{26} n/m^2 with 7.4×10^{26} n/m^2 ($E > 0.1$ MeV), or 37.2 displacements per atom (dpa). Specimens in Pin D received 8.3×10^{26} n/m^2 total with 7.3×10^{26} n/m^2 ($E > 0.1$ MeV), or 35.4 dpa. These fluences and dpa values were calculated by the Fast Reactor Materials Dosimetry Center (FRMDC) at Hanford Engineering Development Laboratory (HEDL) [*2*]. Fluences quoted in this report will be for ($E > 0.1$ MeV),except where noted.

The initial and final irradiation temperatures for the capsules in each pin are given in Table 3 [*3*]. Final irradiation temperature for the capsule in Pin D varied from 520 °C (968 °F) at the top to 553 °C (1027 °F) at the bottom and will be referred to as nominally 535 °C (995 °F). Assuming a linear temperature gradient, the gage section of the tension specimens in this pin varied from 532 to 541 °C (990 to 1006 °F), while the cylindrical and foil specimens were in a temperature region of 547 to 552 °C (1016 to 1026 °F). Also included in Table 3 are the temperatures for the capsules in Pins A and B.

Percent swelling was determined from immersion density measurements [3] on the right-circular cylinders, and calculated from void size and density data from foil and tension specimens. Swelling data for tension specimens were obtained from grip ends after testing was completed. Void size and concentration data were obtained from electron photomicrographs using a particle-size analyzer. Immersion densities for the unirradiated cylindrical specimens were obtained from archive samples.

[2]The italic numbers in brackets refer to the list of references appended to this paper.
[3]Density measurements were made at ANL's Idaho Facility, Analytical Laboratory.

TABLE 1—*Composition of Type 316 stainless steel specimens.*

Type of Specimen	Preirradiation Treatment	Weight, %										
		C	Mn	P	S	Si	Ni	Cr	Cu	Mo	Co	Fe
Tension	A, B, C	0.06	1.68	0.022	0.017	0.51	13.63	17.33	0.075	2.32	0.01	balance
Cylinder	C	0.037	1.51	0.021	0.015	0.42	11.56	16.65	0.13	2.39	0.13	balance
Foil	D	0.052	1.72	0.024	0.011	0.64	13.49	16.89	0.10	2.25	...	balance

TABLE 2—*Preirradiation treatments.*

Designation	Treatment	Condition
A	980°C/1 h + 760°C/8 h	solution-annealed and aged (SA + A)
B	980°C/1 h + 760°C/8 h + 22% cold-rolled (CR)	solution-annealed, aged, and cold-rolled (SA + A + CR)
C	1120°C/30 min + 25% CR	solution-annealed and cold-rolled (SA + CR)
D	980°C/1 h + 20% CR	solution-annealed and cold-rolled (SA + CR)

TABLE 3—*Initial and final irradiation temperatures.*

Pin	Initial Temperature °C	Final Temperature °C
A	500	530
B	600	620
C	500	500
D	600	520 to 553
E	500	545
F	600	600

Tension tests were performed in a vacuum ($\sim 7 \times 10^{-3}$ Pa) at a strain rate of 3.3×10^{-4} s^{-1}. Specimens from Pin E were tested at 525 °C (977 °F), while those from Pin D were tested at 575 °C (1067 °F). There was a 15-min hold prior to testing to allow for temperature stabilization.

Helium analysis was determined by mass spectrometry [*4*] at Atomics International (AI) on a piece cut from the grip end of a tension specimen irradiated in Pin E. The analysis showed 18-appm helium in the specimen.

Results and Discussion

Tension Tests

The results of the tension tests are given in Table 4. These results indicate that, for SA + A specimens, irradiation between 500 and 600 °C (932 and 1112 °F) leads to an increase in yield and ultimate strengths and a decrease in uniform and total elongations. For specimens that are SA + CR, however, irradiation in this temperature region produces a reduction in yield and ultimate strengths and a slight increase in uniform and total elongations. These trends are the same as those reported earlier for specimens irradiated in Pins A and B to a fluence of 3.9×10^{26} n/m^2 [*1*], and similar to the observations of Fahr et al [*5*] and Fish et al [*6,7*] for specimens irradiated in the same temperature range.

TABLE 4—*Summary of tension[a] data for Type 316 stainless steel.*

Treatment	Fluence, $E > 0.1$ MeV (n/m^2)	Irradiation Temperature, °C	Test Temperature, °C	Strength		Elongation	
				Yield, MPa	Ultimate, MPa	Uniform, %	Total, %
A	...	...	525	165	461	32	33
A	7.4×10^{26}	500 to 545	525	413	506	12	14
B	...	...	525	580	647	2.4	3.0
B	7.4×10^{26}	500 to 545	525	449	521	6.6	7.4
C	...	...	525	796	831	2.6	2.9
C	7.4×10^{26}	500 to 545	525	463	547	5.0	5.4
A	...	...	575	162	428	33	34
A	7.3×10^{26}	600 to <535>	575	340	433	12	13
B	...	...	575	564	623	3.8	4.4
B	7.3×10^{26}	600 to <535>	575	409	479	7.3	8.0
C	...	...	575	719	786	2.6	2.8
C	7.3×10^{26}	600 to <535>	575	407	478	4.0	4.3

[a]Strain rate = $3.3 \times 10^{-4}\ s^{-1}$.

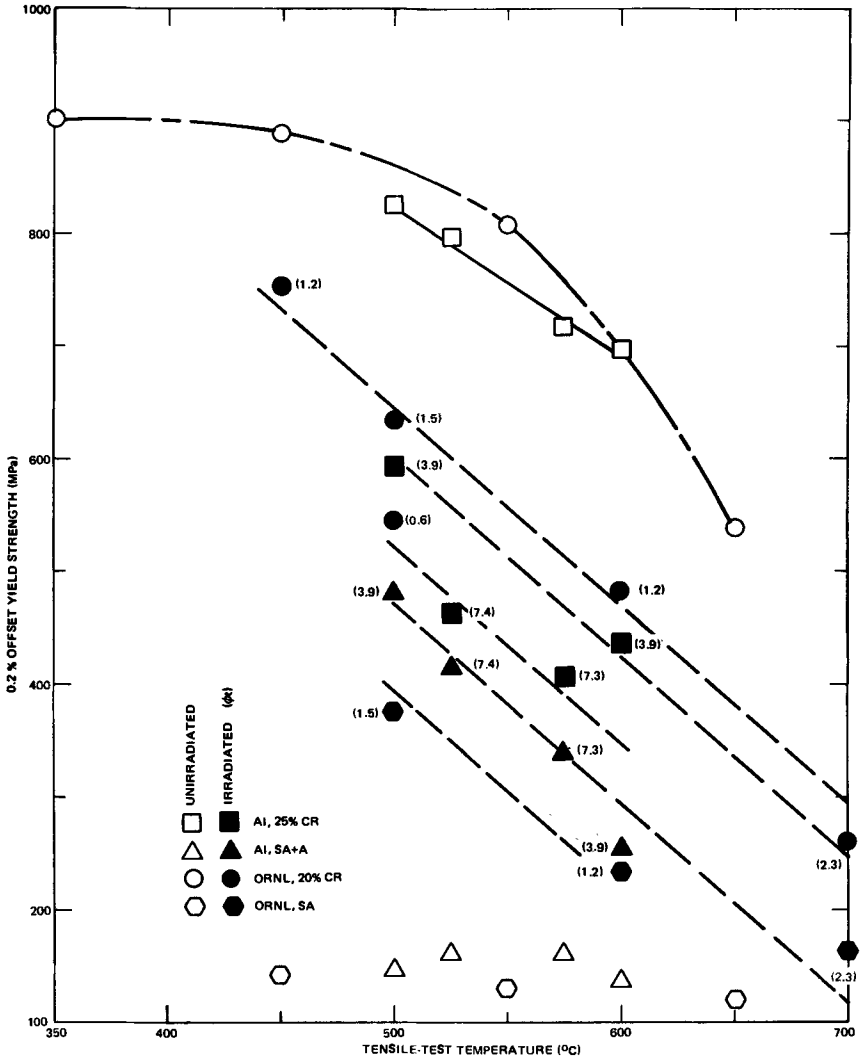

FIG. 1—*Yield strength versus tension test temperature for type 316 stainless steel irradiated near the test temperature.*

Data in Table 4 reveal that the yield strengths of irradiated SA + A and SA + CR specimens are not too different. Figure 1 is a plot of the 0.2 percent yield strength versus tension test temperature for data from Table 4, our previously reported data [*1*], and data of Fahr et al [*5*]. In all cases the irradiation temperature is near the test temperature. The numbers in parentheses are the fast fluence. The data show a shifting of the yield strengths

with fluence to a common value for both cold-worked and annealed materials. The dash lines are only an indication of the trends and have been arbitrarily drawn parallel. It must be pointed up, however, that both Fahr et al [5] and Fish et al [6] reported that the yield strength of specimens that were cold-worked and aged, but not irradiated, was essentially the same as that of the cold-worked and irradiated specimens. Also, transmission electron microscopy (TEM) on our specimens, to be discussed later, does reveal a loss of cold-worked structure in all the cold-rolled specimens. Thus, the reduction in yield strength of the cold-worked material is probably due simply to the time at temperature.

To assess more quantitatively the changes that had occurred in the specimens, the stress-strain curves of several specimens were analyzed. Stress-strain data for each specimen were fitted, by a least-squares method, to the following equations

$$\sigma = K_1\varepsilon^{n_1} \tag{1}$$

$$\sigma = \sigma_0 + K_2\varepsilon^{n_2} \tag{2}$$

and

$$\sigma = K_3\varepsilon^{n_3} + \exp(K_4 + n_4\varepsilon) \tag{3}$$

where

σ = true stress,
ε = true plastic strain, and
K_i, n_i, σ_0 = constants.

Equation 1 is commonly referred to as the power law, while Eq 2 is referred to as the Ludwik equation after the work of Ludwik [8]. Equation 1 is also often referred to as the Ludwik equation; however, we will call it the power law to distinguish it from Eq 2. Equation 3 is a recent modification of Eq 1 by Ludwigson [9]. In the foregoing equations, K_1, K_2, and K_3 are called the strength factors, while n_1, n_2, and n_3 are called the work-hardening exponents. The values of σ_0 and $\exp(K_4)$ represent the true stress at a true plastic strain of zero.

The standard estimate of error (SEE) was computed and used as an indication of the goodness of fit of each equation to the data. SEE was used instead of the coefficient of determination, R^2, because all the equations had high values of R^2 (>0.9999), and SEE was easier to work with.

The values of SEE were computed from the equation

$$\text{SEE} = \left[\sum_{i=1}^{n} (Y_i - Y_{ci})^2/N\right]^{1/2} \tag{4}$$

where

Y_i = the ith data point, and
Y_{ci} = the calculated value of the ith data point.

In addition, the value of ε_u, the true uniform plastic strain before necking, was calculated for each equation and compared with the experimentally determined value. The experimental values of ε_u were obtained by taking the value of elongation at maximum load and converting it to true plastic strain. The value of ε_u was obtained for each of the Eqs 1, 2, and 3 by solving the relationship $d\sigma/d\varepsilon = \sigma$ for ε. The resulting expressions for ε_u are

$$\varepsilon_u - n_1 = 0 \tag{5}$$

$$K_2\varepsilon_u^{n_2-1}(\varepsilon_u - n_2) + \sigma_0 = 0 \tag{6}$$

$$K_3\varepsilon_u^{n_3-1}(\varepsilon_u - n_3) + (1 - n_4)\exp(K_4 + n_4\varepsilon_u) = 0 \tag{7}$$

for Eqs 1, 2, and 3, respectively. Having values for the constants K_i, n_i, and σ_0 from the least-squares fit of the data to Eqs 1, 2, and 3 allows ε_u to be calculated from the foregoing expressions for comparison with the experimentally determined values.

Values of ε_u were the easiest to obtain from Eq 5. Values from Eqs 6 and 7 were obtained by an iterative method. When calculating ε_u from Eq 7, it was found that the exponential term was negligible in all cases. Equation 7 then reduces to the form of Eq 5 with n_3 instead of n_1. If data are analyzed to the experimentally determined value of uniform elongation, the power-law term in Eq 3 will always describe the material behavior in this region, that is, the region of ε_u. Thus, the exponential term in Eq 7 will always be negligible. We believe this is a general feature of Ludwigson's method [*9*] to determine the constants in Eq 3. Numerical solutions have been obtained and plotted by Ono [*10*] for Eq 6.

In general, Eq 1 could be fitted to the data in all cases. However, if one plots log true stress versus log true plastic strain, one observes that the data for most of the specimens do not correspond to a straight line. Most specimens exhibit either a concave or a convex shape when so plotted. Concave-shaped curves have been observed many times and often can be fitted to Eq 2. It was the concave-shaped curves that also led Ludwigson to develop his modification of the power law [*9*].

To our knowledge convex curves have been previously observed only once, by Fahr et al [*5*]. Fahr et al, however, observed convex curves for data from some of the unirradiated as well as irradiated specimens, whereas all of the convex curves that we observed were for data from irradiated specimens.

In order to fit the data of specimens exhibiting convex curves on a log true stress versus log true strain plot, Eqs 2 and 3, were changed slightly. Equation 2 was written as $\sigma = -\sigma_0 + K_2\varepsilon^{n_2}$. Even with this modification, considerable difficulty was encountered. The values of σ_0 were of the order of 3000 to 4000 with a loss of sensitivity, that is, the data were small compared to these values. This produced a strong linear correlation between σ_0 and K_2 which, in turn, made computation impossible. Graphical solutions for specimens with convex curves were obtained with $\sigma_0 \approx 3000$ to 4000, $K_2 \approx 3500$ to 5000, and $n_2 \approx 0.02$. Equation 3 was changed to read $\sigma = K_3\varepsilon^{n_3} - \exp(K_4 + n_4\varepsilon)$. This generally produced satisfactory results. These changes also changed Eqs 6 and 7 slightly.

Changing the sign of σ_0 and the exponential term in Eqs 2 and 3 resulted in equations that no longer corresponded to a physical model. For example, Ono [*10*] has pointed up that σ_0 in Eq 2 may be interpreted as the thermally activated component of the flow stress. Also, σ_0 in Eq 2 and the term $\exp(K_4)$ in Eq 3 are the true stress at the true plastic strain of zero. Changing the sign of these terms produces a negative stress at zero true plastic strain which we knew to be physically unrealistic. We realized these discrepencies when we made these changes. Our intent, however, was simply to see if they would fit the data mathematically, and we were not concerned with the physical model *per se*.

A summary of the constants obtained upon fitting the data to each of Eqs 1, 2, and 3, or their modifications, is given in Tables 5, 6, and 7, respectively. Also included in each table is the value of SEE, the value of ε_u obtained using the appropriate constants in Eqs 5, 6, or 7 or their changes, and the observed value of ε_u. Table 5 also has the preirradiation treatment, irradiation history, and tension test temperature.

Examination of the tables reveals that the best fit to the data for all specimens was obtained with Eq 3 (smaller values of SEE). In general, the calculated values of ε_u do not agree with the observed values, and the work-hardening exponents n_1, n_2, and n_3 are lower in the irradiated specimens compared with their unirradiated counterparts. The strength factors K_1, K_2, and K_3 do not vary in the same manner in all cases for the irradiated specimens.

Looking specifically at Table 7, which gives the constants obtained for Eq 3, for which the best fit to the data was obtained, reveals that the strength factor, K_3, and the work-hardening exponent, n_3, are lower in the irradiated specimens for both preirradiated treatments. Also, values of K_3 and n_3 are about the same for all irradiated specimens, particularly K_3. The values of K_4 do not reveal a systematic variation, whiie n_4 is lower, more negative, in the SA + A irradiated specimens and higher, less negative, in the SA + CR irradiated specimens. The values of K_3 and n_3 describe the behavior of the material at higher strains while K_4 and n_4 describe the deviation from this

TABLE 5—*Summary of constants for data fit to* $\sigma = K_1 \varepsilon^{n_1}$.

Specimen	Treatment	Fluence $E > 0.1$ MeV (n/m^2)	Irradiation Temperature, °C	Test Temperature, °C	Observed ε_u	K_1, MPa	n_1	SEE	Calculated ε_u
901	A	...	...	500	0.305	564	0.238	103.4	0.238
920	A	...	...	525	0.267	534	0.214	87.7	0.214
927	A	...	...	575	0.269	749	0.306	27.0	0.306
907	A	...	...	600	0.295	677	0.275	42.7	0.275
A1	A	3.9×10^{26}	500 to 530	500	0.049	722	0.066	2.8	0.066
A2	A	3.9×10^{26}	500 to 530	500	0.059	751	0.095	11.4	0.095
E3	A	7.4×10^{26}	500 to 545	525	0.109	712	0.109	5.7	0.109
E4	A	7.4×10^{26}	500 to 545	525	0.102	600	0.059	12.1	0.059
D3	A	7.3×10^{26}	600 to <535>	575	0.098	567	0.089	7.0	0.089
B2	A	3.9×10^{26}	600 to 620	600	0.134	583	0.149	11.2	0.149
896	C	...	...	500	0.014	1780	0.154	12.1	0.154
914	C	...	...	525	0.013	1807	0.174	12.5	0.174
917	C	...	...	575	0.016	2013	0.213	13.2	0.213
912	C	...	...	600	0.016	2243	0.255	14.1	0.255
A3	C	3.9×10^{26}	500 to 530	500	0.018	1275	0.14	8.3	0.14
E1	C	7.4×10^{26}	500 to 545	525	0.029	1436	0.251	19.7	0.251
E2	C	7.4×10^{26}	500 to 545	525	0.054	880	0.126	12.6	0.126
D1	C	7.3×10^{26}	600 to <535>	575	0.030	780	0.123	6.2	0.123
B6	C	3.9×10^{26}	600 to 620	600	0.037	850	0.130	11.2	0.130

TABLE 6—*Summary of constants for data fit to* $\sigma = \sigma_0 + K_2 \varepsilon_u^{n_2}$.

Specimen[a]	Observed ε_u	σ_0, MPa	K_2, MPa	n_2	SEE	Calculated ε_u
901	0.305	130	1291	0.715	6.9	0.627
920	0.267	121	921	0.555	17.6	0.462
927	0.269	128	1100	0.68	4.4	0.582
907	0.295	103	986	0.587	6.0	0.508
A1	0.049	−3000	3699	0.01	...	...
A2	0.059	689	−64.9	−2.36	4.8	...
E3	0.109	...	...	...	...	...
E4	0.102	373	383	0.34	4.7	0.111
D3	0.098	204	416	0.20	4.4	0.114
B2	0.134	214	602	0.46	2.5	0.281
896	0.014	513	3193	0.472	6.3	0.376
914	0.013	430	3099	0.45	8.0	...
917	0.016	342	3361	0.46	10.2	0.398
912	0.016	219	3049	0.41	12.2	0.370
A3	0.018	...	...	...	...	...
E1	0.029	−4484	5467	0.022	15.9	...
E2	0.054	911	−198	−0.16	6.4	...
D1	0.030	...	...	...	...	...
B6	0.037	...	...	...	...	...

[a] See Table 5 for specimen history.

behavior at the lower strains. Thus, the behavior of the irradiated material at higher strains, regardless of the preirradiation treatment, is about the same while the deviation at low strains shows some variation.

Microstructural Observations

Solution-Annealed and Aged Specimens—Prior to irradiation, the microstructure consisted of austenitic grains with $M_{23}C_6$ carbides primarily on the grain boundaries and some in the matrix. The dislocation density was typical of an annealed structure, about 10^{12} to $10^{13}/m^2$.

Specimens previously irradiated to 3.9×10^{26} n/m^2 at 500 and 600 °C (932 and 1112 °F) were examined along with the specimens irradiated to the higher fluence of 7.3×10^{26} n/m^2. The irradiations resulted in considerably more precipitates at the grain boundaries. After the higher fluence, some boundaries had a continuous layer of precipitate. A greater quantity of matrix carbides also resulted, as well as unidentified rod-shaped precipitates.

Voids were observed in all specimens. The low-fluence specimen irradiated at 600 °C (1112 °F) had a significant number of voids associated with precipitates. They tended to be larger than isolated voids. Large local variations in void density were apparent in the high-fluence specimen

TABLE 7—*Summary of constants for data fit to* $\sigma = K_3\varepsilon^{n_3} \pm exp\,(K_4 + n_4\varepsilon)$.

Specimen[a]	Observed ε_u	± exp	K_3, MPa	n_3	K_4	n_4	SEE	Calculated ε_u
901	0.305	+	1108	0.457	4.55	−80.7	3.9	0.457
920	0.267	+	1093	0.453	4.51	−45.4	1.9	0.453
927	0.269	+	993	0.434	4.52	−84.5	2.9	0.434
907	0.295	+	979	0.430	4.30	−84.5	3.0	0.430
A1	0.049	−	710	0.062	3.6	−868	1.5	0.062
A2	0.059	−	684	0.068	4.6	−390	3.0	0.068
E3	0.109	+	784	0.15	4.0	−38.2	4.6	0.148
E4	0.102	+	718	0.113	4.44	−142	1.6	0.113
D3	0.098	+	660	0.14	4.2	−96	1.0	0.140
B2	0.134	+	675	0.20	4.38	−140	1.7	0.204
896	0.014	+	2032	0.182	5.24	−1062	3.9	0.182
914	0.013	+	2041	0.199	5.4	−1354	5.3	0.199
917	0.016	+	2270	0.239	5.4	−1302	6.0	0.239
912	0.016	+	2266	0.276	5.5	−1462	9.5	0.276
A3	0.018	−	954	0.074	4.89	−254	5.56	0.074
E1	0.029	−	772	0.093	5.41	−187	10.7	0.093
E2	0.054	−	720	0.067	4.94	−186	2.4	0.067
D1	0.030	−	526	0.019	5.05	−162	1.7	0.031
B6	0.037	−	606	0.038	5.11	−184	2.1	0.040

[a]See Table 5 for specimen history.

irradiated at 600 to 535 °C (1112 to 995 °F); this was not the case for the specimen irradiated at 500 to 545 °C (932 to 1013 °F), which had a very high swelling value (Table 8).

The dislocation structure for irradiated SA + A specimens consisted mostly of line segments with loops. Most of the loops were unfaulted; there were some faulted loops in the low-fluence specimen irradiated at 500 °C (932 °F). This is in variance with our earlier observations of foil specimens irradiated to 3.9×10^{26} n/m^2 at 500 and 600 °C (932 to 1112 °F) where faulted loops were more prevalent [*1*]. Small cavities, which we believe to be helium bubbles, were observed in the low-fluence specimen irradiated at 600 °C (1112 °F). They were observed in the matrix, primarily attached to dislocations. They ranged in size from 2 to 3 nm, which was considerably smaller than the smallest voids observed in that specimen. They were not found at lower temperatures nor in the high-fluence specimen which began irradiation at 600 °C (1112 °F). The general features mentioned in the foregoing are similar to those of Brager and Straalsund [*11*] for SA Type 316 stainless steel.

Solution-Annealed and Cold-Rolled Specimens—Preirradiation microstructure was typical of cold-worked structures with a high dislocation density. No precipitates were observed. After irradiation, polygonization was evident in all cases. However, in the low-fluence specimen irradiated at 500 °C (932 °F), polygonization was not as obvious as in the other specimens. The specimen irradiated at 500 to 545 °C (932 to 1013 °F) to 7.4×10^{26} n/m^2 had polygonization restricted to those areas that were probably the most heavily cold-worked originally. The specimens with an initial irradiation temperature of 600 °C (1112 °F) showed more recovery than specimens with lower initial irradiation temperatures. The high-fluence specimens initially irradiated at 600 °C (1112 °F) were the most advanced in this regard.

The void distribution was inhomogeneous in all cases, being located in regions between deformation bands in low-fluence specimens and between deformation bands and in polygonized regions in high-fluence specimens. Similar low-fluence results have been observed by Brager [*12*]. The void density in these recovered areas was high in some cases, but showed considerable variation even in the same specimen (Fig. 2). Nucleation of voids appears to be continuing in the high-fluence specimens. For the specimen irradiated in Pin E (Fig. 3), swelling in the regions with high void densities reached 11 percent although the overall swelling in the sample was only 2 percent.

Precipitation occurred in all the irradiated SA + CR specimens, mostly in the deformation bands, but also in the grain boundaries. The grain boundary precipitation was not as heavy nor as continuous as in the SA + A specimens. Small cavities were observed in all specimens except in the low-fluence specimen irradiated at 500 °C (932 °F). They were in the matrix

TABLE 8—*Summary of swelling data for Type 316 stainless steel.*

Pin	Specimen Type	Preirradiation Treatment	T_i,[a] °C	T_f,[b] °C	Fluence, $E > 0.1$ MeV (n/m^2)	$(\varrho_0 - \varrho_i)/\varrho_0$, %	$\Delta V/(V - \Delta V)$, %	ϱ_v, voids/m^3	$\bar{d}$, nm
C	cylinder	C	500	500	7.4×10^{26}	$+0.1 \pm 0.2$	...	...	...
D	cylinder	C	600	<535>	7.3×10^{26}	-1.0 ± 0.2	...	...	...
E	cylinder	C	500	545	7.4×10^{26}	$+0.0 \pm 0.2$	...	...	...
F	cylinder	C	600	600	7.4×10^{26}	-3.3 ± 0.2	...	...	...
C	foil	D	500	500	7.4×10^{26}	...	2.0 ± 0.7	3.8×10^{20}	39.5
F	foil	D	600	600	7.4×10^{26}	...	7 ± 2	6.4×10^{20}	53.0
A	tensile	C	500	530	3.9×10^{26}	...	0.1 ± 0.03	3.8×10^{19}	15.8
B	tensile	C	600	620	3.9×10^{26}	...	[c]	...	...
D	tensile	C	600	<535>	7.3×10^{26}	...	1.8 ± 0.6	2.1×10^{20}	37.0
E	tensile	C	500	545	7.4×10^{26}	...	2.1 ± 0.7	1.5×10^{20}	47.3
A	tensile	A	500	530	3.9×10^{26}	...	3.2 ± 1	1.1×10^{21}	33.5
B	tensile	A	600	620	3.9×10^{26}	...	0.8 ± 0.3	3.3×10^{19}	71.1
D	tensile	A	600	<535>	7.3×10^{26}	...	8.8 ± 3	2.3×10^{20}	69.0
E	tensile	A	500	545	7.4×10^{26}	...	22.6 ± 7	4.6×10^{20}	82.1

[a] T_i = initial irradiation temperature.
[b] T_f = final irradiation temperature.
[c] Few voids, no swelling calculated.

FIG. 2—*Electron micrograph of a grip end (unstrained) of a tension specimen of Type 316 stainless steel, 25 percent cold-rolled, irradiated at 600 to 535°C (1112 to 995°F) to 7.3 × 10^{26} n/m^2 (E > 0.1 MeV) and tension at 575°C (1067°F).*

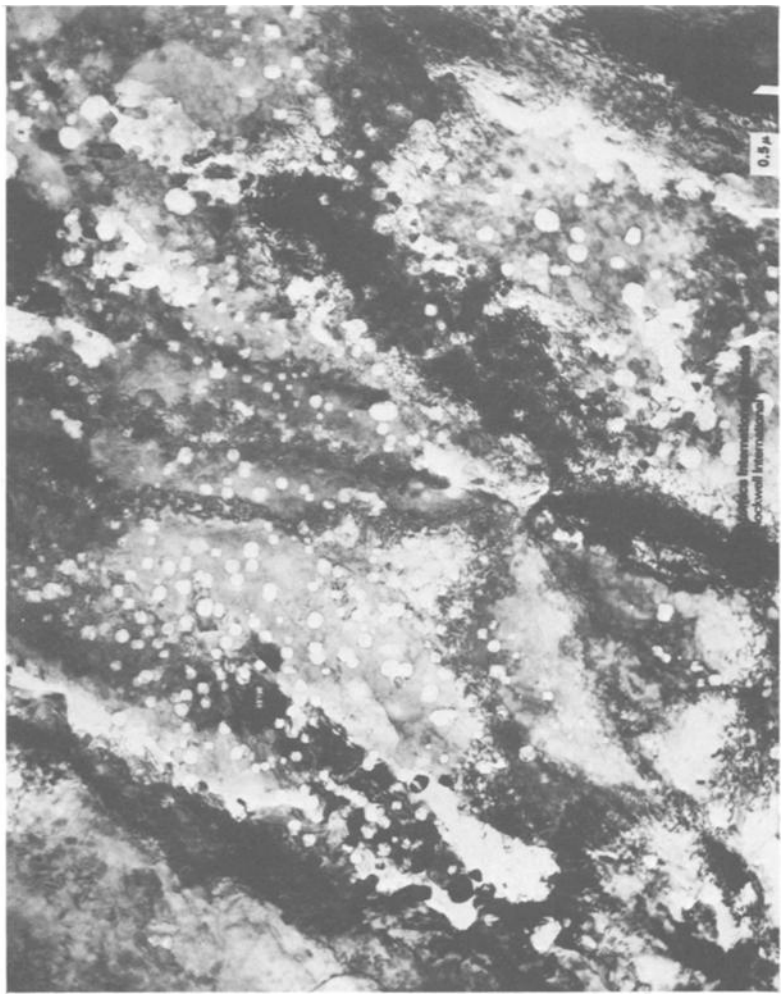

FIG. 3—*Electron micrograph of a grip end (unstrained) of a tension specimen of stainless steel, 25 percent cold-rolled, irradiated at 500 to 545°C (932 to 1013°F) to 7.4 × 10^{25} n/m^2 (E > 0.1 MeV) and tension tested at 525°C (977°F).*

primarily attached to particles and dislocations. We believe these small cavities to be helium bubbles.

Swelling—Results of immersion density measurements and calculations performed on void concentrations and sizes taken from electron photomicrographs are summarized in Table 8. Voids were observed in all specimens; however, the SA + CR tension specimen irradiated in Pin B had very few voids and no swelling value was calculated.

The results have been compared with the equations of Garner et al [*13*], and Garner and Bielein [*14*]. These equations are currently being used in the Nuclear Systems Materials Handbook (NSMH) for design purposes. We find that the immersion density results from Pin F do not agree with the equation of Garner et al [*13*]. In order to get agreement, it was necessary to reduce the incubation fluence, τ, to a value of about 3.8×10^{26} n/m^2.

Swelling calculated from photomicrographs taken of the SA + CR specimens irradiated in Pins D and E is in agreement with the equations of Garner et al [*13*], using a value of $\tau_{mod} - 2$ and temperatures of 525 °C (977 °F) for Pin E and 550 °C (1022 °F) for Pin D. These represent about average temperatures for the pins. The void densities and sizes are also in agreement with the recently reported results of Busboom [*15*].

Using these average temperatures to calculate the swelling for the SA + A specimens from Pins D and E produces good agreement with observed values for Pin D but not for Pin E. The observed swelling vale for the Pin E SA + A specimen is about 2.5 times greater than that calculated using the correlation equation of Garner and Bierlein [*14*].

In an attempt to explain the large swelling in the SA + A specimen from Pin E, and the variations observed in the different heats used in the experiment, we used the equivalent chromium content relationship developed by Bates and Guthrie [*16*]. Using the values given in Table 1 did not produce a significant variation in equivalent chromium, and therefore does not explain the observed variation.

Conclusions

1. Irradiation at temperatures between 500 and 600 °C (932 and 1112 °F) produces an increase in yield and tensile strengths and a decrease in uniform and total elongations of solution-annealed and aged SA + A, Type 316 stainless steel.

2. Irradiation at these temperatures to high fluences ($>3 \times 10^{26}$ n/m^2) produces a decrease in yield and ultimate strengths with a slight increase in ductility in specimens that were solution-annealed and cold-rolled, SA + CR, prior to irradiation.

3. The true stress-true plastic strain relationship is best described by the Ludwigson equation

$$\sigma = K_3\varepsilon^{n_3} \pm \exp(K_4 + n_4\varepsilon)$$

4. In all cases, irradiation causes a decrease in the work-hardening exponent, n_3, and in general also in the strength factor, K_3.

5. After irradiation, the values of K_3 and n_3 are tending toward common values, respectively, for both the SA + A and SA + CR conditions.

6. Significant amounts of recovery occur in cold-rolled material irradiated at 500 to 600 °C (932 to 1112 °F) to fluences greater than 7×10^{26} n/m^2 ($E >$ 0.1 MeV). Voids were observed in all specimens.

7. Results of tension tests and metallography indicate that pre-irradiation thermomechanical treatment will have little effect on the tensile properties of Type 316 stainless steel at the projected goal LMFBR fluence at temperatures of 500 to 600 °C (932 to 1112 °F).

8. Voids were observed in all specimens. Polygonization had occurred in all the cold-worked specimens.

Acknowledgment

We are pleased to acknowledge the assistance of E. M. Działak with specimen preparation, J. A. Mellor with the tension testing, M. D. Ellis and H. Hori with part of the metallography, and P. A. Conners with the computer analysis of the tension data. We thank E. E. Bloom of Oak Ridge National Laboratory for his cooperation on the irradiation of the specimens in EBR-II. We also thank D. W. Keefer and D. Kramer for a critical reading of the manuscript. This work was supported by the U.S. Energy Research and Development Agency under Contract AT(04-3)-824.

References

[1] Garr, K. R., Pard, A. G., and Kramer, D., "The Effect of Neutron Irradiation on Types 316, 321, and Sandvik 12R72 Stainless Steels," *Properties of Reactor Structural Alloys After Neutron or Particle Irradiation, ASTM-STP 570,* American Society for Testing and Materials, 1975, pp. 143–155, or AEC Report AI-AEC-13130, June 1974.

[2] Ulseth, J. A., Fast Reactor Materials Dosimetry Center, Hanford Engineering Development Laboratory, Specimen Fluence (private communications).

[3] Bloom, E. E., Oak Ridge National Laboratory, Specimen Temperatures (private communications).

[4] Farrar, H. and Knox, C. H., *Transactions,* American Nuclear Society, Vol. 11, 1968, p. 503.

[5] Fahr, D., Bloom, E. E., and Stiegler, J. O., *Proceedings,* BNES Conference, British Nuclear Energy Society, Nov. 1972, p. 167.

[6] Fish, R. L., Lovell, A. J., Brager, H. R., and Holmes, J. J., *Proceedings,* BNES Conference, British Nuclear Energy Society, Nov. 1972, p. 187.

[7] Fish, R. L. and Holmes, J. J., *Journal of Nuclear Materials,* Vol. 46, 1973, p. 113.

[8] Ludwik, P., *Elemente der Technologischen Mechanik,* Springer, Berlin, 1909.

[9] Ludwigson, D. C., *Metallurgical Transactions,* Vol. 2, 1971, p. 2825.

[10] Ono, K., *Metallurgical Transactions,* Vol. 3, 1972, p. 749.

[11] Brager, H. R. and Straalsund, J. L., *Journal of Nuclear Materials,* Vol. 46, 1973, p. 134.

[12] Brager, H. R., *Journal of Nuclear Materials,* Vol. 57, 1975, p. 103.
[13] Garner, F. A., Guthrie, G. L., and Bierlein, T. K., HEDL-TME-75-23, Hanford Engineering Development Laboratory, 1975, p. HEDL–95.
[14] Garner, F. A. and Bierlein, T. K., HEDL-TME-75-23, Hanford Engineering Development Laboratory, 1975, p. HEDL–104.
[15] Busboom, H. J., McClellan, G. C., Bell, W. L., and Appleby, W. K., "Swelling of Types 304 and 316 Stainless Steel Irradiated to 8×10^{22} n/cm^2," GEAP-14062, July 1975.
[16] Bates, J. F. and Guthrie, G. L., *Nuclear Technology,* Vol. 27, 1975, p. 286.

R. L. Fish[1] *and J. D. Watrous*[1]

Effect of Fast Reactor Irradiation on the Tensile Properties of 20 Percent Cold-Worked Type 316 Stainless Steel

REFERENCE: Fish, R. L. and Watrous, J. D., **"Effect of Fast Reactor Irradiation on the Tensile Properties of 20 Percent Cold-Worked Type 316 Stainless Steel,"** *Irradiation Effects on the Microstructure and Properties of Metal, ASTM STP 611,* American Society for Testing and Materials, 1976, pp. 91–100.

ABSTRACT: Fast neutron irradiation effects on the tensile properties of 20 percent cold-worked Type 316 stainless steel are presented to fluences of 3.6×10^{22} neutrons (n)/cm^2, $E > 0.1$ MeV (3.6×10^{26} n/m^2, $E > 16$ fJ), at irradiation temperatures of 700 to 1125°F (644 to 880 K). The tests were performed over the range of room temperature to 1600°F (1144 K) employing strain rates of 1.82×10^{-3} to 1.82/min (3×10^{-5} to 3×10^{-2}/s).

Irradiation defect hardening at irradiation temperatures below 900°F (755 K) resulted in strength increases. Thermal annealing of the original cold-work operated to reduce the strength of material irradiated near 1000 and 1100°F (811 and 866 K), in the fluence range investigated. Elongation values initially increased at most irradiation temperatures and then decreased with fluence beyond 10^{22} n/cm^2 (10^{26} n/m^2). Both strength and ductility decreased with increasing temperature at fluences beyond 10^{22} n/cm^2 (10^{26} n/m^2). The 450°F (505 K) unirradiated elongation level was maintained or improved for all irradiation conditions investigated, which suggests that low ductility will not present a problem during refueling operations.

KEY WORDS: radiation, irradiation, stainless steels, tensile strength, fast reactor, strain rate, ductility

Future liquid metal fast breeder reactor (LMFBR) power plants will utilize stainless steels in many core structural applications. The Fast-Flux Test Facility (FFTF) in particular will use 20 percent cold-worked Type 316 stainless steel for fuel cladding, duct components, and other critical core structures. Characterization of the effect of fast reactor environ-

[1] Advanced engineer and manager, Duct, Cladding and Control Elements, respectively, Hanford Engineering Development Laboratory, Westinghouse Hanford Company, Richland, Wash. 99352.

ments on the mechanical properties of this material is therefore essential to the sound design and safe operation of the LMFBR.

The effect of fast neutron irradiation on the tensile properties of 20 percent cold-worked Type 316 stainless steel has been investigated to only a limited extent [*1-3*].[2] Until recently, the data generated by these studies have been sparse above 10^{22} neutrons (n)/cm^2, 10^{26} n/m^2 ($E > 0.1$ MeV, $E > 16$ fJ, used throughout). The present work describes the effects of fast reactor irradiation on the tensile properties to fluences of 3.6×10^{22} n/cm^2 (3.6×10^{26} n/m^2) over the irradiation temperature range of 700 to 1125°F (644 to 880 K). Test temperatures investigated ranged from room temperature to 1600°F (1144 K) at initial strain rates of 1.82×10^{-3}/min to 1.82/min (3×10^{-5} to 3×10^{-2}/s).

Experimental Technique

Tension specimens (2.45 in., 62.2 mm, long) were sectioned from 0.230 in. (5.8 mm) outside diameter by 0.015-in. (0.38 mm) wall tubing. The tubing material was 20 percent cold-worked (20 percent reduction in cross-sectional area by plug drawing) Type 316 stainless steel made to the FFTF developmental specification and designated as N-lot. Table 1 pre-

TABLE 1—*Chemical composition for N-lot tubing.*

Element	Weight %
Nickel	0.006
Carbon	0.054
Manganese	1.59
Phosphorus	0.010
Sulfur	0.006
Silicon	0.48
Nickel	13.48
Chromium	16.45
Molybdenum	2.48
Copper	0.07
Boron	0.0025
Iron	balance

sents the chemical composition for this material. For purposes of irradiation, some of the tubular specimens were placed in sodium-filled subcapsules to minimize temperature gradients while in the Experimental Breeder Reactor-II (EBR-II). The subcapsules were positioned in an irradiation pin to provide a predetermined helium gas gap which, by utilizing gamma heating, provided the desired irradiation temperatures. Melt pellet senti-

[2] The italic numbers in brackets refer to the list of references appended to this paper.

nels with known melting points were used to help provide knowledge of the irradiation temperatures. Low irradiation temperature specimens were obtained using a "weeper" pin which allowed free ingress of reactor sodium coolant.

The tension tests were performed on a hard-beam testing machine with a load-extension recorder. A linear variable differential transformer (LVDT) extensometer was used to measure specimen elongation during the initial stages of each test. At strain levels greater than about 1.5 percent, crosshead movement was used in conjunction with the extensometer to calculate the specimen strain. Compression fittings were used to grip the tubular specimens. A vacuum furnace was used to obtain the desired test temperature with about 15 to 20 min (900 to 1200 s) for specimen heat-up and thermal stabilization. Tests were performed at the irradiation temperature as well as at lower and higher temperatures to simulate refueling, hot cell manipulation, and reactor upset conditions.

Properties Near the Irradiation Temperature

Plots of yield strength and total elongation for each of the nominal irradiation temperatures are presented in Fig. 1 and 2. These figures sum-

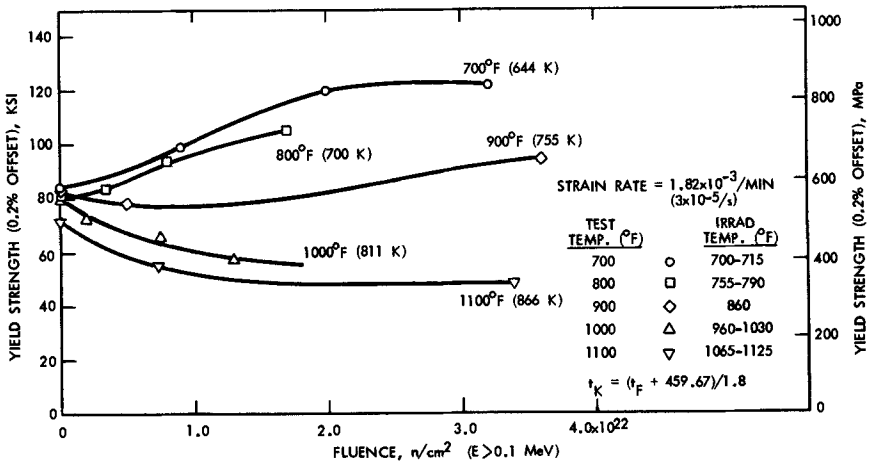

FIG. 1—*Effect of fluence on the yield strength of 20 percent cold-worked Type 316 stainless steel irradiated between 700 and 1125°F (644 and 880 K).*

marize the effect of irradiation temperature on the strength and ductility as a function of fast neutron fluence. The specimen irradiation temperatures are within 50°F (28 K) of the test temperatures. The strain rate used to obtain these data was 1.82×10^{-3}/min (3×10^{-5}/s).

The strength properties shown in Fig. 1 were affected primarily by two

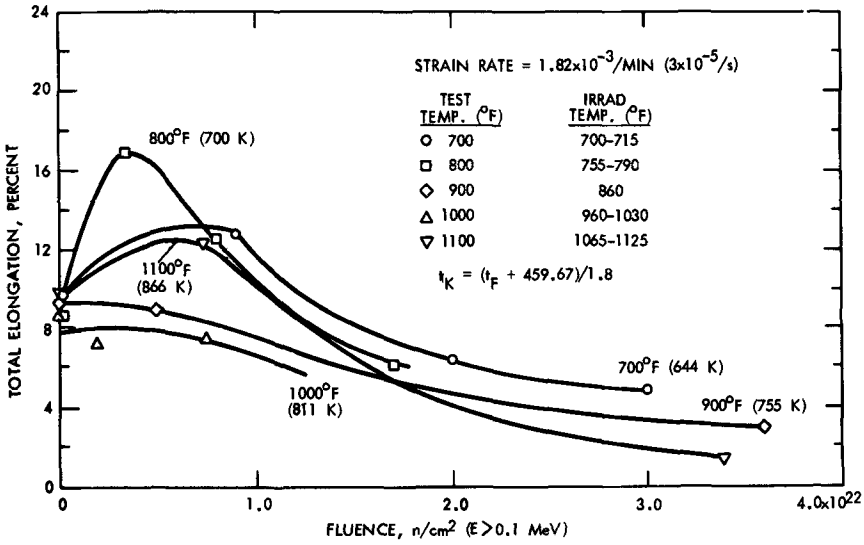

FIG. 2—*Effect of fluence on the total elongation of 20 percent cold-worked Type 316 stainless steel irradiated between 700 and 1125 °F (644 and 880 K).*

competing mechanisms: irradiation defect hardening [*4*], which operates to increase strength properties, and thermal annealing [*5*], which tends to reduce the strength. Irradiation hardening was dominant at 700 °F (644 K) and 800 °F (700 K) where the strength was greater than the unirradiated levels at all fluence conditions investigated. Thermal annealing predominated at 1000 °F (811 K) and 1100 °F (866 K) where the strength decreased rapidly with increasing fluence until about 10^{22} n/cm^2 (10^{26} n/m^2), beyond which the fluence dependence decreased and the strength values leveled out. The interaction of the defect hardening and thermal annealing processes was best demonstrated by the strength parameters measured at 900 °F (755 K) on specimens irradiated at 860 °F (733 K). Initially, the strength decreased from the unirradiated level, reflecting the dominance of the thermal annealing in determining the material strength. At a much higher fluence level (3.6×10^{22} n/cm^2, 3.6×10^{26} n/m^2), the strength was greater than the unirradiated level. This increase in strength was the result of irradiation defect hardening, which evidently has a dominant influence on the strength at high fluences at 900 °F (755 K). At all fluences investigated, the strength properties decreased with increasing irradiation temperature.

Ductility of 20 percent cold-worked Type 316 stainless steel is affected by helium embrittlement [*6,7*] as well as by the thermal annealing and irradiation defect hardening processes. The complex interaction of these processes resulted in the array of curves shown in Fig. 2.

Thermal annealing normally results in increased ductility at the higher temperatures. In the present study, however, an "irradiation assisted" annealing occurred at 700°F (644 K) and 800°F (700 K) to increase the elongation significantly above the unirradiated level at fluences below 10^{22} n/cm^2 (10^{26} n/m^2) as shown in Fig. 2. Material thermally aged at comparable conditions revealed only a slight increase in elongation. At higher fluence levels, the low-temperature irradiation hardening reduced the work hardenability (which leads to premature plastic instability), resulting in the elongation being decreased to below the unirradiated levels.

Helium embrittlement is only effective in reducing ductility in the intergranular failure region, $\geq$ 900°F ($\geq$ 755 K) at 1.82×10^{-3}/min (3×10^{-5}/s). The elongation levels were consequently lower at these higher temperatures with the thermal annealing process operating to produce slightly higher ductilities at 1100°F (866 K). At fluences beyond $\sim 10^{22}$ n/cm^2 (10^{26} n/m^2), the high-temperature ductility, controlled primarily by the helium embrittlement process, decreased continuously with increasing fluence. At the highest fluences investigated (>3×10^{22} n/cm^2, 3×10^{26} n/m^2) the elongation values decreased with increasing temperature, reaching values as low as 0.7 percent uniform and 1.4 percent total elongation at 1100°F (866 K).

Properties at Other Than the Irradiation Temperature

Tension tests performed at temperatures other than the irradiation temperature provide insight as to the material properties under reactor upset, refueling, and hot cell conditions. The yield strength and total elongation are shown in Figs. 3 through 6 for specimens irradiated at temperatures near 700 and 1100°F (644 and 866 K) and tested across a temperature spectrum. These plots illustrate the effect of test temperature and fluence on the tensile properties. The data were obtained at the nominal tensile strain rate of 1.82×10^{-3}/min (3×10^{-5}/s).

At all fluence levels and irradiation temperatures investigated, the strength decreased with increasing test temperature. Evidence of the low-temperature irradiation defect hardening existed to 1000°F (811 K) test temperature with some indication of existence as high as 1200°F (922 K), as shown in Fig. 3. The irradiation hardening was not retained to test temperatures of 1400°F (1033 K) or greater. Predominance of thermal annealing at irradiation temperatures near 1100°F (866 K) is shown in Fig. 5.

Below about 10^{22} n/cm^2 (10^{26} n/m^2) ductility trends are changing rapidly with both test and irradiation conditions due to the complex interaction of the processes affecting ductility. However, above 10^{22} n/cm^2 (10^{26} n/m^2) and at irradiation temperatures of 860°F (733 K) and below,

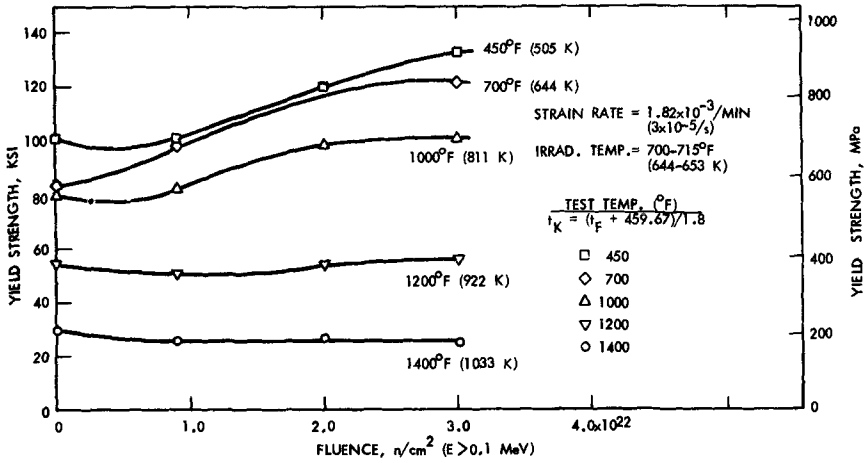

FIG. 3—*Effect of fluence on the yield strength of 20 percent cold-worked Type 316 stainless steel irradiated near 700°F (644 K).*

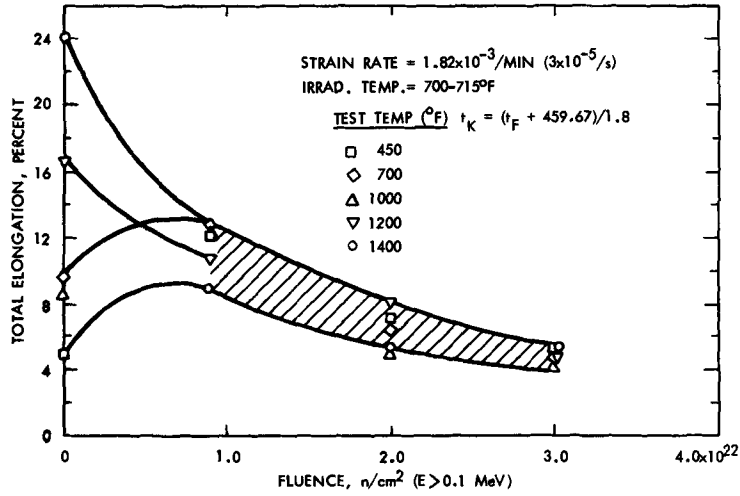

FIG. 4—*Effect of fluence on the total elongation of 20 percent cold-worked Type 316 stainless steel irradiated near 700°F (644 K).*

both uniform and total elongations measured at temperatures above the irradiation temperature were relatively independent of test temperature and decreased with fluence, as illustrated in Fig. 4 for the steel irradiated near 700°F (644 K). At irradiation temperatures of 960°F (789 K) and above, the total elongation decreased with increasing test temperatures,

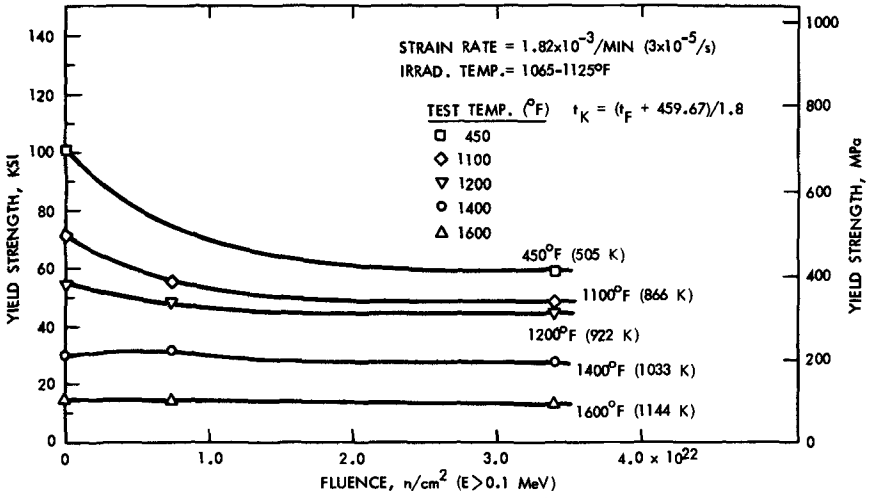

FIG. 5—*Effect of fluence on the yield strength (0.2 percent offset) of 20 percent cold-worked Type 316 stainless steel irradiated near 1100°F (866 K).*

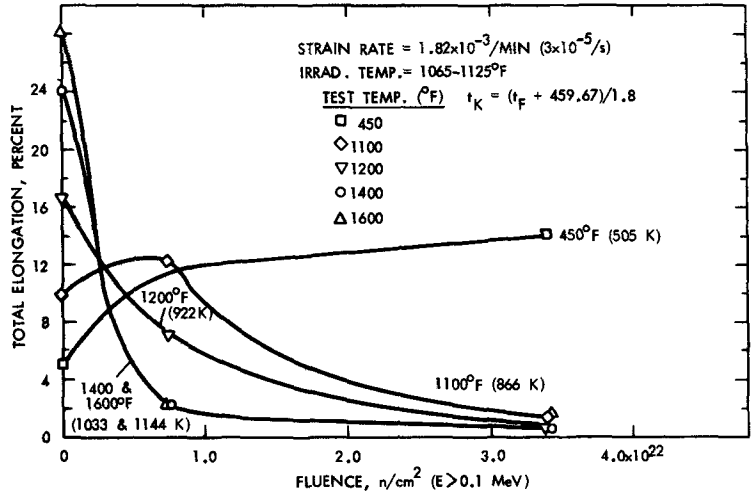

FIG. 6—*Effect of fluence on the total elongation of 20 percent cold-worked Type 316 stainless steel irradiated near 1100°F (866 K).*

reaching values of slightly less than 1 percent at 1200 to 1400°F (922 to 1033 K) at the higher fluence levels (>3 × 10^{22} n/cm², 3 × 10^{26} n/m²), as illustrated in Fig. 6 for the steel irradiated near 1100°F (866 K). At all irradiation temperatures and fluence levels investigated, the total elonga-

tion at the refueling temperature of 450°F (505 K) was maintained equal to or higher than the unirradiated value of 5 percent. This retention of ductility portends that manipulation of fuel pins and ducts during refueling operations will not be a problem from the standpoint of low component ductility, at least within the fluence range investigated.

High Fluence Strain-Rate Effects

Testing was performed over a range of strain rates from 1.82 to 1.82 × 10^{-3}/min (3 × 10^{-2} to 3 × 10^{-5}/s) on specimens irradiated near and tested at temperatures of 900°F (755 K), 1000°F (811 K), and 1100°F (866 K). Tests were not performed at strain rates other than 1.82 × 10^{-3}/min (3 × 10^{-5}/s) on specimens irradiated below 860°F (733 K) because of limited numbers of specimens.

The plot of ultimate tensile strength as a function of strain rate in the fluence range of 1.3 to 3.6 × 10^{22} n/cm^2 (1.3 to 3.6 × 10^{26} n/m^2), Fig. 7, clearly illustrates two regions of deformation behavior. At the higher

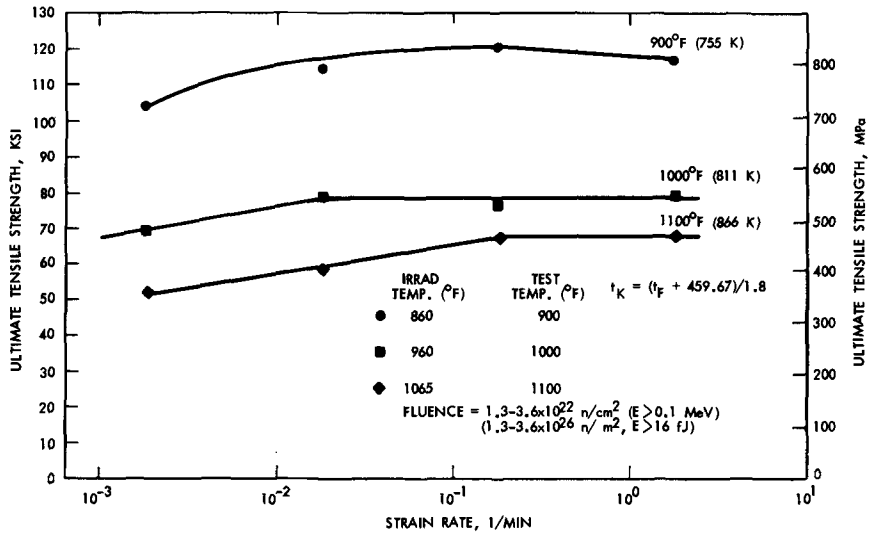

FIG. 7—*Effect of strain rate on the ultimate tensile strength of EBR-II irradiated 20 percent cold-worked Type 316 stainless steel.*

strain rates, strength is independent of strain rate, characteristic of an athermal, transgranular deformation mechanism. Below a "critical strain rate," which depends on temperature, the strength is strain-rate depen-

dent, characteristic of thermally activated deformation processes and intergranular failure. The unirradiated critical strain rates for 20 percent cold-worked Type 316 stainless steel at 1000°F (811 K) and 1100°F (866 K) are approximately 6×10^{-5}/min and 6×10^{-3}/min (10^{-6} and 10^{-4}/s), respectively [*8*]. The critical strain rates for the same temperatures after irradiation to beyond 1.3×10^{22} n/cm^2 (1.3×10^{26} n/m^2) have shifted to higher rates as shown in Fig. 7. This shift is probably due to the helium-assisted separation of grain boundaries during the deformation of irradiated material. The helium embrittlement process thus renders intergranular failure possible over a wider range of strain rates for a given temperature. Although the strain-rate affected behavior of elongation is somewhat more complex than for strength, the general critical strain rate behavior is not inconsistent with that discussed for strength.

Conclusions

Postirradiation tension tests performed on material irradiated in the EBR-II from 700 to 1125°F (644 to 880 K) to fluences of 3.6×10^{22} n/cm^2 (3.6×10^{26} n/m^2) have provided an improved basis for understanding the irradiation effects on 20 percent cold-worked Type 316 stainless steel. Low-temperature irradiation, $\leq$ 900°F (755 K), produced irradiation defect hardening of the matrix, resulting in strength increases. Thermal annealing effects were observed at temperatures of 1000°F (811 K) and 1100°F (866 K) where the strength initially decreased and then leveled out at fluences beyond about 10^{22} n/cm^2 (10^{26} n/m^2). The elongation parameters at 700°F (644 K) and 800°F (700 K) exhibited an increase at low fluence levels that could be attributed to an "irradiation assisted" annealing. Higher temperature ductility at fluences below 10^{22} n/cm^2 (10^{26} n/m^2) was affected by competition between helium embrittlement and thermal annealing processes. Ductility parameters, measured at the irradiation temperature, decreased continuously with fluence beyond 10^{22} n/cm^2 (10^{26} n/m^2), reaching values as low as 0.7 percent uniform and 1.4 percent total elongation at 1100°F (866 K) at a fluence of 3.4×10^{22} n/cm^2 (3.4×10^{26} n/m^2).

At test temperatures above the irradiation temperature, the irradiation defect hardening was retained to temperatures of up to 1200°F (922 K). Total elongation values of slightly less than 1 percent were measured at 1200 to 1400°F (922 to 1033 K) at fluences beyond 3×10^{22} n/cm^2 (3×10^{26} n/m^2). The unirradiated total elongation of 5 percent at the refueling temperature of 450°F (505 K) was retained or improved for all irradiation conditions investigated.

A shift in the critical strain rate required to produce athermal, transgranular deformation and failure was evidenced at 1000°F (811 K) and 1100°F (866 K) after neutron irradiation to fluences greater than 10^{22} n/cm^2 (10^{26} n/m^2).

References

[1] Kawasaki, S., et al, *Journal Atomic Energy Society of Japan*, Vol. 14, No. 6, 1972, pp. 283–289.

[2] Fahr, D., Bloom, E. E., Stiegler, J. O., "Postirradiation Tensile Properties of Annealed and Cold-Worked Type 316 Stainless Steel," *Proceedings*, BNES Conference on Irradiation Creep and Embrittlement, 1973, p. 167.

[3] Garr, K. R., Pard, A. G., and Kramer, D., in *Properties of Reactor Structural Alloys After Neutron or Particle Irradiation, ASTM STP 570*, American Society for Testing and Materials, 1975, pp. 143–155.

[4] Fish, R. L. and Holmes, J. J., *Journal of Nuclear Materials*, Vol. 46, 1973, p. 116.

[5] Guy, A. G., *Elements of Physical Metlalurgy*, July 1960, pp. 421–423.

[6] Barnes, R. S., *Nature*, Vol. 206, 1965, p. 1307.

[7] Kramer, D., Brager, H. R., Rhodes, C. G., and Pard, A. G., *Journal of Nuclear Materials*, Vol. 25, 1968, p. 121.

[8] "Effect of Strain Rate on Flow Stress," *Nuclear Systems Materials Handbook*, TID-26666, Vols. 1 and 2, Part I Structural Materials, Group 1, High Alloy Steels, Section 5, 20% CW 316 Stainless Steel, Property Code 2301.

C. W. Hunter[1] *and G. D. Johnson*[1]

Mechanical Properties of Fast Reactor Fuel Cladding for Transient Analysis

REFERENCE: Hunter, C. W. and Johnson, G. D., "**Mechanical Properties of Fast Reactor Fuel Cladding for Transient Analysis,**" *Irradiation Effects on the Microstructure and Properties of Metals, ASTM STP 611,* American Society for Testing and Materials, 1976, pp. 101-118.

ABSTRACT: In order to determine mechanical behavior under various simulated reactor transient events, internally pressurized specimens of fast flux-irradiated 20 percent cold-worked Type 316 stainless steel fuel pin cladding were rapidly heated until they burst. Tests were conducted at heating rates of 10F°/s and 200°F/s with pressures of 2500 to 14 300 psi (17.2 to 98.6 MPa), resulting in failure temperatures from 1000 to 2000°F (811 to 1366 K). The specimens were taken from subassemblies irradiated in the Experimental Breeder Reactor-II at temperatures from 700 to 1300°F (644 to 978 K). Peak burnup and fluence levels ranged from 28 000 to 50 000 megawatt days per metric ton metal (MWd/MTM) and 2.5 to 4.0 $\times$ 10^{22} neutrons (n)/cm^2 ($E > 0.1$ MeV), respectively.

Irradiation degraded both the failure strain and failure strength, when the transient test conditions resulted in intergranular fracture; intergranular fracture occurred above 1000 to 1200°F (811 to 922 K), depending on strain rate. Below these temperatures the fracture mode is transgranular, so that the failure strength is not reduced.

A correlation based on the ratio of irradiated material failure strain and failure strength was developed to describe the effects of irradiation on the mechanical properties of the cladding. The strain ratio correlation indicates that the failure strain does not further decrease beyond a fluence of 2 $\times$ 10^{22} n/cm^2. The mechanical properties of cladding which had contained fuel during irradiation were degraded more than were the properties of unfueled material.

KEY WORDS: radiation, irradiation, stainless steels, mechanical properties, pinholes, nuclear fuel claddings, ductility, strain rate, safety analysis

The design and licensing of liquid metal fast breeder reactors (LMFBR) require an extensive and basic understanding of fuel pin response to a wide range of off-normal events, which vary from the anticipated mild events to purely hypothetical conditions. These events have been primarily

[1] Senior scientist and senior engineer, respectively, Hanford Engineering Development Laboratory, Westinghouse Hanford Company, Richland, Wash. 99352.

characterized as either loss-of-flow (LOF) or transient overpower (TOP), although undercooling and power/cooling mismatch are also considered.

During severe LOF or TOP transients the temperature of the fuel pin cladding is elevated rapidly above its steady-state service temperature. Such severe events are hypothetical and, even if initiated, would be terminated; nevertheless, the fuel pin behavior must be known for safety analyses. To model properly the fuel pin transient behavior and to predict failure, the mechanical properties (specifically failure strength and ductility) of the 20 percent cold-worked Type 316 stainless steel cladding must be known under thermal and stress conditions encountered in transients. The temperature transient alters the strength, ductility, and deformation behavior by causing recovery, recrystallization, and annealing of the microstructure of the cold-worked and irradiated cladding. Since the extent of the property alteration is dependent upon time as well as temperature, it is imperative that the mechanical properties be determined under appropriate time/temperature conditions. Therefore, a specific testing program is underway at Hanford Engineering Development Laboratory (HEDL), utilizing a recently developed Fuel Cladding Transient Tester (FCTT) [*1-5*][2] to generate the requisite mechanical property information on irradiated and unirradiated fast reactor fuel cladding under temperature ramp conditions.

In a LOF transient, cladding loading is from the plenum fission gas pressure, which is sufficiently low to produce cladding deformation and failure only at high temperatures above 2000°F (1366 K). The failure behavior of low-fluence cladding [1×10^{22} neutrons (n)/cm^2, $E > 0.1$ MeV (1×10^{26} n/cm^2, $E > 16$ fJ)] during high-temperature LOF transients has been characterized with the FCTT and is reported in Ref *2*.

During a TOP event, differential fuel-cladding thermal expansion, intragranular fission gas-induced fuel swelling, and transient release of the intergranular fission gases generate local cladding loadings [*3,5,6*] sufficient to strain the cladding at low temperatures. For example, the seven integral fuel pin TOP tests in the Transient Reactor Test Facility (TREAT), which are reported in Ref *5*, failed at cladding temperatures from 1300 to 1800°F (978 to 1255 K). Therefore, high gas pressures, which simulate the cladding loadings produced by fuel-cladding mechanical interaction, are employed in FCTT tests intended for TOP analyses. The effects of irradiation at 700 to 1300°F (644 to 978 K) to fluence levels of 4×10^{22} n/cm^2 ($E > 0.1$ MeV) (4×10^{26} n/cm, $E > 16$ fJ) on cladding properties for TOP analyses is the subject of this paper.

Fuel Cladding Specimens

Fuel pins, from which cladding specimens were taken for FCTT testing,

[2] The italic numbers in brackets refer to the list of references appended to this paper.

were irradiated in the Experimental Breeder Reactor-II (EBR-II) as part of the fast-flux test facility (FFTF) Driver Fuel Development Program [7]. The dimensions of the 20 percent cold-worked Type 316 cladding were 0.230 outside diameter by 0.015 in. wall (5.84 by 0.381 mm). The fuel pins were irradiated in Subassemblies X096, X097, X158, X193 and X194 at temperatures from 700 to 1300°F (644 to 978 K). Neutron fluences ranged from 0.1 to 4.0 $\times$ 10^{22} n/cm^2 ($E > 0.1$ MeV). Specimens, 2.45 in. (62.2 mm) in length, were cut from various fuel pins from these subassemblies. The fuel was removed by drilling with a $\frac{3}{16}$-in. (4.76 mm) drill. The specimens were filled with a fused-silica rod to reduce the gas volume before end caps were attached to the specimens.

Test Method

Thermal transient tests were performed by pressurizing the tubular specimen to a predetermined load and increasing the temperature from an initial temperature of 700°F (644 K) at a constant rate of 10 or 200F°/s (5.6 or 111 K/s) until rupture occurred. Specimen heating was achieved with an induction generator which was controlled by a function generator to give the desired heating rate. A thermocouple, spot-welded to the specimen, provided the closed-loop control element and temperature measurement. Primary pressure measurement was made with a calibrated Heise gage; during the test the pressure was measured with a strain-gage pressure transducer. The pressures used in testing were from 2500 to 14 300 psi (17.2 to 98.6 MPa). Diametral strain information was obtained by taking posttest-diameter measurements at fixed increments along the axis of the specimen. Additional experimental details are described in Ref *1*.

Unirradiated Cladding Results

Results with FCTT for unirradiated 20 percent cold-worked Type 316 stainless steel cladding have been previously reported [*1*]. It was shown that the failure temperatures increased with decreasing internal pressure. Specimens heated at 200F°/s (111 K/s) were "stronger" than the 10F°/s (5.6 K/s) specimens because less thermal recovery and annealing of the cold-worked microstructure occurred. Under constant-pressure conditions, the majority of the deformation occurred during the last stages of the transient and the cladding strain rate increased rapidly as the failure temperature was approached. Diametral strains at 10F°/s (5.6 K/s) were greater than at 200F°/s (111 K/s) because of more time for recovery or annealing or both. The results for the unirradiated cladding are given as the solid curves in Figs. 1 through 4 and serve as a baseline reference for comparing with the data on the irradiated specimens.

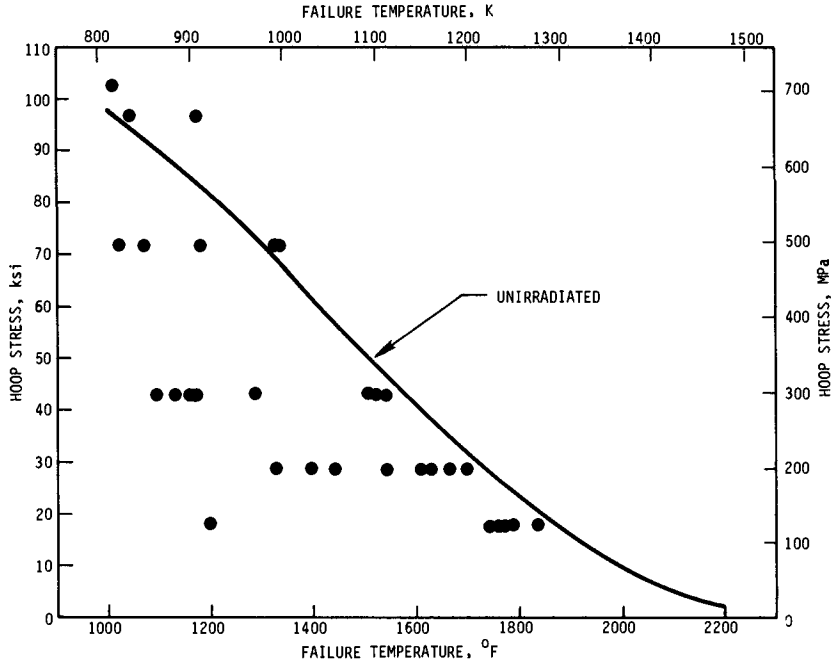

FIG. 1—*Failure stress for 10F°/s (5.6 K/s) thermal transients for irradiated cladding.*

Irradiated Cladding Results

The irradiated cladding specimens may be characterized as exhibiting reduced ductility, and failing at lower temperatures during the transient, than did the unirradiated cladding material. Comparisons of the unirradiated and irradiated cladding failure temperatures are shown in Figs. 1 and 2 for heating rates of 10 and 200F°/s (5.6 and 111 K/s), respectively. In general, the data points lie below the unirradiated cladding curves. This decrease in failure temperature implies that the failure strength of the irradiated material has been decreased. Several high-stress specimens failed at temperatures greater than the corresponding unirradiated material. Test conditions permitted these specimens to fail in a transgranular mode. This increase in strength was due to irradiation hardening [*4*].

Figures 3 and 4 show the cladding diametral failure strain as a function of failure temperature for heating rates of 10 and 200F°/s (5.6 and 111 K/s), respectively. Minimum failure strains are on the order of 0.1 percent at the lower temperatures. For both heating rates, the failure strains increase with increasing failure temperature. At the higher temperatures the maximum strains are 1 to 1.3 percent.

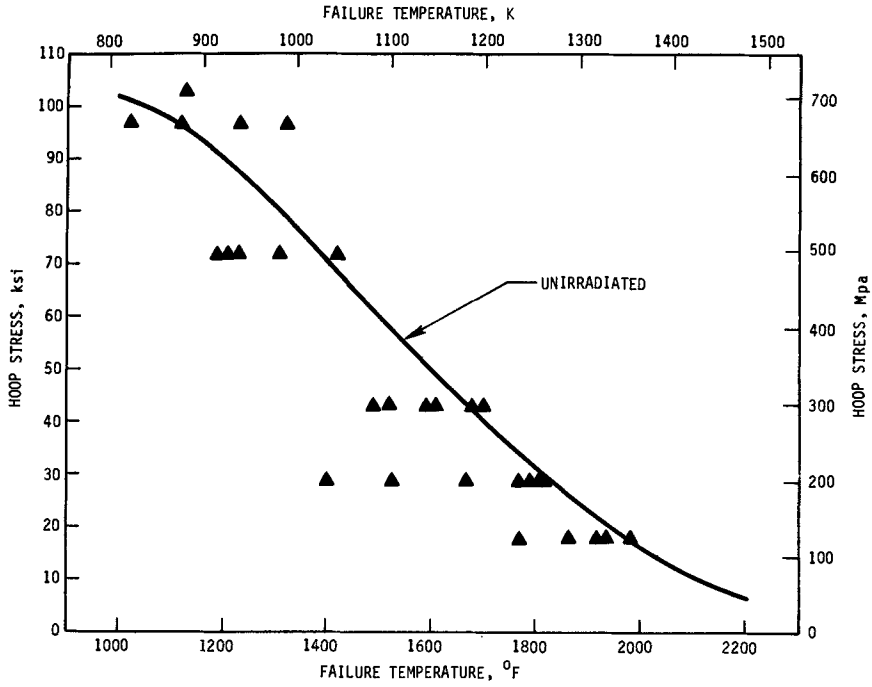

FIG. 2—*Failure stress for 200F°/s (111 K/s) thermal transients for irradiated cladding.*

Irradiation Parameter Dependence

The effect of neutron fluence on the diametral failure strain for specimens tested at 10F°/s (5.6 K/s) is shown in Fig. 5. Dashed lines have been drawn to show the general trend of the data; namely, a decrease in failure strain is observed for increasing neutron fluence.

Figure 6 illustrates the effect of neutron irradiation on the failure temperature by showing the decrease in failure temperature as a function of fluence. Except for the high-pressure tests which failed in a transgranular mode, increased fluence resulted in a greater decrease in failure temperature. Again, the dashed lines are drawn to show the general trend. The data fields of Figs. 5 and 6 are fairly broad due to the wide range of test conditions.

Figures 5 and 6 reveal that an increase in the neutron fluence results in decreases in both the failure strain and failure temperature. Thus the decrease in ductility due to fluence is compounded with an inherent ductility reduction associated with decreasing failure temperature. A proper evaluation of the effect of fluence on the failure strain can be obtained by employing a strain ratio, defined as the ratio of the irradiated failure

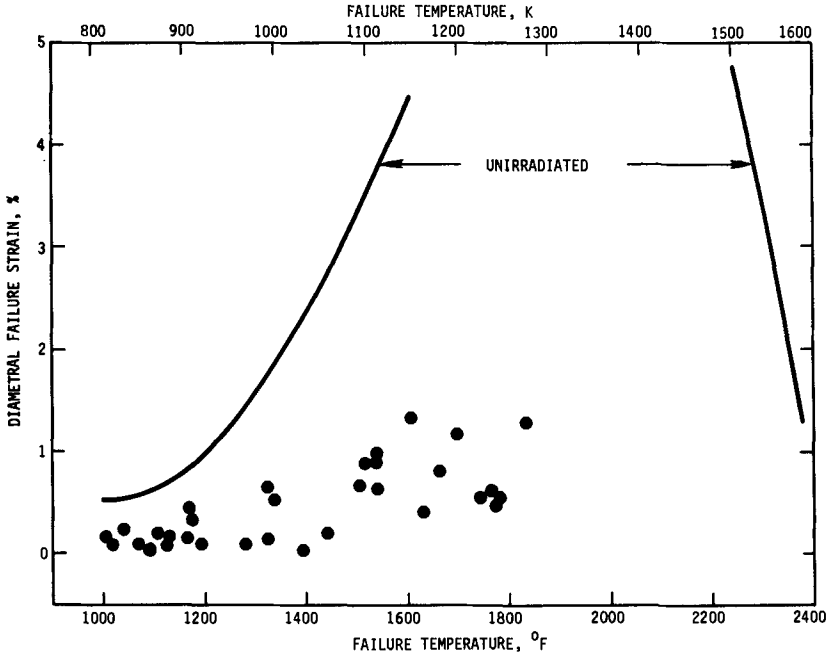

FIG. 3—*Diametral failure strain for 10F°/s (5.6 K/s) thermal transients for irradiated cladding.*

strain to the unirradiated failure strain at the failure temperature for the irradiated specimen. Strain ratio curves were fit to all the failure strain data and are summarized in Figs. 7 and 8. These results indicate that the reduction in ductility occurred at low fluences and has saturated at a fluence of 2×10^{22} n/cm^2.

In the FCTT burst test, a decrease in the failure temperature for an irradiated specimen, relative to the failure temperature at the same gas pressure for an unirradiated specimen, implies that the failure strength has been decreased. For example, an irradiated specimen at 28.8/ksi (198.6 MPa) hoop stress, which failed at 1400°F (1033 K), exhibited only 50 percent of the unirradiated failure strength at that temperature. The results in Figs. 1 and 2 show that the majority of the irradiated specimens failed at a lower temperature than the unirradiated specimens. A stress ratio of the irradiated failure stress to the unirradiated failure stress, at the failure temperature of the irradiated specimen, provides a normalized indication of how the cladding strength has been changed. Figure 9 presents summary stress ratio curves for both heating rates at various gas pressures. While the majority of the curves show a reduction in the stress ratio with fluence, there is a strengthening observed at the higher pres-

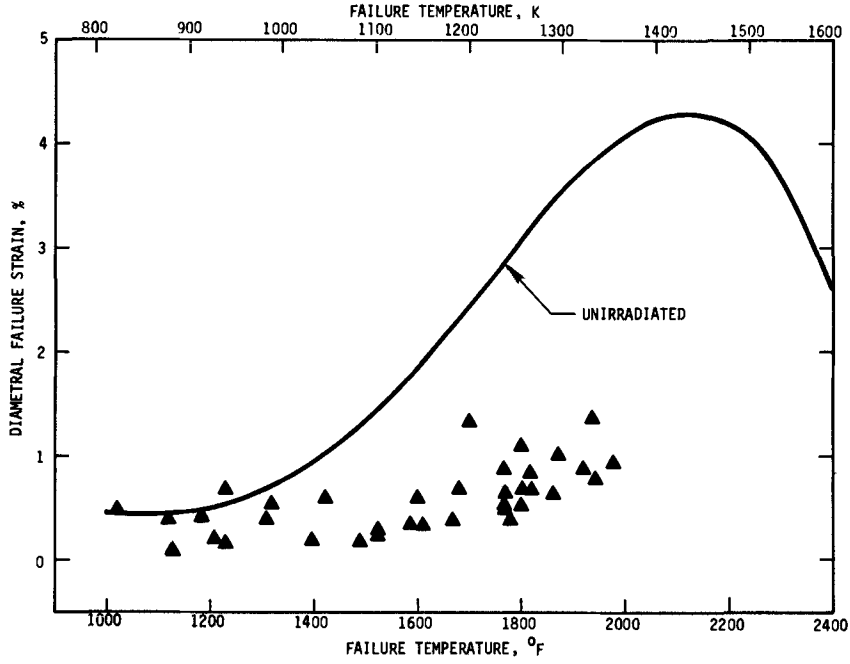

FIG. 4—*Diametral failure strain for 200F°/s (111 K/s) thermal transients for irradiated cladding.*

sures. The occurrence of both a strengthening and reduction in strength is dependent upon test and irradiation conditions, and is discussed in the next section.

Analysis of Irradiated Cladding Failure Behavior

In Fig. 10 the decrease in failure temperature is shown as a function of the failure strain, which demonstrates that the cladding with lower failure strain exhibited the larger decrease in failure temperature, and, consequently, failure strength. This behavior is opposite to that of increasing strength with decreasing ductility commonly exhibited by metals, and is a definite sign that a cracking (noncontinuum) process interferes with the ability of the cladding hoop ligament to bear tensile loads. The decrease in load-bearing capability occurred only under conditions of partial or total intergranular fracture. Intergranular fracture does not inherently require extensive local strain. Hence, if the irradiation and test conditions are appropriate for low-ductility intergranular fracture, then at any highly stressed local region a grain boundary opening or microcrack can occur before the remaining material across the section can bear stress. Conse-

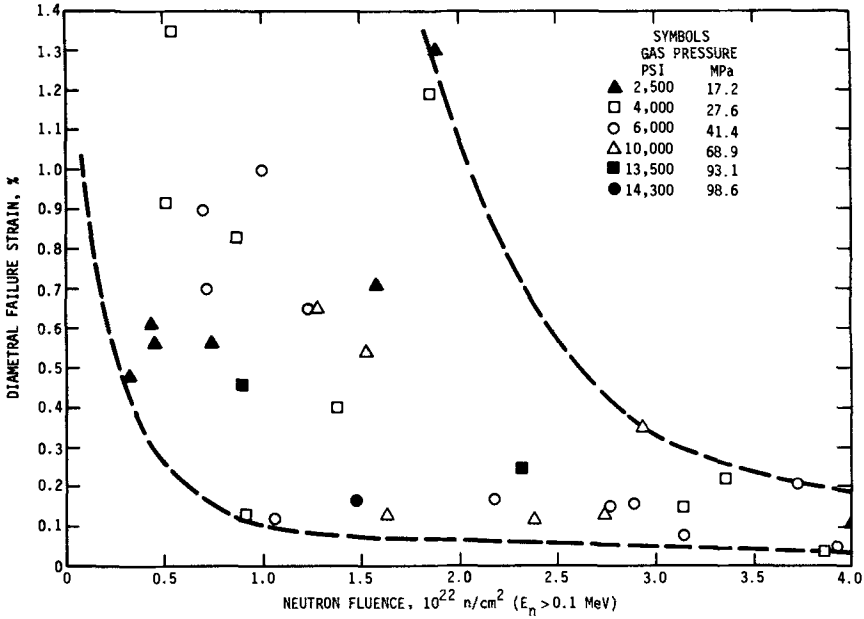

FIG. 5—*Effect of neutron fluence on cladding diametral failure strain for 10F°/s (5.6 K/s) thermal transient.*

quently, the failure strength in tension is reduced. The ductility of intergranular fracture is reduced by helium embrittlement [*8*] and a hard or strong crystal (matrix) [*9*]. Therefore, a higher irradiation fluence should decrease the ductility and reduce the failure strength under conditions of low-ductility intergranular fracture. An example of an intergranular fracture is shown in Fig. 11.

Figures 1 and 2 show that several of the tests at hoop stresses greater than 97.2 ksi (670.3 MPa) had failure temperatures greater than that for the unirradiated material. These test conditions forced a high strain rate at sufficiently low temperatures that transgranular failure occurred, which allowed the radiation hardening to increase the failure strength. Therefore, below about 1200°F (922 K) at 200F°/s (111 K/s) and below about 1000°F (811 K) at 10F°/s (5.6 K/s) transgranular failure can occur, and irradiated failure strengths equal to or greater than those for the unirradiated material are anticipated.

A cross section of a specimen which failed in a transgranular mode is shown in Fig. 12. This specimen failed at a temperature about 200°F (111 K) greater than an unirradiated specimen at the same pressure. It was irradiated at 825°F (714 K) to a fluence of 1.6×10^{22} n/cm^2 ($E > 0.1$ MeV). A small specimen of the fracture surface was examined by scan-

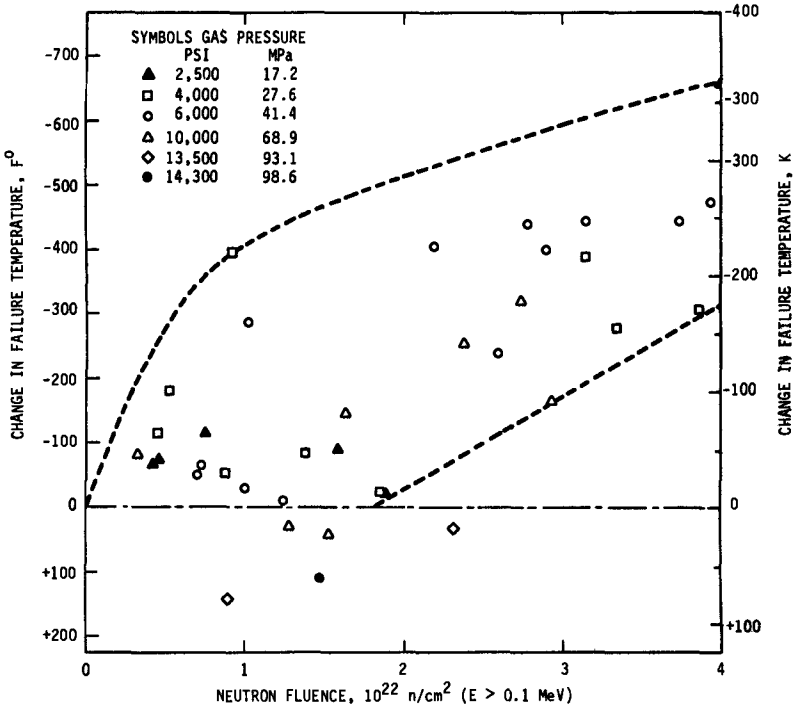

FIG. 6—*Effect of neutron fluence on change in failure temperature for 10F°/s (5.6 K/s) thermal transients.*

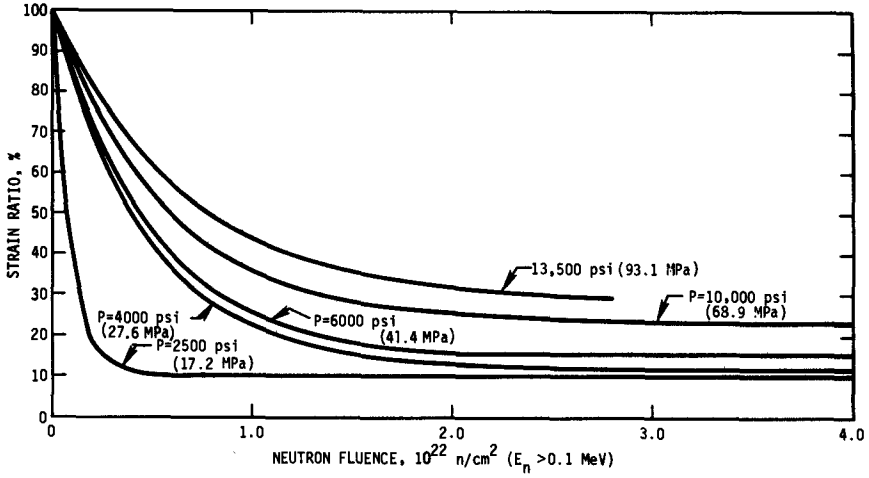

FIG. 7—*Effect of neutron fluence on transient strain ratio for a heating rate of 10F°/s (5.6 K/s).*

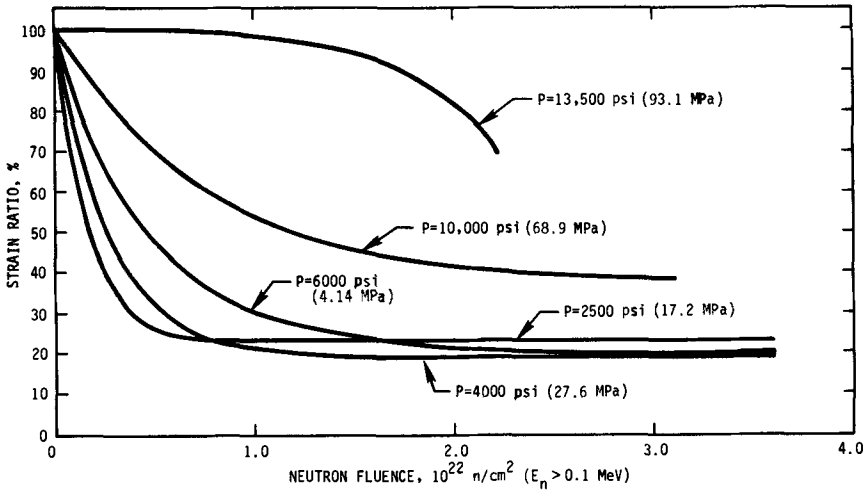

FIG. 8—*Effect of neutron fluence on transient strain ratio for a heating rate of 200F°/s (111 K/s).*

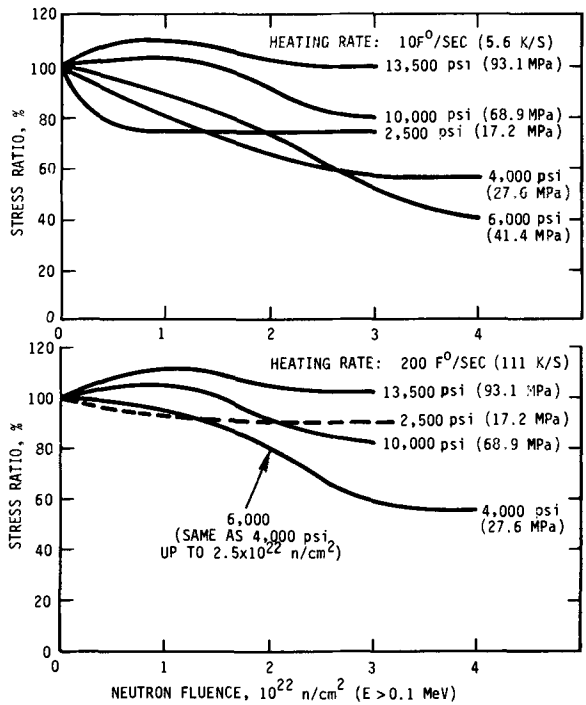

FIG. 9—*Effect of neutron fluence on transient stress ratio.*

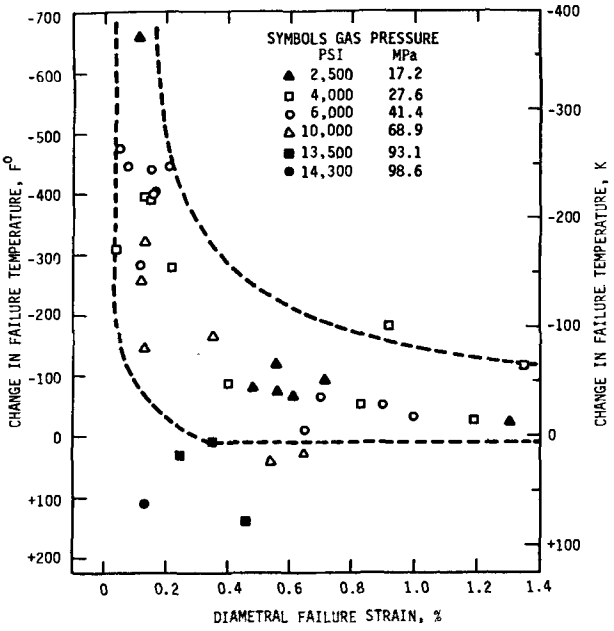

FIG. 10—*Relationship between change in failure temperature and diametral failure strain during a 10F°/s (5.6 K/s) thermal transient.*

ning electron microscopy (SEM). The SEM fractograph of this specimen in Fig. 13 shows that plastic dimpling has occurred. These dimples are microvoids which have been formed at interfaces between the matrix and particles such as carbides, and at imperfections. These voids grow by shear deformation processes until they coalesce to give the cavities or dimples shown in the picture.

The two types of fracture, intergranular and transgranular, require large differences in the energy absorbed before failure occurs. In a standard tension test the total area under the stress-strain curve is indicative of the toughness of the material. Also, this area is a measure of the amount of work done on the specimen per unit volume. Similarly, in a FCTT test, the product of the hoop stress and failure strain is also a measure of toughness. In a cladding transient test the hoop stress is essentially constant throughout the test; thus, the product $\sigma_H \cdot \varepsilon_f$ is a measure of the toughness and is analogous to the work done in a tension test.

Values for the product $\sigma_H \cdot \varepsilon_f$ at a heating rate of 10F°/s (5.6 K/s) are shown in Fig. 14 as a function of neutron fluence. Similarly Fig. 15 is for 200F°/s (111 K/s). Fracture modes are indicated in the figures for those specimens which have been examined metallographically. The product

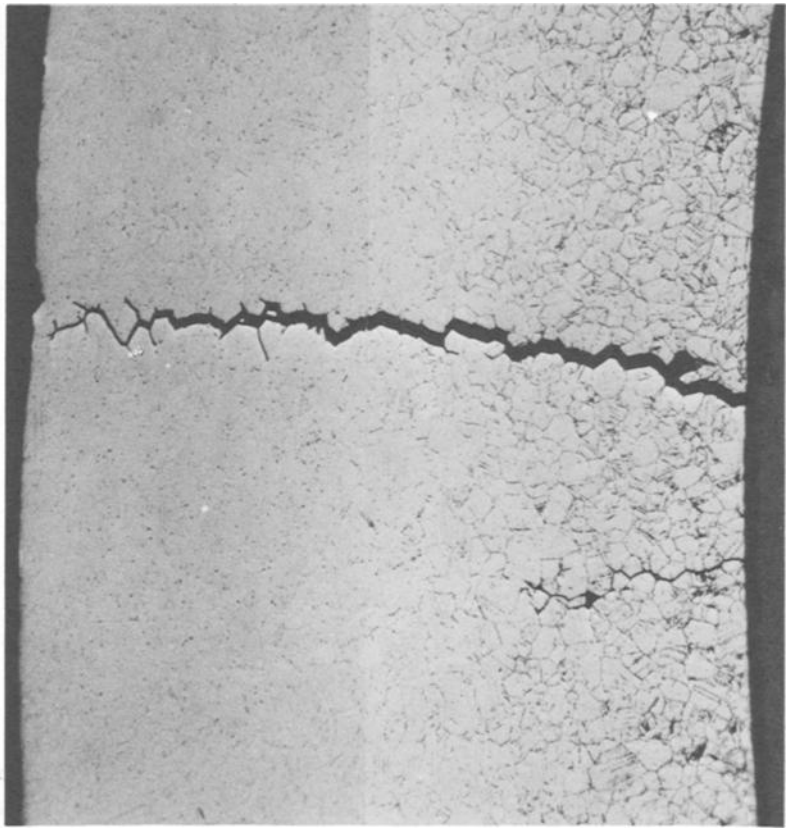

FIG. 11—*Transverse section of a specimen tested at 10F°/s (5.6 K/s) with 4000 psi (27.6 MPa) gas, which failed at 1325°F (991 K) and exhibiting intergranular fracture* (×200).

$\sigma_H \cdot \varepsilon_f$ is more affected by failure strain than by hoop stress, since the ε_f values vary by a factor of 20 while σ_H values vary by only a factor of 7.

In Fig. 14, the lower edge of the data field is bounded by specimens exhibiting an intergranular fracture of the "pinhole" type. Data points with higher $\sigma_H \cdot \varepsilon_f$ values are for intergranular fractures occurring at higher failure temperatures (under which conditions the failure strain was much greater) or for mixed mode (intergranular → transgranular). The general trend of the data field is toward lower values of $\sigma_H \cdot \varepsilon_f$ at higher fluences. There were only three tests at the highest fluence of 4×10^{22} n/cm^2; more tests under different test conditions might produce higher $\sigma_H \cdot \varepsilon_f$ values.

In Fig. 15 there are three major differences compared with Fig. 14. First, the number of pinhole failures has decreased significantly. Next, the

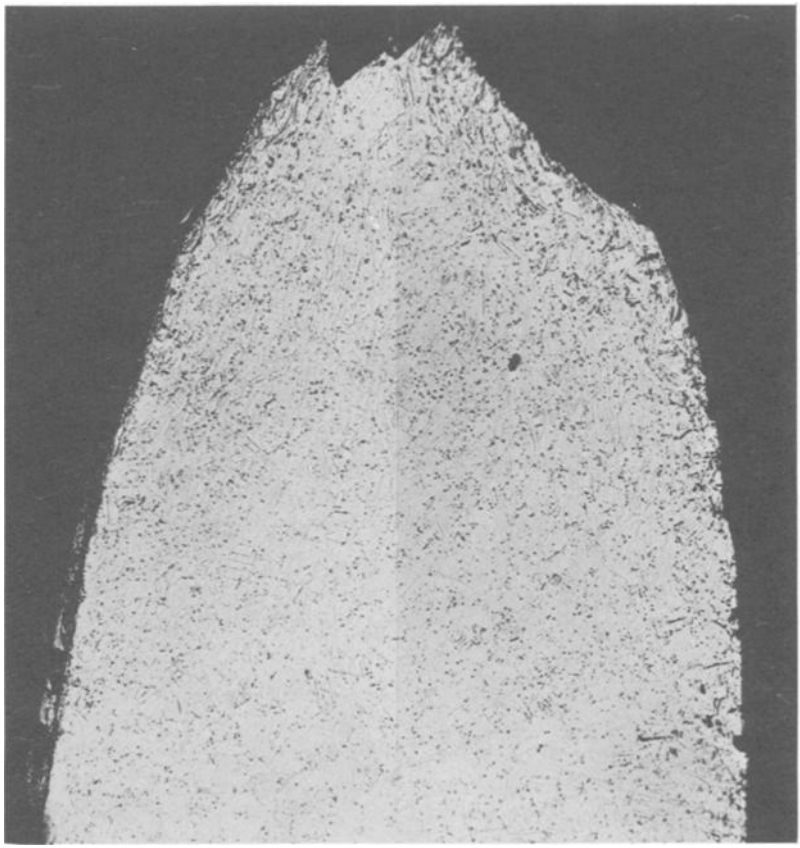

FIG. 12—*Transverse section through the failure site of a specimen tested at 200F°/s (111 K/s) with 14 300 psi (98.6 MPa) gas, which failed at 1125F° (880 K) by a transgranular fracture mode (×200).*

lower and upper limits of the data field lie at higher values of $\sigma_H \cdot \varepsilon_f$. Finally, the specimens exhibiting the higher $\sigma_H \cdot \varepsilon_f$ values exhibit a transgranular fracture. These differences can be attributed to the difference in strain rates associated with the heating rates. The strain rates for the specimens heated at 10F°/s (5.6 K/s) are on the order of 10^{-4} to 10^{-3} s^{-1}, while at 200F°/s (111 K/s) the strain rates are 10^{-2} to 10^{-1} s^{-1}. As pointed up by Dieter [*10*], decreasing the strain rate increases the tendency for intergranular fracture. Thus, at the slower heating rate, there are many pinhole intergranular fractures with no specimens (metallographically examined) exhibiting transgranular fracture. Increasing the heating rate, and therefore the strain rate, tends to eliminate the pinhole fractures and favors transgranular fractures.

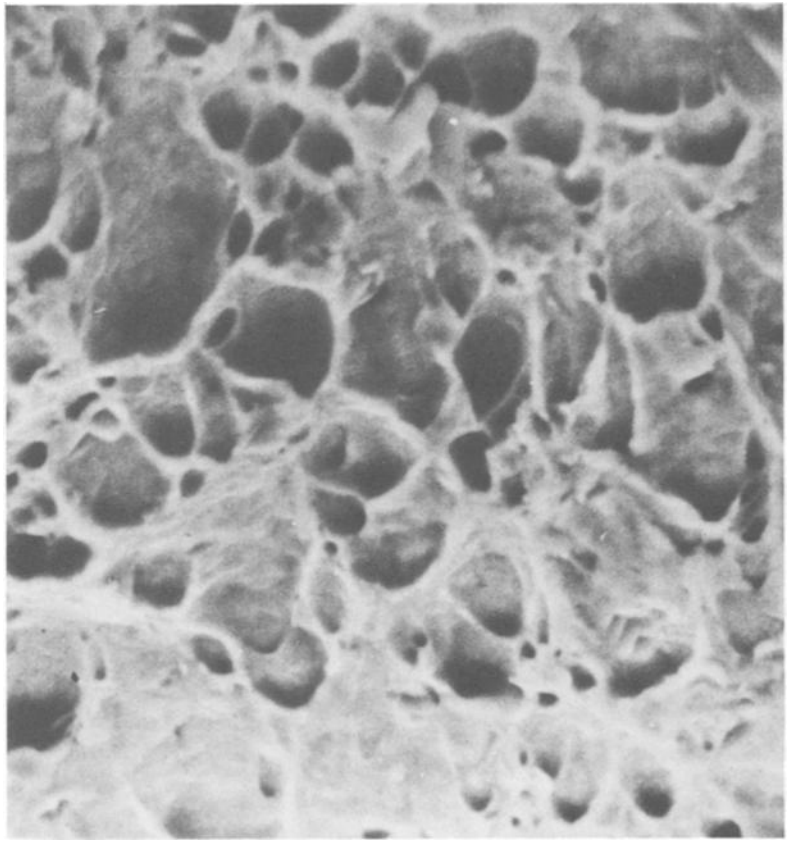

FIG. 13—*Transgranular plastic dimpling of fracture surface of the specimen in Fig. 12 (×2000).*

The results in Fig. 14 and 15 again indicate that the cladding properties are degraded by increasing fluence. Also, the irradiation-produced decrease in ductility is only partially offset by an increase in strength, since the product $\sigma_H \cdot \varepsilon_f$ is seen to decrease with fluence. Further, the specimens from the fuel column region had the lowest values of $\sigma_H \cdot \varepsilon_f$. This degrading effect of fuel is described in the next section.

Effect of Fuel Column on Mechanical Properties

In Ref *4* it was shown that cladding specimens from the fuel column region of the pins exhibited lower failure strengths then did either plenum specimens or unfueled, unstressed specimens from structural materials

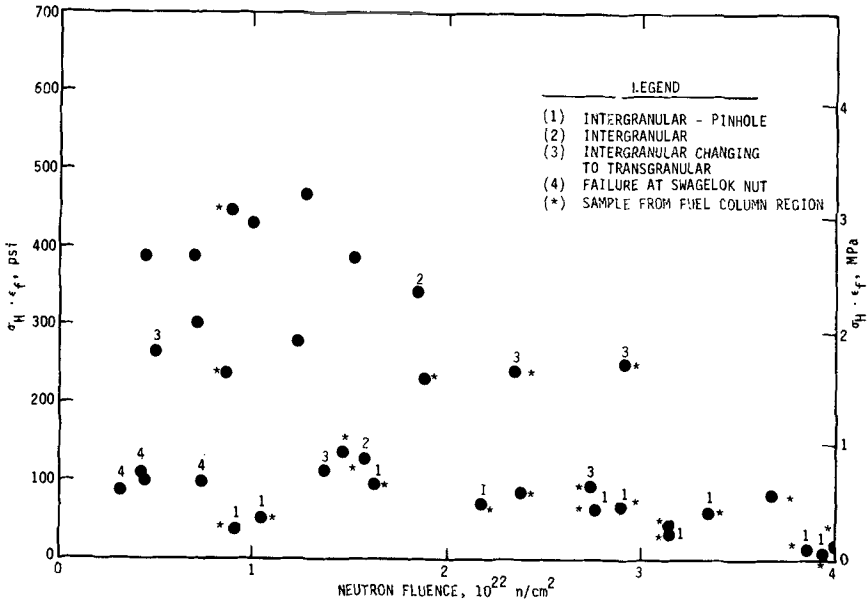

FIG. 14—*Failure energy of transient specimens tested 10F°/s (5.6 K/s).*

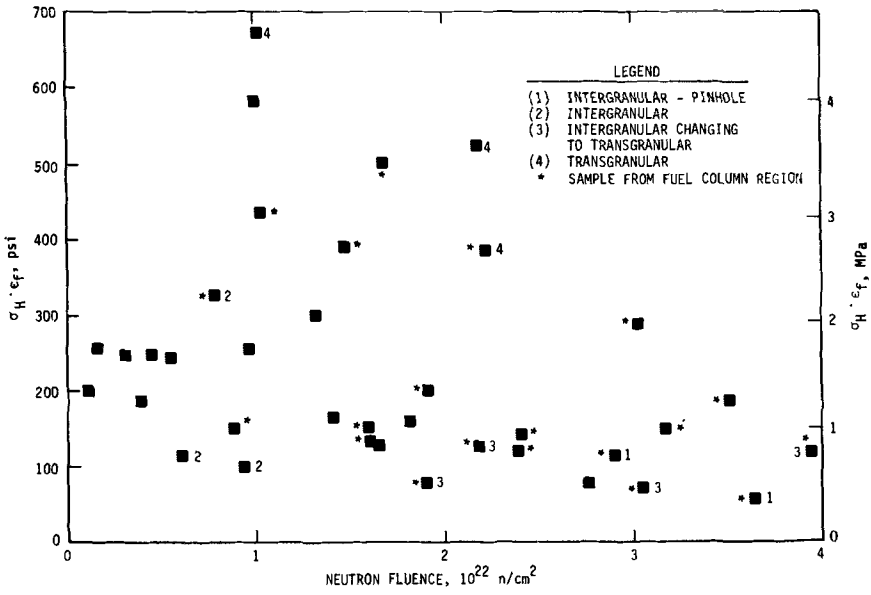

FIG. 15—*Failure energy of transient specimens tested at 200F°/s (111 K/s).*

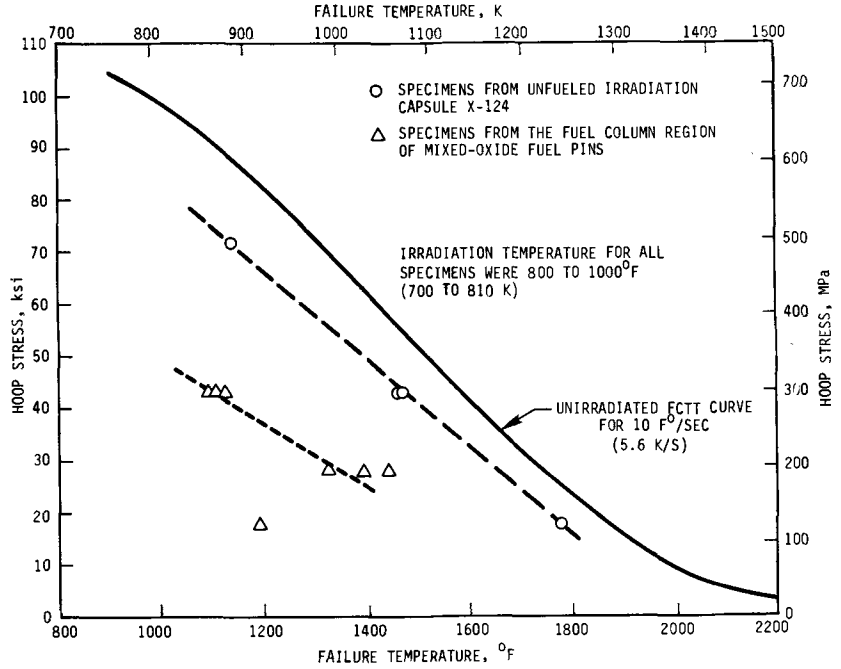

FIG. 16—*Comparison of fueled and unfueled specimen transient behavior for a neutron fluence of 3 to 4 × 10^{22} n/cm² (E > 0.1 MeV).*

irradiations. Recent data from both fuel pin specimens and other structural materials irradiation specimen testing have further substantiated this observation. Figure 16 gives a comparison of fueled and unfueled specimen 10F°/s transient behavior for a neutron fluence of 3 to 4 × 10^{22} n/cm². The unfueled specimens show about a 20 percent reduction in strength, while the fueled specimens exhibit more than a 50 percent reduction in strength. Thus there is an additional 30 percent reduction in strength beyond the fluence effect.

Several mechanisms have been proposed to explain the poorer behavior of fuel column cladding specimens: (*a*) unrelieved thermal stresses after irradiation, (*b*) enhanced helium embrittlement, (*c*) stress concentration from inner surface grain boundary attack or cracking, (*d*) fuel-cladding mechanical interaction during reactor start-up, (*e*) loading from thermal gradients during irradiation, and (*f*) fission gas pressure loading. The current effort is directed toward evaluation of these various mechanisms.

Summary of Irradiation Effects

The irradiated cladding failure stress and ductility data are summarized in Fig. 17. At 200F°/s (111 K/s) above 1200°F (922 K) the ductility and

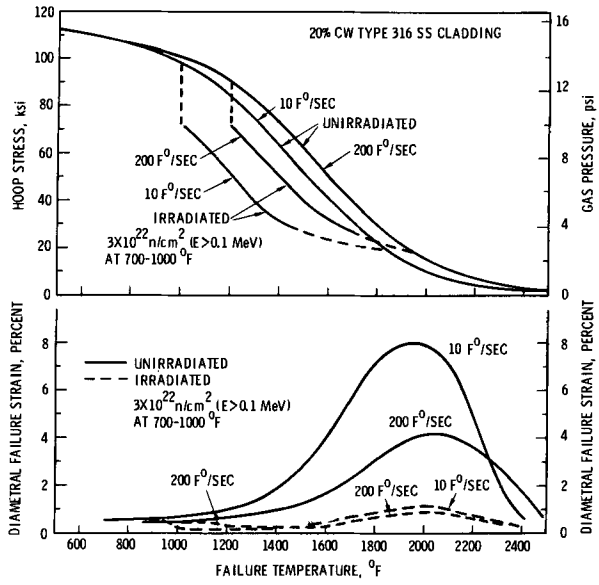

FIG. 17—*Effect of irradiation on failure strength and ductility.*

failure strength of the cladding are reduced; however, above 1600 °F (1144 K) the ductility increases and the available results do not show decreased failure strength. The fracture mode is still intergranular, but the ductility is not low enough to interfere with load-bearing capability. At 10F°/s (5.6 K/s) similar trends are exhibited, except that the slower strain rate allows low-ductility intergranular fracture to occur at temperatures as low as 1000 °F (811 K) and the ductility is increased above about 1400 °F (1033 K).

For both heating rates, at lower failure temperatures and higher stresses, the irradiated material failure stress curve is shown to rise discontinuously to the unirradiated material curve as the fracture changes from intergranular to transgranular. At temperatures above 1400 and 1600 °F (1033 and 1144 K) the failure stress curves gradually approach the unirradiated curves, as the reduced crystal shear strength allows blunting of stress concentrations.

References

[1] Hunter, C. W., Fish, R. L., and Holmes, J. J., *Nuclear Technology*, Vol. 27, Nov. 1975, pp. 376–388.

[2] Hunter, C. W., and Fish, R. L., "Deformation and Failure of Fast Reactor Fuel Cladding Specimens During High-Temperature Simulated Loss-Of-Flow Transients," Fast Reactor Safety Conference, American Nuclear Society, USAEC-Conference 740401, 2–4 April 1974.

[3[Scott, J. H., Culley, G. E., Hunter, C. W., and Hanson, J. E., "Microstructural Dependence of Failure in Mixed-Oxide LMFBR Fuel Pins," Fast Reactor Safety Conference, American Nuclear Society, USAEC Conference 740401, 2–4 April 1974.

[4] Hunter, C. W., Johnson, G. D., and Fish, R. L., "Mechanical Properties During Simulated Overpower Transients of Fast Reactor Cladding Irradiated from 700–1000°F," HEDL-TME 75-28, Hanford Engineering Development Laboratory, Richland, Wash., June 1975.

[5] Scott, J. H., Baars, R. E., Culley, G. E., and Hunter, C. W., "Microstructural Dependence of Failure Threshold in Mixed Oxide LMFBR Fuel Pins," HEDL-TME 75-9, Hanford Engineering Development Laboratory, Richland, Wash., Oct. 1974.

[6] Culley, G. E., Hanson, J. E., Partain, W. L., Scott, J. H., and Waltars, A. E., "Fast Reactor Safety Implications of Recent Assesssments of Fuel Pin Transient Behavior," HEDL-SA 393S, Hanford Engineering Development Laboratory, Richland, Wash., presented at International Conference on Engineering of Fast Reactors for Safe and Reliable Operation, Karlsruhe, Germany, 9–13 Oct. 1972.

[7] Hanson, J. E., and Roake, W. E., *Proceedings,* Fast Reactor Fuel Element Technology, American Nuclear Society, April 1971, pp. 497–515.

[8] Kramer, D., Brager, H. R., Rhodes, C. G., and Park, A. G., *Journal of Nuclear Materials,* Vol. 25, 1968, pp. 121–130.

[9] Holmes, J. J., Robbins, R. E., and Brimhall, J. L., *Journal of Nuclear Materials,* Vol. 32, 1969, pp. 330–339.

[10] Dieter, G. E., *Mechanical Metallurgy,* McGraw-Hill, New York, 1961, p. 345.

R. L. Fish[1] *and C. W. Hunter*[1]

Tensile Properties of Fast Reactor Irradiated Type 304 Stainless Steel

REFERENCE: Fish, R. L. and Hunter, C. W., **"Tensile Properties of Fast Reactor Irradiated Type 304 Stainless Steel,"** *Irradiation Effects on the Microstructure and Properties of Metals, ASTM STP 611,* American Society for Testing and Materials, 1976, pp. 119–138.

ABSTRACT: Tension tests were performed on annealed Type 304 stainless steel specimens sectioned from Experimental Breeder Reactor-II (EBR-II) duct thimbles. The specimens had accumulated neutron fluences of up to 10.3×10^{22} neutrons (n)/cm^2, $E > 0.1$ MeV (10.3×10^{26} n/m^2, $E > 16$ fJ). Irradiation temperatures for the material tested ranged from 700 to 750°F (644 to 672 K). The tests were performed at temperatures of room temperature to 1400°F (1033 K), employing strain rates of 2×10^{-3} to 2/min (3.3×10^{-5} to 3.3×10^{-2}/s).

At test temperatures below 800°F (700 K), the strength increased with fluence until about 7×10^{22} n/cm^2 (7×10^{26} n/m^2), beyond which no further increase was observed. The elongation decreased with fluence, reaching levels as low as 0.5 percent uniform and 1.3 percent total elongation at 700°F (644 K). High-fluence failures below 800°F (700 K) occurred by transgranular channel fracture.

At test temperatures above 1000°F (811 K), elongations were reduced to very low levels at high fluences (average total elongation (TE) = 0.03 percent). Extensive intergranular fracture at the high fluences produced the low ductility and resulted in failure of the specimens before reaching the strength characteristic of the true hardness of the material.

KEY WORDS: radiation, irradiation, stainless steels, ductility, strain rate, neutron irradiation

Tension testing of annealed Type 304 stainless steel specimens taken from Experimental Breeder Reactor-II (EBR-II) duct thimbles has provided an important basis for understanding the mechanical properties of high-fluence fast reactor core structural materials. Investigations of Type 304 stainless steel in the past [*1–5*][2] have focused on the description of tensile properties at the irradiation temperatures of 700 to 900°F (644 to 755 K) over the fluence range to 1×10^{23} neutrons (n)/cm^2, $E > 0.1$ MeV

[1] Advanced engineer and senior scientist respectively, Hanford Engineering Development Laboratory, Westinghouse Hanford Company, Richland, Wash. 99352.

[2] The italic numbers in brackets refer to the list of references appended to this paper.

(1×10^{27} n/m^2, $E > 16$ fJ). Only limited testing has been performed above the irradiation temperature for analysis of reactor components during transient conditions. In addition to the need for tensile properties above the irradiation temperature, knowledge of mechanical properties is required for analysis of reactor components during low-temperature refueling and hot-cell operations.

This paper describes the effects of fast neutron fluence on the tensile properties of annealed Type 304 stainless steel over a test temperature range from room temperature to 1400°F (1033 K). Tensile strain rates from 2×10^{-3} through 2 per min (3.3×10^{-5} through 3.3×10^{-2}/s) were employed. The specimens were irradiated to a maximum fluence of 10.3×10^{22} n/cm^2, $E > 0.1$ MeV (10.3×10^{26} n/m^2, $E > 16$ fJ) and were cut from portions of EBR-II thimbles which had operated at 700 to 750°F (644 to 672 K).

Experimental Technique

Material Irradiation History

The irradiation conditions for EBR-II irradiated, Type 304 stainless steel duct thimbles used in this testing are summarized in Table 1. Irradiation temperatures for specimens sectioned from the thimbles were estimated from temperature curves supplied by the EBR-II project [6]. The fluence estimates were based on Run 31F dosimetry tests [7].

TABLE 1—*Summary of EBR-II irradiated duct thimbles.*

EBR-II Thimble Identification	Exposure, MWd[a]	Peak Fluence, $E > 0.1$ MeV	Irradiation Temperature, °F
3A1 SRT	37 490	11.7×10^{22} n/cm^2	700 to 860 (644 to 733 K)
5A3 CRT	36 785	7.6×10^{22} n/cm^2	700 to 870 (644 to 739 K)
5C3 CRT	15 541	3.7×10^{22} n/cm^2	700 to 870 (644 to 739 K)
5F3 CRT	42 321	10.3×10^{22} n/cm^2	700 to 870 (644 to 739 K)
5F1 CRT	49 967	10.2×10^{22} n/cm^2	700 to 870 (644 to 739 K)

[a]MWd = megawatt day

A plot of the estimated irradiation conditions for one of the thimbles, control rod thimble (CRT) 5A3, is shown in Fig. 1. The axial neutron flux gradient in the EBR-II produced neutron fluences about three times higher at the midplane than at 10 in. (0.25 m) away from the midplane.

The temperature in Fig. 1 rises fairly rapidly through the core region (±6¾ in., ±0.17 m) and becomes approximately constant again for distances more than about 10 in. (0.25 m) above the midplane. Below the core, the thimble temperature was equal to the inlet sodium coolant tem-

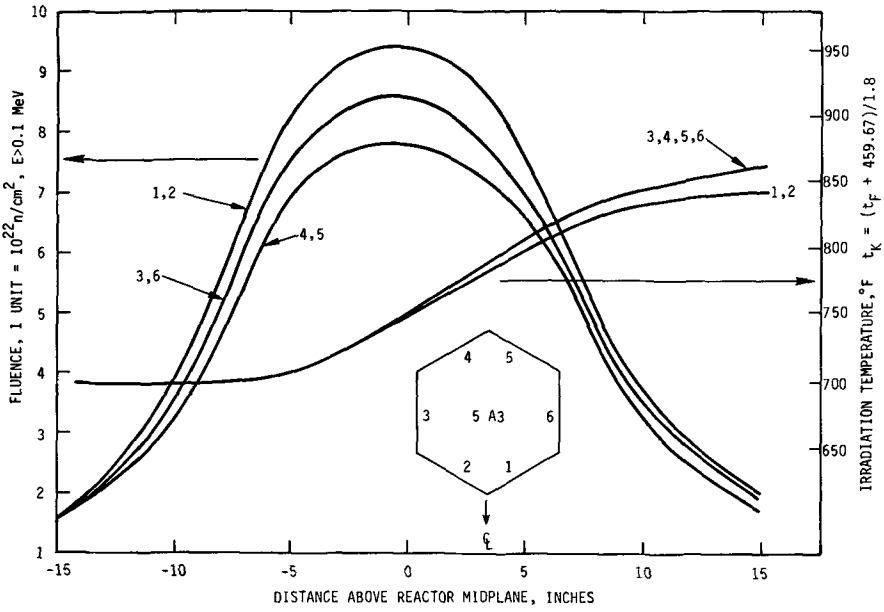

FIG. 1—*Estimated irradiation conditions for control rod thimble 5A3.*

perature, which is maintained at a constant 700°F (644 K). The temperatures at the upper ends of the thimbles vary from flat to flat depending upon the loading of adjacent subassemblies. The temperature profiles in Fig. 1, as well as the temperatures in Tables 1 and 2, represent averages over the lifetime of the in-reactor service.

Tension Testing

The tension specimens were cut from regions of the thimbles irradiated at 700 to 750°F (644 to 672 K). The tension specimen shown in Fig. 2 is a modification of the pin-loaded flat specimen described in ASTM Tension Testing of Metallic Materials (E 8-69). The overall dimensions were 2⅝ in. (66.7 mm) long by 0.040 in. (1 mm) thick; the reduced gage section was effectively 1 in. (25.4 mm) long by ⅛ in. (3.2 mm) wide. The specimens were machined from the flats of the thimbles with the specimen tensile axis parallel to the longitudinal axis of the thimble.

Tension tests were performed on a hard-beam testing machine equipped with a high-temperature vacuum furnace. Both load and elongation were recorded throughout the test. A linear variable differential transformer (LVDT) extensometer, capable of ×700 strain magnification, was employed for strain measurements during the low-strain (<1.5 percent) por-

TABLE 2—*Tensile properties of fast neutron irradiated, annealed Type 304 stainless steel.*

Specimen Identification	Strain Rate, 1/min	Irradiation Temperature, °F	Fluence, $E > 0.1$ MeV (n/cm^2)	Test Temperature, °F	Strength, ksi			Ductility, %		
					Proportional Elastic Limit	Yield Strength	Ultimate Tensile Strength	Uniform Elongation	Total Elongation	Reduction in Area
C1A1	2×10^{-3}	700 (644 K)	3.8×10^{22}	RT[a]	102.3	128.0	133.2	3.0	8.9	50.0
C2A1	2×10^{-2}	700 (644 K)	3.5	RT	93.2	120.2	126.1	5.2	9.2	53.2
C5A1	2×10^{-1}	700 (644 K)	3.5	RT	96.1	118.4	123.7	3.4	6.9	58.8
C6A1	2	700 (644 K)	3.8	RT	110.2	138.8	140.6	3.7	8.1	54.9
C1C1	2×10^{-3}	700 (644 K)	7.8×10^{22}	RT	102.3	133.3	141.4	1.7	4.5	47.9
C2C1	2×10^{-2}	700 (644 K)	7.2	RT	103.6	135.2	143.6	3.4	8.9	50.0
C5C1	2×10^{-1}	700 (644 K)	7.2	RT	104.3	137.6	148.0	4.5	9.0	45.2
C6C1	2	700 (644 K)	7.8	RT	109.6	139.1	145.1	1.8	4.9	45.4
C1E1	2×10^{-3}	730 (661 K)	10.3×10^{22}	RT	84.6	127.1	137.9	2.1	3.5	26.8
C2E1	2×10^{-2}	730 (661 K)	9.4	RT	94.7	129.8	140.2	3.0	4.9	28.4
C3E1	2×10^{-1}	730 (661 K)	8.8	RT	108.2	136.9	147.6	3.8	8.2	47.5
C6E1	2	730 (661 K)	10.3	RT	101.9	135.8	149.1	3.9	5.1	17.0
C1A2	2×10^{-3}	700 (644 K)	3.8×10^{22}	450 (505 K)	75.0	105.2	106.7	0.6	2.5	37.2
C2A2	2×10^{-2}	700 (644 K)	3.5	450 (505 K)	84.3	109.3	111.0	0.7	2.8	31.0
C5A2	2×10^{-1}	700 (644 K)	3.5	450 (505 K)	95.7	117.0	119.6	0.7	3.2	40.1
C6A2	2	700 (644 K)	3.8	450 (505 K)	95.8	125.4	126.9	0.8	2.4	44.3
C1C2	2×10^{-3}	700 (644 K)	7.8×10^{22}	450 (505 K)	90.9	116.6	118.0	0.4	1.9	41.4
C2C2	2×10^{-2}	700 (644 K)	7.2	450 (505 K)	99.8	127.1	131.2	0.8	2.7	34.9
C5C2	2×10^{-1}	700 (644 K)	7.2	450 (505 K)	93.4	124.3	129.1	0.7	2.1	48.9
C6C2	2	700 (644 K)	7.8	450 (505 K)	102.2	134.8	139.3	0.8	1.4	37.0
C1E2	2×10^{-3}	730 (661 K)	10.3×10^{22}	450 (505 K)	90.0	120.8	123.6	0.4	1.5	24.0
C2E2	2×10^{-2}	730 (661 K)	9.4	450 (505 K)	100.0	129.3	133.8	0.9	2.2	26.8
C3E2	2×10^{-1}	730 (661 K)	8.8	450 (505 K)	97.9	130.0	135.2	0.9	2.2	38.0
C6E2	2	730 (661 K)	10.3	450 (505 K)	100.0	130.4	133.3	0.7	1.2	20.4

B6D1	2×10^{-3}	700 (644 K)	2.8×10^{22}	700 (644 K)	74.5	104.9	109.0	0.5	1.6	29.4
B6E1	2×10^{-3}	700 (644 K)	4.5	700 (644 K)	72.9	108.1	112.5	0.4	1.5	22.9
B6F1	2×10^{-3}	700 (644 K)	6.6	700 (644 K)	82.4	111.6	116.1	0.5	2.6	21.6
D2E2	2×10^{-3}	725 (658 K)	9.7×10^{22}	700 (644 K)	93.1	105.9	108.0	0.5	1.3	24.5
D3E2	2×10^{-2}	725 (658 K)	9.2	700 (644 K)	84.0	110.6	114.4	).6	1.2	25.2
D4E2	2×10^{-1}	725 (658 K)	9.7	700 (644 K)	88.5	109.0	115.8	).8	1.3	31.5
D5E2	2	725 (658 K)	10.2	700 (644 K)	84.6	111.2	115.8	).5	2.1	26.6
H06451 (5C3)	0.05	704 (646 K)	0.93×10^{22}	1100 (866 K)	44.3	60.2	60.6	0.9	2.0	30.6
H06461 (5C3)	0.05	704 (646 K)	1.6	1100 (866 K)	44.9	60.4	60.4	1.0	1.1	11.4
H06493 (5C3)	0.05	750 (672K)	3.0	1100 (866 K)	43.4	56.3	56.3	0.4	0.5	7.9
B6B1	2×10^{-3}	700 (644 K)	1.1×10^{22}	1100 (866 K)	43.3	55.2	57.5	0.6	1.4	17.3
B6C1	2×10^{-3}	700 (644 K)	1.8	1100 (866 K)	57.1	67.3	68.1	0.3	0.7	19.2
A5A2	2×10^{-3}	700 (644 K)	2.8	1100 (866 K)	65.7	73.5	73.5	0.15	0.4	24.1
A5C2[b]	2×10^{-3}	700 (644 K)	5.85	1100 (866 K)	51.0	...	53.1	0.02	0.02	...
A5E2[b]	2×10^{-3}	730 (661 K)	7.56	1100 (866 K)	47.1	...	48.1	0.01	0.015	...
H06455 (5C3)	0.05	704 (646 K)	0.93×10^{22}	1300 (978 K)	14.6	21.1	26.6	5.6	9.8	18.3
H06463 (5C3)	0.05	704 (646 K)	1.6	1300 (978 K)	21.5	34.9	35.8	0.8	0.9	11.1
H06494 (5C3)	0.05	750 (672 K)	3.0	1300 (978 K)	19.1	30.8	30.8	0.25	0.3	9.4
D1D1	2×10^{-3}	710 (650 K)	9.7×10^{22}	1000 (811 K)	69.8	81.3	81.3	0.15	0.30	10.0
D2D1[b]	2×10^{-3}	710 (650 K)	9.2	1100 (866 K)	51.2	...	56.4	0.02	0.02	...
D3D1	2×10^{-3}	710 (650 K)	8.7	1200 (922 K)	31.4	...	38.1	0.03	0.04	3.3
D4D1[b]	2×10^{-3}	710 (650 K)	9.2	1300 (978 K)	22.9	...	27.7	0.03	0.04	...
D5D1	2×10^{-3}	710 (650 K)	9.7	1400 (1033 K)	19.4	...	23.7	0.03	0.04	4.6

[a] RT = room temperature.
[b] Broke at extensometer point.
A-5A3 CRT
B-3A1 SRT
C-5F3 CRT
D-5F1 CRT

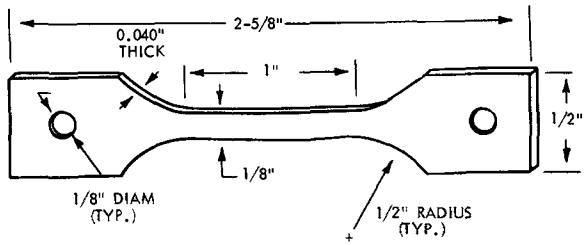

FIG. 2—*Schematic of EBR-II thimble tension specimen.*

tion of all tests. For the specimens which failed at low plastic strain, the extensometer recorded the entire strain history of the specimen, and the elongation values were obtained from the extensometer record. The elongation on specimens exhibiting greater strain was estimated by summing both the extensometer record and the crosshead movement. The specimen temperature during each test was measured and controlled with a chromel-alumel thermocouple. Approximately 20 to 30 min (1200 to 1800 s) were allowed for thermal equilibration and stabilization prior to initiating each tension test.

Experimental Results

The tension test results are presented in Table 2 along with the respective specimen irradiation temperatures and fluences. Also included in the table are test temperature and strain rate. The major groupings within the table are based on test temperature.

Effect of Test Temperature

The tensile properties listed in Table 2 for the high-fluence ($>8.7 \times 10^{22}$ n/cm^2, 8.7×10^{26} n/m^2) material, at the nominal strain rate of 2×10^{-3}/min (3.3×10^{-5}/s) are plotted as a function of test temperature in Figs. 3 and 4. The 0.2 percent offset yield strength and ultimate tensile strength are shown in Fig. 3. At these high fluences of 8.7 to 10.3×10^{22} n/cm^2 (8.7 to 10.3×10^{26} n/m^2), the strength parameters continually decreased with increasing test temperature from room temperature to 1400°F (1033 K). At temperatures above 1000°F (811 K), the strength decreased more rapidly with temperature; concurrently, the uniform elongation (plastic strain at maximum load) decreased to below the 0.2 percent level, rendering the 0.2 percent offset yield strength parameter irrelevant above this temperature. From the limited data it appears that the temperature dependence of the ultimate tensile strength decreased at 1300°F (978 K) and above.

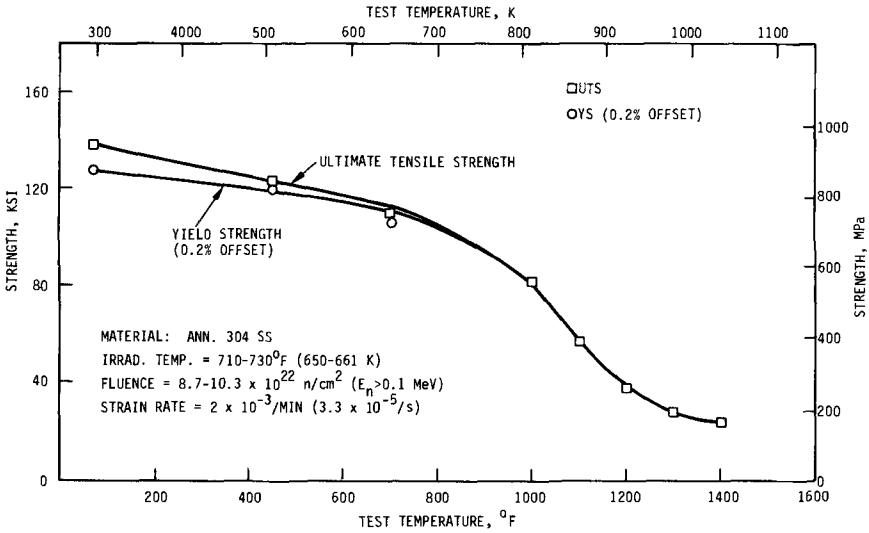

FIG. 3—*Effect of test temperature on the yield strength (0.2 percent offset) and ultimate tensile strength at high fluence.*

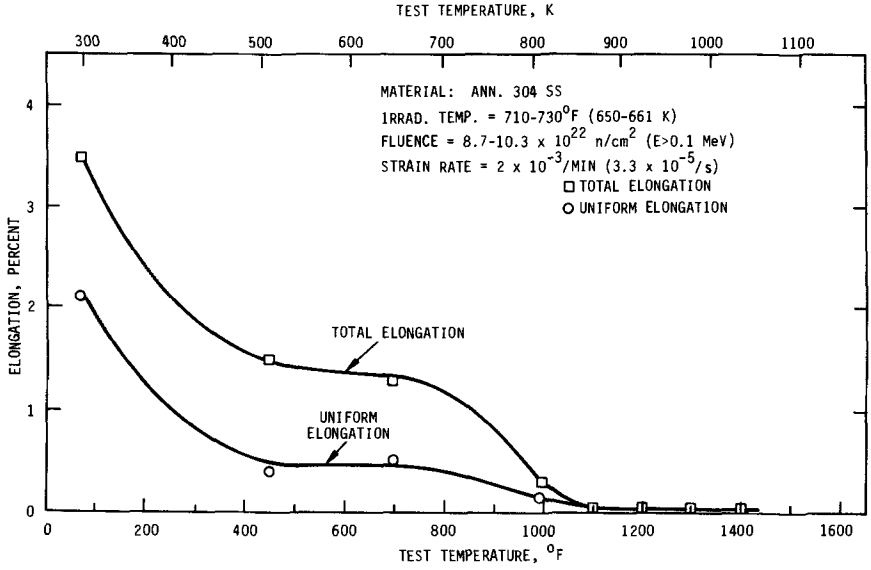

FIG. 4—*Effect of test temperature on the high-fluence ductility of EBR-II Type 304 stainless steel.*

The uniform and total elongation at the high fluences are plotted as a function of test temperature in Fig. 4. These ductility parameters decreased with increasing temperature between room temperature and 450°F (505 K). Between 450°F (505 K) and 700°F (644 K) the parameters were relatively temperature independent, with uniform elongation at 0.5 percent and total elongation at about 1.4 percent. As the test temperature was increased from 700°F (644 K) to 1100°F (866 K), the ductility further decreased to a very low level, averaging 0.03 percent from 1100 to 1400°F (866 to 1033 K). At these high temperatures (≥1100°F, 866 K) uniform and total elongation were practically identical, because essentially no plastic strain occurred beyond the peak load.

Strain Rate Effects

Strain rate effects were investigated at the lower test temperatures of room temperature, 450°F (505 K) and 700°F (644 K). The ultimate tensile strengths, measured at these temperatures, are plotted as a function of strain rate in Fig. 5. A slight increase in ultimate tensile strength of about

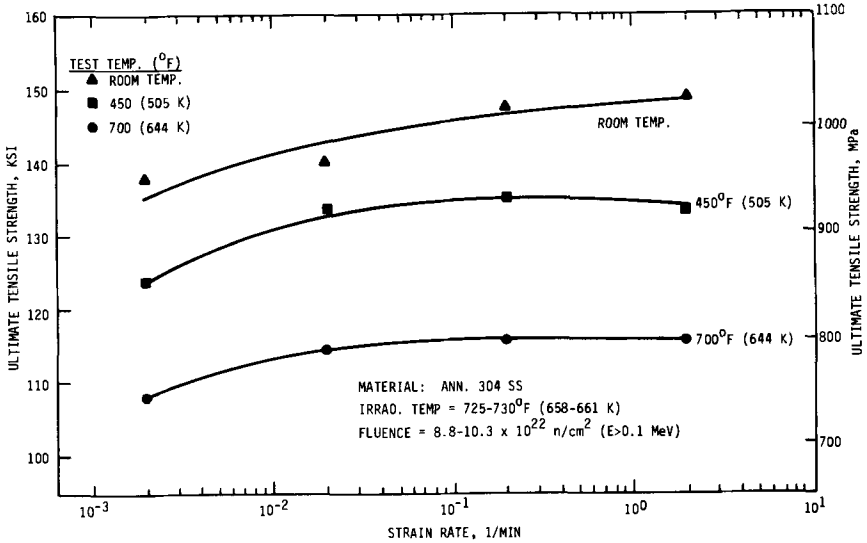

FIG. 5—*Effect of strain rate on the ultimate tensile strength of high-fluence EBR-II Type 304 stainless steel.*

8 percent was observed as the strain rate increased from 2×10^{-3}/min to 2/min (3.3×10^{-5} to 3.3×10^{-2}/s). This modest strain rate dependence was similar for all test temperatures.

The uniform elongation, at the high fluence levels of 8.8 to 10.3 $\times$ 10^{22} n/cm^2 (8.8 to 10.3 $\times$ 10^{26} n/m^2), is plotted as a function of strain rate in Fig. 6. The strain rate dependence of uniform elongation was more pro-

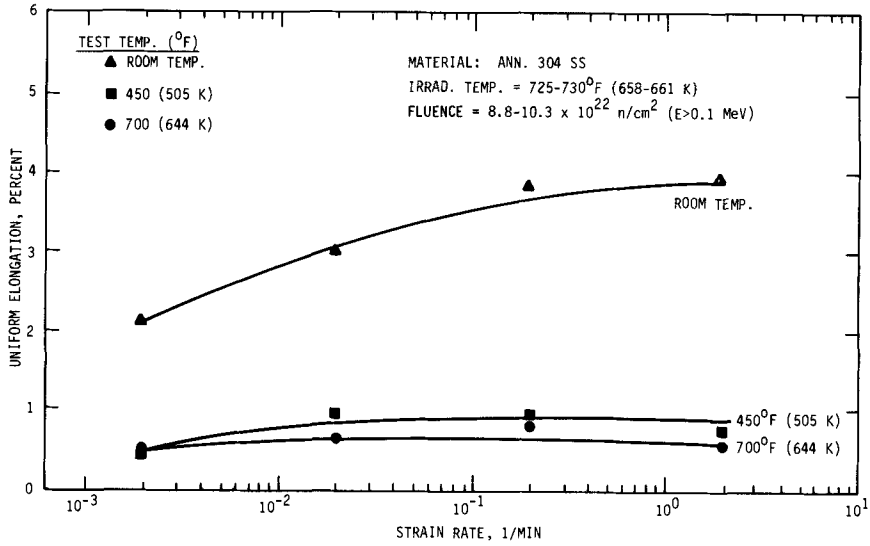

FIG. 6—*Effect of strain rate on the uniform elongation of high-fluence EBR-II Type 304 stainless steel.*

nounced than that observed in the strength. Particularly at room temperature, the uniform elongation increased substantially (86 percent) as the strain rate increased from 2 $\times$ 10^{-3}/min to 2/min (3.3 $\times$ 10^{-5} to 3.3 $\times$ 10^{-2}/s).

Effect of Fluence

The effect of fluence on the ultimate tensile strength of annealed Type 304 stainless steel is presented in Fig. 7. At all fluence levels investigated, strength decreased with increasing test temperature. At test temperatures less than and equal to the 700°F (644 K) irradiation temperature, the strength increased rapidly with increasing fluence until about 3 $\times$ 10^{22} n/cm^2 (3 $\times$ 10^{26} n/m^2), above which the fluence dependence diminished; above 7 $\times$ 10^{22} n/cm^2 (7 $\times$ 10^{26} n/m^2) the strength leveled out and became fluence independent. The low-fluence strength representations shown in Fig. 7 were established on the basis of previously published data at 700°F (644 K) [*5*] and assuming similar trends for the 450°F (505 K) and room temperature curves. At the 1100°F (866 K) and 1300°F (978 K)

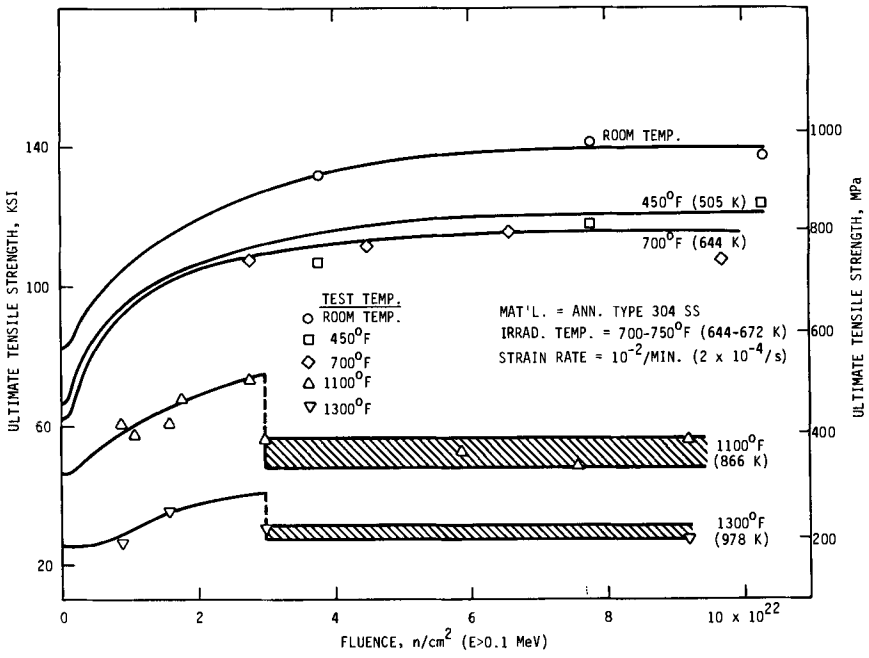

FIG. 7—*Effect of fluence on ultimate tensile strength.*

test temperatures, the ultimate tensile strength exhibited a different fluence dependence than at the lower test temperatures. The strength increased with fluence to about 3×10^{22} n/cm^2 (3×10^{26} n/m^2), above which the strength dropped abruptly and became independent of fluence.

Total elongation determined at and below the 700°F (644 K) irradiation temperature is shown as a function of fluence in Fig. 8. Over the fluence range investigated, 3 to 10×10^{22} n/cm^2 (3 to 10×10^{26} n/m^2), the total elongation at 700°F (644 K) remained fluence independent. There was a greater fluence dependence at test temperatures below 700°F (644 K). Both the uniform and total elongation at 1100°F (866 K) and 1300°F (978 K) are presented as a function of fluence in Fig. 9. These ductility parameters decreased with increasing fluence to about 5×10^{22} n/cm^2. Above 5×10^{22} n/cm^2 (5×10^{26} n/m^2), the total plastic strain to failure corresponded very closely with the plastic strain at the peak load. Therefore, the uniform and total elongation values were essentially identical and leveled out at an average value of 0.03 percent.

Correlation of Properties with Fracture Mode

The correlation of fracture modes and mechanisms with tensile properties contributes to the basis for understanding the mechanical properties

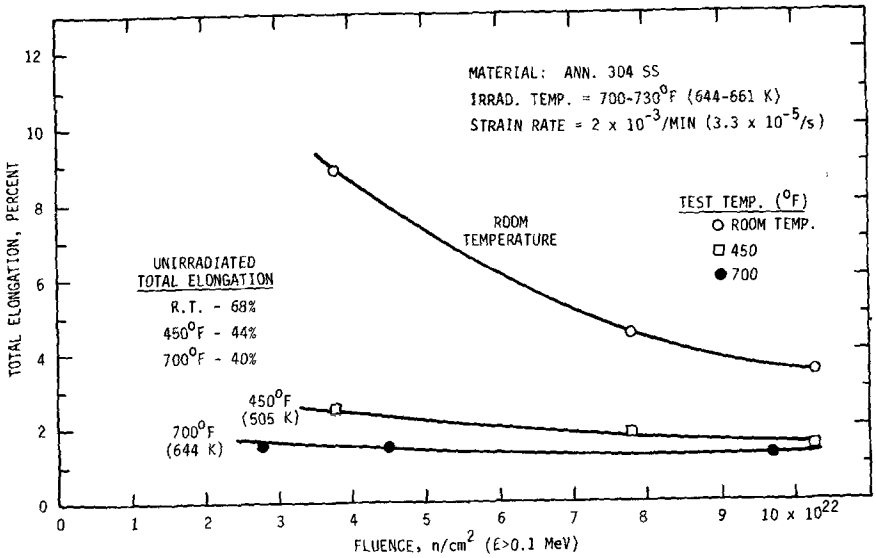

FIG. 8—*Effect of fluence on total elongation of EBR-II Type 304 stainless steel.*

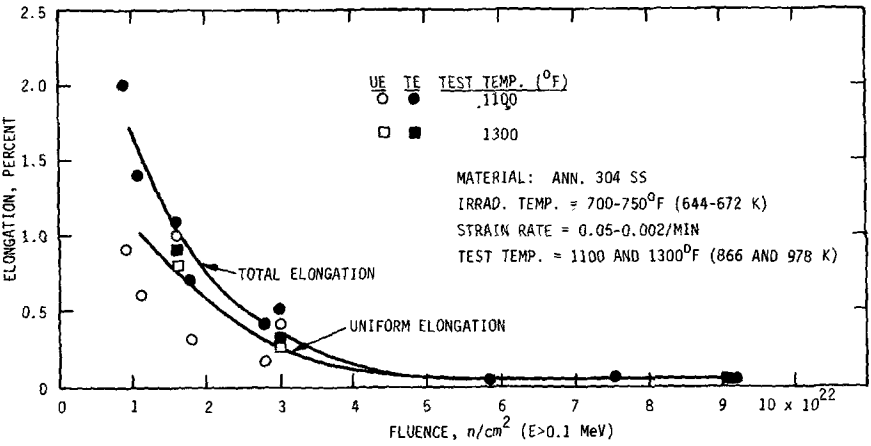

FIG. 9—*Effect of fluence on high-temperature ductility of EBR-II Type 304 stainless steel.*

exhibited by this material. Both irradiation fluence and test temperature exert a pronounced effect on the deformation and fracture characteristics.

Fractography

Fracture surfaces from 22 tension specimens were examined using a scanning electron microscope (SEM). A composite SEM fractograph was

developed for each specimen fracture using ×75 magnification photos. This composite was utilized for locating key regions for high magnification photographs, up to ×3000. The fracture mode and mechanisms were identified and confirmed at the higher magnifications, and correlated with the low-magnification appearance. Based on the low-magnification appearance, and confirming observations at high magnifications, the fracture surface percentage of each type of fracture was estimated for each specimen. These estimates are summarized in Table 3. Several tension specimens from other Type 304 stainless steel studies were analyzed and have been included in this table in order to facilitate an overall interpretation.

Fracture Modes and Mechanisms

Below 900 to 1000°F (755 to 811 K) the dominant fracture mode was transgranular [*8*]. However, irradiation does affect the fracture mechanism in this temperature range: unirradiated specimens exhibit plastic dimpling [*8*], while the fracture mechanism in highly irradiated material is channel fracture. This fracture mechanism, which has been observed only in irradiated stainless steel [*9*], results from dislocation channeling [*5,10–12*] confining the crystal slip to narrow bands of planes or channels within the grain. At high fluences the slip along one of these bands is so extensive that the crystals literally slide apart on that channel. Each fracturing channel produces a relatively flat facet and the polycrystalline character of the specimen leads to intersecting and interrupted channels. The macroscopic fracture appearance of a specimen fracturing by channel fracture was a slant fracture, 45 deg to the tensile stress axis, which eliminated the possibilities of either transgranular cleavage [not observed in face-centered-cubic (fcc)] or intergranular fracture. At temperatures above 900 to 1000°F (755 to 811 K), the dominant fracture mode was intergranular.

Correlation of Fracture with Strength

The relationship between fracture character, ultimate tensile strength, and irradiation fluence is shown in Fig. 10 for two different test temperatures. The low-temperature fracture mode is transgranular at all fluence levels. However, the irradiation hardening, which is very fluence dependent at low fluence levels and becomes relatively fluence independent at above 3 to 4 × 10^{22} n/cm^2 (3 to 4 × 10^{26} n/m^2), is accompanied by a transition in the fracture mechanism. At low fluences, fracture occurred by transgranular plastic dimpling. As the fluence increased, the shear processes ceased to be homogeneous throughout the entire crystal and became restricted to narrow channels to such an extent that complete chan-

TABLE 3—*Summary of SEM fractograph analysis.*

Specimen Identification	Irradiation Temperature, °F	Fluence, $E > 0.1$ MeV (n/cm^2)	Test Temperature, °F	Strain Rate, 1/min	Estimated Percent of Fracture Surface		
					Dimpling	Channel	Intergranular
C1A1	700 (644 K)	3.8×10^{22}	RT[a]	2×10^{-3}	80	20	0
C1E1	730 (661 K)	10.3	RT	2×10^{-3}	3	97	0
C6E1	730 (661 K)	10.3	RT	2	0	100	0
C1A2	700 (644 K)	3.8×10^{22}	450 (505 K)	2×10^{-3}	85	15	0
C1E2	730 (661 K)	10.3	450 (505 K)	2×10^{-3}	0	100	0
C6E2	730 (661 K)	10.3	450 (505 K)	2	0	100	0
6A1	700 (644 K)	0.9×10^{22}	700 (644 K)	5×10^{-2}	100	0	0
A5A1	700 (644 K)	2.8	700 (644 K)	2×10^{-3}	70	30	0
A5C1	700 (644 K)	5.9	700 (644 K)	2×10^{-3}	30	70	0
A5E1	730 (661 K)	7.6	700 (644 K)	2×10^{-3}	4	96	0
B6H1	750 (672 K)	10.7	700 (644 K)	2×10^{-3}	0	100	0
D5E2	725 (658 K)	10.2	700 (644 K)	2	0	100	0
A5H1	840 (722 K)	2.8×10^{22}	800 (700 K)	2×10^{-3}	20	78	2
B6I1	795 (697 K)	9.4	800 (700 K)	2×10^{-3}	1	98	1
A5J1	870 (739 K)	0.76×10^{22}	900 (755 K)	2×10^{-3}	95	0	5
A5I1	860 (733 K)	1.8	900 (755 K)	2×10^{-3}	50	30	20
B6J2	840 (722 K)	6.6	900 (755 K)	2×10^{-3}	0	80	20
ALW4	...	0.0×10^{22}	1000 (811 K)	2×10^{-3}	99	0	1
A5E2	730 (661 K)	7.5×10^{22}	1100 (866 K)	2×10^{-3}	5	5	90
D2D1	710 (650 K)	9.2	1100 (866 K)	2×10^{-3}	10	65	25
ALW5	...	0.0×10^{22}	1200 (922 K)	2×10^{-3}	20	0	80
D5D1	710 (650 K)	9.7×10^{22}	1400 (1033 K)	2×10^{-3}	1	0	99

[a] RT = room temperature.

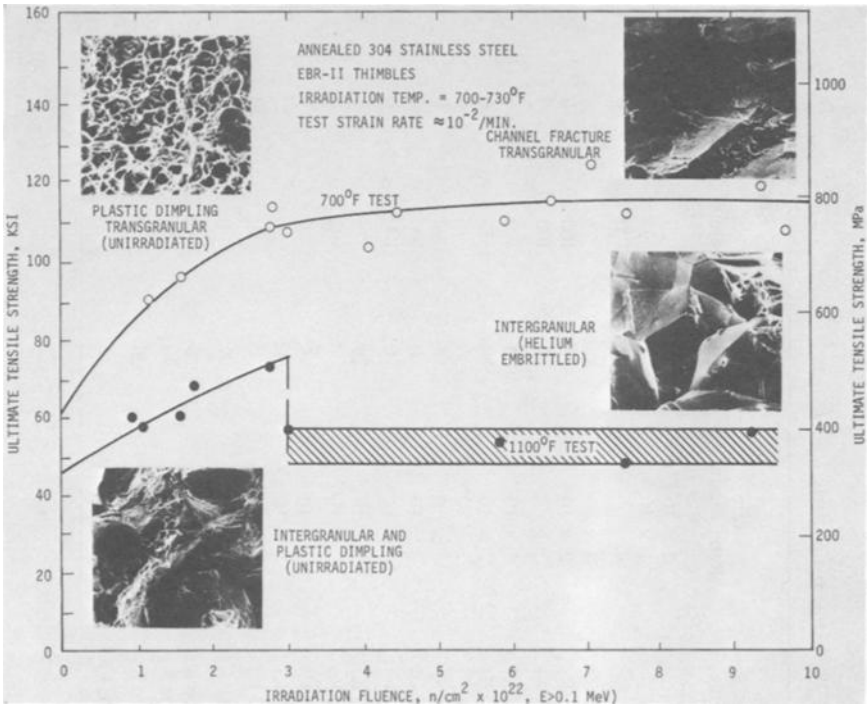

FIG. 10—*Fracture mode and irradiated tensile strength of EBR-II Type 304 stainless steel.*

nel fracture resulted at the highest fluence levels. An example of channel fracture is shown in Fig. 11, which is typical of irradiated specimen fracture for test temperatures of room temperature, 450 °F (505 K), and 700 °F (644 K), and tensile strain rates from 2×10^{-3}/min (3.3×10^{-5} to 3.3×10^{-2}/s.

At the 1100 °F (866 K) test temperature, fracture occurred at the low fluences by a mixed plastic dimpling and intergranular fracture. As the fluence increased, the tensile strength increased, as illustrated in Fig. 10. Above about 3×10^{22} n/cm^2 (3×10^{26} n/m^2) the grain boundary embrittlement from helium [*13*] became sufficient to interfere with the load-bearing capability of the material; consequently, the tensile strength dropped abruptly. The high-fluence 1100 °F (866 K) fracture in Fig. 10 reflects a greater degree of intergranular failure, indicative of helium embrittled grain boundaries.

Correlation of Fracture with Ductility

The relationship between fracture and elongation at the high-fluence level is presented in Fig. 12. In general, the continual decrease in both

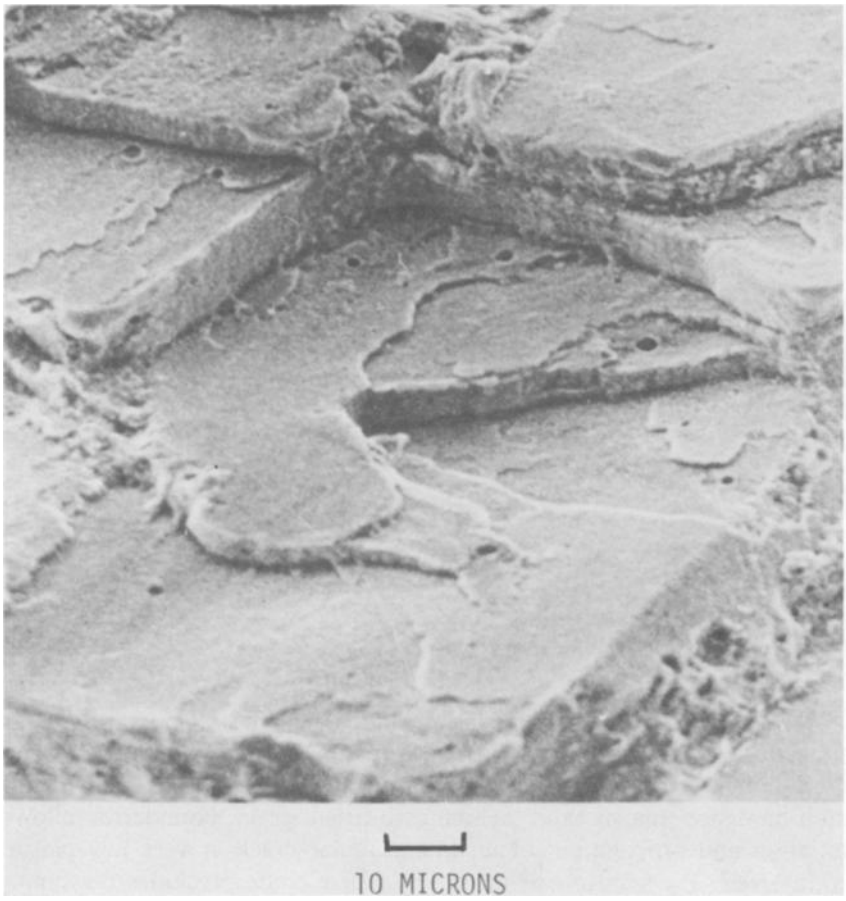

FIG. 11—*Channel fracture (700°F) (644 K) of Specimen B6H1 (3A1 SRT) irradiated at 750°F (672 K) to 10.7 × 10^{22} n/cm^2 (E > 0.1 MeV).*

uniform and total elongation with increasing test temperature is associated with a decreasing tendency for flow within the grains. From room temperature to 700°F (644 K), crystal deformation decreased due to a greater tendency for dislocation channeling, while above 900 to 1000°F (755 to 811 K) intergranular fracture further reduced the deformation. The decreased propensity for dislocation channeling at room temperature from that at 700°F (644 K) allows more homogeneous shear, which results in the greater measured ductilities at room temperature. The channel fracture observed at the lower temperatures, room temperature to 700°F (644 K), resulted in relatively high elongation values compared with the higher test temperature behavior.

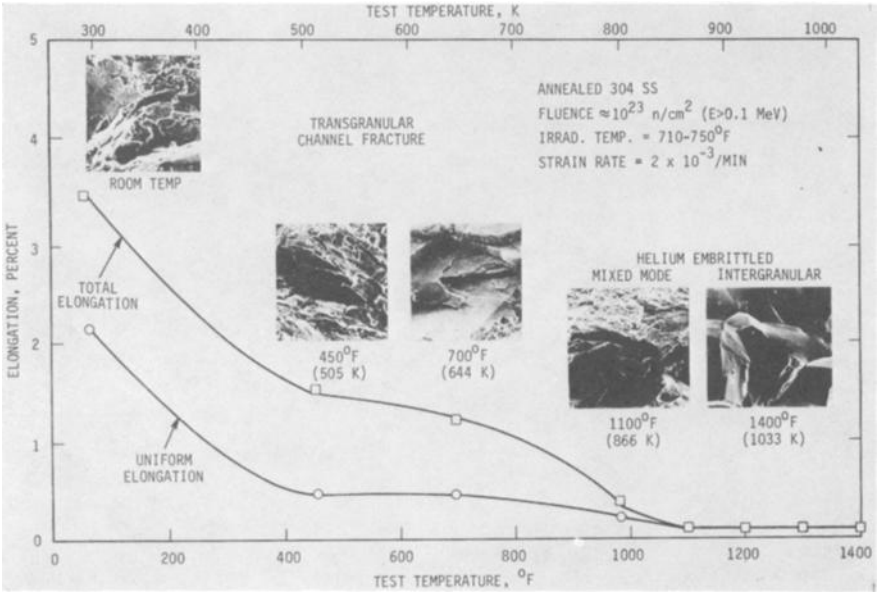

FIG. 12—*Effect of test temperature on high-fluence ductility and fracture.*

The further decrease in elongation at the high test temperatures was associated with the preclusion of matrix (within the grain) deformation by intergranular fracture. The combination, at high fluences, of an irradiation-hardened matrix and helium-embrittled grain boundaries allows initiation and propagation of an intergranular crack at very low plastic strain levels. Propagation of an intergranular crack precludes the possibility of further extensive deformation within the grains of the material. The extreme intergranular character of the high-fluence, high-temperature specimens is illustrated in Fig. 12.

Fracture Map

The fracture characteristics, evaluated with the SEM and listed in Table 3 for specimens tested at 2×10^{-3}/min (3.3×10^{-5}/s) strain rate, provide a basis for mapping the fracture modes and mechanisms of annealed Type 304 stainless steel as a function of fluence and test temperature. The onset and completion of the channel fracture mechanism may be established by plotting the channel fracture percent as a function of fluence, as shown in Fig. 13. The largest amount of data exists at 700 to 900°F (644 to 755 K). The scatterband for this temperature range was used to help establish bands for room temperature to 450°F (505 K) and 1100°F (866 K) temperatures. The intersection of the scatterbands with the zero channel frac-

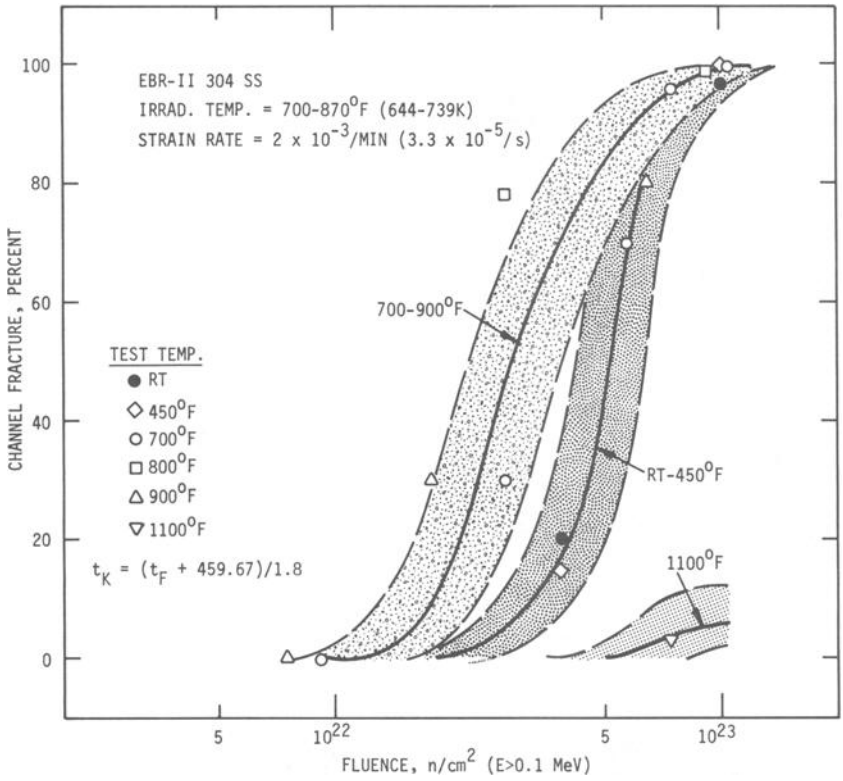

FIG. 13—*Effect of fluence on percent of channel fracture.*

ture level established the "onset of channel fracture" zone presented on the fracture map in Fig. 14. The intersection of the 700 to 900°F (644 to 755 K) scatter band with the 100 percent channel fracture level established the "completion of channel fracture transition" zone for that temperature range as shown in Fig. 14. Data points (C1E1 and C1E2) for room temperature and 450°F (505 K) temperature indicate that the completion of channel fracture occurs near the same fluence level for these temperatures also. The "completion of channel fracture transition" zone is dashed above about 800°F (700 K) to indicate the anticipated trend.

The onset of intergranular fracture was established using four tension specimens (A5H1, B6I1, A5J1, and ALW 4) that show a minimal amount of intergranular fracture. The unirradiated specimen (ALW 4) was tested at 1000°F (811 K). A specimen at $\sim 0.7 \times 10^{22}$ n/cm^2 (0.7×10^{26} n/m^2), A5J1, was tested at 900°F (755 K) and the other two at higher fluences tested at 800°F (700 K). The similar low amounts of intergranular fracture displayed by these four specimens, tested at decreasing temperatures

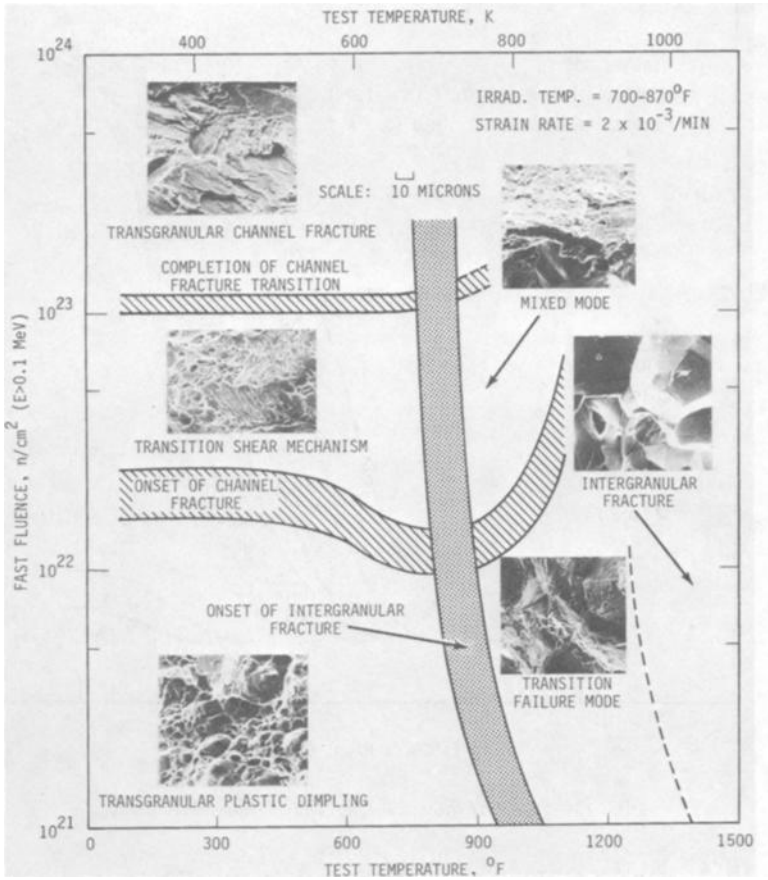

FIG. 14—*Fluence-test temperature fracture map for EBR-II Type 304 stainless steel.*

with increasing fluence, is the basis for the fluence dependent "onset of intergranular fracture." Additional evidence for the existence of the shift in onset of intergranular fracture due to irradiation is the set of tensile fracture surfaces evaluated at 900°F (755 K), B6J2, A5I1, and A5J1. As may be observed in Table 3, the higher-fluence 900°F (755 K) specimens exhibited a factor of four greater amount of intergranular fracture mode than the lowest-fluence specimen. The width of the onset of intergranular fracture zone is arbitrary. A lack of an adequate number of high-temperature (≥1200°F, 922 K) tensile fracture surfaces rendered determination of the completion of intergranular fracture transition impossible. A dashed line is shown in Fig. 14 to merely represent an anticipated trend for the completion of the intergranular fracture transition.

Conclusions

The effects of fast neutron irradiation at 700 to 750°F (644 to 672 K) on the tensile properties of annealed Type 304 stainless steel are dependent upon the test temperature and neutron fluence. At test temperatures below 800°F (700 K), the strength increased rapidly with increasing fluence until about 3×10^{22} n/cm^2, $E > 0.1$ MeV (3×10^{26} n/m^2, $E >$ 16 fJ), above which the fluence dependence weakened; above 7×10^{22} n/cm^2 (7×10^{26} n/m^2) the strength became fluence independent. Concomitantly, the elongation decreased with increasing fluence, reaching levels as low as 0.5 percent uniform and 1.3 percent total elongation at the 700°F (644 K) test temperature. Failure below 800°F (700 K) at low fluences occurred by transgranular plastic dimpling, consistent with the high ductility observed under these conditions. At high fluences, failure below 800°F (700 K) was by transgranular channel fracture. The dislocation channeling which leads to channel fracture precludes extensive matrix deformation, thus resulting in the low, but necessarily finite, ductilities observed at high fluences.

At test temperatures above 1000°F (811 K) the strength increased and elongation decreased rapidly with increasing fluence until about 3×10^{22} n/cm^2. Beyond 3×10^{22} n/cm^2 (3×10^{26} n/m^2) the total elongation continued to decrease until it reached a constant low level of 0.03 percent beyond 5×10^{22} n/cm^2 (5×10^{26} n/m^2). The low ductility at the high fluences resulted from extensive helium-embrittled intergranular fracture which occurred before reaching the tensile strength characteristic of the true hardness of the material. Thus, a drop in the ultimate tensile strength was observed at fluences beyond $\sim 3 \times 10^{22}$ n/cm^2 ($\sim 3 \times 10^{26}$ n/m^2).

An 8 percent increase in strength between strain rates of 2×10^{-3}/min and 2/min (3.3×10^{-5}/s and 3.3×10^{-2}/s) was observed at the highest fluence and temperatures below 800°F (700 K). The increase in uniform elongation with strain rate over the same range was 86 percent at room temperature.

References

[1] Holmes, J. J., Robbins, R. E., Brimhall, J. L., and Mastel, B., *Acta Metallurgica*, Vol. 16, 1968, pp. 955-967.

[2] Bloom, E. E. and Stiegler, J. O., *Transactions*, American Nuclear Society, Vol. 14, Oct. 1971, pp. 557-558.

[3] Carlander, R., Harkness, S. D., and Yagee, F. L., *Nuclear Applications and Technology*, Vol. 7, July 1969, pp. 67-75.

[4] Ring, P. J., Busboom, H. J., and Duncan, R. N., *Transactions*, American Nuclear Society, Vol. 14, Oct. 1971, pp. 552-553.

[5] Fish, R. L., Straalsund, J. L., Hunter, C. W., and Holmes, J. J. in *Effects of Radiation on Substructure and Mechanical Properties of Metals and Alloys, ASTM STP 529,* American Society for Testing and Materials, 1973, pp. 149-164.

[6] Phipps, R. D., "A Study of the Deformations Produced by Long Irradiation of EBR-II Control and Safety Rod Thimbles," a thesis presented in partial fulfillment of the requirements for the degree of Master of Science, Major in Metallurgy, University of Idaho Graduate School, April 1973.

[7] McElroy, W. N., Jackson, J. L., Ulseth, J. A., and Simons, R. L., "EBR-II Dosimetry Test Data Analysis (Reactor Runs 31E and 31F)," BNWL-1402, Battelle-Northwest, Richland, Wash., 1970.

[8] Sullivan, C. P., "A Review of Some Microstructural Aspects of Fracture in Crystalline Materials," Bulletin No. 122, Welding Research Council, May 1967.

[9] Hunter, C. W., Fish, R. L., and Holmes, J. J., *Transactions*, American Nuclear Society, Vol. 15, June 1972, pp. 254–255.

[10] Bloom, E. E. and Stiegler, J. O., "Void Damage in Neutron Irradiated Structural Metals," U.S.-Japan Seminar on Radiation Effects in Metals and Structural Materials, Kyoto, Japan, Sept. 28–30, 1971.

[11] Sharp, J. V., *Philosophical Magazine,* Vol. 16, No. 139, July 1967, pp. 77–95.

[12] Mastel, B., Kissinger, H. E., Laidler, J. J., and Bierlein, T. K., *Journal of Applied Physics*, Vol. 34, No. 12, Dec. 1963, PP. 3637–3638.

[13] Kramer, D., Brager, H. R., Rhodes, C. G., and Pard, A. G., *Journal of Nuclear Materials*, Vol. 25, 1968, pp. 121–130.

P. S. Sklad,[1] *R. E. Clausing,*[1] *and E. E. Bloom*[1]

Effects of Neutron Irradiation on Microstructure and Mechanical Properties of Nimonic PE-16

REFERENCE: Sklad, P. S., Clausing, R. E., and Bloom, E. E., "**Effects of Neutron Irradiation on Microstructure and Mechanical Properties of Nimonic PE-16,**" *Irradiation Effects on the Microstructure and Properties of Metals, ASTM STP 611,* American Society for Testing and Materials, 1976, pp. 139–155.

ABSTRACT: Specimens of Nimonic PE-16, a γ'-hardened austenitic alloy, were irradiated in the Experimental Breeder Reactor-II (EBR-II) in order to determine the effect of neutron irradiation on the microstructure and mechanical properties. Specimens with two different aging treatments were irradiated at temperatures ranging from 650 to 823 K and fluences ranging from 1.2×10^{26} neutrons (n)/m^2 to 4.0×10^{26} n/m^2. The aging treatments were: (A) 2h at 1313 K + 2 h at 1073 K + 16 h at 973 K; and (B) 4 h at 1313 K + 1 h at 1173 K + 8 h at 1023 K. Postirradiation transmission electron microscopy (TEM) revealed the presence of voids in all irradiated specimens. No difference in the fluence dependence of swelling at an irradiation temperature of 773 K was observed between the specimens with Preirradiation Treatment A and the specimens with Preirradiation Treatment B. In contrast, the temperature dependence of swelling appears to be sensitive to the particular preirradiation aging treatment used. TEM also shows that existing precipitates coarsen slightly during irradiation and that precipitation of γ'-precipitates occurs on irradiation-produced dislocation loops and voids.

Specimens irradiated at 773 K were tensile tested at 683, 773, 873, and 973 K. There is no significant difference in postirradiation mechanical properties between the two preirradition heat treatments. There is a large increase in yield strength after irradiation, which is consistent with the observed changes in microstructure. The ductility decreases as the test temperature increases. The low ductilities observed at the higher test temperatures are associated with a tendency for intergranular fracture. Auger spectroscopy of fracture surfaces on a specimen fractured at 823 to 873 K in the Auger chamber indicates that the concentrations of phosphorus and sulfur are a factor of two or three higher, and that the concentrations of iron and chromium are a factor of two lower, on surfaces of grain boundary fracture than on surfaces resulting from ductile fracture within the same specimen. There is also an enrichment of nickel at grain boundaries. In addition, helium release was observed at the time of fracture.

KEY WORDS: radiation, neutron irradiation, nickel-based austenitic alloys, precipitation hardening, radiation damage, mechanical properties, swelling, voids, Auger spectroscopy, transmission electron microscopy, precipitation

[1]Research staff members, Oak Ridge National Laboratory, Metals and Ceramics Division, Radiation Effects and Microstructural Analysis Group, Oak Ridge, Tenn. 37830.

Nimonic PE-16 is a γ'-hardened austenitic alloy which has been shown to have attractive strength properties and swelling resistance [*1*][2]. It is thus a candidate for fuel element cladding and fuel subassembly duct applications in future breeder reactors. To begin to understand the relationship between neutron irradiation-induced microstructural changes, mechanical property changes, and the initial microstructure, several specimens of this alloy with two different aging treatments were irradiated in the Experimental Breeder Reactor-II (EBR-II). Irradiation temperatures were in the range 650 to 823 K and the maximum fluence was 4×10^{26} neutrons (n)/m^2 (>0.1 MeV).

Experimental Procedure

Nimonic PE-16 rod having the composition given in Table 1 was fabricated according to the following schedule: As-received rod (13.0 mm

TABLE 1—*Chemical composition of PE-16.*

Element, weight %									
Ni	Cr	Mo	C	Al	Ti	Si	Mn	B	Fe
43.8	16.65	3.38	0.06	1.1	1.03	0.26	0.13	0.0020	balance

diameter) was annealed 1 h at 1313 K, swaged at 1253 K to 7.11 mm diameter, cold swaged to 6.88 mm diameter, swaged at 1253 K to 6.22 mm diameter, and cold swaged to 6.17 mm diameter. Cyclindrical density specimens (5.97 mm diameter by 10.2 mm long) and mechanical property test specimens (with gage section 3.175 mm diameter by 28.575 mm long) were machined from the rod and heat treated as follows: Treatment A—2 h at 1313 K plus 2 h at 1073 K plus 16 h at 973 K, or Treatment B—4 h at 1313 K plus 1 h at 1173 K plus 8 h at 1023 K. These two treatments are suggested by the manufacturers, Henry Wiggen & Company Limited, to provide high-creep rupture properties at longer times and greater metallurgical stability, respectively. Specimens were irradiated in the EBR-II. The fluences and temperatures are given in Table 2.

The microstructure of the material in the as-irradiated condition was characterized by transmission electron microscopy (TEM) of specimens sectioned from density blanks or unstressed portions of tensile specimens and prepared in the usual way. Quantitative measures of void swelling parameters were obtained by determining foil thickness by stereomicroscopy. Postirradiation examination also included tensile tests, scanning electron

[2] The italic numbers in brackets refer to the list of references appended to this paper.

TABLE 2—*Nimonic PE-16 irradiation history.*

Irradiation Temperature, K	Fluence, n/m^2 (>0.1 MeV)
650	1.2×10^{26}
708	2.9×10^{26}
748	4.0×10^{26}
773	1.2×10^{26}
773	1.7×10^{26}
773	2.3×10^{26}
773	4.0×10^{26}
823	2.9×10^{26}

microscopy (SEM) of fracture surfaces, and Auger spectroscopy of fracture surfaces created within the Auger apparatus. Specimens for *in situ* fracture within the Auger apparatus were machined from irradiated density blanks to a size of 10 mm long and 1 by 1 mm in cross section, with the center portion reduced to a 0.5 by 0.5 mm or 0.5 by 1 mm cross section to facilitate fracture at the desired position. Details of the specimen holder, tensile apparatus, and temperature control of the specimens in the Auger analysis are reported elsewhere [*2*].

Results

Microstructures

Transmission electron microscopy revealed the presence of voids in all irradiated specimens. Stereomicroscopy techniques were used to measure foil thickness and obtain values of volume change. Table 3 is a summary of the void swelling parameters for irradiated specimens with both preirradiation heat treatments. In all cases the number of voids, as well as the average diameter of the voids, was small. The volume change calculated from these values was in all cases less than 0.5 percent. A measured swelling of 0.18 to 0.34 percent in specimens irradiated to 4×10^{26} n/m^2 ($\sim$20 dpa) at 823 K in this study compares well with published data for examination of specimens of fuel pin cladding irradiated to $\sim$30 dpa at the same temperature, that is, 0.22 to 0.44 percent [*3*]. The magnitude of the swelling is low in both cases, although the swelling in the cladding material is higher. It must be remembered, however, that data from fuel pin cladding are on material stressed to some indeterminate level so that direct quantitative comparison is difficult.

Examination of the data reveals that preirradiation heat treatment had no effect on the swelling rate of specimens irradiated at 773 K. For specimens with both preirradiation heat treatments, the measured volume change increased as a function of fluence at this temperature from 0.04 percent at 1.2

TABLE 3—*Summary of void statistics in neutron-irradiated Nimonic PE-16.*

Irradiation Temperature, K	Neutron Fluence, n/m^2 (>0.1 MeV)	Void Concentration, voids/m^3	Volume Change, %	Average Void Diameter, nm
	Treatment A			
	2 h at 1313 K + 2 h at 1073 K + 16 h at 973 K			
650	1.2×10^{26}	75.0×10^{19}	0.05	10
708	2.9×10^{26}	11.2×10^{19}	0.08	21
748	4.0×10^{26}	8.8×10^{19}	0.15	30
773	1.2×10^{26}	5.4×10^{19}	0.04	22
773	1.7×10^{26}	2.0×10^{19}	0.02	27
773	2.3×10^{26}	5.9×10^{19}	0.04	21
773	4.0×10^{26}	13.4×10^{19}	0.22	28
823	2.9×10^{26}	7.0×10^{19}	0.34	40
	Treatment B			
	4 h at 1313 K + 1 h at 1173 K + 8 h at 1023 K			
650	1.2×10^{26}	70.0×10^{19}	0.08	13
708	2.9×10^{26}	5.4×10^{19}	0.09	30
748	4.0×10^{26}	22.2×10^{19}	0.29	29
773	1.2×10^{26}	2.8×10^{19}	0.04	27
773	1.7×10^{26}	3.4×10^{19}	0.03	24
773	2.3×10^{26}	5.2×10^{19}	0.06	27
773	4.0×10^{26}	10.3×10^{19}	0.23	33
823	2.9×10^{26}	4.7×10^{19}	0.18	39

$\times 10^{26}$ n/m^2 to ~0.22 percent at 4.0×10^{26} n/m^2. This increase is due to an increase in both the number of voids and the average void diameter as fluence increases. In contrast, the volume changes in specimens irradiated at different temperatures to approximately the same fluence (normalized to 4.0×10^{26} n/m^2 assuming a linear dependence of swelling on fluence and no incubation fluence) suggest a sensitivity of the temperature dependence of swelling to the preirradiation heat treatment. A summary of this normalized data is given in Table 4. In particular, the measured volume change in specimens with Treatment A increases continuously with temperature from 0.1 percent at 708 K to 0.47 percent at 823 K for a fluence normalized to 4.0×10^{26} n/m^2. For specimens with Preirradiation Treatment B the measured volume change for fluences normalized to 4.0×10^{26} n/m^2 increases from 0.1 percent to 708 K to a maximum value of 0.29 percent at 748 K and then remains relatively constant up to 823 K. The volume change in a specimen with Treatment B at the highest irradiation temperature is only one half as large as that measured in the specimen with Treatment A at the same irradiation temperature. This latter observation suggests that while the preirradiation heat treatment had no effect on the swelling rate of specimens irradiated at 773 K, the same is not true at other temperatures.

TABLE 4—*Temperature dependence of swelling in neutron-irradiated Nimonic PE-16.*

Irradiation Temperature, K	Neutron Fluence, n/m^2 (>0.1 MeV)	Volume Change, %
	Treatment A	
	2 h at 1313 K + 2 h at 1073 K + 16 h at 973 K	
708	4.0×10^{26}	0.10[a]
748	4.0×10^{26}	0.15
773	4.0×10^{26}	0.22
823	4.0×10^{26}	0.47[a]
	Treatment B	
	4 h at 1313 K + 1 h at 1173 K + 8 h at 1023 K	
708	4.0×10^{26}	0.10[a]
748	4.0×10^{26}	0.29
773	4.0×10^{26}	0.23
823	4.0×10^{26}	0.25[a]

[a]Normalized to 4.0×10^{26} n/m^2, assuming linear dependence of swelling on fluence and no incubation fluence.

Changes in dislocation structure were also observed in these specimens. Although no attempt was made to measure dislocation densities, some qualitative observations were made. The unirradiated specimens with both heat treatments are characterized by an almost dislocation-free microstructure. Although the postirradiation dislocation structure is much different, it does not appear to be sensitive to preirradiation heat treatment. In general, for constant irradiation temperature, the structure varies from a high concentration of small loops, many of which are faulted, at low fluence to a complex configuration of larger loops and loop segments at high fluence. The variation in dislocation structure as a function of irradiation temperature for approximately the same fluence follows a similar trend, changing from a high concentration of small loops at low temperature to a complex configuration of loops and segments at high temperature.

Since γ'-precipitates in PE-16 are known to have an important effect on mechanical properties and possibly swelling resistance, the effect of neutron irradiation on the morphology and distribution of the precipitates was investigated. The two preirradiation treatments produced γ'-precipitate distributions which were noticeably different. In particular, a specimen with Preirradiation Treatment A was characterized by a narrow and relatively symmetrical distribution of precipitate sizes, with diameters ranging from $\sim$10 nm to 33 nm and having a mean of $\sim$22 nm. The precipitates appear to be very regular in shape. A specimen with Preirradiation Treatment B

was also characterized by a narrow symmetrical distribution of precipitate particles. In this latter case, however, the size of the particles was smaller, ranging from ~6.0 nm to ~13.0 nm and having a mean size of ~10 nm. In order to characterize some of the changes in γ'-distribution and morphology which result from neutron irradiation, several specimens with Preirradiation Treatment A and different irradiation histories were examined by TEM.

The distribution of γ'-particle sizes in a specimen with Preirradiation Treatment A irradiated to a fluence of 1.2×10^{26} n/m^2 at 650 K is essentially the same as in the unirradiated specimen. No significant redistribution of precipitates nor coarsening of existing precipitates was observed. It was not possible to determine positively whether small γ'-precipitates were present on loops due to the fine scale of the irradiation-produced dislocation structure.

Although many of the γ'-precipitates seen in the specimen irradiated to a fluence of 1.2×10^{26} n/m^2 at 773 K are similar in size to those in the unirradiated specimen, there is also a significant number of large (~45 nm diameter) irregularly shaped γ'-precipitates. These are associated with large perfect loops or dislocation segments. In addition, examples of small (~5 nm diameter) γ'-precipitates which have formed on the dislocation lines of irradiation-produced loops, and also of thin layers of γ' which have precipitated at void surfaces, are observed. Similar observations were made in specimens irradiated to a fluence of 4×10^{26} n/m^2 at 773 K. These observations are illustrated in Fig. 1. The appearance of an unirradiated specimen is shown in Fig. 1*a*. Here the γ'-precipitates are imaged in dark-field contrast using a [110] superlattice reflection on a (200) matrix pattern. The appearance of a specimen after neutron irradiation to a fluence of 4×10^{26} n/m^2 at 773 K is shown in Fig. 1*b* as imaged in dark-field contrast using the [110] superlattice reflection. In addition to regularly shaped precipitates similar to those seen in the unirradiated case, large irregularly shaped γ'-precipitates associated with perfect loops or dislocation segments, small γ'-precipitates on the dislocation lines of loops, and γ' precipitated at void surfaces can be clearly seen. The decorated loops are identified as *L* and the voids as *V* in the micrograph. The changes which occur during irradiation become more pronounced with increasing fluence. Furthermore, a slight coarsening of the uniformly distributed, regularly shaped γ'-precipitates occurs at the higher fluence, producing a size distribution which is skewed toward larger sizes. Although no quantitative analysis of kinetics was performed, this coarsening appears to be fluence dependent since it was not observed in the specimens irradiated to a lower fluence at the same temperature.

The observation of precipitates associated with dislocations is in agreement with similar observations by Sharpe and Whapham [*4*] in neutron-irradiated PE-16, and by Hudson [*5*] in both neutron-irradiated

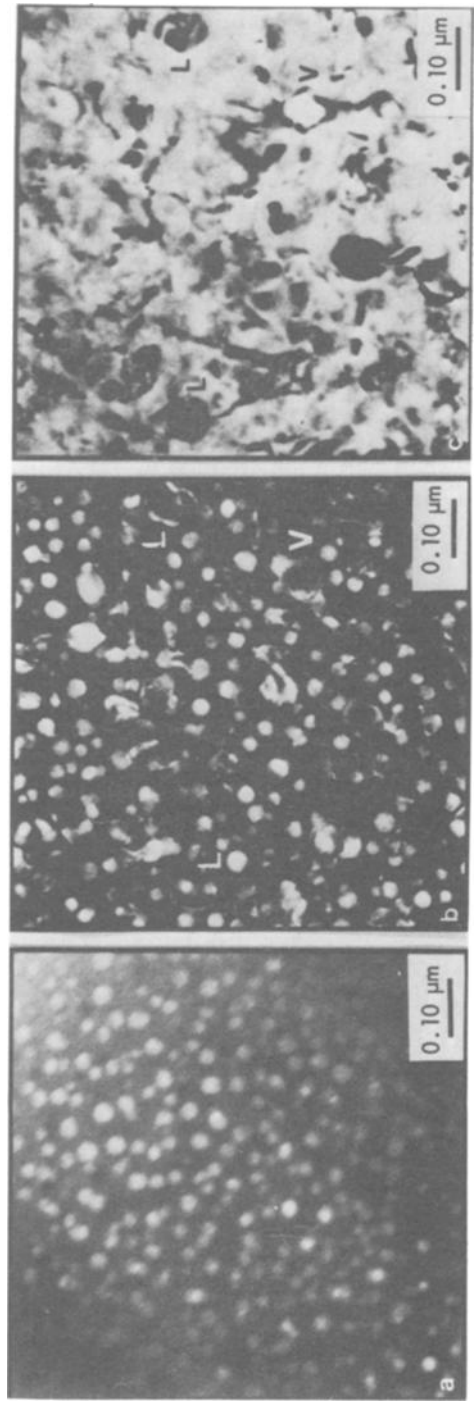

FIG. 1—*Neutron irradiation-induced changes in distribution and morphology of γ′-precipitates in PE-16.* (a) *Precision dark-field images of γ′-precipitates in unirradiated PE-16 with the following heat treatment: 2 h at 1313 K + 2 h at 1073 K + 16 h at 973 K: [110] superlattice reflection on (200) matrix pattern.* (b) *Precision dark-field images of γ′-precipitates in PE-16 irradiated to a fluence of* 4×10^{26} *n/m*^{2} *at 773 K using [110] superlattice reflection. Preirradiation treatment same as in* (a), *precipitates on irradiation-produced loops and voids identified as* L *and* V, *respectively.* (c) *Bright-field image of* (b).

and ion-bombarded PE-16. Although the precipitation of γ'-precipitates on dislocations observed in the present study is on a much finer scale due to the fact that the dislocation structure is not as well developed at our lower irradiation temperatures, the phenomenon is the same, that is, heterogeneous precipitation of γ' on dislocations. The precipitation of γ' on dislocations may be significant in two ways. First the precipitates may pin the dislocations and thus provide increased strength, and second, precipitation of γ' on dislocations may inhibit the ability of dislocations to act as preferential sinks for interstitials. Segregation of alloying elements to void surfaces has been predicted by Anthony [*6*] and has been experimentally observed in several systems [*7*]. Sharpe and Whapham [*4*] and the present authors have observed the precipitation of γ' at void surfaces in PE-16. The precipitation of γ' at void surfaces may indicate that significant segregation of nickel, titanium, and aluminum to the voids occurs during irradiation. It cannot be shown from our results, however, that this is an irradiation effect rather than an equilibrium phenomenon. Two other possible explanations for the presence of γ' precipitates at void surfaces exist: (*a*) The void may provide a preferential nucleation site for the precipitates, or (*b*) the void is nucleated and grows until it intersects existing γ'-precipitates which subsequently coat the void surface.

If the precipitation of γ' at void surfaces is due to segregation, it implies similar segregation to other internal surfaces such as grain boundaries. Compositional changes of this type may influence other properties such as ductility or may provide a possible mechanism for limiting void growth.

Mechanical Properties

Specimens with both preirradiation heat treatments irradiated to a fluence of 1.2×10^{26} n/m^2 at 773 K were tensile tested at 673, 773, 873, 973 K. The results of these tests, along with those for unirradiated as-heat-treated specimens, are tabulated in Table 5. It can be seen that the two preirradiation treatments produce different properties in unirradiated specimens. In particular, specimens given Treatment A have a higher yield stress as well as a higher uniform elongation. After irradiation, there is an increase in yield strength in all specimens; however, there is no significant difference in postirradiation properties between specimens with Preirradiation Treatments A and B. Figure 2 illustrates the variation in properties with test temperature and compares them with handbook values [*8*]. The yield strength, ultimate tensile strength, and ductility all decrease with increasing test temperature. In considering the results of tests at 873 and 973 K, it should be noted that the specimens were irradiated at 773 K, and, thus, the matrix hardening (as indicated by the increase in yield strength) is greater than would be expected in specimens irradiated to the same fluence at 873 and 973 K.

Fracture surfaces from the irradiated specimens tested at 673, 773, 873,

TABLE 5—*Tensile properties of neutron-irradiated Nimonic PE-16.*

Heat Treatment	Irradiation Conditions		Test Conditions		Tensile Properties			
	Temperature, K	Fluence, n/m^2 (>0.1 MeV)	Temperature, K	$\dot{\epsilon}$, min^{-1}	σ_y, ksi	σ_{uts}, ksi	ϵ_u, %	ϵ_r %
Treatment A	...	...	673	0.002	80.9	124.1	12.8	32.1
2 h at 1313 K + 2 h at 1073 K + 16 h at 973 K	...	...	773	0.002	81.6	140.1	18.6	22.5
	773	1.2×10^{26}	773	0.20	119.2	157.3	9.7	12.2
	773	1.2×10^{26}	773	0.02	120.4	161.2	10.6	13.8
	773	1.2×10^{26}	773	0.002	116.9	149.6	10.2	12.3
	773	1.2×10^{26}	873	0.002	112.5	126.1	1.6	1.6
Treatment B	...	...	473	0.002	63.7	132.8	24.5	27.8
4 h at 1313 K + 1 h at 1173 K + 8 h at 1023 K	...	...	673	0.002	63.2	124.7	25.5	32.5
	...	...	773	0.002	64.1	125.5	23.4	27.8
	773	1.2×10^{26}	773	0.20	116.4	151.5	12.3	14.7
	773	1.2×10^{26}	773	0.02	116.8	154.0	11.9	12.6
	773	1.2×10^{26}	973	0.002	97.3	99.7	0.5	0.5
	773	1.2×10^{26}	673	0.002	113.7	145.0	12.0	14.8

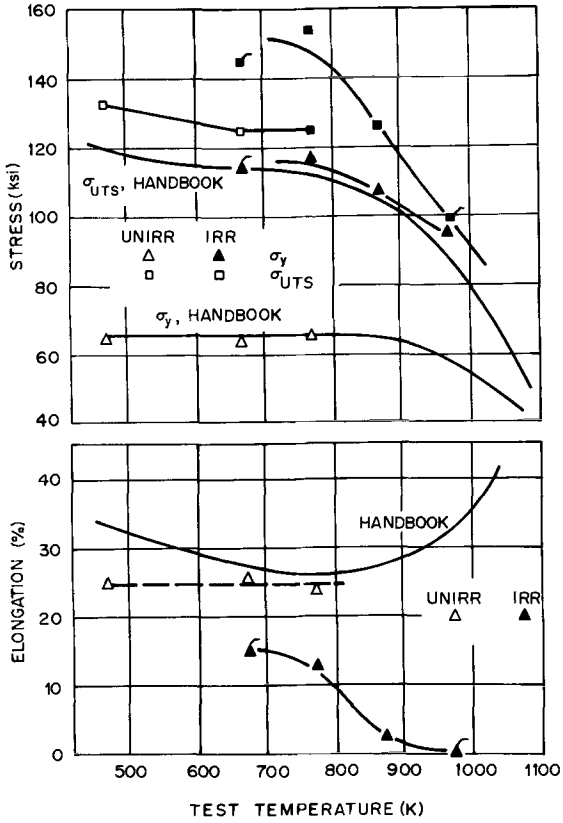

FIG. 2—*Tensile properties of Nimonic PE-16 irradiated at 773 K to 1.2 × 10^{26} n/m² (>0.1 MeV). Heat treatment: 4 h at 1313 K + 1 h at 1173 K + 8 h at 1023 K. (Flags signify 2 h at 1313 K + 2 h at 1073 K + 16 h at 973 K.) Handbook values from Ref 8.*

and 973 K have been examined by SEM. The fracture surfaces varied gradually with increasing test temperature from primarily transgranular shear character in the specimen tested at 673 K to completely intergranular character in the specimen tested at 973 K (Fig. 3). The low ductilities observed at higher test temperatures are associated with this tendency for intergranular fracture. Note that the fracture surfaces shown in Fig. 3*a* and *d* are from specimens given Preirradiation Treatment B while the fracture surfaces shown in Fig. 3*b* and *c* are from specimens given Treatment A.

The increase in yield strength over the unirradiated value observed in specimens irradiated at 773 K to a fluence of 1.2 × 10^{26} n/m² is not unexpected and follows the trends seen by Broomfield [*9*] at lower fluences. The values given in Table 5 are significantly higher than those reported by

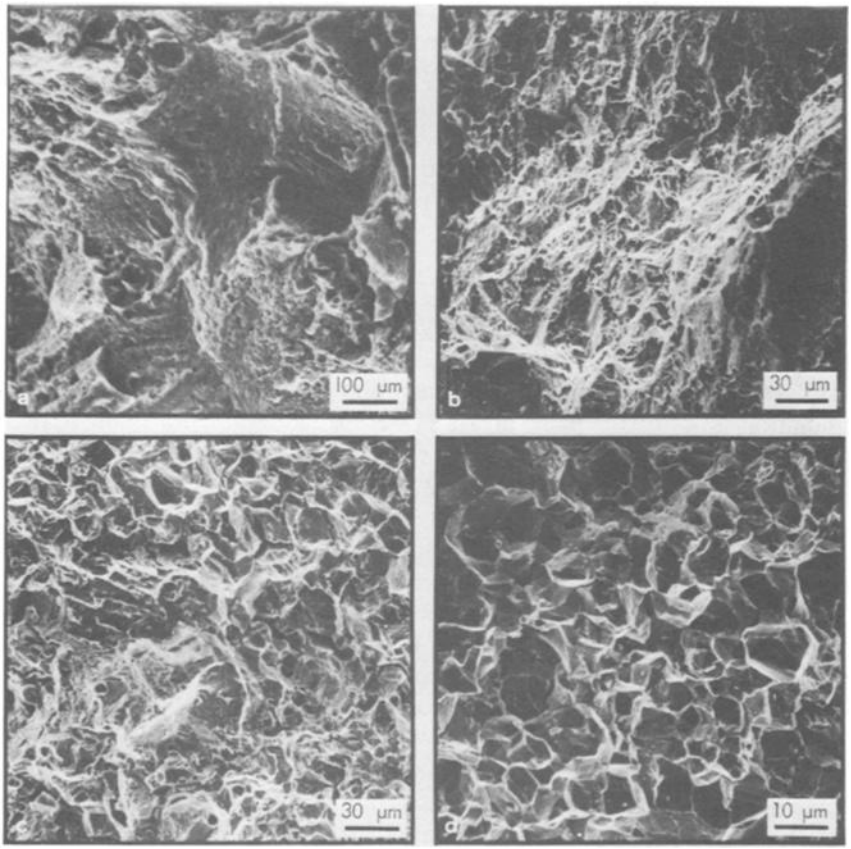

FIG. 3—*SEM's of fracture surfaces in PE-16 irradiated at 773 K to a fluence of 1.2 × 10^{26} n/m². Strain rate = 0.02 min^{-1}. (a) Test temperature 673 K; fracture primarily transgranular. (b) Test temperature 773 K; fracture-mixed transgranular and intergranular. (c) Test temperature 873 K; fracture-mixed transgranular and intergranular. (d) Test temperature 973 K; fracture primarily intergranular. (Note: Specimens tested at 673 K and 973 K had Preirradiation Treatment B while specimens tested at 773 K and 873 K had Preirradiation Treatment A.)*

Broomfield; however, this may be the result of the lower irradition temperature and test temperatures used in the present study. The increase in strength is due to the combined effect of high densities of irradiation-produced dislocations and a redistribution of γ'-precipitates on the dislocations. In contrast to the foregoing results, the yield strength values reported by Fraser et al [*10*] are significantly lower. The reason for this disagreement is not presently known.

The decrease in strength which is observed in specimens tested at temperatures higher than the irradiation temperature is due to partial recovery

of the irradiated dislocation structure and to the decrease associated with thermally activated processes. In general, the strength of PE-16 remains higher until the test temperature reaches a critical value approximately equal to the irradiation temperatures and then begins to drop drastically. The uniform ductility measured in the irradiated PE-16 parallels the tensile behavior; that is, it remains fairly constant until the test temperature is greater than 773 K and then drops sharply.

Auger Spectroscopy

In order to determine whether segregation to grain boundaries contributes to the intergranular fracture and low ductilities, several specimens of PE-16 which had been given Preirradiation Treatment A before neutron irradiation to 4×10^{26} n/m^2 at 773 K were fractured *in situ* in an Auger spectrometer at temperatures between 823 and 973 K. A mass spectrometer incorporated in the Auger apparatus was used to determine if helium was released as the specimens were fractured. The first specimen was fractured at 823 to 873 K. The fracture was predominantly transgranular except for a small area of intergranular fracture, marked "I" in Fig. 4. The second specimen was fractured at 923 to 973 K. Helium release occurred; however, an estimate of the amount could not be obtained because the mass spectrometer became saturated. The fracture was predominantly along grain boundaries as shown in Fig. 5. Many of the grain boundary surfaces contained sharp ledges or offsets, Fig. 6, which are thought to result from channel deformation. The final specimen was tested between 823 and 873 K. Again helium release was detected. Based on system pumping rate, volume, and observed pressure increase, a helium release of $\sim$0.03 helium atoms per atom of grain boundary is calculated assuming 1.5×10^{19} grain boundary atoms/m^2. This value is in agreement with the helium release value measured in Type 304 stainless steel irradiated to approximately the same fluence at about 650 K and fractured at 823 K [*2*].

Auger spectra were taken at several positions on each of the fracture surfaces. Table 6 compares the compositions in a region of ductile fracture and a region of grain boundary fracture on a specimen fractured at 823 to 873 K. Concentrations of phosphorous and sulfur are about a factor of three higher and the concentrations of iron and chromium about a factor of two lower on surfaces of grain boundary fracture than on surfaces resulting from ductile fracture within the same specimen. The concentrations of nickel and titanium are also higher at the grain boundary surface. Similar observations were made on grain boundary fractures in the specimens tested at 923 to 973 K. Carbon concentration was high on all surfaces although this effect is probably due to surface contamination rather than a real segregation effect. The fracture surface produced at 923 to 973 K was sputtered with 1000 eV argon ions at 5×10^{-5} torr using a normal incidence

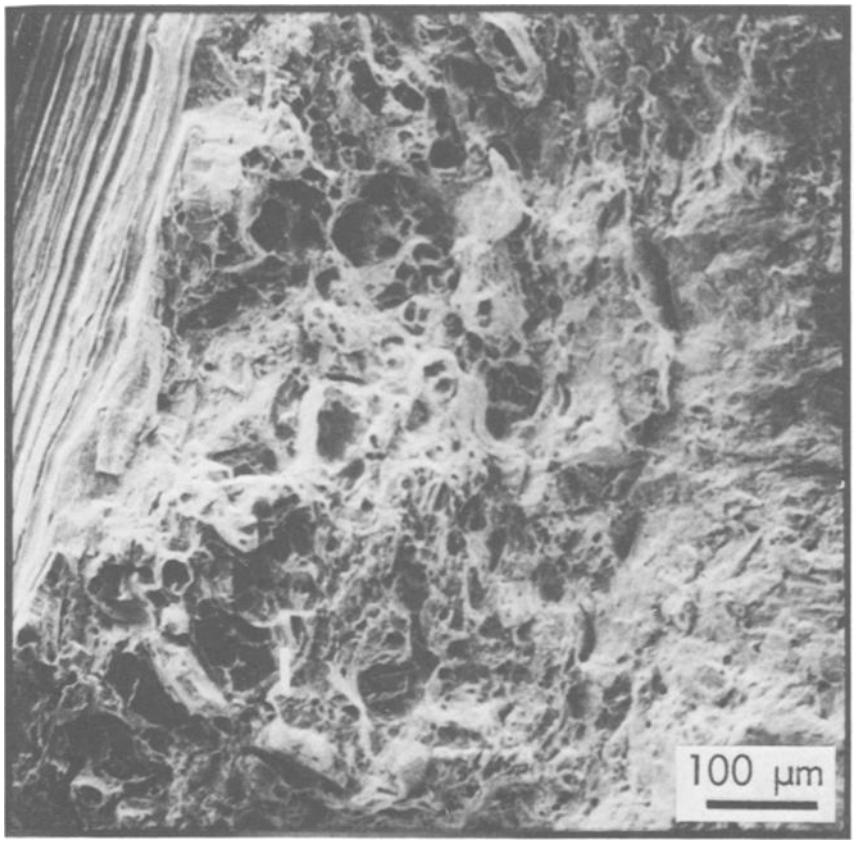

FIG. 4—*SEM of fracture surface of specimen of PE-16 irradiated at 773 K to a fluence of 4* $\times$ 10^{26} *n/m*^{2} *and fractured* in situ *in the Auger spectrometer at 823 to 873 K. Area of intergranular fracture marked* "I."

beam. Removal rates are estimated to be 1 atom layer per minute. After 40 min of sputtering, the phosphorous and sulfur concentrations in the sputtered area decreased from 2.2 and 3.8 atomic percent to 0.6 and 0.4 atomic percent respectively. On the initial fracture surface the carbon peaks were not typical of a carbide phase whereas after sputtering they were.

The iron, nickel, and chromium concentrations at the grain boundaries are significantly different than in the bulk. Table 7 gives the relative concentrations of these three elements normalized to 100 for different areas of a fracture surface. It is evident that the grain boundary is significantly enriched in nickel and depleted in iron and chromium. As was the case with phosphorous and sulfur, the nickel, chromium, and iron composition of the boundary approaches that in the bulk after 40 min of sputtering. Such

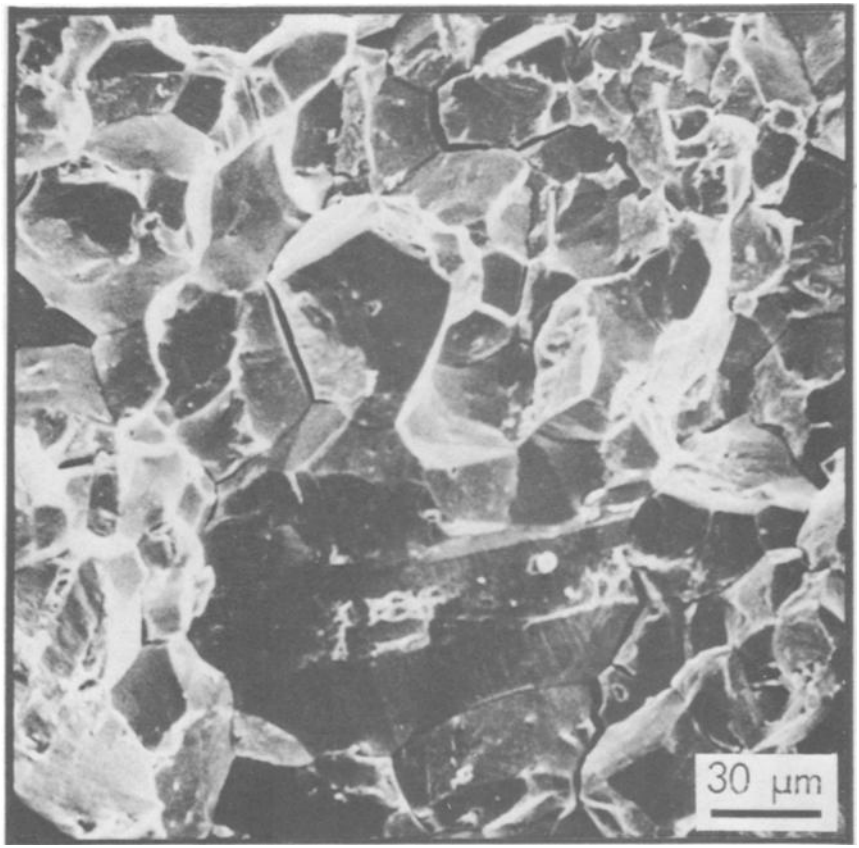

FIG. 5—*SEM of fracture surface of specimen of PE-16 irradiated at 773 K to a fluence of 4* $\times$ 10^{26} *n/m*^{2} *and fractured* in situ *in the Auger spectrometer at 923 to 973 K. Fracture is predominantly intergranular.*

segregation of iron, nickel, and chromium could be qualitatively predicted. If we assume that the grain boundary acts as a sink for vacancies during irradiation, a relative enrichment of nickel and depletion of iron at the grain boundary would occur if $D_{Fe} > D_{Ni}$. Duiraldenq and Poyet [*11*] have shown that this is the case in an alloy of Fe-45Ni-19Cr at 1173 K, and it is not unreasonable to expect similar behavior in PE-16 (Fe-43Ni-17Cr) irradiated at 773 K.

The segregation of sulfur and phosphorous to grain boundaries as determined by Auger spectroscopy is of interest since the presence of these elements at grain boundaries may be detrimental to ductility. It is not possible to determine from our results whether such segregation is an equilibrium phenomenon or the result of the boundary acting as vacancy of interstitial sink during irradiation.

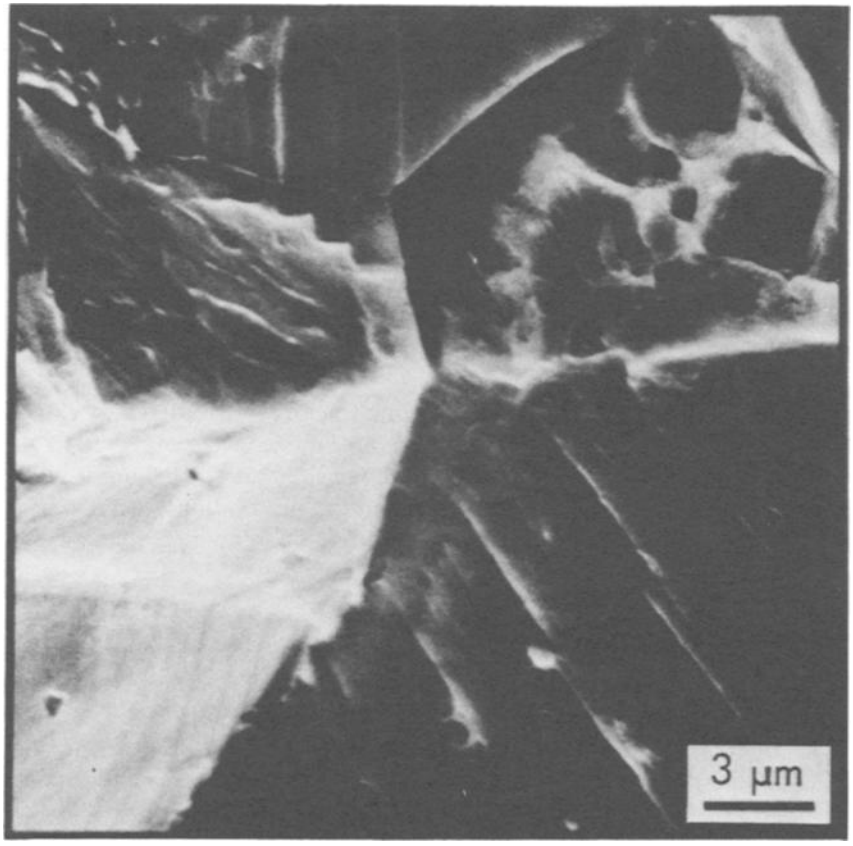

FIG. 6—*SEM of fracture surface of PE-16 specimen irradiated at 773 K to a fluence of 4 × 10^{26} n/m² and fractured* in situ *in the Auger spectrometer at 923 to 973 K. Ledges or offsets are thought to result from channel deformation.*

TABLE 6—*Estimated composition of fracture surfaces from Auger spectroscopy.*

Type of Fracture	Element, atomic %						
	Fe	Cr	Ni	P	S	C	Ti
Ductile fracture at 823 to 873 K[a]	21.1	13.4	36.1	1.4	0.6	24.3	1.9
Grain boundary at 823 to 873 K[a]	11.3	8.4	37.1	5.0	1.9	33	2.5

[a]Comparison of ductile and grain boundary fracture areas on same specimen.

TABLE 7—*Relative concentrations of iron, nickel, and chromium on fracture surfaces*[a].

Type of Fracture	Relative Atomic Concentration, %		
	Fe	Ni	Cr
Bulk composition	35	45	20
Ductile fracture at 823 to 873 K	30	52	18
Grain boundary fracture at 923 to 973 K[b]	16	72	12
Grain boundary fracture at 923 to 973 K[b] after 40 min of sputtering	36	48	16

[a]Σ Fe, Ni, Cr = 100 percent.
[b]Comparison of grain boundary fracture area on same specimen before and after sputtering.

The observation of helium release during fracture of irradiated specimens is significant in terms of ductility. Since no bubbles were observed at the boundaries by TEM, it is reasonable to conclude that the helium is either segregated to the boundary but remaining "in solution" as a partial monolayer or precipitated into bubbles less than 1 to 2 nm in diameter.

Conclusions

1. Void swelling was observed in all specimens of solution-treated and aged PE-16 irradiated at temperatures ranging from 650 to 823 K and fluences ranging from 1.2×10^{26} n/m^2 to 4.0×10^{26} n/m^2. Swelling was less than 0.5 percent in all cases.

2. No difference in the fluence dependence of swelling at an irradiation temperature of 773 K was observed between specimens with the two preirradiation treatments investigated.

3. The temperature dependence of swelling appears to be sensitive to preirradiation heat treatment for a fluence of approximately 4.0×10^{26} n/m^2.

4. Significant changes occur in the distribution and morphology of γ'-precipitates during neutron irradiation. Irradiation at 773 K to a fluence of 4.0×10^{26} n/m^2 causes coarsening of some existing γ'-precipitates as well as precipitation of γ' on irradiation-produced dislocation loops and voids.

5. There is no significant difference in postirradiation mechanical properties of specimens with the preirradiation heat treatments investigated in this study.

6. Neutron irradiation produces a large increase in yield strength. Ductility decreases with increasing test temperature. The low ductilities at higher test temperature are associated with a tendency for intergranular fracture.

7. Auger spectroscopy indicates that concentrations of phosphorous and sulfur are higher and concentrations of iron and chromium lower on sur-

faces of grain boundary fracture than on ductile fracture surfaces in the same specimen. The concentration of nickel is also higher at grain boundary surfaces.

8. Helium release was observed at the time of fracture in specimens tested at 823 to 873 K and 923 to 973 K.

Acknowledgements

The research reported herein was sponsored by the U.S. Engery Research and Development Administration under contract with Union Carbide Corporation.

The authors would like to thank J. Bentley for invaluable assistance in transmission electron microscopy.

References

[1] Hudson, J. A., Mazey, D. J., and Nelson, R. S., "Void Formation in Nickel, 316 Steel, and Nimonic PE-16 During 20 MeV C^{++} Irradiation," *Voids Formed by Irradiation of Reactor Materials,* British Nuclear Energy Society Conference, S. F. Pugh, M. H. Loretto, and D.I.R. Norris, Eds., Reading, England, 1971.

[2] Clausing, R. E. and Bloom, E. E. in *Grain Boundaries in Engineering Materials,* Proceedings of the 4th Bolton Landing Conference J. L. Walter, J. H. Westbrook, and D. A. Woodford, Eds., June 1974, pp. 491–505.

[3] Bramman, J. I., Bagley, K. Q., Cawthorne, C., and Fulton, E. J., "Void Formation in Cladding and Structural Materials Irradiated in DFR," *Radiation-Induced Voids in Metals,* Proceedings of the 1971 International Conference, J. W. Corbett and L. C. Ianniello, Eds., Albany, N.Y., 1971.

[4] Sharpe, R. M. and Whapham, A. D., "Effects of Irradiations on γ' Precipitation in Nimonic PE-16 Alloy," *Proceedings,* Conference on Irradiation Behavior of Fuel Cladding and Core Component Materials, Karlsruhe, Germany, 1974.

[5] Hudson, J. A., *Journal of British Nuclear Energy Society,* Vol. 14, No. 2, April 1975, pp. 127–136.

[6] Anthony, T. R., *Radiation-Induced Voids in Metals,* Proceedings of the 1971 International Conference, J. W. Corbett and L. C. Ianniello, Eds., Albany, N.Y., 1971, pp. 630–646.

[7] Okamoto, P. R. and Weidersich, H., *Consultant Symposium in the Physics of Irradiation Produced Voids,* R. S. Nelson, Ed., Harwell, England, 9–11, Sept. 1974, pp. 231–238.

[8] "Nimonic Alloy PE-16," Henry Wiggin & Company Limited, Hereford, England, Publication 3349A.

[9] Broomfield, G. H. in *Irradiation Effects in Structural Alloys for Thermal and Fast Reactors, ASTM STP457,* American Society for Testing and Materials, 1969, pp. 38–66.

[10] Fraser, A. S., Gillies, M. A., and Sinclair, W. D. J., "Irradiation Embrittlement of a Nickel Base Precipitation Hardening Alloy-Nimonic PE-16," *Proceedings,* Conference on Irradiation Behavior of Fuel Cladding and Core Component Materials, Karlsruhe, Germany, 1974.

[11] Guiraldenq, P. and Poyet, P., *Memoires Scientifiques de la Revue de Metallurgie,* Vol. 70, No. 10, 1973, pp. 715–23.

A. L. Ward,[1] *J. M. Steichen,*[1] *and R. L. Knecht*[1]

Irradiation and Thermal Effects on the Tensile Properties of Inconel-718

REFERENCE: Ward, A. L., Steichen, J. M., and Knecht, R. L., **"Irradiation and Thermal Effects on the Tensile Properties of Inconel-718"** *Irradiation Effects on the Microstructure and Properties of Metals, ASTM STP 611,* American Society for Testing and Materials, 1976, pp. 156–170.

ABSTRACT: The effects of neutron irradiation and out-of-flux aging on the tensile properties of wrought and weld-deposited Inconel-718 have been investigated following fast-reactor irradiation to total fluences ranging from 0.55×10^{22} neutrons (n)/cm^2 (~400 °C) (752 °F) to 6.6×10^{22} n/cm^2 (649 °C) (1200 °F) and thermal exposure at 538 and 649 °C (1000 and 1200 °F) for durations to 10 000 h. Classical irradiation hardening is exhibited by this very strong material following irradiation at low temperature (~400 °C) (752 °F) to relatively low fluence (~10^{22} n/cm^2) and also at high temperature when very high fluence (6.6×10^{22} n/cm^2) is accumulated. At test temperatures ≥538 °C (1000 °F), ductility losses arising from helium embrittlement are evident for all irradiation conditions and at high fluences are so severe as to restrict the strength to lower than expected values.

Low postirradiation strength, compared to that following out-of-flux aging for equivalent durations, suggests that irradiation accelerates the thermal overaging process at 538 °C (1000 °F). At 649 °C (1200 °F), the results are obscured by embrittlement and coincident limitations on strain hardenability.

KEY WORDS: radiation, irradiation, thermal stability, helium, thermal reactors, tensile properties, nickel alloys, strain hardening

Inconel-718, a precipitation hardenable nickel-base alloy, is a candidate material for a variety of structural applications in liquid metal fast breeder reactor (LMFBR) systems. Knowledge of the response of this alloy to neutron fluence and elevated-temperature exposure is thus required for design, design confirmation, operations support, and safety analyses.

Irradiation effects on the short-term tensile properties of wrought Inconel-718 have been investigated following exposure in the Experimental Breeder Reactor-II (EBR-II) to a variety of neutron fluence levels and a

[1]Senior engineer, advanced engineer, and manager, Materials Analysis Section, respectively, Hanford Engineering Development Laboratory, Westinghouse Hanford Company, Richland, Wash. 99352.

number of irradiation temperatures ranging from 0.55 × 10^{22} neutrons (n)/cm^2 (total) at 404 °C (759 °F) to 6.6 × 10^{22} n/cm^2 (total) at 649 °C (1200 °F). The wrought materials included in this study represent a conventional solution anneal and duplex precipitation-heat treatment. In addition, weld-deposited (gas tungsten-arc) Inconel-718 specimens were irradiated to total fluences in the range from 2.55 to 3.05 × 10^{22} n/cm^2 at 538 °C (1000 °F) to 3.19 to 3.35 × 10^{22} n/cm^2 at 649 °C (1200 °F).

Irradiation effects on the properties of the wrought material are examined by comparison of preirradiation trend values and postirradiation measured values. Comparisons are also made between postirradiation properties and those representing out-of-reactor thermal exposures at 538 and 649 °C (1000 and 1200 °F) for periods of 1000, 4000, and 10 000 h.

Materials and Procedures

The wrought Inconel-718 used in this study was obtained in the form of 12.7-mm-thick plate. Miniature buttonhead tension specimens (48 mm long, 3.18 mm gage diameter, 28.6 mm gage length, and 6.4 mm buttonhead diameter) were taken from the plate such that the specimen axis was parallel to the longitudinal forming direction of the plate. Weld metal specimens of identical configuration were obtained from a gas tungsten-arc butt weld in the base plate. The plate was solution annealed prior to welding and specimens were taken both from longitudinal and transverse orientations relative to the weld axis.

All specimens from the wrought material and most of the weld specimens were solution annealed at 954 °C (1749 °F) for one half hour and then aged at 717 °C (1323 °F) for 8 h, furnace cooled to 621 °C (1150 °F), and held until the total aging time reached 18 h (AMS 5596C). A limited number of weld specimens were retained in the as-welded condition for both pre- and postirradiation testing. The chemical compositions of the wrought plate and weld filler metal are given in Table 1.

All irradiated specimens were contained in experiments exposed in EBR-II, Row 2, core positions. Irradiation conditions (Table 2) included total fluence levels from 0.55 to 10^{22} n/cm^2 to 6.6 × 10^{22} n/cm^2 and temperatures from 395 °C (743 °F) to 649 °C (1200 °F). Exposure durations (residence time at full-power reactor operation) were 1121 h for the low-fluence irradiations (<10^{22} n/cm^2), 3888 h for the intermediate fluences (1.3 to 2.98 × 10^{22} n/cm^2) at 593 and 649 °C (1100 and 1200 °F), and 7528 h for the balance (Table 2). Specimens irradiated at 391 and 404 °C (736 and 759 °F) were contained in "weeper" capsules which permitted free ingress of the reactor primary coolant sodium. Specimens irradiated at the higher temperatures were contained in closed subcapsules in a static sodium environment. Results describing the effects of out-of-reactor thermal aging

TABLE 1—*Chemical composition of Inconel-718 base and weld materials (weight percent).*

	Plate, Ht52C9EK	Filler Metal, Ht60C7E
C	0.07	0.04
Mn	0.08	0.09
Fe	18.19	17.97
S	0.007	0.007
Si	0.17	0.18
Cu	0.11	0.10
Ni	53.44	53.84
Cr	18.11	18.04
Al	0.59	0.55
Ti	1.08	1.01
P	0.007	0.01
Co	0.03	0.03
Mo	3.0	3.0
B	0.0032	0.0042
Cb + Ta	5.10	5.12

TABLE 2—*Summary of irradiation conditions for Inconel-718 wrought and weld specimens.*

Material Type	Total Fluence, n/cm^2	Irradiation Temperature, °C	In-Flux Residence Time, h
Wrought	0.55×10^{22}	404	1121
Wrought	0.93×10^{22}	391	1121
Wrought	0.86 to 0.98×10^{22}	593	1121
Wrought	1.78 to 2.44×10^{22}	593	3888
Wrought	2.18 to 4.63×10^{22}	538	7528
Wrought	3.18 to 5.79×10^{22}	620	7528
Wrought	3.13 to 3.42×10^{22}	649	3888
Wrought	6.49 to 6.66×10^{22}	649	7528
Weld	2.55 to 3.05×10^{22}	538	7528
Weld	3.19 to 3.35×10^{22}	649	3888

were obtained from specimens which also were contained in closed, sodium-filled capsules.

All tension tests were conducted on hard-beam universal test machines at a constant crosshead rate of 8.5×10^{-4} mm/s (strain rate = 3.0×10^{-5}/s). Conventional engineering stress-strain curves were obtained from autographic records of the applied load and specimen extension. Total elongation and reduction-of-area values are based on pre- and post-test specimen measurements. Uniform elongation (elongation at maximum load) values were obtained from the test records and then adjusted in proportion to the difference between the measured and indicated total elongation values.

Results and Discussion

Wrought Base Metal

The tensile properties for the wrought and age-hardened Inconel-718 included in the present study are illustrated graphically in Figs. 1 and 2 as functions of test temperature over the range from room temperature to 760°C (1400°F). The results of multiple tests at each temperature are shown by dashed-line bands to represent the maximum range of the data at any given

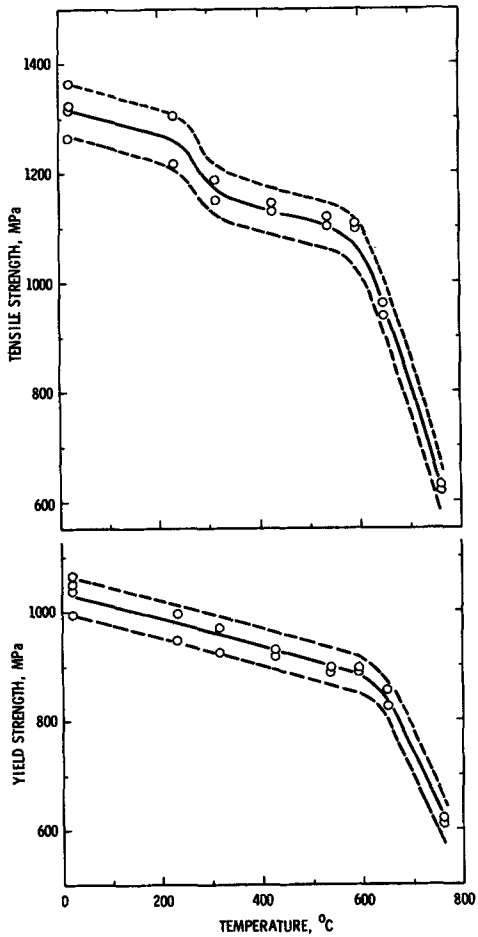

FIG. 1—*Preirradiation strength of wrought Inconel-718.*

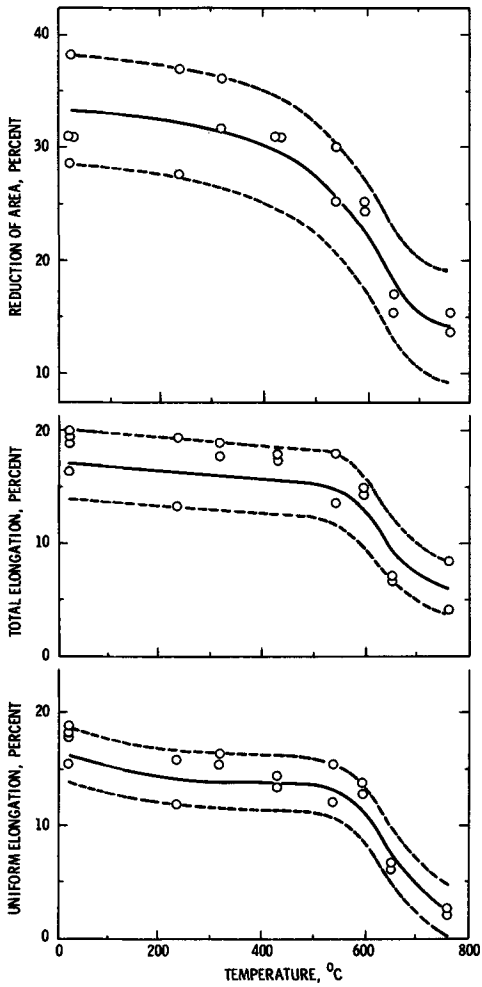

FIG. 2—*Preirradiation ductility of wrought Inconel-718.*

temperature in the range. For purposes of comparison with postirradiation properties, trend lines representing the locus of mean values based only on the scatterbands have also been constructed.

In general, the overall magnitude of the properties and the behavioral trends—decreasing strength and ductility with increasing temperature—are consistent with those reported by Brinkman and Korth [*1*][2] for the same heat of material and with those reported elsewhere for other Inconel-718

[2]The italic numbers in brackets refer to the list of references appended to this paper.

[2–5]. The properties also conform to the minimum strength and ductility requirements specified by AMS 5596B. The apparent discontinuity in the tensile strength curve, in the range from 200 to 300 °C (392 to 572 °F) (Fig. 1), evidently has not been reported previously and is believed to be associated with the onset of strain aging at these temperatures and this relatively low strain rate [6,7]. The time-dependent nature of the strain-aging phenomenon is such that the yield strength, which is obtained from the very early portion of the stress-strain curve, is not affected. All ductility parameters fall sharply as the temperature exceeds ~600 °C (1112 °F) (Fig. 2) coincident with a transition in fracture mode which is transgranular at low temperatures and predominantly intergranular at temperatures of 649 and 760 °C (1200 and 1400 °F). As a point of general interest, tests conducted at 871 °C (1600 °F) produced results which showed that minima occur in the total elongation and reduction of area curves at about 700 to 800 °C (1292 to 1472 °F); values approaching 35 and 70 percent, respectively, were obtained at 871 °C (1600 °F).

Changes in mechanical properties of austenitic materials from fast-reactor irradiation have been a subject of intensive study in recent years [8–10]. Classical irradiation damage takes the form of increases in strength, loss in strain hardening capacity, and reductions in ductility at temperatures generally below about one half the absolute melting point. At high temperatures, damage may anneal at rates approaching the damage accumulation rate, thus reducing the net effect observed in postirradiation tests. At test temperatures greater than the homologous temperature ($T_m/2$), however, the phenomenon of helium embrittlement can severely limit postirradiation ductility irrespective of the classical hardening state [11–13].

Evaluation of irradiation effects in Inconel-718 requires consideration of the thermal stability and the irradiation damage state, both of which depend upon the irradiation temperature, fluence, time at temperature, and the test temperature. The effects of neutron fluence and test and irradiation temperature are summarized in Figs. 3 through 5, in which the postirradiation measured properties are plotted against the preirradiation trend values given by the curves of Figs. 1 and 2. Taken as a whole, the body of yield strength data (Fig. 3) appears simply to scatter about the diagonal line representing no effect of irradiation; however, some trends are apparent upon closer examination. At the lowest fluence and temperature, the data do, in fact, scatter rather closely about the line at all test temperatures. When the fluence is approximately doubled (0.93×10^{22} n/cm^2) at essentially the same temperature (391 °C versus 404 °C) (736 °F versus 759 °F), the yield strengths tend to fall above the line. At a higher irradiation temperatures (593 °C (1100 °F) and about the same fluence (0.86 to 0.98×10^{22} n/cm^2), the data invariably fall below the line. Such loss of strength can be attributed only to thermal effects since strength increases were noted when

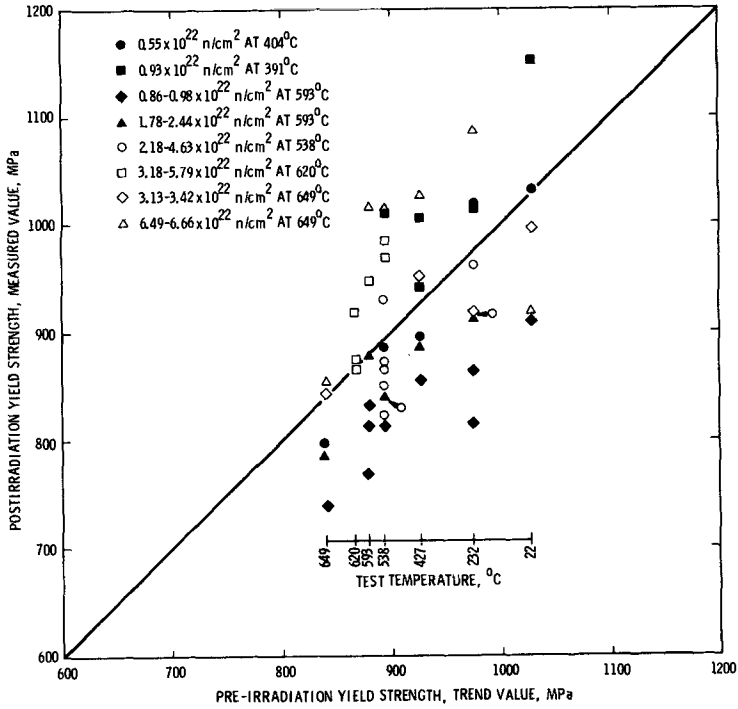

FIG. 3—*Effects of neutron fluence, irradiation temperature, and test temperature on the yield strength of wrought Inconel-718.*

this fluence level was accumulated at 391 °C (736 °F) and the ductility loss is not sufficiently severe to restrict the strength. The tendency toward strength loss at 593 °C (1100 °F) is still apparent at 1.78 to 2.44 $\times$ 10^{22} n/cm^2. A fluence range of 2.18 to 4.63 $\times$ 10^{22} n/cm^2 at 538 °C (1000 °F) produced somewhat mixed results with data falling generally below the line and one [tested at 538 °C (1000 °F)] above. Limited results for the fluence range 3.18 to 5.79 $\times$ 10^{22} n/cm^2 at 620 °C (1148 °F) indicate that the irradiation-induced strengthening dominates any tendencies toward strength loss due to thermal effects. This is also apparent at 649 °C (1200 °F) where generally higher strengths are observed for the fluence range of 6.49 to 6.66 $\times$ 10^{22} n/cm^2 than for 3.13 to 3.42 $\times$ 10^{22} n/cm^2.

While the preirradiation strength constitutes the minimum postirradiation strength in annealed austenitic stainless steels, Inconel-718 can undergo losses associated with thermal instability at elevated irradiation temperatures. Comparison of Inconel-718 results prior to and following irradiation in Fig. 4 shows that strength losses occurred more frequently than did strength increases. Significantly higher postirradiation tensile

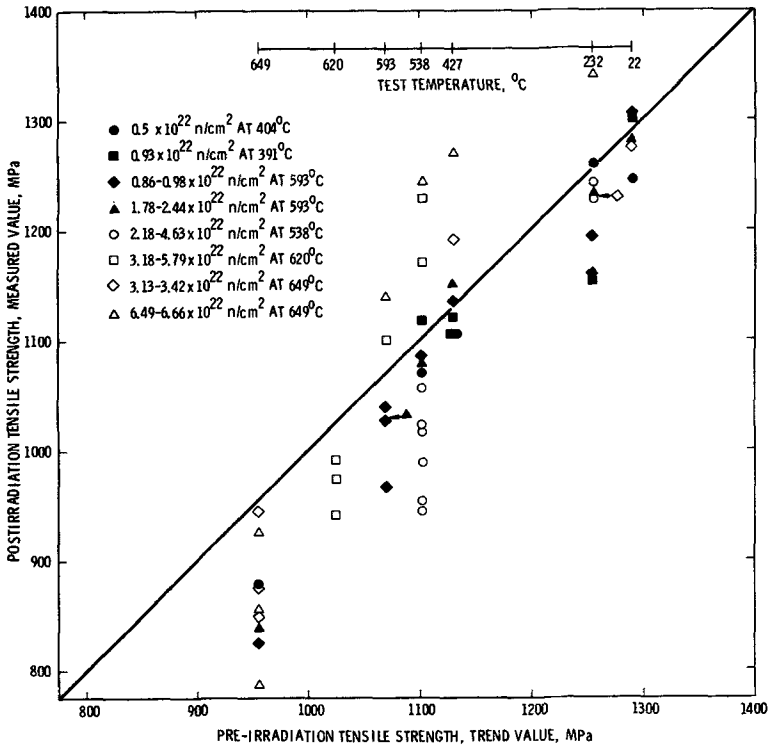

FIG. 4—*Effects of neutron fluence, irradiation temperature, and test temperature on the tensile strength of wrought Inconel-718.*

strengths were observed only in those specimens representing the highest fluence levels and test temperatures of 593 °C (1100 °F) and lower. At higher test temperatures, all results show lower postirradiation tensile strengths.

The effects of the irradiation and test conditions on the ductility are illustrated in Fig. 5, which compares the pre- and postirradiation total elongation values. Total elongation was selected for this representation because it is a commonly used ductility quantity and because it typifies the general trends observed for the uniform elongation and reduction of area. Test temperature is clearly the controlling factor in postirradiation ductility. Ductility losses associated with irradiation hardening are clearly evident, for those conditions which produced increases in yield strength, only when the test temperature was below 538 °C (1000 °F). At test temperatures of 538 °C (1000 °F) and above, all postirradiation total elongation values fall below the preirradiation trend values. Ductility losses above 538 °C (1000 °F) are certainly attributable to the combined effects of irradiation hardening and helium embrittlement. The relative contributions of the two effects cannot be determined precisely although it is expected that helium embrittlement

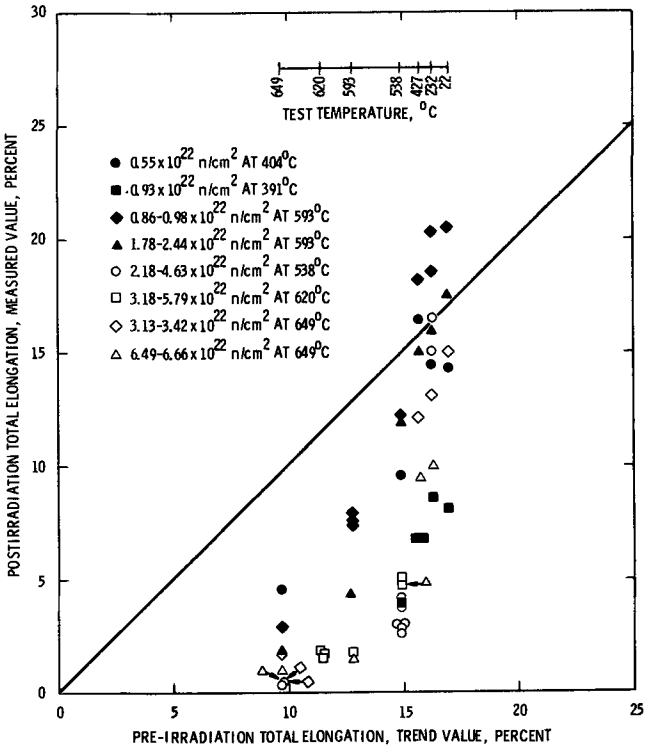

FIG. 5—*Effects of neutron fluence, irradiation temperature, and test temperature on the total elongation of wrought Inconel-718.*

becomes the progressively dominant factor as the deformation temperature increases.

Yield strength increases and ductility losses which were observed following low-temperature irradiation when the fluence reached approximately 10^{22} n/cm^2 and following high-temperature irradiation to much higher fluence levels can be attributed to classical irradiation hardening. High-temperature ductility losses for all irradiation conditions would seem to point strongly toward the operation of the helium embrittlement mechanism. Premature failure due to such embrittlement would also impose severe restrictions on the tensile strength by reducing or by virtually eliminating the ability of the material to strain harden. The extent of such limitations is illustrated by several tests at 649 °C (1200 °F) for which only the maximum stress values are plotted (Fig. 4) since the 0.2 percent offset strain normally used for yield strength determination was not reached.

Exposure of fully age-hardened Inconel-718 to a fast neutron flux at elevated temperatures for extended durations clearly gives rise to the poten-

tial for operation of competing property-controlling mechanisms. Properties measured after irradiation are the net result of irradiation damage, which tends to strengthen, and thermal overaging, which tends to weaken the material. In an attempt to separate the effects of irradiation and thermal instability, postirradiation results are compared with those obtained from specimens aged out-of-flux at 538 and 649 °C (1000 and 1200 °F) for periods of 1000, 4000, and 10 000 h in Fig. 6. The postirradiation data are placed on the time-scale according to the duration of residence in the reactor at the irradiation temperature (Table 2). The apparent maxima in the strength versus time curves suggest well-known age-hardening, overaging process typical of precipitation-hardenable alloys. Thus, the lower strengths following irradiation, particularly at 538 °C (1000 °F), would seem initially to indicate that the overaging process was accelerated by irradiation. The effects of thermal exposure alone are generally consistent with results reported by Barker et al [*14*] for Inconel-718 specimens tension tested following long-term aging under various stresses. They showed that, when tested at 649 °C (1200 °F), specimens exposed at 538 °C (1000 °F) for periods in excess of 10 000 h exhibited slight gains in strength with no detectable change in reduction of area, and those exposed at 649 °C (1200 °F) produced maxima in both the yield and ultimate strengths at about 1000 h. The evidence for irradiation enhancement of the thermal process is strongest at 538 °C (1000 °F), since the helium embrittlement mechanism apparently does not restrict the strength properties to the extent noted at 649 °C (1200 °F). Lower strength measured in specimens at 649 °C (1200 °F) is clearly attributable to the severe losses in strain-hardening capacity associated with the embrittlement.

Weld Materials

Weld-deposited Inconel-718, when subjected to the same age-hardening treatment given the wrought product, exhibits preirradiation yield strengths comparable to those measured for the wrought materials, slightly lower tensile strength and lower ductility (Fig. 7). Better agreement between weld- and wrought-material yield strength indicates similarity in behavior during the early stages of plastic deformation with the substantive differences arising in those parameters measured at larger deformations associated with instability and fracture. For example, the greatest difference is noted in the reduction of area. As might be expected in weld-metal with relatively coarse grains and a generally less homogeneous microstructure, the data show significantly more scatter than do the data for the wrought material, again primarily in those properties associated with large deformations. No well-defined difference in strength appears to exist between specimens taken from longitudinal and transverse orientations to the weld axis. There does appear, however, a tendency for the transverse specimens to exhibit lower

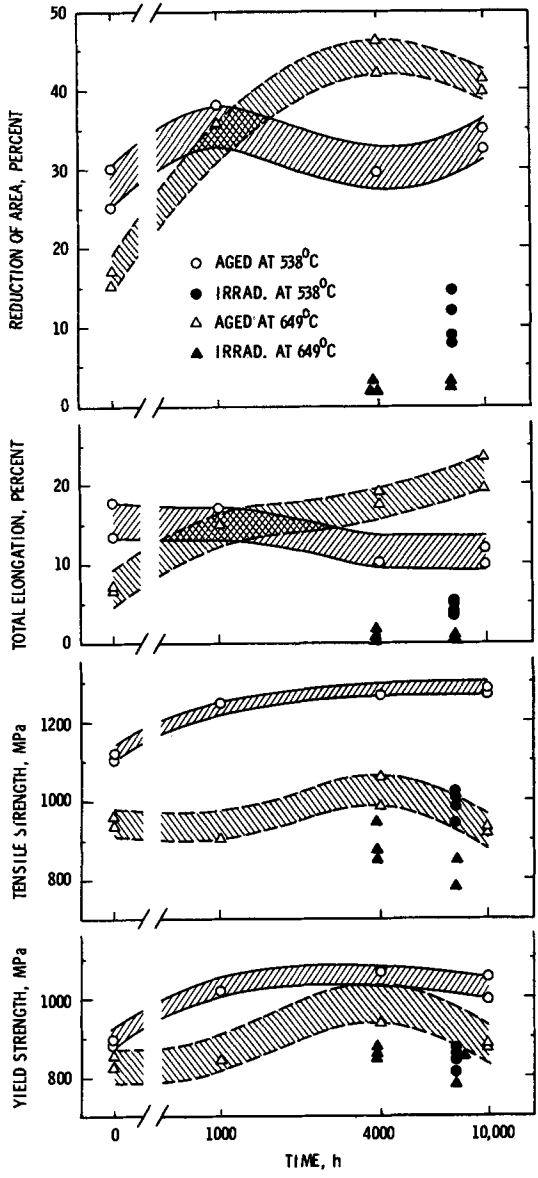

FIG. 6—*Combined effects of thermal exposure and neutron irradiation on the tensile properties of wrought Inconel-718. Tests were conducted at the respective irradiation and aging temperatures.*

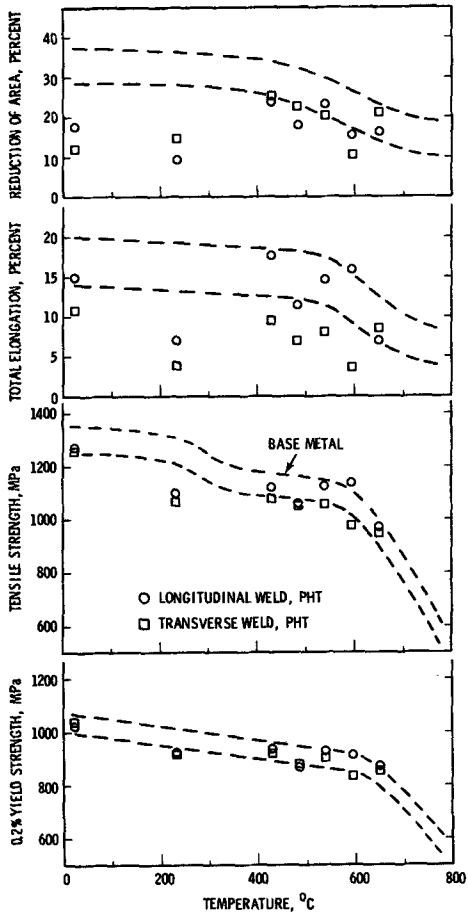

FIG. 7—*Preirradiation tensile properties of weld-deposited Inconel-718.*

uniform and total elongation values and to fracture in the weld rather than the base metal. In the as-welded condition, both transverse and longitudinal specimens showed very low strength and high ductility. In this case, the transverse specimens produced substantially greater uniform and total elongations than did the longitudinal specimens as a result of the contribution from the annealed base metal contained in the gage sections.

The effects of irradiation on the tensile properties of weld-deposited Inconel-718 are summarized in Fig. 8, which indicates the relative magnitude and direction of the property changes resulting from the irradiation and test conditions. Consistent with the results described in the foregoing for the wrought materials, reductions in ductility are observed for all irradiation

MATERIAL[a] CONDITION	FLUENCE (TOTAL) 10^{22} n/cm^2	IRRADIATION TEMPERATURE °C	TEST[b] TEMPERATURE RANGE	COMPARATIVE IRRADIATION EFFECTS ON PROPERTIES			
				STRENGTH		DUCTILITY	
				← DECREASE	INCREASE →	← DECREASE	INCREASE →
L, PHT	3.05	538	LOW				
			HIGH				
L, PHT	3.35	649	LOW				
			HIGH				
L, AW	2.55	538	LOW				
			HIGH				
L, AW	3.19	649	LOW				
			HIGH				
T, PHT	2.55-2.80	538	LOW				
			HIGH				
T, PHT	3.19-3.26	649	LOW				
			HIGH				
T, AW	2.55	538	LOW				
			HIGH				
T, AW	3.19	649	LOW				
			HIGH				

[a] L - LONGITUDINAL SPECIMEN
T - TRANSVERSE SPECIMEN
PHT - SOLUTION ANNEALED/DUPLEX PRECIPITATION HEAT TREATMENT
AW - AS WELDED

[b] LOW: ROOM TEMPERATURE - 482°C
HIGH: 538°C - 649°C

FIG. 8—*Summary of irradiation effects on weld-deposited Inconel-718.*

conditions [2.55 to 3.05 × 10^{22} n/cm^2 at 538 °C (1000 °F) and 3.19 to 3.35 × 10^{22} n/cm^2 at 649 °C (1200 °F)] and, for a given fluence and irradiation temperature, the severity of the ductility loss is greater in the high test temperature range. No clear evidence of strength increases attributable either to irradiation hardening or aging is observed in the age-hardened metal; however, those specimens irradiated in the as-welded condition exhibit very strong increases (factors of 2 to 2.5) in yield strength and severe losses in ductility despite the high irradiation temperatures. Postirradiation total elongation values ranged from 3 to 30 percent of the control value in the as-welded material.

These results for as-welded Inconel-718, which might be considered to be in an "annealed" condition, afford an interesting qualitative view of the combined effects of irradiation damage, thermal aging, and helium embrittlement. Large irradiation-induced strength increases are commonly observed—for example, in austenitic stainless steels—but two- and threefold increases would generally be associated with lower temperatures at the fluence levels represented here. It is thus likely that thermal aging contributes a significant strength increment at 649 °C (1200 °F) and, if aging is accelerated by the neutron flux, at 538 °C (1000 °F) as well. Finally, the postirradiation ductility, which can be interpreted as disproportionately low based on values measured in the unirradiated age-hardened material of

similar strength, is certainly as susceptible to helium embrittlement limitations as is that of the wrought alloy form.

Summary

The effects of neutron irradiation and out-of-flux thermal aging on the tensile properties of age-hardened Inconel-718 (base and weld metal) have been examined. Irradiation conditions ranged from 0.55×10^{22} n/cm^2 (total) at 404°C (759°F) to 6.6×10^{22} n/cm^2 (total) at 649°C (1200°F). Control specimens were aged at 538 and 649°C (1000 and 1200°F) for periods of 1000, 4000, and 10 000 h. The results of this study are summarized as follows:

1. Inconel-718 exhibits increases in strength and losses in ductility, associated with classical irradiation hardening, when irradiated to low fluences ($\sim 10^{22}$ n/cm^2) at low temperatures ($\sim$400°C) (752°F) and when irradiated to very high fluences (6.6×10^{22} n/cm^2) at high temperatures (649°C (1200°F), but generally only when tested at 538°C (1000°F) or lower. At higher test temperatures, the effects on strength are obscured by premature failure caused by severe restrictions on the strain-hardening capacity, presumably imposed by helium embrittlement.

2. Comparison of results from irradiated specimens and those aged out-of-flux at 538 and 649°C (1000 and 1200°F) provides evidence of irradiation-enhanced overaging. The evidence is strongest at 538°C (1000°F), since lower strengths at 649°C (1200°F) may well be attributable to embrittlement rather than overaging.

3. Age-hardened weld metal exhibited severe ductility losses at high test temperatures following irradiation to $\sim 3 \times 10^{22}$ n/cm^2 at 538 and 649°C (1000 and 1200°F); however, there was no clear indication of irradiation hardening in the strength results.

4. The most pronounced irradiation effect of this study was observed in limited results for specimens irradiated in the as-welded condition. Twofold increases in yield strength and reductions in ductility to <10 percent of the preirradiation values were observed.

Acknowledgment

This work was conducted under the auspices of the U.S. Energy Research and Development Administration, Contract No. E(45-1)-2170. Permission to publish is gratefully acknowledged.

References

[1] Brinkman, C. R. and Korth, G. E., *Journal of Testing and Evaluation*, Vol. 2, No. 4, 1974, pp. 249-259.

[2] "Thermal and Mechanical Treatments for Nickel and Some Nickel-Base Alloys: Effects on Mechanical Properties," NASA SP-5106, National Aeronautics and Space Administration Report, Washington, D.C., 1972.

[3] Wagner, H. J., Burns, R. S., Carroll, T. E., and Simon, R. C., "Nickel Base Alloys—Alloy 718," *DMIC Handbook,* Battelle Memorial Institute, Columbus, Ohio, 1968.

[4] *Inconel Alloy 718,* Huntington Alloys, The International Nickel Company, 1968.

[5] Eiselstein, H. L. in *Advances in the Technology of Stainless Steels and Related Alloys, ASTM STP 369,* American Society for Testing and Materials, 1965, pp. 62–79.

[6] Steichen, J. M. and Ward, A. L., "Effect of Strain Rate on the Tensile Properties of Irradiated Inconel-718" HEDL-TME 76-14, Hanford Engineering Development Laboratory Report, Richland, Wash., Jan. 1976.

[7] Steichen, J. M., "High Strain Rate Tensile Properties of AISI Type 304 Stainless Steel," *Journal of Engineering Materials and Technology,* Vol. 95, July 1973, pp. 182–185.

[8] Holmes, J. J., Robbins, R. E., Brimhall, J. L., and Mastel, B., "Elevated Temperature Irradiation Hardening in Austenitic Stainless Steel," *Acta Metallurgica,* Vol. 16, 1968, pp. 955–967.

[9] Bement, A. L., "Void Formation in Irradiated Austenitic Stainless Steels," *Advances in Nuclear Science and Technology,* Vol. 7, 1973, p. 1.

[10] Claudson, T. T., Barker, R. W., and Fish, R. L., "The Effects of Fast Flux Irradiation on the Mechanical Properties and Dimensional Stability of Stainless Steel," *Nuclear Applications and Technology*, Vol. 9, July 1970, pp. 10–23.

[11] Barnes, R. S., in *Flow and Fracture of Metals and Alloys in Nuclear Environments, ASTM STP 380,* American Society for Testing and Materials, 1964, pp. 40–68.

[12] Kramer, D., Garr, K. R., Rhodes, C. G., and Pard, A. G., "Helium Embrittlement of Type 316 Stainless Steel," *Journal of The Iron and Steel Institute,* Aug. 1969, p. 1141.

[13] Ward, A. L. and Holmes, J. J., "Ductility Loss in Fast Reactor Irradiated Stainless Steel," *Nuclear Applications and Technology*, Vol. 9, Nov. 1970, p. 771.

[14] Barker, J. F., Ross, E. W., and Radavich, J. F., "Long Time Stability of Inconel-718," *Journal of Metals,* Jan. 1970, pp. 31–41.

L. M. Lowry,[1] *J. S. Perrin,* [1] *and A. A. Bauer*[1]

Tensile and Hardness Property Evaluations of Irradiated Zircaloy Cladding Under Off-Normal and Transient Conditions

REFERENCE: Lowry, L. M., Perrin, J. S., and Bauer, A. A., "**Tensile and Hardness Property Evaluations of Irradiated Zircaloy Cladding Under Off-Normal and Transient Conditions,**" *Irradiation Effects on the Microstructure and Properties of Metals, ASTM STP 611,* American Society for Testing and Materials, 1976, pp. 171–180.

ABSTRACT: A program is being conducted to determine the mechanical behavior of irradiated Zircaloy-4 fuel rod cladding subjected to anneals under temperature and time conditions that simulate various off-normal and transient reactor operating conditions. This paper reports the initial phase of the program, which is a study of changes in hardness and tensile properties that accompany isothermal and transient anneals. A special transient annealing apparatus was built to subject specimens to the desired temperature/time conditions. Hardness and tensile strength decreased with increase in the maximum annealing temperature from 800 °F (425 °C) to 1300 °F (705 °C). Changes above 1100 °F (595 °C) were related to recrystallization and grain growth.

KEY WORDS: radiation, mechanical properties, cladding, annealing, strength, grain growth, recrystallization

The mechanical properties of irradiated Zircaloy fuel rod cladding have been studied using various techniques to determine the mechanical behavior under conditions applicable to normal steady-state reactor operating conditions [*1–3*].[2] However, there is also a current need to predict fuel cladding performance under various postulated off-normal, transient, and accident conditions. The data available on the mechanical properties of irradiated Zircaloy cladding as functions of such variables as irradiation level, texture, temperature, and condition of loading are not sufficient to permit predicting cladding performance to the desired level of accuracy.

To provide the data needed for fuel rod behavior code development, ex-

[1]Researcher and research leaders, respectively, Nuclear Materials Technology Section, Battelle's Columbus Laboratories, Columbus, Ohio 43201.

[2]The italic numbers in brackets refer to the list of references appended to this paper.

perimental studies are being conducted at a number of sites through the support of the Division of Reactor Safety Research/Fuel Behavior Branch of the U. S. Nuclear Regulatory Commission. The program at Battelle's Columbus Laboratories includes a determination of strength and ductility characteristics on irradiated Zircaloy-4 cladding from commercial power reactors that will include tension, burst, and expanding mandrel tests [*4*]. The work reported herein includes tensile and hardness evaluations before and after both isothermal and transient annealing. Annealing conditions were chosen to simulate various postulated off-normal and transient reactor heating conditions.

Experimental Procedures

Material

The material used for specimens is Zircaloy-4 cladding obtained from a single fuel rod from the Wisconsin Electric Company Point Beach nuclear plant. The nuclear steam supply systems for Point Beach Units No. 1 and No. 2 are pressurized water reactors. The cladding material is nuclear grade Zircaloy-4, cold reduced and stress relieved. Table 1 is a typical analysis of Zircaloy-4; an analysis of the actual material used in the present study is not available. The initial length of the fuel rod was approximately 151 in., the outer diameter was nominally 0.422 in., and the wall thickness was nominally 0.024 in. The fluence varied moderately as a function of position along the length of the rod. The average cladding fluence was 2.9×10^{21} n/cm^2 ($E >$ MeV). The corresponding burnup of the UO_2 fuel in the rod was 15 500 megawatt days per ton.

The fuel rod was γ-scanned before sectioning into specimens in order to identify the length of cladding over which fuel burnup, and therefore neutron fluence, was relatively uniform. Experimental procedures for γ-scanning are described elsewhere [*5*]. The γ-profile for the rod was relatively flat along a 94-in. length, being within ± 5 percent of the average value except for four local regions. These four regions of the rod were at grid positions where the gamma intensity was about 10 percent below that of adjacent regions.

After γ-scanning, the fuel rod was punched and the fission gases were removed. The rod was then cut into sections for tension, hardness, and metallography specimens. The sectioning was performed by cutting with a water-cooled, abrasive cutoff wheel.

The fuel was then removed from the individual specimens. This was accomplished on shorter specimens (metallography and hardness specimens) by tapping or pressing out the fuel using an aluminum mandrel. The fuel was removed from the 5-in.-long tension specimens by using a specially designed water-inundated diamond core drilling apparatus.

TABLE 1—*Chemical composition of reactor grade Zircaloy-4.*

Element	Composition, weight, %
Tin	1.20 to 1.70
Iron	0.18 to 0.24
Chromium	0.07 to 0.13
Nickel	... ...
Iron + chromium + nickel	0.28 to 0.37
	Maximum Impurities, weight, %
Aluminum	0.0075
Boron	0.00005
Cadmium	0.00005
Carbon	0.027
Chromium	...
Cobalt	0.0020
Copper	0.0050
Hafnium	0.020
Iron	...
Hydrogen	0.0025
Oxygen	...
Manganese	0.0050
Nickel	0.0070
Nitrogen	0.0080
Silicon	0.0120
Titanium	0.0050
Tungsten	0.010
Uranium (total)	0.00035

Annealing

Specimens were annealed under both isothermal and transient heating conditions for subsequent hardness and tensile property evaluations. The experimental heating apparatus designed and constructed to perform these annealing sequences is shown schematically in Fig. 1. The apparatus incorporates an inner heating element (which fits inside specimens) for rapid heating, a resistance furnace to provide a constant-temperature zone, and a quench manifold for cooling the specimen. The heating system is enclosed in a bell jar, and the annealing treatments were conducted under a vacuum of 10^{-2} torr or less.

For isothermal annealing, the specimens were mounted in the specimen holder and a chromel-alumel thermocouple was attached. With the inner heating element and resistance furnace at predetermined temperatures, the specimen was lowered over the inner heating element until the specimen temperature reached the annealing temperature. The specimen was then raised into the constant-temperature zone, held at temperature, and finally

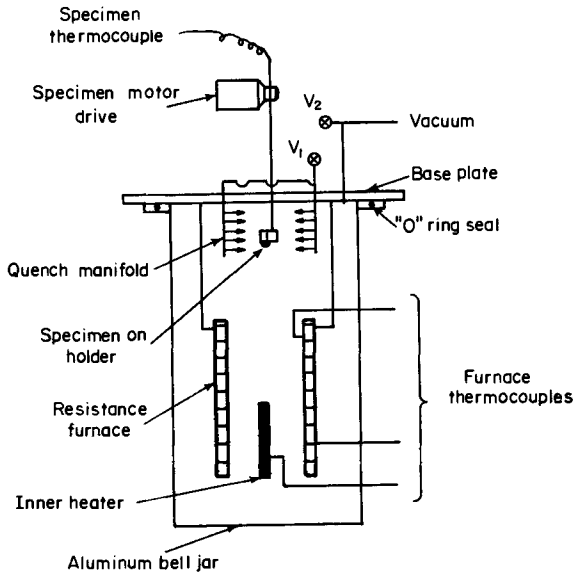

FIG. 1—*Schematic of the annealing apparatus.*

withdrawn from the furnace and quenched with helium to complete the isothermal annealing sequence. For transient annealing, the foregoing procedure was followed with the inner heating element and resistance furnace set at predetermined temperatures to heat the specimen at a linear rate to the maximum annealing temperature. The specimen was then drawn into the quench manifold and cooled with helium. Typical isothermal and transient annealing curves are shown in Figs. 2 and 3.

Hardness Tests

The hardness specimens were prepared from ½-in.-long rings. The rings were cut longitudinally using a jewelers saw, producing half-ring sections. A number of half-ring sections were mounted in Bakelite metallographic mounts for hardness measurements in the as-irradiated condition, using a Tukon microhardness tester with a diamond indenter and 1-kg load.

The half-rings used for isothermal and transient annealing were cleaned by grinding with a small silicon carbide wheel to remove the oxide from both the outside and inside surfaces. A 5-min etch at room temperature with 50 percent HNO_3 and 50 percent H_2O was applied to the specimen to further clean the surface. A chromel-alumel thermocouple was spot welded to the specimen which then was mounted on the annealing-apparatus specimen

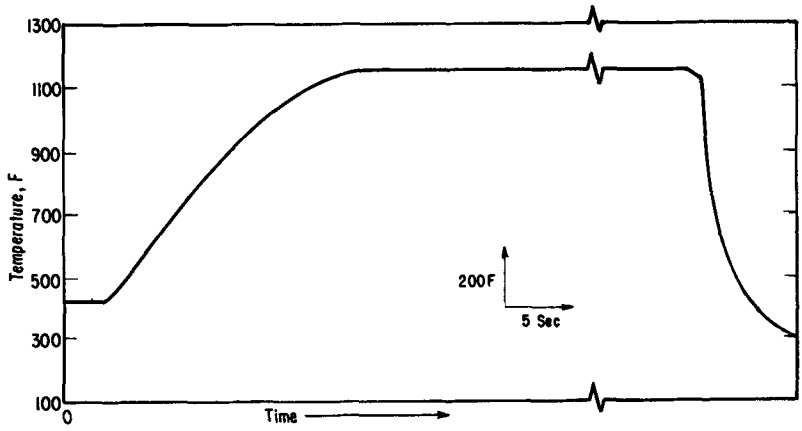

FIG. 2—*Typical isothermal annealing sequence. Specimen was heated from 425 to 1100°F (218 to 593°C), held for 10 min at 1100°F (593°C), and then quenched.*

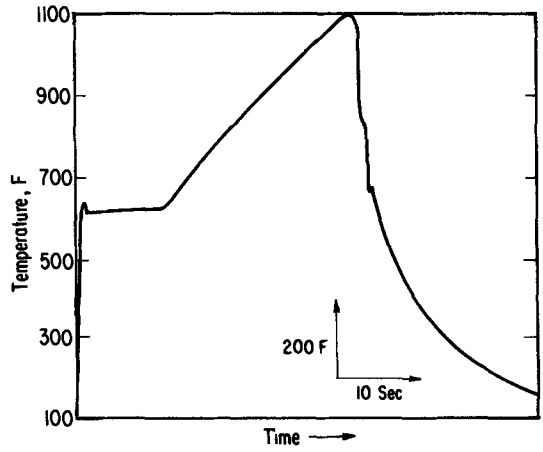

FIG. 3—*Typical transient annealing sequence. Specimen was heated at a rate of 25°F/s (−4°C/s) to a maximum temperature of 1100°F (593°C).*

holder. At this point the specimen was ready for either an isothermal or transient anneal as described in the preceding section.

After annealing, the specimen was mounted in a metallographic mount such that a circular cross section was exposed. It was ground and polished, and then tested using a Tukon microhardness tester with a diamond

pyramid indenter and a 1-kg load. Tests were made with the indenter axis oriented both parallel and perpendicular to the tube radius. Five indents were made at each orientation.

Tension Tests

The tension specimens were 5-in. lengths of cladding from which the fuel was removed. Specimens were first measured and then fitted with steel plugs [made to the ASTM Tension Testing of Metallic Materials (E 8–69) specifications] to prevent tubing collapse within the specimen grips. A knife-edge extensometer fitted with a clip gage was used to measure the strain over a 2-in. gage length. The specimens were tested in a 20 000-lb tension test machine. All tests were conducted at 700 °F (370 °C). The crosshead speed was 0.01 in./min through the yield point, and then 0.05 in./min for the remainder of the test.

Specimens to be annealed were cleaned in a HNO_3 solution for 5 min and in a HCl solution for 5 min to remove surface deposits (crud) and fuel. The specimens were next ultrasonically cleaned in a soap solution for 10 min to remove any remaining loose contamination, rinsed in distilled water, and then rinsed in alcohol. The specimens were then annealed under both isothermal and transient heating conditions as described in the preceding section on annealing. Both annealed and as-irradiated specimens were tension tested using the procedures described in the foregoing .

Experimental Results and Discussion

Hardness

Knoop hardness (HK) data were obtained at room temperature for both isothermally and transient-annealed specimens. Hardness data were obtained by making hardness indents both parallel and perpendicular to the tube radius.

Figure 4 is a plot of room temperature hardness as a function of annealing time at various isothermal annealing temperatures, based on hardness indents that were made perpendicular to the tubing radius. Data similar to that shown in Fig. 4 were obtained for hardness indents parallel to the tube radius. The figure shows that the hardness is not a function of annealing time for the time ranges shown.

There is no effect of annealing time in the data shown, the shortest annealing time at each temperature being sufficient to anneal out the defects responsible for the as-irradiated hardness. The horizontal lines through the data represent arithmetic averages of the hardness values obtained for the various times at each annealing temperature. The as-irradiated hardness values are shown in the upper left-hand corner of Fig. 4, and average approximately 265 HK. The 700 °F (370 °C) anneal produces no significant

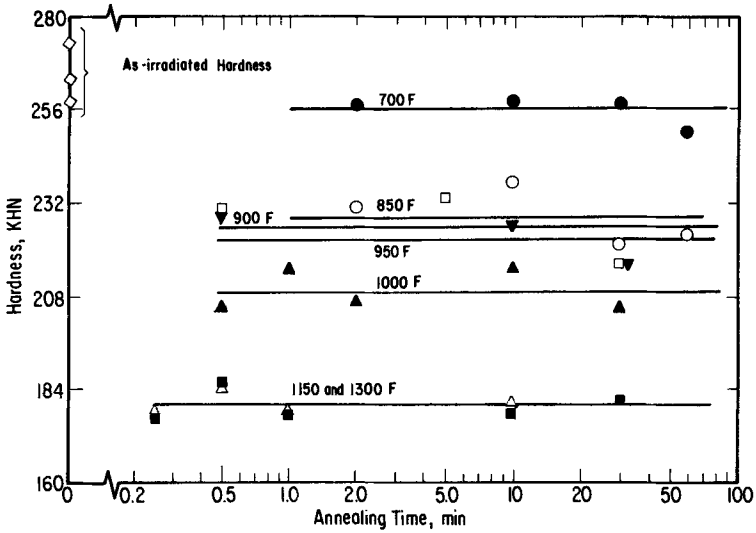

FIG. 4—*Hardness of irradiated Zircaloy as a function of time for various isothermal annealing temperatures (hardness indents perpendicular to tube radius).*

change in hardness, but the hardness progressively drops as the annealing temperature is raised from 800 °F (425 °C) to 1150 °F (620 °C), reaching an average value of approximately 180 HK. There is no further drop in hardness when the annealing temperature is increased from 1150 °F (620 °C) to 1300 °F (705 °C).

Figure 5 is a plot of room temperature hardness as a function of the heating rate and maximum temperature of a transient anneal. One figure is for hardness indents parallel to the tube radius, and the other is for hardness indents perpendicular to the tube radius. The heating rate and maximum temperature both have a significant effect on the resultant hardness. For a given heating rate, the hardness decrease becomes greater as the maximum temperature of the transient anneal increases. The hardness decrease also becomes greater as the rate of heating decreases.

These results indicate an effect of time as well as of temperature on the annealing of irradiation-damage induced hardening. Note that the greatest change in hardness behavior appears to occur between the heating rate of 1 and 10 °F/s (0.55 and 5.5 °C/s).

Tension Tests

Tension tests were run at 700 °F (370 °C) on three as-irradiated and seven isothermally annealed specimens. Two additional 700 °F (370 °C) tension tests were conducted on transient-annealed specimens. Figure 6 is a plot of

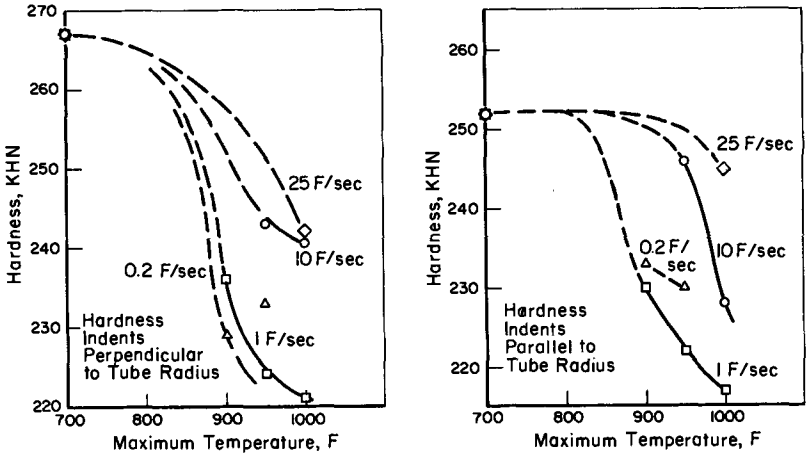

FIG. 5—*Hardness of irradiated Zircaloy as a function of heating rate and maximum temperature of transient annealing.*

the 700 °F (370 °C) yield strength and ultimate tensile strength as a function of annealing time for various isothermal annealing temperatures. Figure 7 is a plot of the 700 °F (370 °C) uniform elongation and total elongation as a function of time for various isothermal annealing temperatures. The as-irradiated values of the tensile properties are shown at an annealing time of 0 min.

Figure 6 shows that a 60-min anneal at 800 °F (425 °C) results in no change of the yield strength (YS) or ultimate tensile strength (UTS). A 60-min anneal at 850 °F (455 °C) causes a slight drop in YS and UTS, indicating moderate annealing of irradiation damage. A somewhat greater effect on strength is produced by annealing at 900 °F (480 °C). However, Fig. 7 shows that the uniform and total elongations show no corresponding increase in ductility. As the annealing temperature is increased above 900 °F (480 °C), substantial decreases in YS and UTS occur. A 30-min anneal at 1300 °F (705 °C) results in essentially the same YS and UTS as a 30-min anneal at 1100 °F (595 °C). At 1100 °F (595 °C) and 1300 °F (705 °C), decreases in strength are accompanied by increases in ductility.

Transient annealing tests were run at the rate of 1 °F/s (0.55 °C/s) to 1100 °F (595 °C), and 0.2 °F/s (0.11 °C/s) to 1000 °F (540 °C). Tension tests conducted at 700 °F (370 °C) on these specimens show significant decreases in YS and UTS, although ductility as determined by uniform elongation is essentially unchanged from the as-irradiated value.

Figure 6 shows the same trends in strength changes as shown in Fig. 4 for hardness changes in response to annealing. Moderate and gradual changes

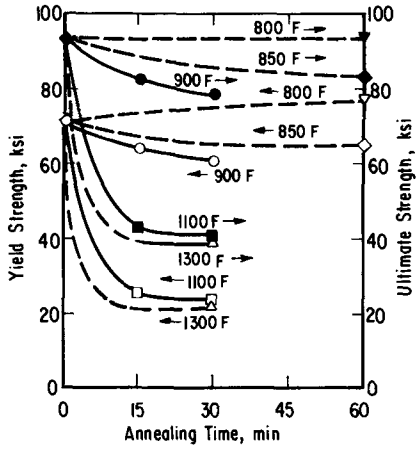

FIG. 6—*Yield strength and ultimate tensile strength for irradiated and annealed Zircaloy cladding tested at 700°F (370°C).*

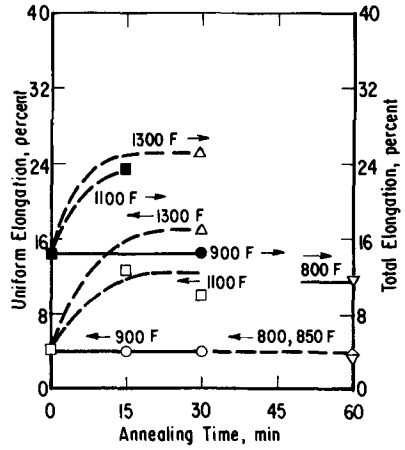

FIG. 7—*Uniform elongation and total elongation of irradiated and annealed Zircaloy cladding tested at 700°F (370°C).*

in hardness and strength occur as the temperature is increased above 800°F (425°C). However, these changes tend to level out in the general temperature range of 1100°F (585°C) or 1150°F (620°C), with only a slight additional change in strength and hardness as the temperature is increased further. The significant observation is that tensile ductility shows evidence of recovery only when the temperature of 900°F (480°C) is exceeded. This resistance of ductility recovery also is exhibited by the tension test specimens subjected to transient rather than to isothermal anneals.

Specimens were examined metallographically to determine the relationship of microstructure to observed changes in hardness and tensile properties. The as-irradiated Zircaloy microstructure is characterized by the original typical cold-worked structure with grains elongated parallel to the tubing axis. Annealing at temperatures up to 1000°F (540°C) for times as long as 30 min does not appreciably alter the cold-worked microstructure. Consequently, annealing of irradiation-produced crystal lattice defects is responsible for changes in properties at temperatures below 1000°F (540°C). However, recrystallization occurs after annealing at 1150°F (620°C) for 10 min, as evidenced by a fine-grained equiaxed structure. Increasing the annealing temperature to 1300°F (705°C) produces a structure with well-defined equiaxed grains that exhibit some growth as compared with those developed after the 1150°F (620°C) anneal. Thus recrystallization and grain growth are responsible for the hardness and tensile strength behavior at the higher temperature.

Acknowledgment

This work was performed under Nuclear Regulatory Commission Contract W-7405-eng-72.

References

[1] Douglas, D. L., *The Metallurgy of Zirconium*, International Atomic Energy Agency, 1971.

[2] Baroch, C. J., Munim, A. V., and Harbinson, E. N. in *Irradiation Effects on Structural Alloys for Nuclear Reactor Applications, ASTM STP 484*, American Society for Testing and Materials, 1970, pp. 176–193.

[3] Hardy, D. G., *Effects of Radiation on Substructure and Mechanical Properties of Metals and Alloys, ASTM STP 529*, American Society for Testing and Materials, 1973, pp. 415–434.

[4] Bauer, A. A., Lowry, L. M., and Perrin, J. S., "Evaluating Strength and Ductility of Irradiated Zircaloy," Quarterly Progress Report, Oct.–Dec. 1975, BMI-1942, Battelle Memorial Institute, Columbus, Ohio, 1975.

[5] Bauer, A. A., Lowry, L. M., and Perrin, J. S., "Progress on Evaluating Strength and Ductility of Irradiated Zircaloy During July through September, 1975," BMI-1938, Battelle Memorial Institute, Columbus, Ohio, 1975.

R. L. Simons[1]

Neutron Energy Dependent Damage Functions for Tensile Properties of 20 Percent Cold-Worked Type 316 Stainless Steel

REFERENCE: Simons, R. L., "**Neutron Energy Dependent Damage Functions for Tensile Properties of 20 Percent Cold-Worked Type 316 Stainless Steel,**" *Irradiation Effects on the Microstructure and Properties of Metals, ASTM STP 611,* American Society for Testing and Materials, 1976, pp. 181–192.

ABSTRACT: Material property measurements from test reactor irradiations cannot always be applied directly to design reactor irradiation conditions because of differences in neutron spectra. A semi-empirical damage function can be derived from the test reactor data for a particular property to describe the damage effectiveness of neutrons as a function of their energies. Such functions have been derived for strength and ductility parameters of 20 percent cold-worked Type 316 stainless steel for irradiation temperatures of 393, 493, and 593 °C (740, 920, and 1100 °F). Both fast and thermal reactor data were used in the analysis. Quantitative conclusions from this analysis were limited by the lack of data; however, damage functions for tensile properties of 20 percent cold-worked Type 316 stainless steel irradiated at 393 and 493 °C (740 and 920 °F) appear to be consistent with the displacement cross section for stainless steel. At 593 °C (1100 °F) the ductility damage functions show substantial deviation from the displacement cross shape when both fast and thermal reactors are included in the analysis. The latter damage functions were found to be consistent with the correlation of ductility with the square root of the product of displacements and helium concentration. Examples of application to fast reactors and fusion reactors are given.

KEY WORDS: radiation, radiation effects, cold working, stainless steels, displaced atoms, helium, tensile properties, swelling

When designing reactor components for service in spectra for which no relevant property change data exist, a technique is needed to utilize existing property change data obtained in various test reactor spectra. Damage

[1] Advanced scientist, Irradiation Analysis Section, Hanford Engineering Development Laboratory, Westinghouse Hanford Company, Richland, Wash. 99352.

functions can be derived to correlate these data on the basis of spectral differences. The damage functions, in the form of energy-dependent cross sections, can then be applied to neutron spectra such as those corresponding to a power reactor pressure vessel, in-vessel structural components, or fuel cladding and ducts to estimate damaging fluences.

The fuel cladding and ducts of the fast test reactor (FTR) and the Clinch River breeder reactor (CRBR) will be 20 percent cold-worked Type 316 stainless steel. Presently available test spectra from Experimental Breeder Reactor-II (EBR-II) and high-flux isotope reactor (HFIR) do not correspond precisely to those expected in FTR or CRBR; hence, a small spectral effect must be accounted for when applying the test reactor data. Some preliminary designs of fusion reactors have employed 20 percent cold-worked Type 316 stainless steel as a first-wall material [*1*].[2] This application will require a substantial spectral extrapolation from present test reactor data.

The primary motivation for using the cold-worked material is to reduce swelling in the cladding since this limits the economical life of the fuel. A knowledge of tensile properties, however, is important for reactor operating safety and handling of irradiated fuel subassemblies during reactor servicing.

The first attempt has been made to develop energy-dependent damage functions for neutron radiation induced changes in tensile strength and ductility of 20 percent cold-worked Type 316 stainless steel. The properties, property levels, and irradiation temperatures employed in the analyses are summarized in Table 1. The measured property levels were corrected to account for the difference in test temperature and irradiation

TABLE 1—*Irradiation temperature, property, and property level for damage function analyses of 20 percent cold-worked Type 316 stainless steel.*

Irradiation Temperature Range, T_I	Property			
	Yield Strength, ksi	Ultimate Tensile Strength, ksi	Uniform Elongation, %	Total Elongation %
740 ± 40°F (393 ± 22°C)	100	110	5, 2	10, 5
920 ± 60°F (493 ± 33°C)	90	100	5	10, 5, 2
1100 ± 30°F (593 ± 17°C)	...	...	5, 2, 1	10, 5, 2

temperatures when differences existed. The lack of data, coupled with the effects of aging, caused large uncertainties in some damage functions. No analyses were made for the tensile strength at 593°C (1100°F) because there was no definite irradiation effect shown by the data. Damage func-

[2] The italic numbers in brackets refer to the list of references appended to this paper.

tions for ductility were limited to those property levels for which the data could be interpolated or extrapolated on a reasonable basis.

Method of Analysis

A damage function, $G(E)$, is derived by solving iteratively the set of integral equations

$$M_i = \frac{P}{(\Phi t)_i} = \int_0^\infty G(E)\phi_i(E)dE, \qquad i = 1, 2, 3, \ldots, N \tag{1}$$

where P is the specific property level of interest resulting from an irradiation to a total fluence $(\Phi t)_i$ in the i_{th} neutron test spectrum $\phi_i(E)$ (normalized to unit flux). There is one equation for each test spectrum. The solution of Eq 1 begins with an assumed energy dependence $G°(E)$ based on a consideration of the prevailing damage mechanisms. The most appropriate $G°(E)$ for irradiation temperature less than about 540°C (1000°F) is a displacement cross section. The displacement cross section used was calculated by Doran [*13*]. Above about 540°C (1000°F), helium apparently plays an important role in the loss of ductility; thus the most appropriate $G°(E)$ would be a helium cross section alone or in combination with a displacement cross section to reflect a synergistic damage mechanism. $G°(E)$ used for all damage functions in this analysis was a displacement cross section because the application of these damage functions will primarily be in liquid metal fast breeder reactor (LMFBR) environments where displacements are the dominate mechanism. The result of adjusting $G°(E)$ to give a best fit to the experimental data is a $G(E)$ that applies specifically to the particular property level P. The damage function $G(E)$ may be weakly or strongly dependent on $G°(E)$, depending on whether data were obtained in dissimilar or similar test reactor spectra, respectively.

Data Compilation

Both Hanford Engineering Development Laboratory (HEDL) [*2,3*] and Oak Ridge National Laboratory (ORNL) [*4,5*] tensile data were considered in this analysis, but they were treated separately because of several differences in the specimens studied by the two laboratories. The specimens came from different heats of steel, were in different forms (tube at HEDL versus round stock at ORNL), exhibited different tensile properties in the unirradiated condition. Specifically, the ductility of ORNL material was lower than that of HEDL material while the strength was considerably higher.

The neutron dosimetry and subsequent fluence and spectrum determinations for specimens irradiated in EBR-II were based upon the Run 50H dosimetry test flux map [*6*]. The fluences and spectrum for ORNL irradi-

ations in HFIR were based on the dosimetry reported in Refs *5* and *7*. The same spectrum was used for all HFIR specimens since they were all irradiated in the core region where the spectrum is not expected to vary significantly.

The exposures and material properties used in the analysis are summarized in Ref *8*.

Data Analysis

The focus of the preliminary data analysis was the determination of the fluence $\Phi_i t$ (and thus $M_i = P/\Phi_i t$) required to achieve the design property level in each test spectrum. Since the experimental data were generally at property levels different from P, it was necessary to establish the fluence dependence of the property change. In doing so, differences in irradiation and test temperatures and the effect of aging had to be considered.

The HEDL data were taken at various test temperatures for each irradiation temperature. Only data for which the test and irradiation temperatures were nearly the same were selected for analysis. The balance of the data were used to account for the remaining difference between irradiation and test temperatures. In nearly all cases the corrections were $\leqslant 10$ percent and were less than the expected experimental errors. ORNL data for different test temperatures were not available and no temperature corrections were assumed; however, the corrections would be small (<10 percent) and not expected to change the results appreciably.

Aging data on 20 percent cold-worked Type 316, obtained at both ORNL [*4*] and HEDL, show significant effects on tensile properties. As a result of aging, some irradiated material data showed lower strengths and higher ductilities than the unaged, unirradiated material properties. For this reason, only data which deviated from the aging data in the direction of expected irradiation damage were used in the analysis. For example, the strength data for irradiated material at 593 °C (1100 °F) are indistinguishable from those for aged material, precluding further analysis. Some effect of aging on yield strength is generally apparent at 493 °C (920 °F) but is absent at 393 °C (740 °F) Ductility changes appear to be dominated by aging at low displacements per atom (dpa) values at all three temperatures.

The number of data points were too limited to define the fluence dependence for each property change in each test spectrum. Hence the data were plotted as a function of dpa [*13*], the dpa value associated with the property level P was determined by interpolation, and these values were converted to the corresponding fluence in each spectrum. Figures 1 and 2 show plots for total elongation (TE) data at 393 and 593 °C (740 and 1100 °F); results for other temperatures and properties are presented in Ref *8*.

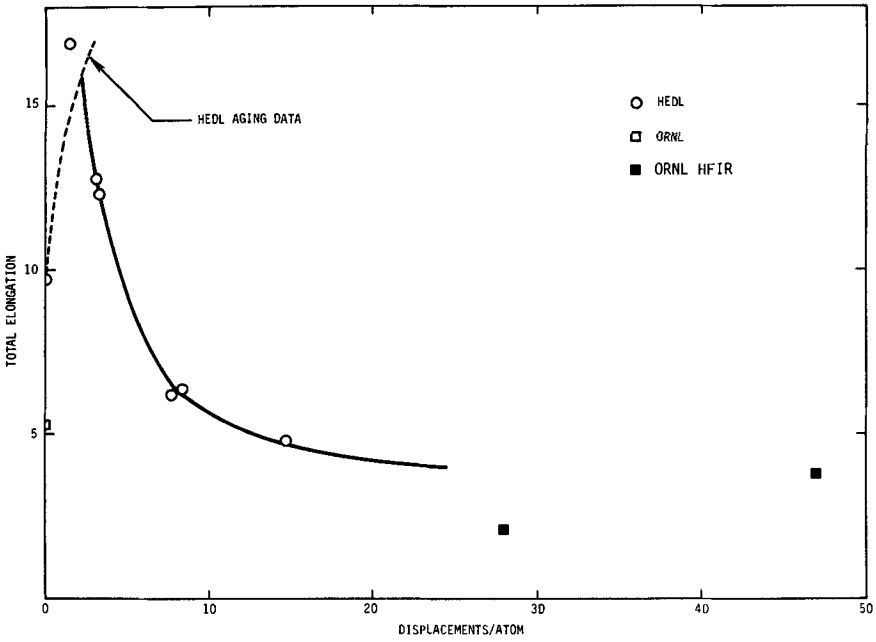

FIG. 1—*Total elongation of 20% cold-worked Type 316 stainless steel irradiated at 393 °C (740 °F) versus displacements per atom.*

The TE data (Fig. 1) at 393 °C (740 °F) are affected by aging at low doses. The aging curve in Fig. 1 is appropriate for the spectrum that corresponds to the point at 1.4 dpa; this point was not used in the analysis. The ORNL data from HFIR, at much higher dpa (and helium content) than the HEDL data, are not inconsistent with the trend of the HEDL EBR-II data. The general belief is that a higher temperature is needed for helium to cause embrittlement. Shorter irradiations which yield higher ductility would be necessary to show the effect of helium on the rate of loss in ductility in HFIR.

At 593 °C (1100 °F), aging undoubtedly affects the ductility for EBR-II irradiations, but the exposures were sufficient to show decreased ductility in all cases. ORNL and HEDL data were analyzed separately. The former include HFIR data which show a pronounced decrease in ductility at very low displacement doses (Fig. 2), presumably due to the high helium generation rate. The dpa dose dependence of the HEDL data was used to extrapolate the single ORNL EBR-II point to the reference property levels.

Results

A total of 18 damage functions was derived from the HEDL (EBR-II)

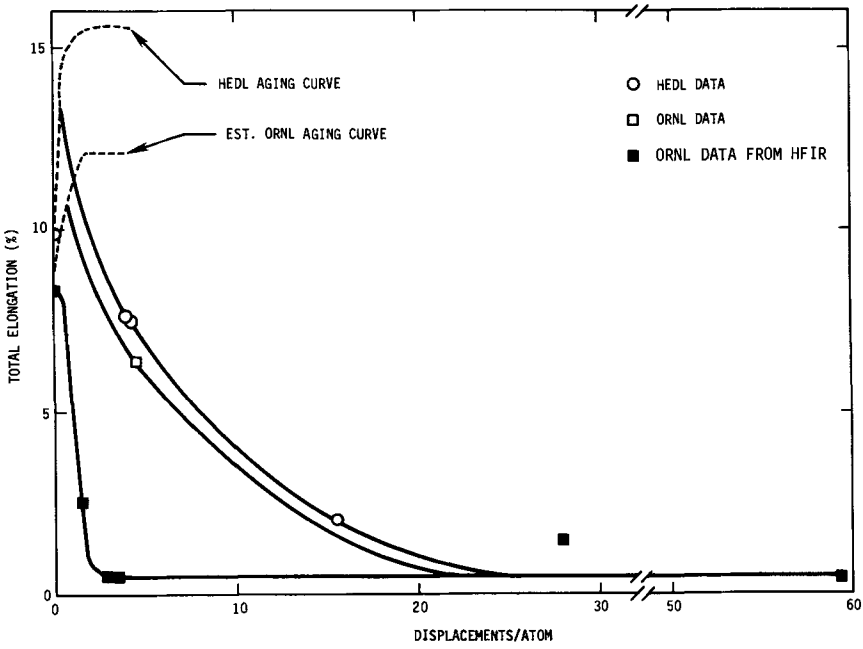

FIG. 2—*Total elongation of 20 percent cold-worked Type 316 stainless steel irradiated at 593 °C (1100 °F) versus displacements per atom.*

tensile data (see Table 1). In addition, two TE damage functions at 593 °C (1100 °F) were derived using ORNL (EBR-II plus HFIR) data.

Plots of damage functions for 2 percent TE at 593 °C (1100 °F) using HEDL and ORNL data are shown in Figs. 3 and 4, respectively. The bars span the energy range in which 90 percent of the damage occurred in each test spectrum used in the unfolding. The difference in the two damage functions presumably illustrates the effect of increased helium production in the HFIR specimens.

The damage function in Fig. 3, derived without the use of thermal reactor data, has the same energy dependence as the displacement cross section used as input to the unfolding procedure. The damage functions derived from EBR-II data at other temperatures have similar shapes. This result was inevitable because there are too few data to suggest that a correlation parameter other than dpa should be used.

Further investigation of the ORNL data at 593 °C (1100 °F) showed that the EBR-II and HFIR data could be correlated with the square root of the product of the displacements and helium content as illustrated in Fig. 5. The HFIR helium concentrations used to determine the exposure parameters in Fig. 5 are up to a factor of two higher than reported by Bloom and Wiffen [5]. The values used here were determined by solving the rate

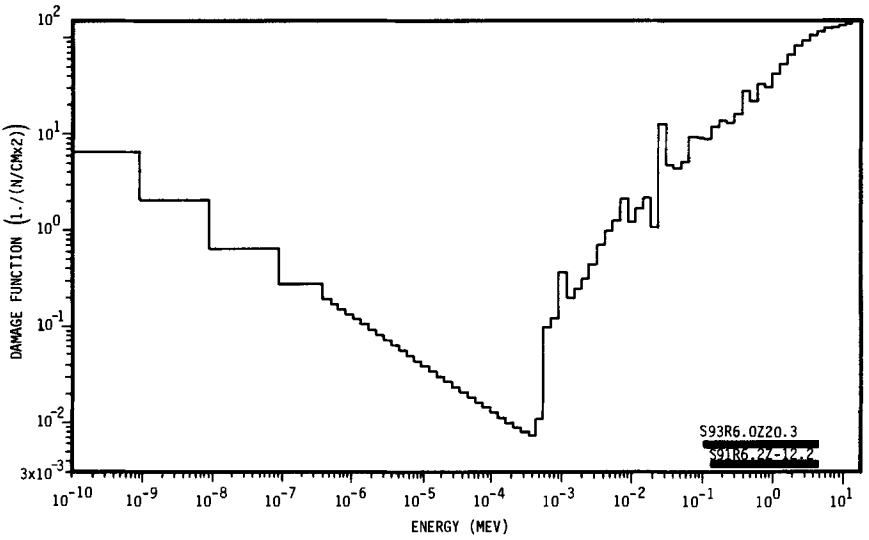

FIG. 3—*Damage function for 2 percent TE in 20 percent cold-worked Type 316 stainless steel irradiated at 593°C (1100°F) (using HEDL data only).*

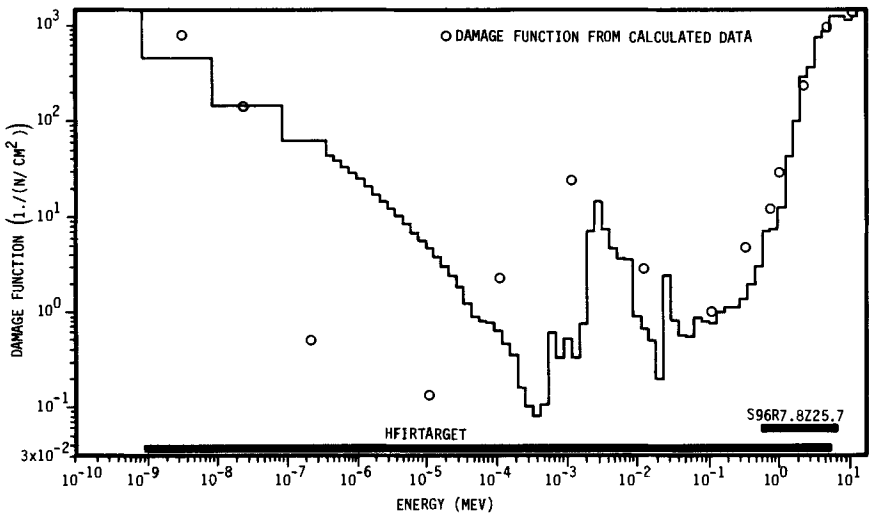

FIG. 4—*Damage function for 2 percent TE in 20 percent cold-worked Type 316 stainless steel irradiated at 593°C (1100°F) (using ORNL data only).*

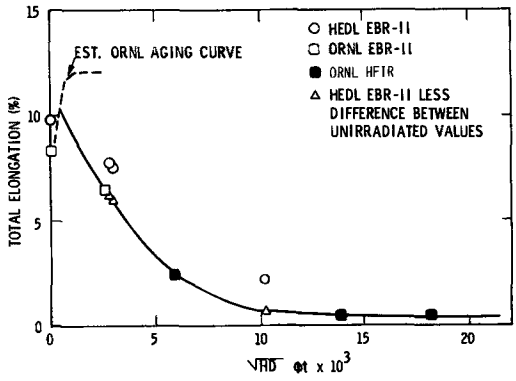

FIG. 5—*Total elongation in 20 percent cold-worked Type 316 stainless steel irradiated at 593 °C (1100 °F) versus square root of product of displacements and helium concentration.*

equations for the two-stage nickel reaction, using cross-sectional data from Ref *9* and normalizing the resulting curve to the single measurement by Wiffen and Bloom [*10*]. The resulting predictions are not inconsistent with those of McElroy and Farrar [*11*], and they account for burn-in/burnout of reaction products. In addition, it was observed that the HEDL data lie above the ORNL data ~1.5 percent TE at all fluences. This is about the same as the difference between the unirradiated values reported by the two laboratories (see Fig. 5). This may be fortuitous since it does not appear to be the case at the other irradiation temperatures.

An equation of the form

$$P = P_0 - P_1(1 - e^{-\beta G \Phi t}) \tag{2}$$

was fit to the data in Fig. 5 by adjusting the parameters P_0, P_1, and β. $G\phi t$ is the square root of the product of displacements ($\bar{D}\Phi t$) and helium concentrations ($\bar{H}\Phi t$).

In order to test the correlation over a wide variety of spectra, the fluence required to achieve 2 percent TE was calculated for a number of spectra using helium and displacement cross sections. The spectra included heavy and light water reactor spectra, fast test reactor (FTR) vessel wall, grid plate, and core center spectra, four EBR-II spectra, and Los Alamos Mason Production Facility (LAMPF) spectra with beryllium and copper beam stops. These calculated fluences were then used to unfold a damage function for 2 percent TE. The results, plotted as points in Fig. 4, show surprisingly good agreement for the energy regions $<10^{-7}$ MeV and $>10^{-3}$ MeV with the damage function unfolded using the ORNL data alone. Thus, the semi-empirical damage function shape for TE at 593 °C

(1100°F) is generally consistent with the correlation of data with the square root of the product of the displacements and helium content.

Uncertainty in the damage function shape and magnitude arises generally from two sources: (1) nonuniqueness of the solution, and (2) data errors. The damage functions derived in this work are nonunique because so few data (that is, different spectra) were available for each analysis. The results are thus highly dependent on $G°(E)$. The nonuiqueness error must be minimized by using a physically realistic input such as the displacement cross section. It would be desirable to determine a $G°(E)$ by theoretical modeling which would reflect the synergistic helium displacement interaction evident in the 593°C (1100°F) ductility damage functions.

The data errors can be further characterized as spectrum shape errors and integral data errors. Both these sources of uncertainty can be studied by a Monte Carlo procedure which has been adequately described elsewhere [*12*]. Because of present data limitations, no error assessment was made.

Application

Application of a damage function to a particular design spectrum is accomplished by using Eq 1. The property level divided by the integral of the damage function over the design spectrum gives the fluence in the design spectrum required to achieve the property level for which the damage function was defined.

Table 2 gives examples of predicted fluence limits to achieve the specific TE value for CRBR and a fusion reactor spectrum. The specific spectra

TABLE 2—*Fluence limit predictions for total elongation.*

Spectrum	$\bar{E}$(MeV)	Total Elongation, T_t	Nominal Fluence, n/cm^2
CRBR upper blanket	0.36	(5%, 593°C)	3.5×10^{22} [a]
CRBR core	0.51	(5%, 493°C)	5.5×10^{22} [a]
CTR first wall	4.2	(2%, 593°C)	1.9×10^{22} [a]
	4.2	(2%, 593°C)	2.7×10^{21} [b]

[a] Damage function using EBR-II (HEDL) data only.
[b] Damage function using EBR-II and HFIR (ORNL) data only.

are CRBR upper blanket [593°C (1100°F)], core center [493°C (920°F)], and fusion reactor first wall [*1*] (593°C) (1100°F). Damage functions derived with and without thermal reactor data were applied to the last case. The uncertainty in the CRBR predictions should be comparable to the errors in the data used to derive the damage function (10 to 30 per-

cent, $\pm 1\sigma$) since the differences between design and test spectra are small. The fusion reaction predictions are subject to substantial error because of the large spectral extrapolation required. It is noteworthy that in HFIR and EBR-II the helium and displacements are produced below 5 to 10 MeV, whereas in a fusion reactor first-wall spectrum they are produced above 5 to 10 MeV. The difference in the two predictions is due to the differences in the shapes of the two damage functions used (see Figs. 3 and 4). In HFIR and EBR-II, both helium and displacements are produced by neutrons of energy less than 10 MeV. Therefore, the damage function determined from EBR-II and HFIR data is poorly defined above 10 MeV. The application of this damage function to a fusion reactor first-wall spectrum, in which half the displacements and all the helium are produced above 10 MeV, hinges on the validity of the helium-displacement correlation shown in Fig. 5. It was already demonstrated that the damage function and the correlation are consistent at high energies.

In other words, in order to apply HFIR data to the first-wall spectrum, it is necessary to assume that the effect of helium on ductility depends only on the total quantity of helium produced and is independent of the neutron (and hence primary knock-on atom) energy. This assumption leads to the low fluence limit in Table 2, indicating that a UWMAK-I first wall of 20 percent cold-worked Type 316 stainless steel would experience a ductility decrease to a 2 percent TE in only a few months if operated at about 600 °C (1100 °F). To make predictions at lower temperatures, data are needed at lower fluences (hence lower helium concentrations) in order to determine the onset of a strong helium effect.

Summary and Conclusions

Quantitative definition of damage functions was severely limited by the lack of data on 20 percent cold-worked Type 316 stainless steel tensile properties. The absence of spectral variation resulted in damage function solutions that were dependent on the theoretical estimate of the damage cross section used as input. This nonuniqueness of solution also affects the solution error magnification; thus, the uncertainty in a fluence limit prediction requiring large spectral extrapolation could be misleading. For this reason, no error analysis was done.

Due to the scarcity of data for irradiation temperatures less than about 540 °C (1000 °F), the damage functions are simply the displacement cross section normalized to the data. In this temperature range, a displacement cross section is a realistic damage function and the available data are not inconsistent with it. Additional data with both wider fluence and spectral variations are necessary to corroborate or improve these results.

The energy dependence of ductility for irradiation temperatures above about 540 °C (1000 °F) was found to be substantially different than that of the

displacement cross section. This difference is presumably due to the synergistic effect of the helium-displacement interaction. Further analysis revealed that the EBR-II and HFIR ductility data could be correlated with the square root of the product of the helium concentration and dpa. Although the ductility damage function is not unique, it was shown to be consistent with that expected from the helium-dpa correlation. Additional data from HFIR and EBR-II would be desirable to test this correlation. Application of this damage function to a fusion reactor first-wall spectrum suggests that a few months (1 MW/m^2) at about 600°C (1100°F) would be sufficient to reduce the ductility of 20 percent cold-worked Type 316 to 2 percent total elongation.

Acknowledgment

This work was supported by the U.S. Energy Research and Development Administration under Contract E(45-1)-2170.

References

[1] Kulcinski, G. L., Brown, R. G., Lott, R. G., and Sarger, P. A., "Radiation Damage Limitations in the Design of the Wisconsin TOKAMAK Fusion Reactor," *Nuclear Technology,* Vol. 22, April 1974.

[2] Fish, R. L., Lovell, A. J., Brager, H. R., and Holmes, J. J., "Tensile and Creep Behavior of Cold Worked Type 316 Stainless Steel After EBR-II Irradiation," British Nuclear Energy Society Conference, *Irradiation Embrittlement and Creep in Fuel Cladding and Core Components,* 9-10 Nov. 1972.

[3] Hunter, C. W., Johnson, G. D., Fish, R. L., and Holmes, J. J., "Effect of Irradiation on the Mechanical Properties of 20% CW Type 316 Stainless Steel Prototypic Cladding," *HEDL Quarterly Technical Report,* Vol. 1, Oct.-Dec. 1974; HEDL-TME 74-4; Hanford Engineering Development Laboratory, Richland, Wash., Jan. 1975.

[4] Fahr, D., Bloom, E. E., and Stiegler, J. O., "Post-Irradiation Tensile Properties of Annealed and Cold Worked Type 316 Stainless Steel, " British Nuclear Energy Society Conference, *Irradiation Embrittlement and Creep in Fuel Cladding and Core Components,* 9-10 Nov. 1972.

[5] Bloom, E. E. and Wiffen, F. W., "The Effect of Large Concentrations of Helium on the Mechanical Properties of Neutron-Irradiated Stainless Steel," ORNL-TM 4861, Oak Ridge National Laboratory, Oak Ridge, Tenn., May 1975.

[6] Simons, R. L., Ulseth, J. A., and Graves, N. J., "EBR-II Spectral Parameters (Reactor Run 50H)," HEDL-TME 74-44, Hanford Engineering Development Laboratory, Richland, Wash., July 1974.

[7] Kam, F. B. K., and Swanks, J. H., "Neutron Flux Spectrum in the HFIR Target Region," ORNL-TM 3322, Oak Ridge National Laboratory, Oak Ridge, Tenn., 1971.

[8] Simons, R. L., "Energy Dependent Damage Functions for 20% CW 316 Stainless Steel," *HEDL Semi Annual Technical Report, Oct.-Dec. 1975,* Vol. 1, HEDL-TME 76-13, Hanford Engineering Development Laboratory, Richland, Wash., Jan. 1976.

[9] Kirouac, G. J. and Eiland, H. M., "Neutron Absorption in ^{59}Ni," Knolls Atomic Power Laboratory, Schenectady, N.Y., KAPL-3980, April 1972.

[10] Wiffen, F. W. and Bloom, E. E., "Effect of High Helium Content on Stainless Steel Swelling," ORNL-TM 4541, Oak Ridge National Laboratory, Oak Ridge, Tenn., May 1974.

[*11*] McElroy, W. N. and Farrar IV, H., *Radiation-Induced Voids in Metals,* J. W. Corbett and L. D. Ianniello, Eds., AEC Symposium Series 26, CONF-710601, Atomic Energy Commission, April 1972, p. 187.

[*12*] Oster, C. A., McElroy, W. N., and Marr, J. M., "A Monte Carlo Program for SAND-II Error Analysis," HEDL-TME 73-20, Hanford Engineering Development Laboratory, Richland, Wash., Feb. 1973.

Irradiation Simulation

J. A. Ellis, Jr.,[1] *W. K. Appleby,*[1] *and T. Lauritzen*[1]

Swelling Simulation Studies of Type 316 Stainless Steel

REFERENCE: Ellis, J. A., Jr., Appleby, W. K., and Lauritzen, T., "**Swelling Simulation Studies of Type 316 Stainless Steel,**" *Irradiation Effects on the Microstructure and Properties of Metals, ASTM STP 611,* American Society for Testing and Materials, 1976, pp. 195–207.

ABSTRACT: The effects of some compositional and processing variations on the irradiation-induced swelling of 20 percent cold-worked Type 316 stainless steel have been investigated. Bombardment by 5-MeV nickel ions was used to simulate the fast neutron irradiation which occurs in breeder reactor core components. Swelling in cold-worked Type 316 was found to be lowered by additions of silicon and molybdenum. Swelling was also reduced by increasing the solution-annealing temperature prior to the final cold-working operation.

KEY WORDS: radiation, irradiation, neutron irradiation, stainless steels, swelling, voids

This study was undertaken to investigate irradiation-induced swelling in the reference fast-flux test facility (FFTF) and Clinch River breeder reactor prototype (CRBRP) core structural material, 20 percent cold-worked Type 316 stainless steel, using a 5-MeV nickel ion swelling simulation technique. Bombardment of specimens of reactor structural materials with highly energetic heavy ions produces lattice atom displacements equivalent to those produced by neutron irradiation, but in a much shorter time period. Thus a given material can sustain equivalent damage displacement in a few hours out-of-reactor as opposed to several years in-reactor. The ion bombardment technique was first applied in this manner by workers at Harwell [*1,2*].[2] A technique subsequently developed at General Electric [*3*] using 5-MeV nickel ions has been employed in the present work. The principal objectives of this work were to define compositional and processing modifications for cold-worked Type 316 stainless steel that could reduce the

[1] Associate engineer, manager, and senior engineer, respectively, Fast Breeder Reactor Department, Structural Materials Unit, General Electric Company, Sunnyvale, Calif. 94086.

[2] The italic numbers in brackets refer to the list of references appended to this paper.

material's tendency to swell. A secondary objective was to provide information concerning the performance of first FFTF cores by defining the variability of swelling in the various Type 316 heats to be used in FFTF.

Experimental

The experimental techniques employed in this work have been described in detail previously [*3*]. The materials used are in the form of a strip 0.15 mm thick. Unless otherwise stated in the text, the Type 316 specimens are 20 percent cold-rolled to the final 0.15-mm dimension and then aged at 593 °C (1100 °F) for 200 h to partially produce the aging occurring in-reactor. These strip specimens are implanted with 15 atomic parts per million (ap pm) helium using 24.5-MeV alpha particles from a cyclotron. Disks, 3 mm in diameter, are then cut from the strip and bombarded with 5-MeV nickel ions using a partial mask to protect parts of the specimen surface from the beam. Measurements of the resultant swelling can then be made in two ways. First, measurement of the "step height" from unexposed to exposed surface gives a relative measure of the swelling in each specimen. These step heights are typically obtained by averaging up to 24 measurements on each specimen. Second, the specimens are examined by transmission electron microscopy (TEM). The bombarded surface is given a calibrated polish to the calculated peak damage region at about 9000 Å, then the specimen is back-thinned so that the peak damage region can be examined in transmission. Swelling is estimated from void size measurements together with foil thickness measurements from stereo pair analysis. The uncertainty in polishing to the required depth is estimated to be ± 500 Å.

Results and Discussion

Effects of Minor Compositional Variations

Bates and co-workers [*4*] at the Hanford Engineering Development Laboratory (HEDL) have studied an extensive series of Type 316 alloys, each of which represents a compositional modification of the standard Type 316 composition. Results after irradiation in the Experimental Breeder Reactor-II (EBR-II) to 2 to 4 × 10^{22} neutrons(n)/cm^2 ($E > 0.1$ MeV) indicated that void swelling is suppressed by silicon, phosphorus, manganese, molybdenum, cobalt, and carbon.

Six alloys from this compositional variations test, two Oak Ridge National Laboratory (ORNL) Type 316 variants, and two separately procured heats have been used to provide a first assessment of the effects of variations in minor element composition on the swelling of 20 percent cold-worked Type 316 stainless steel at displacement doses which are the equivalent of liquid metal fast breeder reactor (LMFBR) target fluences.

The alloys have fixed composition of the principal alloying constituents and variable composition of the minor alloying elements carbon, nitrogen, silicon, and molybdenum. Table 1 gives the compositions of these alloys and shows the minor elements varied in this experiment. Alloys HEDL-3 and heat 820467 were included as control specimens since they conform to the chemical composition of a commercial Type 316 steel.

Apart from the ORNL alloys which were solution annealed only, all alloys were bombarded in the 20 percent cold-worked condition. Step-height measurements for these alloys following bombardment at 625 °C (1157 °F) to 140 displacements per atom (dpa) (E_d = 33 eV) are also given in Table 1.

Using alloys HEDL-3 and 820467 as the base composition, comparisons between the other alloys can be made. The test matrix allows the effects of silicon and molybdenum to be examined separately. Figure 1 shows swellings plotted separately as a function of silicon and molybdenum content for those alloys in which the contents of other elements were essentially constant. It is seen that the swelling decreases dramatically as the molybdenum content is increased from 0.1 to 4.9 percent. Similarly the 1.4 weight-percent silicon alloy shows much reduced swelling compared to alloys containing the nominal silicon content.

The effect of other elements could not be uniquely separated because of the limitations of the test matrix. However, comparison of alloys HEDL-4 (530 Å) and HEDL-45 (1710 Å) suggests that carbon may be more effective than nitrogen in suppressing swelling in that the increased nitrogen content in HEDL-45 has not been as effective as the increased carbon in HEDL-4.

Effects of Titanium Modifications

A titanium-modified Type 316 heat under investigation by ORNL was included in this program for comparison with the compositional variables matrix and other 20 percent cold-worked Type 316 irradiated in the program.

Four specimens of 20 percent cold-worked titanium-modified Type 316 were bombarded to ~100 dpa (E_d = 33 eV) at 575, 625, 675, and 725 °C (1067, 1157, 1247, and 1337 °F). Results from the TEM examination of these specimens are given in Table 2 together with the alloy composition.

Figure 2 shows a comparison of these results with those previously obtained for Type 316 with varying extents of cold work [*5*]. It is seen that the maximum swelling is approximately as great as that previously found in the higher-swelling 20 percent cold-worked Type 316 heat No. 820467. Thus, the 0.23 percent titanium has not lowered the swelling of this material as anticipated from results obtained from minor alloying element additions to a pure ternary alloy [*6*]. However, attention is drawn to the processing conditions. The major difference in the swelling of heats 820467 and 81621 in

TABLE 1—*Compositions of "metallurgical variables" alloys (weight percent) and step-height swelling results.*

	HEDL No.						ORNL Pure	ORNL Commercial	Heat No. 820467	Heat No. 81621
	3	4	28	30	34	45				
Constants										
P	0.010	0.012	0.010	0.010	0.011	0.010	0.006	0.01	0.018	0.004
S	0.007	0.008	0.008	0.007	0.008	0.007	0.002	0.01	0.009	0.006
Cr	16.99	17.06	17.07	16.89	17.09	16.98	17.5	17.8	17.03	17.4
N	12.05	12.08	12.30	12.31	12.24	12.12	14.4	13.0	13.17	13.6
Cu	0.10	0.10	0.10	0.10	0.10	0.10	...	...	0.12	0.01
Co	0.12	0.11	0.11	0.11	0.11	0.11	...	...	0.13	0.018
B	0.0008	0.0010	0.0007	0.0011	0.0010	0.0012	0.0001	0.001	<0.001	0.006
Mn	0.94	0.96	0.93	0.99	0.87	1.12	<0.001	1.5	1.86	1.61
Variables										
C	0.047	0.127	0.044	0.044	0.045	0.012	0.005	0.05	0.05	0.055
N	0.050	0.006	0.054	0.049	0.051	0.13	0.0003	0.05	0.038	0.004
Si	0.39	0.38	1.47	0.40	0.40	0.41	0.01	0.75	0.73	0.54
Mo	2.33	2.32	2.38	0.01	4.93	2.31	2.8	2.5	2.08	2.29
Average step height Å	1218	530	≤200	1970	~200	1710[a]	2680	1030	1070	840

[a]TEM data from average of four areas: $\Delta V/V_0 = 15.8 \pm 6.6$ percent.
Average void diameter = 975 ± 212 Å.
Void density = $(2.4 \pm 0.9) \times 10^{14}$ cm^{-3}.

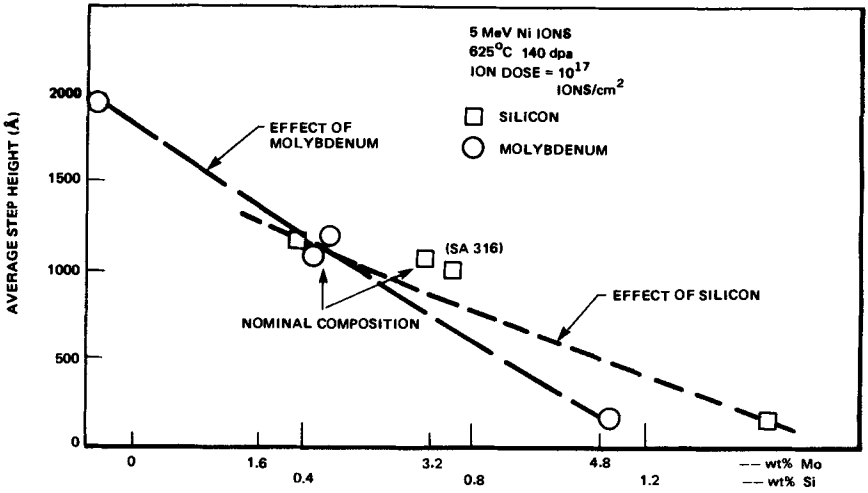

FIG. 1—*Effects of some minor elements on cold-worked Type 316 swelling.*

TABLE 2—*5 MeV Ni^{++} results for titanium-modified 20 percent cold-worked Type 316.*

Specimen	Temperature, °C	Dose, dpa	Step Height, Å	$\Delta V/V$, % (TEM)	Average Void Diameter, Å	Number Density, cm^3
VIII C7	575	104	no mask	4.4 ± 1.5	415	9.9×10^{14}
VIII C8	625	96	740	9.8 ± 6	558	8×10^{14}
VIII D7	675	106	540	9.6 ± 4	792	2.5×10^{14}
VIII E7	725	106	<200	5.7 ± 4.7	926	8.7×10^{13}

All bombardment times = 1.5 h

Chemical Composition (weight%)

	C	Cr	Ni	Mo	Ti	Mn	Si	B
Heat R-1	0.06	17.0	12.0	2.4	0.23	0.5	0.4	0.0007

Processing

Solution-anneal at 1050 °C (1922 °F) for 30 min, air-cool, 20 percent cold work by rolling, plus a service-simulation age of 593 °C (1100 °) for 200 h.

Fig. 2 is ascribed to their differing annealing temperatures (1010 °C versus 1149 °C) (1850 °F versus 2100 °F), and it is noted that the titanium-modified Type 316 was solution annealed at a low temperature (1050 °C) (1922 °F). It is most probable that minor elements such as titanium, silicon, carbon, and nitrogen are only beneficial in reducing swelling if they are in solid solution. Thus the importance of annealing temperature arises because, if the tem-

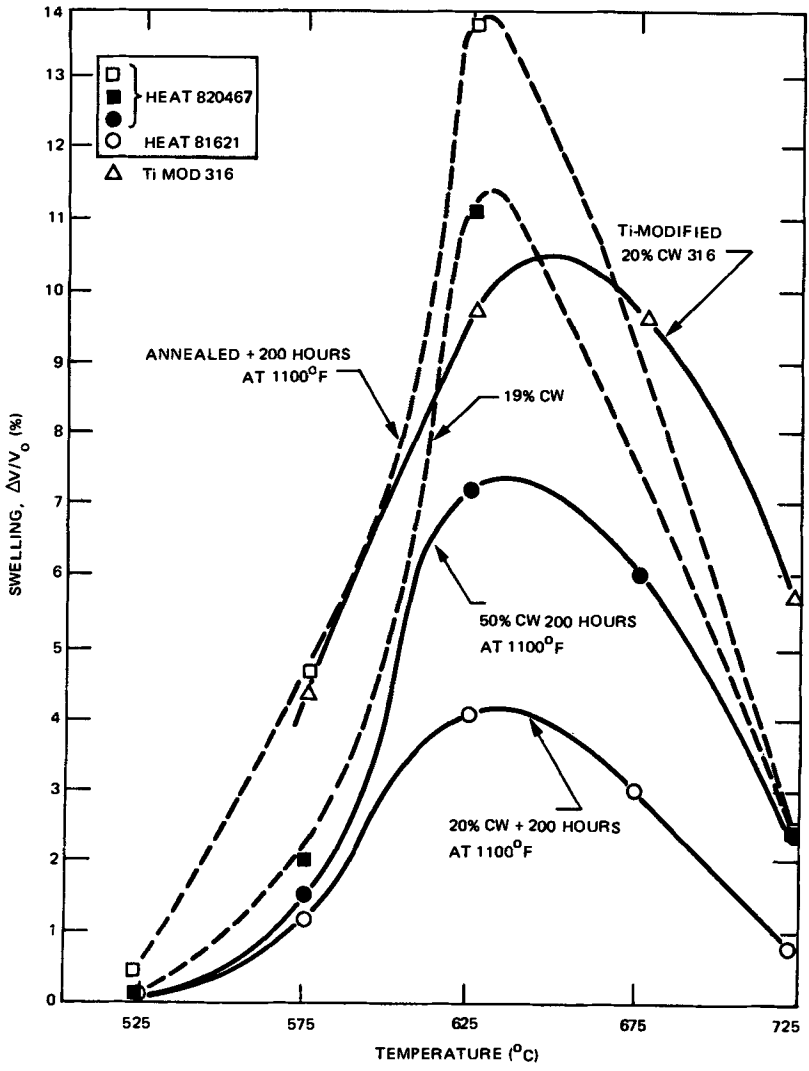

FIG. 2—*Temperature dependence of swelling in Type 316 stainless steel after 105 dpa (Ref 5).*

perature is too low, only a portion of these elements will be in solution. The remainder will appear as carbide and nitride particles, which probably have a deleterious effect on swelling by acting as void nucleation sites as, for example, observed in Ref. *7.*

It can be expected that these various alloying elements will have very different effects on swelling. The effects of silicon and molybdenum appear to

be acute while any effect of titanium appears in this case to be swamped by effects of processing. Results from reactor irradiations of Type 321 (essentially titanium-modified Type 304) have shown that while titanium can apparently delay the onset of swelling, the eventual swelling rate can be as high as or higher than Type 304. However, the results for molybdenum suggest more than merely an effect on incubation fluence, since at 140 dpa ($\sim 2 \times 10^{23}$ n/cm^2) up to a factor of 10 difference in swelling is still apparent. Obviously some of these effects of compositional variations are subtle and require further study for full elucidation.

Effects of Annealing Temperature

Results from previous work [5] showed that the swelling in 20 percent cold-worked Type 316 stainless steel from heat No. 81621 was less than a like material from heat No. 820467. Figure 3 shows the results of these data. The major difference in the two heats of materials reported in Fig. 3 is the annealing temperature prior to the final 20 percent cold work: heat 820467—1010 °C (1850 °F), heat 81621—1177 °C (2151 °F). Heat 81621 was reprocessed according to the procedures used for 820467 and bombarded to

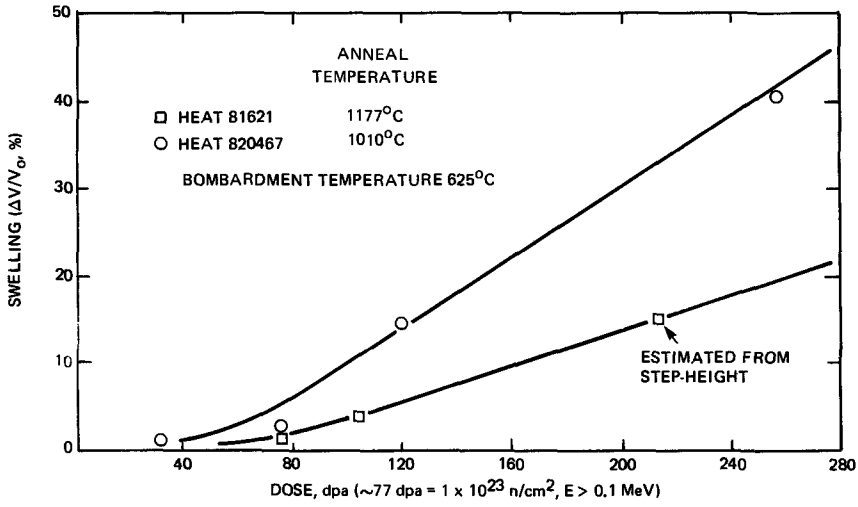

FIG. 3—*Heat-to-heat variation in swelling of 20 percent cold-worked Type 316 stainless steel.*

approximately 77 and 150 dpa at 625 °C (1157 °F) (E_d = 33 eV). Figure 4 shows a comparison between the data from the reprocessed heat No. 81621 and the data in Fig. 3. It is seen from Fig. 4 that annealing temperature can be an important processing parameter.

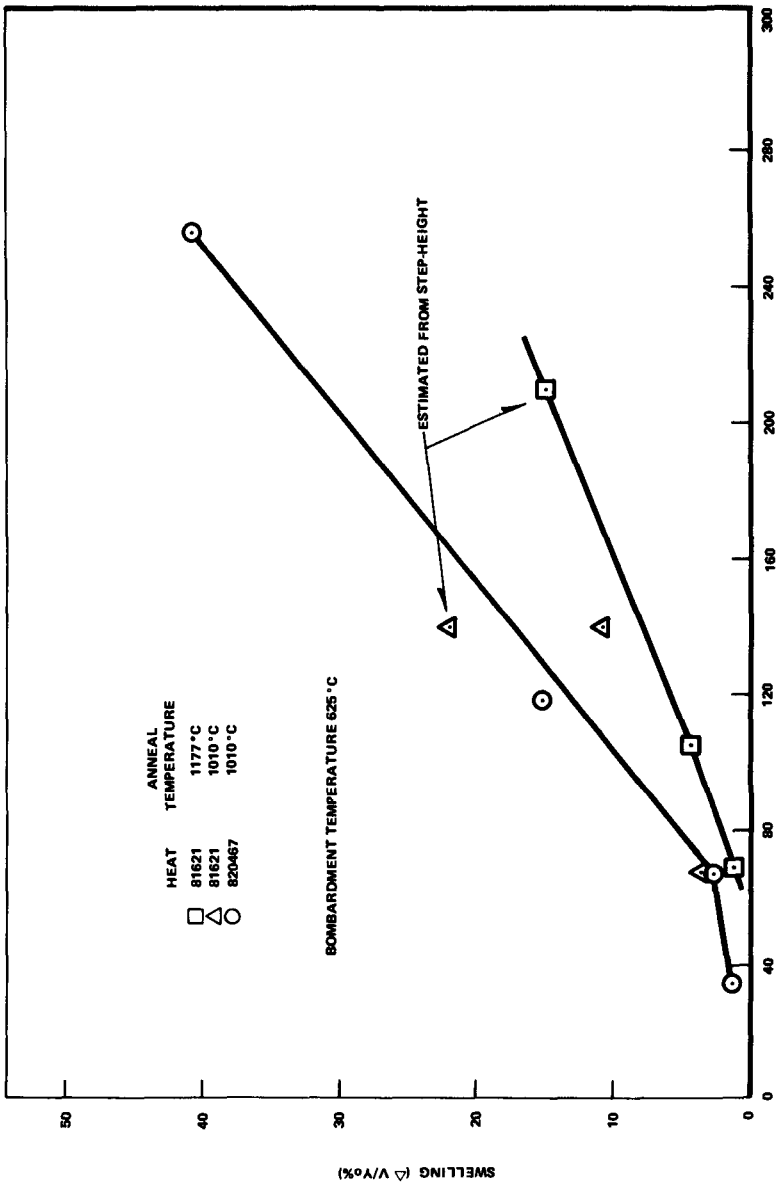

FIG. 4—*Effect of solution-annealing temperature on swelling of 20 percent cold-worked Type 316 stainless steel.*

Heat-to-Heat Variations

The purpose of this study was to investigate swelling variations between different heats of 20 percent cold-worked Type 316 stainless steel. Tubing specimens were received from HEDL from seven different lots of 20 percent cold-worked Type 316 tubing representing six different heats of vacuum-melted steel to be used in the first core loading of FFTF. The compositions of these lots are given in Table 3. Twenty percent cold-worked 316 tubing from an air-melted heat irradiated in the L-16 materials irradiation test in Subassembly X-098 of EBR-II was added to the test matrix for comparison. All lots were processed to the same U.S. Reactor Development and Technology standard.

Table 3 summarizes the bombardment conditions, composition, and step-height results for each specimen. The step-height results in Table 3 show clearly a variation in swelling between the different heats of material. Two of the lots (N and 24) are from the same heat and provide duplicate data points which indeed show almost equal swellings.

It was surprising to discover that the specimen exhibiting the highest swelling was from the air-melted heat irradiated in the GE L-16 test in Subassembly X-098. This heat has presently been examined after reactor irradiation to fluences of ~4 (~30 dpa) and 8.5 10^{22} n/cm^2 (65 dpa), $E > 0.1$ MeV and has shown only moderate swelling [*8*]. The peak volume increase in the 20 percent cold-worked material was ~2 percent at 600°C (1112°F). It is now discovered that at 140 dpa (E_d = 33 eV) the air-melted heat No. M2783 is showing more than twice the swelling of some of the vacuum-melted heats. Whether this is a result of a shorter incubation period or higher swelling rate remains to be determined.

It is of interest to note that if one attempts to link the observed swelling behavior in these heats to compositional effects one could conclude that increases in the total phosphorus + nitrogen + sulphur content can cause increased swelling. The only discernible difference in these heats (apart from uncertainties in processing) is the nitrogen, phosphorus, and sulfur contents. Major alloying element contents are consistent. Figure 5 shows the step-height measurements of swelling plotted as a function of combined nitrogen + phosphorus + sulfur.

It has been suggested that all cold-worked Type 316 heats will exhibit the same swelling rate after incubation. Thus a second objective in the evaluation of swelling in FFTF tubing is to determine whether there are differences in the steady-state swelling rates of the various heats. Lots N, DD, and S were each bombarded to 35 and 70 dpa to investigate this point. Specimen HEDL-30 was also included. This is a low-molybdenum Type 316 which exhibited high swelling in the effects of minor compositional variations experiments. It was of interest to learn whether its higher swelling was due to a shorter incubation period, higher swelling rate, or both.

TABLE 3—*FFTF tubing, heat-to-heat variations in swelling.*

	HEDL Lot Number							
	CN 13	N[a]	24[a]	—[b]	CN 17	X	DD	S
Specimen	74-2-13	74-2-14	74-2-15	74-2-16	74-2-17	74-2-18	74-2-19	74-2-20
C	0.054	0.057	0.057	0.06	0.053	0.051	0.050	0.037
N	0.006	0.007	0.007	0.026	0.005	0.005	0.006	0.027
Si	0.58	0.49	0.49	0.51	0.55	0.52	0.53	0.45
Mo	2.32	2.50	2.50	2.51	2.31	2.35	2.31	2.50
V	0.02	...	...	...	...	...	...	...
P	0.004	0.013	0.013	0.022	0.004	0.005	0.005	0.009
S	0.006	0.006	0.006	0.015	0.006	0.003	0.006	0.007
Cr	17.45	16.51	16.51	16.43	17.43	17.54	17.43	17.25
Ni	13.71	13.54	13.54	13.28	13.71	13.86	13.73	12.92
Cu	0.01	0.07	0.07	0.09	0.01	0.01	0.01	0.02
Co	0.016	...	...	0.06	0.012	0.01	0.021	...
B (ppm)	<5	32	32	1.5	<5	9	<5	9
Mn	1.65	1.60	1.60	1.77	1.71	1.63	1.75	1.38
Step-height (Å)	790	900	980	2100	1230	870	820	1540

[a] Heat No. 87210.
[b] Heat No. M2783 (GE-X098, L-16 Irradiation).

NOTES—Compositions in weight percent except where noted.
Bombardment conditions: 2 h at 625°C (1157°F) for a dose of 140 dpa (E_d = 33 eV).

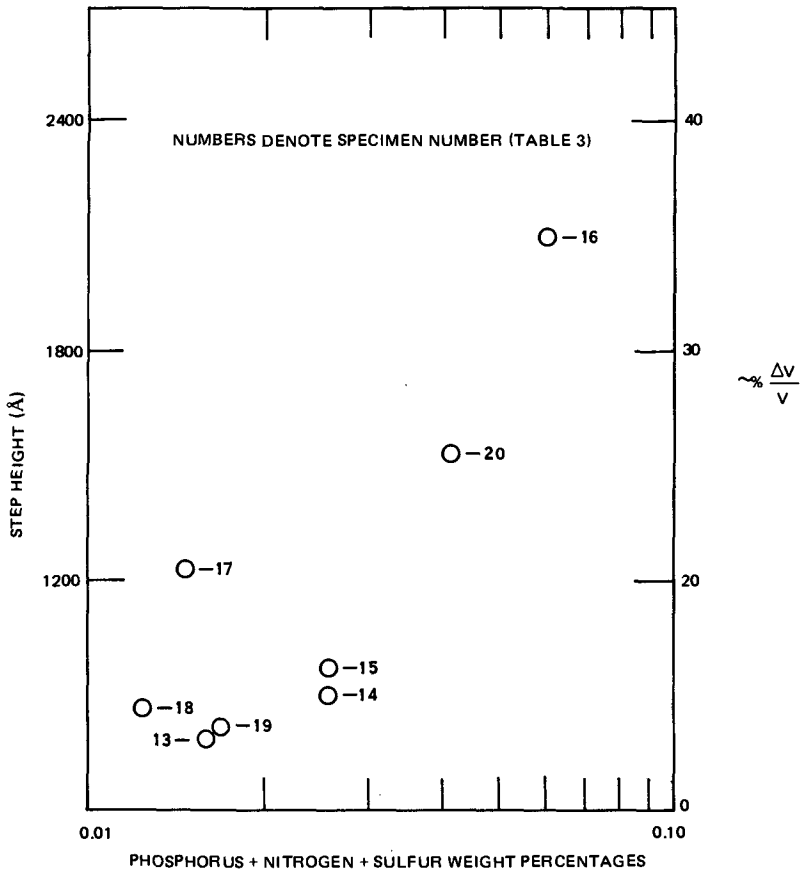

FIG. 5—*Combined effects of phosphorus, nitrogen, and sulfur weight percentages on swelling.*

Swelling was measured in the 35 and 70-dpa specimens by TEM, because step heights were too small to resolve, and then compared with the step height data from the specimens bombarded to 140 dpa. The dose dependence of swelling in the four lots is shown in Fig. 6. Comparison of the steady-state swelling rate is valid only if the intermediate-dose (60 to 70 dpa) data points are beyond the void incubation period. Specimens HEDL-30, N, and DD show sufficient swelling for this to be the case and it is found that their steady-state swelling rates vary by a factor of two. It is additionally observed that the low-molybdenum specimen HEDL-30 apparently shows higher swelling as a result of both a shorter void incubation period and a higher steady-state swelling rate. The complete data including void size and number density data are given in Table 4.

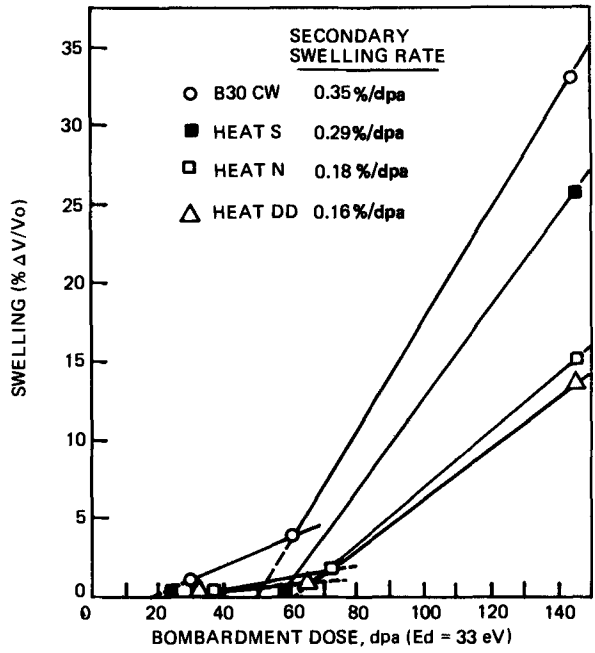

FIG. 6—*Dependence of swelling in Type 316 20 percent cold-worked steel: heat-to-heat variation; 5-MeV nickel-ion bombardment at 625°C (1157°F).*

TABLE 4—*Dose dependence of swelling in various lots of 20 percent cold-worked Type 316—data summary.*

Lot	Dose, dpa (E_d = 33 eV)	Void Diameter, Å			Average Void Density, cm^{-3}	Average Swelling, % $\Delta V/V_0$
		Min	Avg	Max		
HEDL-30	29	154	322	580	3.9×10^{14}	0.88
HEDL-30	60	176	515	1060	3.7×10^{14}	3.38
HEDL-30	144	...	...	...	...	32.8[a]
N	36	120	285	547	5.9×10^{13}	0.17
N	72	122	437	733	2.3×10^{14}	1.55
N	144	...	...	...	...	15.0[a]
DD	33	63	159	314	1.4×10^{14}	0.05
DD	66	74	291	577	3.7×10^{14}	0.68
DD	144	...	...	...	...	13.7[a]
S	23	99	238	349	1.6×10^{14}	0.12
S	59	87	272	475	1.7×10^{14}	0.25
S	144	...	...	...	...	25.7[a]

[a] From step-height measurement.

Conclusions

Certain minor alloying elements, particularly silicon and molybdenum, were found to reduce the extent of swelling in 20 percent cold-worked Type 316 when irradiated with 5-MeV nickel ions to 140 dpa (E_d = 33 eV). It was additionally found that lower swelling can result from a higher solution-annealing temperature prior to the final cold-working operation. This result suggests that minor alloying elements are effective in reducing swelling only when in solid solution. The smaller swelling observed in certain cold-worked Type 316 heats was found to be a consequence of both a longer incubation time for void formation and a lower eventual swelling rate.

This work has shown that some of the dependencies of swelling on alloy composition observed in pure alloy systems [6] are also found for Type 316 series stainless steel. This offers the possibility that acceptably low swelling can be achieved in stainless steel for LMFBR core components through suitable control of alloy composition and processing conditions.

Acknowledgments

We gratefully acknowledge the invaluable assistance of W. G. Johnston for ion bombardments, W. L. Bell for transmission microscopy, and G. M. Konze and E. S. Darlin for specimen preparation.

This work was performed under Contract E(04-3)-893, Task 3, 189 No. SG044 between the Energy Research and Development Administration and General Electric Company.

References

[1] Nelson, R. S. and Mazey, D. J. in *Radiation Damage in Reactor Materials,* Symposium Proceedings STI/PUB/230, Vol. 2, International Atomic Energy Agency, Vienna, 1969, p. 157.

[2] Nelson, R. S., Mazey, D. J., and Hudson, J. A., *Journal of Nuclear Materials*, Vol. 37, 1970, p. 1.

[3] Johnston, W. G., Rosolowski, J. H., Turkalo, A. M., and Lauritzen, T. in *Effects of Radiation on Substructure and Mechanical Properties of Metals and Alloys, ASTM STP 529,* American Society for Testing and Materials, 1973, pp. 213–227.

[4] Bates, J. F. in *Properties of Reactor Structural Alloys after Neutron or Particle Irradiation, ASTM STP 570,* American Society for Testing and Materials, 1975, pp. 369–387.

[5] Challenger, K. D., "Irradiation Induced Void Swelling in Type-316 Stainless Steel Resulting from 5 MeV Nickel Ion Bombardment," PhD. thesis, University of Cincinnati, Cincinnati, Ohio, 1973; also, Report No. NEDO-13990, General Electric Company.

[6] Johnston, W. G., Lauritzen, T., Rosolowski, J. H., and Turkalo, A. M., *Proceedings,* American Society for Metals Materials Science Seminar on Radiation Damage in Metals, Cincinnati, Ohio, Nov. 1975.

[7] Appleby, W. K. and Wolff, U. E. in *Effects of Radiation on Substructure and Mechanical Properties of Metals and Alloys, ASTM STP 529,* American Society for Testing and Materials, 1973, pp. 122–136.

[8] Busboom, H. J., McClellan, G. C., Bell, W. L., and Appleby, W. K., GEAP-14062, General Electric Company, Sunnyvale, Calif., July 1975.

F. A. Garner,[1] *J. J. Laidler,*[1] *and G. L. Guthrie*[1]

Development and Evaluation of a Stress-Free Swelling Correlation for 20 Percent Cold-Worked Type 316 Stainless Steel

REFERENCE: Garner, F. A., Laidler, J. J., and Guthrie, G. L., "**Development and Evaluation of a Stress-Free Swelling Correlation for 20 Percent Cold-Worked Type 316 Stainless Steel,**" *Irradiation Effects on the Microstructure and Properties of Metals, ASTM STP 611,* American Society for Testing and Materials, 1976, pp. 208–226.

ABSTRACT: Sufficient data have been accumulated on the swelling behavior of 20 percent cold-worked Type 316 stainless steel to make predictions of the anticipated swelling in the fast test reactor (FTR). A predictive stress-free swelling correlation has been developed employing a limited data base developed in the Experimental Breeder Reactor-II (EBR-II). Insight gained from electron and ion simulation experiments aided in the correlation development. Application of this correlation to environments other than fast reactor core regions requires consideration of the differences in neutron spectrum and displacement rate in such environments.

KEY WORDS: radiation, irradiation, swelling, stainless steels, evaluation, nuclear reactors, voids

The prediction of radiation-induced property changes in structural materials exposed to high neutron fluence is a major requirement for design and evaluation of fast breeder reactors. Although reactor components will not be operated to fluences beyond the available data base, predictive correlations are necessary to assess the impact of variations in operating parameters such as the coolant inlet temperature. They also aid in design optimization studies and the assignment of lifetimes for experimental subassemblies and replaceable core components. The development of predictive correlations necessitates a continuous review and improvement process as new data are developed in the Experimental Breeder Re-

[1] Senior research scientist, manager-Materials Development, and senior research scientist, respectively, Hanford Engineering Development Laboratory, Westinghouse Hanford Company, Richland, Wash. 99352.

actor-II (EBR-II). For fast test reactor (FTR) applications, the data base is now large enough to make predictions of the swelling behavior of the major structural material, 20 percent cold-worked Type 316 stainless steel.

The swelling data base developed in EBR-II comprises three categories: unstressed prototypic[2] steel at low fluence, unstressed steel which is non-prototypic but nominally similar and exposed to moderate fluences, and stressed prototypic fuel pin cladding exposed to fluence levels close to the FTR goal fluence. This data base is not large enough, however, to define both the empirical form of the swelling equation and the major parametric dependencies simultaneously and uniquely, which are known to include the irradiation temperature, total neutron fluence and spectrum, and the stress state. It had been possible, however, to combine the available data with knowledge gained from charged particle simulation studies and produce a predictive correlation for stress-free swelling. The development of the correlation evolved in two stages, the first of which culminated in late 1973 and which was very dependent on the results of simulation experiments. The second stage included subsequent data and insight available at the end of 1974 and was influenced both by simulation studies and new neutron data.

1973 Swelling Position

Laidler [*1*][3] demonstrated that the swelling behavior observed in electron irradiations of prototypic (N-lot) fuel cladding was linear with displacement dose after an incubation period. Noticing that the low-fluence prototypic neutron data showed no observable swelling, Laidler employed moderate-fluence [$\leqslant 7 \times 10^{22}$ neutrons (n)/cm^2 ($E > 0.1$ MeV)] unprototypic data which also showed little or no swelling as a lower estimate of the duration of the incubation period. A swelling position was developed which combined the incubation behavior observed in neutron irradiations with swelling rate profiles observed in electron irradiation experiments. Theoretical estimates of the atomic displacement cross sections were employed along with estimates of the rate-dependent temperature shift of the swelling regime. The form of the swelling equation is illustrated in Fig. 1 and given in the following, where the neutron fluence is in units of 10^{22} n/cm^2 ($E > 0.1$ MeV)

$$\text{swelling} = \frac{\Delta V}{V_0} = R\left[\phi t + \frac{1}{\alpha} \ln \left\{\frac{1 + \exp\left[\alpha(\tau - \phi t)\right]}{1 + \exp(\alpha\tau)}\right\}\right]$$

[2]Prototypic steels are defined as Type 316 stainless steels prepared in accordance with RDT Standard M7-3, which defines the requirements for FTR and Clinch River breeder reactor (CRBR) applications.

[3]The italic numbers in brackets refer to the list of references appended to this paper.

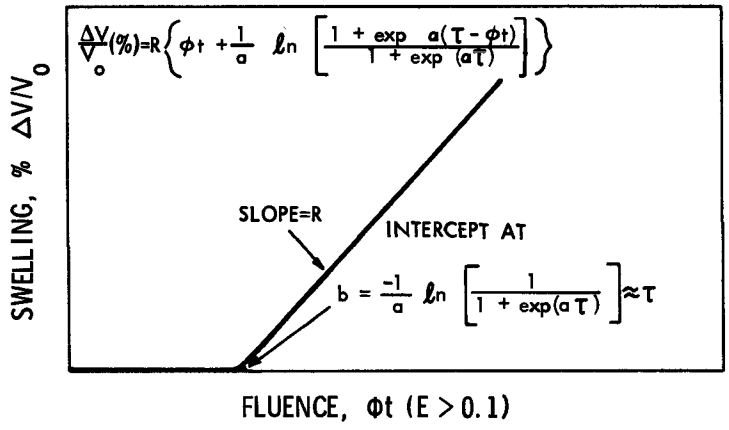

FIG. 1—*Model and mathematical form of empirical swelling equation presently used in core design for 20 percent cold-worked Type 316 stainless steel components.*

The parameters R, α, and τ model the steady-state swelling rate, the degree of curvature in the transition region, and the zero-swelling intercept of the steady-state swelling regime, respectively. All three of these parameters are dependent on temperature. When the swelling $\Delta V/V_0$ is expressed as a percentage

$$R(T) = \exp(-88.5499 + 0.531072T - 1.24156 \times 10^{-3}T^2 + 1.37215 \times 10^{-6}T^3 - 6.140 \times 10^{-10}T^4)$$

$$\tau(T) = \exp(-16.7382 + 0.130532T - 3.81081 \times 10^{-4}T^2 + 5.51979 \times 10^{-7}T^3 - 3.26491 \times 10^{-10}T^4)$$

$$\alpha(T) = -1.12 + 6.89 \times 10^{-3}T$$

where T is the centigrade temperature. Tabulations of these parameters are given in Table 1. Note again that the incubation parameter $\tau(T)$ in general represents a lower limit, since the data field used at that time did not exhibit swelling at all temperatures. In addition, the data were so sparse that 50°C (90°F) temperature increments were required in this analysis to accumulate sufficient data points in each determination of the incubation parameter. The confidence limits for the 1973 position were established by consideration of the uncertainties in electron and neutron displacement equivalencies, and ranged from 133 to 78 percent of the nominal prediction. The lower limit set by Laidler was reduced subsequently

TABLE 1—*Previous design swelling correlation temperature-dependent parameters for 20 percent cold-worked Type 316 stainless steel.*

Temperature, °C	R	τ	α
350	0.0058	2.81	1.29
375	0.0023	3.57	1.47
400	0.0691	4.35	1.64
425	0.165	5.08	1.81
450	0.352	5.72	1.98
475	0.539	6.17	2.16
500	0.771	6.35	2.33
525	0.968	6.21	2.50
550	1.077	5.68	2.67
575	1.068	4.80	2.84
600	0.943	3.69	3.02
625	0.737	2.53	3.19
650	0.502	1.50	3.36
675	0.294	0.76	3.53
700	0.144	0.31	3.71
725	0.0574	0.10	3.88
750	0.0179	0.026	4.05

to 50 percent, based on a consensus reached by peer review groups on possible alternative interpretations of the neutron data.

Recent Insights and Additional Data

Since the development of this correlation, the relevant unstressed data field has been expanded to include the data given in Table 2. All of these data are from air-melted heats, which have less stringent specifications on minor element composition and processing than do the vacuum-melted FTR first-core and vendor qualification cladding heats. The addition of small amounts of impurities has been shown to retard neutron-induced swelling in pure metals such as copper, nickel, and aluminum. The swelling of 300 series stainless steels has been found to be sensitive to the levels of minor elements such as carbon, titanium, silicon, zirconium, and columbium. An extensive review of the effects of composition and other variables on swelling is contained in Ref *3*. Removal of almost all impurities has led to greatly enhanced swelling in neutron-irradiated solution-annealed Type 316 stainless steel [*2*]. Subsequent ion bombardment studies [*3*] indicated that the primary effect of removing the impurities was to decrease the incubation period substantially, as shown in Fig. 2.

The expanded data field is still too small to allow the simultaneous determination of the form of the swelling equation and the nature of the major parametric dependencies, which are known to include the irradia-

TABLE 2—*Compilation of recent swelling data for 20 percent cold-worked Type 316 stainless steel.*

Material	Experiment Designation	Reference No.	Irradiation Temperature, °C	Fluence, 10^{22} n/cm^2 ($E > 0.1$ MeV)	$\Delta V/V_0$, %
20% cold-worked Type 316 Drawn tubing Heat #M2783	X-098 (General Electric)	19	454	8.6	0.13
			454	8.4	0.05
			535	8.9	0.42
			535	8.6	0.26
			609	8.8	2.30
			609	8.6	1.60
			689	9.4	0.01
			689	9.2	−0.10
27% cold-worked Type 316 Swaged rod Program heat	X-157 (B-92) (Westinghouse Hanford)	20	390	5.6	0.31
			430	7.6	0.83
			460	6.6	0.42
			625	9.5	1.42
			685	9.9	0.46
			750	10.1	−0.03
			810	10.1	−0.02
20% cold-worked Type 316 Rolled sheet Heat #34357	X-100 (Atomics International)	21	500	8.0	−0.1
			600	8.0	3.3
20% cold-worked Type 316 DO heat	X-100 (Oak Ridge National Lab)	22	500	6.6	−0.10
			600	6.6	0.40

tion temperature, total neutron fluence and spectrum, and the stress state. In this data set the latter parameter should not be operating, however.

Rather than attempt to recorrelate the data, it was decided to analyze the data in Table 2 for consistency with predictions of the previous correlation. Figure 3 is a graphical compilation of the recent cold-worked data tabulated in Table 2. The largest uncertainties are not associated with the magnitude of the swelling but with the assignment of fluence and temperature. Since these data were derived in uninstrumented experiments, the temperature is the most difficult parameter to estimate in-reactor.

In performing a consistency analysis on these data, it was found that there is a very large variation between the magnitude and the predicted value for each data point. Recent insights gained from simulation experiments have led to a realization that the apparent variations, while large at relatively low fluence, do not necessarily imply equally large variations at higher fluences.

First of all, the linear-after-incubation swelling model was confirmed in full-range ion bombardment studies on 20 percent cold-worked Type 316 [*4*] and electron irradiation studies [*5*] on the various heats of pro-

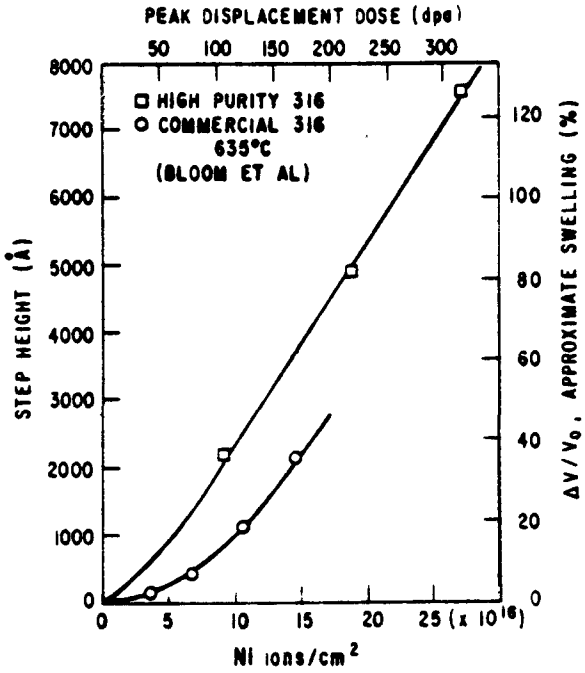

FIG. 2—*Swelling observed in ion bombardment of commercial Type 316 and high-purity (reduced carbon, nitrogen, and silicon) stainless steels. This figure was reproduced direclty from Johnston et al* [3].

totypic and qualification steels employed in the FTR development program. The electron irradiation studies also showed that although the steady-state swelling rates for all heats are similar, there is a large variability in the local incubation period, as shown in Figs. 4 and 5. This is a consequence of the small volume sampled in a high-voltage electron microscope (HVEM) irradiation experiment [*6*], since the incubation parameter in a given material depends strongly on local composition and microstructure. In broad-beam irradiation techniques such as 5 MeV Ni^+ ion irradiations, the variability is much easier to observe, although the local variability is often seen in the small areas irradiated with electrons. Similar local variations in swelling are routinely observed in neutron-irradiated cold-worked stainless steels in the United States and abroad. Figure 6 shows that the bulk-integrated swelling behavior measured in ion bombardment experiments for various nominally similar heats can be quite variable [*7*]. The range for the various first-core heats of steel is quite small, however, reflecting the stringent specifications placed on the composition and processing of reactor-grade materials.

Based on these observations, it appears that in both electron and neutron

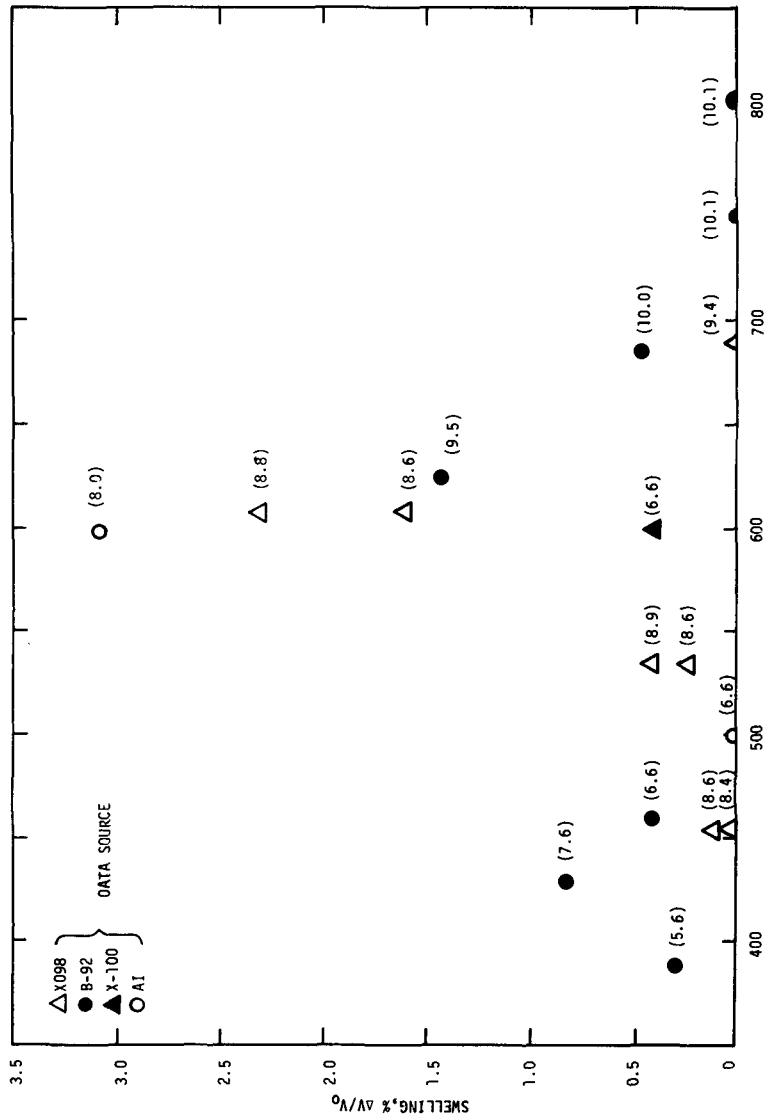

FIG. 3—*Graphical compilation of recent cold-worked Type 316 swelling data shown in Table 2. Numbers in parentheses are fluences above 0.1 MeV, in units of* 10^{22} *n/cm*^{2}.

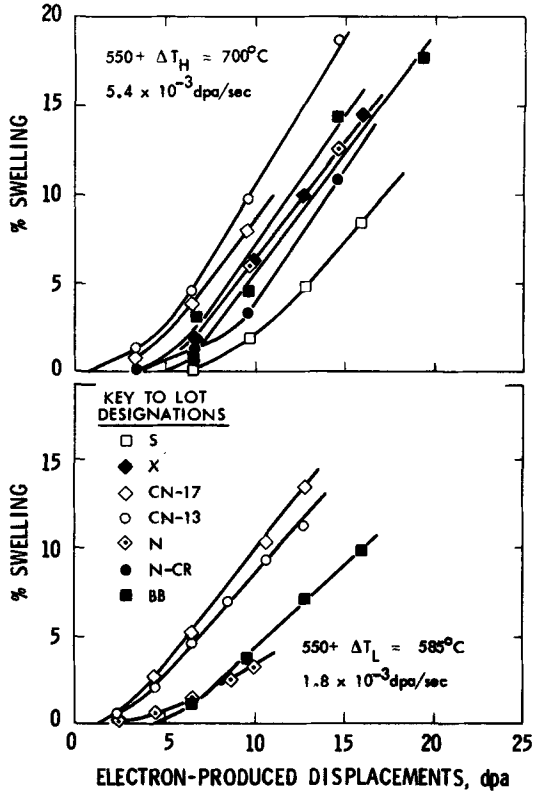

FIG. 4—*Results of HVEM irradiation at two temperatures of various lots of prototypic 20 percent cold-worked Type 316 stainless steel fuel cladding [5].*

irradiations there will be some bulk-integrated incubation parameter for each material

$$\bar{\tau}_i(T) = \frac{\int \tau_i(T, \text{ composition, structure})\, dV}{\int dV}$$

where

dV = individual volume element,
T = temperature, and
i = material identity.

If a normal distribution of $\tau(T)$ values throughout the material is assumed, then the probability of any volume having a given $\tau(T)$ is

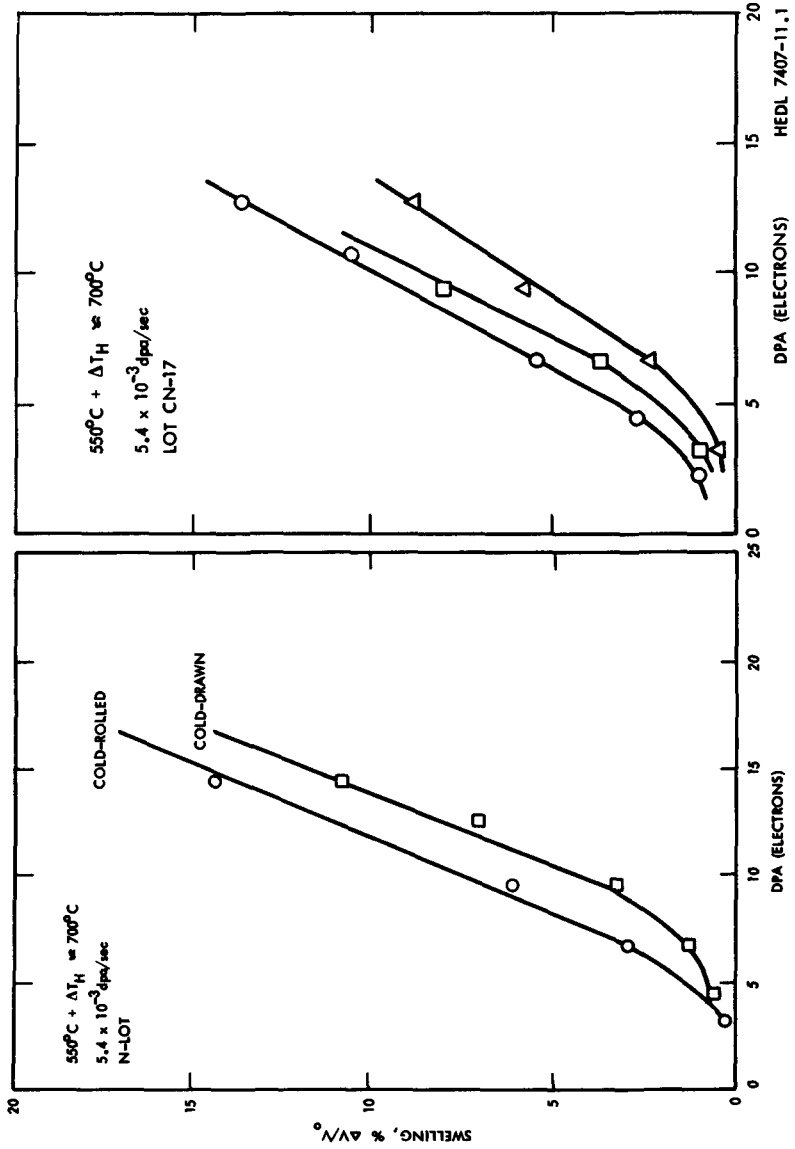

FIG. 5—*The spot-to-spot incubation period for swelling is sensitive to the manner in which the heat was processed and varies from grain to grain within a single heat* [5].

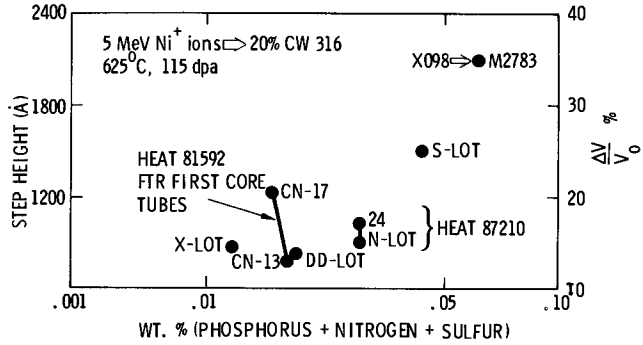

FIG. 6—*Tube lot-to-lot variations in total swelling observed in ion bombardment of various cold-worked steels of interest to the FTR development program* [23]. *The bars connect tube lots which were derived from the same heat. Lots X, DD, CN-13, and CN-17 are designated as first-core steels.*

$$P_i(\tau) = \frac{1}{\sqrt{2\pi}\sigma_i} \exp\left(\frac{[\tau - \bar{\tau}_i(T)]^2}{2\sigma_i^2}\right)$$

As shown in Fig. 7, two different heats might have macroscopic or bulk-averaged values of $\bar{\tau}_i$ which are different, even though there may be overlap in the microscopic τ-values. At low fluences the influence of the incubation period will lead to large relative differences. At higher fluences, only a small absolute difference will be maintained.

Development of an Updated Correlation (1975 Position)

If it is assumed that the compositional and microstructural dependence is contained only in the incubation parameter τ, the complexity of the problem can be reduced by visualizing the data in τ-space rather than swelling space. This has the benefit of automatically normalizing all data, removing the dimension of fluence.

The following approach was used in this analysis:

1. $R(T)$ and $\alpha(T)$ were preserved from the previous correlation.
2. The new data points were correlated by finding τ^*-values necessary to reproduce the observed swelling at that temperature and fluence.
3. These τ^*-values were then analyzed for trends.

Figure 8 shows the new data plotted in τ-space, as well as the data used by Laidler in developing the previous $\tau(T)$ correlation. With the exception of the X-157 data points below 500°C (932°F), all data lie above the current correlation, which was expected to be a lower bound. With an additional exception of the lowest data point at 600°C (1112°F), all points lie

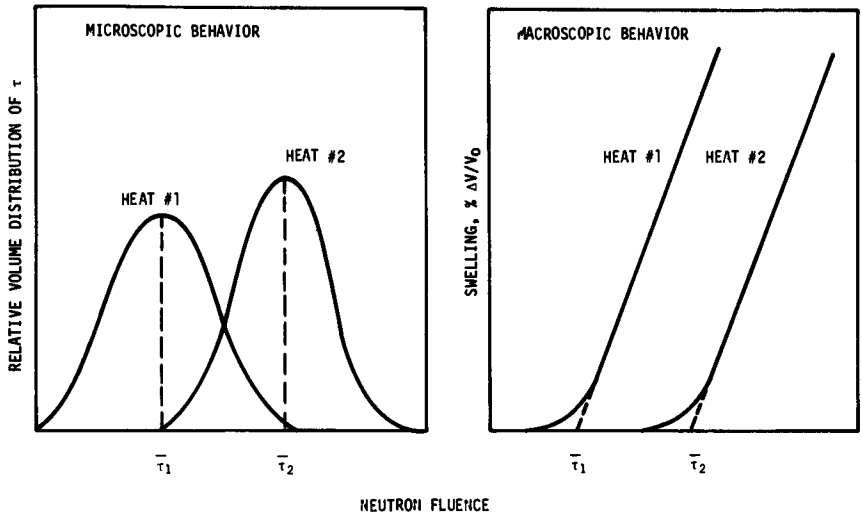

FIG. 7—*Schematic representation of statistical distribution of incubation parameters, τ, and the effect of this distribution on the observed bulk swelling.*

in a relatively tight band which is best defined by the X-098 data, the only data set that spans the full temperature range. This reduction technique has reconciled apparently large differences in the X-098 and X-100 swelling data. The large difference in observed swelling in these two materials is due to the fact that the X-100 experiment was irradiated to a fluence of the order of the incubation period, while the X-098 experiment was irradiated to higher levels.

A modified incubation parameter curve, labeled τ_{mod}, was placed through the upper-bound data and has the following form

$$\tau_{mod}(T) = 2.57262 \times 10^2 - 2.39381T + 8.16677 \times 10^{-3}T^2 - 1.18508 \times 10^{-5}T^3 + 6.21367 \times 10^{-9}T^4$$

The form of this curve requires some comment since a nearly straight line placed around $\tau = 8.0$ for all temperatures would probably fit as well. Recent data confirm a trend noted by Brager [*8*] that there is a peak in the incubation period of 20 percent cold-worked Type 316 around 500°C (932°F), and that above 600°C (1112°F) it again becomes difficult to nucleate voids. As shown in Fig. 9, the shape of the τ-curve is consistent with the experimental observations, whereas a constant τ is not.

The B-92 data below 500°C (932°F) are completely inconsistent with this curve and require negative values for τ below 400°C (752°F). This

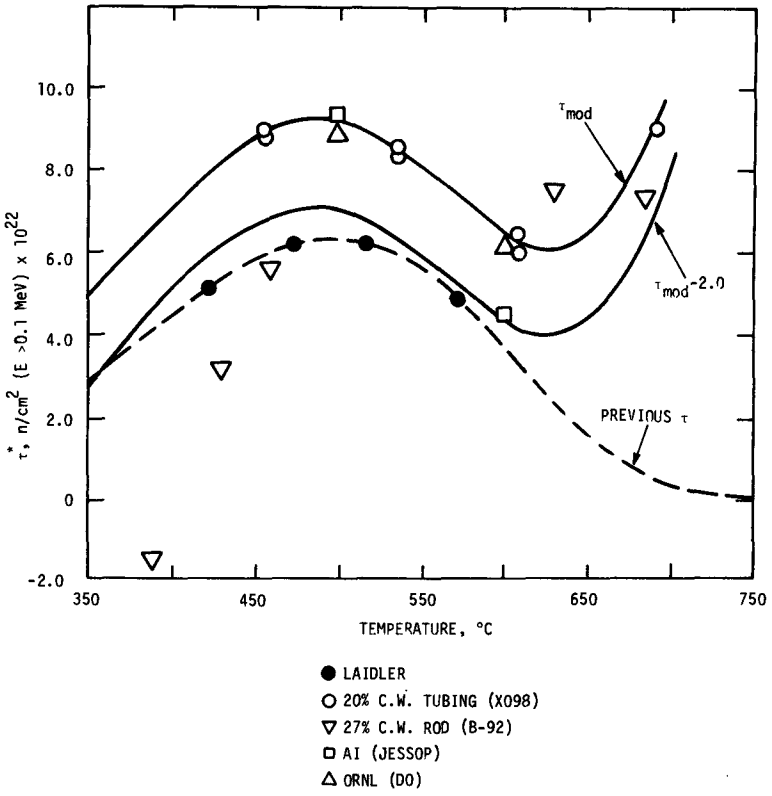

FIG. 8—*Swelling data of Table 2 reduced to τ-space.*

material has a higher level of cold work (27 percent), however, and there is considerable uncertainty in the estimated irradiation temperatures. The agreement at higher temperatures may be due to the irradiation-induced recovery of 20 and 27 percent cold work to the same dislocation density. Note that the $[\tau_{mod}(T) - 2.0]$ curve is in rough agreement with the lowest data point at 600°C (1112°F) and the earlier data of Laidler, and forms a lower-bound estimate of $\tau(T)$. Reconciliation of the low temperature B-92 data would require $[\tau_{mod}(T) - 4.0]$.

The new nominal design equation is chosen so that the middle of the τ-band is used. Therefore, the incubation parameter is now $(\tau_{mod} - 1.0)$ or

$$\tau(T) = 2.56262 \times 10^2 - 2.39381T + 8.16677 \times 10^{-3}T^2 - 1.18508 \times 10^{-5}T^3 + 6.21367 \times 10^{-9}T^4$$

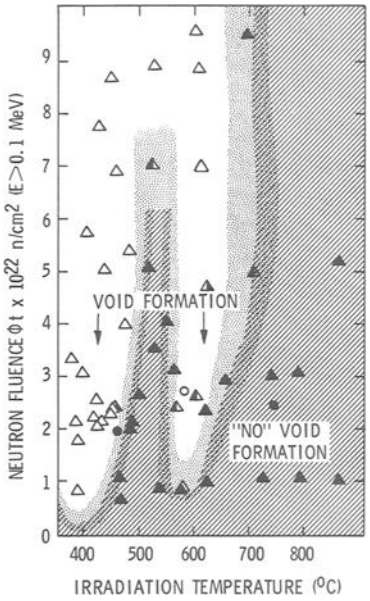

FIG. 9—*Data of Brager* [20] *show that using void densities greater than* 10^{12} cm^{-3} (*open triangles*) *as a nucleation criterion, cold-worked Type 316 stainless steel has an incubation period that is strongly temperature-dependent. Note the peak in nucleation resistance around 500°C (932°F).*

The R and α parameters remain unchanged from the previous position. Note that the coefficients in these equations should not be truncated in application. At all temperatures the coefficients are generated by small differences between nearly equal terms, and substantial deviations from the values intended can be obtained with truncated coefficients, particularly above 600°C (1112°F).

Recent Fuel Pin Data

This new nominal equation was compared [*9,10*] with recent swelling data generated from density measurements on the cladding of fuel pin PNL-11-9R. The details of temperature, fluence, and stress history are given in the referenced papers. This pin utilized fully prototypic cladding and was part of the PNL-11 (X-194) subassembly, containing 37 mixed-oxide fuel pins and irradiated to a peak neutron fluence of 1.0×10^{22} n/cm^2 ($E > 0.1$ MeV). Although the swelling data from this cladding cannot be considered stress-free data, the stress level was relatively low, with the calculated stress contribution due to stress-affected swelling being less than 10 percent of the total. This fuel pin had a low smear density

and was not expected to experience fuel-clad contact and subsequent stress interaction. Note the rather good agreement shown in Fig. 10, which tends to confirm the general applicability of the equation.

Confidence Limits and Predictions

With such a limited data field, the assignment of confidence limits is quite difficult. Since the swelling equation appears to describe the swelling of prototypic tubing quite well, arguments directed toward uncertainties involved in extrapolation from simultation studies can be discounted. Limits of 125 and 75 percent of the nominal prediction were chosen, based on a consensus reached by members of an advisory peer group on current best estimates of the uncertainties in the peak swelling rate R. At fluences near or below the incubation level, however, the variability in the incubation period can lead to percentage variations which are much larger. If the confidence limits were to be set by the upper and lower bounds of the τ-band shown in Fig. 8, then the percentage variation is much larger at lower fluences and diminishes to unrealistically small values at high fluences. Therefore, it is recommended that the ± 25 percent confidence limits not be applied below 0.5 percent swelling. Another reason for not using these confidence limits below 0.5 percent swelling is that the total density change below this level is often dominated by independent companion processes—precipitate-related thermal densification and recovery of cold work—which yield strains on the order of 0.1 to 0.2 percent for FTR steels [*11*]. The contribution due to these processes is shown in Fig. 10.

The original correlation predicted that the maximum swelling of FTR fuel cladding would be 8 and 21 percent at the goal fluences of 1.2×10^{23} and 2.5×10^{23} n/cm^2 ($E > 0.1$ MeV), which are approximate target goals for FTR and proposed commercial breeders, respectively. The new correlation proposed here predicts 6.2 and 20 percent, reflecting relatively minor changes in the predicted swelling levels. At lower fluences the relative difference between the two swelling predictions becomes progressively larger. If the peak flux region does not coincide with the location of the peak swelling rate, the levels of swelling will be even smaller.

Application of Swelling Correlations to Other Reactor Environments

These correlations were developed on the basis of the conventional concept of a threshold fluence, in which only the portion of the fluence above 0.1 MeV is considered to contribute to radiation-induced property changes. In effect, the damage potential of the spectrum is approximated by weighting the total fluence, ϕt, by $F(0.1)$, the fraction of the flux above

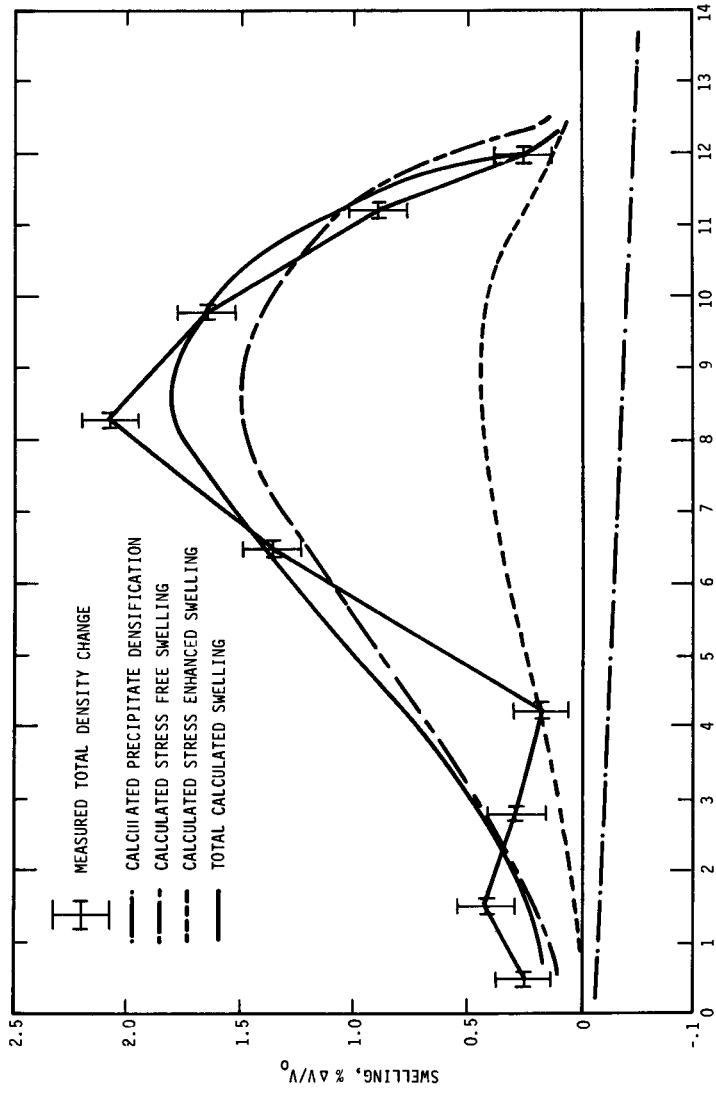

FIG. 10—*Comparison of measured total density changes of fuel pin PNL-11-9R with predictions of nominal equations for density changes due to swelling and precipitate-related densification. This figure was reproduced from Jackson et al* [9].

0.1 MeV. As documented elsewhere [*12*], the use of $F(0.1)$ as a spectrum weighting factor is not physically defensible, but it functions fairly well nonetheless as an approximate spectral weighting factor in the core regions of fast reactors. In reflector regions and beyond, however, $F(0.1)$ does not adequately approximate the decreasing displacement potential of the local neutron spectrum. The net effect is to overpredict the amount of swelling expected outside of the core. The reduced atomic displacement potential of the fluence can be included in the swelling correlation by dividing the input fluence by the factor K, where

$$K = \left[\frac{\bar{\sigma}_d}{F(0.1)}\right]_{\text{EBR-II}} * \left[\frac{F(0.1)}{\bar{\sigma}_d}\right] = \left(\frac{445}{0.87}\right) * \frac{F(0.1)}{\bar{\sigma}_d} = 511 * \frac{F(0.1)}{\bar{\sigma}_d}$$

The validity of this procedure is documented in Ref *12*, which employs the spectrum-averaged atomic displacement cross section $\bar{\sigma}_d$ (barns), calculated according to the standard procedure [*13*]. In the FTR core center the spectrum is softer than in the EBR-II core center, with $\bar{\sigma}_d = 280$ barns and $F(0.1) = 0.62$, which leads to $K_{\text{FTR}} = 1.13$. Although this implies that the FTR flux is 12 percent less effective than the EBR-II flux in creating damage, this consideration has not been included in swelling predictions for FTR, since the error is small compared with the other uncertainties involved. In out-of-core fast reactor environments, however, this consideration can lead to much larger changes in the predicted swelling.

In the application of any swelling equation developed for the liquid metal fast breeder reactor (LMFBR) to fusion or thermal reactor environments, there are additional considerations which must be included. First of all, the spectra in these reactors are quite different from those of fast reactors, containing contributions from 14 MeV neutrons in a fusion reactor spectrum, and involving both a more energetic fast spectrum as well as a thermal neutron distribution in a thermal reactor. While the factor K can be used to account for displacement effects in these environments, it cannot completely compensate for accompanying changes in displacement rates and helium production, both of which are known to influence the swelling behavior of stainless steels.

The swelling phenomenon is known to span a temperature regime which shifts with displacement rate. For a given displacement rate $\Phi_1 = \phi\bar{\sigma}_d$, the swelling regime ranges from $T_s(\Phi_1)$ to $T_f(\Phi_1)$, peaking at an intermediate temperature $T_p(\Phi_1)$. As the displacement rate increases or decreases to Φ_2, there is an increase or decrease in all three characteristic temperatures.

Theory [*14*] predicts a temperature shift based on the upper end of the swelling regime such that

$$\Delta T_f(\Phi_1, \Phi_2) \approx \Delta T_p \approx T_1^2 \frac{K}{E_v} \left[\frac{1}{1 + \frac{KT_1}{E_v} \ln \frac{\Phi_2}{\Phi_1}} \right] \ln \frac{\Phi_2}{\Phi_1}$$

where

T_1 = irradiation temperature in degrees Kelvin at Φ_1,
K = Boltzman's constant, and
E_v = self-diffusion energy.

As a first approximation, the temperature shift is assumed to operate equally at all temperatures in the swelling regime.

For small enough changes in Φ

$$\Delta T_p \approx J \ln(\Phi_2/\Phi_1)$$

The best current estimates [*15,16*] of the magnitude of this shift at fast reactor displacement rates is 25 °C (45 °F) per flux decade (J = 10.9), and 38 °C (68 °F) per flux decade at typical charged particle displacement rates. Therefore, for reactor applications at fluxes substantially different from EBR-II, the temperature T in the swelling equation can be replaced by T' where

$$T' = T + 10.9 \ln \left[\frac{\bar{\sigma}_d \phi}{(445)(3.1 \times 10^{15})} \right]$$

where

T' = effective temperature and
T = actual irradiation temperature.

For the FTR core center region, ($T' - T$) is less than 10 °C (18 °F).

Note again that ϕ is the total flux and $\bar{\sigma}_d$ the average displacement cross section for the entire spectrum. This distinction is very important for thermal and fusion reactors.

While some adjustment can be made for the effect of displacement rate, the effect of the increased helium concentrations generally obtained in other reactors [*17*] is not so easily modeled. Wiffen and Bloom [*18*] have investigated the swelling of Type 316 stainless steel in the high-flux isotope reactor (HFIR) and found that the swelling level was influenced strongly by the much higher helium levels produced in this reactor, suggesting that helium production may dominate the swelling behavior in such conditions.

It is suggested that prior to application of this correlation to a new

environment, the spectrum-averaged helium production cross section should be compared with the EBR-II value of ~0.2 millibarns. If the cross section exceeds the EBR-II value by more than a factor of five, the predictions of this correlation should be interpreted only as a lower estimate of the swelling.

Conclusions

With insight gained from analysis of simulation and charged-particle irradiation data, a correlation has been developed that successfully predicts the magnitude of void swelling in 20 percent cold-worked Type 316 stainless steel at fluences near that of the FTR goal. Upon extrapolation to the long-term fast breeder goal fluence of about 2.5×10^{23} n/cm^2 ($E > 0.1$ MeV), the swelling is expected to be about 20 percent. With some caution, this correlation can be employed as an estimate of swelling in other reactor environments. The modifications required in such applications arise due to spectral and flux level considerations.

Acknowledgment

This paper is based on work performed by Hanford Engineering Development Laboratory, Richland, Washington, operated by Westinghouse Hanford Company, a subsidiary of Westinghouse Electric Corporation, under United States Energy Research and Development Administration Contract E(45-1)-2170.

References

[1] Laidler, J. J., "Simulation of Neutron-Induced Swelling in FTR Fuel Cladding," *Proceedings*, International Conference on Physical Metallurgy of Reactor Fuel Elements, Berkeley, Gloucestershire, England, 2–7 Sept. 1973.

[2] Leitnaker, J. M., Bloom, E. E., and Steigler, J. O., *Journal of Nuclear Materials*, Vol. 49, 57, 1973.

[3] Johnston, W. G., Lauritzen, T., Rosolowski, J. H., and Turkalo, A. M., "The Effect of Metallurgical Variables on Void Swelling," *Proceedings*, ASM Materials Science Seminar on Radiation Damage in Metals, Cincinnati, American Society for Metals, 9–10 Nov. 1975; also General Electric Report No. 76CRD019, Jan. 1976.

[4] Rowcliffe, A. F., Diamond, S., Bleiberg, M. L., Spitznagel, J., and Choyke, J. in *Properties of Reactor Structural Alloys After Neutron or Particle Irradiation, ASTM STP 570*, American Society for Testing and Materials, 1975, pp. 565–583.

[5] Laidler, J. J., Mastel, B., and Garner, F. A. in *Properties of Reactor Structural Alloys After Neutron or Particle Irradiation, ASTM STP 570*, American Society for Testing and Materials, 1975, pp. 451–468.

[6] Laidler, J. J., Garner, F. A., and Thomas, L. E., "Simulation Experiments with the High Voltage Electron Microscope," *Proceedings*, ASM Materials Science Seminar on Radiation Damage in Metals, American Society for Metals, Cincinnati, Nov. 9–10, 1975.

[7] "Reference Fuel Studies, First Semiannual Report," GEAP-14032-3, General Electric Report Aug. 1975, pp. 2–18.

[8] Brager, H. R. and Straalsund, J. L., *Journal of Nuclear Materials*, Vol. 46, 1973, pp. 103–106.

[9] Jackson, R. J., Washburn, D. F., Garner, F. A., and Gilbert, E. R., "Correlation of Creep and Swelling with Fuel Pin Performance," *Transactions*, Vol. 22, No. 184, American Nuclear Society, 1975.

[10] Garner, F. A., Gilbert, E. R., Jackson, R. J., and Washburn, D. F., "Cladding and Structural Materials Semiannual Progress Report, January–July 1975," HEDL-TME 75-77, Hanford Engineering Development Laboratory, Richland, Wash., pp. 110–120.

[11] Garner, F. A., Bates, J. F., and Gilbert, E. R., "Precipitate-Related Densification of 316 Stainless Steel," "Cladding and Structural Materials Quarterly Report, July–September 1975," HEDL-TME 76-13, Hanford Engineering Development Laboratory, Richland, Wash.

[12] Garner, F. A., "Cladding and Structural Materials Semiannual Progress Report, January–July 1975," HEDL-TME 75-77, Hanford Engineering Development Laboratory, Richland, Wash., pp. 90–101.

[13] Doran, D. G. et al, "Report of the Working Group on Displacement Models and Procedures for Damage Calculations," HEDL-TME 73-6, Hanford Engineering Development Laboratory, Richland, Wash., Dec. 1973.

[14] Bullough, R. and Perrin, R. C. in *Voids Formed by Irradiation of Reactor Materials*, British Nuclear Energy Society, Reading, England, 1971, p. 79.

[15] Garner, F. A. and Guthrie, G. L., "The Influence of Displacement Gradients on the Interpretation of Charged Particle Simulation Experiments," *Proceedings*, International Conference on Radiation Effects and Tritium Technology for Fusion Reactors, Gatlinburg, Tenn. Oct. 1975.

[16] Sprague, J. A. et al, *Journal of Nuclear Materials*, Vol. 54, 1974, pp. 286–298.

[17] Kulcinski, G. L., Doran, D. G., and Abdou, M. A., in *Properties of Reactor Structural Alloys After Neutron or Particle Irradiation, ASTM STP 570*, American Society for Testing and Materials, 1975, pp. 329–351.

[18] Wiffen, F. W. and Bloom, E. E., *Nuclear Technology*, Vol. 25, 1975, pp. 113–123.

[19] Busboom, H. J., McClellan, G. C., Bell, W. L., and Appleby, W. K., "Swelling of Types 304 and 316 Stainless Steel Irradiated to 8×10^{22} n/cm^2," General Electric Report GEAP-14062, General Electric Company, July 1975.

[20] Brager, H. R., "Microstructure of Neutron Irradiated Stainless Steels," *Proceedings*, U.S.-Japan Seminar on Radiation-Produced Defects and Defect Clusters and Their Effects in Metals, Ames, Iowa, 28–30 Sept. 1975.

[21] Garr, K. R. and Pard, A. G., "Swelling and Tensile Property Changes in Neutron-Irradiated Type 316 Stainless Steel," *Proceedings*, 8th International Symposium on Radiation Damage to Reactor Materials, St. Louis, Mo., 4–6 May 1976.

[22] Sklad, P. S. and Bloom, E. E., "Semi-Annual Progress Report: Irradiation Effects on Reactor Structural Materials, August 1974 to February 1975," HEDL-TME 75-23, Hanford Engineering Development Laboratory, Richland, Wash., pp. ORNL-1–10.

[23] Ellis, J. A., Appleby, W. K., and Lauritzen, T., "Swelling Simulation Studies of Type 316 Stainless Steel," *Proceedings*, 8th International Symposium on Radiation Damage to Reactor Materials, St. Louis, Mo., 4–6 May 1976.

F. A. Smidt, Jr.,[1] *P. R. Malmberg,*[2] *J. A. Sprague,*[1] *and J. E. Westmoreland*[2]

Swelling Behavior of Commercial Ferritic Alloys, EM-12 and HT-9, as Assessed by Heavy Ion Bombardment

REFERENCE: Smidt, F. A., Jr., Malmberg, P. R., Sprague, J. A., and Westmoreland, J. E., **"Swelling Behavior of Commercial Ferritic Alloys, EM-12 and HT-9, as Assessed by Heavy Ion Bombardment,"** *Irradiation Effects on the Microstructure and Properties of Metals, ASTM STP 611,* American Society for Testing and Materials, 1976, pp. 227–241.

ABTRACT: Ferritic alloys have some promise for duct and cladding applications for liquid metal fast breeder reactors (LMFBR) because of their favorable neutron absorption cross sections. Two alloys of the 10 to 12 percent chromium class, EM-12 and HT-9, have been selected for study in the National Alloy Development Program. Bombardment with 2.8 MeV $^{56}Fe^{+}$ ions and transmission electron microscopy (TEM) observations were used to determine the temperature dependence of swelling at 150 displacements per atom (dpa) and the swelling rate at the peak swelling temperature up to 250 dpa. Both alloys were found to be more swelling resistant than Type 316 stainless steel, with EM-12 having a swelling rate of 0.011 percent/dpa at the peak swelling temperature of 550°C (1022°F) while HT-9 had a swelling rate of 0.017 percent/dpa at the peak swelling temperature of 500°C (932°F). An unusual feature of swelling in these materials was the formation of very large voids on precipitates along the grain boundaries.

KEY WORDS: radiation, swelling, ferritic stainless steels, radiation effects, transmission electron microscopy, ion bombardment, voids

The discovery of swelling in 1967 presented a new challenge to the nuclear metallurgy community. Not only was this a new and unexpected phenomenon, but it also had engineering and economic implications. It was soon found that swelling resistance was influenced by composition

[1] Research metallurgists, Thermostructural Materials Branch, Engineering Materials Division, Naval Research Laboratory, Washington, D.C. 20375.

[2] Physicists, Materials Modification and Analysis Branch, Radiation Technology Division, Naval Research Laboratory, Washington, D.C. 20375.

and metallurgical state. It also became apparent that the doubling time was influenced by neutron absorption cross section; therefore, economics became a factor in material selection. New design criteria and a different set of trade-offs developed for cladding and duct applications in the liquid metal fast breeder reactor (LMFBR), and conventional alloy design wisdom had to be modified. To meet this need, the National Alloy Development Program was initiated in 1974 under sponsorship of the Energy Research and Development Administration (ERDA); the research reported here is a part of that effort.

Ferritic alloys are of potential interest for duct and cladding applications in LMFBR because of their lower neutron absorption cross section and because a few scattered observations suggested that they might be swelling resistant [*1–4*].[3] The major deficiency of ferritic alloys is their poor creep strength above 600°C (1112°F), which results from overaging and transformation of the metastable precipitate phases that provide the strengthening mechanism. The class of commercial ferritic alloys with the best high-temperature strength was considered to be the 10 to 12 percent chromium alloys with additions of molybdenum, columbium, tungsten, or tantalum to provide solid-solution hardening and more stable alloy carbides at high temperatures. Two commercial alloys from this class were selected for study in the National Alloy Development Program, EM-12 and HT-9.

No neutron irradiation data were available on either of these materials, so ion bombardment with 2.8 MeV $^{56}Fe+$ ions was utilized to rapidly assess the temperature dependence of swelling in them and their swelling rate at the peak swelling temperature. The results of those ion-bombardment experiments are described in this paper.

Experimental Methods

The two alloys selected for this study, EM-12 and HT-9, were procured from vendors by Hanford Engineering Development Laboratory (HEDL) and specimens in the form of 3-mm-diameter rods in the heat-treated conditions were supplied for these experiments. Chemical compositions for the heats of these alloys are given in Table 1.

These combinations of composition and heat treatment produce microstructures that are primarily overaged tempered martensite. Coarse precipitates, which are probably $M_{23}C_6$ or M_6C [*5*], formed along many of the grain boundaries. The tempering temperature selected for the experiments was higher than commonly employed in commercial practice for similar super chrome steels, although it was within the range recommended by Sandvik for high-temperature service for HT-9. Tempering at 780°C

[3] The italic numbers in brackets refer to the list of references appended to this paper.

TABLE 1—*Chemical analysis of ferritic alloys.*

	C	Mn	Fe	Cu	Ni	Cr	Mo	Si	Cb + Ta	Co
EM-12	0.059	1.08	86.5	0.055	0.15	10.50	2.05	0.18	0.36	0.033
HT-9	0.19	0.61	85.0	0.045	0.44	12.05	0.92	0.50	0.30	0.026

Heat Treatments

EM-12—solution anneal at 1050°C (1925°F) for 30 min/air cool; temper at 755°C (1390°F) for 1½ h/air cool
HT-9—solution anneal at 1050°C (1925°F) for 30 min/air cool; temper at 780°C (1436°F) for 2½ h/air cool

(1436°F) should provide stability of the microstructure at the irradiation temperature, but at the sacrifice of strength. Also, as will be seen later, the coarse precipitate morphology adversely influences void nucleation. The carbon content of the heat of EM-12 used was on the low side of the commercial range, and this resulted in the presence of large grains of delta ferrite in the structure.

Specimens were prepared for ion bombardment from the rod material received from HEDL by slicing off wafers approximately 0.015 in. thick, using a silicon-carbide abrasive wheel. The slices were then ground flat and parallel and reduced to approximately 0.005 in. on 600-grit abrasive paper. Specimens were mechanically polished with 0.3-μm alumina and then electropolished for 30 s in a solution of 15-ml perchloric acid, 250-ml methyl alcohol, and 150-ml butyl alcohol at −65°C (−85°F) at a potential of 45 V.

The specimens were then implanted with helium in the Naval Research Laboratory (NRL) cyclotron with a 30-MeV α-particle beam. An aluminum sheet was used to reduce the energy of the α-particles so they would come to rest in the surface region of the foils. The helium concentration profile resulting from this implant was one half of a Gaussian-shaped peak with full width half maximum of 11.8 μm and a maximum concentration of 1-ppm helium. This concentration of helium corresponds to the calculated accumulation of helium from (n, α) reactions for a fluence of 1×10^{22} neutrons (n)/cm^2 $E > 0.1$ MeV.

The ion irradiations were performed using the NRL 5-MV Van de Graaff accelerator with a beam of 2.8 MeV ^{56}Fe+ ions. The experimental irradiation system and procedures used for the bombardment are the same as those described in Ref *6* and will not be repeated here. The beam current density for all of the bombardments was 8 μA/cm^2, which produced 37°C (67°F) beam heating of the specimen. This temperature rise is included in all irradiation temperatures reported herein.

The irradiations were performed in two experiments so as to first determine the temperature dependence of swelling and then determine the

swelling rate at the peak swelling temperature. In the temperature-dependence experiment, specimens of EM-12 and HT-9 were each bombarded at temperatures of 650, 600, 550, 500, and 450°C (1202, 1112, 1022, 932, and 842°F) in that sequence, to a dose of 150 dpa. The swelling rate experiment involved bombardment at the peak swelling temperature to doses of 250, 150, 80, and 40 dpa, in that order.

The deposition of damage energy by the incident iron ions as a function of depth into the foil was determined from the Manning-Mueller E-DEP-1 computer code [7], assuming densities of 7.8 g/cm^3 for EM-12 and 7.7 g/cm^3 for HT-9. The region of peak energy deposition was calculated to be 0.61 μm below the front surface for EM-12 and decreased to 20 percent of the maximum at 0.47 and 0.72 μm. In HT-9 the peak damage region was 0.62 μm below the surface and decreased to 20 percent of the maximum at 0.47 and 0.72 μm. Displacement doses were calculated on the basis of a Kinchin-Pease secondary displacement model with an efficiency of 0.8 and a displacement energy of 40 eV. The corresponding dose rate for these irradiations was 6×10^{-2} dpa/s.

Specimens were prepared for microscopy by removing 0.52 $\pm$ 0.05 μm from the front face by electropolishing in a chromic-acetic acid polishing cell, using a laser interferrometer [8] to monitor removal of the metal. The specimens were then back thinned to perforation by masking off the front surface and using a single-jet electropolisher with the perchloric-alcohol solution previously described. Some of the specimens had unusually large voids, and they perforated at these locations prior to thinning to suitable electron transparent thickness. Where this occurred, the specimens were further thinned from the backside using an ion milling unit.

The specimens were examined using a 200-kV JEM-200A electron microscope, equipped with a double-tilt side-entry goniometer stage. To obtain quantitative microstructural information on an area, a stereo pair showing the voids was taken under weakly diffracting conditions (dislocations out of contrast) with a stereo angle $\geqslant$12 deg, and a third micrograph of the same area was taken with the dislocation structure in contrast. Void densities and distributions were measured using a particle-size analyzer. The thickness of a given area was determined from the stereo pair by measuring the distance between voids obviously intersecting opposite foil surfaces.

Microscopy in these materials is exceedingly difficult because the magnetic specimen causes a beam shift and attendant loss of resolution with each movement and tilt of the specimen. In addition, the martensitic structure is highly strained and has small grain sizes so that widely varying diffraction conditions exist in any given field of view. To add to the difficulties of analysis, large variations in void size were encountered which required modifications in the usual void analysis techniques. This

required sampling both thin sections of the specimen to characterize the small voids which had relatively high densities, and thick sections to characterize the large voids which were few in number.

The case of the large voids also required a special approach to calculate swelling. The assumption was made that voids intersecting the surface with sharply defined edges had their centers in the foil and were counted as voids. Those with rounded edges were assumed to be less than half in the foil and were not counted. The effective thickness for the void number density in cases where the void diameter exceeded the foil thickness, but where the center was within the foil, was calculated by setting the effective foil thickness equal to the diameter. Swelling was then calculated from the equation

$$S(\%) = \frac{100\Delta V}{V - \Delta V}$$

where

$$\Delta V = \pi/6 \sum_i n_i d_i^3$$

and where d_i is the center of the ith-size interval for void diameters measured by the particle size analyzer. Also, n_i is the number of voids/cm^3 in that size class which has been normalized to an effective foil thickness of $t - d_i$, where the voids are smaller than the foil thickness, and to an effective thickness of $t = d_i$, where very large voids are present.

TEM Observations of Temperature-Dependence Experiments

The temperature dependence of swelling in these alloys was evaluated at 150 dpa using transmission electron microscopy (TEM) determinations of swelling. The more significant observations are described in some detail in the following section, and the characteristics of the void microstructures are summarized in Table 2.

EM-12 specimens have been examined from each of the five temperatures bombarded, and voids were found in the 500, 550, and 600 °C (932, 1022, and 1112 °F) specimens. The specimen at 500 °C (932 °F) had large voids, with a mean diameter of 80 nm, which were associated with precipitates along the grain boundaries. These voids were rather inhomogeneously distributed in the specimen, and a sampling of several areas was required to determine the average density and estimated swelling in Table 2. The inhomogeneity of void distributions in EM-12 is best illustrated in the 550 °C (1022 °F) specimen shown in Fig. 1. Three different size classes of voids were observed: A few exceptionally large voids with diameters up

TABLE 2—*Void microstructures in commercial ferritics at 150 dpa.*

	EM-12			HT-9		
Temperature, °C	d(nm)	ϱ(cm^{-3})	$\frac{\Delta V}{V}$ (%)	d(nm)	ϱ(cm^{-3})	$\frac{\Delta V}{V}$ (%)
450	...	no voids	...	79.0	1.0×10^{13}	0.4
500	80.0	6.5×10^{12}	0.4	117.5	3.3×10^{13}	3.7
550	34.5	1.5×10^{14}	1.5	76.5	1.7×10^{13}	0.7
600	33.0	2.7×10^{13}	0.1	89.0	1.5×10^{13}	0.8
650	...	no voids	...	...	not examined	...

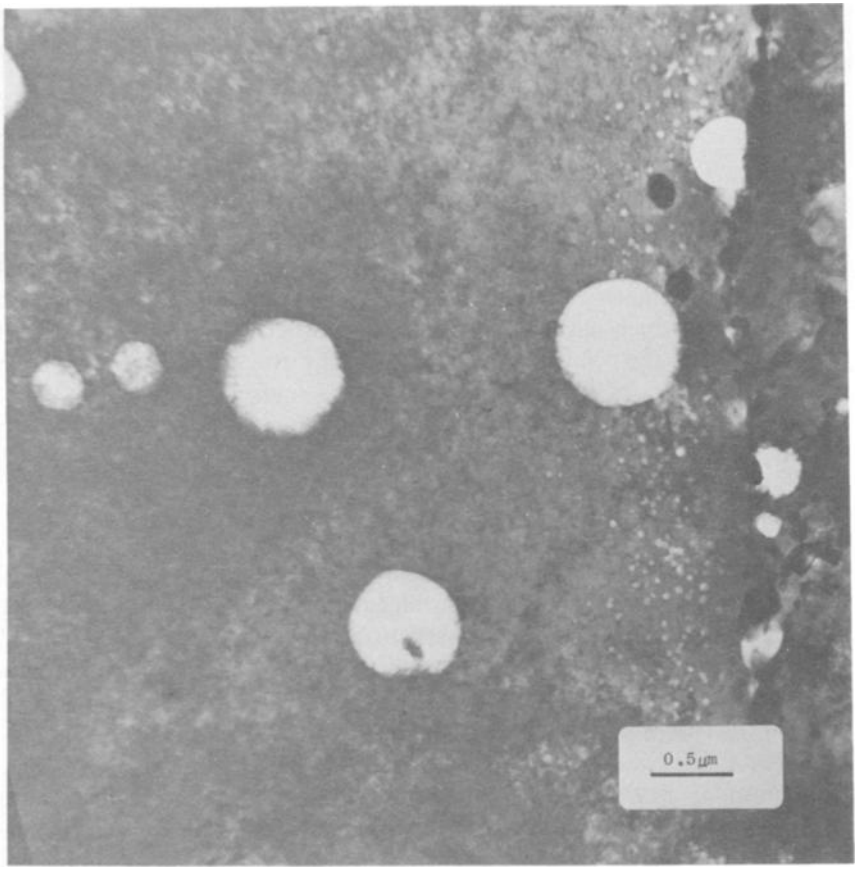

FIG. 1—*TEM of voids in EM-12 after bombardment to a dose of 150 dpa at 550°C (1022°F). Note the three different populations of voids; the large voids in the grain interior which nucleated on precipitates, the voids along the grain boundary which nucleated on precipitates, and the small voids in the band adjacent to the grain boundary. Swelling was 1.5 percent in this specimen.*

to 700 nm which formed on blocky precipitates in the interior of grains; voids of around 80 nm associated with the grain-boundary precipitates; and, finally, a population of smaller 34-nm mean diameter voids which formed in a band adjacent to the grain boundaries. The region containing the small voids was found to have a maximum swelling of 0.4 percent with a void density of $1.5 \times 10^{14} cm^{-3}$, but estimates based on averaging over the total volume of the grain gave about 0.2 percent swelling from this void population. Low magnification shots from thicker sections were required to obtain micrographs with enough of the larger voids to count. These voids had a mean diameter of 325 nm, a density of $2.5 \times 10^{11} cm^{-3}$, and a swelling of 1.3 percent. Total swelling from both the large- and small-size populations was then estimated by combining the two sets of data to give a swelling of 1.5 percent. This example illustrates the difficulty in measuring swelling in these alloys. In addition, the calculations of swelling involving the larger voids which extend beyond the region of uniform damage must be considered with some reservation since they encompass regions with gradients in the displacement damage and gradients in the point-defect concentrations. The 600°C (1112°F) specimen had a relatively uniform distribution of voids with a smaller mean diameter, higher-density voids, and a fine dispersion of precipitates in the grain interiors, most of which were associated with voids.

The HT-9 alloy had a wider range of temperatures at which voids were observed, greater swelling at the peak swelling temperature, and a peak at 500°C (932°F) rather than the 550°C (1022°F) peak observed for EM-12. As in the EM-12, the voids were closely associated with grain boundary precipitates, and, because of the more extensive precipitation along grain boundaries in the HT-9, the void densities and swelling were greater. In fact, void formation along the boundaries was extensive enough to cause concern about degradation of mechanical properties. See Fig. 2 for an example of this void morphology.

A summary of the void microstructures for the temperature dependence of swelling is provided in Table 2. The temperature dependence of both the void size and density is unusual in these materials and probably reflects the influence of the precipitates on void nucleation and growth. In EM-12 the large void size at 500°C (932°F) reflects nucleation of a few large voids on precipitates, but at 550°C (1022°F) and higher the nucleation of many small voids in the matrix causes the mean diameter to decrease. In HT-9 the void size and density are fairly constant with temperature except at 500°C (932°F), the peak swelling temperature, where both size and density increased.

The dislocation structure in these alloys was difficult to characterize because of the very high dislocation density resulting from the martensite transformation in the starting material and the loop structure resulting from the displacement damage in the ion-bombarded specimens. At the

FIG. 2—*TEM of voids associated with precipitates along a grain boundary in a thick section of HT-9 specimen bombarded to a fluence of 250 dpa at 500°C (932°F).*

lowest irradiation temperature of 450°C (842°F), both alloys had a very high dislocation density, which appeared as a mass of black-and-white contrast in which individual dislocations could not be resolved. This appeared to be a combination of overlapping dislocations and small loops or clusters. At 500°C (932°F) the dislocation density was still very high, but in the HT-9, in particular, individual dislocations could be resolved. At 550°C (1022°F) the dislocation structures were characterized by dense tangles, containing small loops less then 10 nm, or small precipitates or both. At 600°C (1112°F) dense tangles, small loops, and fine precipitates were observed in the EM-12, while in HT-9 a tangled network had formed. At 650°C (1202°F) in the EM-12, where no voids were observed, the dislocation structure had relaxed into a fairly regular network with a few small angle boundaries. Also, precipitation had occurred on the network, especially at nodes. In general, the dislocation structure decreased in density with increasing irradiation temperature from 450 to 650°C (842 to 1202°F), and the HT-9 appears to show recovery at lower temperatures than the EM-12.

TEM Observations of the Dose-Dependence Experiments

After the peak swelling temperature had been established, another set of specimens was ion bombarded to establish the swelling rate at the peak swelling temperature. Specimens of EM-12 were bombarded at 550°C (1022°F) to doses of 40, 80, and 250 dpa while specimens of HT-9 were bombarded at 500°C (932°F) to doses of 40, 80, 150, and 250 dpa. The duplicate specimen at 150 dpa was included to confirm the rather large variations in void size and morphology from grain to grain observed in the temperature-dependence experiment.

The swelling trends observed in the experiment fit quite well with results of the previous temperature-dependence experiments. The 40- and 80-dpa specimens of EM-12 had a low density of the large voids associated with precipitates along grain boundaries, which had previously been noted in the 150-dpa specimen at 550°C (1022°F). The mean void size was about 95 nm, and the density increased from 4.6×10^{12} cm^{-3} at 40 dpa to 9.3×10^{12} at 80 dpa with an attendant increase in swelling from 0.4 to 0.7 percent. As noted in the previous study, at 150 dpa a new population of small voids appeared which was not associated with precipitates. Because of the large numbers of the voids, the mean diameter of the total void population dropped to 34.5 nm while the void density increased to 1.5×10^{14} cm^{-3}. The swelling continued to increase to 1.5 percent, but most of the swelling still came from the larger voids. The 250-dpa specimen also showed the multiple population. Mean size increased to 37 nm, and density increased to 3.6×10^{14} with an attendant increase in swelling to 2.6 percent. Again the larger voids (>50 nm) produced most of the swelling, 2.2 percent out of 2.6 percent.

The HT-9 did not have two distinct size populations of voids but did have rather large variations in void density from one region of the specimen to another. This trend had previously been noted in the 150-dpa specimen from the temperature-dependence run, and a duplicate specimen for the 150-dpa point was made in this experiment to check consistency. The same variability in swelling was noted in the duplicate 150-dpa specimen and in the 250-dpa specimen, and it was concluded that these variations from one area to another are real. The cause is not known, but may result from composition variations in the specimen or the distribution of precipitates in the specimen. An example of the association between precipitates and voids is shown in Fig. 2, for a very thick section of the 250-dpa foil.

A void density of $\sim 2 \times 10^{13}$ cm^{-3} was found from 40 dpa to 250 dpa in the HT-9, and most of these voids were associated with precipitates. The mean void size, on the other hand, increased from 92.5 nm at 40 dpa to 142.5 nm at 250 dpa, and the swelling likewise increased from 1.2 percent at 40 dpa to 4.7 percent at 250 dpa. It appears that the voids nucleate early in the irradiation on precipitates and then grow slowly. The matrix, however, appears to be more resistant to swelling then EM-12 because no small voids were seen in the matrix. Data from the dose-dependence experiments are summarized in Table 3.

TABLE 3—*Summary of void microstructures for dose dependence of swelling at peak swelling temperature.*

Material	Parameter	Fluence, dpa			
		40	80	150	250
EM-12 (550 °C)	$\bar{d}$ (nm)	96.0	95.0	34.5	37.0
	ϱ (cm^{-3})	4.6×10^{12}	9.3×10^{12}	1.5×10^{14}	3.6×10^{14}
	$\frac{\Delta V}{V}$ (%)	0.4	0.7	1.5	2.6
HT-9 (500 °C)	$\bar{d}$ (nm)	92.5	106.5	117.5	142.5
	ϱ (cm^{-3})	1.9×10^{13}	1.7×10^{13}	3.3×10^{13}	2.4×10^{13}
	$\frac{\Delta V}{V}$ (%)	1.2	1.8	3.7	4.7

Discussion

The temperature dependence of swelling for these alloys at a dose of 150 dpa is plotted in Fig. 3. Error bars on HT-9 indicate the range of swelling observed in different areas of the specimen examined. Inhomo-

geneity of this degree makes it difficult to obtain accurate measurements of swelling by TEM. Error bars on the EM-12 measurements represent ±30 percent values. Swelling in HT-9 is a maximum at 500°C (932°F) while that in EM-12 is a maximum at 550°C (1022°F). The range of swelling is greater in HT-9 possibly because of the association of voids with the precipitates.

Very little data are available on swelling of ferritic materials with which to compare the results of the present investigation. Johnston et al [*9*] have examined a series of binary alloys containing 7, 15, and 20 percent chromium, using 5-MeV Ni^+ ion bombardment. The maximum swelling temperature in the 15 percent chromium alloy was a 550°C (1022°F) for a dose of 115 dpa (using E_d of 40 eV). A compositional effect on swelling was found with a maximum of 7 percent swelling in the 15 percent chromium alloy, with lower swelling at higher and lower chromium contents. A commercial 2.25Cr-1Mo alloy examined after bombardment under the

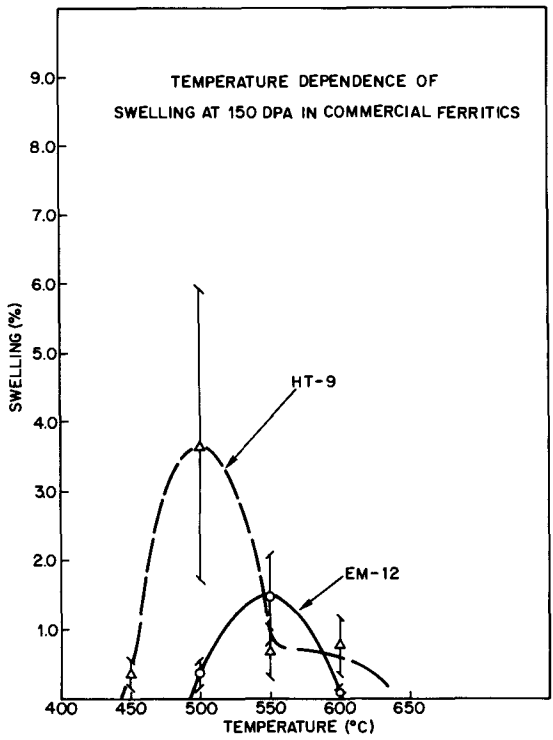

FIG. 3—*Temperature dependence of swelling at 150 dpa for EM-12 and HT-9. Error bars represent ±30 percent for EM-12 and range of observations for different specimen areas in HT-9.*

same conditions showed only 0.8 percent swelling. The authors [*1*], in a previous study of pure iron and several dilute iron alloys, using Ni^+ ion bombardment to study swelling in the 10 to 20 dpa range (for $E_d = 40$ eV), found that the maximum swelling of ~0.3 percent occurred at 650°C (1202°F) in pure iron but at 450°C (842°F) in an Fe-0.3Cu alloy. Neutron irradiation of Type 405 stainless steel [*2*], a steel of the same class as those studied in this experiment, produced no void formation after a total fluence of 3.3×10^{22} n/cm^2 (~15 dpa) in the Experimental Breeder Reactor-II (EBR-II) at a temperature between 400 and 425°C (752 and 797°F). If a dose rate shift in the peak swelling temperature of about 100°C (180°F) were assumed, the irradiation temperature should have been in the temperature range where high swelling would be expected. Heat treatments given the Type 405 in the experiment produced larger carbides or a delta ferrite structure, however, so a direct comparison may not be that significant. Thus the limited amount of previous data on less complex iron-base alloys indicates that swelling occurs in the same temperature range found for the present experiments and is sensitive to alloy additions.

The dose dependence of swelling at the peak swelling temperature is plotted in Fig. 4. As in Fig. 3, error bars for the data points for HT-9 approximate the variations in swelling observed from different regions in the specimen, while those for EM-12 are ±30 percent. Higher-dose data points for both materials are derived from analysis of four to six different micrographs from different regions of the specimen. As can be seen in Fig. 4, both sets of data can be fitted to a linear swelling relation. EM-12 extrapolates to an incubation period of about 10 dpa, while the data for HT-9 indicate a region of higher swelling rate between 0 and 40 dpa from the data fitting. It should be noted, however, that a linear swelling rate line can be drawn from the origin and pass within the indicated error bars. The lines plotted in Fig. 4 represent a least-squares fit to the data in Table 3 with the following equations

$$\text{HT-9} \qquad \frac{\Delta V}{V}(\%) = 0.0170\ (\text{dpa}) + 0.61$$

$$\text{EM-12} \qquad \frac{\Delta V}{V}(\%) = 0.0109\ (\text{dpa}) - 0.12 \qquad \text{dpa} > 11$$

$$= 0 \qquad \text{dpa} < 11$$

The observations on the binary Fe-15Cr alloy [*8*] showed a swelling rate higher by a factor of 5 to 10 with 0.118 percent/dpa, and showed an incubation period of about 60 dpa before the onset of linear swelling.

The apparent rapid swelling observed at low fluences in HT-9 is unusual for a complex alloy, which more commonly shows the behavior of

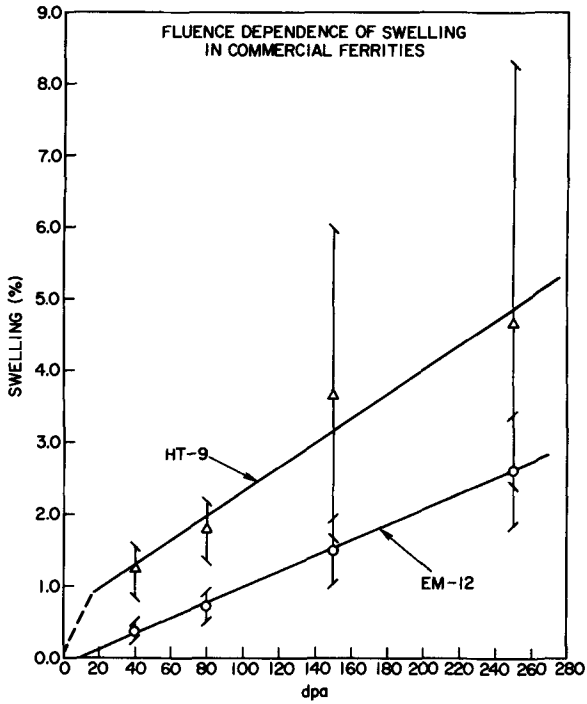

FIG. 4—*Dose dependence of swelling at peak swelling temperatures for EM-12, 550°C (1022°F); and HT-9, 500°C (932°F). Lines shown on the figure represent a least-squares fit to the data points. Error bars on EM-12 represent ±30 percent while those for HT-9 represent variations in swelling observed in different areas of the specimen.*

EM-12 with an initial incubation period followed by a more rapid linear swelling regime. Pure nickel and molybdenum, however, have shown a rapid initial swelling rate [*10,11*]. The close association between the voids and precipitates observed in HT-9 would lead one to suspect easy nucleation as the cause of the rapid initial swelling. Precipitates are believed to influence nucleation by either depleting the surrounding matrix of elements which suppress swelling or by some unique feature of the interface. It has not been possible to identify the precipitates observed in these alloys by electron diffraction techniques because of the multiple grain and precipitate orientations and the distorted structure. The grain boundary morphology and heat treatment conditions, however, should produce $M_{23}C_6$ and M_6C as the predominant precipitate phases [*5*], and electron diffraction patterns of $M_{23}C_6$ or M_6C, or both, have been identified in HT-9 aged for longer times to produce larger precipitates. Both these phases are rich in chromium, molybdenum, and carbon [*12*] and thus would deplete the surrounding matrix of these elements. Another

possibility is that the precipitate-matrix interface serves to nucleate voids, perhaps as a response to the formation of interfacial dislocations on the precipitates. It is not possible to resolve this question with the data available in this experiment. Another possibility considered was that porosity in the stock material or preferential etching of the precipitates could cause an apparent rapid nucleation; however, examination of unirradiated specimens prepared in the same manner showed no porosity or preferential attack on precipitates.

The formation of voids on precipitates along the grain boundaries may also degrade the mechanical properties. Indeed some grains were bordered by voids along 50 to 75 percent of their boundary in the planar section observed by TEM. An investigation of the precipitate distribution after tempering at lower temperatures shows that the massive precipitation along grain boundaries can be reduced substantially by tempering at 650 °C (1202 °F) for 4 h. This should also improve the creep strength while, it is hoped, preserving alloy stability at the service temperature. Another study of the swelling behavior of HT-9 with this optimized heat treatment is in progress.

Conclusions

An investigation of the swelling resistance of the commercial ferritic alloys EM-12 and HT-9, using heavy ion bombardment with 2.8 MeV $^{56}Fe+$ ions, has shown the following:

1. The maximum swelling at 150 dpa occurs at 500 °C (932 °F) in HT-9 and at 550 °C (1022 °F) in EM-12.
2. The maximum swelling rate in HT-9 is 0.017 percent/dpa while it is 0.011 percent/dpa in EM-12, some 20 times lower than the maximum swelling rate of Type 316 stainless steel.
3. Large voids are associated with precipitates, most likely $M_{23}C_6$ and M_6C, along grain boundaries in the materials studied in this investigation and may degrade the mechanical properties.

Acknowledgments

The authors wish to thank A. G. Pieper for performing the helium implants and J. R. Reed for assistance with specimen preparation and ion bombardment.

References

[1] Smidt, F. A., Jr., Sprague, J. A., Westmoreland, J. E., and Malmberg, P. R. in *Defects and Defect Clusters in BCC Metals and Their Alloys,* R. J. Arsenault, Ed., National Bureau of Standards, Gaithersburg, Md., 1973, pp. 341–362.

[2] Garr, K. R., Rhodes, C. G., and Kramer, D. in *Effects of Radiation on Substructure and Mechanical Properties of Metals and Alloys, ASTM STP 529,* American Society for Testing and Materials, 1973, pp. 109–118.
[3] Johnston, W. G., Rosolowski, J. H., Turkalo, A. M., and Lauritzen, T., *Journal of Nuclear Materials,* Vol. 54, 1974, p. 24.
[4] Little, E. A, *Radiation Effects,* Vol. 16, 1972, p. 135.
[5] Briggs, J. Z. and Parker, T. D., *The Super 12% Cr Steels,* Climax Molybdenum Company, New York, 1965, p. 8.
[6] Sprague, J. A., Smidt, F. A., Jr., Westmoreland, J. E., and Malmberg, P. R., this publication, pp. 227–241.
[7] Manning, I. and Mueller, G. P., *Computer Physics Communications,* Vol. 7, 1974, p. 85.
[8] Sprague, J. A., *Review of Scientific Instruments,* Vol. 46, 1975, p. 1171.
[9] Johnston, W. G., Lauritzen, T., Rosolowski, J. H., and Turkalo, A. M., in Seminar on *Radiation Damage in Metals,* Cincinnati, Ohio, 9–10 Nov. 1975, American Society for Metals, Metals Park, Ohio, to be published.
[10] Sprague, J. A., Westmoreland, J. E., Smidt, F. A., Jr., and Malmberg, P. R. in *Effects of Radiation on Structural Materials, ASTM STP 570,* American Society for Testing and Materials, 1975, pp. 505–524.
[11] Smidt, F. A., Jr., unpublished research, 1976.
[12] Weiss, B. and Stickler, R., *Metallurgical Transactions,* Vol. 3, 1972, p. 851.

N. Igata,[1] *F. Watari,*[1] *and H. Murakami*[1]

Observation of Defect Clusters of Columbium and Columbium Alloys *In Situ* Irradiated Under a High-Voltage Electron Microscope

REFERENCE: Igata, N., Watari, F., and Murakami, H., **"Observation of Defect Clusters of Columbium and Columbium Alloys *In Situ* Irradiated Under a High-Voltage Electron Microscope,"** *Irradiation Effects on the Microstructure and Properties of Metals, ASTM STP 611,* American Society for Testing and Materials, 1976, pp. 242-255.

ABSTRACT: The nucleation and growth mechanisms of self-interstitial dislocation loops in columbium, columbium-oxygen, columbium-zirconium, and columbium-molybdenum, were studied by the electron irradiation and *in situ* observation in the temperature range from 10 K to 500 K, using a high-voltage electron microscope. The loop density increased in proportion to the square root of interstitial oxygen concentration. The density first decreased and then increased with the increase in zirconium and molybdenum concentrations. The logarithm of loop density was proportional to the reciprocal irradiation temperature. The growth rate of loops was suppressed by interstitial oxygen atoms; it was enhanced and then suppressed as the concentrations of substitutional zirconium and molybdenum atoms increased. The nucleation and growth mechanisms of self-interstitial loops were discussed from the viewpoint of the trapping effect of self-interstitials and vacancies by alloying atoms. The scavenging effect by zirconium and molybdenum atoms was also discussed.

KEY WORDS: radiation, columbium, columbium-oxygen, columbium-zirconium, columbium-molybdenum, radiation damage, point defects, dislocation loop, high voltage electron microscope, scavenging effect

There have been studies of defect clusters in neutron-irradiated columbium [*1-5*].[2] It was pointed up that interstitial oxygen atoms [*6*] and substitutional zirconium atoms [*4*] affect the process of void formation.

There have been few studies of the effects of substitutional and inter-

[1]Professor, graduate, and research associate, respectively, Department of Materials Science, University of Tokyo, 7-3-1, Bunkyoku, Tokyo, Japan.

[2]The italic numbers in brackets refer to the list of references appended to this paper.

stitial alloying atoms on defect cluster formation by electron irradiation [*7–10*]. Since the high-flux irradiation and *in situ* direct observation of the damage process are possible, the high-voltage electron microscope (HVEM) is used frequently to simulate the damage process by neutron irradiation. The objectives of this study are to observe the nucleation and growth processes of defect clusters in columbium and columbium alloys by HVEM and to discuss the role of interstitial and substitutional alloying atoms in the radiation damage processes. The dominant interstitial atoms in columbium are oxygen atoms because of their large solubility. Therefore, oxygen atoms were chosen as interstitial alloying atoms. As substitutional alloying atoms, zirconium and molybdenum atoms were chosen, taking into consideration their scavenging effect on interstitial alloying atoms and their production by transmutation in columbium used in the nuclear fusion reactor [*11,12*].

Experimental Procedures

The heat treatments and interstitial impurity contents of materials used are summarized in Table 1.

Specimens for the electron microscope were obtained by a twin-jet technique using an electrolyte of 97 percent methyl alcohol CH_3OH + 2 percent sulfuric acid (H_2SO_4) + 1 percent hydrofluoric acid (HF) at 230 K. The electron irradiation and *in situ* observation were performed by the HVEM JEM 1250. The accelerating voltage was set at 1000 kV since the threshold energy of columbium is reported to be 36 eV [*13*], corresponding to about 900 kV of accelerating voltage. The beam intensity was kept 4.8×10^{18} e/cm^2 s. A cold stage was used for irradiation at 10 and 77 K with a vacuum of 3×10^{-7} torr, and a hot stage was used for irradiation above 300 K with a vacuum of 2×10^{-6} torr. The foil thickness was estimated by the equal-thickness fringe method.

Results

The nature of defect clusters formed by the electron irradiation was determined by the Hirsch et al method [*14*] to be the self-interstitial type dislocation loop on {111} plane with Burgers vector, (a/2) <111> [*7*]. The density of dislocation loops was determined by the thickness dependency of the density per unit area [*7,15*]. The densities of observed loops were almost constant throughout the irradiation time. This fact shows that the number of loops is fixed just after the start of irradiation, as shown in other investigations [*7,16,17*].

Figure 1 shows the dislocation loops in outgassed columbium and columbium-530 weight ppm oxygen alloys irradiated at various temperatures. Note that the density of dislocation loops increased with the in-

TABLE 1—*Interstitial impurity contents and heat treatments of columbium and columbium alloys.*

		Heat Treatment,			Interstitial Impurity, weight ppm			
		Temperature, °C	Vacuum, torr	Time, min	O	N	C	H
Cb[a]	Outgassed	2450	10^{-7}	5	...	...	...	...
Cb[a]-O	30 ppm O	950	4×10^{-8}	70	30	17	10	1.5
	70 ppm O	1890	1.4×10^{-8}	90	71	5.9	trace	1.6
	530 ppm O	650 → 1150	$10^{-4} \rightarrow 10^{-7}$	30 → 60	530	11	90	1.3
	2 700 ppm O	800 → 1120	$10^{-3} \rightarrow 2 \times 10^{-6}$	30 → 60	2 700	18	80	1.3
	3 100 ppm O	800 → 1120	$10^{+2} \rightarrow 6 \times 10^{-7}$	30 → 90	3 100	75	80	5.4
	27 500 ppm O	1600	(0_2 gas) 10^{-5}	40	27 500	...	...	...
Cb[b]-Mo	0.15Mo	1100	1.4×10^{-8}	30	64	22	...	...
	0.75Mo	1160	2.0×10^{-8}	30	80	25	...	...
	4.95Mo	1280	3.5×10^{-8}	30	87	16	...	...
Cb[b]-Zr	0.07Zr	1100	1.4×10^{-8}	30	44	19	...	...
	0.14Zr	1160	2.0×10^{-8}	30	110	24	...	...
	1.70Zr	1280	3.5×10^{-8}	30	120	21	...	...

[a]The purity of columbium is 99.95 percent up, supplied by MRC.
[b]The purity of columbium is 99.8 percent, supplied by Nihon Gaishi Co. Ltd.

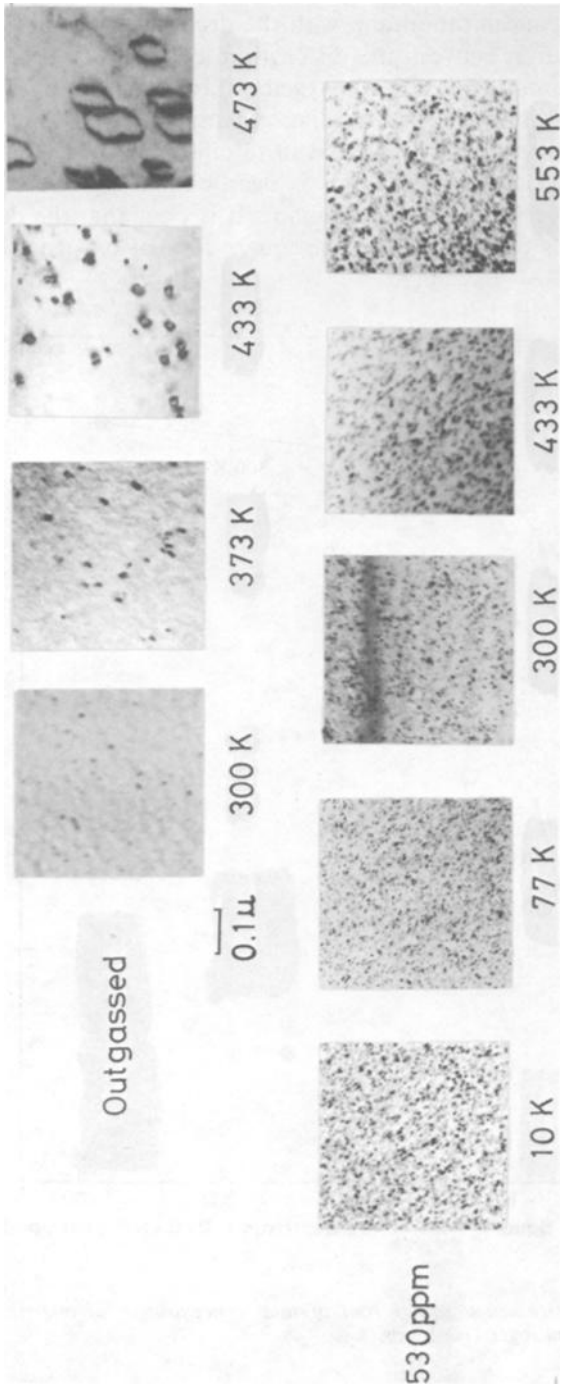

FIG. 1—*Dislocation loops in an outgassed columbium and columbium-530 weight ppm oxygen alloys irradiated at various temperatures. Total dose = 8.6 × 10^{21} e/cm² at 10 K, and 2.3 × 10^{21} e/cm² above 300 K.*

crease of oxygen concentration and with the decrease of irradiation temperature. The relation between the dislocation loop density and the concentration of the sum of interstitial oxygen (O), carbon (C), and nitrogen (N) atoms is shown in Fig. 2 for irradiation temperatures of 300 and 433 K, where the horizontal axis is plotted in (atoms ppm)$^{1/2}$. The change of the sum of interstitial alloying atoms is nearly equal to that of oxygen atoms because oxygen atoms are dominant. It is clear that the density of dislocation loops is proportional to the square root of oxygen concentra-

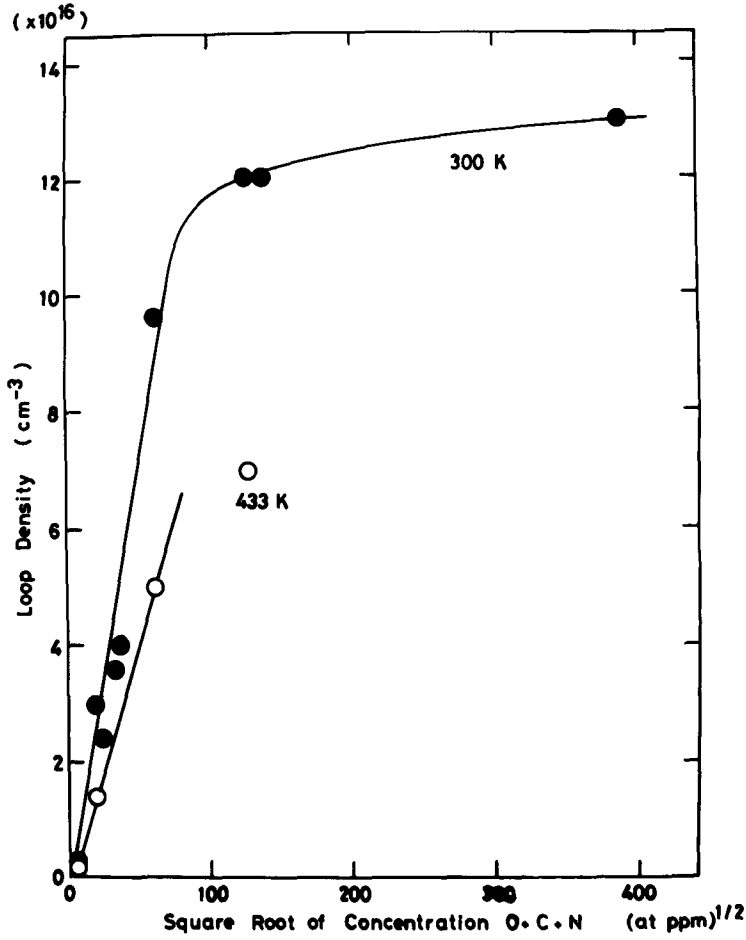

FIG. 2—*Loop density versus square root of total concentration of interstitial oxygen (O), carbon (C), and nitrogen (N) atoms.*

tion. The density of loops seems to saturate at the level of about 10^{17} cm^{-3} when the oxygen concentration is above 10^4 atoms ppm (1700 weight ppm).

The relation between the density of dislocation loops and the irradiation temperature is shown in Fig. 3. The density of dislocation loops saturated at the level of about 10^{17} cm^{-3} at the irradiation below 77 K. The logarithmic density is proportional to the reciprocal of irradiation temperature above 300 K.

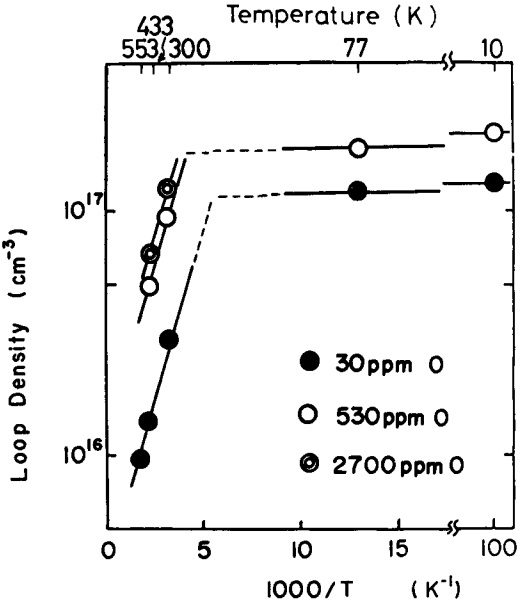

FIG. 3—*Logarithmic loop density versus reciprocal irradiation temperature.*

The dislocation loops formed in columbium-0.14 percent zirconium, columbium-1.70 percent zirconium, columbium-0.15 percent molybdenum, and columbium-4.95 percent molybdenum alloys at 300 and 433 K are shown in Fig. 4. The concentration dependence of loop density in columbium-zirconium and columbium-molybdenum alloys is shown in Fig. 5. In both alloys, the loop density became lower around the concentration of 0.1 percent than in columbium containing about the same content of oxygen atoms, and then increased with the concentration of zirconium and molybdenum atoms. The loop density in columbium-zirconium alloy was higher than that in columbium-molybdenum alloy, as shown in Fig.

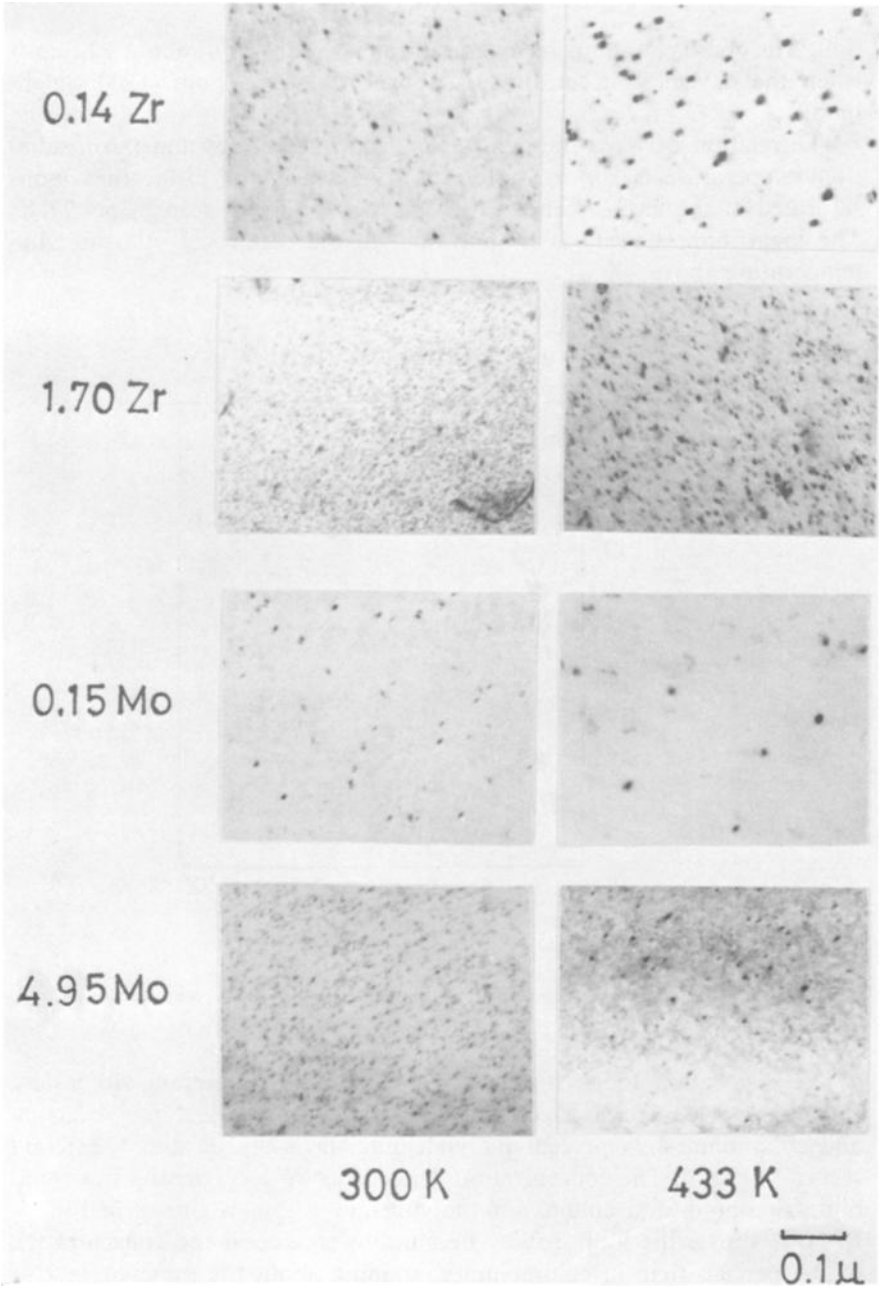

FIG. 4—*Dislocation loops formed in columbium-0.14 percent zirconium, columbium-1.70 percent zirconium, columbium-0.15 percent molybdenum, and columbium-4.95 percent molybdenum alloys irradiated at 300 and 433 K. Total dose* = 2.3×10^{21} *e/cm*^{2}.

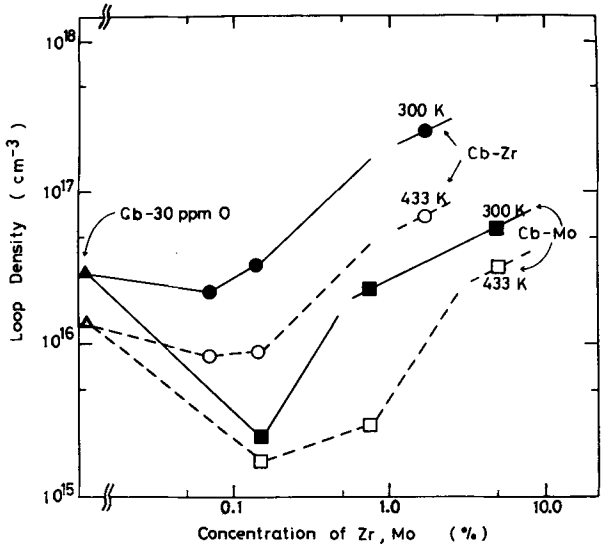

FIG. 5—*Concentration dependence of loop density in columbium-zirconium and columbium-molybdenum alloys.*

5. The relations between the loop density and irradiation temperature are shown in Fig. 6.

The loop diameter was measured as the function of the irradiation time, and results are shown in Figs. 7 through 9. As shown in figures, the loop grew with the irradiation time as $d = At^n$, where d is the loop diameter, t the irradiation time, A a constant, and n the exponent of loop growth. The value of the growth exponent in outgassed columbium was ⅓ at 300 K and one at above 373 K as shown in Fig. 7. The effects of substitutional molybdenum atoms on the loop growth are shown in Fig. 9. It is clear that molybdenum atoms suppress the value of the growth exponent. This phenomenon was also observed in columbium-zirconium alloys. The suppression of the growth exponent by substitutional atoms is weaker than that by interstitial atoms at the same concentration. It is noticeable in Fig. 9 that the low-concentration molybdenum enhances the growth of loops.

Discussion

The foregoing results suggest that the trapping of self-interstitials by alloying atoms is an important factor in the nucleation of dislocation loops. The mobility of self-interstitials in alloys becomes lower because of the binding energy between self-interstitials and alloying atoms. On the consideration of the trapping effect, Igata et al [*7–9*] modified Makin's

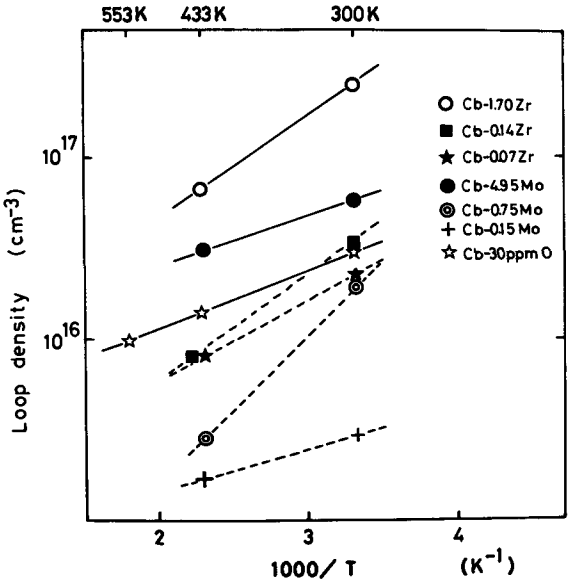

FIG. 6—*Relations between loop density and irradiation temperature in columbium-zirconium and columbium-molybdenum alloys.*

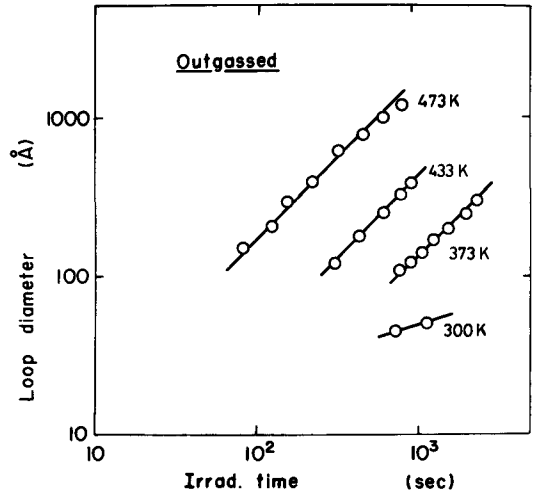

FIG. 7—*Loop diameter versus irradiation time in an outgassed columbium.*

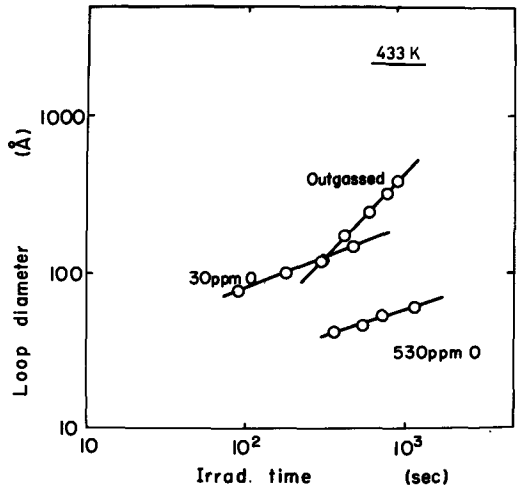

FIG. 8—*Loop diameter versus irradiation time in columbium-oxygen alloys at 433 K.*

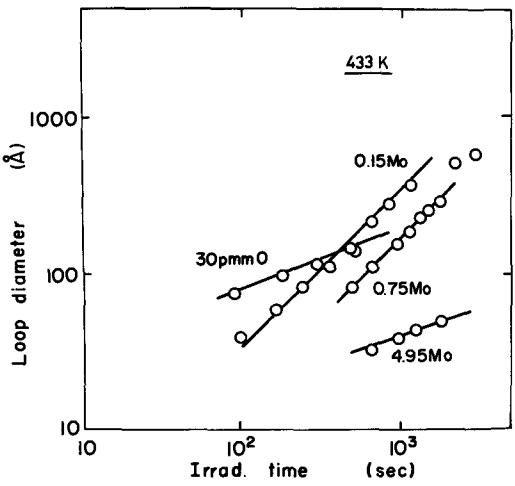

FIG. 9—*Loop diameter versus irradiation time in columbium-molybdenum and columbium-30 weight ppm oxygen alloys at 433 K.*

equation [*18*] for the nucleation process of dislocation loops in the vacancy immobile temperature range. That is

$$N = \left[\frac{K\{1 - wC + wC\exp(B/kT)\}\exp(E_m/kT)}{\nu_0 \nu(4z + \sqrt{2}z')}\right]^{1/2} \quad (1)$$

where

N = density of dislocation loops,
K = defect production rate,
w = number of atoms within the trapping volume,
C = concentration of alloying atoms,
B = binding energy between a self-interstitial and an alloying atom,
E_m = migration energy of self-interstitials,
k = Boltzman constant,
T = absolute irradiation temperature,
ν_0 = pre-exponential factor,
ν = atomic volume, and
z and z' = numbers of atoms within the self-interstitial-vacancy recombination volume and that within the self-interstitial mutual combination volume, respectively.

The loop density is proportional to the square root of oxygen atom concentration as shown in Fig. 2. This shows that the term $1 - wC$ in Eq 1 is neglected. Therefore, it is concluded that the trapping effect of self-interstitials by interstitial oxygen atoms controls the nucleation of interstitial dislocation loops. The saturation phenomenon at high oxygen concentration above 10^4 atoms ppm (1700 weight ppm) may be understood as follows: The increase of interstitial oxygen atoms causes the increase of trapped self-interstitials, and the same number of vacancies is accumulated in matrix in the vacancy immobile temperature range. This increase of the vacancy concentration suppresses further nucleation of dislocation loops because the probability of the recombination between self-interstitials and vacancies becomes higher, and the loop density is saturated.

It is shown in Eq 1 that the logarithmic loop density is proportional to the reciprocal of irradiation temperature because $1 - wC \ll wC \exp(B/kT)$. This temperature dependency is in agreement with the results in Fig. 3. The value of $(E_m + B)$ was estimated to be about 0.13 eV for columbium-oxygen. This value agrees with Faber's result [*19*].

The minimum loop densities in columbium-zirconium and columbium-molybdenum alloys at low concentrations (Fig. 5) may be understood by the scavenging effect for oxygen atoms by zirconium and molybdenum atoms. These effects of zirconium and molybdenum were pointed up from the results of internal friction by Haason et al [*20*] and others [*21–24*],

and Szkopiak et al [*22*], respectively. From their studies, 0.75 percent molybdenum atoms and 0.07 percent zirconium atoms seem enough to scavenge oxygen atoms contained in the specimens. The values of $(E_m + B)$ in columbium-1.70 percent zirconium and columbium-4.95 percent molybdenum are estimated to be about 0.2 and 0.1 eV, respectively, from Fig. 6. Results of other alloys were excluded from the estimation since it seems by the later discussions on the growth kinetics of dislocation loops that vacancies may be mobile at 433 in these alloys, and so Eq 1 is not applicable. Equation 1 is applicable in the case of the vacancy immobile temperature range. The binding energy of a zirconium atom to a self-interstitial atom seems to be larger than that of a molybdenum atom. The loop density in columbium-zirconium alloy is higher than that in columbium-molybdenum alloy at the same concentration (Fig. 5), which is in agreement with the foregoing relation.

The growth kinetics of dislocation loops under electron irradiation was discussed by Makin [*18*] and Kiritani et al [*25*]. The authors derived similar equations [*9*] as follows

$$d = \frac{2}{a}\left(\frac{3}{\pi}\right)^{1/3} \nu^{1/4}(4z + \sqrt{2}z')\left(\frac{p}{z}\right)^{1/3} K^{1/4} \nu_i^{1/4} t^{1/3} \tag{2}$$

in the vacancy immobile temperature range, and

$$d = \frac{2\nu^{1/2}}{a^2}\left[p\left(\frac{S_\nu}{zS_i}\right)^{1/2} - p'\left(\frac{S_i}{zS_\nu}\right)^{1/2}\right] K^{1/2} \nu_\nu^{1/2} t \tag{3}$$

in the temperature range where vacancies are mobile and the steady state is attained. In Eqs 2 and 3

where

d = loop diameter,
a = interatomic distance,
p = number of atoms per one atomic site along dislocation lines within the self-interstitial-dislocation combination volume,
p' = that within the vacancy-dislocation combination volume,
ν_i and ν_ν = jump frequencies of self-interstitials and vacancies, and
S_i and S_ν = total sink densities for self-interstitials and for vacancies, respectively.

The growth exponent in an outgassed columbium is one above 373 K as shown in Fig. 7. This suggests that the vacancy may be mobile above 373 K when the foregoing analysis is applicable. The migration energy of a vacancy seems to be $\lesssim$1 eV, and this inference does not conflict with Faber's

result [*19*] and Vabra et al's result [*26*]. The oxygen and molybdenum atoms suppress the vacancy mobility by the trapping effect shown in Figs. 8 and 9. There is a similar effect in the case of zirconium atoms. The strength of this suppressing effect on vacancy mobility by interstitial oxygen atoms seems to be larger than that by substitutional molybdenum and zirconium atoms. It is supported by Faber's result [*19*] that the binding energy of an oxygen atom to a vacancy is large.

Conclusions

1. Alloying atoms such as interstitial oxygen atoms, substitutional zirconium, and molybdenum atoms affects the mobilities of both self-interstitials and vacancies because of the binding between alloying atoms and self-interstitials or vacancies. The nucleation mechanism of self-interstitial dislocation loops in the vacancy immobile temperature range is controlled by the trapping of self-interstitials by alloying atoms.

2. The growth exponent in the loop growth depends on the vacancy mobility which is affected by alloying atoms.

3. The scavenging effect in columbium-zirconium and columbium-molybdenum alloys was observed in both nucleation and growth processes.

4. The values of $(E_m + B)$ are estimated to be about 0.13 eV in columbium-oxygen, 0.2 eV in columbium-zirconium and 0.1 eV in columbium-molybdenum respectively.

5. Vacancies in an outgassed columbium seem to migrate above 373 K when the analysis is applicable.

Acknowledgment

The authors are very grateful to J. Uchida and H. Nishizawa of the Japan Electron Optics Laboratory Campany for their help with this work. They wish also to acknowledge H. Tsunakawa and T. Kaneko of Tokyo University for their assistance.

References

[*1*] Loomis, B. A. and Gerber, S. B., *Acta Metallurgica*, Vol. 21, 1973, pp. 165–172.
[*2*] Tucker, R. P. and Wechsler, M. S., *Radiation Effects*, Vol. 3, 1970, pp. 73–87.
[*3*] Elen, J. D., Hamburg, G., and Mastenbroek, A., *Journal of Nuclear Materials*, Vol. 39, 1971, pp. 194–202.
[*4*] Michel, D. J. and Moteff, J., *Radiation Effects*, Vol. 21, 1974, pp. 235–243.
[*5*] Mitchell, J. B., Van Konynenburg, R. A., Guinan, M. W., and Echer, C. J., *Philosophical Magazine*, Vol. 31, 1975, pp. 919–927.
[*6*] Loomis, B. A., Taylor, A. T., Klippert, T. E., and Gerber, S. B., *Defects and Defect Clusters in BCC Metals and Their Alloys*, R. J. Arsenault, Ed., National Bureau of Standards, Gaithersburg, Md., 1973, pp. 332–340.

[7] Igata, N., Watari, F., and Murakami, H., "Effect of Interstitial Impurity Atoms on Electron Bombarded Niobium Studied by High Voltage Electron Microscope," United States-Japan Seminar on Radiation-Produced Defects and Defect Clusters and Their Effects in Metals, Ames, Iowa, 28–30 Sept., 1975.

[8] Igata, N., Watari, F., and Murakami, H., 4th International Conference on High Voltage Electron Microscopy, Toulouse, France, 1–4 Sept., 1975, to be published.

[9] Igata, N., Watari, F., Murakami, H., International Conference on Fundamental Aspects of Radiation Damage in Metals, Gatlinburg, Tenn., 8–10 Oct., 1975, to be published.

[10] Igata, N. and Watari, F., *JEOL News,* Japan Electron Optics Laboratory Company, Vol. 12, No. 1, 1974, pp. 2–5.

[11] Steiner, D., ORNL-TM-3094, Oak Ridge National Laboratory, Oak Ridge, Tenn., 1970.

[12] Blow, S., AERE-R 6581, Atomic Energy Research Establishment, Harwell, England, 1971.

[13] Youngblood, G., Myhra, S., and DeFord, J. W., *Physical Review,* Vol. 188, 1969, p. 1101.

[14] Hirsch, P. B., Howie, A., Nicholson, R. B., Pashley, D. W. and Whelan, M. J., *Electron Microscopy of Thin Crystals,* Butterworth, London, 1965, p. 263.

[15] Hirsch, P. B., Howie, A., Nicholson, R. B., Pashley, D. W., and Whelan, M. J., *Electron Microscopy of Thin Crystals,* Butterworth, London, 1965, p. 424.

[16] Makin, M. J., *Philosophical Magazine,* Vol. 18, 1968, pp. 637–653.

[17] Yoshida, N. and Kiritani, M., *Journal of the Physical Society of Japan,* Vol. 35, 1973, pp. 1418–1429.

[18] Makin, M. J., *Philosophical Magazine,* Vol. 19, 1969, pp. 1133–1146.

[19] Faber, K., "Die Erhorlung des elektrischen Widerstandes von Niob und Tantal nach Elektronenbestrahlung bei 4.5K," Thesis, Universitat Stuttgart, 1973.

[20] Haason, D. F. and Arsenault, R. J., *Treatise on Materials Science and Technology,* H. Herman, Ed., Vol. 1, Academic Press, New York and London, 1972, pp. 179–246.

[21] Bunn, P. M., Cummings, D. G., and Leavenworth, H. W., *Journal of Applied Physics,* Vol. 33, 1962, pp. 3009–3013.

[22] Szkopiak, Z. C. and Ahmad, M. S., *High Temperature Materials,* 6th Plansee Seminar, F. Benesovsky, Ed., Springer-Verlag, Vienna-New York, 1969, pp. 345–356.

[23] Mosher, D., Dollins, C., and Wert, C., *Acta Metallurgica,* Vol. 18, 1970, pp. 797–803.

[24] Miner, R. E., Gibbons, D. F., and Gibala, R., *Acta Metallurgica,* Vol. 18, 1970, pp. 419–428.

[25] Kiritani, M., Yoshida, N., Takata, H., and Maehara, Y., *Journal of the Physical Society of Japan,* Vol. 38, 1975, pp. 1677–1686.

[26] Vávra, F., Dönitz, W., and Böning, K., *Physica Status Solidi* (*a*), Vol. 20, 1973, pp. 511–519.

Johannes Weertman[1] *and W. V. Green*[2]

Void Growth Suppression by Dislocation Impurity Atmospheres

REFERENCE: Weertman, Johannes and Green, W. V., **"Void Growth Suppression by Dislocation Impurity Atmospheres,"** *Irradiation Effects on the Microstructure and Properties of Metals, ASTM STP 611,* American Society for Testing and Materials, 1976, pp. 256-269.

ABSTRACT: A detailed calculation is given of the effect of an impurity atmosphere on void growth under irradiation damage conditions. Norris has proposed that such an atmosphere can suppress void growth. We have found the hydrostatic stress field of a dislocation that is surrounded by an impurity atmosphere and from it have calculated the change in the effective radius of a dislocation line as a sink for interstitials and vacancies. The calculation of the impurity concentration in a Cottrell cloud takes into account the change in hydrostatic pressure produced by the presence of the cloud itself. It is assumed that the hydrostatic pressure field of an impurity atom exists over a radial distance larger than the radius of the impurity atom. It is found that void growth is eliminated whenever dislocations are surrounded by a condensed atmosphere of either oversized substitutional impurity atoms or interstitial impurity atoms. A condensed atmosphere will form whenever the average impurity concentration is larger than a critical concentration.

KEY WORDS: radiation, voids, growth, irradiation, damage, dislocations (materials), impurities, interstitials, atoms, vacancies

Norris [*1*][3] recently suggested that a dislocation line is a less efficient sink for interstitial atoms if an impurity atmosphere is attached to it that contains oversized substitutional or interstitial impurity atoms. Void growth under irradiation damage conditions presumably is a direct consequence of the higher efficiency of a dislocation line as an interstitial atom sink than as a lattice vacancy sink [*2-12*]. Void growth can be suppressed by decreasing the efficiency of a dislocation line as an interstitial sink by the impurity atmosphere mechanism suggested by Norris, or by

[1] Consultant, Los Alamos Scientific Laboratory, University of California, Los Alamos, N. Mex. 87544 and professor, Department of Materials Science and Engineering Technological Institute, Northwestern University, Evanston, Ill. 60201.

[2] Staff member, Los Alamos Scientific Laboratory, Los Alamos, N. Mex. 87544.

[3] The italic numbers in brackets refer to the list of references appended to this paper.

increasing the efficiency as a sink for vacancies by the vibrating dislocation line mechanism suggested by us [*13,14*].

Norris has given only a rough calculation of the effect of an impurity atmosphere on the behavior of a dislocation line as a vacancy or interstitial sink. In this paper we present a more detailed study of the atmosphere effect. Our analysis is based partly on the results of the fundamental paper of Ham [*15*] on the stress-assisted diffusional motion of point defects around a dislocation line, as well as on our earlier papers [*13,14*].

Theory

Effective Core Radius

Were it not for its stress field, an edge dislocation would act as a sink for vacancies and interstitials in the same manner as does a cylindrical hole of radius equal to the core radius of the dislocation. The larger the radius of the cylindrical hole, the more effective a sink it is for vacancies and interstitials. The stress field of an edge dislocation alters the diffusive motion of vacancies and interstitials in such a manner that the effective core r_0 of the dislocation as a sink for point defects is increased in value [*13–17*]. The effective core radius can be calculated as follows. Let the concentration c of vacancies at a distance R, where $R \gg r_0$, be maintained at the level $c = c_0$, and let the concentration at the dislocation be kept at the level $c = 0$. The diffusion equation is [*15*]

$$\partial c/\partial t = D\nabla\cdot(\nabla c - \beta c\nabla V) \tag{1}$$

where

D = diffusion coefficient,
β = $1/kT$ where k is Boltzmann's constant, T is the temperature,
t = time, and
$V(r, \theta)$ = elastic interaction energy of a point defect situated at a distance r at the azimuthal angle θ measured from the slip plane of the dislocation.

(The extra half-plane of atoms of the edge dislocation exists at $\theta = \pi/2$.) Note that $V(r, \theta)$ is the energy that must be supplied to the crystal when a point defect situated at r, θ is moved to a position $r \to \infty$. Under steady-state conditions, $\partial c/\partial t = 0$. For the case when $V = 0$, the solution of Eq 1 is

$$c = [c_0/\log(R/r_0)]\log(r/r_0) \tag{2}$$

and the number N of point defects that arrive at a unit length of dislocation line is a unit time equal to

$$N = D\int_0^{2\pi} [\partial c/\partial r - \beta c\partial V/\partial r]d\theta = 2\pi Dc_0/\log(R/r_0) \tag{3}$$

When $V = 0$, the appropriate value of r_0 is the actual core radius of the dislocation: $r_0 \approx b$, where b is the length of the Burgers vector of the dislocation.

When the stress field of the edge dislocation is taken into account, the value of N is given by Eq 3 provided that r_0 in that equation is set equal to [*14,15,17,19*]

$$r_0 = (|A|\beta \exp\gamma)/4 \tag{4}$$

where $\gamma = 0.5772 \ldots$ is Euler's constant and A is approximately equal to $4\mu\varepsilon a^3 b/3$ where μ is the shear modulus, a the atomic radius of an atom in the lattice or interstitial site, and $\varepsilon = (a^* - a)/a$ where a^* is the radius of the vacancy or the interstitial.

The efficiency E of the dislocation line as a sink can be defined by the relationship

$$E = N/N_b \cong 1 + [\log(r_0/b)]/\log(R/b) \tag{5}$$

where N_b is the value of N when $r_0 = b$. If r_{0v} and r_{0i} represent, respectively, the effective core radius of the dislocation as a vacancy and as an interstitial sink, the difference $\Delta E = E_i - E_v$ in efficiency of the dislocation line as a sink for interstitials and for vacancies is

$$\Delta E = E_i - E_v = [\log(r_{0i}/r_{0v})]/\log(R/b) \tag{6}$$

Interaction Energy

The interaction energy with a hydrostatic pressure field of a point defect considered to be an oversized or undersized spherical elastic inclusion of the same elastic constant is [*20*]

$$V(r, \theta) = -[3(1 - \nu)/(1 + \nu)]P(r, \theta)(4\pi/3)\varepsilon a^3 \tag{7}$$

where $(4\pi/3)\varepsilon a^3$ is the difference in volume of the point defect with respect to a lattice atom as measured in a stress-free state, and ν is Poisson's ratio. The term $P(r, \theta)$ is the hydrostatic pressure; it has a positive value when in compression.

The hydrostatic pressure field $P_d(r, \theta)$ of the edge dislocation is given by

$$P_d(r, \theta) = \{(\mu b/3\pi)(1 + \nu)/(1 - \nu)\}(\sin\theta)/r \tag{8}$$

Combining Eqs 7 and 8 gives

$$V(r, \theta) = -A(\sin\theta)/r \tag{9}$$

for the elastic interaction energy of the point defect with the dislocation (assuming that $|\varepsilon| < 1$).

Pressure Change Produced by Variation in Impurity Concentration

At equilibrium the concentration $c(r, \theta)$ of impurity atoms in the vicinity of a dislocation line is given by the Cottrell-Bilby expression

$$c(r, \theta) = c_0 \exp(\beta V\{r, \theta\}) \tag{10}$$

where c_0 is the concentration at a large distance from the dislocation.

The interaction energy given by Eq 9 ordinarily is used in Eq 10. However, use of $V(r, \theta)$ given by Eq 9 takes no account of the fact that a variation of the concentration c with r and θ will itself produce a change in the hydrostatic pressure. For example, suppose that an infinitely long cylinder of inner radius r' and outer radius $r' + \delta r'$ were cut out of a solid. Suppose that the impurity concentration in this cylinder were changed from the value c_0 to the value $c_0 + \Delta c$. A length L of this infinitely long cylinder would now be changed to the length $L(1 + \alpha\Delta c)$, and the inner and outer radii would have the values $r'(1 + \alpha\Delta c)$ and $(r' + \delta r')(1 + \alpha\Delta c)$, respectively. The constant α is equal to $4\pi\varepsilon^* a^3/3$, where ε^* is the value of ε of the impurity atoms. Now let the cylinder be forced back into the hole it left in the solid in such a way that each length $L(1 + \alpha\Delta c)$ of the cylinder is restored to its original length L. The self-stresses set up in the solid by this restoration can be obtained from the solution of a simple problem in elasticity. The hydrostatic pressure component P_c of this stress field is equal to zero for values of r where the composition was unchanged and is equal to

$$P_c = \{4\mu(1 + \nu)/3(1 - \nu)\}\alpha\Delta c \tag{11}$$

in the region $r' < r < r' + \delta r'$.

This result is easily generalized. For any arbitrary variation of the concentration of the impurity atoms

$$\Delta c(r, \theta) = c(r, \theta) - c_0$$

produces the hydrostatic pressure

$$P_c(r, \theta) = \{4\mu(1 + \nu)/3(1 - \nu)\}\alpha\Delta c(r, \theta) \quad (12)$$

The Thomson Effect

Thomson [*21*] has pointed out that if a point defect is considered to be a spherical elastic oversized or undersized elastic inclusion (whose radius is equal to the atomic radius) in an elastic matrix, the dilational strain field around a dislocation is not saturated by a point-defect atmosphere. The hydrostatic stress around an impurity atom at radial distances larger than the radius of the impurity atom is always zero. Hence, the hydrostatic stress near a dislocation is unchanged at any lattice site that does not contain an impurity atom. The hydrostatic stress at radial distances smaller than the radius of an impurity atom is not equal to zero. Thus, the pressure P_c given by Eq 12 is the hydrostatic pressure averaged over both the impurity atoms (where it is not equal to zero) and the host atoms (where it is equal to zero).

When an impurity atom is considered to be an elastic inclusion of diameter equal to the lattice spacing, it is implicitly assumed that the impurity atom interacts only with its nearest neighbor atoms. However, if the impurity atom interacts appreciably with atoms at larger distances than its nearest neighbor atoms, it can be considered to be equivalent to an elastic inclusion of an effective diameter larger than the lattice spacing. In this situation, whenever the mean spacing between impurity atoms is of the order of or smaller than this effective diameter, the average hydrostatic pressure P_c given in Eq 12 will approximate the actual hydrostatic pressure at *every* lattice site.

In the sections that follow, it is assumed that the hydrostatic pressure produced by an impurity atom is not equal to zero at radial distances larger than the lattice spacing. We realize this assumption may be controversial. Because the concentration of impurity atoms in a Cottrell atmosphere is relatively large, the effective diameter of the hydrostatic stress field of an impurity atom need only be two or three lattice distances to serve our purpose.

Cottrell Atmosphere Modified by Pressure Relaxation

The pressure $P(r, \theta)$ that appears in Eq 7, the equation for the interaction energy $V(r, \theta)$, should be the sum of $P_d(r, \theta)$ given by Eq 8 and $P_c(r, \theta)$ given by Eq 12. The concentration of impurity atoms in the Cottrell cloud thus is given by the equation

$$\Delta c(r, \theta) = c_0\{\exp[-A^*\beta\{4\pi\alpha b^{-1}\Delta c(r, \theta) + r^{-1}\sin\theta\}] - 1\} \quad (13)$$

where A^* is the value of A calculated for the impurity atoms.

At large distance from the dislocation, this last equation reduces to

$$\Delta c(r, \theta) = -c_0 A^* \beta (1 + 4\pi\alpha c_0 b^{-1} A^* \beta)^{-1} \sin\theta / r \tag{14}$$

The hydrostatic pressure is given by

$$P(r, \theta) = (1 - f) P_d(r, \theta) \tag{15}$$

where $P_d(r, \theta)$ is given by Eq 8 and the term f is equal to

$$f = 4\pi c_0 \alpha A^* \beta / b(1 + 4\pi\alpha c_0 b^{-1} A^* \beta) \tag{16}$$

The term f is always a positive quantity. Equations 14 and 15 are also valid near the dislocation if the interaction energy is small compared with $kT = 1/\beta$ at distances of the order $r \sim b$.

When the interaction energy is large compared with $kT = 1/\beta$, the concentration in the vicinity of the dislocation is given by

$$\Delta c(r, \theta) = -c_0 \tag{17a}$$

on the side of the slip plane for which $A^* \sin\theta > 0$, and by

$$\Delta c(r, \theta) = -\{(3/\mu\alpha)(1 - \nu)/4(1 + \nu)\} P_d(r, \theta) - G \tag{17b}$$

where $G = (b/4\pi\alpha A^* \beta) \log(1 + \Delta c/c_0) \sim b/\alpha A^* \beta$ on the side of the slip plane for which $A^* \sin\theta < 0$. Equation 17*b* breaks down if the average concentration c_0 is made sufficiently small. If $c_0 < (b/4\pi\alpha A^* \beta) \exp(-|A^*|\beta/b)$, the concentration $\Delta c(r, \theta)$ is given by

$$\Delta c(r, \theta) \approx c_0 \{\exp(-A^* \beta \sin\theta / r) - 1\} \tag{17c}$$

The hydrostatic pressure is equal to

$$P(r, \theta) = P_d(r, \theta) - 4\alpha\mu c_0 (1 + \nu)/3(1 - \nu) \tag{18a}$$

where $A^* \sin\theta > 0$, and to

$$P(r, \theta) = -4\alpha\mu G(1 + \nu)/3(1 - \nu) \tag{18b}$$

if $c_0 > (b/4\pi\alpha A^* \beta \exp(-|A^*|\beta/b)$ and $A^* \sin\theta < 0$, and to

$$P(r, \theta) = P_d(r, \theta) - c_0 \alpha \{4\mu(1 + \nu)/3(1 - \nu)\} \exp(|A^*|\beta \sin\theta / r) \tag{18c}$$

if $c_0 < (b/4\pi\alpha A^* \beta) \exp(-|A^*|\beta/b)$ and $A^* \sin\theta < 0$.

It should be noted that the concentration given by Eq 17*b* is only very weakly temperature-dependent. This result is in marked contrast to the usual result obtained when no correction is made for the reduction of the hydrostatic pressure. Equation 17*b* represents the concentration of a condensed Cottrell cloud.

Change in Effective Core Radius

Weak Impurity-Dislocation Interaction

When the impurity atoms of the Cottrell cloud interact only weakly with the dislocation, according to Eq 15 the hydrostatic pressure field of the dislocation is reduced by the constant factor f. The effective core radius of the dislocation line as a vacancy or an interstitial sink is thus given by

$$r_0 = (1 - f)(A\beta \exp\gamma)/4 \tag{19}$$

where A is calculated with the value of ε for a vacancy or for an interstitial (not with the value of ε for an impurity atom). The value of f is the same for a vacancy and for an interstitial.

Although the presence of the atmosphere reduces the efficiency of a dislocation line as a sink for point defects because r_0 is reduced in value, the difference in efficiency ΔE as a vacancy and as an interstitial sink (see Eq 6) is not changed. Thus an impurity cloud of weakly bonded impurity atoms cannot eliminate the bias of a dislocation line as an interstitial sink that ultimately causes the growth of voids under high-temperature irradiations.

Strong Impurity-Dislocation Interaction When c_0 *Is Relatively Large*

When impurity atoms interact strongly with a dislocation line and $c_0 > (b/4\pi\alpha A^*\beta) \exp(-|A^*|\beta/b)$, the pressure field near the dislocation is given by Eqs 18*a* and 18*b*, and far away from the dislocation line is given by Eq 15. To a first approximation, the interaction energy $V(r, \theta)$ of a vacancy or an interstitial and an edge dislocation is given by

$$V(r, \theta) = -AJ(\theta)(\sin\theta)/r \tag{20}$$

where

$$J(\theta) = \begin{cases} 1 & (0 < \theta < \pi) \\ 0 & (\pi < \theta < 2\pi) \end{cases} \tag{21}$$

if the impurity atoms of the Cottrell cloud are oversized substitutional atoms or are interstitial atoms. [If the impurity atoms are undersized substitutional atoms, $J(\theta) = 0$ for $0 < \theta < \pi$ and $J(\theta) = 1$ for $\pi < \theta < 2\pi$. We will consider in what follows only the case when Eq 21 applies.]

The general steady-state solution of Eq 1 on the side of the slip plane of the dislocation for which $J(\theta) = 0$ and which satisfies the symmetry conditions [that is, $c(r, \theta) = c(r, \pi - \theta)$ and $\partial c(r, \theta)/\partial\theta = -\partial c(r, \pi - \theta)/\partial\theta$] is

$$c(r, \theta) = a_0 \log(r/r_0) + \sum_{1,3,5}^{\infty} (a^*_n r^n + a_n/r^n) \sin(n\theta) + \sum_{2,4,6}^{\infty} (a^*_n r^n + a_n/r^n) \cos(n\theta) \tag{22}$$

where a_0, a_n, and a^*_n are constants. The general solution of Eq 1 on the side of the slip plane for which $J(\theta) = 1$ and which satisfies the symmetry conditions is [*15*]

$$c(r, \theta) = b^*_0 \exp(-A\beta \sin\theta/r) + \exp(-A\beta \sin\theta/2r) \Big\{ \sum_{1,3,5}^{\infty} [b_n K_n(|A|\beta/2r) + d_n I_n(|A|\beta/2r)] \sin(n\theta) + \sum_{0,2,4}^{\infty} [b_n K_n(|A|\beta/2r) + d_n I_n(|A|\beta/2r)] \cos(n\theta) \Big\} \tag{23}$$

where b^*_0, b_n, and d_n are constants and K_n and I_n are modified Bessel functions (Ham [*15*] has argued, for the particular problem he considered, that the function I_0 should not be used. Later workers [*17, 18*] have retained, correctly we believe, this Bessel function in Ham's solution.)

The boundary conditions that Eqs 22 and 23 must satisfy are: at $r = b$ the concentration $c(b, \theta) = 0$, and at $r = R$ the concentration $c(R, \theta) = c_0$. (We are considering in these equations only the concentration of point defects in excess of the thermal equilibrium concentration.) The flux of vacancies or interstitials across the slip plane must be continuous; the concentration itself also must have the same value on either side of the slip plane.

At large distances from the dislocation, the binding energy $V(r, \theta)$ is very small in magnitude. The dependence of the concentration on the azimuthal angle must disappear in this region and the concentration must depend logarithmically on radial distance as given by Eq 2. The terms a_n/r^n and $d_n I_n(|A|\beta/2r)$ in Eqs 22 and 23 do approach zero as $r \to \infty$ for $n \geqslant 1$ and can be neglected at large values of r. [Note that $I_n(x) \sim x^n$ for small values of x.] In order that the terms $ma^*_n r^n$ and $b_n K_n(|A|\beta/2r)$ do not lead to a large angular dependence of $c(r, \theta)$ at large values of r, the constants a^*_n and b_n for $n \geqslant 1$ must have small enough values that these

terms can be ignored at all values of r. [Note that $K_n(x) \sim 1/x^n$ for small values of x when $n \geqslant 1$.] Thus at large values of r

$$c(r, \theta) \approx c_0 \log(r/r_0)/\log(R/r_0) \approx b^*_0 + d_0 + b_0 \log(4r/|A|\beta \exp\gamma) \quad (24)$$

where use has been made of the following approximations, valid for large values of r: $K_0(|A|\beta/2r) \approx \log(4r/|A|\beta \exp\gamma)$ and $I_0(|A|\beta/2r) \approx 1$.

With the use of condition $c(b, \theta) = 0$, the relationship $I_n(x) = (-1)^n I_n(-x)$, and the expansion

$$\begin{aligned} \exp(x \sin\theta) = I_0(x) &+ 2 \sum_{1,3,5}^{\infty} (-1)^{(n-1)/2} I_n(x) \sin(n\theta) \\ &+ 2 \sum_{2,4,6}^{\infty} (-1)^{n/2} I_n(x) \cos(n\theta) \end{aligned} \quad (25)$$

it is possible to show that the constant b^*_0 can be set equal to zero. The constant b_0 in Eq 24 is, of course, equal to $b_0 = a_0 = c_0/\log(R/r_0)$. Thus d_0 is the only unknown constant that appears in Eq 24. Once its value is found, the value of r_0 is determined and the effectiveness of the dislocation line as a sink for point defects is known. The effective radius r_0 is then given by the equation

$$d_0 = c_0 \log(\{|A|\beta \exp\gamma\}/4r_0)/\log(R/r_0) \quad (26)$$

At large distances, the concentration $c(r, \theta)$ given by Eq 24 has associated with it a total integrated flux N of point defects given by the right-hand side of Eq 3. At the dislocation core ($r = b$), the flux N is unchanged in value. The number N_- of point defects that enter the core in unit time from below the slip plane is given by

$$N_-/D = \int_{\pi}^{2\pi} (\partial c/\partial r)_{r=b} d\theta = \pi a_0 + 2 \sum_{1,3,5}^{\infty} a_n/b^n \quad (27)$$

where $c(r, \theta)$ is given by Eq 22.

The number N_+ of point defects that enter the core from above the slip plane per unit time is given by

$$\begin{aligned} N_+/D &= b \int_0^{\pi} [(\partial c/\partial r) - \beta c(\partial V/\partial r)]_{r=b} d\theta \\ &= b(\partial/\partial r)\Big\{ \int_0^{\pi} \exp(-A\beta \sin\theta/2r)[b_0 K_0(|A|\beta/2r) \\ &\quad + d_0 I_0(|A|\beta/2r) + \sum_{1,3,5}^{\infty} d_n I_n(|A|\beta/2r) \sin(n\theta) \\ &\quad + \sum_{2,4,6}^{\infty} d_n I_n(|A|\beta/2r) \cos(n\theta)] d\theta \Big\}_{r=b} \end{aligned} \quad (28)$$

where $c(r, \theta)$ is given by Eq 23.

The sum of the fluxes $N = N_- + N_+$ given by Eqs 27 and 28 must satisfy the equation

$$(N_- + N_+)/D = 2\pi a_0 = 2\pi c_0/\log(R/r_0) \tag{29}$$

Consider the limits that can be set on the value of the expression $(N_- + N_+)/D$. Consider first the case when $A > 0$. In this situation $(N_- + N_+)/D$ must be smaller than the value of N/D calculated for the case when $V(r, \theta) = 0$ for all values of $\theta (0 \leqq \theta \leqq 2\pi)$. Thus

$$2\pi c_0/\log(R/r_0) < 2\pi c_0/\log(R/b) \tag{30}$$

The term $(N_- + N_+)/D$ must be larger than the value of N/D calculated for the case when a barrier is placed across the slip plane of the dislocation ($\theta = 0$ and $\theta = \pi$) that prevents point defects from diffusing across it, but the potential $V(r, \theta)$ for all other values of θ otherwise is not changed. The value of N_-/D for this situation is simply $(1/2)2\pi c_0/\log(R/b)$. The value of N_+/D for this situation in turn is smaller than the value of N_+/D calculated for the problem where $V = -A \sin\theta/r$ for *all* values of θ $(0 \leqq \theta \leqq 2\pi)$. The value of N_+/D for this latter problem is approximately equal to 0 when the magnitude of the term $A\beta/2b$ is large. Thus

$$\pi c_0/\log(R/b) < 2\pi c_0/\log(R/r_0) \tag{31}$$

The value of r_0 for the case when $A > 0$ thus lies between the limits

$$b(b/R) < r_0 < b \tag{32}$$

The term $(N_- + N_+)/D$ given by Eq 29 when $A < 0$ must be larger than the value of N/D calculated for the case when $V = -A \sin\theta/r$ for *all* values of θ. Thus from Eq 4

$$2\pi c_0/\log(4R/|A|\beta \exp\gamma) < 2\pi c_0/\log(R/r_0) \tag{33}$$

The term $(N_- + N_+)/D$ must be smaller than the value of N/D calculated for the case where $V = -A/r$ for all values of θ. Thus (from Ref *14*)

$$2\pi c_0/\log(R/|A|\beta \exp\gamma) < 2\pi c_0/\log(R/r_0) \tag{34}$$

Therefore

$$(|A|\beta \exp\gamma)/4 < r_0 < |A|\beta \exp\gamma \tag{35}$$

It is easy to understand why the effective core radius r_0 must have a

value within the limits in Eqs 32 or 35. When the magnitude of the term $A\beta/2b$ is large and $A > 0$, the large negative interaction energy $V(r, \theta)$ (given by Eq 20) acts as a strong barrier to a point defect that attempts to move into the core of the dislocation from above the slip plane ($0 < \theta < \pi$). In this situation it is to be expected that almost all the point defects move into the core from below the slip plane ($\pi < \theta < 2\pi$). The potential $V(r, \theta) = 0$ is on this side of the slip plane. The effective core radius, therefore, should be smaller than the core radius $r_0 = b$ found for this when $V(r, \theta) = 0$ on both sides of the slip plane. On the other hand, when $A < 0$, the interaction energy $V(r, \theta)$ causes point defects to be strongly attracted to the region near the core that is above the slip plane ($0 < \theta < \pi$). In this situation most of the point defects will diffuse into the core from above the slip plane. However, there is no barrier to the motion of a point defect that comes to the dislocation from beneath the slip plane. Therefore, the core radius r_0 should be somewhat larger than $r_0 = (|A|\beta \exp\gamma)/4$, which is the core radius calculated for the case in which the potential $V(r, \theta)$ acts as a barrier to point defects moving into the dislocation core from beneath the slip plane and acts in addition as an attractive force to point defects moving into the dislocation core from above the slip plane.

Strong Impurity-Dislocation Interaction When c_0 is Very Small

When the impurity atoms interact strongly with a dislocation line but the average concentration is so small that $c_0 < (b/4\pi\alpha A^*\beta) \exp(-|A^*|\beta/b)$, the pressure field near the dislocation is given by Eqs 18*a* and 18*c*. In this situation it is clear that the effective radius r_0 for interstitial atoms is reduced from the value $(|A|\beta \exp\gamma)/4$ by a small factor whose value increases as the value of c_0 is made larger. For vacancies the effective radius is increased by approximately the same amount.

Discussion

The effect of a condensed Cottrell cloud of oversized or interstitial impurity atoms on the relative efficiency of a dislocation line as a sink for vacancies and interstitial atoms is quite clear. For vacancies the effective core radius is increased from the value $(|A_v|\beta \exp\gamma)/4$, where A_v is the appropriate constant for a vacancy, to a value between $(|A_v|\beta \exp\gamma)/4$ and $|A_v|\beta \exp\gamma$. The impurity cloud makes the dislocation a more effective sink for vacancies. For interstitial atoms the effective core radius r_0 is reduced from the value $(|A_i|\beta \exp\gamma)/4$ to a value smaller than b. In other words, the dislocation, rather than being a more effective sink for interstitial atoms, now is a more effective sink for vacancies than for interstitial atoms. This reversal in behavior will prevent the growth of voids that occurs when interstitial atoms are annihilated preferentially at dislocation lines.

If the impurity cloud is made up of undersized impurity atoms the dislocation line will become an even better sink for interstitial atoms and an even worse sink for vacancies. In this circumstance, void growth would be enhanced.

We have assumed implicitly throughout this paper that the diffusion coefficients are not a function of the impurity content. Obviously they are, and a more accurate theory would take this concentration dependence into account whenever the dependence is a strong one. We have also assumed implicity in this paper that interactions between dislocations and point defects and between point defects other than elastic ones are unimportant. Clearly, new theories could be developed for the cases when nonelastic interactions are the dominant ones. We point out again that our assumption that the hydrostatic stress field of a point defect may extend out a distance larger than the atomic radius may be controversial.

Appreciable void growth under irradiation damage produced by the energetic bombardment by neutrons, heavy ions, or electrons occurs at relatively high temperatures, of the order of one third to one half of the melting point of the material. The interaction energy of an impurity atom with a dislocation has to be relatively high in order to have an appreciable Cottrell cloud exist at these temperatures. Interstitial atoms in metals with body-centered-cubic crystal structure are known to have large interaction energies. For carbon in iron, the energy is estimated from theory and experiment [*20*] to be of the order of 0.52 to 0.75 eV. An interaction energy of 0.52 eV is sufficiently large to cause a thousand-fold increase of the carbon concentration at a dislocation line at a temperature equal to one half of the melting temperature of iron.

If the concentration c_0 is quite small, no condensed Cottrell atmosphere will form even if the interaction energy is large. In this situation, although void growth may not be eliminated, the growth rate of voids can be reduced appreciably in value. If the impurity atoms only interact weakly with dislocations, there is no possibility of reducing the rate of growth of voids.

The critical concentration c^*_0 above which an atmosphere will form is of the order of

$$c^*_0 = (b/4\pi\alpha A^*\beta) \exp(-|A^*|\beta/b) \tag{36}$$

As an example, if $|A^*|\beta/b = 6$ and $\varepsilon = 0.1$, the critical concentration c_0^* is of the order of 0.1 atomic percent. There is no equation similar to Eq 36 in Norris's paper [*1*] with which comparison can be made.

A referee of our paper has brought to our attention the paper of Kuhlmann-Wilsdorf [*18*], in which it is suggested that the presence of oversized solute atoms near a dislocation could suppress void nucleation there. Kuhlmann-Wilsdorf does not develop a quantitative theory in her short paper (she references a longer paper of hers which is still in press),

but suggests that void nucleation near a dislocation is made more difficult by oversize impurity atoms because the dilational strains are reduced, because the concentration of excess vacancies bound to the dislocation also is reduced, and because the activation energy of formation of a critical void nucleous is increased.

A paper by Wolfer and Ashkin [*22*] that appeared in print after we wrote the present paper has developed further Ham's theory of the flow of point defects to a dislocation line. Wolfer and Ashkin consider the flow of lattice vacancies and interstitials to an edge dislocation. They use their analysis to consider the problem of void nucleation in the vicinity of a dislocation line.

Conclusion

If the average concentration c_0 of oversized substitutional impurity atoms or interstitials impurity atoms that can interact strongly with a dislocation is greater than the critical concentration c^*_0, void growth under irradiation damage by energetic particles should be completely suppressed. Our results are only valid if the hydrostatic pressure field of an impurity atom extends out to distances larger than the lattice spacing. If the hydrostatic pressure field of an impurity atoms exists only within a radial distance equal to or less than the radius of the impurity atom, then, because of the Thomson effect, the hydrostatic stress field of a dislocation line cannot be neutralized by a Cottrell cloud and this impurity atmosphere cannot suppress the growth of voids.

Acknowledgments

This work was performed under the auspices of the Energy Research and Development Administration. The authors wish to express their appreciation to R. J. Bard for his interest, encouragement, and support.

References

[*1*] Norris, D. I. R., *The Physics of Irradiation Produced Voids*, R. S. Nelson, Ed., AERE-R7934, Atomic Energy Research Establishment, Harwell, England, H. M. Stationery Office, 1975, pp. 134–139.

[*2*] Greenwood, G. W., Foreman, A. J. E., Rimmer, D. E., *Journal of Nuclear Materials,* Vol. 1, 1959, pp. 305–324.

[*3*] Harkness, S. D. and Li, C. -Y., *Metallurgical Transactions,* Vol. 2, 1971, pp. 1457–1470.

[*4*] Bullough, R. and Perrin, R. C., *Radiation-Induced Voids in Metals,* J. W. Corbett and L. C. Ianniello, Eds., U. S. Atomic Energy Commission, 1972, pp. 769–797.

[*5*] Adda, Y., *Radiation-Induced Voids in Metals,* J. W. Corbett and L. C. Ianniello, Eds., U. S. Atomic Energy Commission, 1972, pp. 31–83.

[*6*] Harkness, S. D. and Li, C. -Y., *Radiation-Induced Voids in Metals,* J. W. Corbett and L. C. Ianniello, Eds., U. S. Atomic Energy Commission, 1972, pp. 798–824.

[*7*] Bullough, R., Eyre, B. L., and Perrin, R. C., *Journal of Nuclear and Applied Technology,* Vol. 9, 1970, pp. 346–355.

[8] Bullough, R. and Perrin, R. C. in *Irradiation Effects on Structural Alloys for Nuclear Applications, ASTM STP 484,* American Society for Testing and Materials, 1970, pp. 317–329.
[9] Foreman, A. J. E., "A Note on the Dose Dependence of Void Growth in Irradiated Materials," Report AERE-R-6358, Atomic Energy Research Establishment, Harwell, England, 1970.
[10] Li, C. -Y., Franklin, D. G., and Harkness, S. D., *Irradiation Effects on Structural Alloys for Nuclear Applications, ASTM STP 484,* American Society for Testing and Materials, 1970, pp. 347–360.
[11] Harkness, S. D. and Li, C. -Y., *Proceedings,* Symposium on Radiation Damage in Reactor Materials, International Atomic Energy Agency, Vienna, 1969, Vol. 2, pp. 189–213.
[12] Bullough, R. and Perrin, R. C., *Voids Formed by Irradiation of Reactor Materials,* British Nuclear Energy Society, Harwell, England, 1971, pp. 79–107.
[13] Green, W. V. and Weertman, J., *Nature,* Vol. 243, 1973, pp. 159–160.
[14] Green, W. V. and Weertman, J., *Radiation Effects,* Vol. 22, 1974, pp. 9–13.
[15] Ham, F. S., *Journal of Applied Physics,* Vol. 30, 1959, pp. 915–926.
[16] Heald, P. T. and Speight, M. V., *Philosophical Magazine,* Vol. 30, 1974, pp. 869–875.
[17] Heald, P. T., *Philosophical Magazine,* Vol. 31, 1975, pp. 551–558.
[18] Kuhlmann-Wilsdorf, D., *Scripta Metallurgica,* Vol. 7, 1973, pp. 1059–1063.
[19] Margvelashvili, I. G. and Saralidze, Z. K., *Soviet Physics—Solid State,* Vol. 15, 1974, pp. 1774–1776.
[20] Nabarro, F. R. N., *Theory of Crystal Dislocations,* Clarendon Press, Oxford, England, 1967, pp. 399–404.
[21] Thompson, R., *Acta Metallurgica,* Vol. 6, 1958, pp. 23–28.
[22] Wolfer, W. G. and Ashkin, M., *Journal of Applied Physics,* Vol. 47, 1976, pp. 791–800.

J. S. Watkin[1]

Dependence of Void Swelling on the Electron Vacancy Concentration

REFERENCE: Watkin, J. S., "**Dependence of Void Swelling on the Electron Vacancy Concentration,**" *Irradiation Effects on the Microstructure and Properties of Metals, ASTM STP 611,* American Society for Testing and Materials, 1976, pp. 270–283.

ABSTRACT: Large variations have been noted between the swelling of different iron, chromium, nickel alloys and suggestions have been made that the differences are due to variations in the carbon, silicon, phosphorus, and nickel content of the alloys. Harries has postulated that variations in the solute concentration of the gamma matrix could be responsible for the different swelling behavior and that the formation of any second phase which leads to a depletion in the solute concentration will in turn lead to an impairment in swelling resistance. The swelling of several commercial alloys irradiated at 600°C (1112°F) in the Dounreay Fast Reactor lend general support to Harries' suggestion and the swelling at 30 atomic displacements per atom (dpa) has been shown to increase with the calculated equilibrium fraction of sigma phase. A superior correlation has been shown to exist between the swelling and calculated electron vacancy concentration of the matrix and a critical value of 2.58 electron vacancies per atom has been observed above which swelling increases rapidly and below which swelling is small.

KEY WORDS: radiation, swelling, voids, vacancies (crystal defects), interstitials, austenitic stainless steels, nickel alloys, electron vacancy concentration, sigma phase

Large variations have been noted between the swelling of different iron, chromium, nickel alloys, and several correlations have been made which suggest that the differences are due to such factors as carbon, silicon, and phosphorus content [*1*].[2] The most consistent correlation, however, has been that between swelling and nickel content [*2*]. These and other observations such as voids forming near precipitates have led Harries [*3*] to suggest a way in which compositional factors might exert a marked influence on neutron-induced void swelling. He postulates that solute atoms

[1] Higher scientific officer, United Kingdom Atomic Energy Authority, Springfields, Preston, England.

[2] The italic numbers in brackets refer to the list of references appended to this paper.

in a gamma matrix might act as trapping sites for gas atoms or aid the recombination of irradiation-produced interstitials and vacancies. The formation of any second phase, such as sigma phase, into which such beneficial solutes tend to segregate would then lead to an impairment in the swelling resistance of the gamma matrix.

Data on the void swelling of a number of commercial alloys irradiated under identical conditions are available from the irradiation of solid cylinders in the Dounreay Fast Reactor (DFR) over a range of temperatures. In this paper the data at 600 °C (1112 °F), which is at or very near to the peak swelling temperature of all the alloys, are analyzed to determine what general support they lend to Harries' hypothesis and whether any further quantification is possible.

Experimental Details

Materials

The compositions of the alloys used in this investigation are given in Table 1. The solution-strengthened stainless steels Types 316, M316, 316L, FV 548, 321, and 347 were given solution treatments of 1050 °C (1922 °F), ½ h; the alloy G 68 (a gamma prime hardened austenitic steel) was given 920 °C (1688 °F), 1 h + 720 °C (1328 °F), 16 h; and the three casts of PE16, a gamma prime hardened nickel-based alloy, were given 1040 °C (1904 °F), 15 min + 700 °C (1292 °F), 16 h. The special alloy GAB 286, similar in composition to PE16 but much lower in the gamma prime forming constituents titanium and aluminum, was also given the same heat treatment as PE16.

Specimen Preparation

The specimens used for these studies are right solid cylinders 10 mm long by 4.7 mm diameter lapped on their end faces to permit accurate length measurements to be made. The materials used were generally in the form of swaged bar. The heat treatment was carried out in evacuated silica capsules after specimen manufacture but prior to the final lapping process, except for the Type 316 specimens, which were machined axially from the wall of already heat-treated, thick-walled tubing.

Irradiation

Irradiation was carried out in a gamma-heated rig in a pitch 13 position in the core of DFR. The specimens were sealed in helium-filled container tubes, and, by a process of measurement and re-irradiation, data were obtained after peak doses of 13 and 30 atomic displacements per

TABLE 1—*Chemical analysis.*

Material	M316	FV 548	321	347	G 68	316	316L	PE16 (1)	PE16 (2)	PE16 (3)	GAB 286
Analysis weight %											
C	0.035	0.09	0.11	0.078	0.058	0.058	0.01	0.057	0.026	0.06	0.039
Si	0.63	0.36	0.74	0.65	0.83	0.51	0.61	0.19	0.18	0.27	0.13
Mn	1.85	1.17	0.97	0.90	1.56	1.47	1.28	0.13	0.2	0.02	0.1
Cr	17.2	17.0	17.5	17.8	13.7	17.8	16.4	16.6	15.4	16.5	16.0
Ni	13.7	11.6	9.5	9.1	25.0	12.2	13.6	43.0	40.3	43.3	42.6
Mo	2.41	1.4	0.45	0.49	1.21	2.34	2.14	3.4	2.9	3.31	3.0
Cb	...	1.09	<0.02	1.10	<0.05	<0.05	...	...	0.04	...	...
Fe	balance	balance	balance	balance	balance	balance	balance	balance	balance	balance	balance
S	0.006	0.011	0.028	0.010	0.005	0.005	0.01	...	0.007	0.005	0.006
P	0.008	0.009	0.032	0.024	0.028	0.026	0.005	...	0.005	...	0.002
B	<0.0006	0.002	0.0004	0.0007	0.0035	0.0023	0.0001	0.0029	0.0029	0.0050	0.0022
Co	0.014	0.026	0.11	0.031	0.19	0.11	...	0.049	0.009	0.12	0.02
Cu	...	...	...	...	...	...	...	...	0.01	0.03	0.01
Ti	...	<0.02	0.44	0.01	0.49	0.063	...	1.31	1.10	1.27	0.35
Mg	...	...	...	...	...	...	...	...	...	...	...
W	...	...	...	...	...	...	...	...	...	...	...
V	...	...	...	...	...	...	...	...	0.05	...	0.04
Al	...	...	...	...	...	...	...	1.23	1.5	1.08	0.22
N	0.024	0.019	0.016	0.045	0.92	0.023	...	0.011	0.0095	...	0.005
O	...	...	...	...	0.0045	...	...	...	...	...	...

atom (dpa); each specimen, therefore, was irradiated and measured twice. Displacement doses were calculated using the Norgett Robinson and Torrens model [4]. (The displacement energy used for these calculations is 40 eV.) The calculated neutron fluences are 2.26 and 5.02 $\times$ 10^{22} neutrons (n) $cm^{-2} > 0.1$ MeV, respectively.

Temperature was derived from the isochronal annealing behavior of silicon carbide. Toward the end of the second irradiation the specimen temperature fell to ~450°C (842°F), but the temperature quoted is believed to be representative of ~80 percent of the total dose received. Nevertheless, because all the alloys were irradiated together in the same rig they all experienced the same temperature history, and therefore the temperature changes should not prejudice comparisons between the alloys.

Measurement of Volume Swelling

The length of each specimen was measured before and after each irradiation cycle to an accuracy of ±0.003 percent. The measurements were supplemented by immersion density determinations from which it has been found that all specimens undergo an initial length shrinkage of ~0.2 percent at constant density [5] prior to the onset of isotropic void swelling. This means that volume swelling cannot be derived from the simple cubic relationship

$$\frac{\Delta V}{V_0} = \left(1 + \frac{\Delta L}{L_0}\right)^3$$

where $\Delta V/V_0$ and $\Delta L/L_0$ are the fractional volume and length changes, respectively, but by the more complex relationship

$$\frac{\Delta V}{V_0} = 0.0062 + 0.96\left[\left(1 + \frac{\Delta L}{L_0}\right)^3 - 1\right]$$

This equation has been used to convert the measured length changes to volume swelling for each alloy, and these data (four to six values for each alloy) have been fitted to the linear swelling equation

$$\frac{\Delta V}{V_0} = A(D - D_0)$$

where D is the displacement dose dpa, and A and D_0 are material constants.

A linear swelling equation with dose was chosen in preference to a

power law because no improvement in fit was obtained using a power law. The values obtained for A and D are given in Table 2.

TABLE 2—*Values of constants* A *and* D_0 *in the swelling equation.*

$$\frac{AV}{V}\% = A(D - D_0)$$

Irradiation Temperature 600°C (1112°F)

Material	A, % per dpa	D_0, NRT	Material	A, % per dpa	D_0, NRT
347	0.77	23.1	G68	0.25	25.3
321	0.49	23.2	PE16(1)	0.08	26.3
FV 548	0.71	21.6	PE16(2)	0.06	20.0
316	0.48	20.9	PE16(3)	0.09	20.0
M316	0.40	21.6	GAB 286	0.07	20.0
316L	0.25	11.5	...	...	...

Discussion of Results

It is the object of this paper to determine whether a relationship exists between the constitution of the alloys and their swelling. Harries [*3*] has suggested that the constitution of the matrix is an important parameter; therefore it has been necessary to compute the matrix composition. This has been achieved by making allowance for the precipitation of carbides and gamma prime by a process similar to that used in the PHACOMP calculations of Woodyatt, Sims, and Beattie [*6*].

Carbide Precipitation

Two types of carbide precipitate have been considered: monocarbides (of the compositions CbC, TiC, VC and WC) and chromium carbides (of the compositions $Cr_{23}C_6$ or, when molybdenum is present, $Cr_{21}Mo_2C_6$). The carbon was assumed to be partitioned in two ways:

(*a*) half to form monocarbides and half to form chromium carbide, or

(*b*) all the carbon initially to form monocarbides, but in understabilized steels, where the atomic concentration of carbon is greater than Ti + Cb + V + W, the remaining carbon partitioned to form chromium carbide.

Hence, for method (*b*) and for a columbium-stabilized steel containing no molybdenum, the columbium content of the matrix is

$$\text{weight \% Cb} - \frac{\text{weight \% C} \times \text{atomic weight Cb}}{\text{atomic weight C}}$$

and chromium content of the matrix is

$$\text{weight \% } C^* \times \frac{\text{atomic weight Cr}}{\text{atomic weight C}} \times \frac{23}{6}$$

where C* is that remaining after columbium-carbide precipitation. In the event, however, that the difference between the two methods has been insignificant in all the correlations examined, only the results given by method (*b*) are presented.

Gamma Prime Precipitate

Three compositions of gamma prime have been considered: Ni_3Ti, Ni_3Al and Ni_3Cb (presented separately to aid computation).

Hence, the nickel remaining in the matrix will be

$$\begin{aligned} \text{Ni} = \text{Ni} &- 3\,(\text{weight \% Ti}^*) \times \frac{\text{atomic weight Ni}}{\text{atomic weight Ti}} \\ &- 3\,(\text{weight \% Al}) \times \frac{\text{atomic weight Ni}}{\text{atomic weight Al}} \\ &- 3\,(\text{weight \% Cb}^*) \times \frac{\text{atomic weight Ni}}{\text{atomic weight Cb}} \end{aligned}$$

where Ti* and Cb* are the amounts remaining after precipitation of the mono-carbides TiC and CbC calculated earlier.

In this way the matrix composition is derived (scaled of course to 100 percent).

Swelling Against Equivalent Nickel Content

Figure 1 shows the swelling at 30 dpa and 600°C (1112°F) plotted against the equivalent nickel content, from which it can be seen that swelling tends to decrease with nickel content. Unlike the work of Bates and Guthrie [*1*], however, no trend was observed with equivalent chromium content. The equations used to derive the equivalent nickel and chromium contents of the matrix are as follows [*7*], where the weight percent of each element is that obtained after making allowance for precipitation as described in the foregoing

$$\begin{aligned} \acute{\text{N}}\text{i} = {} & \text{weight \% Ni} + \text{weight \% Co} + 0.5\ \text{weight \% Mn} + \\ & 30\ \text{weight \% C} + 0.3\ \text{weight \% Cu} + 25\ \text{weight \% N} \end{aligned}$$

$$\begin{aligned} \acute{\text{C}}\text{r} = {} & \text{weight \% Cr} + 2\ \text{weight \% Si} + 1.5\ \text{weight \% Mo} + \\ & 5\ \text{weight \% V} + 5.5\ \text{weight \% Al} + 1.75\ \text{weight \% Cb} + \\ & 1.5\ \text{weight \% Ti} + 0.75\ \text{weight \% W} \end{aligned}$$

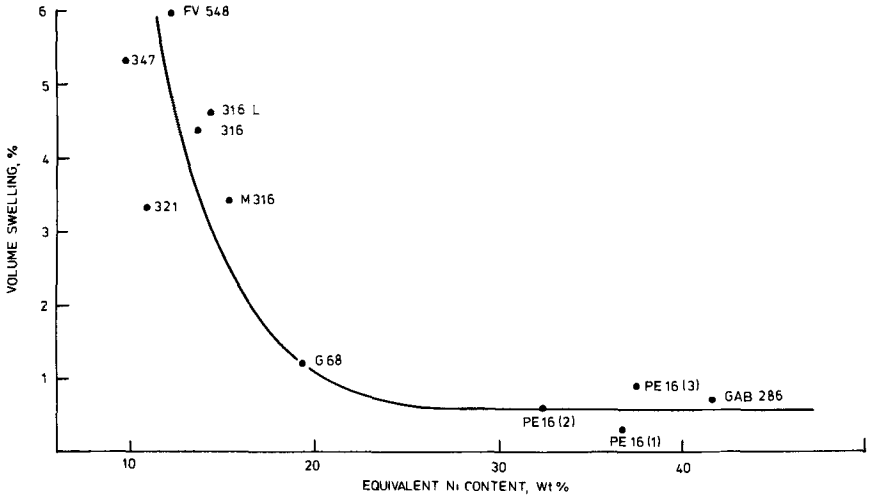

FIG. 1—*Volume swelling at 30 dpa and 600°C (1112°F) as a function of equivalent nickel content.*

Determination of the equivalent nickel and chromium contents of the alloys is a convenient method for the normalization of the minor alloying constituents onto nickel and chromium scales. For example, the normalization factor used for carbon on the equivalent nickel scale was 30, and this high value reflects the strong austenitizing influence of carbon in solution. This approach has been fully established for austenitic and ferritic steels but may not be justified for nickel-based alloys.

Swelling Against Sigma Phase

Examination of the equilibrium iron/chromium/nickel (Fe/Cr/Ni) ternary diagram at 650°C (1202°F) reveals that the residual matrix composition of most of the alloys studied lies within the two-phase $\gamma + \sigma$ region. Therefore it is not unreasonable, if Harries' hypothesis is true, to expect some correlation between swelling and σ-content of the steels such that swelling should increase with σ-content. In the absence of metallographic estimates of the sigma content in these alloys (the actual specimens having been returned to the reactor for further irradiation), values have been calculated for each alloy. In this calculation the equivalent nickel and chromium values calculated in the foregoing are positioned on the Fe/Cr/Ni equilibrium diagram and, using the "lever rule," an estimate of sigma content is obtained. Because no comprehensive Fe/Cr/Ni equilibrium diagram could be found at 600°C (1112°F), the 650°C (1202°F) diagram of Kinzel and Franks [*8*] was used but with the γ, $\gamma + \sigma$ boundary modi-

fied in accordance with the work of Cook and Brown [*9*]. The values so calculated for sigma content must only be treated as an indication of the propensity of the alloy to form sigma phase, because:

(*a*) the equilibrium diagram is approximate,

(*b*) irradiation itself might alter the phase boundaries and also cause precipitation of new phases [*10*], and

(*c*) the normalizing factors used to convert elements onto an equivalent nickel and chromium base are uncertain; for example, Pryce and Andrews [*11*] suggest that the potency of molybdenum can increase from 1 to 4 as molybdenum content increases to 3 weight percent.

Nevertheless, swelling tends to increase, as expected, with the calculated sigma content. In Fig. 2 the swelling at 30 dpa is plotted against the

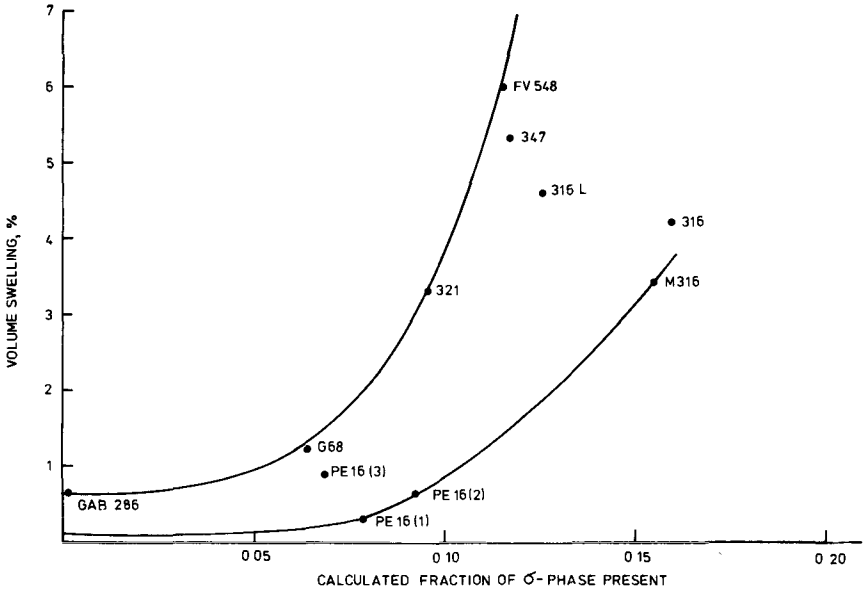

FIG. 2—*Swelling at 30 dpa and 600°C (1112°F) as a function of calculated sigma content.*

calculated fraction of sigma phase. The data lie within a band rather than being described by a unique relationship, and this could be associated with the uncertainties in the calculation mentioned earlier. The data lend general support, however, to Harries' suggestion that the formation of a second phase is deleterious.

The correlation observed by Bates and Guthrie [*1*] that the swelling decreases with increasing equivalent chromium content (that is, alloys with a greater propensity to form sigma phase) is not inconsistent with Harries' suggestion because their data were obtained at 390°C (734°F), at which temperature it is probable that little or no second phase will have

formed. The reduction in swelling with equivalent chromium content can thus be interpreted as being due to increasing solute content in the gamma matrix. Harries' hypothesis, however, would predict that the swelling at temperatures >550°C (1022°F) should increase with chromium content because the alloys are then likely to form a second phase and reduce the solute content of the matrix.

Swelling Against Electron Vacancy Concentration

Because of the uncertainties associated with the estimation of fractional-amount sigma phase present in the alloys after irradiation, a second approach has been used to determine the propensity of the matrix to form a second phase. In this approach, use is made of Pauling's [*12*] model for the electronic structure of the transitional elements and the fact that sigma phase can be regarded as an electron compound [*13*]. For this calculation, allowance is again made for the precipitation of carbides and gamma prime, and the electron vacancy concentration (N_v) is calculated using the equation

$$N_v = 4.66\,(\mathrm{Cr} + \mathrm{Mo}) + 3.66\mathrm{Mn} + 2.66\mathrm{Fe} + 1.7\mathrm{Co} + 0.66\mathrm{Ni}$$

where Cr, Mo, Mn, Fe, Co and Ni are the atomic concentrations of chromium, molybdenum, manganese, iron, cobalt, and nickel. The values used for the number of electron vacancies per atom for each element are those suggested by Pauling, except for molybdenum, where a value similar to that of chromium is used as suggested by Rideout [*14*]. It is argued that because molybdenum follows chromium in the same column of the periodic table it might be assumed that the electron vacancies in the 4-d sub-band equate to those of the 3-d sub-band. Figure 3 shows the swelling of the alloys at 40 dpa and 600°C (1112°F) plotted against the electron vacancy concentration N_v.

It can be seen that a good correlation exists between swelling and the calculated electron vacancy concentration for values above 2.58 (a figure close to the 2.52 value derived by Woodyatt et al [*6*] for the appearance of sigma phase in high-nickel alloys). The critical value of 2.58 electron vacancies per atom has been deduced from the data by fitting a linear relationship to the swelling against N_v when $N_v > 2.5$ and by assuming that swelling is constant at 0.62 when $N_v < 2.5$. The correlation coefficient for swelling against electron vacancy concentration when $N_v > 2.5$ is 0.82 (that is, the correlation is significant at the 5 percent level, using 7 data points) compared with a correlation, coefficient of 0.5 (which is not significant at the 10 percent level) for swelling against σ-content. Therefore, it is concluded that this second approach offers a much more reliable method of correlating swelling.

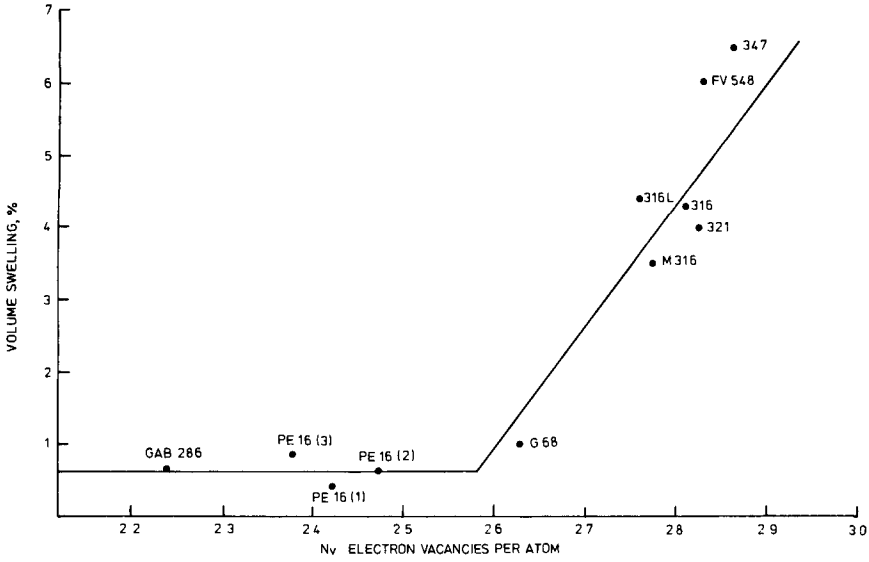

FIG. 3—*Swelling at 30 dpa and 600°C (1112°F) against electron vacancy concentration.*

As a further test of this correlation—in the absence of another similarly comprehensive data set from reactor irradiations—the results of the 5-MeV nickel ion irradiations of Johnston et al [*2*] have been assessed. Figure 4 shows these data for the swelling of a range of alloys irradiated at 625°C (1157°F) to 140 dpa plotted against equivalent nickel content. They show a trend similar to the present results with swelling falling with equivalent nickel content, but, when the results are plotted against calculated sigma content, no obvious correlation can be detected (Fig. 5). This lack of a correlation with sigma content is hardly surprising because the irradiation time was only ~8 h and sigma phase is notoriously slow in formation, even allowing for the fact that about half these alloys were aged at 593°C (1098°F) for 200 h, to simulate in-service conditions. However, when these data are plotted against the electron vacancy concentration calculated as described in the foregoing, a correlation is obtained (Fig. 6) which is as good as that found for the neutron data. The correlation coefficient is 0.77 (that is, the correlation is significant at the 1 percent level, using 10 data points). These results also suggest a critical value for N_v in commercial alloys of ~2.5 electron vacancies per atom above which significant swelling is observed and below which swelling is small or insignificant. An interesting feature of Johnston's results is that the four "base alloys" (alloys manufactured from high-purity starting material) indicate a critical value of N_v which is approximately 0.3 electron vacancies per atom less than that for commercial materials. The correlation for

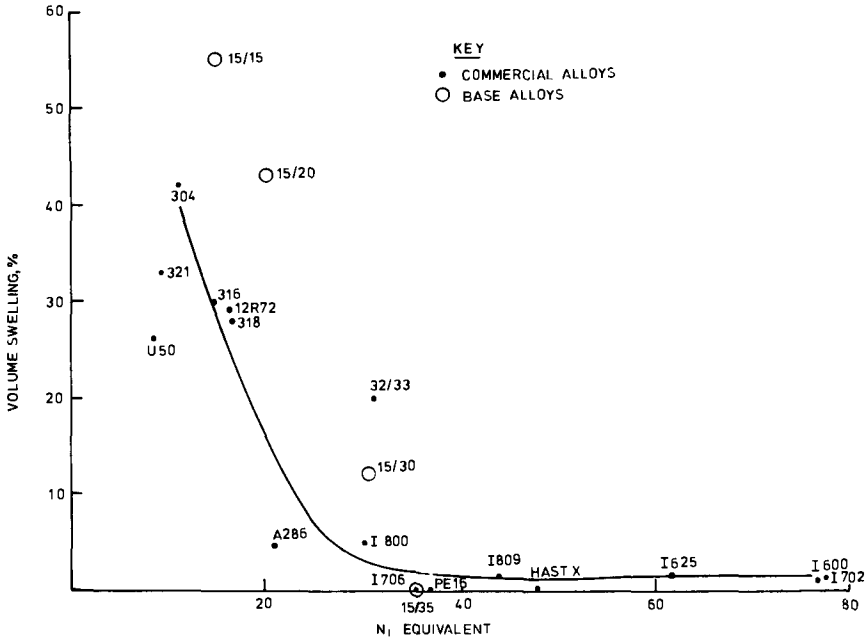

FIG. 4—*Swelling against equivalent nickel content [Johnston's 5-MeV nickel ion irradiations at 625°C (1157°F) and 140 dpa].*

the four base alloys of swelling with N_v must be treated with some reservation because it might only be a reflection of the fact that N_v decreases linearly with nickel content at constant chromium content. If true, however, then the difference between the two lines (the line for high-swelling commercial alloys and that for the base alloys) could be associated with minor alloying elements such as silicon and phosphorus.

General Discussion

The starting point for the interpretation of the high-temperature swelling behavior in this paper was Harries' suggestion [*3*] that sigma phase formation would have an important effect on swelling. Sigma-free alloys should, it was thought, be less prone to swelling than those which contain that phase. It has been shown, however, that there is a better correlation between swelling and electron vacancy concentration than with sigma content for the neutron data and for the 5-MeV nickel ion data. The sigma content was estimated using experimentally derived multiplying factors to determine the equivalent nickel and chromium contents and from an experimentally derived phase diagram. And it was the realization that such a procedure might be inaccurate that led to the study of electron

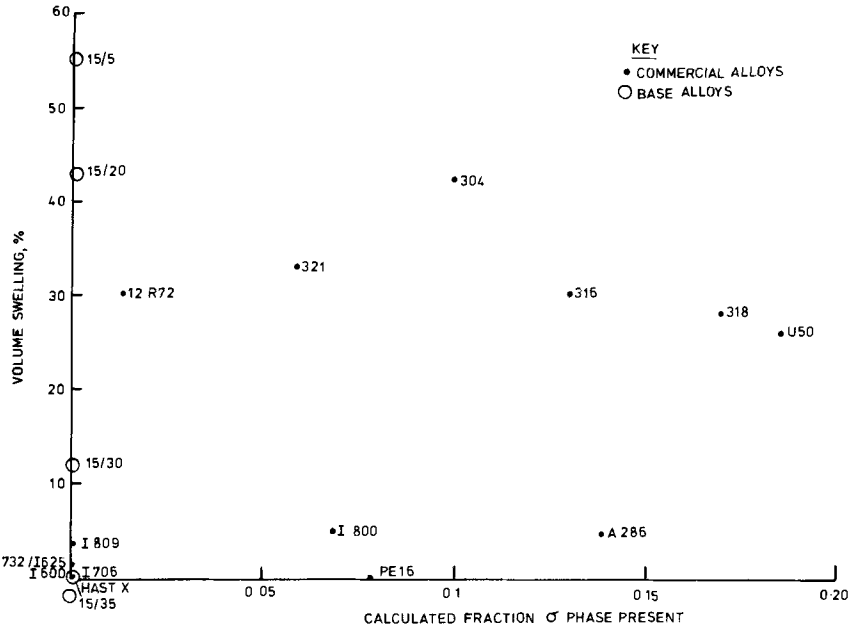

FIG. 5—*Swelling against calculated sigma content [Johnston's 5-MeV nickel ion irradiations at 625°C (1157°F) and 140 dpa].*

vacancy concentration as an alternative means of estimating sigma-forming tendency. The resulting correlations are remarkably good, particularly in the case of our own data for materials irradiated at high temperatures, and strongly suggest that a mechanism of basic importance has been identified.

It may be, of course, that the electron vacancy concentration is merely a more precise reflection of the sigma content of the alloys than is the estimate derived from the phase diagram. Alternatively, there may be an intrinsic effect of electron vacancy concentration upon some important property of the austenite matrix itself. For example, if a low electron vacancy concentration reduces the diffusion coefficients for irradiation-induced interstitials and vacancies, then it would be equivalent to a reduction in the temperature of irradiation and, by increasing the tendency for point defects to recombine on the lattice, it would produce the observed reduction in swelling. Another possibility is that raising the electron vacancy concentration causes the formation not only of sigma (perhaps in amounts equal to those here inferred from analysis of the phase diagram) but also of other electron compounds. These latter might share with sigma phase a tendency to absorb impurities whose presence in the gamma phase would have conferred swelling resistance. Metallography will help to distinguish between these hypotheses.

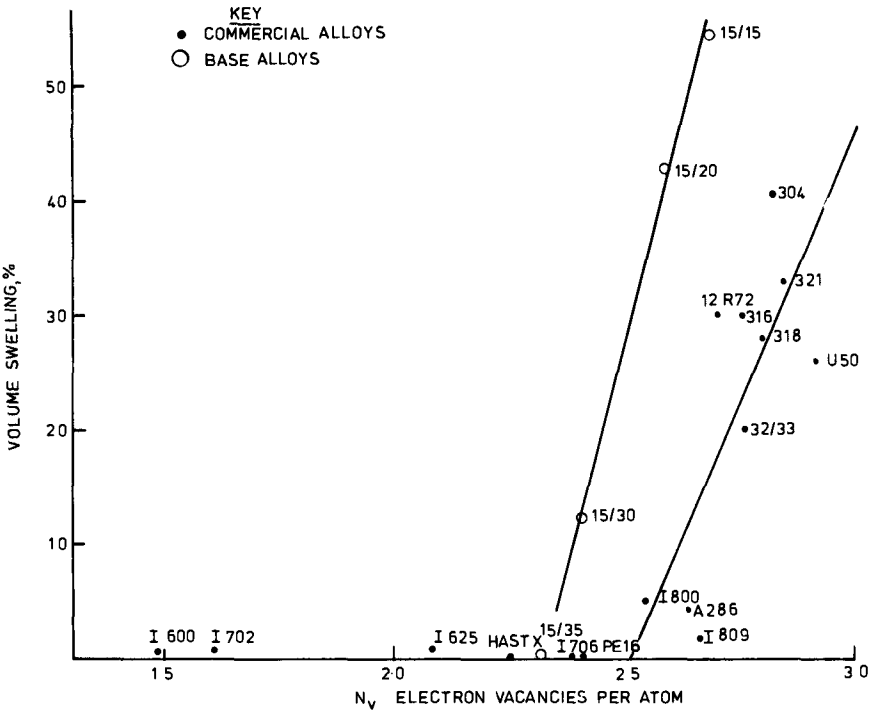

FIG. 6—*Swelling against electron vacancy concentration [Johnston's 5-MeV nickel ion irradiations at 625°C (1157°F) and 140 dpa].*

Whatever the scientific reason for the correlation between swelling and electron vacancy concentration, its practical utility as a means of selecting materials of low swelling content is very clearly established by the analysis reported here. Experiments are in progress to explore the swelling of materials of varying electron vacancy concentration at high fluences to see if the trend is maintained.

Conclusions

The results reported here for the swelling of some austenitic stainless steels and nickel alloys irradiated at 600°C (1112°F) in the DFR lend general support to the recent suggestion of Harries [*3*] that swelling in austenitic and nickel-based alloys could be influenced by elements in solid solution. The swelling at 30 dpa has been shown to increase with the calculated equilibrium fraction of sigma phase.

A superior correlation has been shown to exist between the swelling and calculated electron vacancy concentration of the matrix, and a value of 2.58 electron vacancies per atom has been observed above which swelling

increases rapidly and below which swelling is small. The concept of a critical value of electron vacancy concentration has been shown to be consistent with the 5-MeV nickel ion irradiations of Johnston et al [2] and, also, that it offers a suitable approach for the design of new alloys with potentially low swelling characteristics.

Acknowledgments

The author wishes to thank J. H. Gittus and J. Standring and J. E. Palentine for useful discussion—the latter for the development of a computer code to calculate equivalent chromium and nickel contents, sigma content, and electron vacancy concentration—and W. N. Miller for his statistical assessment of the correlations.

References

[1] Bates, J. F. and Guthrie, G. L., "A Relationship Between Equivalent Chromium Content and Irradiation-Induced Swelling in Type 316 Stainless Steel," *Nuclear Technology,* Vol. 27, Oct. 1975.

[2] Johnston, W. G., Rosolowski, J. H., and Turakalo, A. M., "An Experimental Survey of Swelling in Commercial Fe-Cr-Ni Alloys Bombarded with 5 MeV Ions," *Journal of Nuclear Materials,* Vol. 54, 1974, pp. 24–40.

[3] Harries, D. R., "Void Swelling in Austenitic Steels and Nickel Based Alloys. Effects of Alloy Constitution and Structure," *Proceeding* of the Consultants Symposium, AERE Report 7934, Harwell, Sept. 1974.

[4] Norgett, H. J., Robinson, M. T., and Torrens, I. M., "A Proposed Method of Calculating Displacement Dose Rates," *Nuclear Engineering and Design,* Vol. 33, 1975, pp. 50–54.

[5] Watkin, J. S., "Some Effects of Fast Reactor Irradiation on the Dimensions of Cladding Alloys," *Proceeding* of the European conference on Irradiation Behaviour of Fuel Cladding and Core Components, BNES/KGDA, Karlsruhe, 3–5 Dec. 1974.

[6] Woodyatt, L. R., Sims, C. T., and Beattie, H. J., "The Prediction of Sigma-Type Phase Occurrence from Compositions in Austenitic Superalloys," *Transactions,* Metallurgical Society of AIME, Vol. 236, April 1966.

[7] Briggs, J. Z. and Parker, T. D., "The Super 12% Cr Steels," Climax Molybdenum Co., 1965.

[8] Kinzel, A. B. and Franks, R., *The Alloys of Fe and Cr,* 1st ed., Vol. II, McGraw-Hill, New York, 1940.

[9] Cook, A. J. and Brown, B. R., "The Constitution of Fe, Ni, Cr Alloys at 550°C–800°C," *Journal of the Iron and Steel Institute,* Aug. 1952.

[10] Hudson, J. A., "Structural Stability During Irradiation," *Journal of British Nuclear Energy Society,* Vol. 14, No. 2, April 1975.

[11] Pryce, L. and Andrews, K. W., "Practical Estimation of Composition Balance in Ferrite Content in Stainless Steels," *Journal of the Iron and Steel Institute,* Aug. 1960.

[12] Pauling, L., "The Nature of the Interatomic Forces in Metals," *Physical Review,* Vol. 54, 1938.

[13] Hume-Rothery, W. and Raynor, G. V., *The Structure of Metals and Alloys,* The Institute of Metals, 1956.

[14] Rideout, S., Manly, W. D., Kamen, E. L., Lement, B. S., and Beck, P. A., "Intermediate Phases in Ternary Alloy Systems of Transition Elements," *Journal of Metals,* Oct. 1951.

D. J. Michel,[1] *P. L. Hendrick,*[2] *and A. G. Pieper*[1]

Microstructure and Mechanisms of Ion-Simulated Irradiation-Induced Creep of Nickel

REFERENCE: Michel, D. J., Hendrick, P. L., and Pieper, A. G., "**Microstructure and Mechanisms of Ion-Simulated Irradiation-Induced Creep of Nickel,**" *Irradiation Effects on the Microstructure and Properties of Metals, ASTM STP 611,* American Society for Testing and Materials, 1976, pp. 284–297.

ABSTRACT: The microstructure of cold-worked, high-purity nickel has been investigated following ion-simulated irradiation-induced creep with 22-MeV deuterons and 70-MeV α-particles. The irradiations were conducted at 224°C (435°F), at stresses between 170 and 345 MPa, and at displacement rates between 13 and 30 $\times$ 10^{-8} displacements per atom per second (dpa/s). Transmission electron microscopy (TEM) procedures were used to prepare, observe, and photograph the microstructure of the ion-irradiated uniaxial creep specimens and companion unirradiated specimens.

Examination of the ion-irradiated microstructure revealed no substantial differences between the deuteron and α-particle irradiated specimens. In all cases, a heterogeneous distribution of defect clusters or small dislocation loops and network dislocations, or both, were observed. A significant reduction in dislocation density from the unirradiated values was seen for the irradiated specimens. It was found that the small loops and defect clusters provided effective obstacles to dislocation motion as evidenced by the bowing of dislocations between adjacent defects.

The microstructural results were evaluated in terms of the theoretical mechanisms proposed for irradiation-induced creep and the previously reported creep simulation results for nickel by Hendrick et al. A model based on the climb-controlled glide of dislocations over dispersed obstacles was found to be consistent with the microstructural results and the experimental creep data.

KEY WORDS: radiation, irradiation, nickel, dislocations, electron microscopy, microstructure, radiation damage simulation, radiation effects, ion irradiation, ion simulation, radiation creep, creep mechanisms

The dimensional stability of structural materials is of major importance in the design of breeder and, in the future, controlled thermonuclear

[1] Research metallurgist and physicist, respectively, Naval Research Laboratory, Washington, D.C. 20375.

[2] Research scientist, Battelle Memorial Institute, Pacific Northwest Laboratories, Richland, Wash. 99352.

reactors. One of the critical parameters to be considered in the evaluation of dimensional stability is irradiation-induced creep. However, despite considerable recent effort to develop theoretical models of irradiation-induced creep [*1–6*],[3] the difficulties of performing in-reactor creep experiments have severely limited the quantity of experimental data available to test the models. Furthermore, the simultaneous effects of external stress and irradiation on the microstructure of materials are poorly understood [*7*].

The lack of prototypical irradiation test facilities for in-reactor creep experiments coupled with the necessity for careful control of all experimental variables motivated the development of techniques for the ion-simulation of irradiation-induced creep. While several experiments have demonstrated that ion simulation can be applied to investigate irradiation-induced creep in several materials [*8–11*], recent experiments have shown that ion simulation can be successfully applied to produce irradiation-induced creep in materials whose thickness is characteristic of proposed breeder fuel cladding material [*12*]. However, the mechanisms responsible for the observed ion-simulated irradiation-induced creep behavior have not been fully evaluated and the relationship of the ion-simulation results to in-reactor data is poorly known [*12,13*].

The purpose of the present work was to characterize the microstructure of high-purity nickel following ion-simulated irradiation-induced creep [*12*] to determine the simultaneous effects of applied stress and ion irradiation. The microstructural results were then examined in terms of the observed creep behavior and possible mechanisms of irradiation-induced creep. The results show that a model for the climb-controlled glide of network dislocations is in good agreement with the observed creep behavior.

Experimental Procedures

Detailed descriptions of the material history and composition, experimental technique, specimen design, and the irradiation-induced creep results for the nickel specimens used in this work have been previously reported [*12–14*]. Briefly, 0.38-mm-thick uniaxial tension specimens of 95 percent cold-worked, 99.995 percent nickel were maintained at a temperature of 224°C (435°F) in vacuum while stressed from 170 to 345 MPa. Simultaneously, the specimens were irradiated with either 22-MeV deuterons or 70-MeV α-particles at displacement rates between 13 and 30×10^{-8} displacements per atom per second (dpa/s) to fluence levels from 0.01 to 0.04 dpa. Instantaneous specimen length was monitored by three linear variable differential transformers (LVDT's). Through careful

[3] The italic numbers in brackets refer to the list of references appended to this paper.

control of experimental variables, the creep rate as a function of applied stress and ion flux was measured. It was also shown that, for the test conditions employed, negligible thermal creep occurred.

Transmission electron microscopy (TEM) disks were prepared from the gage section of the creep specimens using electrical-discharge cutting techniques. Similar disks were obtained from unirradiated end-tab areas of the creep specimens as well as from as-received specimen material. Since preliminary studies indicated that foils prepared directly from the 0.38-mm specimen thickness did not contain sufficient thin area for quantitative microscopy, careful low-speed, water-cooled grinding procedures were used to reduce the thickness of the TEM disks to approximately 0.19 mm. During preparation of the disks from the specimen gage section, the grinding was done uniformly from both the front and rear surfaces of the specimen.

The TEM disks were thinned using a twin-jet electropolishing technique [*15*] and a 9:1 (by volume) acetic-perchloric electrolyte. The thin foils were examined in a JEM 200A electron microscope operated at 200 kV and equipped with a double-tilt goniometer stage. During TEM examination, the irradiated disks were oriented such that the direction of applied stress was coincident with the goniometer x-tilt axis.

The dislocation density and cell diameters were determined by previously described line intercept methods [*16*]. The dislocation density measured was the average density of the network dislocations as opposed to the localized density of the dislocation cell walls. Weak-beam, dark-field procedures were employed to observe the defect clusters (presumed to be unresolvable dislocation loops) and dislocation loops in the irradiated specimens whenever possible. However, the highly deformed nature of the specimens coupled with the small defect cluster/dislocation loop size prevented the use of the weak-beam, dark-field method in all cases. The defect cluster/loop sizes and distributions were evaluated from enlarged micrographs using a particle size analyzer. In addition, individual size measurements were made from the central region of highly enlarged micrographs to confirm the results from the particle size analyzer. Foil thickness was determined using dynamical stereomicrographs. At least three thickness determinations were used to compute the dislocation and defect cluster/loop densities for each specimen. These values are believed to be accurate to only within ± 50 percent due to the high density of defects and initial deformation structure.

Results

Examination of TEM specimens prepared from unirradiated, as-received nickel stock material and from unirradiated portions of the creep specimens indicated a deformation microstructure characteristic of severely

cold-worked material. Small dislocation cells, deformation bands, and slip traces were observed in most cases. A typical example of the dislocation cell structure is shown in Fig. 1*a*. The dislocation density of the cell wall was estimated to be $>1 \times 10^{13}$ cm/cm^3. Small dislocation loops were occasionally observed within the cell interiors in these specimens, Fig. 1*b*.

The TEM evaluation of the irradiated microstructures revealed no substantial difference between the deuteron and α-particle irradiated specimens. A heterogeneous distribution of small defect clusters, dislocation loops, individual dislocations, and larger dislocation cells with reduced cell wall dislocation densities ($\sim 10^{11}$ cm/cm^3) was distinctly visible in all specimens. Typical examples of the defect cluster/dislocation loop structure and network dislocations are shown in Fig. 2*a* and *b*. In both, the pinning of individual dislocations by the defect clusters/dislocation loops can be seen. In certain specimens, resolvable dislocation loops were observed as shown in Fig. 2*c* and *d*. Repeated attempts to deduce the character of these loops by weak-beam, dark-field stereo methods [*17*] and bright-field tilting procedures [*18*] were inconclusive due to the small loop size and high loop density. In certain specimens, limited evidence of loop orientation on {111} habit planes was observed. However, efforts to determine the extent, if any, of preferential loop alignment with respect to the applied stress direction were inconclusive.

The microstructural results from all specimens examined in this study are given in Table 1. It was noted that the defect cluster/dislocation loop diameters exhibited a very narrow distribution about the mean values given in the table. The normalized steady-state creep rates were computed from the experimental results in the manner described by Hendrick et al [*12*]. The microstructural results indicate that the combined effects of both ion irradiation and applied stress produced an increase in dislocation cell size with an accompanying net decrease in dislocation density. The defect cluster/loop size and density were found to vary inversely with the applied stress as shown in Fig. 3.

Discussion

The previously published ion-simulated irradiation-induced creep experimental results for the specimens examined in this work have shown that the stress dependence of the steady-state creep rate[4] was approximately quadratic ($\dot{\varepsilon} \propto \sigma^2$) and the flux dependence was approximately linear [*12,13*]. By comparison, it was shown that these results were in overall agreement, within experimental error, with previous ion-simulated irradia-

[4]The steady-state creep rate, as used in this study, may be temporal in nature (that is, specimens irradiated to higher fluence levels may exhibit lower values of steady-state creep rate due to hardening effects).

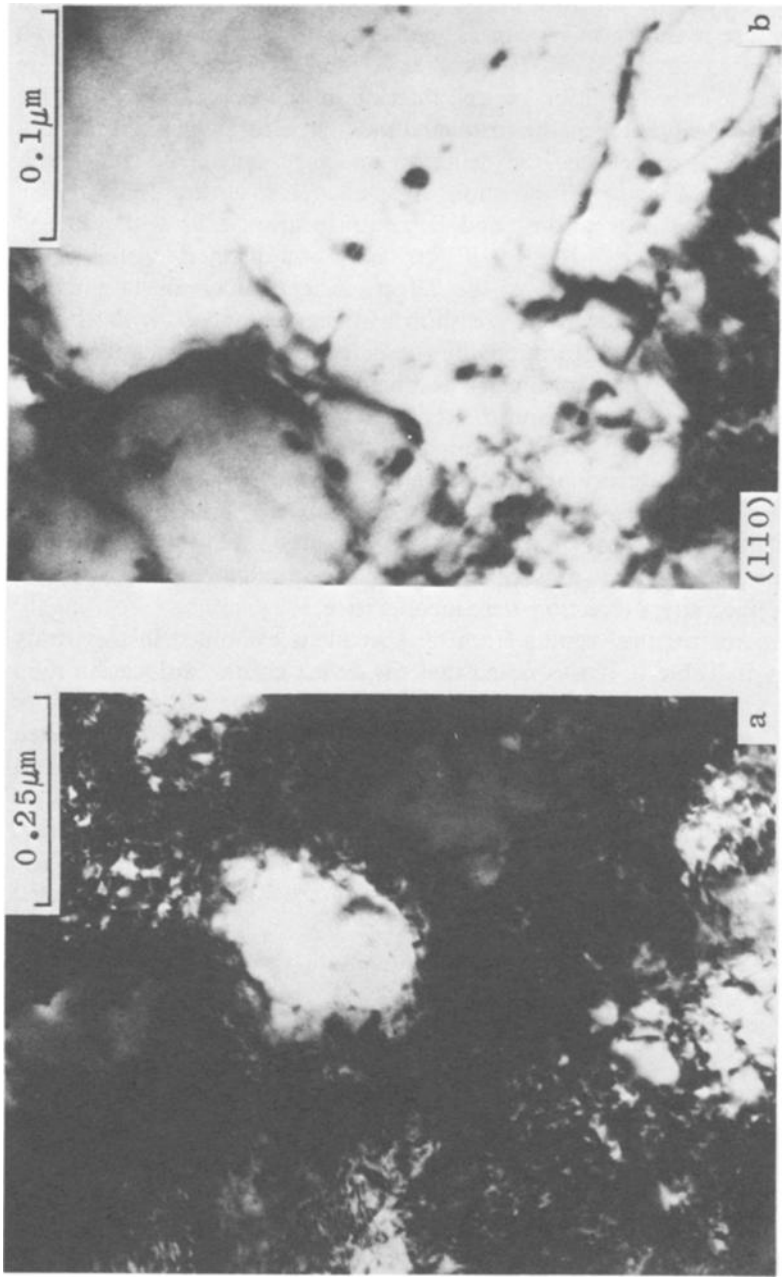

FIG. 1—*Microstructure of unirradiated nickel specimen material.* (a) *Dislocation cells characteristic of the cold-work level of the material.* (b) *Example of dislocation loops observed in the dislocation cell interior.*

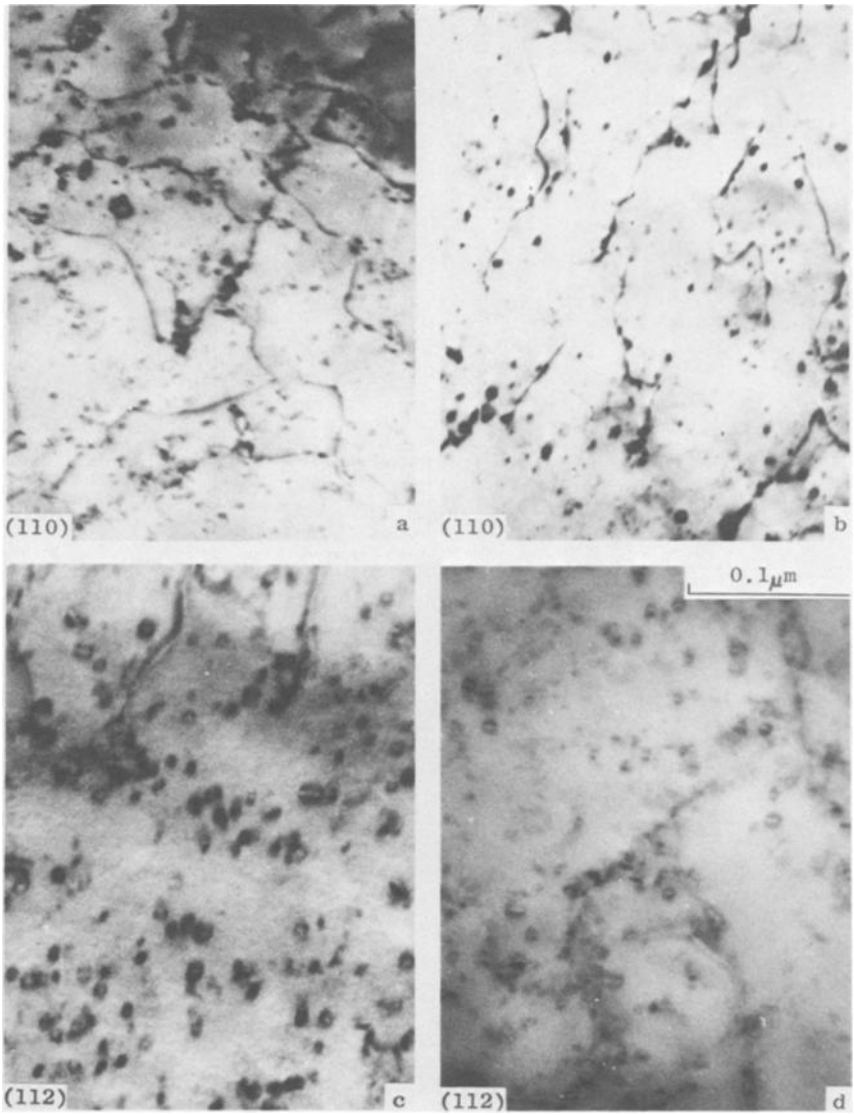

FIG. 2—*Microstructure of ion-simulated irradiation-induced creep specimens. The direction of applied stress in all micrographs was left to right within the plane of the paper.* (a) *and* (b) *Defect cluster/dislocation loop structure and network dislocations. Note the pinning of individual dislocations by the defect clusters/dislocation loops.* (c) *and* (d) *Distinct dislocation loops observed in Specimen 4D-2-5.*

TABLE 1—*Summary of ion-simulated irradiation-induced creep test and microstructure results.*

Material No.-Specimen No.-Test No.[a]	Irradiation Test Temperature,[a] °C	Stress,[a] MPa	Displacement Rate[a] $\times 10^8$, dpa/s	Fluence[b] $\times 10^2$, dpa	Steady-State Creep Rate $\times 10^5$, h^{-1}	Normalized Steady-State Creep Rate[a] $\times 10^2$, dpa^{-1}	Defect Cluster/Loop Number Density, #/cm^3	Mean Defect Cluster/Loop Diameter, Å	Dislocation Density, cm/cm^3	Mean Dislocation Cell Diameter, μm
4D-2-5	224	345	30.40	3.6	4.3	4.9	1.6×10^{16}	46	3.6×10^{10}	0.82
4D-3-2	224	170	30.40	1.6	1.2	1.4	2.5×10^{16}	58	3.4×10^{10}	1.20
4D-4-2	224	345	27.17	2.3	4.8	4.9	1.4×10^{16}	43	3.2×10^{10}	0.85
4D-5-2	224	345	13.53	0.9	2.7	5.5	2.0×10^{16}	42	2.8×10^{10}	1.00
4E-1-2	224	170	27.17	1.9	1.8	1.8	2.2×10^{16}	52	3.6×10^{10}	1.20
4E-2-2	224	207	27.17	2.1	1.4	1.4	3.0×10^{16}	67	3.5×10^{10}	1.15
4E-4-2	224	247	27.17	1.7	2.6	2.7	1.8×10^{16}	50	2.9×10^{10}	1.10
4D	...	unirradiated, unstressed material			...	...	$<10^{13}$	~30	$>2 \times 10^{11}$	~0.28

[a] Data from Ref *12*.
[b] Includes particle factor (Ref *12*).

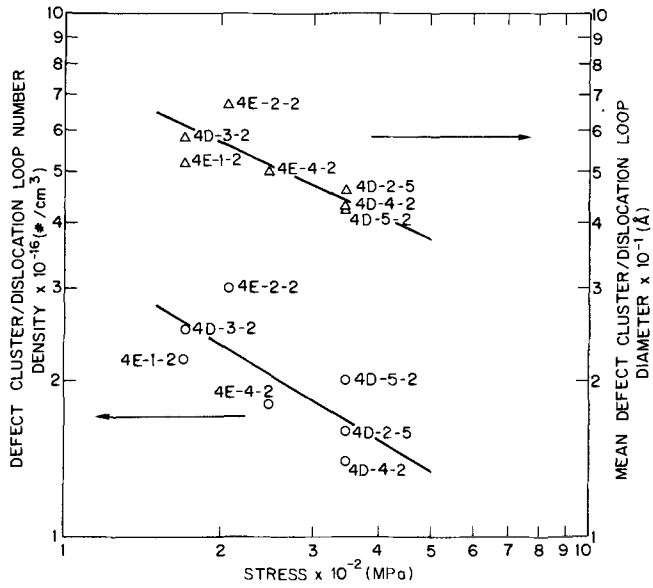

FIG. 3—*Stress dependence of defect cluster/dislocation loop number density and mean diameter.*

tion-induced creep results for nickel obtained by Hendrick et al [*11,19*] using 3.0- and 5.25-MeV protons. Other simulation results reported by Harkness et al [*10*] for austenitic stainless steel show a stress dependence of the creep rate between one and two at stresses and homologous temperatures comparable to those used for the nickel experiments. Although no microstructural data were obtained in the previous studies for comparison with the present results, the experimental data in all cases suggest that irradiation-induced climb-controlled glide could be responsible for the observed creep behavior.

Several climb-controlled glide creep models have been published by Harkness et al [*20,21*] and by Wolfer et al [*22,23*] to account for the climb of dislocations over dispersed obstacles by the absorption of irradiation-induced point defects. Depending on the parameters chosen, the models predict a squared stress dependence of the irradiation-induced creep rate at high stresses and a linear stress dependence at low stresses [*22,23*]. A climb-controlled glide mechanism is entirely consistent with the microstructural results obtained in this study in view of the decreased dislocation density produced by irradiation-induced dislocation climb and the observation that defect clusters/dislocation loops were apparently effective as barriers to dislocation motion.

The agreement between the climb-controlled glide mechanism and both the previous experimental results and the present microstructural observa-

tions for the same nickel specimens was analyzed by computing the steady-state creep rate on the basis of the microstructural data. For the case where a metallic material is undergoing irradiation, the steady-state defect concentrations may be calculated according to the models proposed by Brailsford and Bullough [*1,24*] using the defect balance equations

$$K - D_i C_i k_i^2 - \alpha C_i C_v = 0 \tag{1}$$

$$K' - D_v C_v k_v^2 - \alpha C_i C_v = 0 \tag{2}$$

where K is the atomic displacement rate, K' the effective defect generation rate (that is, the displacement rate augmented by vacancy emission from sinks), C_i and C_v the concentrations of interstitials and vacancies, D_i and D_v the diffusion coefficients for interstitials and vacancies, k_i^2 and k_v^2 the total strengths of fixed sinks for interstitials and vacancies, and α the recombination coefficient. The sink strengths were then expressed as

$$k_i^2 = Z_i \varrho_d \tag{3}$$

$$k_v^2 = Z_v \varrho_d \tag{4}$$

where ϱ_d is the dislocation density (network dislocations and loops), and Z_i and Z_v are the sink strengths for interstitials and vacancies. The dislocation cell walls were assumed to act as neutral sinks and their strength was estimated as $1/r_c^2$, where r_c is the cell radius. From the results in Table 1, their maximum strength is approximately 6×10^8 cm^{-2}, which is considerably less than that of the network dislocations and loops. Therefore, the effect of these sinks on the calculated creep rates was negligible. The interstitial and vacancy diffusion coefficients were calculated by

$$D_i = D_i^0 \exp(-E_i^m/kT) \tag{5}$$

$$D_v = D_v^0 \exp(-\mathrm{E}_v^m/kT) \tag{6}$$

where D_i^0 and D_v^0 are the diffusion pre-exponentials, E_i^m and E_v^m the activation energies for interstitials and vacancies, T the absolute temperature, and k Boltzmann's constant.

The creep rate, $\dot{\varepsilon}$, was evaluated according to the expression for climb-controlled glide [*22,23*]

$$\dot{\varepsilon} = \varrho_d^n b |v_c| (L/d) \tag{7}$$

where

ϱ_d^n = network dislocation density,

b = Burger's vector,
L = obstacle spacing, and
d = obstacle height.

The dislocation climb velocity, v_c, was evaluated from the expression for a stressed solid [3]

$$v_c = \frac{\sigma\Omega}{6(1 - \nu)bkT}(C_v D_v Z_v^s - C_i D_i Z_i^s) \tag{8}$$

where

σ = applied stress,
Ω = atomic volume,
ν = Poisson's ratio, and
Z_i^s and Z_v^s = dislocation bias for interstitial and vacancy capture under stress, respectively.

The thermal vacancy concentration term was not included in Eq 8 since preliminary calculations confirmed that it was negligible at the irradiation temperatures where the experimental data were obtained. For purposes of calculation, the material parameters for nickel given by Sprague et al [25] were used. The bias terms used were $Z_i = 1.01$ and $Z_v = 1.00$. The bias terms under stress were taken as $Z_i^s = -1.2$ and $Z_v^s = 2.7$ following Heald and Speight [3]. The obstacle spacing was determined from the loop density, N_l, and $L = \frac{1}{2}(N_l^{-1/3})$, and the obstacle height was taken as the defect cluster/loop diameter given in Table 1.

The creep rates computed from Eq 7 are compared in Fig. 4 with the experimental creep rates for the same specimens [12] as a function of stress. It can be seen that the creep rates calculated from the values in Table 1 are in reasonable agreement with the experimental results. The extremes of the vertical lines in Fig. 4 represent the creep rates calculated from the maximum and minimum observed defect cluster/dislocation loop diameters. The solid line through the experimental data points indicates a slope of two in accord with the results obtained by Hendrick et al [12]. In addition, the creep rates expected on the basis of the dislocation climb model of Wolfer and Ashkin [4] and the loop orientation model of Brailsford and Bullough [1] were computed using the same material and microstructural parameters. The creep rates from both of these models are several orders of magnitude below those calculated for the climb-controlled glide model and those observed experimentally. The calculations confirm that, of those models considered, only the climb-controlled glide model is in reasonable agreement with the steady-state ion-simulated irradiation-induced creep behavior observed in the present specimens. Evidence which supports this suggestion has been published recently by Wolfer [26], who shows that, for low fluence ($\lesssim 10^{22}$ neutrons

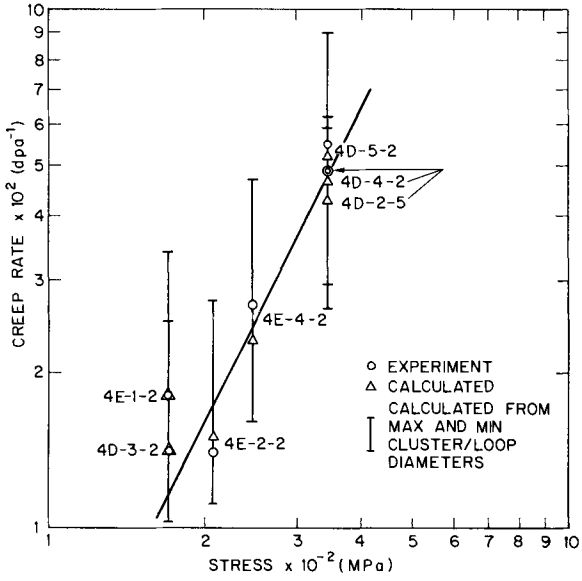

Fig. 4—*Stress dependence of calculated and measured ion-simulated irradiation-induced creep rate.*

(n)/cm²) and temperatures, the primary contribution to creep is provided by dislocation loops in agreement with the experimental data of Mosedale et al [*27*].

The quadratic dependence of creep rate on stress as calculated from the microstructural data results from both the linear dependence of the ratio of obstacle spacing to height, L/d, on stress, and from the stress term contained within the expression for climb velocity. The microstructural calculations predict a linear dependence of creep rate on flux, which results from the nearly linear relationship between atomic displacement rate and defect concentrations as given by Eqs 1 and 2, in agreement with the experimental results [*12*].

Previous calculations of creep rates using a climb-controlled glide model by Harkness et al [*20,21*] did not distinguish between the transient and steady-state neutron irradiation-induced creep, but predicted a decrease in creep rate with dose, reflecting the accumulation of defects with increasing fluence. Since the microstructural results obtained in the present study represent the defect parameters after steady-state creep was achieved, no effect of fluence on the creep rate was calculated. However, the experimental data given by Hendrick et al [*12*] for these specimens show that transient creep is essentially saturated at fluences greater than approximately 0.01 dpa. This evidence indicates that the initial accumulation of irradiation defects occurs very rapidly, and may continue to flu-

ence levels beyond those achieved experimentally to produce further growth of the defect clusters/dislocation loops. It is reasonable, therefore, to expect that climb-controlled glide will continue to operate at these higher fluences, but that the creep rate will diminish with the increase in defect cluster/dislocation loop size. When this occurs, other mechanisms may become dominant and provide the primary contribution to the creep rate.

Summary and Conclusions

The microstructure of high-purity nickel was characterized following ion-simulated irradiation-induced creep by 22-MeV deuterons and 70-MeV α-particles at 224°C (435°F). The principal microstructural features observed were defect clusters/dislocation loops and a decreased network dislocation density as compared with unirradiated material. The results were compared with previously reported experimental creep data for these specimens on the basis of a climb-controlled glide mechanism.

The following conclusions can be drawn from this work:

1. The effect of both ion irradiation and applied stress was to increase defect cluster/dislocation loop number density and size and dislocation cell diameter and to decrease network dislocation density. No evidence of preferential dislocation loop alignment with respect to the applied stress direction was observed.
2. The defect clusters/dislocation loops appeared to act as effective obstacles to network dislocation motion during steady-state irradiation-induced creep. This observation together with the decreased network dislocation density is consistent with a climb-controlled glide mechanism.
3. Calculations based on the microstructural results confirmed that a climb-controlled glide mechanism was in agreement with the squared stress dependence and linear flux dependence observed during ion-simulated irradiation-induced creep experiments.
4. Creep rates calculated from the microstructural results using dislocation climb and loop orientation models were several orders of magnitude less than those calculated for the climb-controlled glide mechanism.
5. The review of a limited number of ion-simulation and neutron irradiation-induced creep results suggests that climb-controlled glide should be a viable creep mechanism at low temperatures and fluences. It is expected that steady-state irradiation-induced creep begins upon stabilization of that part of the irradiated microstructure which contributes to transient creep.

Acknowledgments

The authors gratefully acknowledge the assistance of J. T. Atwell in the preparation and examination of the TEM specimens. The authors

thank J. A. Sprague for useful comments and for a critical review of the manuscript.

This work was supported by the Office of Naval Research at the Naval Research Laboratory. Support provided to co-author P. L. Hendrick, through the Pacific Northwest Laboratory of Battelle Memorial Institute by the Division of Physical Research, U.S. Energy Research and Development Administration, is acknowledged.

References

[1] Brailsford, A. D. and Bullough, R., *Philosophical Magazine*, Vol. 27, 1973, p. 49.
[2] Bullough, R. and Hayns, M. E., *Journal of Nuclear Materials*, Vol. 57, 1975, p. 348.
[3] Heald, P. T. and Speight, M. V., *Philosophical Magazine*, Vol. 29, 1974, p. 1075.
[4] Wolfer, W. G. and Ashkin, M., *Journal of Applied Physics*, to be published.
[5] Wolfer, W. G. and Ashkin, M., *Journal of Applied Physics*, Vol. 46, 1975, p. 547.
[6] Dollins, C. C. and Tucker, R. P., *Journal of Nuclear Materials*, Vol. 52, 1974, p. 277.
[7] Brager, H. R., Gilbert, E. R., and Straalsund, J. L., *Radiation Effects*, Vol. 21, 1974, p. 37.
[8] Buckley, S. N., "Irradiation Growth and Irradiation Creep in fcc and bcc Metals," AERE-R-5944, Atomic Energy Research Establishment, Vol. 2, 1968, p. 547.
[9] Bodde, D. L., "Irradiation-Induced Stress Relaxation and Creep in Reactor Materials," S.M. thesis, Massachusetts Institute of Technology, Cambridge, Mass., Feb. 1972.
[10] Harkness, S. D., Yaggee, F. L., and Nolfi, F. V., in *Irradiation Embrittlement and Creep in Fuel Cladding and Core Components*, British Nuclear Energy Society, London, 1972, p. 259.
[11] Hendrick, P. L., Bement, A. L., Jr., and Harling, O. K., *Nuclear Instruments and Methods*, Vol. 124, 1975, p. 389.
[12] Hendrick, P. L., Michel, D. J., Pieper, A. G., Surratt, R. E., and Bement, A. L., Jr. in *Proceedings* of International Conference on Radiation Effects and Tritium Technology for Fusion Reactors, Gatlinburg, Tennessee, 1975, to be published.
[13] Hendrick, P. L., "Ion Simulated Irradiation-Induced Creep," Ph.D. thesis, Massachusetts Institute of Technology, Cambridge, Mass., Sept. 1975.
[14] Hendrick, P. L., Michel, D. J., Pieper, A. G., Surratt, R. E., and Bement, A. L., Jr., *Nuclear Instruments and Methods*, Vol. 133, 1976, to be published.
[15] Schoone, R. D. and Fischione, E. E., *Review of Scientific Instruments*, Vol. 37, 1966, p. 1351.
[16] Michel, D. J., Moteff, J., and Lovell, A. J., *Acta Metallurgica*, Vol. 21, 1973, p. 1269.
[17] Mitchell, J. B. and Bell, W. L. in *Proceedings*, Thirty-Third Annual Meeting, Electron Microscopy Society of America, Claitor's Publishing Division, Baton Rouge, La., 1975, p. 160.
[18] Edmunson, B. E. and Williamson, G. F., *Philosophical Magazine*, Vol. 9, 1964, p. 277.
[19] Hendrick, P. L., "Proton Simulated Irradiation-Induced Creep," S.M. thesis, Massachusetts Institute of Technology, Cambridge, Mass., Feb. 1974.
[20] Harkness, S. D., Tesk, J. A., and Li, Che-Yu, *Nuclear Applications and Technology*, Vol. 9, 1970, p. 24.
[21] Harkness, S. D., Grappel, R., and McDonald, S. G., *Nuclear Technology*, Vol. 16, 1972, p. 25.
[22] Wolfer, W. G., Foster, J. P., and Garner, F. A., *Nuclear Technology*, Vol. 16, 1972, p. 55.
[23] Wolfer, W. G. and Boltax, A. in *Irradiation Embrittlement and Creep in Fuel Cladding and Core Components*, British Nuclear Energy Society, London, 1972, p. 283.
[24] Brailsford, A. D. and Bullough, R., *Journal of Nuclear Materials*, Vol. 54, 1974, p. 286.

[25] Sprague, J. A., Westmoreland, J. E., Smidt, F. A., Jr., and Malmberg, P. R., *Journal of Nuclear Materials,* Vol. 54, 1974, p. 286.
[26] Wolfer, W. G., *Scripta Metallurgica,* Vol. 9, 1975, p. 801.
[27] Mosedale, D., Lewthwaite, G. W., and Ramsey, I. in *Irradiation Embrittlement and Creep in Fuel Cladding and Core Components,* British Nuclear Energy Society, London, 1972, p. 233.

S. C. Agarwal,[1] *D. I. Potter,*[1] *and A. Taylor*[1]

Effects of Interstitial Solutes on the Microstructures of Self-Ion Irradiated Vanadium*

REFERENCE: Agarwal, S. C., Potter, D. I., and Taylor, A., **"Effects of Interstitial Solutes on the Microstructures of Self-Ion Irradiated Vanadium,"** *Irradiation Effects on the Microstructure and Properties of Metals, ASTM STP 611,* American Society for Testing and Materials, 1976, pp. 298–311.

ABSTRACT: Vanadium and vanadium containing 0.1 percent carbon, 0.4 percent carbon, 1.0 percent nitrogen, and 1.0 percent oxygen were irradiated with 3-MeV $^{51}V^{+}$ ions in the temperature range 650 to 880 °C (1202 to 1616 °F) to a dose level of ~20 dpa. The results show that nitrogen is most effective in controlling the void swelling. Carbon and oxygen also suppress the swelling considerably when compared with unalloyed vanadium. Except for vanadium-1.0 percent nitrogen, all compositions exhibit a fine platelet precipitate with {012} habit at 650 °C (1202 °F). In the case of vanadium-carbon alloys, this phase persisted even at higher temperatures. Vanadium and vanadium-1.0 percent oxygen showed fine precipitation on dislocations and void surfaces at 880 °C (1616 °F). Vanadium-0.1 percent carbon exhibited a metastable {013} carbide precipitate at 880 °C (1616 °F), whereas vanadium-0.4 percent carbon showed equilibrium V_2C phase with some {012} precipitates. This {012} precipitation was irradiation induced and was dependent upon the carbon concentration. Vanadium-1.0 percent nitrogen did not show any evidence of precipitation over the entire temperature range.

KEY WORDS: radiation wall materials, body-centered-cubic metals, interstitial solutes, radiation effects, swelling, voids, dislocations, metastable precipitation.

Strong effects of interstitial solutes on the irradiation-induced microstructure of body-centered-cubic (bcc) metals and alloys have recently been demonstrated in ion-bombardment experiments. For example, a reduction in the void swelling of dilute columbium-oxygen alloys compared with pure columbium has been reported [*1*],[2] and our preliminary studies indicated similar behavior in vanadium-oxygen alloys. The theoretical

*Work supported by the U. S. Energy Research and Development Administration.
[1]Materials Science Division, Argonne National Laboratory, Argonne, Ill. 60439.
[2]The italic numbers in brackets refer to the list of references appended to this paper.

calculation of Schilling and Schroeder [*2*], based primarily on vacancy trapping by interstitial solutes in bcc metals, also predicts significant suppression of swelling with solute content. In addition, irradiation may produce precipitates in alloys which, under thermal equilibrium, would not contain precipitates. Such irradiation-induced precipitates have been observed in ion-irradiated vanadium [*3,4*] and are thought to arise from very low concentrations of interstitial impurities.

To determine the effects of these interstitial solutes on the void swelling as a function of temperature, we have prepared and irradiated dilute binary alloys of vanadium containing known amounts of carbon, oxygen, and nitrogen. In addition, our early results suggested a correlation between irradiation-induced precipitation and carbon content. Thus we also investigated a normally two-phase vanadium-carbon alloy containing V_2C phase. A dose level of ~20 dpa was selected on the basis of previous dose-dependence studies of swelling that indicated a maximum swelling in the vicinity of this dose level [*3*].

Experimental Procedure

Vanadium was obtained in the form of 0.02-cm sheet from Wah Chang, Albany. The supplier's analysis, an independent mass spectrographic analysis for substitutional elements, and vacuum-fusion analysis of interstitial elements are given in Table 1. As shown in Table 1, the carbon,

TABLE 1—*Chemical analyses of vanadium.*

Element	Supplier, weight ppm	Mass Spectrograph, weight ppm	Fusion Analysis, weight ppm
H	4	...	...
C	80	...	125
N	100	...	39
O	350	...	136
Al	80	<40	...
Cu	<40	2	...
Fe	90	33	...
Si	295	150	...
Remainder	...	<10	...

oxygen, and nitrogen contents of the vanadium correspond to ~0.05, 0.04, and 0.01 atomic percent, respectively. Sheets (20 by 0.4 by 0.02 cm) of vanadium containing an additional 0.1 percent and 0.4 percent carbon, 1.0 percent oxygen, and 1.0 percent nitrogen were made by reacting the vanadium at 1250°C (2282°F) with methane, oxygen, or nitrogen in an ultrahigh vacuum system. In the case of carbon alloys, the residual hydrogen was removed by evacuating the system to $\lesssim 10^{-8}$ torr before cooling the sheet. When possible, nominal compositions were checked by com-

paring specimen weight gain based on the amount of gas reacted with those actually measured. These quantities agreed within 1 percent of the weight of solute added.

Specimens for irradiation were obtained by punching 3-mm disks from the sheet stock just described. One surface was polished by procedures described previously [5]. Hydrogen picked up during polishing was removed by final degassing for 15 min at 1050°C (1922°F) just prior to inserting the specimens into the ultrahigh vacuum irradiation chamber. Groups of specimens from each composition were clamped in a 4 by 5 array in a tungsten specimen holder and irradiated with 3.0-MeV $^{51}V^{+}$ ions in the Argonne National Laboratory (ANL) dual ion-irradiation facility [5]. A given array contained three disks of each alloy. The ion flux and fluence were typically 0.55 $\mu A\ cm^{-2}$ and 4.0 $mC\ cm^{-2}$. One disk of each composition was shielded from the beam and acted as a control specimen in that it experienced the same thermal treatment and gaseous environment as the irradiated specimens. The nominal irradiation temperatures were 650, 700, 750, 800, and 880°C (1202, 1292, 1382, 1472, and 1616°F). The temperature was controlled by thermocouples in the specimen holder, and individual specimen temperatures were read using an infrared pyrometer calibrated for these materials and specimen-preparation procedures. Total gas pressures during the ~2-h irradiation were in the low 10^{-8} torr range, dropping to 10^{-9} torr as the run proceeded. Residual gas-pressure measurement showed approximate partial pressures for water (H_2O) of $\sim 3 \times 10^{-9}$ torr and for combined nitrogen (N_2) and carbon monoxide (CO) $\sim 5 \times 10^{-9}$ torr.

Following irradiation, the specimens were sectioned to depths between 7100 and 8500 Å from the irradiated surface, then thinned from the backside to perforation. The section depth for a particular specimen was determined with an interference microscope and was used in computing the dose for that specimen. Deposited energy densities as a function of depth, calculated from Brice Codes RASE3 and DAMG2 [6], were converted to displacements per atom (dpa) using a threshold energy of 40 eV. For the 3-MeV V^{+} irradiation, the depth of maximum displacement damage was 9300 Å, and an ion flux of 1 $\mu A/cm^2$ corresponded to a displacement rate of 5.5×10^{-3} dpa/s. The void and precipitate microstructures were examined by procedures described previously [5].

Void and Dislocation Data

Comparisons of data for the void and dislocation microstructure of four interstitial doped alloys with those for unalloyed vanadium are shown in Figs. 1 through 4. Plots show, respectively, void volume fraction, void number density, mean void diameter, and dislocation density plotted as a function of irradiation temperature. For the vanadium, vanadium-0.1 percent carbon, vanadium-1.0 percent oxygen, and vanadium-1.0 percent

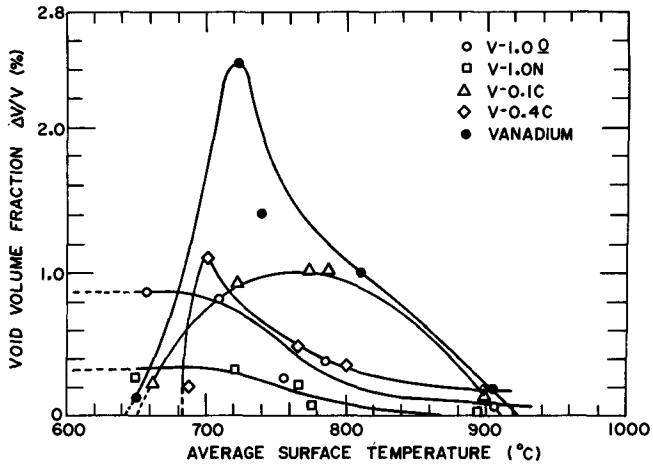

FIG. 1—*Void volume fraction as a function of irradiation temperature.*

nitrogen, the dose level of the transmission electron microscopy (TEM) specimens was 20 ± 2 dpa, whereas that of vanadium-0.4 percent carbon was 16 ± 2 dpa. The curves on the plots show the trends in the parameters.

The temperature dependence of the void volume fraction for vanadium is consistent with previous data for Ni^+ ion irradiations at a dose level of ~50 dpa [7]. The swelling rises rapidly with temperature, peaks in the vicinity of 700 °C (1292 °F), and drops off slowly on the high-temperature side. Within limits of the present data set, it appears that the shape of the swelling curve for vanadium-0.4 percent carbon is not affected strongly, although the magnitude of the swelling is depressed significantly. Vanadium-0.1 percent carbon exhibits swelling over the same temperature range as the vanadium. In vanadium-1.0 percent oxygen and vanadium-1.0 percent nitrogen swelling is decreased over this temperature range, but for vanadium-1.0 percent oxygen it is increased at lower temperatures. A comparison of these swelling data with those obtained previously in a $^{58}Ni^+$ irradiation shows that, although the magnitude of the swelling is similar, the void number density was an order of magnitude lower in the self-ion irradiation. The void number density is strongly dependent upon the solute, although in all cases the density decreases rapidly as the temperature increases. Interstitial solutes cause large variations in void number density, particularly at the lower temperatures: oxygen appears to promote void nucleation, nitrogen depresses it, whereas carbon in solution exhibits an intermediate behavior closely paralleling that for unalloyed vanadium. The void size, however, tends to increase with irradiation temperature; only vanadium-0.4 percent carbon exhibits the more generally observed monotonic increase [8]. The variations in the other curves, although not presently understood, appear to

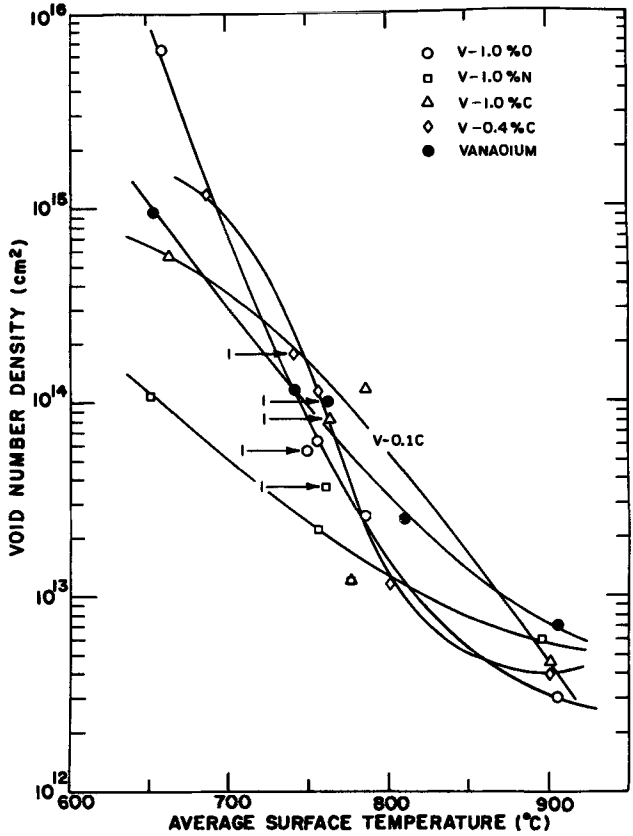

FIG. 2—*Void number density as a function of irradiation temperature. (Arrows represent a +40°C (104°F) temperature excursion for about 10 min in the beginning of the run. The total run time was about 2 h.)*

be valid as they are well outside the limits of the relative error in the mean void diameters (± 10 percent).

Micrographs showing the void structure of the various alloys after irradiation at 700°C (1292°F) are shown in Fig. 5. Nonrandomness in the void distributions can be seen in vanadium and in the carbon alloys where the voids tend to form a network pattern and, to a lesser extent, in the oxygen-doped alloy where a few void clusters are visible. At temperatures above and below 700°C (1292°F), however, all specimens tended to exhibit more random void structures. A precipitate structure can be seen in vanadium-0.1 percent carbon (Fig. 5*b*), whereas the dislocation microstructure is visible in the oxygen- and nitrogen-doped alloys (Figs. 5*c* and 5*d*). In all the alloys, dense dislocation tangles were observed, the density of which decreased with an increase in the irradiation temperature (Fig. 4). Vanadium exhibited a

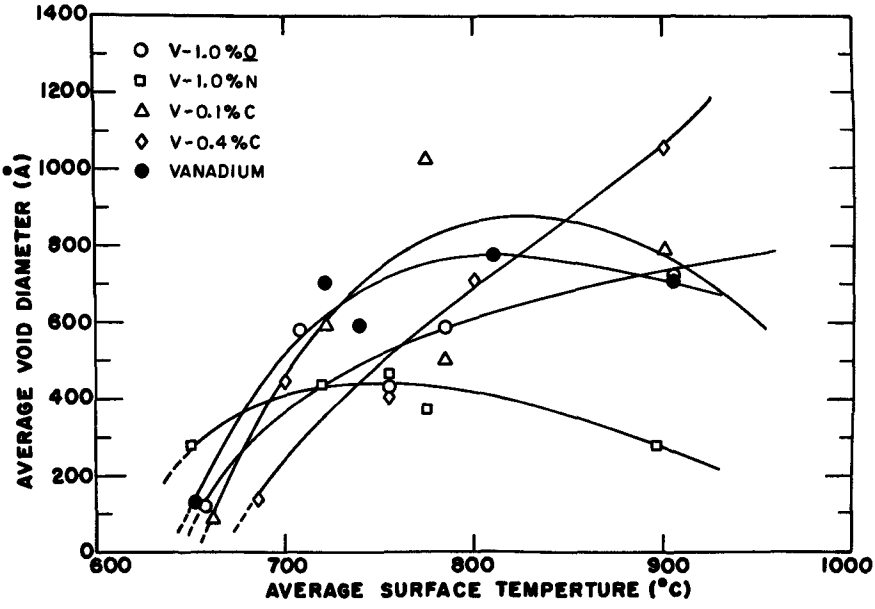

FIG. 3—*Average void diameter as a function of irradiation temperature.*

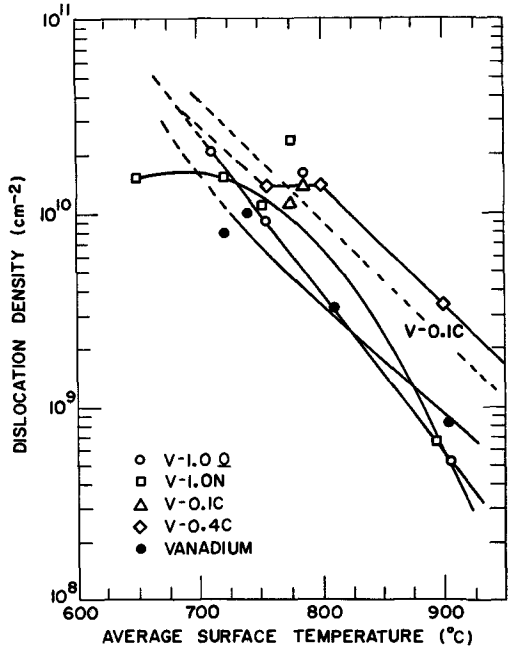

FIG. 4—*Dislocation density as a function of irradiation temperature.*

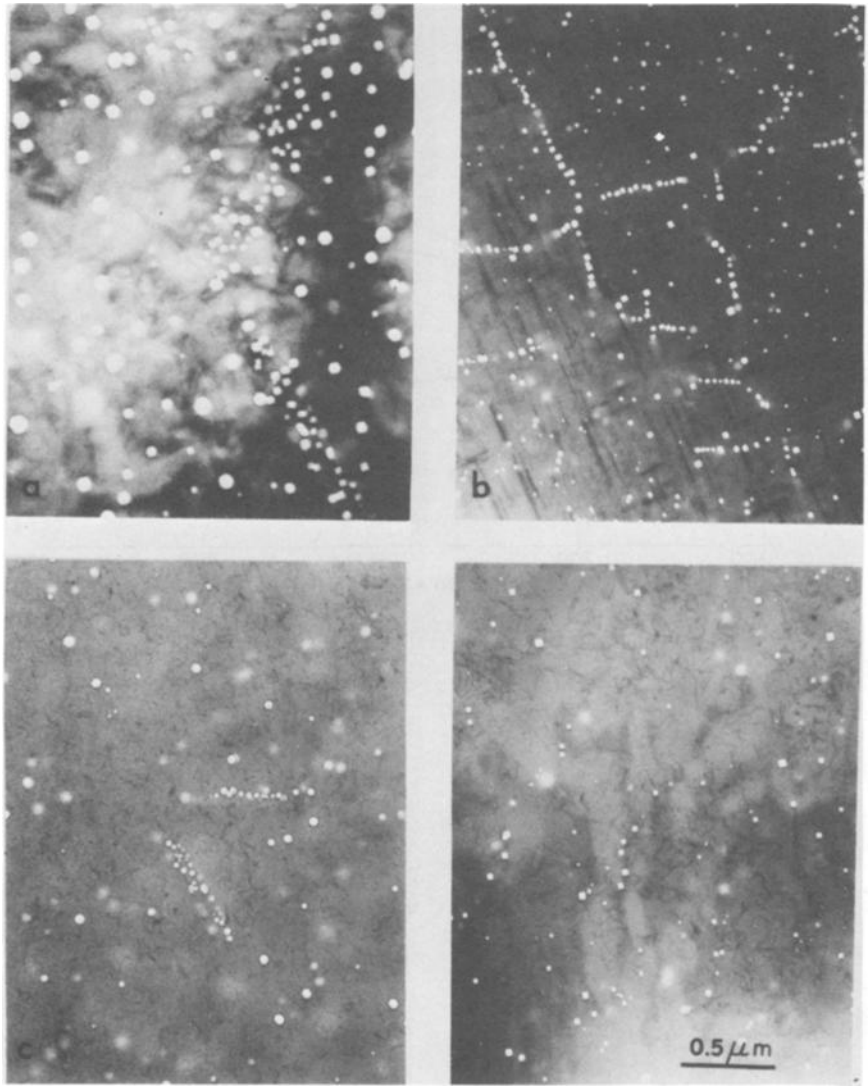

FIG. 5—*Void microstructure in vanadium and vanadium alloys irradiated at 700°C (1292°F). (a) Vanadium. (b) Vanadium-0.1 percent carbon. (c) Vanadium-1.0 percent oxygen. (d) Vanadium-1.0 percent nitrogen.*

significantly lower dislocation density than the other alloys, whereas in the 0.4 percent carbon alloy, the dislocation density at high temperatures was significantly greater than the other compositions. This is ascribed to the generation of additional dislocations by prismatic punching at V_2C particles [*9*].

Precipitation Phenomena

Under normal conditions of thermal equilibrium, all alloys investigated, except vanadium-0.4 percent carbon, are single phase at the irradiation temperatures [*10,11*]. Vanadium-0.4% carbon contains the V_2C phase and a bcc solid solution, as described by Diercks and Wert [*9*]. These authors have demonstrated that formation of V_2C at temperatures $\lesssim$500°C (932°F) is preceded by a metastable carbide with {013} habit. Our vanadium-0.4 percent carbon unirradiated control specimen from the 880°C (1616°F) irradiation showed V_2C precipitates on the external surface and at a depth corresponding to the peak damage (9300 Å). The morphology and electron diffraction patterns from the internal V_2C phase were the same as those reported by Diercks and Wert [*9*].

The various precipitate types observed in the irradiated specimens are shown in Fig. 6. Figure 6*a* shows a platelet precipitate that trace analysis confirmed had an {012} habit, henceforth called the {012} precipitate. This precipitate was previously observed by Agarwal and Taylor [*3*]. It is extremely thin, perhaps only one or two atom layers thick, as evidenced by profuse streaking along <012> in the electron diffraction patterns. Furthermore, it displays well-developed displacement fringe contrast when inclined to the electron beam. Figure 6*b* shows irregular, three-dimensional precipitates identified as V_2C by electron diffraction. As previously stated, these are surrounded by dense tangles of dislocations. In addition to V_2C precipitates, Fig. 6*c* shows thin, disk-shape precipitates that are visible by displacement fringe contrast. Trace analysis of these precipitates showed a {013} habit. They produced diffraction effects identical to the metastable carbide phase described by Diercks and Wert (Fig. 6 of their paper [*9*]). In the present case, this precipitate clearly forms heterogeneously on dislocations and void surfaces. The presence of precipitates along dislocations was also observed in vanadium at the highest irradiation temperatures (Fig. 6*d*). These precipitates are very thin disks of {013} habit with a ~500 Å diameter. They frequently occur as parallel sets along the dislocations, for example, the region labeled *A*. In other orientations visible in Fig. 6*d*, the overlapping strain contrast of these precipitates causes the fringed appearance of some portions of the dislocations.

Table 2 is a summary of the various kinds of precipitates observed as a function of irradiation temperature and alloy composition. The vanadium-1.0 percent nitrogen alloy showed no precipitates over the entire temperature range investigated. Vanadium and vanadium-1.0 percent oxygen exhibited qualitatively similar behavior, namely, a high density of {012} precipitates at the lowest irradiation temperature only and precipitates on dislocations at the highest temperatures. The vanadium-0.1 percent carbon and vanadium-0.4 percent carbon showed high densities of {012} precipitates at 650°C (1202°F). Unlike vanadium and vanadium-1.0 percent oxygen, the {012} precipitate in the carbon alloys persisted to much higher

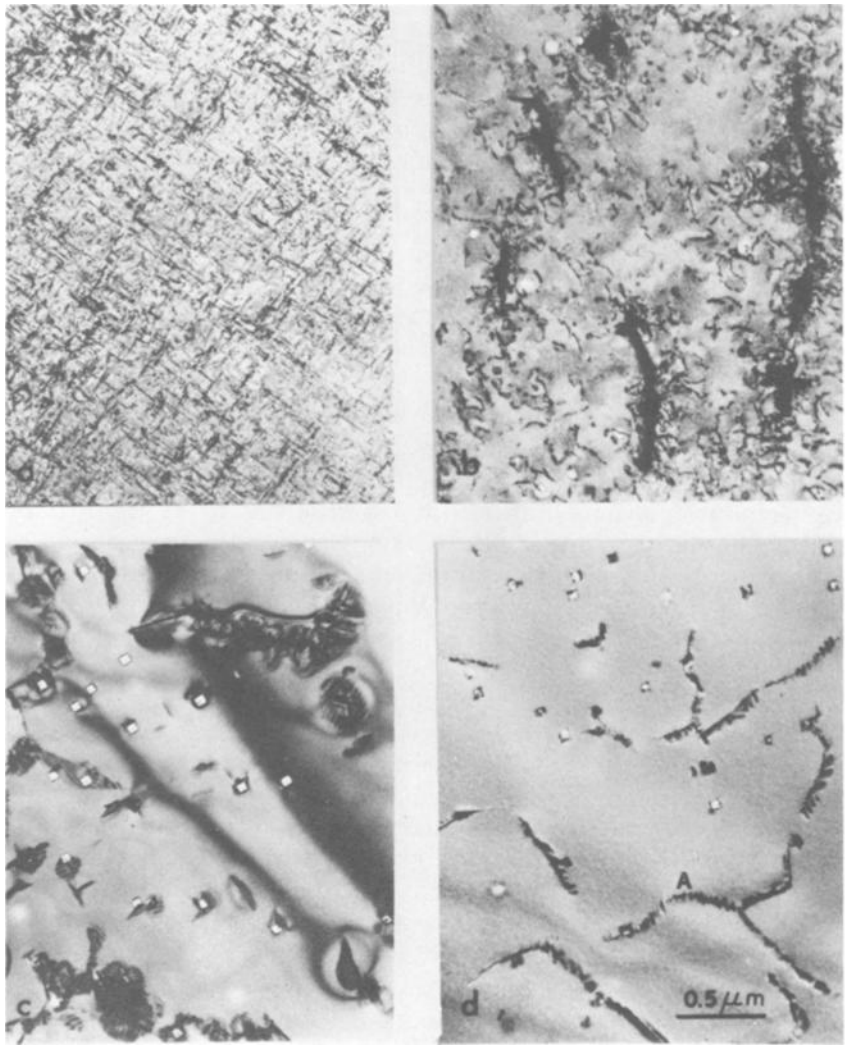

FIG. 6—*Various precipitate microstructures observed in vanadium and vanadium alloys irradiated in the temperature range 650 to 880°C (1202 to 1616°F) [(100) foil]. (a) Vanadium-0.4 percent carbon at 650°C (1202°F). (b) Vanadium-0.4 percent carbon at 800°C (1472°F). (c) Vanadium-0.1 percent carbon at 880°C (1616°F). (d) Vanadium at 880°C (1616°F).*

temperatures (~800°C) (1472°F). This is demonstrated in the case of vanadium-0.1 percent carbon in Fig. 7, which shows that the precipitates become less dense and coarser as the irradiation temperature increases. The {012} precipitate was not observed in specimens irradiated at 880°C (1616°F). These did show, however, the metastable carbide phase described

TABLE 2—*Summary of the precipitate microstructures observed in vanadium and vanadium alloys at various irradiation temperatures.*

Irradiation Temperature, °C	Vanadium	Vanadium-0.1 Percent Carbon	Vanadium-0.4 Percent Carbon	Vanadium-1.0 Percent Oxygen	Vanadium-1.0 Percent Nitrogen
650	very high density of {012} precipitates	very high density of {012} precipitates	very high density of {012} precipitates; no V_2C	high density of fine {012} precipitates	no precipitates
700	no precipitates	dense {012} precipitates	V_2C + {012} precipitates	no precipitates	no precipitates
750	no precipitates	low density coarse {012} precipitates	V_2C + {012} precipitates	no precipitates	no precipitates
800	fine precipitation on dislocations	coarse {012} precipitates	V_2C + some coarse {012} precipitates	no precipitates	no precipitates
880	fine precipitation on dislocations and void surfaces	metastable carbide exhibiting displacement fringe contrast	fine V_2C on the surfaces of the specimen + V_2C in bulk + some metastable carbide	fine precipitates on dislocations (similar to vanadium)	no precipitates

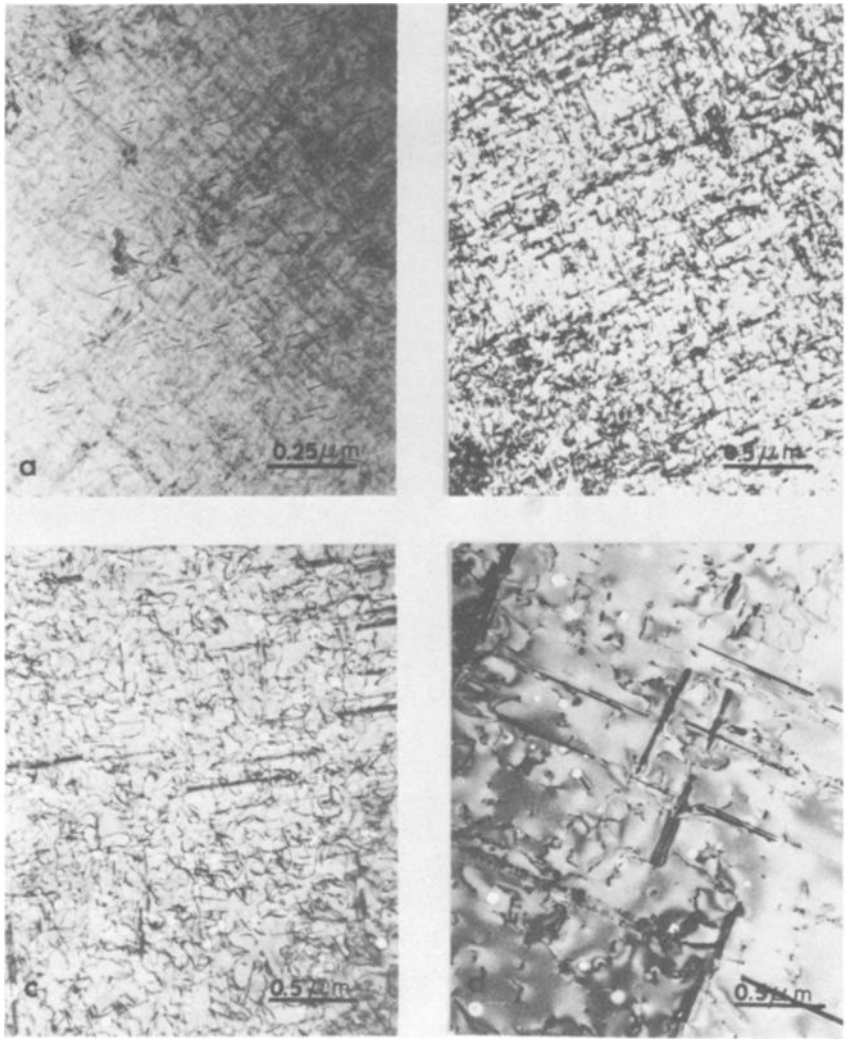

FIG. 7—*Coarsening of {012} precipitate in vanadium-0.1 percent carbon as a function of temperature [(100) foil]. (a) 650°C (1202°F). (b) 700°C (1292°F). (c) 750°C (1382°F). (d) 800°C (1472°F).*

earlier (Fig. 6*c*), which is believed to form during cooling from the irradiation temperature.

Conventional thermal aging of vanadium-0.4 percent carbon at temperatures above 600°C (1112°F) produced only V_2C precipitates, which was also the case for specimens irradiated at 880°C (1616°F). At 650°C (1202°F), however, no V_2C precipitate was observed in the irradiated

specimen, but instead only a very high density of {012} precipitate (Fig. 6*a*). With an increase in temperature, the relative proportion of {012} precipitate decreased and that of V_2C increased (Fig. 6*b*). At 880°C (1616°F), the presence of V_2C in the external surface of the irradiated vanadium-0.4 percent carbon was noted, which was similar to the unirradiated control sample.

Discussion

The present investigation of the influence of interstitial solutes on the void microstructure of vanadium indicates systematic dependence of the microstructure upon the solute species. To a first approximation, possible effects due to impurity contamination from the vacuum environment during the irradiation have been limited by bombarding all alloy compositions simultaneously. Nitrogen doping produces the largest effect, in that both the void number density and the void swelling are lower than in the unalloyed vanadium. Alloying with oxygen reduces the swelling and causes a large increase in the observed void number density at the lowest temperature. In both oxygen and nitrogen alloys, an indication has been found that the swelling curve shifted to lower temperatures when compared with unalloyed vanadium. The lower carbon concentrations of 0.1 and 0.4 percent produce significant depressions in swelling mainly through reduction in void size. The origin of the irregularities in the temperature dependence of the void size is not understood. Complications arising from segregation and precipitation of impurities and the temperature dependence of these effects require additional investigation.

The influence of oxygen concentration on swelling can be inferred from a comparison of the present data with some of our previous observations [*12*] of a vanadium-5.0 percent oxygen alloy that showed negligible swelling at 700°C (1292°F), that is, <0.001 percent, because of the $\sim 10^{12}$ cm^{-3} void density. Thus, a progressive decrease in swelling with an increase in oxygen content [*1*] is apparent.

The mechanism by which interstitial solute atoms inhibit void swelling is not clear. The Schilling and Schroeder [*2*] model, which involves vacancy trapping by immobile interstitial solutes, predicts a reduction in swelling and a shift of the swelling-temperature curves to higher temperatures. A decrease in the swelling is observed in the present work. With the addition of interstitial solutes, however, the direction of the shift in the peak swelling implied by the oxygen and nitrogen data is opposite that predicted by the Schilling and Schroeder model. Okamoto et al [*13*] have developed a model consistent with the observed trends in our data.

The present results shed new light on the {012} precipitate noticed in previous investigations [*3*]. This precipitate seems quite definitely associated with carbon in the vanadium. The {012} precipitate is present to higher

irradiation temperatures than 650 °C (1202 °F), when carbon is added to the vanadium. The presence of {012} at 650 °C (1202 °F) in the starting vanadium is probably due to small carbon concentration (≈0.05 percent). Also, it competes with V_2C for the available carbon. At lower irradiation temperatures, where any irradiation-induced carbon segregation effect would be most noticeable, the {012} precipitate replaces V_2C observed under equilibrium thermal aging. At the higher temperatures, where irradiation-induced segregation would be less dominant [*13*], one observes the V_2C phase. Perhaps the {012} precipitate acts as a sink not only for carbon atoms but also for vacancies, self-interstitials or both [*14*].

Conclusion

1. The addition of the interstitial solutes nitrogen, oxygen, and carbon strongly suppresses void swelling of vanadium induced by ion bombardment.
2. These solutes influence both the number density of voids and the mean void size.
3. Identical {012} metastable precipitates were observed in ion-irradiated vanadium and in vanadium-0.1 percent carbon and vanadium-0.4 percent carbon alloys. This precipitate replaces some of the V_2C phase observed in specimens of vanadium-0.4 percent carbon alloy under thermal equilibrium.

Acknowledgments

The authors wish to express their gratitude to all those who contributed their talents so necessary to the execution of our work. D. Ryding, B. Kestel, and C. Steves of the Kinetics Group worked on specimen preparation and analysis; J. Wallace assisted by J. Kaplenk provided irradiation services with the dual ion irradiation system; and R. Amrein and the Dynamitron staff of the Physics Division operated the accelerator. H. Wiedersich reviewed the manuscript and discussed the work. The manuscript was edited by F. Adams.

This work was supported by the Division of Physical Research and Controlled Thermo-Nuclear Fusion of the U.S. Energy Research and Development Administration.

References

[*1*] Loomis, B. A., Taylor, A., Klippert, T. E., and Gerber, S. B., *Proceedings of the 1973 International Conference on Defects and Defect Clusters in B.C.C. Metals and Their Alloys,* R. J. Arsenault, Ed.; *Nuclear Metallurgy,* Vol. 18, 1973, p. 332.

[*2*] Schilling, W. and Schroeder, K., *Proceedings of the Consultant Symposium on the Physics of Irradiation Produced Voids,* R. S. Nelson, Ed., Harwell, Sept. 1974, p. 212.

[3] Agarwal, S. C. and Taylor, A., *Proceedings of the International Conference on Radiation Effects and Tritium Technology for Fusion Reactors,* Gatlinburg, Tenn., Oct. 1975.
[4] Weber, W. J., Kulcinski, G. L., Lott, R. G., Wilkes, P., and Smith, H. V., Jr., *Proceedings of the International Conference on Radiation Effects and Tritium Technology for Fusion Reactors,* Gatlinburg, Tenn., Oct. 1975.
[5] Taylor, A., Wallace, J. R., Potter, D. I., Ryding, D. G., and Okray Hall, B., *Proceedings of the International Conference on Radiation Effects and Tritium Technology for Fusion Reactors,* Gatlinburg, Tenn., Oct. 1975.
[6] Brice, D. K., Research Report SLA-73-0416, Sandia Laboratories, Albuquerque, N. Mex., April 1973.
[7] Santhanam, A. T., Taylor, A., and Harkness, S. D., *Proceedings of the 1973 International Conference on Defects and Defect Clusters in B.C.C. Metals and Their Alloys,* R. J. Arsenault, Ed.; *Nuclear Metallurgy,* Vol. 18, 1973, p. 302.
[8] Norris, D. I. R., *Radiation Effects,* Vol. 14, 1972, p. 1.
[9] Diercks, D. R. and Wert, C. A., *Metallurgical Transactions,* Vol. 3, 1972, p. 1699.
[10] Potter, D. I., Epstein, H. D., and Goldstein, B. M., *Metallurgical Transactions,* Vol. 5, 1974, p. 2075.
[11] Henry, J. L., O'Hare, S. A., McCune, R. A., and Krug, M. P., *Journal of the Less-Common Metals,* Vol. 21, 1970, p. 115.
[12] Potter, D. I. and Hoff, H., *CTR Quarterly Progress Report,* Argonne National Laboratory, Argonne, Illinois, April 1975.
[13] Okamoto, P. R., Wiedersich, H., Lam, N., and Johnson, R., private communication.
[14] Loomis, B. A., Taylor, A., and Gerber, S. B., *Journal of Nuclear Materials,* Vol. 56, 1975, p. 25.

Void Growth and Microstructural Changes

M. L. Bleiberg,[1] *R. Bajaj,*[1] *I. M. Baron,*[1] *A. Chang,*[1]
R. W. Chickering,[1] *and S. Diamond*[1]

Swelling and Gamma-Prime Particle Stability of Ion-Bombarded Iron-Chromium-Nickel Alloys

REFERENCE: Bleiberg, M. L., Bajaj, R., Baron, I. M., Chang, A., Chickering, R. W., and Diamond, S., "**Swelling and Gamma-Prime Particle Stability of Ion-Bombarded Iron-Chromium-Nickel Alloys,**" *Irradiation Effects on the Microstructure and Properties of Metals, ASTM STP 611,* American Society for Testing and Materials, 1976, pp. 315-336.

ABSTRACT: Nickel-ion bombardment studies were conducted on experimental alloys which were designed to provide basic information on the influence of composition, residual elements, and γ'-precipitates on swelling in the iron-chromium-nickel alloy system. Bombardments were conducted at temperatures ranging from 550 to 750°C (1022 to 1382°F) to maximum damage of 250 displacements per atom (dpa).

Comparison of identical alloys with and without γ'-precipitates showed that titanium and aluminum additions to the matrix compositions suppressed swelling. It is inferred that the aluminum increases the incubation dose while titanium reduces the swelling rate. The γ'-precipitates influence swelling only as they affect matrix chemistry.

Fine γ'-particles (8 to 18 nm) were precipitated under irradiation and approached an equilibrium size at high damage levels. A slight coarsening of 30-nm particles was observed, but there was only a slight increase in the volume fraction of the γ'-particles due to the irradiation. It was concluded that disorder dissolution was not an important mechanism in these alloys.

KEY WORDS: radiation, iron-chromium-nickel alloys, ion bombardment, electron microscopy, voids, radiation effects, γ'-precipitation

The damage produced in metals and alloys by fast neutron fluences has been simulated in many experiments by bombardment with high-energy charged particles [*1,2*].[2] The void formation, swelling, and irradiation-related microstructural evolution during these particle bombardments occur

[1]Manager, Advanced Materials, senior engineers, engineer, and senior engineer, respectively, Westinghouse Advanced Reactors Division, Madison, Pa. 15663.

[2]The italic numbers in brackets refer to the list of references appended to this paper.

a thousand-fold more rapidly than during neutron exposure. This permits rapid detailed study of the damage process and of the possible mechanisms for the avoidance or suppression of swelling.

In addition to void swelling, precipitation-hardened alloys must be investigated for phase stability, morphological changes, and precipitate particle stability under irradiation to be considered for application in a fast breeder reactor environment. A series of experimental alloys was designed in the iron-chromium-nickel phase field to specifically investigate this and also to provide information to aid in interpreting the irradiation changes observed in more complicated alloys. This report summarizes the test results obtained to date on several of the alloys in this test program.

Experimental Techniques

The alloys were fabricated by International Nickel Company by vacuum melting 45-kg heats, extruding into 15.9-mm-diameter bar stock, and cutting into 305-mm lengths. The material was then swaged at room temperature to about 10.2 mm diameter, annealed at 1093 °C (2000 °F) for one hour in a H_2 atmosphere, centerless ground to 9.5 mm diameter, copper plated, and drawn into wire about 3.18 mm diameter. The alloy compositions as determined by spectrographic and X-ray analyses are given in Table 1. Examination of these compositions shows that this test series con-

TABLE 1—*Experimental alloy compositions.*

Alloy No.	E-20	E-48	E-42	E-54
Fe	balance	balance	balance	balance
Ni	24.4	25.0	34.6	45.7
Cr	14.9	14.6	15.1	14.6
Ti	...	3.04	1.99	1.6
Al	...	1.51	1.7	1.05
C	0.003	0.006	0.04	0.001
O_2	0.017	0.0055	0.0024	0.0039
N_2	0.0017	0.0019	0.0014	0.0006
Si	...	...	0.69	...
B	...	...	0.15	...

sists of a simple Fe-15Cr-24Ni ternary-base alloy (E-20), a similar alloy with γ'-alloying additions (E-48), and two additional γ'-containing alloys with increased nickel content, namely, E-42 (35 percent nickel and E-54 (45 percent nickel). Also, Alloy E-42 contained small additions of the residual elements silicon and boron. The alloy compositions and heat treatments were designed to produce a nearly constant preirradiation volume fraction of γ'-precipitate of about 5 percent.

The wire material was solution treated at 1150 °C (2102 °F) for 1 h.

Alloys E-42, E-48, and E-54 were aged at 815°C (1500°F) for 10 h which produced an average γ'-particle diameter of 25 to 30 nm.

The specimens were then injected with 5 atomic parts per million (appm) helium to 1 μm sequentially so that the helium distribution was nearly homogeneous. Subsequently the specimens were mounted in tungsten alloy holders and irradiated with 3 MeV or 3.5 MeV nickel ions in the Argonne National Laboratory Dynamitron at temperatures ranging from 550 to 750°C (1022 to 1382°F). The displacement doses ranged from 35 to 250 dpa. The maximum damage rate was about 5×10^{-3} dpa per second. The typical displacement energy deposition variation through the specimen was shown by Diamond et al [*3*]. For 3 MeV the maximum damage was at 580 nm and for 3.5 MeV the maximum damage was at 670 nm. One additional test was run on selected specimens using the Oak Ridge National Laboratory Van Der Graff operating at 4 MeV. In this case, only step-height measurements were made on the specimens.

The energy deposition profile, dE/dX, was calculated using the EDEP-1 computer code [*4*]. For the atomic displacement calculations, the threshold energy was assumed to be 40 eV in a modified Kinchin Pease secondary displacement model. A typical lattice parameter for these alloys is 0.357 nm[5], which yielded an atomic density of 8.79×10^{28} atoms per cubic meter for the EDEP-1 calculation.

After bombardment, specimens were prepared for examination in one of two ways. In some cases the specimens were prepared for full-range high-voltage electron microscope (HVEM) examination by backthinning to the ion entry surface [*3*]. Other specimens were ion sectioned to 430 and 550 nm for 3 and 3.5 MeV nickel ions, respectively. The sectioning depth was based upon E DEP-1 calculations but verified by HVEM [*3*].

Results

Swelling

The swelling and dislocation structure of the simple ternary Alloy E-20 was obtained by full-range HVEM examination [*3*]. The void swelling data are summarized in Fig. 1. The swelling increased, the void concentration decreased, and the void size increased with temperature up to 700°C (1292°F). At 750°C (1382°F) the void concentration increased slightly but the void size was very much smaller and the swelling was thus greatly diminished. The maximum swelling occurred at 700°C (1292°F).

For convenience these swelling data were represented by two straight lines, representing a low damage level (Stage I) swelling and a high damage level (Stage II) swelling. Regression analyses were performed on these data and the swelling at the peak swelling temperature of 700°C (1292°F) was calculated as [*3*]

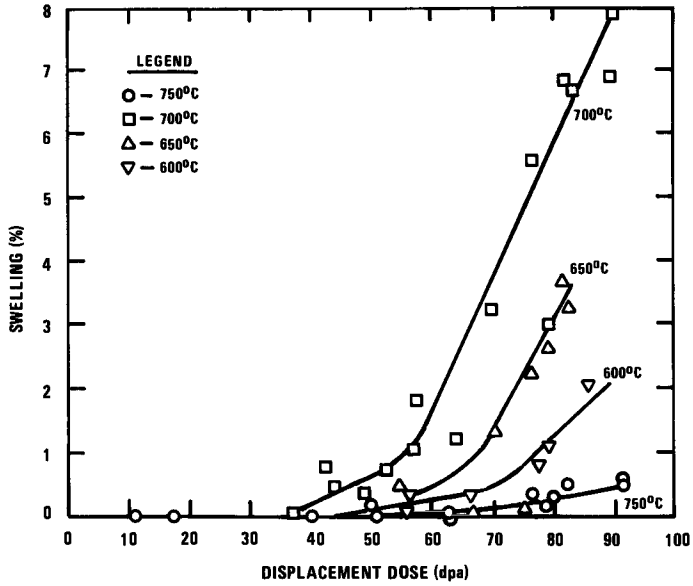

FIG. 1—*Swelling of Fe-25Ni-15Cr alloy as a function of dose and temperature.*

Stage I	$S = 0.04\,(D\text{-}35)$	$35 < D < 58$	$\gamma = 0.87$
Stage II	$S = 0.19\,(D\text{-}51)$	$58 < D < 90$	$\gamma = 0.93$

where

S = percent swelling,
D = dose in dpa, and
γ = correlation coefficient.

These results on the simple ternary alloy may be compared to those obtained on solution-annealed and solution-annealed and aged specimens of Alloy E-48, which has about the same nickel and chromium content but contains titanium and aluminum to precipitate γ'-particles after aging heat treatments. Examination of these data showed that the aged specimens exhibited about ten times the void swelling as the solution-annealed specimens. This is shown in Fig. 2 for material bombarded to 135 dpa at 600°C (1112°F).

The void swelling exhibited by specimens of E-48 solution annealed and aged after bombardment at 500, 550, and 600°C (932, 1022, and 1112°F) is shown in Fig. 3. Electron microscopy data combined with step-height data indicate that the swelling dependence with damage level is similar for this material in the 500 to 600°C (932 to 1112°F) temperature range. The step height to swelling conversion factor was taken to be 60 Å per percent void

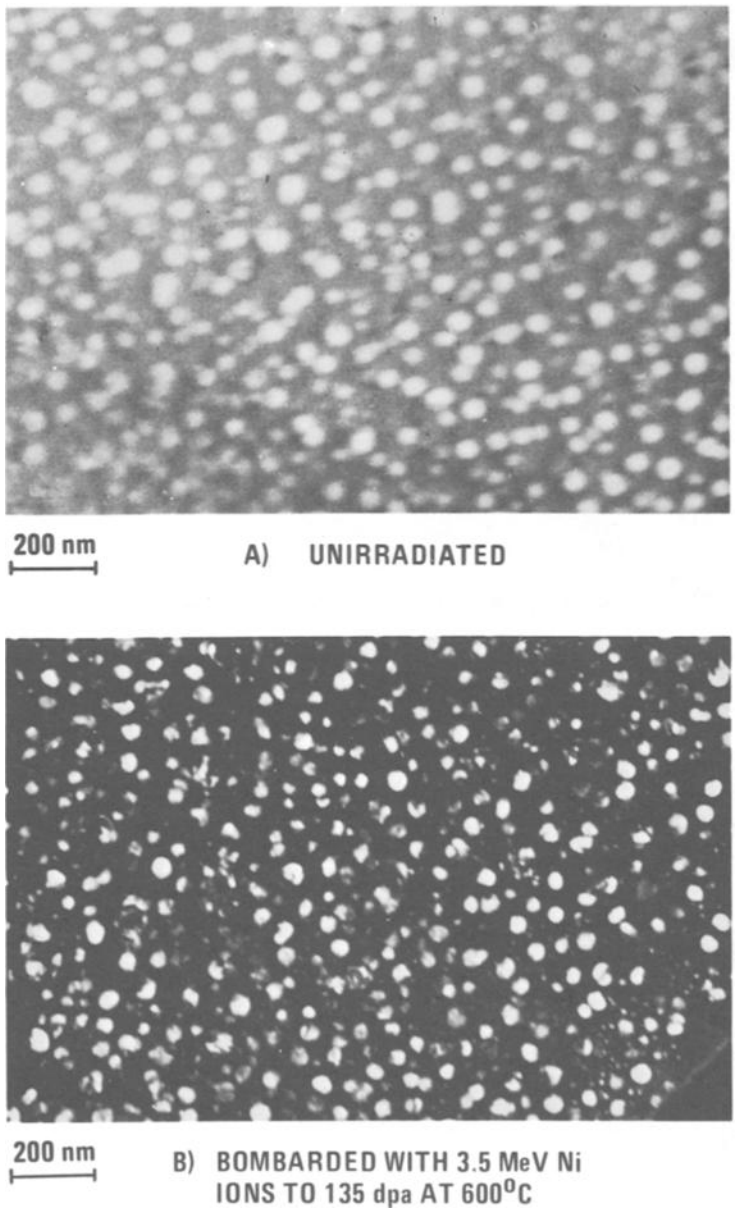

FIG. 2—*Void formation in Alloy E-48 bombarded to 135 dpa with 3.5-MeV nickel ions at 600°C (1112°F).*

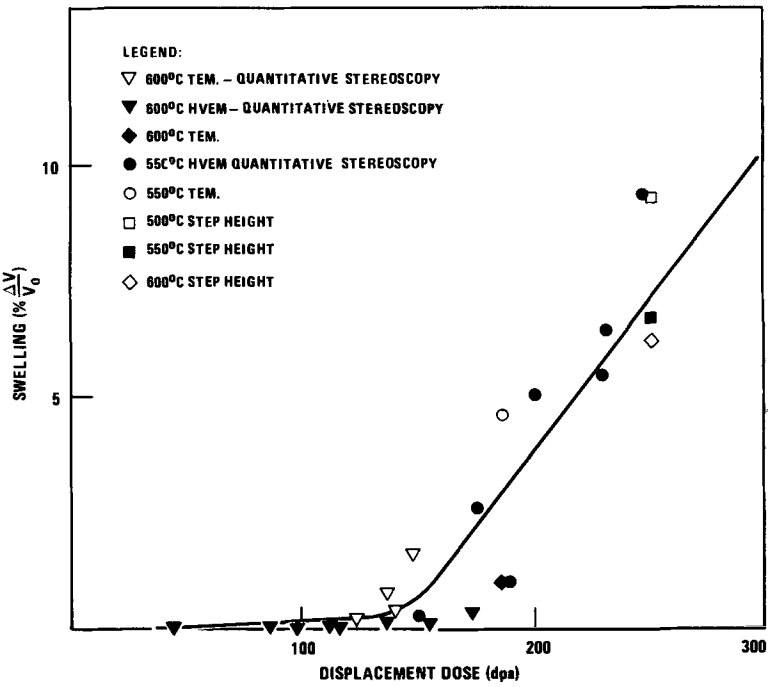

FIG. 3—*Nickel-ion bombardment swelling of aged E-48.*

swelling in the maximum damage region using the same assumptions as Johnston et al [*6*].

Using the same formulation for swelling as in the foregoing for Alloy E-20, the swelling equations for the peak swelling temperature for Alloy E-48 in the aged condition were represented as a two-stage linear function with damage.

A least-squares fit of the void swelling data and step-height data gave Stage I and Stage II swelling rates as follows:

$$\text{Stage I} \quad S = 0.002\,(D\text{-}58) \quad 0 < D < 115 \text{ dpa} \quad \gamma = 0.67 \tag{3}$$

$$\text{Stage II} \quad S = 0.066\,(D\text{-}141) \quad 150 < D < 250 \text{ dpa} \quad \gamma = 0.92 \tag{4}$$

The swelling of the higher nickel alloys E-42 and E-54 was found to be small. A maximum swelling of 0.5 percent observed in E-42 after 204 dpa at 600 °C (1112 °F). The swelling of E-54 at 600 °C (1112 °F) after 130 dpa was negligible.

In the case of Alloys E-42 and E-54 the voids were found along grain boundary precipitates and carbide precipitates inside the grains. The average void size along grain boundary precipitates was measured to be 66

nm. The morphology of voids formed around grain boundary precipitates and carbides is shown in Figs. 4 and 5, respectively. The precipitates along grain boundaries were identified to be the Laves phases (probably $TiFe_2$, $TiCr_2$, or Ti_2Ni_3Si) by selected-area diffraction technique. The carbides were found to be of M_6C-type (probably Cr_3Ni_2SiC).

Gamma-Prime Precipitate Stability

The irradiation of Alloy E-48 produced no coarsening of the original γ'-particles as shown in Figs. 6 and 7. A fine precipitate about 10 nm in diameter, however, was observed to have precipitated out of solution. The total volume fraction gamma prime did not change significantly, increasing from about 6 ± 2 percent to 7 ± 2 percent after the irradiation.

As shown in Fig. 8, γ' precipitated in the solution-annealed E-48 specimens during bombardment. Fine γ' did not appear when control samples were thermally aged for 13 h at 600 °C (1112 °F), which was the bombardment time period. The postirradiation γ' size distribution in the solution-annealed E-48 was similar in size and concentration to the fine γ' size component in the aged E-48.

The influence of irradiation temperature on the nickel-ion bombardment of the γ'-particle size distribution of Alloy E-42 is shown in Fig. 9. It may be seen that after 35 dpa at 600, 650, and 700 °C (1112, 1202, and 1292 °F) extensive precipitation of fine γ'-particles occurred. In this temperature range, the concentration of fine particles was inversely related to temperature. Also, the degree of bimodality (that is, the ratio of the average large and small particle sizes) varied inversely with temperature. At 750 °C (1382 °F) after 100 dpa, as shown in Fig. 9*d*, only a general broadening of the original particle size distribution was noted. The effect of increased exposure on the size distribution for E-42 (aged) is summarized in Fig. 10. These results indicate that the temperature effect noted at 35 dpa on the small particle sizes [that is 18 nm at 700 °C (1292 °F) and 8 nm at 650 and 600 °C (1202 and 1112 °F)] disappears at higher doses, and an "equilibrium" fine particle size of about 10 nm occurs at 100 dpa. The initial particle size of about 30 nm showed a slight coarsening with exposure, increasing to about 35 nm after 100 dpa.

Solution-annealed E-54 bombarded to 100 and 130 dpa at 600 °C (1112 °F) exhibited two competing precipitation modes. Inhomogeneous nucleation of strings of γ'-particles parallel to dislocation line segments was observed along with randomly distributed homogeneous nucleation of small spherical γ' particles, as shown in Fig. 11. Investigation of thermal control specimens aged 13 h at 600 °C (1112 °F) showed that γ' cannot be precipitated with this heat treatment. It is concluded that all the precipitation observed is radiation-enhanced. It is interesting to note that the size of the γ'-precipitate from the solution-annealed E-54 is similar to

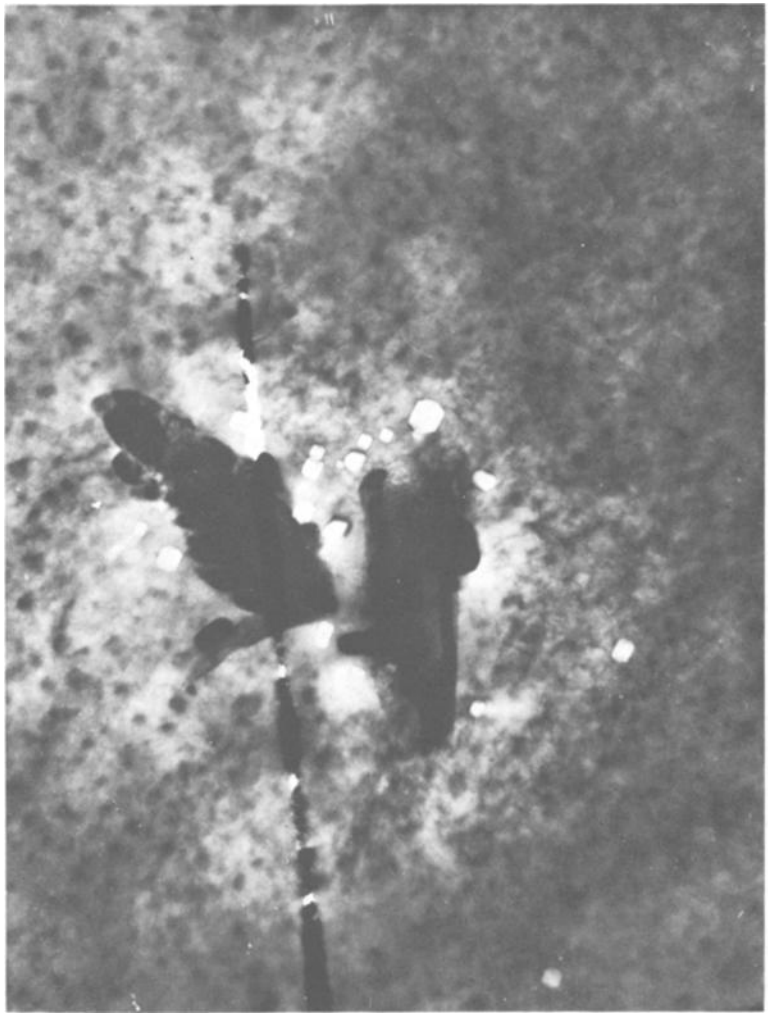

FIG. 4—*Voids around carbide precipitates in E-42 aged at 815°C (1500°F) for 10 h, and nickel ion irradiated to 101 dpa at 650°C (1202°F).*

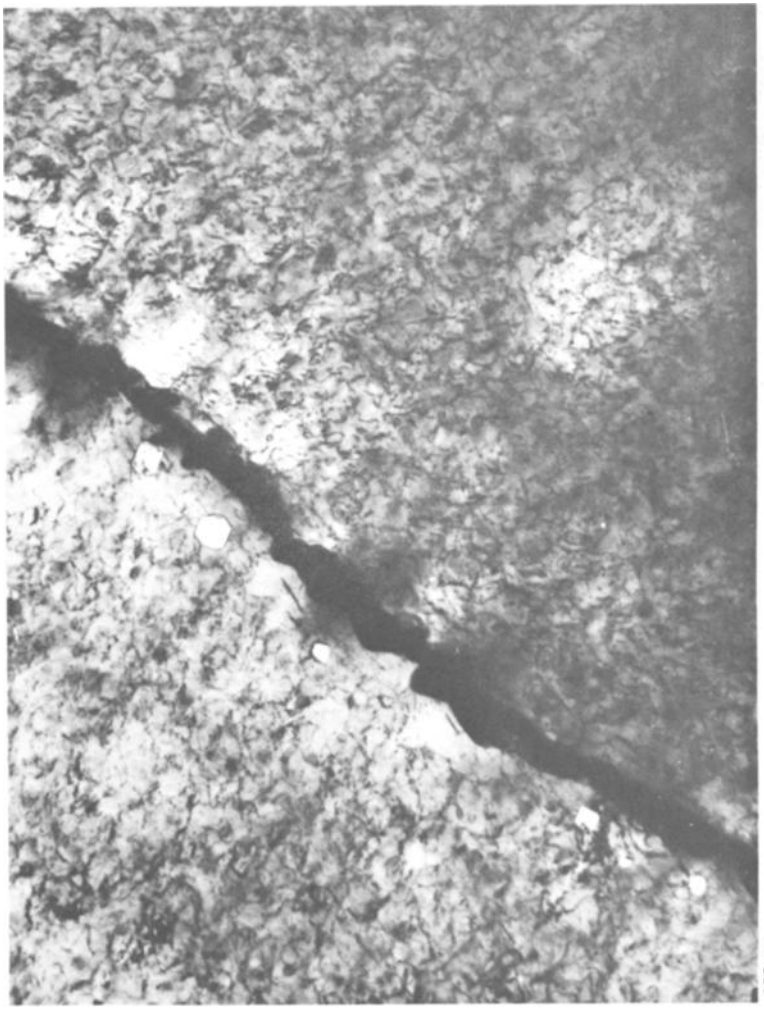

FIG. 5—*Voids along grain boundary precipitates in E-42 aged at 815°C (1500°F) for 10 h, and nickel ion irradiated to 101 dpa at 650°C (1202°F).*

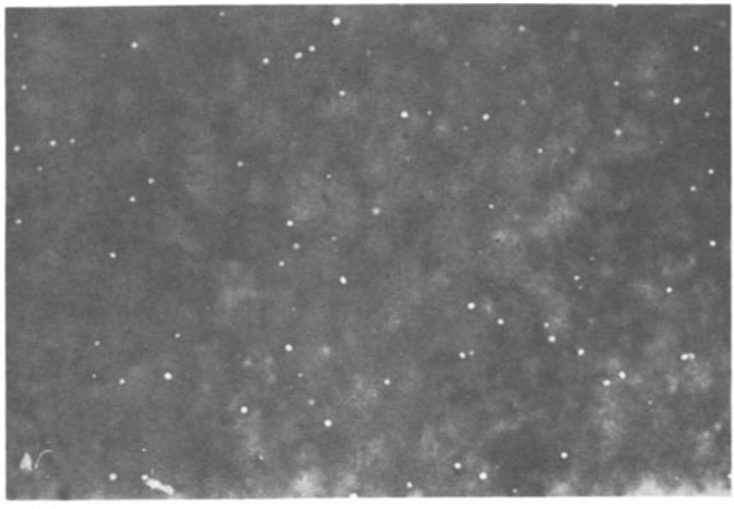

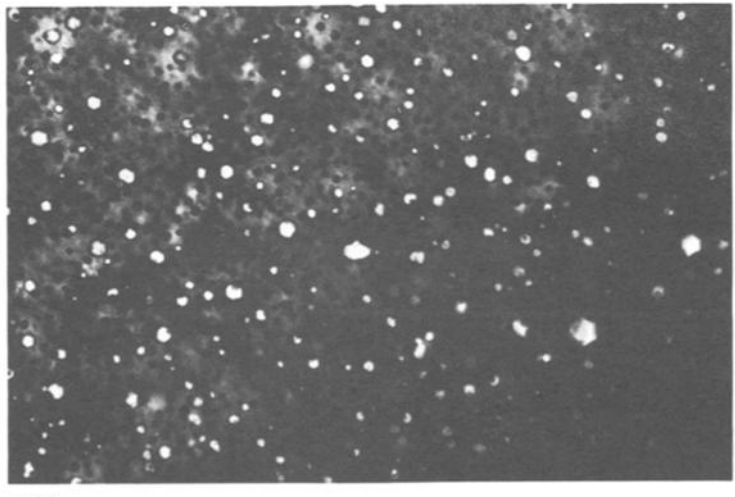

FIG. 6—*γ′ precipitated in Alloy E-48 solution annealed at 1150°C (2102°F) for 1 h and aged at 815°C (1500°F).*

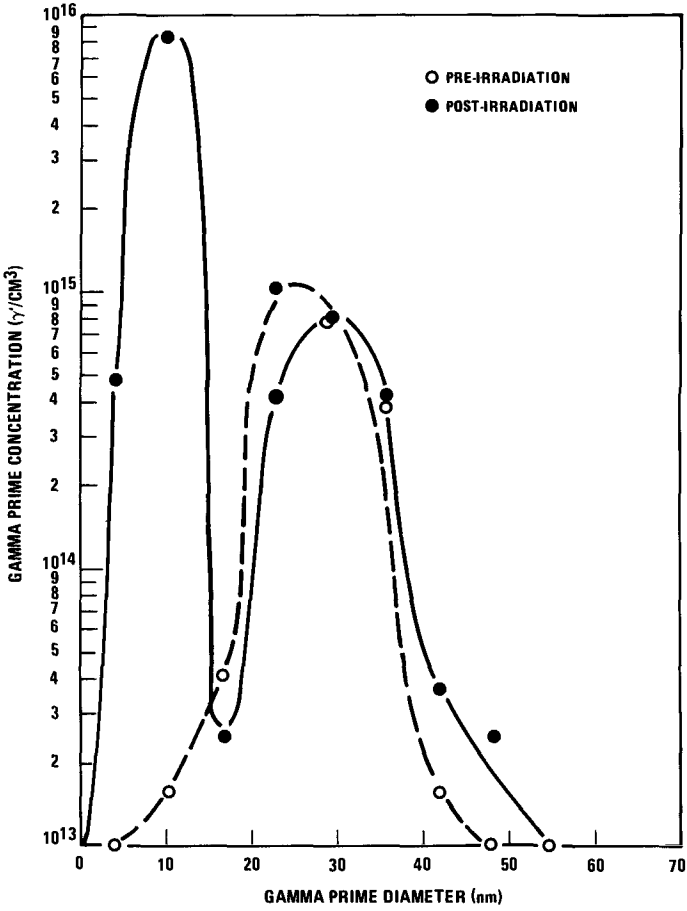

FIG. 7—*Unirradiated and irradiated γ'-size distribution in E-48 (solution annealed and aged) at 135 dpa at 600°C (1112°F) for 6-nm-size intervals.*

the fine precipitate noted in E-42 and also from E-48. This indicates that the irradiation-enhanced effect is independent of composition over the range of 25 to 45 percent nickel. Furthermore, it substantiates the premise of an "equilibrium" size for these fine γ'-precipitates.

Discussion of Results

Swelling

The reduction in swelling of these alloys with increasing nickel content is consistent with the results of Johnston et al [*6*] on swelling of simple ternary

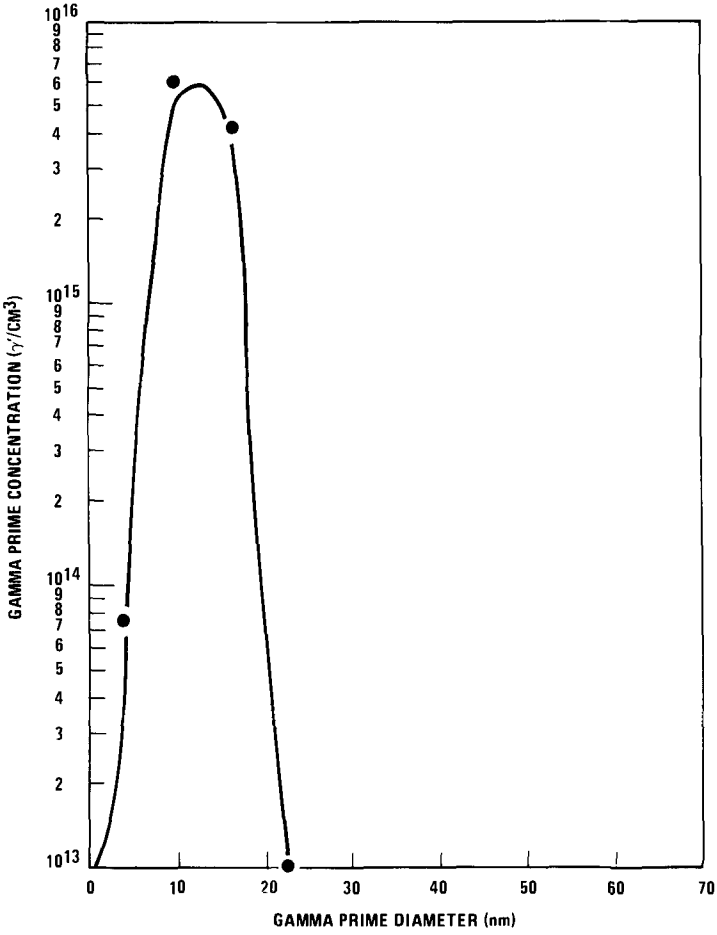

FIG. 8—*Postirradiation γ′ distribution for E-48 (solution annealed) specimens at 135 dpa at 600°C (1112°F) for 6-nm-size intervals.*

iron-chromium-nickel alloys. Note that although the absolute values of swelling are not identical between Johnston et al and this test series, due to material differences, differing amounts of preinjected helium, etc., the effects of alloying additions of nickel and titanium to the iron-chromium-nickel matrix are similar. It is apparent that the swelling of these alloys is significantly suppressed by the addition of titanium and aluminum to the matrix composition. This is evident in the comparison of the results of Alloy E-48 in the solution-annealed and the aged condition with the simple ternary Alloy E-20. These results are shown in Fig. 12, where the void swelling is compared with the percentage of titanium plus aluminum in the

matrix. It is assumed that all the titanium and aluminum are present in the matrix of E-48 in the solution-annealed condition. In the aged condition, a lower-bound value was assumed based upon matrix chemistry extractive analysis of overaged E-48 heat-treated at 815 °C (1500 °F) for 136 h. This produced a volume fraction of γ' of 10 ± 2 percent and a matrix chemistry of Fe 63.0-Ni 19.1-Cr 15.2-Ti 1.5-Al 0.9 which approximates the upper bound of volume fraction γ' of the irradiated alloy of 7 ± 2 percent.

Equations 3 and 4 that described the swelling equation of Alloy E-48 can be compared with the swelling equation of the simple ternary alloy Eqs 1 and 2 to determine quantitatively the effect of the titanium and aluminum additions on the Fe-15Cr-25Ni alloy at the peak swelling temperature. Following the procedure of Johnston et al [*6*], a relative peak swelling value was calculated by dividing the swelling of Alloy E-48 by that of E-20 at the same dose. These results are shown in Fig. 13.

The swelling suppression effect of the titanium and aluminum is shown to be dependent upon displacement dose since the relative peak swelling varies from about 0.03 at 150 dpa to 0.22 at 300 dpa. This is compared with the value of 0.2 to 0.3 at 115 dpa estimated from Johnston's data for the equivalent titanium addition in the matrix, which is assumed to vary during the bombardment from about 2.5 to about 1.5 percent as discussed in the foregoing. Note that Johnston et al noted no effect of 0.7 percent aluminum on the swelling of the ternary alloys.

Examination of these data shows that it is logical to assume that at high displacement doses the suppression would be essentially that due to titanium alone. Therefore, the effect of aluminum is evidenced by the suppression of the swelling at the lower doses. Examination of the Stage II swelling equations supports this premise. The ratio of the swelling rate of E-48 and E-20 is 0.066/0.190 = 0.34, which is reasonably close to the high displacement dose (that is, titanium) suppression effect noted by Johnston et al. Therefore, the effect of titanium may be assumed to be reflected in the steady-state swelling rate. By similar reasoning, the effect of aluminum may be inferred to be in the suppression of the threshold dose of Stage II swelling. For E-48, this value is 141 dpa, while for the simple ternary it is 51 dpa. These interactions of aluminum and titanium on the base alloy are shown schematically in Fig. 14.

Johnston et al saw no swelling suppression effect of 0.7 percent aluminum in Fe-15Cr-20Ni. These investigators preinjected their specimens with 20 appm helium as compared with the 5 appm used in the present experiments. It is reasonable to assume that the higher value of helium used by Johnston et al is sufficient to mask subtleties in the incubation dose. Thus they would see no change in the swelling at a single displacement dose since aluminum apparently does not influence the swelling rate. It is concluded therefore that the Johston et al data are consistent with these results.

Although the reason for the reduction in swelling of iron-chromium-

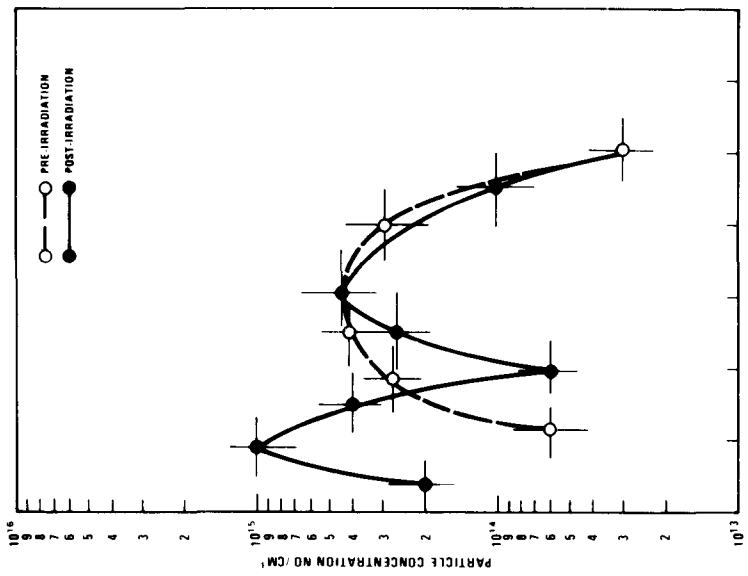

(b) 650°C AT 35 dpa

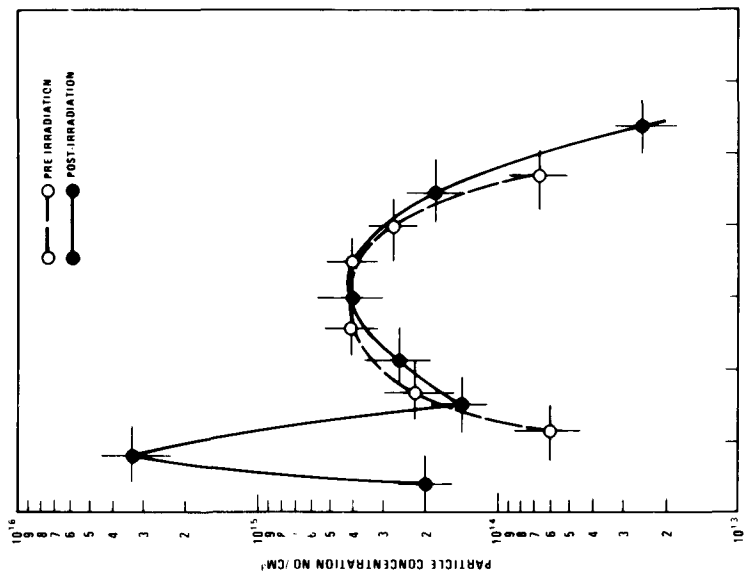

(a) 600°C AT 35 dpa

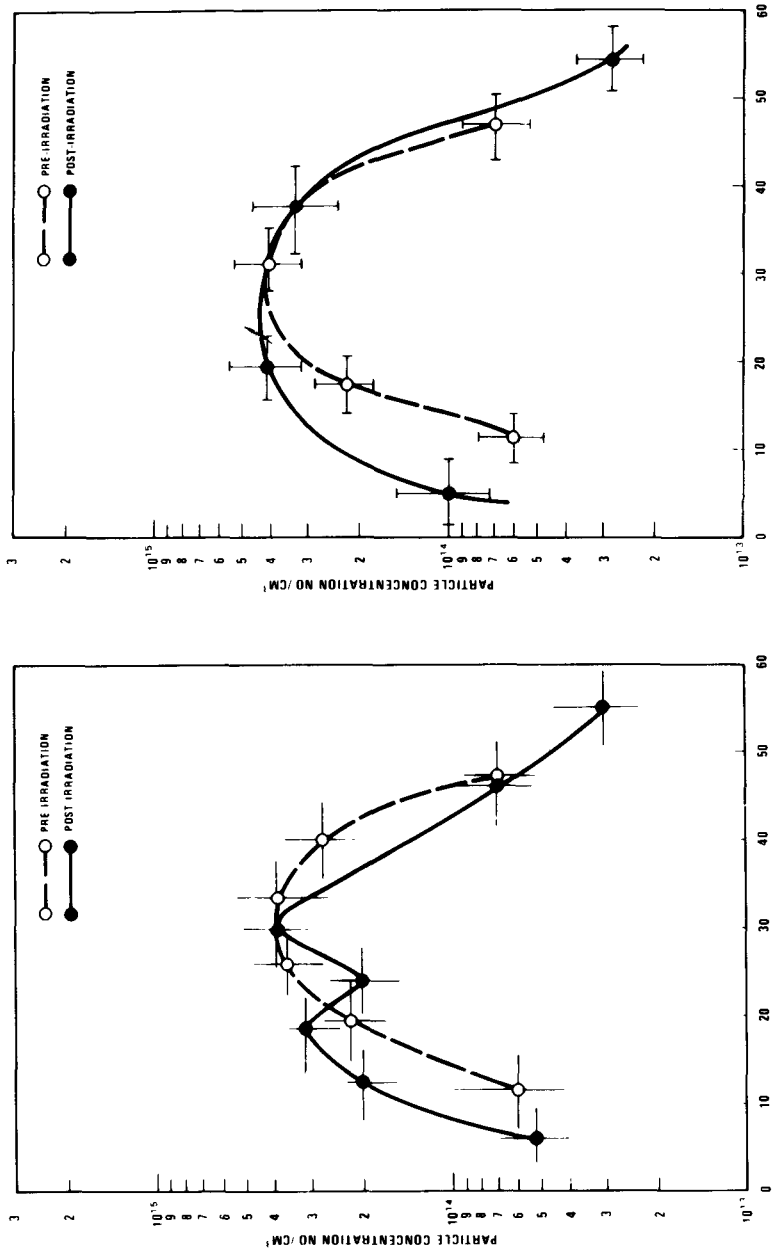

FIG. 9—*Size distribution for E-42 aged 10 h at 815°C (1500°F). Size interval:* (a), (b), *and* (c)—*6 nm;* (d)—*15 nm.*

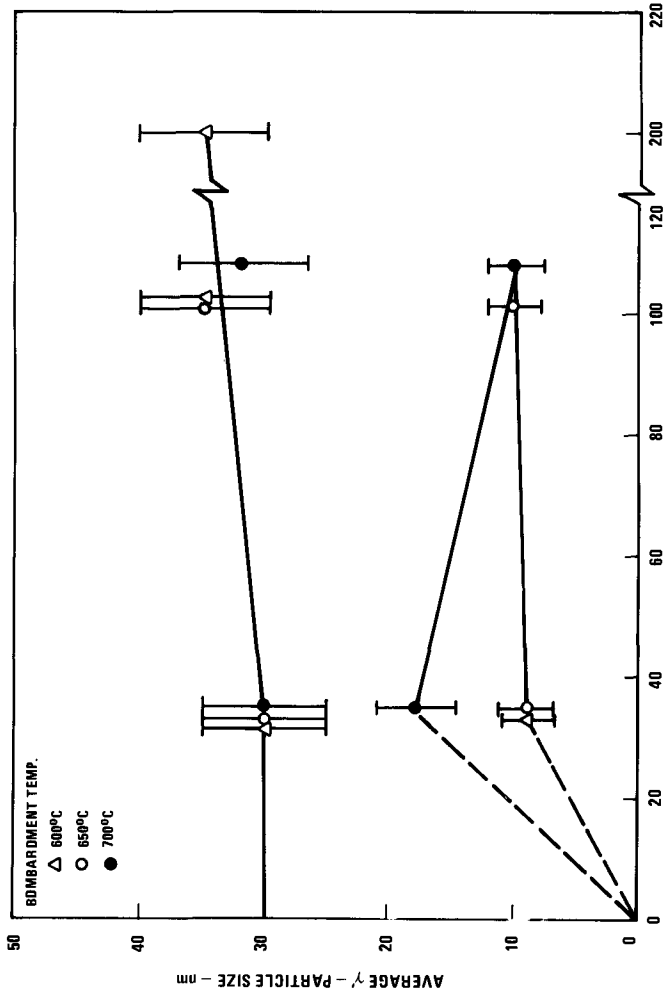

FIG. 10—*Dose dependence of γ'-particle size of Alloy E-42 aged at 815°C (1500°F) for 10 h.*

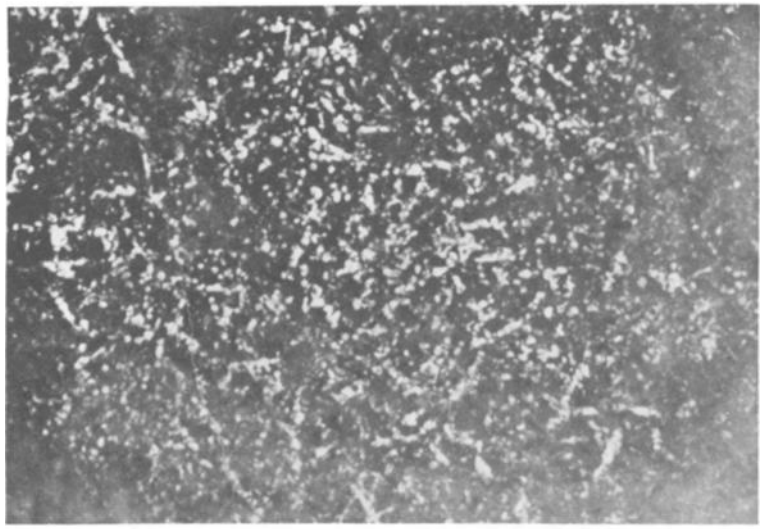

FIG. 11—*γ′ morphology in E-54 (solution annealed) irradiated to 130 dpa at 600°C (1112°F). Superlattice dark field* $\vec{g}$ = *[011].*

nickel alloys by aluminum and titanium cannot be specifically defined, the effect of these two elements is not inconsistent with current theories [*7*]. Smidt and Sprague have shown that vacancy trapping by substitutional impurities could account for reduced void nucleation rates [*8*]. Similarly, Koehler [*9*] has shown that interstitial trapping can reduce the swelling rate. It can also affect nucleation by reducing the mobility of substitutionally diffusing helium. Also, Norris has shown that poisoning of dislocation by impurity atmospheres can suppress void growth [*10*]. All of these mechanisms could be relevant to the effect of titanium and aluminum in solution in the iron-chromium-nickel system. The average Goldschmidt radius characterizing the iron-chromium-nickel solid solutions in these tests is about 0.126 nm, whereas the Goldschmidt radii of aluminum and titanium are 0.143 and 0.147 nm, respectively. Thus aluminum and titanium in solution could exert a misfit strain up to 20 percent on the matrix lattice. A portion of this strain will be relaxed locally, but appreciable strain will remain. This could lead to possible vacancy binding to aluminum and titanium atoms and to dislocation poisoning by the local impurity atmosphere buildup. It was shown by Hasiguti, however, that when crystalline effects are considered, oversized impurity atoms could also trap interstitials [*11*].

Based upon this analysis of swelling data in E-48, it is concluded that the γ'-particles, per se, influence swelling only as they affect matrix chemistry.

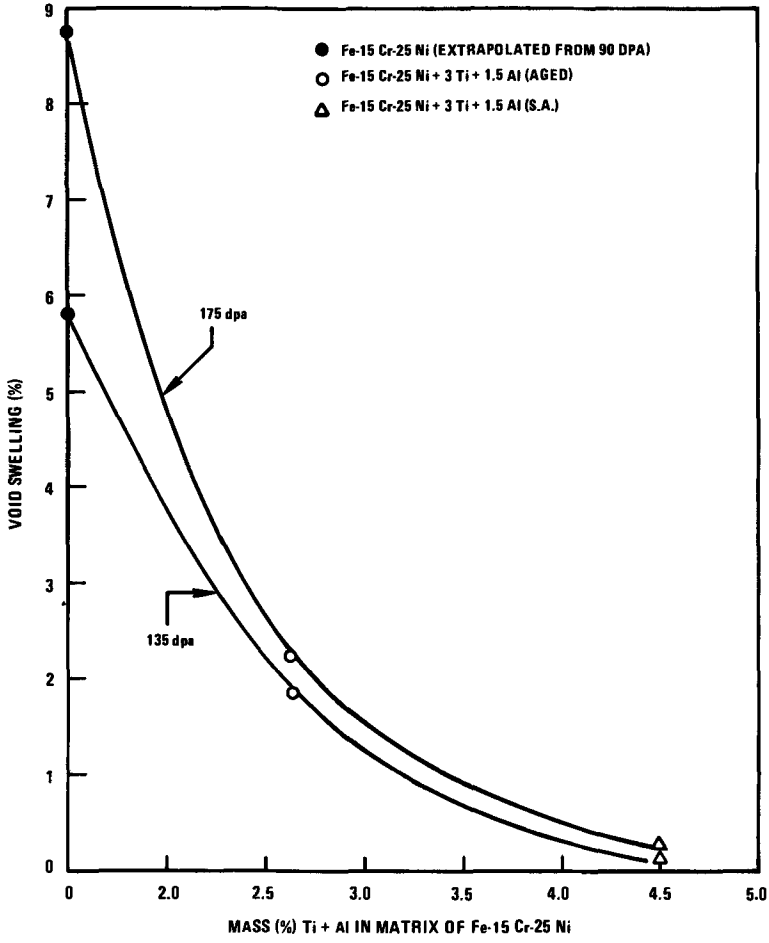

FIG. 12—*Effect of titanium and aluminum content on void swelling of Alloy E-48 at 600 °C (1112 °F).*

Thus swelling control can be separated from considerations of microstructural interactions as long as the desired matrix chemistry is maintained. This premise is supported by the nonuniform swelling noted in the higher nickel alloys E-42 and E-54 as shown in Figs. 4 and 5. Voids were observed only at carbide and grain boundary precipitates. In the case of these alloys, the matrix chemistry is swelling resistant, and only where the nickel and titanium are depleted by second-phase precipitation were voids observed.

γ′-Precipitate Stability

These nickel-ion irradiation tests on Fe-15Cr-25Ni to Fe-15Cr-25Ni alloys containing γ′-precipitates over the temperature range 600 to 750 °C (1112 to

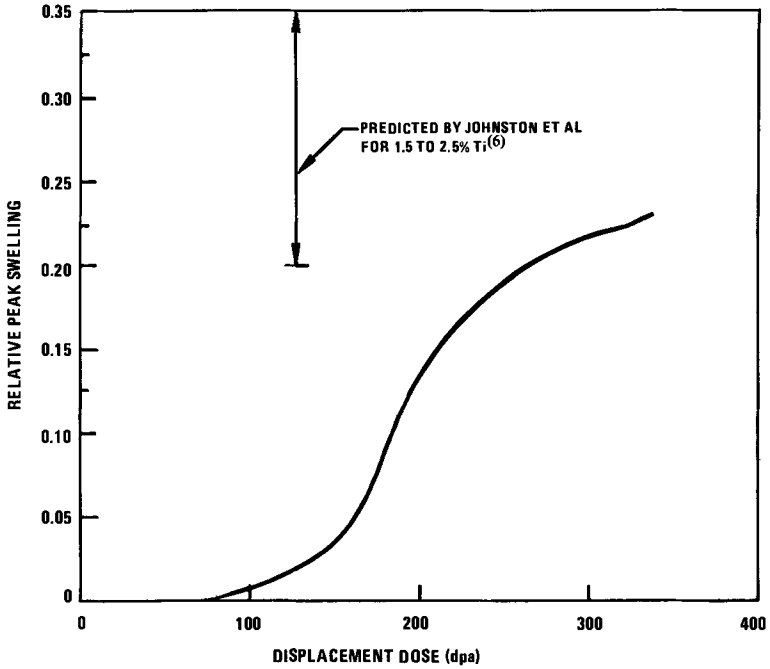

FIG. 13—*Peak swelling suppression of 1.5 percent titanium and 0.9 percent aluminum in matrix of Fe-15Cr-19Ni alloy as a function of dose.*

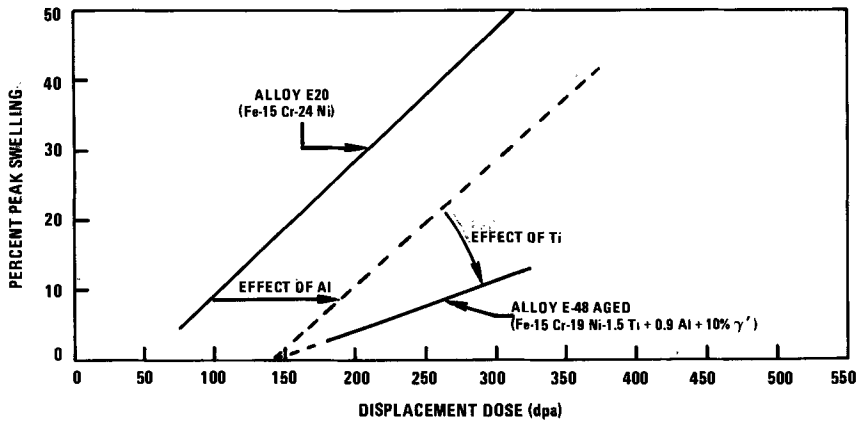

FIG. 14—*Effect of aluminum and titanium additions on swelling of iron-chromium-nickel alloys.*

1382 °F) and up to 200 dpa showed that the irradiations produced a slight change in the size distribution and small change in the volume fraction of the precipitates. If these results are substantiated by neutron irradiation, this would indicate no appreciable degradation of the mechanical properties of this class of alloys under liquid metal fast breeder reactor conditions.

The structural stability of the γ'-particles in these alloys may be compared to that observed in neutron-irradiated PE-16. Hudson showed that an equilibrium structure was attained in solution-annealed and in aged PE-16 after bombardment to 6 dpa at 640 °C (1184 °F) [*12*]. Although the size of the PE-16 γ'-particles is not specified, they appear to be of the order of 5 to 10 nm. It may be noted that, if the initial aged particle size of the alloys in this test were about 10 nm, then these alloys would also have attained "equilibrium."

Two mechanisms originally suggested by Nelson, Hudson, and Mazey [*13*] may contribute to the dissolution of γ'-particles subjected to heavy ion bombardment; namely, recoil dissolution and disorder dissolution. Other irradiation-enhanced mechanisms may be responsible for nucleation of virgin γ'-particles under irradiation. Growth of irregularly shaped particles may occur by radiation-enhanced Oswald ripening or other diffusion-accelerated processes. Analysis of morphological features of the test results described in the foregoing could be interpreted as evidence for diverse mechanisms, and it is apparent that no single mechanism would be sufficient to rationalize these results. The temperature and dose dependence of the size and morphology changes, however, indicate some important general trends. The volume fraction γ' after irradiation is nearly independent of temperature, over a temperature range from 600 to 750 °C (1112 to 1382 °F); it is also nearly independent of total dose. It is concluded, therefore, that disorder dissolution is not an important mechanism at these temperatures; reordering apparently takes place on a very fast time scale. Recoil dissolution does not contribute to large-scale changes in the distribution, although some evidence for its existence can be detected. The most obvious change in the distribution is the nucleation, homogeneous and inhomogeneous, of small γ'-particles approximately 10 nm in diameter. The concentration of these particles is fairly high at 600 °C (1112 °F) (about 10^{22} particles/m^3); however, they contribute little to the volume fraction of the precipitated phase.

Some coarsening is evident at all temperatures, but the effect is small. Nucleation γ' on a fine scale is much more pronounced at low temperatures than at the higher ones investigated and is probably due to the higher supersaturation of γ'-forming elements in the matrix. The nucleation is clearly radiation-enhanced due to the removal of kinetic barriers. Whether it is a radiation-induced phenomenon (that is, due to primary knock-on events) still needs to be investigated. At 750 °C (1382 °F) the distribution of particle

sizes closely resembles thermal distributions, although the fluctuation in particle sizes is more pronounced.

Conclusions

1. Nickel-ion bombardment of iron-chromium-nickel alloys containing γ'-forming additions of titanium and aluminum showed that swelling is significantly suppressed by additions of titanium and aluminum to the matrix. Based upon the peak swelling kinetics, it has been inferred that the effect of aluminum is to increase the incubation dose while titanium acts to reduce the swelling rate.

2. The γ'-particles influence swelling only as they affect the matrix composition. This pronounced effect of matrix composition on swelling in the Fe-15Cr-25Ni to Fe-15Cr-45Ni composition range is evidenced by a large effect of aging heat treatment on swelling.

3. Extensive precipitation of fine γ'-particles (8 to 18 nm) occurs in these alloys at 35 dpa. The concentration of the fine particles is inversely related to temperature in the range 600 to 700 °C (1112 to 1292 °F). Large particles (30 nm) showed a slight coarsening with dose to about 35 nm at 200 dpa.

4. The fine particles approach an equilibrium size at higher damage values (100 dpa), and this effect is temperature independent. Also, this irradiation-enhanced effect was found to be independent of composition in the range 25 to 45 percent nickel.

5. Comparison of these results with neutron-irradiated PE-16 shows a similarity in the formation of an equilibrium-size fine particle.

6. The volume fraction of γ' after irradiation is nearly independent of temperature and damage over the range of 600 to 750 °C (1112 to 1382 °F) and 35 to 200 dpa, respectively. Therefore, it is concluded that disorder dissolution is not an important mechanism for the 30-nm particles in these materials in the temperature range investigated.

Acknowledgments

We wish to acknowledge the cooperation and participation of Scott Lally and the staff at the U. S. Steel Research Laboratories in the high-voltage microscope; the participation of R. Kossowsky and J. Choyke of the Westinghouse Research and Development Center for the extraction analysis and helium preinjection of the specimens; the assistance of A. Taylor, members of the staff of the Material Sciences Division, and the Dynamitron staff at Argonne National Laboratory for the nickel-ion bombardments; the indispensable efforts of T. Dimuzio in the preparation of the specimens and the performance of the irradiation; the technical contribution of F. Venskytis in the prebombardment specimen preparation and techniques. This

work was performed within the National Alloy Development Program under the auspices of the U. S. Energy Research and Development Administration.

References

[1] *Radiation Induced Voids In Metals*, J. W. Corbett and L. C. Ianniello, Eds., U. S. Atomic Energy Commission Office of Information Service, Washington, D. C., 1972.
[2] Johnston, W. G., Rosolowski, J. H., Turkalo, A. M., and Lauritzen, T., *Journal of Nuclear Materials*, Vol. 47,1973, p. 155.
[3] Diamond, S., Bleiberg, M. L., Baron, I. M., Bajaj, R., and Chickering, R. W., International Conference on Radiation Effect and Tritum Technology for Fusion Reactors, Gatlinburg, Tenn., 1-3 Oct., 1975.
[4] Manning, I. and Muller, G. P., *Computer Physics Communications*, Vol. 7, 1974, p. 85.
[5] Gibson, R., Private communication, International Nickel Company.
[6] Johnston, W. G., Rosolowski, J. H., Turkalo, A. M., and Lauritzen, T., Seminar on Radiation Damage in Metals, American Society of Metals, Cleveland, Ohio Nov., 1975, to be published.
[7] A general reference of various mechanisms is presented in *Consultant Symposium—The Physics of Irradiation Produced Voids* R. S. Nelson, Ed., AERE-R7934, Atomic Energy Research Establishment, Harwell, England, 9-11 Sept. 1974.
[8] Smidt, F. A. and Sprague, J. A., *Scripta Metallurgica*, Vol. 1, 1973 p. 495; and Smidt, F. A. et al, "The Effect of Alloy Additions on Void Nucleation and Growth" *Defects and Defect Clusters in B.C.C. Metals* R. J. Asenault, Ed., National Bureau of Standards, Gaithersburg, Md., 1973.
[9] Koehler, J. S., "Decrease In The Void Growth Rate By Interstitial Trapping," *Journal of Applied Physics*, Vol 46 No. 6, June 1975, p. 2423.
[10] Norris, D. I. R., "The Poisoning of Dislocations by Impurity Atmospheres as a Mechanism for Control of Void Swelling During Irradiation," *Consultant Symposium*—The Physics of Irradiation Produced Voids, R. S. Nelson, Ed., AERE-R7934, Atomic Energy Research Establishment, Harwell, England, 9-11 Sept. 1974.
[11] Hasiguti, R. R., *Journal of the Physical Society of Japan*, Vol. 15, No. 10, Oct. 1960.
[12] Hudson, J. A., "Structural Stability During Irradiation," *Journal of the British Nuclear Energy Society*, No. 2, 14 April 1975, pp. 127-136.
[13] Nelson, R. S. et al, *Journal of Nuclear Materials*, Vol. 44, 1972, pp. 318-330.

J. A. Sprague,[1] *F. A. Smidt, Jr.,*[1] *J. E. Westmoreland,*[2] *and P. R. Malmberg*[2]

Effect of Ion Irradiation on the Microstructure of an Iron-Nickel-Chromium Alloy

REFERENCE: Sprague, J. A., Smidt, F. A., Jr., Westmoreland, J. E., and Malmberg, P. R., "**Effect of Ion Irradiation on the Microstructure of an Iron-Nickel-Chromium Alloy,**" *Irradiation Effects on the Microstructure and Properties of Metals, ASTM STP 611,* American Society for Testing and Materials, 1976, pp. 337–352.

ABSTRACT: Void and dislocation structures in an Fe-25Ni-15Cr alloy were studied following irradiation with 2.8 MeV $^{58}Ni^{+}$ ions at temperatures between 600 and 750°C (1112 and 1382°F) to maximum damage levels up to 80 displacements per atom (dpa). Void formation was observed at all the temperatures investigated, with the maximum swelling between 650 and 700°C (1202 and 1292°F). The swelling versus dose relationships exhibited an incubation dose followed by swelling at a rate that increased with increasing damage level. These data were consistent with previous swelling results for austenitic alloys irradiated with charged particles, which indicate that the swelling should become linear with irradiation dose at higher damage levels. Tangled dislocation networks were observed to form at low doses and to be fairly stable up to the highest damage levels examined. With the assumption of the observed stable dislocation networks, the dose dependence of swelling could be explained by a general form of the chemical rate theory for swelling due to void growth.

KEY WORDS: radiation, irradiation, voids, swelling, dislocations, microstructure, iron base alloys, stainless steels, radiation effects, radiation damage simulation, ion irradiation

The dimensional instability of cladding and core structural components caused by the formation of voids during irradiation presents a serious design limitation for high-temperature fast reactors. The austenitic stainless steels are an important class of alloys for these applications, both in

[1] Metallurgists, Thermostructural Materials Branch (Code 6390), Engineering Materials Division, Naval Research Laboratory, Washington, D.C. 20375.

[2] Physicists, Materials Modification and Analysis Branch (Code 6670), Radiation Technology Division, Naval Research Laboratory, Washington, D.C. 20375.

presently operating reactors and in future units. Since the microstructures of most commercial alloys are complex, it is useful to study the mechanisms of swelling basic to the austenite lattice with high-purity model systems, such as iron-nickel-chromium ternary alloys. The present experiment was performed as part of the Alloy Development Intercorrelation Program, an interlaboratory comparison of the swelling produced by fast neutrons and a variety of charged particles. In addition to their part in the intercomparison, which will be reported elsewhere, the results of this individual experiment provide a detailed analysis of the initial swelling behavior of an ion-irradiated iron-nickel-chromium alloy, giving some insights into the important void formation mechanisms.

Experimental Procedure

The alloy used for this experiment was nominally Fe-25Ni-15Cr, which had been swaged into 3.2-mm-diameter rod and given a final anneal at 1093°C (2000°F) for one hour in hydrogen followed by a furnace cool. The actual chemical composition of the alloy is given in Table 1. The rod

TABLE 1—*Composition of alloy (weight percent).*

Fe	Ni	Cr	C	Cu	Si	Mn	N_2	O_2
60.1	25.04	14.80	0.01	0.02	0.02	0.005	0.0028	0.0154

was sliced into disks 0.23 to 0.33 mm thick, which were ground to thicknesses of 0.15 to 0.18 mm with 600-grit abrasive paper. One surface of each disk was polished with 0.3-μm alumina and then electropolished to remove the polishing scratches. The specimens were implanted with a uniform concentration of approximately 5 atomic parts per million (appm) helium.

Following helium implantation, the polished surface of each specimen was lightly repolished with 0.3-μm alumina, and an additional 80 μm was removed from the surface by jet electropolishing with an electrolyte of 250-ml methyl alcohol, 150-ml butyl alcohol, and 15-ml perchloric acid at −60°C (−76°F).

The nickel-ion irradiations were performed using the Naval Research Laboratory (NRL) 5 MV Van de Graaff accelerator. A beam of 2.8 MeV $^{58}Ni^{+}$ was produced with this accelerator using a sputter ion source of the Hill-Nelson type, which had been extensively modified to adapt it to the accelerator and increase the attainable beam current. The beam from the accelerator was bent 16 deg by an energy-analyzing magnet, then defocused by the first section of a standard electrostatic quadrupole

strong focusing lens doublet. The specimen was located 1.2 cm above the centerline of the drift tube, and the single-charged component of the beam was steered to this position with a set of electrostatic deflection plates. This procedure greatly reduced the effect of ions with other charge states, created by charge exchange collisions with residual gas atoms in the tube. The specimens were irradiated with a 3 mm by 3 mm beam, selected from the center of the large defocused beam by an aperture. The uniformity of the ion flux within this 3 mm by 3 mm area was monitored periodically during irradiation with a vane-type beam profile monitor, and variations were kept to less than ±15 percent. The ion fluence was measured by integrating the current directly from the entire target chamber, which was electrically isolated and formed a deep Faraday cup. The average beam current density for all of the bombardments was (2.2 to 2.4) $\mu A/cm^2$. At each irradiation temperature, specimens were irradiated to integrated charge densities of 1210, 3630, 6050, and 8470 $\mu C/cm^2$. Additional specimens were irradiated to 10 890 $\mu C/cm^2$ at 650 and 700°C (1202 and 1292°F).

The target chamber specimen holder was a resistance-heated columbium block with ten faces, to which the specimens were mechanically clamped. The irradiation temperature was monitored with a thermocouple embedded in the block. The calibration of this thermocouple was previously checked with a small thermocouple spot-welded directly to a dummy nickel specimen. This same arrangement was used to measure the temperature rise due to beam heating, which was found to be 12°C (22°F) for the range of irradiation temperatures used in this investigation. The reported irradiation temperatures include this 12°C (22°F) temperature rise and have an overall accuracy within ±10°C (±18°F). Specimens were irradiated at 50°C (90°F) intervals between 600 and 750°C (1112 and 1382°F).

The deposition of initial damage energy by the nickel ions as a function of distance into the target foils was determined by the E-DEP-1 code [*1*].[3] For this calculation, the bulk density of the material was assumed to be 7.8 g/cm^3. The energy deposition was converted to displacements per atom (dpa) with the modified Kinchin-Pease model proposed by Torrens and Robinson [*2*], using a displacement energy of 40 eV and a displacement efficiency of 0.8. This procedure yielded peak displacement densities (located at 5600 Å depth) of 10, 30, 50, 70, and 90 dpa and a range of average peak displacement rates between 1.8×10^{-2} and 2.0×10^{-2} dpa/s.

Following ion irradiation, a nominal 0.4 μm was removed from the front surface of each specimen using an interferometric electropolisher that has been described elsewhere [*3*]. Since some difficulty was experienced in following the interference fringes during polishing of this alloy,

[3] The italic numbers in brackets refer to the list of references appended to this paper.

the actual depth of the electropolish was determined by a subsequent interference microscopy measurement of the height of a step at the edge of a masked area. The range of these measured depths was 0.3 to 0.5 μm. The front surface of each specimen was then masked off with petroleum jelly and a thin piece of transparent plastic, and the back surface was polished to perforation with an electrolyte of 20 percent perchloric acid and 80 percent acetic acid at room temperature. Some of the specimens which did not contain sufficiently thin areas following electropolishing were further thinned from the back surface by ion milling.

The specimens were examined in a 200-kV electron microscope equipped with side-entry goniometer stage. For each area examined, a stereo pair of micrographs was taken in void contrast (weakly diffracting with slightly underfocused objective) conditions and a third micrograph was taken with the dislocations in contrast. Void size distributions were measured with a variable light spot type particle size analyzer. The size of the physical projection of a void was measured at the inside of any visible dark ring at the edge of the void image. Since the voids formed in this material were irregularly shaped, the equivalent diameter of a void was taken to be the maximum diameter of a circle inscribed within the void image. Voids intersecting specimen surfaces were not measured. The thickness of each area was determined by a stereo measurement of the distance between voids intersecting foil surfaces. Dislocation densities were determined by counting intersections with randomly oriented lines drawn on the micrographs. The damage level (dpa) for each area was taken to be the mean value calculated across the specimen, using the measured front face depth and the thickness of the region examined.

Discussion of Experimental Results

Qualitative examination of the irradiated microstructures revealed that all of the irradiation conditions of this experiment produced voids and tangled dislocation networks, with the exceptions of 9 dpa at 700 and 750°C (1292 and 1382°F), for which no voids were detected. A few loops were seen within the dislocation networks, but these accounted for a relatively small fraction of the total dislocation line length in most specimens. The effects of irradiation temperature on the observed microstructures are illustrated in Fig. 1. The voids and dislocations at 600°C (1112°F) are shown in separate micrographs because the small void sizes made it impossible to effectively image both types of defects with the same diffraction condition. The general trends with increasing irradiation temperature were, as expected from many previous experiments, to lower dislocation and void number densities and to larger void sizes. The progression of microstructures with increasing irradiation dose at 650°C (1202°F) is illustrated in Fig. 2. Again, small void sizes made it necessary to show the

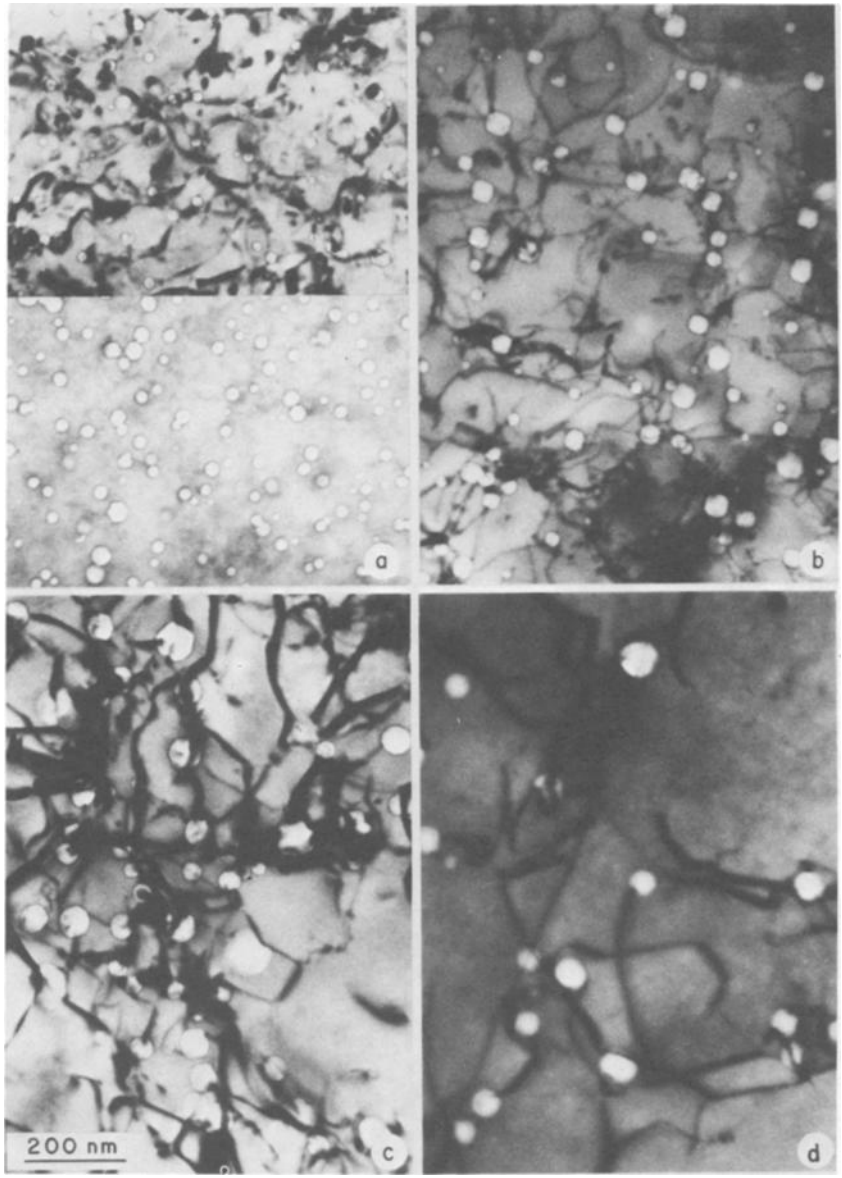

FIG. 1—*Effect of irradiation temperature on the void and dislocation structures:* (a) *35 dpa at 600°C (1112°F) (dislocations above, voids below)*; (b) *42 dpa at 650°C (1202°F)*; (c) *43 dpa at 700°C (1292°F)*; (d) *42 dpa at 750°C (1382°F)*.

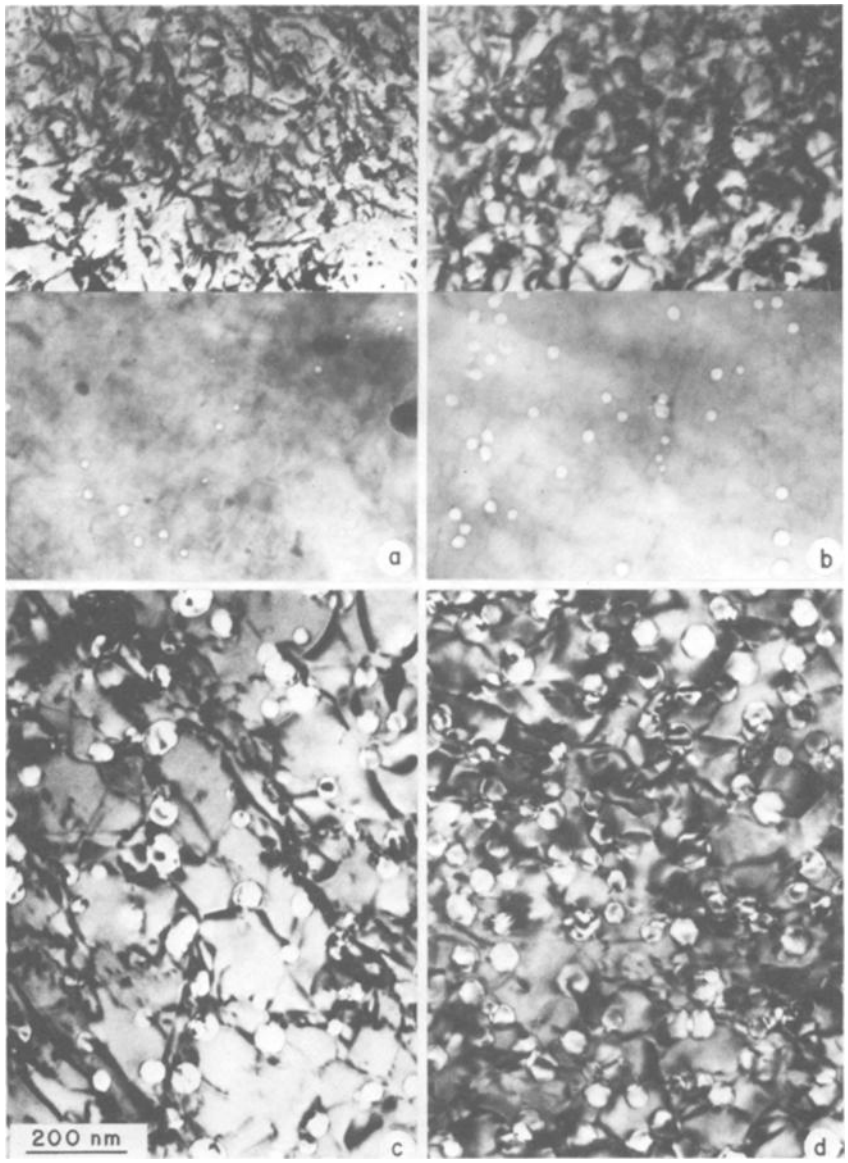

FIG. 2—*Effect of irradiation dose at 650°C (1202°F) on the void and dislocation structures (see also Fig. 1b)*: (a) *9 dpa (dislocations above, voids below)*; (b) *22 dpa (dislocations above, voids below)*; (c) *60 dpa*; (d) *80 dpa.*

voids and dislocations in separate micrographs for 9 and 22 dpa. It can be seen that the dislocation network became very dense at low damage levels and then progressed to slightly more open structures with the onset of significant void formation.

This relationship of dislocation structure to dose, similar to that seen at the other temperatures of the experiment, was somewhat different from that reported in a previously published study of this same alloy irradiated with 3.5-MeV nickel ions [*4*]. In that experiment, the full range of the ions was examined in stereo with a 1-MV electron microscope. The variation of the damage production with depth from the irradiated surface was used to convert the observed depth dependence of microstructures to dose dependence. With this technique, the progression of dislocation structure with increasing depth (and thus increasing dose) was from a coarse dislocation network to large faulted loops to large unfaulted loops to a dense tangled dislocation network. The irradiation dose at the surface of the Ref *4* specimens, and thus the dose at which the aforementioned progression began, was approximately 30 dpa.

The quantitative parameters of the void and dislocation distributions are given in Table 2. The dependence of dislocation density on dose that was apparent in Fig. 2 can be seen for all four irradiation temperatures.

TABLE 2—*Void and dislocation data.*

Temperature, °C	Dose, dpa	Total Voids Measured	Mean Void Size, nm	Void Density, cm^{-3}	Swelling, %	Dislocation Density, cm^{-2}
600	9	646	9.1	1.2×10^{15}	0.06	2.6×10^{10}
600	26	513	12.5	8.3×10^{14}	0.11	4.9×10^{10}
600	35	2025	16.8	8.6×10^{14}	0.28	1.5×10^{10}
600	64	2844	25.4	9.4×10^{14}	0.98	1.6×10^{10}
650	9	119	11.7	1.1×10^{14}	0.01	4.7×10^{10}
650	22	500	18.6	4.2×10^{14}	0.17	2.8×10^{10}
650	42	1116	25.6	3.6×10^{14}	0.47	1.4×10^{10}
650	60	929	39.6	4.5×10^{14}	1.95	1.7×10^{10}
650	80	1617	50.3	9.3×10^{14}	7.72	1.4×10^{10}
700	9	...	...	...	...	1.8×10^{10}
700	26	328	25.6	9.3×10^{13}	0.11	2.6×10^{10}
700	43	339	42.1	7.4×10^{13}	0.40	1.2×10^{10}
700	75	790	67.3	3.8×10^{14}	8.12	1.1×10^{10}
750	9	...	...	...	...	9.8×10^{9}
750	26	30	37.0	1.0×10^{13}	0.33	4.0×10^{9}
750	42	98	56.2	3.8×10^{13}	0.44	4.5×10^{9}
750	57	102	68.4	3.1×10^{13}	0.72	4.5×10^{9}

An especially interesting point is that the apparently stable dislocation density reached at high doses was nearly constant between 600 and 650°C

(1112 and 1202°F), decreased by ~25 percent between 650 and 700°C (1202 and 1292°F), and decreased by ~60 percent between 700 and 750°C (1292 and 1382°F). Although there was some scatter in the behavior of the void number densities with dose, the maximum values observed showed a similar dependence on irradiation temperature, with a large decrease between 700 and 750°C (1292 and 1382°F). The general swelling behavior with increasing dose was an incubation period followed by a rate of swelling that increased with increasing dose, which can be seen most dramatically at 650 and 700°C (1202 and 1292°F), for which specimens were irradiated to higher doses.

In both electron [*5*] and heavy-ion [*4,6*] irradiation of many austenitic stainless steels and model austenitic alloys, the observed swelling behavior has been a variable incubation dose with little or no measurable void formation, a transition dose regime in which the swelling rate increased with increasing dose, and a high-dose regime in which the swelling was linear with dose. Insufficient data were gathered in the present experiment to determine whether or not the high-dose swelling was linear, but the volume of published data [*4–6*] on similar materials tends to justify that assumption. It therefore appears that the bulk of the present data represent the transition regime that is a precursor to linear swelling.

The void size distributions as functions of dose are shown in Fig. 3. The fractional distributions are presented as Gaussian curves fitted to the measured size histograms. This presentation of the fraction of voids per 1-nm-size interval masks the differences in void number density seen in Table 2, but it has the advantage that differences in the distributions themselves are more apparent. The effect of increasing dose on the size distributions may best be discussed with reference to 650°C (1202°F), for which the most extensive data were taken. Up to 42 dpa, the distribution simply broadened, with little movement of the lower size limit. Above 42 dpa, the entire distribution moved to larger sizes. Between 60 and 80 dpa, in fact, the width of the distribution actually decreased. The dose range over which the change in behavior occurred coincided with the onset of rapid swelling. At 700°C (1292°F), there were fewer data points, but the same mechanism seemed to be operating. The onset of rapid swelling was accompanied by a change in the behavior of the void size distribution. Based on these observations, it would appear that the highest dose examined at 600°C (1112°F), 64 dpa, was at the beginning of the rapid swelling regime for that temperature. Due to the low void number density formed at 750°C (1382°F), a relatively small number of voids were measured (see Table 2). The 750°C (1382°F) size distributions must therefore be interpreted with some caution, but one can say in general that they broadened with increasing dose.

Interpretation of the Swelling Behavior

As discussed in the foregoing section, the swelling observed in this experiment appeared to follow the same swelling-dose relationship previously reported by a number of investigators for charged-particle irradiation of austenitic alloys. Specifically, this is a swelling rate that increases with increasing dose followed by swelling that is linear with dose. This behavior is discussed in the following with reference to the chemical rate theory of swelling due to void growth. The results of these calculations have important implications for the comparison of charged-particle and neutron-irradiation experiments.

The fundamentals of the chemical rate theory [*7–10*] are contained in a pair of coupled equations for the point defect concentrations

$$G + G_v^{\text{th}} - Q_v D_v C_v - R C_v C_i = 0 \tag{1}$$

$$G - Q_i D_i C_i - R C_v C_i = 0 \tag{2}$$

which determine the vacancy and interstitial concentrations C_v and C_i, in terms of the atomic displacement rate G; the thermal rate of vacancy production G_v^{th}; the mutual recombination coefficient R; the strengths of all fixed sinks for vacancies and interstitials, Q_v and Q_i; and the diffusion coefficients for vacancies and interstitials, D_v and D_i. The sink strengths are usually calculated as sums of terms for the various types of sinks

$$Q_v = Q_v^V + Q_v^D + \ldots \tag{3}$$

$$Q_i = Q_i^V + Q_i^D + \ldots . \tag{4}$$

voids dislocations

A number of models have been proposed to calculate these sink strengths, including those for which the point-defect absorption is diffusion-controlled [*7–9*] and surface-reaction controlled [*10*]. The simplest class of these models that suit the present purpose considers voids and dislocations as the dominant sinks, the voids having equal strength for vacancies and interstitials and the dislocations having an effective bias in favor of interstitial absorption

$$Q_v^V = Q_i^V = Q^V \tag{5}$$

$$Q_v^D = Q_0^D \tag{6}$$

$$Q_i^D = (1 + \delta) Q_0^D \tag{7}$$

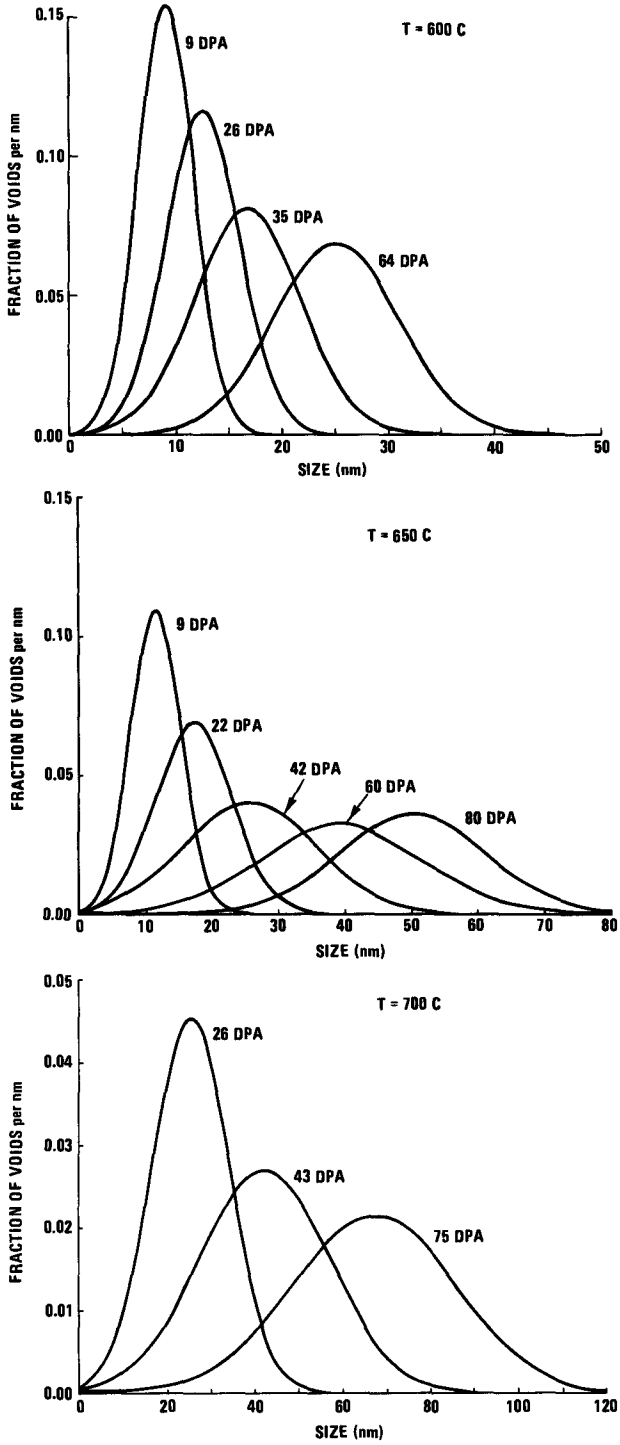
T = 600 C
9 DPA
26 DPA
35 DPA
64 DPA
FRACTION OF VOIDS per nm
SIZE (nm)
T = 650 C
9 DPA
22 DPA
42 DPA
60 DPA
80 DPA
FRACTION OF VOIDS per nm
SIZE (nm)
T = 700 C
26 DPA
43 DPA
75 DPA
FRACTION OF VOIDS per nm
SIZE (nm)

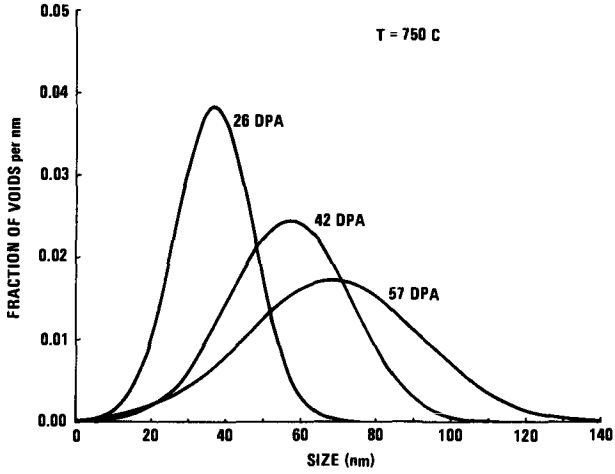

FIG. 3—*Fractional void size distributions observed*: (a) *600°C (1112°F)*; (b) *650°C (1202°F)*; (c) *700°C (1292°F)*; (d) *750°C (1382°F)*.

where δ is commonly taken to be 0.01 to 0.1. The rate of swelling may then be calculated by

$$\frac{d}{dt}(\Delta V/V) = (C_v D_v - C_i D_i) Q^V \tag{8}$$

For purposes of discussion, we can assume that the temperature is sufficiently low that we can safely ignore G_v^{th}, and we will consider two limiting cases: (*a*) almost all of the point defects are annihilated at fixed sinks, and (*b*) almost all of the point defects are annihilated by mutual recombination. For the first case, representative of temperatures near the peak swelling temperature for neutron irradiation, the approximate results are

$$C_v \approx \frac{G}{Q_v D_v} \tag{9}$$

$$C_i \approx \frac{G}{Q_i D_i} \tag{10}$$

$$\frac{d}{dt}\left(\frac{\Delta V}{V}\right) \approx \left(\frac{\delta Q_0^D}{Q^V + (1+\delta) Q_0^D}\right)\left(\frac{Q^V}{Q^V + Q_0^D}\right) G \tag{11}$$

If dislocations are the dominant sinks, the swelling rate approaches

$$\frac{d}{dt}\left(\frac{\Delta V}{V}\right) \xrightarrow{Q_0^D \gg Q^V} \sim G\delta \left(\frac{Q^V}{Q_0^D}\right) \tag{12}$$

If voids are the dominant sinks, the swelling rate approaches

$$\frac{d}{dt}\left(\frac{\Delta V}{V}\right) \xrightarrow{Q^V \gg Q_0^D} \sim G\delta \left(\frac{Q_0^D}{Q^V}\right) \tag{13}$$

The maximum swelling rate is predicted for the void and dislocation sink strengths being equal. The important point of this is that if all point defects are annihilated at voids or dislocations, and the displacement rate and dislocation bias are constant, then a constant swelling rate implies that the ratio of void sink strength to dislocation sink strength is constant.

The second case, dominant recombination, is representative of the low-temperature portion of the neutron-irradiation swelling range and, as discussed previously [*11*], much of the temperature range for swelling in a high dose rate charged-particle experiment. In this limit

$$C_v \approx \left(\frac{GQ_iD_i}{RQ_vD_v}\right)^{1/2} \tag{14}$$

$$C_i \approx \left(\frac{GQ_vD_v}{RQ_iD_i}\right)^{1/2} \tag{15}$$

$$\frac{d}{dt}\left(\frac{\Delta V}{V}\right) \approx \left(\frac{GD_iD_v}{R}\right)^{1/2} \left(\frac{\delta Q_0^D Q^V}{Q_0^D + Q^V}\right) \tag{16}$$

In this case, if the dislocations are the dominant sinks

$$\frac{d}{dt}\left(\frac{\Delta V}{V}\right) \xrightarrow{Q^D \gg Q^V} \sim \left(\frac{GD_iD_v}{R}\right)^{1/2} \delta Q^V \tag{17}$$

while dominance of the voids as sinks gives

$$\frac{d}{dt}\left(\frac{\Delta V}{V}\right) \xrightarrow{Q^V \gg Q_0^D} \sim \left(\frac{GD_iD_v}{R}\right)^{1/2} \delta Q_0^D \tag{18}$$

For a constant dislocation sink strength, the maximum swelling rate is described by Eq 18 in this approximation.

This second limiting case implies, then, that if a large fraction of the radiation-produced defects are lost by mutual recombination, the swelling

rate will be approximately proportional to the void sink strength when the dislocations are much stronger sinks than the voids, and the swelling rate will be approximately proportional to the dislocation sink strength when the voids are the stronger sinks. In other words, if the dislocation network is stable and voids are the dominant sinks, then the swelling rate will be constant, independent of moderate changes in the void sink strength.

To determine if the limiting case of dominant recombination could be applied to explain the dose dependence of swelling in charged-particle irradiated austenitic alloys, swelling rates were calculated by Eq 1-8, thus considering both recombination and point-defect loss to fixed sinks. Swelling rates were calculated as a function of void sink strength for a constant dislocation sink strength [9] of $Q_0^D = 1 \times 10^{10}$ cm^{-2} with $\delta = 0.01$, using material parameters representative of an austenitic steel [9]. The following cases were considered: a temperature of 700°C (1292°F) and a displacement rate of 2×10^{-2} dpa/s, representing the peak swelling condition in the present experiment; a temperature of 550°C (1022°F) and a displacement rate of 1×10^{-6} dpa/s, representing the peak swelling condition for neutron irradiation of the same alloy, allowing for the 150°C (270°F) shift of the peak swelling temperature observed for Type 316 stainless steel [6]. Two features of the results of these calculations, shown in Fig. 4, are worthy of note. The swelling rates for the charged-particle case were much lower (note the different scales for the two curves) than those for the neutron-irradiation case, due to the larger fraction of point

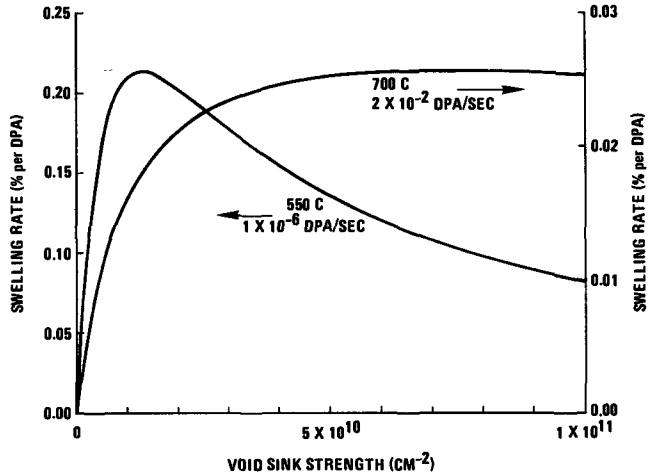

FIG. 4—*Swelling rates due to void growth as functions of void sink strength predicted for a stainless steel irradiated under conditions representing the peak swelling temperatures for neutron irradiation [1 × 10^{-6} dpa/s at 550°C (1022°F), left-hand ordinate] and the present ion irradiation [2 × 10^{-2} dpa/s at 700°C (1292°F), right-hand ordinate].*

defects lost to recombination. Also, in the charged-particle case, the swelling rate increased with increasing void sink strength up to approximately $Q^V \approx 2 \times Q_0{}^D$, beyond which the swelling rate was relatively insensitive to further increases in void sink strength. In the neutron-irradiation case, however, most of the point defects were being annihilated at the voids and dislocations, and the ratio of the two sink strengths strongly affected the swelling rate over the entire range.

These calculations, coupled with experimental observations, suggest a simplified mechanism for the swelling-dose relationships in charged-particle irradiation of austenitic steels. A relatively stable dislocation structure first forms at low irradiation doses. With increasing dose, void nucleation and growth increase the sink strength of the voids, resulting in an increasing swelling rate. Beyond the dose for which the voids become slightly stronger sinks than the dislocations, the swelling rate becomes nearly constant, and the swelling is essentially linear with dose. The rate of void nucleation will determine both the magnitude of the incubation dose and the swelling in the transition dose regime.

This model is definitely an oversimplified one, but it does point out a significant difference between neutron and charged-particle swelling experiments. Near the peak swelling temperature for neutron irradiation, nearly all of the point defects are lost at fixed sinks. In this case, a constant swelling rate implies a constant ratio of void to dislocation sink strength. For a charged-particle irradiation, a large fraction of the point defects may be lost by mutual recombination at the peak swelling temperature, and, with a stable dislocation network, a constant swelling rate may be achieved for a wide range of the sink strength ratio.

For this picture to be valid, some factor outside the simple void growth theory must intervene in charged-particle experiments to reduce the swelling rate at temperatures above the peak. Both the present experimental results and a previous study of the temperature dependence of nickel-ion damage in nickel [*11*] suggest that the sharp decrease of the swelling rate for temperatures above the peak is related to a sharp decrease in the void nucleation rate. Furthermore, the experimental evidence also suggests that the decrease in void nucleation is related to a decrease of the dislocation density due to dynamic annealing of the dislocation structure during irradiation.

Conclusions

An investigation of nickel-ion damage in Fe-25Ni-15Cr at temperatures between 600 and 750°C (1112 and 1382°F) produced the following results:

1. The peak swelling temperature was between 650 and 700°C (1202 and 1292°F), with some void formation observed at all temperatures.

2. At all temperatures, the dislocation density increased to a maximum at relatively low irradiation doses and then decayed slightly to a stable value.

3. The observed swelling-dose relationships were in the form of an incubation dose followed by a region where the rate of swelling increased with increasing irradiation dose. The relationships were consistent with previously reported results for charged-particle irradiations of similar alloys: incubation dose, followed by transition regime with increasing swelling rate, followed by swelling that is linear with dose.

4. The onset of rapid swelling at 650 and 700°C (1202 and 1292°F) coincided with a change in the behavior of the void size distributions from a broadening of the distribution with increasing dose to a movement of the entire distribution.

Analyses of the dose dependence of void and dislocation structures of this and other austenitic alloys irradiated with charged particles indicate that the swelling data can be understood in terms of a general form of the chemical rate theory for swelling due to void growth. Due to the high displacement rates achieved in charged-particle experiments, the theory predicts that a large fraction of the radiation-produced point defects will be annihilated by mutual recombination, even at the peak swelling temperature. If, as in the present experiment, fairly stable dislocation networks form at low damage levels, the theory predicts that initial void nucleation and growth will cause the swelling rate to increase with increasing dose until the voids become the dominant sink. If the dislocation network remains stable, the swelling rate will be approximately constant at higher doses.

Acknowledgments

This research was financially supported by the Office of Naval Research. The experiments were performed as part of an interlaboratory program coordinated by the Energy Research and Development Administration. The technical cooperation of the other participants in this program, including several individuals from Atomics International, General Electric, Hanford Engineering Development Laboratory, International Nickel Co., and Westinghouse is also gratefully acknowledged.

References

[1] Manning, I. and Mueller, G. P., *Computer Physics Communications,* Vol. 7, 1974, pp. 85–94.

[2] Torrens, I. M. and Robinson, M. T. in *Radiation-Induced Voids in Metals,* J. W. Corbett and L. C. Ianniello, Eds., U.S. Atomic Energy Commission Symposium Series 26, 1972, pp. 739–756.

[3] Sprague, J. A., *Review of Scientific Instruments,* Vol. 46, 1975, pp. 1171–1173.
[4] Diamond, S., Baron, I. M., Bleiberg, M. L., Bajaj, R., and Chickering, R. W., "HVEM Quantitative Stereoscopy Through the Full Damage Range of an Ion-Bombarded Fe-Ni-Cr Alloy," *Proceedings,* International Conference on Radiation Effects and Tritium Technology for Fusion Reactors, Gatlinberg, Tenn., 1–3 Oct. 1975, to be published.
[5] Makin, M. J. and Walters, G. P., *Proceedings,* Symposium on the Physics of Irradiation Produced Voids, Atomic Energy Research Establishment Report R7934, Harwell, England, 9–11 Sept. 1974, pp. 299–312.
[6] Johnston, W. G., Lauritzen, T., Rosolowski, J. H., and Turkalo, A. M., "The Effect of Metallurgical Variables on Void Swelling," *Proceedings,* American Society for Metals Materials Science Seminar on Radiation Damage in Metals, Cincinnati, Ohio, 9–10 Nov. 1975, to be published.
[7] Harkness, S. D. and Li, Che-Yu, *Metallurgical Transactions,* Vol. 2, 1971, p. 1457.
[8] Wiedersich, H., *Radiation Effects,* Vol. 12, 1972, pp. 111–125.
[9] Brailsford, A. D. and Bullough, R., *Journal of Nuclear Materials,* Vol. 44, 1972, pp. 125–135.
[10] Mansur, L. K., Okamoto, P. R., Taylor, A., and Li, Che-Yu in *Properties of Reactor Structural Alloys After Neutron or Particle Irradiation, ASTM STP 570,* American Society for Testing and Materials, 1976, pp. 272–289.
[11] Sprague, J. A., Westmoreland, J. E., Smidt, F. A. Jr., and Malmberg, P. R., *Journal of Nuclear Materials,* Vol. 54, 1974, pp. 286–298.

W. L. Bell,[1] *T. Lauritzen,*[2] *E. S. Darlin,*[1] *and R. W. Warner*[1]

Microstructural Changes in Ion-Irradiated Commercial Alloys

REFERENCE: Bell, W. L., Lauritzen, T., Darlin, E. S., and Warner, R. W., **"Microstructural Changes in Ion-Irradiated Commercial Alloys,"** *Irradiation Effects on the Microstructure and Properties of Metals, ASTM STP 611,* American Society for Testing and Materials, 1976, pp. 353-369.

ABSTRACT: The effect of heavy ion bombardment on the microstructural stability of several high-nickel superalloys was evaluated by transmission electron microscopy techniques. The work was intended to simulate the type and magnitude of radiation damage occurring with high-fluence exposure in a liquid metal fast breeder reactor (LMFBR) core.

Results revealed a general acceleration in precipitation kinetics in alloys with high titanium-to-aluminum ratios, over the temperature range 475 to 725°C (887 to 1337°F). In the Inconel alloys 706 and 718, for example, bombardment produced the stable overaging precipitate η Ni_3Ti at the expense of the preexisting phases γ', γ'', and δ. Thermal control data over the same temperature range did not reveal the presence of η. Little or no changes in precipitate microstructure were observed in Nimonic PE16, an age-hardenable alloy with a titanium/aluminum ratio of unity.

KEY WORDS: radiation, ion bombardment, simulation, radiation damage, overaging, precipitation hardening, transmission electron microscopy

The irradiation behavior of several high-nickel superalloys is being studied by participants in the National Alloy Development Program to assess the applicability of this group of alloys for use as liquid metal fast breeder reactor (LMFBR) core structural materials. Interest in the superalloys is based principally on their high-temperature strength and their apparent resistance to swelling in an irradiation environment [*1*].[3] The

[1] Metallurgist and technologists, respectively, General Electric Co., Vallecitos Nuclear Center, Pleasanton, Calif. 94566.

[2] Engineer, Fast Breeder Reactor Department, General Electric Co., Sunnyvale, Calif. 94086.

[3] The italic numbers in brackets refer to the list of references appended to this paper.

development of high mechanical strength in these alloys is due to the precipitation of nickel-rich intermetallic phases upon proper heat treatment; their swelling resistance, although not fully understood, is related to their high matrix nickel content as well as to the solubility of certain minor alloying elements.

In view of their complex aging response and the acute dependence of strength, and, likely, irradiation-induced swelling on the resulting microstructure, the stability of these alloys is of considerable practical concern in the ultimate selection of candidates for in-reactor applications.

In the work reported here, high energy nickel-ion bombardment techniques were used to provide a rapid simulation of neutron irradiation. Three potential candidates were studied: Inconel 706, Inconel 718, and Nimonic PE16. All are precipitation-hardenable grades and were bombarded in the fully heat-treated condition. The Inconel 706 and Nimonic PE16 were, in addition, studied in the solution-annealed condition. The objective of the work was the microstructural characterization of the alloys after high-dose, high-temperature ion bombardment and an assessment of the effect of such bombardments on phase stability.

Experimental Details

Heavy ion-bombardment techniques have been used for a number of years to simulate the type and magnitude of void formation that occurs in metals and alloys with high-temperature fast neutron irradiation [*2*]. In the present investigation, positively charged nickel ions accelerated to 5 MeV in a tandem Van de Graff accelerator were used to bombard thin foils of test material. [Preparation of the foils prior to bombardment included cyclotron implantation of 5 atom parts per million (appm) of helium into the foils to simulate the in-reactor production of helium by the (n, α) reaction.] Bombardments were made over a range of temperatures selected to span the peak swelling temperature in each alloy. All alloys were bombarded to a damage level of 115 dpa (E_d = 40 eV),[4] which corresponds to a fluence of 2 to 3 $\times$ 10^{23}neutrons/cm^2 ($E > 0.1$ MeV) [*1*].

Since 5-MeV nickel ions have a range of only about 1400 nanometres (nm) in these materials and the peak damage zone lies only 900 nm from the surface, transmission electron microscopy (TEM) foils must be carefully prepared to provide a final foil thickness that lies within the peak damage region. Calibrated removal of material from the front surface was performed by argon ion micromilling, after which the nominally 150-μm foil was perforated by electropolishing from the back surface. The

[4] Displacements per atom (dpa) were calculated using a minimum displacement energy (E_d) of 33 eV and then converted to values corresponding to E_d = 40 eV.

foregoing experimental procedures were developed in earlier ion-bombardment simulation programs and were discussed in some detail in previous publications [*1,3*]. Following perforation, the ion-bombarded regions of the thin foils were examined in a JEM 6A electron microscope operated at 100 kV.

Materials

The three commercial precipitation-hardening alloys used in this study (Inconel 706, Inconel 718, and Nimonic PE 16) were procured by the Hanford Engineering Development Laboratory (HEDL) for use by participants in the Energy Research Development Administration (ERDA) sponsored National Alloy Development Program. Chemical compositions were verified and heat treatments and prebombardment microstructural characterizations were also performed by HEDL[5] and are mentioned here to allow comparisons with the microstructures observed after bombardment.

Precipitation in these alloys depends primarily upon the amounts and types of elements used for alloying—aluminum, titanium, and columbium being the most important [*4*]. Table 1 shows that Inconel 718 contains the most columbium while Inconel 706 contains the most titanium and has the highest titanium-to-aluminum ratio. The γ'-precipitate formed in all three alloys is cuboidal Ni_3 (Ti,Al) and the average length of a cube edge is generally used to specify the precipitate size. The γ'' formed in the Inconels is body-centered tetragonal Ni_3Cb and generally occurs as disk-like platelets for which an average thickness and an average diameter can be used to specify size.

Triple-aged Inconel 706 [1 h at 954°C (1750°F) and water quenched, followed by 3 h at 843°C (1550°F) and air cooled, followed by 8 h at 718°C (1325°F) and furnace cooled to 621°C (1150°F), held for an additional 10 h and air cooled] contained γ'-precipitates (39 nm) and γ''-platelets (5 nm thick, 16 nm in diameter).

Double-aged Inconel 718 [1 h at 954°C (1750°F) and water quenched, followed by 8 h at 718°C (1325°F) and furnace cooled to 621°C (1150°F), held for an additional 10 h and air cooled] contained γ''-platelets (5 nm thick, 15 nm in diameter).

Double-aged Nimonic PE16 [4 h at 1079°C (1975°F) and air cooled, followed by 1 h at 899°C (1650°F) and air cooled, followed by 9 h at 749°C (1380°F) and air cooled] contained γ' (15.5 nm).

Solution-annealed Inconel 706 [1 h at 1066°C (1950°F) and water quenched] and Nimonic PE16 [4 h at 1079°C (1975°F) and air cooled) contained no γ' or γ'' precipitates.

[5] Gelles, D. S., Mastel, B., and Bates, J. F., Hanford Engineering Development Laboratory, Richland, Wash., private communication, 1974.

TABLE 1—*Alloy compositions*[a].

Alloy	Fe	Ni	Cr	Mo	Mn	C	Cb (+Ta)	Al	Ti	S	Si	Cu	Co
Inconel 706	balance	41.49	16.09	...	0.10	0.03	2.95	0.27	1.66	0.0002	0.10	0.02	...
Inconel 718	balance	52.83	18.57	2.83	0.10	0.04	5.28	0.5	0.92	0.007	0.23	0.12	0.03
PE16[b]	balance	43.37	16.5	3.15	<0.01	0.082	...	1.20	1.27	0.001	<0.01	<0.01	0.03

[a] See Footnote 4.
[b] Also <0.01 V, <0.01 Zr, 0.0032 B, 0.001 P.

Both γ' and γ'' are metastable, and overaging will result in their disappearance and replacement by stable phases which habit {111} planes of the austenitic matrix. Overaging of γ' results in plates of η-phase, a hexagonal Ni_3Ti, while overaging of γ'' results in plates of δ-phase, an orthorhombic Ni_3Cb [*4*]. During prebombardment characterizations, coarse δ-phase plates were observed on the grain boundaries of the aged Inconels.

Results

Figure 1 shows the microstructures of aged Inconel 706 after 2 h ion bombardments at temperatures between 550 and 725°C (1022 and 1337°F). Representative selected area diffraction patterns are shown in Fig. 2 where streaks due to thin precipitates can be detected even for the material bombarded at the lowest temperature. Faint streaks were also observed in diffraction patterns of an additional specimen bombarded at 475°C (887°F). The obvious effects of increasing the bombardment temperature are the enhanced coarsening of the precipitate platelets and the appearance of intensity maxima on relrods (reciprocal lattice rods arising from thin platelets in real space) due to the development of stronger form factor effects with the coarser plates.

The precipitates habit {111} planes of the matrix and relrods in diffraction patterns pass through, and eventually connect, matrix reciprocal lattice points along <111> directions. However, even with the coarsest plates the intensity maxima developing along the relrods are not localized enough to allow accurate interplanar spacings to be determined.

The preirradiation precipitate phases, γ' and γ'', are degraded or dissolved during ion bombardment. With increasing bombardment temperature the superlattice reflections became weakened and dark-field imaging disclosed fewer particles.

Annealed Inconel 706 was studied after similar ion bombardments, and precipitate platelets were also observed as shown in Fig. 3. In both images and diffraction patterns, however, it appeared that the degree of coarsening of the platelets was lower than observed in aged material bombarded at similar temperatures. In addition to the relrods due to the platelets, superlattice spots corresponding to γ' or γ'' were observed in the diffraction patterns. Since neither of the metastable precipitate phases were present during the preirradiation characterization, ion bombardment must also have produced these in addition to the coarser platelet phase. However, in dark-field images using the superlattice reflections, the metastable precipitates could not be easily detected or distinguished from the diffuse background.

To emphasize the difference in coarsening between aged and annealed Inconel 706, during heavy ion bombardment, Fig. 4 shows typical grain

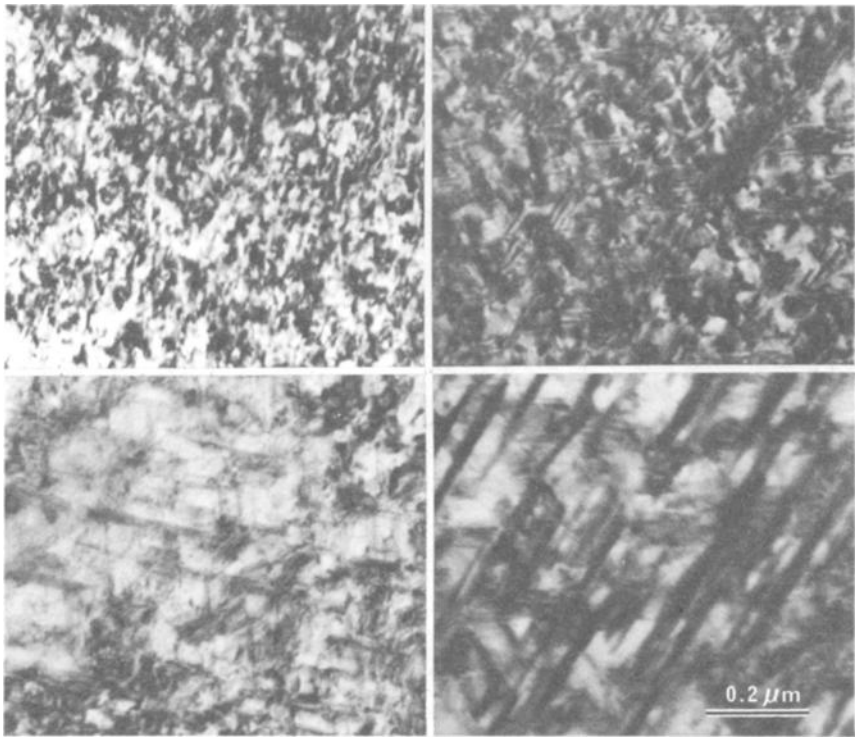

FIG. 1—*Triple-aged Inconel 706 ion bombarded to 115 dpa at the temperatures indicated.* (upper left) *550°C (1022°F), dark-field image;* (upper right) *625°C (1157°F), dark-field image;* (lower left) *675°C (1247°F), bright-field image;* (lower right) *725°C (1337°F), bright-field image.*

boundaries in the materials bombarded at 625°C (1157°F). Characteristic overaging behavior is exhibited by the aged material [*4*] and cellular precipitation is advanced at the grain boundaries. In contrast, the annealed material still has straight grain boundaries and no noticeable greater coarsening of precipitate plates in these regions.

The microstructural features of double-aged Inconel 718 after 2 h bombardments are shown in Fig. 5 where the coarsening of precipitate platelets, similar to those observed in Inconel 706, can be seen to increase with increasing bombardment temperature. Molybdenum masks had been used to shield certain areas of the target specimens from ion bombardment for purposes of obtaining step heights which can be correlated to swelling behavior. In each specimen, perforations were made in the ion-bombarded region and also in an area that had been shielded. Thus thermal control information could be obtained from the same specimen that had undergone bombardment. In all cases the unirradiated material appeared

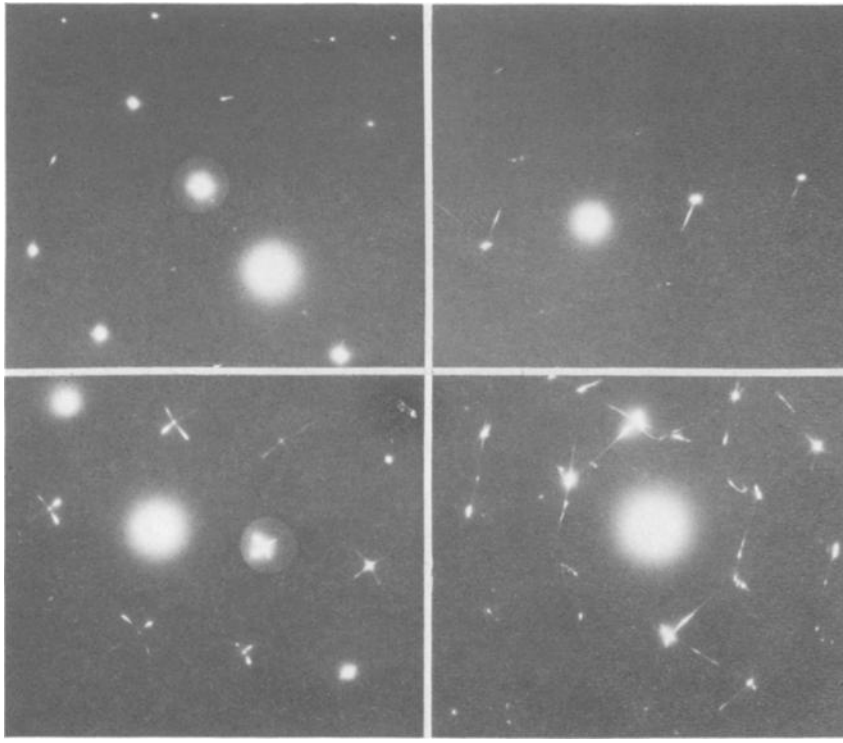

FIG. 2—*Representative selected area electron diffraction patterns from triple-aged Inconel 706 after ion bombardment at the temperatures indicated.* (upper left) *550°C (1022°F)*, (upper right) *625°C (1157°F)*, (lower left) *675°C (1247°F)*, (lower right) *725°C (1337°F)*.

as characterized in the preirradiation study, and γ'' could be imaged using appropriate dark-field techniques. The appearance of the material under the masked area of the 725°C (1337°F) bombarded specimen is also shown in Fig. 5 and is representative of that observed in specimens bombarded at lower temperatures.

Figure 6 shows representative selected area diffraction patterns obtained from Inconel 718 after ion bombardments. After the 625°C (1157°F) bombardment, only very faint streaks can be detected along {111} directions due to the thin nature of the precipitating platelets. After 675°C (1247°F) bombardment, relrods are clearly evident although no tendency exists to exhibit intensity maxima along the streaks. After bombardment at 725°C (1337°F), diffuse intensity maxima are appearing on the streaks, indicating that form factor effects are becoming stronger as the platelets thicken. In the masked areas of the specimens, no streaks along {111} directions could be detected in the diffraction patterns and

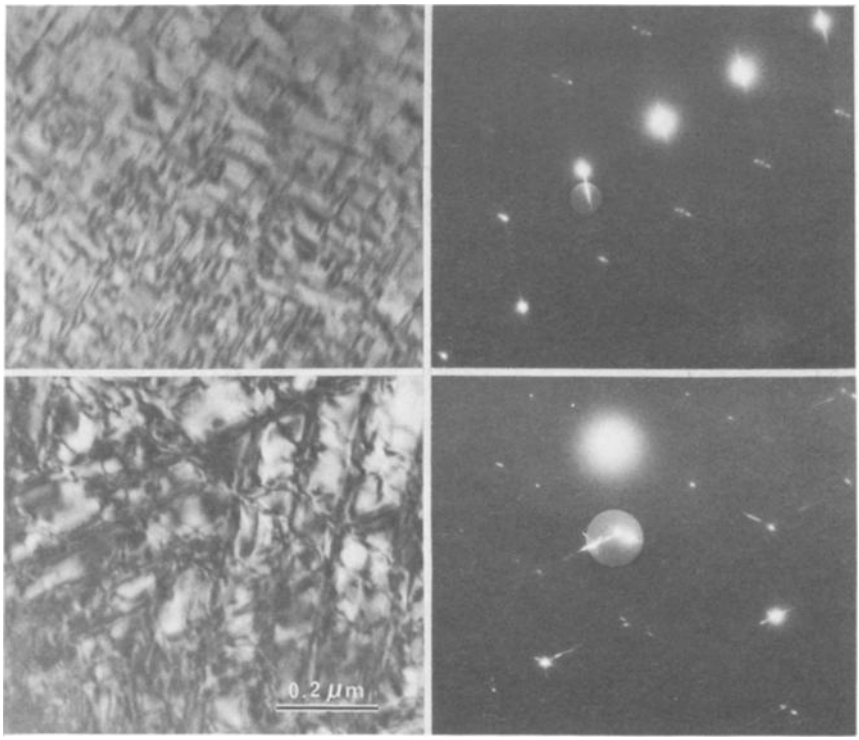

FIG. 3—*Bright-field images and representative selected area diffraction patterns from solution-annealed Inconel 706 ion bombarded to 115 dpa at the temperatures indicated.* (top) *625°C (1157°F)*, (bottom) *725°C (1337°F)*.

only the characteristic superlattice reflections of the precipitates produced by the double-aging treatment were observed.

A general statement about the behavior of Nimonic PE16 during ion bombardment is that no evidence of changes in precipitate microstructures was noted. In aged materials, the γ' distribution appears to be the same after ion bombardment as before. In annealed materials, no tendency was noted for the formation of γ' during bombardment. The only noticeable difference between the two materials is that dislocation arrays appeared to be more fully developed in the annealed specimens. A low density of fringed planar defects on {111} planes was present in annealed material bombarded at 625°C (1157°F) in addition to unfaulted loops and dislocation segments. These planar defects produced relrods in diffraction patterns and therefore might be thought to be similar to the precipitating phase detected in the bombarded Inconels. However, fewer such defects were found after 675°C (1247°F) bombardment and practically none were present after the 725°C (1337°F) bombardment. Since

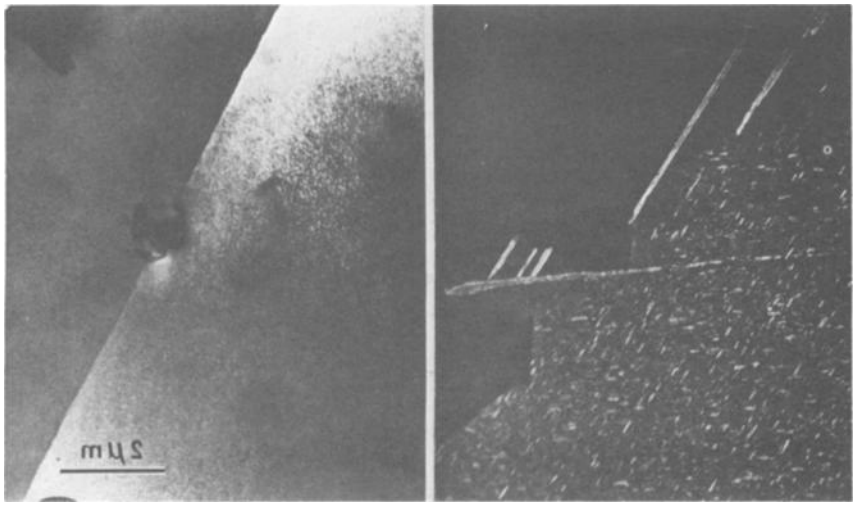

FIG. 4—*Dark-field images of grain boundary regions in ion-bombarded Inconel 706.* (left) *triple aged,* (right) *solution annealed.*

coarsening with increased bombardment temperature did not occur, these defects are most likely faulted loops and are probably thermally unstable. The microstructures and representative diffraction patterns of bombarded annealed PE16 are shown in Fig. 7.

Through-focus, high-resolution, dark-field image sets were obtained for the precipitates observed in each specimen. Such sets form the basis for the stereo imaging technique called "2½-D electron microscopy" by introducing artificial parallax at the sacrifice of image detail [5]. Depth in 2½-D images is produced by objects with different reciprocal lattice vectors and bears no inherent relationship to the actual spatial distribution of objects since specimen tilting is not involved. Studies of precipitation effects represent one of the elemental applications of this technique. For platelets producing relrods, the objective aperture is so positioned as to include the intersections of these relrods with the reflecting sphere. Through-focus imaging produces stereo pairs which are the equivalent of multiple individual dark-field images, each with its characteristic parallax, but with problems of image exposure, specimen manipulation, specimen lifetime, etc., reduced or eliminated.

Figure 8 shows 2½-D stereo image pairs, at the same magnification, obtained from the four materials studied. The images have been so arranged that, with a small stereo viewer, two defect systems can be observed in each case. The Inconels are illustrated for the 725 °C (1337 °F) bombardments where the coarsest plates were developed and high-intensity relrod intersections were obtained well away from the matrix spot

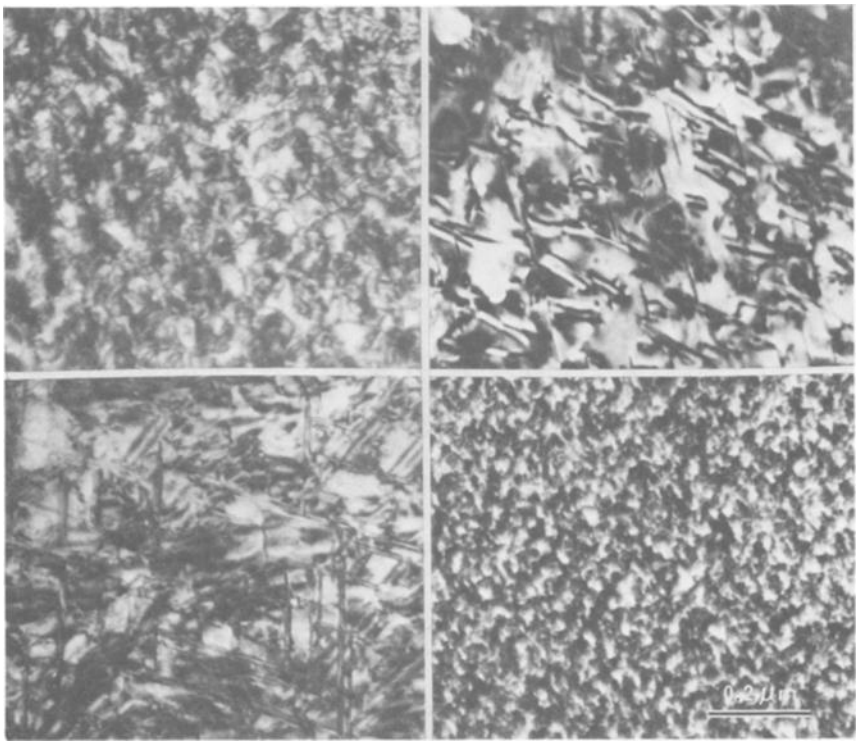

FIG. 5—*Double-aged Inconel 718 ion bombarded to 115 dpa at the temperatures indicated.* (upper left) *625°C (1157°F), dark-field image;* (upper right) *675°C (1247°F), dark-field image;* (lower left) *725°C (1337°F), bright-field image;* (lower right) *725°C (1337°F), under mask, dark-field image.*

positions on the diffraction patterns, allowing excellent depth to be obtained in the 2½-D images. With the stacking faults in PE16 bombarded at 625°C (1157°F), however, the relrods are so weak that only intersections quite near the matrix spot can be used; hence the noticeably smaller depths in the last 2½-D image pair.

It is not possible to identify the precipitates produced in the Inconels by ion bombardment solely on the basis that they habit {111} planes, since both δ- and η-phases have this characteristic and both are stable phases produced by overaging. Distinction between the two possibilities must be accomplished using interplanar spacings. However, relrod intersections with diffraction patterns of arbitrary orientations will not allow correct interplanar spacings to be determined and, even when the relrods lie in the diffraction patterns, the diffuse nature of the intensity maxima makes difficult the measurements required to obtain interplanar spacings accurate enough to identify the proper phase. One way to avoid

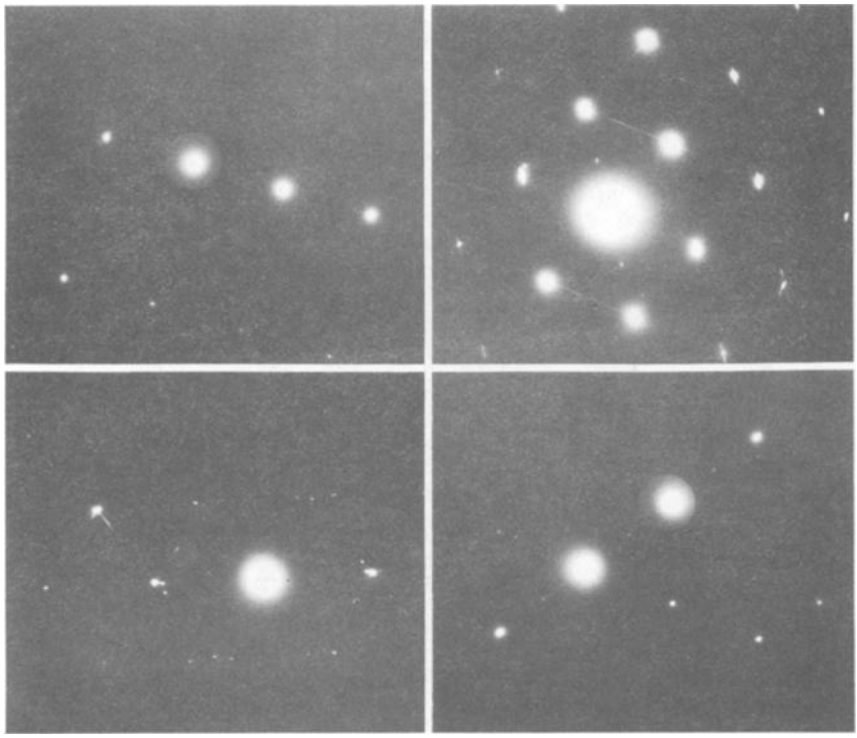

FIG. 6—*Representative selected area electron diffraction patterns from double-aged Inconel 718 after ion bombardment at the temperatures indicated.* (upper left) *625°C (1157°F)*; (upper right) *675°C (1247°F)*; (lower left) *725°C (1337°F)*; (lower right) *725°C (1337°F), under mask.*

these problems is to use a <111> matrix orientation and determine the positions of the intersections of relrods which are normal to the electron diffraction pattern. These intersections will then be in the proper positions for reflections belonging to the zone axis of the precipitate parallel with the <111> matrix direction—the <0001> for the η-phase or the <010> for the δ-phase. Figure 9 is a <111> diffraction pattern from the material containing the coarsest platelets, aged Inconel 706 bombarded at 725°C (1337°F). The weak interior spots have sixfold symmetry with corresponding interplanar spacings of 2.21 Å (0.221 nm) in agreement with published values for $\{20\bar{2}0\}$ planes of hexagonal Ni_3Ti [6]. To match published data on orthorhombic Ni_3Cb, these spots would need to correspond to {002} and {201} planes with spacings of 2.28 and 2.23 Å (0.228 nm and 0.223 nm), respectively [7], with interplanar angles of 61 and 58 deg; the measured angles are all within half degrees of 60 deg. It is

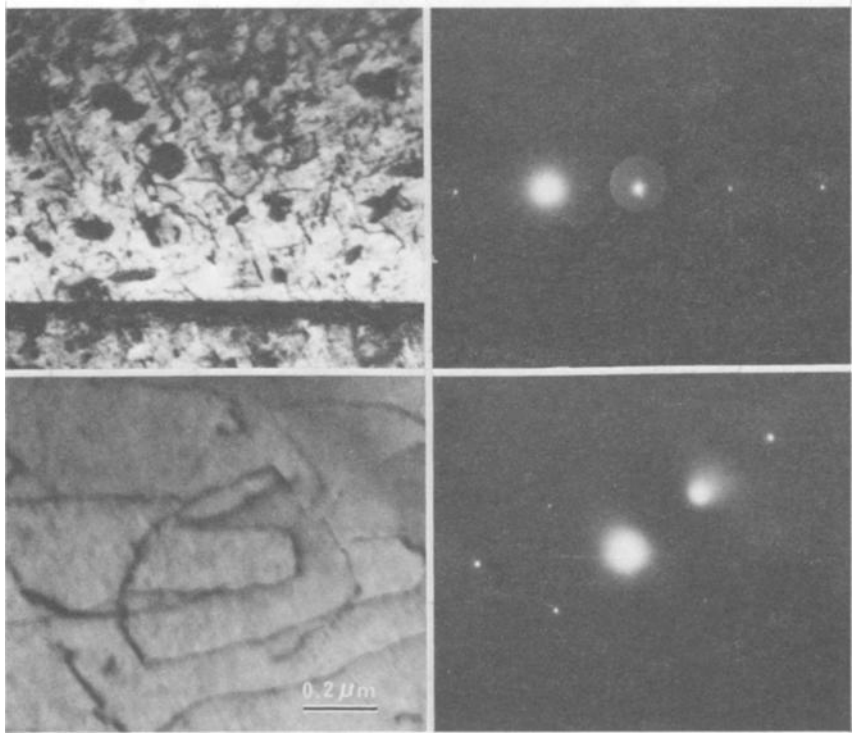

FIG. 7—*Images and representative selected area diffraction patterns from solution-annealed Nimonic PE16 ion bombarded to 115 dpa at the temperatures indicated.* (top) *625° C (1157°F), dark-field image;* (bottom) *725°C (1337°F), bright-field image.*

thus clear that the better choice of precipitate species, based upon experimental evidence, is η-phase, the hexagonal form of Ni_3Ti.

Discussion

Without the diffraction pattern data of Fig. 9, it might seem reasonable to expect the precipitating platelets to be δ-phase, since δ was present in both Inconels prior to bombardment, and PE16, containing no columbium, did not develop any precipitates during irradiation. The diffraction data themselves might be considered suspect in that they represent a section through a relrod lattice connecting matrix relpoints, and the spots measured might not even be present if the plates were coarser.

The fact that the platelets coarsened much more readily in Inconel 706 than in Inconel 718 is inconsistent with an analysis that they are δ-phase, since the kinetics of δ formation are significantly slower in the first alloy [*8*]. Higher titanium/aluminum ratios are more favorable for

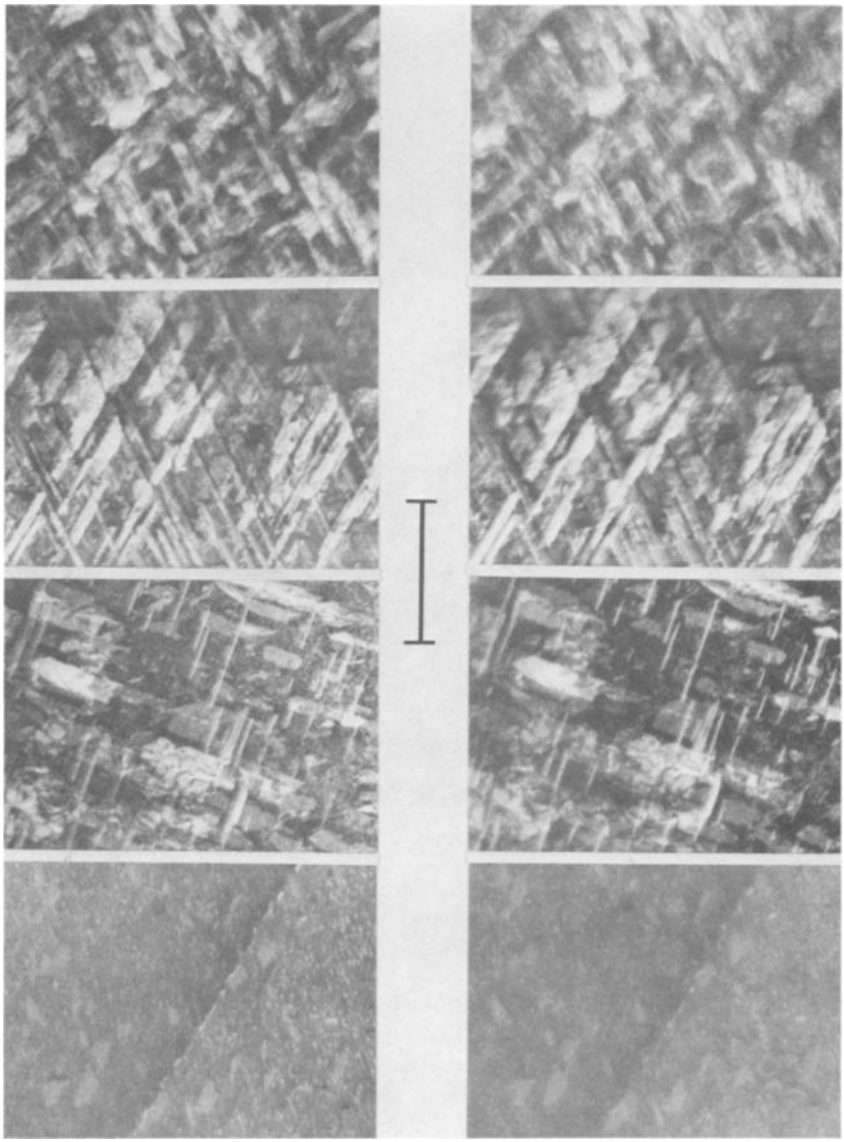

FIG. 8—*2½-D stereo image pairs of precipitates in the Inconels and faulted loops in Nimonic PE16 after ion bombardment at the temperatures indicated. In-focus images are on the left and defocused images on the right. Scale mark indicates 0.5 μm.* (top) *725°C (1337°F), triple-aged Inconel 706;* (upper middle) *725°C (1337°F), solution-annealed Inconel 706;* (lower middle) *725°C (1337°F), double-aged Inconel 718;* (bottom) *625°C (1157°F), solution-annealed Nimonic PE16.*

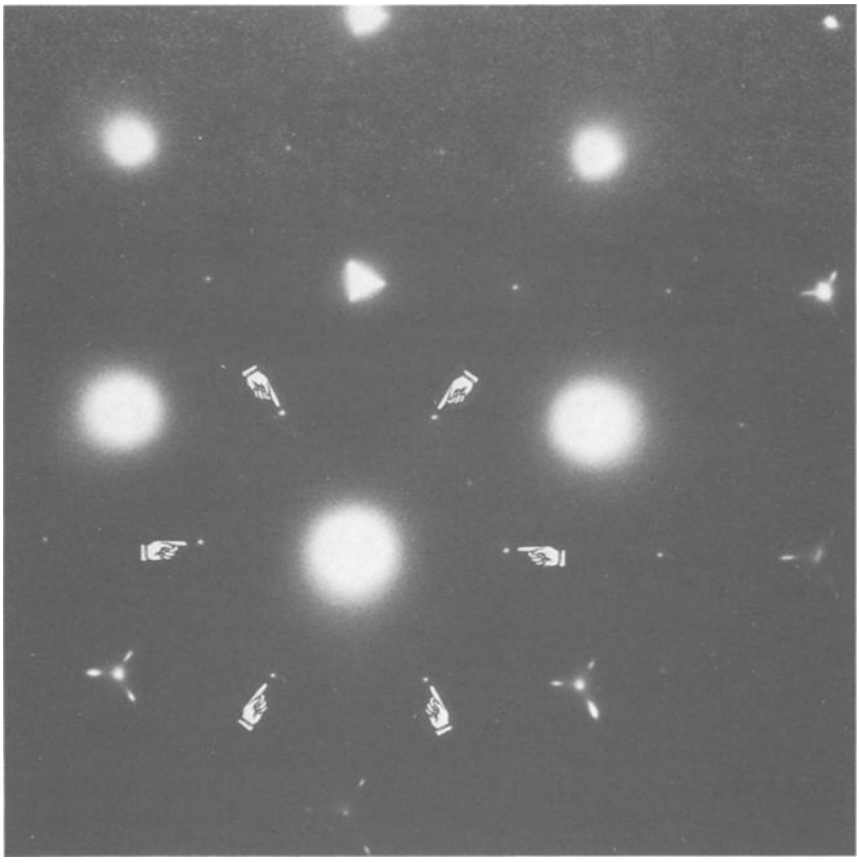

FIG. 9—*Selected area <111> electron diffraction pattern from Inconel 706 bombarded at 725°C (1337°F). The reflections indicated correspond to {20$\bar{2}$0} planes of hexagonal η-phase platelets in the plane of the specimen. Satellite spots around outer reflections are caused by relrods produced by thin precipitates on inclined {111} planes.*

the formation of η-phase [9], and Inconel 706 has a higher ratio of these species than does Inconel 718; thus the obviously greater coarsening of the platelets in the first alloy is consistent with titanium and aluminum concentrations. Nimonic PE16 has a titanium/aluminum ratio of about one (compared with 6.2 for Inconel 706 and 1.8 for Inconel 718), and the absence of precipitates after ion bombardment can be ascribed to this low ratio and the corresponding sluggishness of the overaging process.

The diffraction pattern analysis is valid because the relrod lattice belongs to the precipitate and not to the matrix. Precipitate intensity maxima must lie on the relrods, and intersections of the relrods with the <111> matrix diffraction pattern must be at positions determined by the

structure of the precipitate, although not all intersections need have a nonzero structure factor for bulk material. The intersections observed in Fig. 9 indicate that the relrods connect matrix relpoints above and below the plane of the diffraction pattern, a situation compatible only with η-plates since not all the relrods produced by δ-plates would pass through matrix relpoints.

Other platelet phases that might be considered are the tetragonal δ-phase, the hexagonal Laves phase, and the trigonal μ-phase—all minor intermetallic phases [*4*]. These can also be ruled out on the basis that either the structures or the interplanar spacings [*10*] involved would not allow relrod intersections to be observed in the positions shown in Fig. 9.

Data obtained from Inconel 718, from areas that were masked from ion bombardment, allow the conclusion to be made that the precipitation of η-plates occurs solely as a response to ion bombardment. No significant microstructural changes occur due to temperature alone during the short bombardment period of 2 h, but in the irradiated areas temperature affects the details of coarsening of the η-platelets.

It is generally accepted that heavy ion bombardment is useful in predicting trends in the swelling behavior that austenitic alloys would exhibit in a fast reactor environment. It is clear from the data presented here that overaging behavior is also accelerated by heavy ion bombardment, but it remains to be established that short-time bombardments simulate the changes in precipitate microstructures that would occur during neutron irradiation. There are no data on neutron-irradiated Inconel alloys with fluences (approximately 2×10^{23} n/cm^2, $E > 0.1$ MeV) that would compare with the 115 dpa obtained by ion bombardments for this study. Inconel 718, however, has been studied after neutron irradiation to 8×10^{22} n/cm^2 at 600°C (1112°F) [due to temperature shift effects, ion bombardment at about 725°C (1337°F) would be roughly comparable]. A moderate density of faulted loops was described as being present.[6] This faulted-loop microstructure is in fact similar in appearance to the precipitate microstructures produced by ion bombardment and analyzed in this investigation. It is therefore possible that valid simulation of overaging behavior is produced by ion bombardment, but more extensive analyses of neutron-irradiated materials must be performed before a firm conclusion can be reached.

Conclusions

1. Bombardment with 5-MeV nickel ions accelerates overaging in the Inconel alloys 706 and 718.

[6] Pard, A. G. and Garr, K. R., Atomics International, private communication, 1975.

2. The stable overaging precipitate caused by ion bombardment between 475 and 725 °C (887 and 1337 °F) is thin platelets of η-phase Ni_3Ti.

3. Preexisting metastable- and stable-phase precipitates of γ', γ'', and δ are degraded or dissolved in the two Inconel alloys during accelerated overaging caused by ion bombardment between 625 and 725 °C (1157 and 1337 °F).

4. Aged Inconel 706 overages more rapidly than does solution-annealed material bombarded under similar conditions.

5. The overaging behavior of the Inconels may simulate in-reactor response.

6. The degree of coarsening of η-phase platelets can be correlated with the titanium/aluminum ratio of the alloys Inconel 706, Inconel 718, and Nimonic PE16.

7. Nimonic PE16, with a low titanium/aluminum ratio of one, does not overage during ion bombardment, nor does preexisting γ' noticeably change as a result of bombardments to 115 dpa between 625 and 725 °C (1157 and 1337 °F).

Acknowledgments

The contribution of W. G. Johnston, General Electric Corporate Research and Development Center, in performing all nickel-ion bombardments is gratefully acknowledged. The assistance of G. M. Konze and the guidance of W. K. Appleby are noted with appreciation. This work was supported by the USERDA-National Alloy Development Program through Contract No. E (04-3)-893, Task 14.

References

[1] Johnston, W. G., Rosolowski, J. H., Turkalo, A. M., and Lauritzen, T., *Journal of Nuclear Materials,* Vol. 54, 1974, pp. 24–40.

[2] See, for example, the compendium of the Proceedings of the 1971 International Conference on Radiation-Induced Voids in Metals, State University of New York, Albany, Atomic Energy Commission Symposium Series, 26 April 1972.

[3] Armijo, J. S. and Lauritzen, T., "Deuteron-Generated Void Formation in Austenitic Stainless Steels," *Proceedings,* 1971 International Conference on Radiation-Induced Voids in Metals, State University of New York, Albany, Atomic Energy Commission Symposium Series, 26 April 1972, p. 481.

[4] Sullivan, C. P. and Donachie, M. J., Jr., *Metals Engineering Quarterly,* Nov. 1971, p. 1.

[5] Bell, W. L., *Journal of Applied Physics,* Vol. 47, No. 4, 1976, p. 1676.

[6] Beattie, M. J., Jr. and Hagel, W. C., *Transactions,* Metallurgical Society of the American Institute of Mining, Metallurgical, and Petroleum Engineers, Vol. 211, 1957, p. 911.

[7] Bohm, H., Ehrlich, K., and Kramer, K. H., *Metallurgy,* Vol. 2, 1970, p. 139.

[8] Eisenstein, H. L., "Properties of Inconel Alloy 706," presented at Materials Engineering Congress, Cleveland, Oct. 1970.

[9] Mihalisin, J. R. and Decker, R. F., *Transactions*, Metallurgical Society of the American Institute of Mining, Metallurgical, and Petroleum Engineers, Vol. 218, 1960, p. 507.

[10] Beattie, H. J., Jr. and Hagel, W. C., *Transactions*, Metallurgical Society of the American Institute of Mining, Metallurgical, and Petroleum Engineers, Vol. 221, 1961, p. 28.

L. G. Kirchner,[1] *F. A. Smidt, Jr.,*[2] *G. L. Kulcinski,*[3]
J. A. Sprague,[2] *and J. E. Westmoreland*[4]

Nickel-Ion Damage in a Precipitation-Hardened Nickel-Aluminum

REFERENCE: Kirchner, L. G., Smidt, F. A., Jr., Kulcinski, G. L., Sprague, J. A., and Westmoreland, J. E., "**Nickel-Ion Damage in a Precipitation-Hardened Nickel-Aluminum Alloys,**" *Irradiation Effects on the Microstructure and Properties of Metals, ASTM STP 611,* American Society for Testing and Materials, 1976, pp. 370–384.

ABSTRACT: A precipitation-hardened nickel 14 atom percent aluminum alloy has been irradiated with 2.8 MeV $^{58}Ni^{+}$ ions at a damage rate of 4.4×10^{-2} displacements per atom (dpa)/s, over a temperature range of 525 to 725 °C (977 to 1337 °F), to a damage level of 20 dpa, and at 625 °C (1157 °F) over a dose range of 4 to 125 dpa. The experiment was designed to examine the stability of Ni_3Al precipitates as a function of temperature and dose as well as their role in reducing swelling.

Prior to irradiation, the precipitates were cuboidal in shape with a mean edge length of 400 Å. Ion bombardment to 20 dpa at 725 °C (1337 °F) generated a higher precipitate density with a reduced and highly uniform size of 85 Å. At all other temperatures, the precipitate structures were less well defined and took on a ragged appearance with a wide spread in sizes as small precipitates formed between the original ones. A few scattered voids were formed at the two highest damage levels at 625 °C (1157 °F), but the swelling was negligible.

KEY WORDS: radiation, precipitate stability, swelling, radiation effects, nickel aluminum alloy, transmission electron microscopy, nickel-ion bombardment.

Swelling is a problem of major engineering significance in advanced nuclear systems and appears to be influenced by practically all metallurgical variables such as dislocation density, composition, and precipitate struc-

[1] Ph.D. candidate of the Department of Nuclear Engineering, University of Wisconsin, Madison, Wis., Naval Research Laboratory, Washington, D.C. 20375.

[2] Thermostructural Materials Branch (Code 6390), Engineering Materials Division, Naval Research Laboratory, Washington, D.C. 20375.

[3] Professor, Department of Nuclear Engineering, The University of Wisconsin, Madison, Wis. 53706.

[4] Materials Modification and Analysis Branch (Code 6670), Radiation Technology Division, Naval Research Laboratory, Wash., D.C. 20375.

ture. The precipitate structure also influences the mechanical properties; therefore, knowledge about the stability of precipitates under irradiation is of considerable importance. The nickel-aluminum alloy system was selected as a good candidate for study because both solid solution and precipitation-hardening effects can be examined in the same system. Rapid simulation techniques to characterize the swelling and alloy stability are advantageous because of the reduced time scale and closer control of experimental variables.

The use of simulation techniques, however, requires an awareness of the differences in irradiation effects between the simulation techniques and neutrons and between different simulation techniques such as heavy ions and electrons. Of particular interest is the difference in damage to precipitates caused by ions and neutrons as compared with electrons because of the difference in displacement cascade effects.

A precipitation-hardened alloy, nickel-14 atom percent aluminum, was studied to determine the stability of the precipitates under nickel-ion bombardment and to determine the influence of coherent Ni_3Al precipitates on the temperature and fluence dependence of swelling. A companion study on the solid solution alloy Ni-6Al is also in progress and will be reported in a later paper.

In earlier work [*1*],[5] nickel-aluminum alloys preinjected with helium and bombarded with either 20 MeV carbon ions or 46.5 MeV nickel ions had shown a decrease in swelling as the aluminum content in solution increased. The presence of precipitates seemed to have little or no effect on the swelling characteristics. In another study, Nelson et al [*2*] observed that Ni_3Al precipitates decreased in size in aged material and grew to the same size in solution-annealed material under the influence of irradiation. They attempted to model the opposing effects of enhanced substitutional solute diffusion and re-solution of precipitated solute atoms and were able to demonstrate limited agreement with observations of precipitation of γ'-phase in nickel-aluminum binary alloys and in PE-16. Their model predicts that an equilibrium size should be reached after a few displacements per atom (dpa). This work was recently reviewed by Hudson [*3*].

Experimental Procedures

The nickel-aluminum alloy used in this investigation was prepared from International Nickel Company nickel (99.995 percent nominal purity) and high-purity Materials Research Corporation aluminum. After vacuum-arc melting, buttons were sectioned into strips which were then rolled to 100-μm foils. Chemical analysis of the material is given in Table 1.

The foil strips were solution annealed in a 1×10^{-6}-torr vacuum at

[5] The italic numbers in brackets refer to the list of references appended to this paper.

TABLE 1—*Chemical analysis of nickel-aluminum alloy in weight percent.*

Al	C	O	Ba	Ca	Cr	Cu	Fe	In
6.84	0.001	0.006	<0.001	<0.003	<0.001	<0.002	<0.002	<0.001
K	Mg	Mn	Na	Si	Ta	B	Ti	Zn
<0.001	<0.001	<0.001	<0.001	<0.001	<0.05	<0.001	<0.001	<0.03

1050°C (1922°F) for 2 h, and aged at 750°C (1382°F) for 4 h to produce the desired precipitate characteristics. Specimens for ion bombardment were prepared in the form of 3-mm-diameter disks. The specimens were ground flat on 600-grit silicon carbide abrasive paper, mechanically polished with 0.3-μm alumina, and the surfaces to be bombarded were electropolished to remove polishing scratches. The nickel-ion irradiations were performed using the Naval Research Laboratory (NRL) 5-MV Van de Graaff accelerator and a 2.8 MeV $^{58}Ni^{+}$ beam. Specimens were irradiated at 50°C (90°F) intervals from 525 to 725°C (977 to 1337°F) to a dose of 20 dpa, at a peak displacement rate of 4.4×10^{-2} dpa/s, to examine the temperature dependence of the radiation damage, and at 625°C (1157°F) to doses of 4, 20, 56, and 125 dpa to examine the dose dependence of the radiation damage.

The deposition of initial damage energy by the nickel ions as a function of distance into the target foils was determined by the Manning-Mueller E-DEP-1 computer code [*4*]. For 2.8 MeV $^{58}Ni^{+}$ ions, this calculation yielded a peak energy deposition for elastic collisions of 1.1568 MeV/μm at a depth of 5400 Å for the Ni-14Al, assuming a Kinchin-Pease secondary displacement model with an efficiency of 0.8 and displacement energy of 40 eV. The aluminum was assumed to be uniformly distributed in the alloy for these calculations.

After ion bombardment, 4000 ± 500 Å of the front surface of each specimen was removed using a laser interferometric polisher [*5*]. The front face was then masked off and the specimen was polished to perforation from the rear surface with one jet of a semi-automatic dual-jet electropolisher. Specimens were examined in a JEM-200A electron microscope equipped with side entry goniometer stage and operated at 200 kV. Ordered face-centered cubic (fcc) precipitates in Ni-14Al have a small positive mismatch of about +0.6 percent with respect to the disordered solid solution matrix [*6*]. The small mismatch and resulting strain field usually make it difficult to image the precipitates by bright-field electron microscopy, so the precipitates were imaged in dark field using an appropriate superlattice spot.

A particle size analyzer was used to characterize the precipitate size distribution and density. Thickness measurements were made using grain-

boundary interference fringes, bright-field stereo pairs of dislocations, and dark-field stereo pairs of the precipitates.

Experimental Results

The precipitates prior to irradiation are cuboidal with a regular spacing and a mean cube edge of about 400 Å with a standard deviation of 100 Å and a precipitate volume fraction of 12 percent. Figure 1 shows the precipitates prior to ion bombardment, which are free of any unusual contrast markings.

The effect of ion bombardment on the precipitate structure was found to be a rather complex phenomenon which was strongly dependent on temperature, with a weaker dose dependence as well. In the lower part of the temperature range, the precipitates developed somewhat irregular shapes and a contrast feature of unknown origin which gave the precipitates a 'fractured' appearance. In addition, a fine precipitate structure appeared between the larger precipitates in the lower-temperature irradiations. At 725 °C (1337 °F), the 400-Å-diameter precipitates produced by the heat treatment were replaced by a smaller and higher-density precipitate structure. Measurements of the mean diameter of the Ni_3Al precipitate structures before and after irradiation are summarized in Table 2.

Ion bombardment at 725 °C (1337 °F) to a dose of 20 dpa produced a marked change in the precipitate structure with a resulting precipitate mean diameter of 85 Å and a standard deviation of 25 Å. Figure 2 shows the appearance of this structure. The 725 °C (1337 °F) experiment was repeated with another lot of material, which contained 230 Å precipitates prior to bombardment, and the same result was observed but with a slightly smaller 72-Å-diameter precipitate as the final product.

Irradiations at all other temperatures led to less well-defined structures as illustrated in Fig. 3, which shows the precipitate structure in a thin section after 20 dpa at 625 °C (1157 °F). The original 400 Å-diameter precipitates have taken on a ragged appearance, in marked contrast to that in Fig. 1. Contrast features which have been interpreted in the sizing measurements reported here as fragmentation of the original precipitates can also be observed in many of the larger precipitates. The origin of these contrast features is as yet unknown, and it must be conceded that alternative explanations, such as antiphase boundaries, which are stacking faults in the ordered γ'-phase, or dislocation structures either within the precipitates or at the interface, cannot be ruled out at this time. This point is examined in more detail in the discussion section which follows. The interpretation of this point, whether fractured precipitates or contrast features on the original precipitate, will have some influence on the measured value of the precipitate size. The measurements in Table 2 are cited as the best value on the basis of current knowledge and are made in an

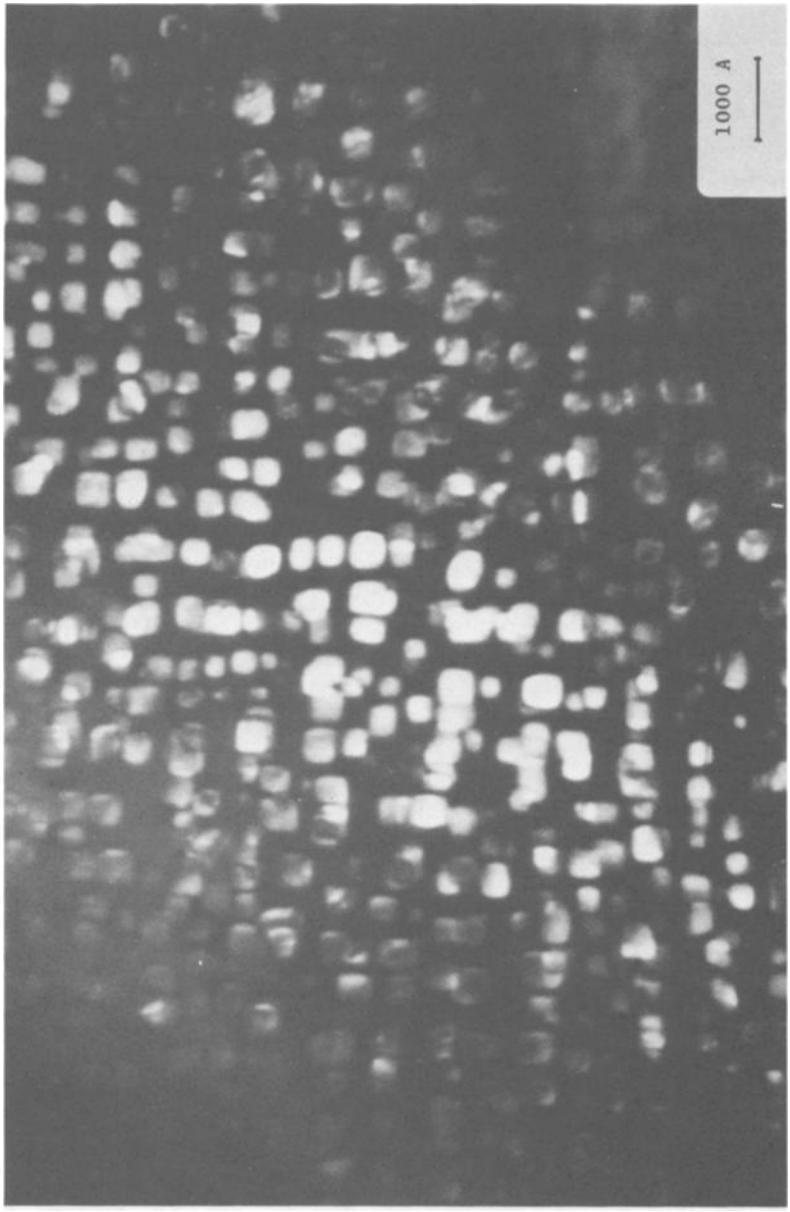

FIG. 1—*Transmission electron micrograph of Ni_3Al precipitates in unirradiated Ni-14Al imaged under [110] superlattice dark-field contrast. Mean cube edge is about 400 Å.*

TABLE 2—*Precipitate size changes in irradiated Ni-14A1.*

Irradiation Temperature, °C	Damage Level, dpa	Average Unirradiated Ni_3Al Size, A, Standard Deviation	Average Irradiated Ni_3Al Size, A, Standard Deviation
525	20	400 (100)	130 (65)
575	20	400	137 (70)
625	20	400	213 (91)
675	20	400	180 (85)
725	20	400	85 (25)
725	20	231 (71)	72 (25)
625	4	400	232 (82)
625	20	400	213 (92)
625	56	400	137 (70)
625	125	400	133 (65)

internally consistent manner.

Another feature of the microstructure is the appearance of much smaller precipitates between the large ones. The histogram of precipitate sizes in Fig. 4 shows clearly the shift in mean diameter of the precipitate size distribution from 400 Å toward smaller sizes as a consequence of the appearance of this finer structure. Several competing trends appear to be present, as can be seen by the temperature dependence of the precipitate mean diameter, which first increases in mean diameter with increasing temperature and then decreases. The dose dependence of precipitate diameter shows an asymptotic approach to the size at 125 dpa.

The precipitate number density increased slightly at lower temperatures but the volume fraction did not change markedly from the unirradiated condition. At 725 °C (1337 °F), however, the number density increased from about 6×10^{15} to more than 6×10^{16} while the volume fraction decreased from about 12 percent in the unirradiated material to what appeared to be two percent after 20 dpa at 725 °C (1337 °F). This low-volume fraction may be more apparent than real because visibility of the precipitates in dark-field contrast from superlattice reflections is low. Section thicknesses examined were approximately 600 to 900 Å thick, but no contrast calculations have been made to assure that precipitates are visible at all depths within the foil. It is also possible that many small clusters may be present which are either below the resolution limit of the microscope (~15 Å) or are too small to produce sufficient contrast above the inelastic background.

Voids were observed in only the 56 and 125 dpa specimens of Ni-14A1, and in both cases the voids were inhomogeneously distributed in the specimen and so few in number that the resulting swelling would be insignificant. Dislocation densities were very high in all specimens.

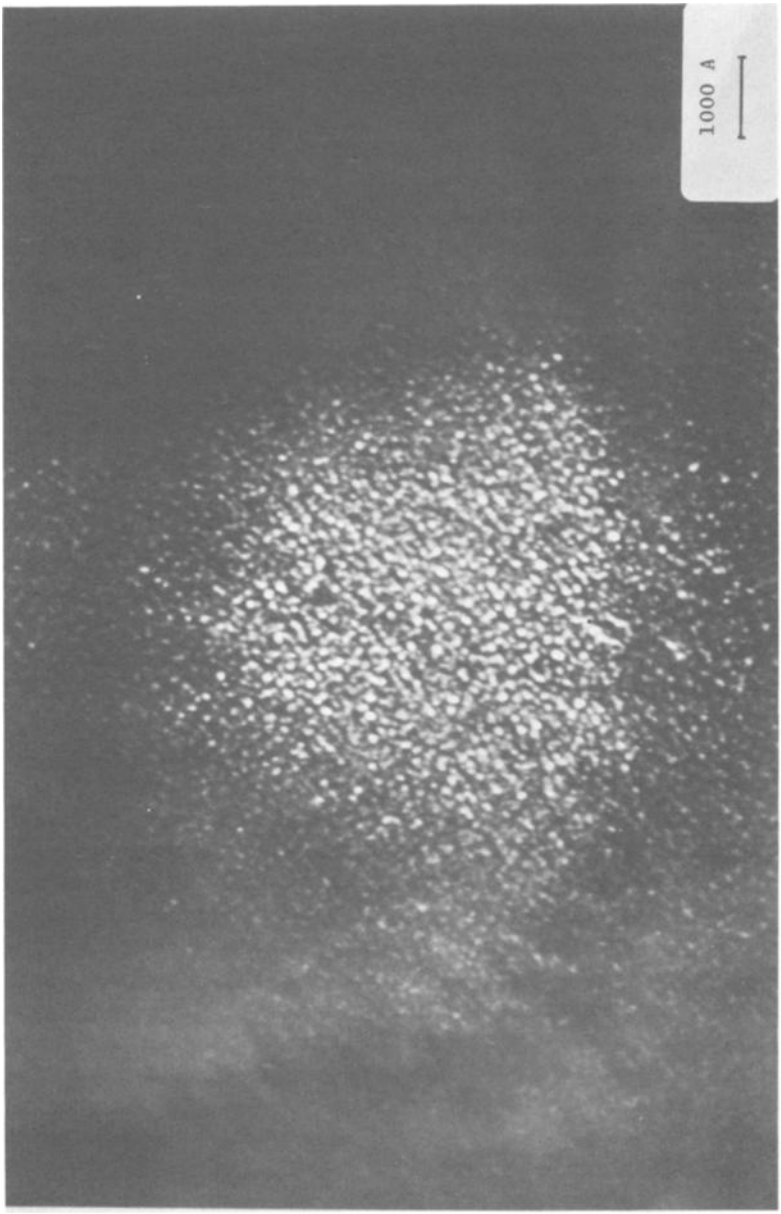

FIG. 2—*Transmission electron micrograph of Ni$_3$Al precipitates after irradiation to 20 dpa at 725°C (1337°F) with nickel ions at a damage rate of 4.4 × 10^{-2} dpa/s. The precipitates are imaged in dark-field contrast using a [100] superlattice reflection and have a mean diameter of 85 Å with a standard deviation of 25 Å.*

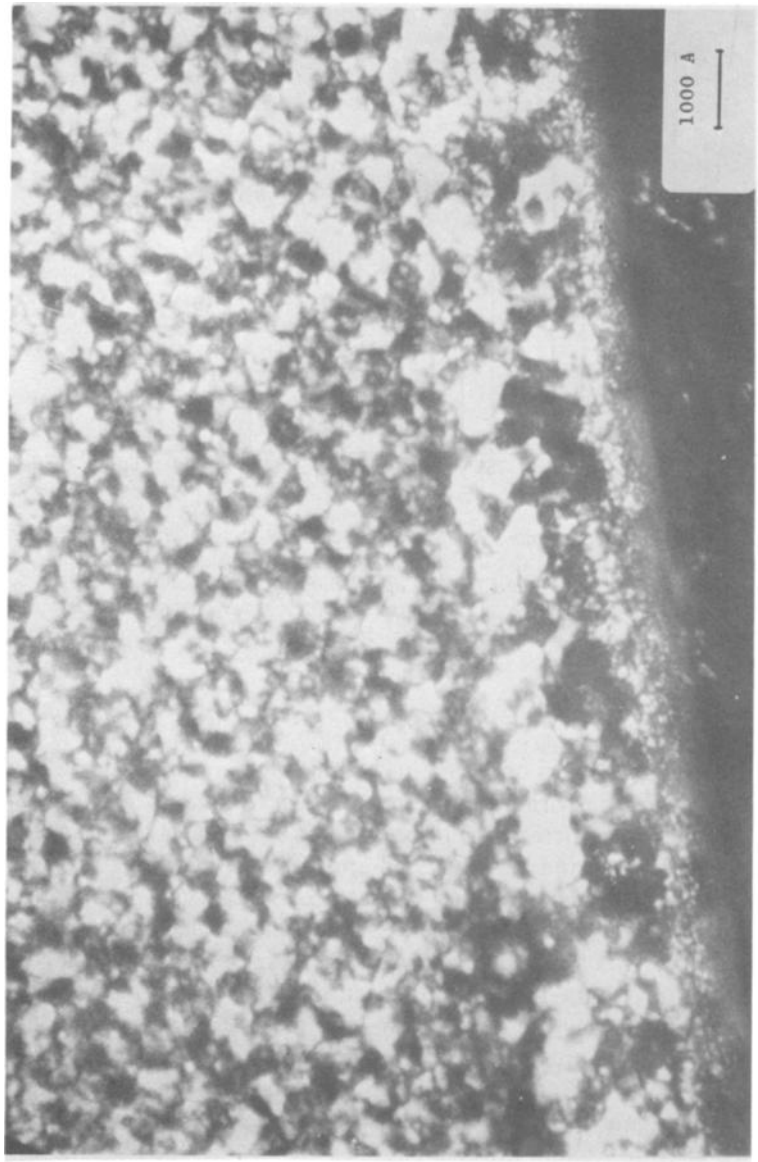

FIG. 3—*Transmission electron micrograph of Ni_3Al precipitates after irradiation to 20 dpa at 625°C (1157°F) with nickel ions at a damage rate of 4.4×10^{-2} dpa/s. The precipitates were imaged in dark-field contrast using a [100] superlattice reflection and have a mean diameter of 213 Å with a very wide spread in the size distribution. The clustering is typical of all the specimens irradiated at temperatures below 725°C (1337°F).*

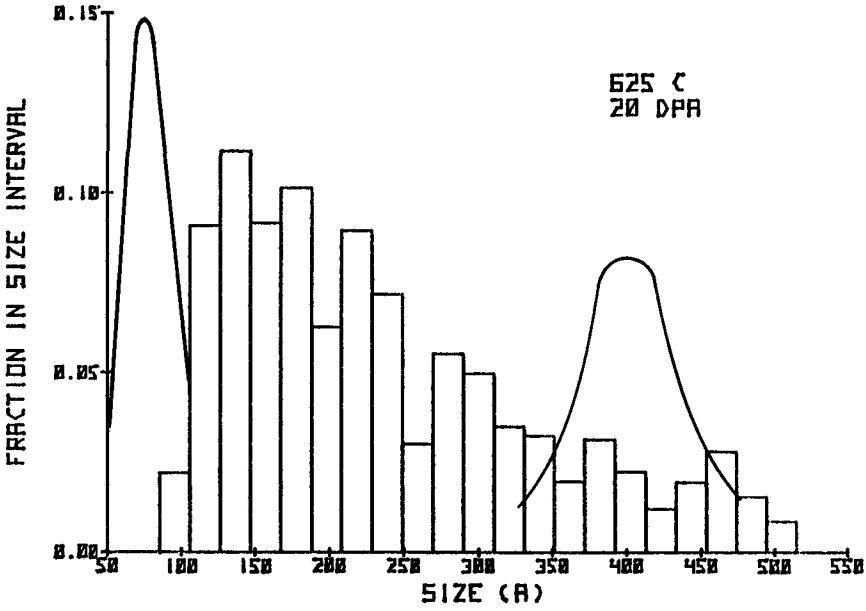

FIG. 4—*Histogram of the precipitate size distribution after ion bombardment at 625°C (1157°F), 20 dpa, compared with the size distribution of precipitates prior to ion bombardment (solid curve centered at 400 Å) and the size distribution of precipitates folowing ion bombardment at 725°C (1337°F) (solid curve centered at 85 Å). Mean diameter for the histogram is 213 Å.*

Discussion

The most significant effects observed in the ion bombardment of Ni_3Al precipitates were the transformation of the original 400 Å precipitates to 85 Å precipitates with an increased number density at 725 °C (1337 °F), the development of a fragmented and clustered appearance to the precipitates during bombardment at temperatures between 525 and 675 °C (977 and 1247 °F), the formation of small precipitates between the larger ones during bombardment at the lower temperatures, the development of unusual contrast features on or in the precipitates after the lower-temperature bombardments, and finally the observation of a low density of voids. In this discussion we compare the present results with other observations cited in the literature on unirradiated and irradiated alloys containing Ni_3Al precipitates, and then we examine the various explanations which have been proposed to explain the results.

The elevated temperature behavior of nickel-aluminum alloys containing Ni_3Al is well characterized. The γ/γ'-phase boundary in this alloy system occurs near 10 atom percent aluminum at 500 °C (932 °F) and 12.4 atom percent at 750 °C (1382 °F). The 13.8 atom percent aluminum alloy

used in this study had a 12 percent volume fraction of Ni_3Al precipitates after aging 4 h at 750°C (1382°F). The precipitates had a mean diameter of about 400 Å, in agreement with predictions in the literature [*6*], and were cuboidal in shape with cube faces parallel to {100}. As the precipitates get smaller, their shape tends to be more spherical. When the precipitates are overaged they start to cluster and align as they depart from a cuboidal shape. The morphology of unirradiated precipitates is generally determined by elastic strain and, since the lattice misfit in Ni-14Al is about +0.6 percent, the precipitate behaves as a large interstitial [*7*]. Precipitate volume fraction has little or no effect on the thermal coarsening behavior of this alloy [*8*], and the lattice misfit decreases slightly as the temperature increases [*9*]. As the misfit decreases with increasing temperature, the preferred precipitate shape tends more toward spherical from cuboidal, and precipitate alignment would be expected to decrease.

The first reported study of the response of Ni_3Al precipitates to irradiation was that of Nelson et al [*2*], who found that at temperatures below 300 to 325°C (572 to 617°¼f) the Ni_3Al was disordered after 0.1 dpa by heavy ion bombardment. At elevated temperatures, Ni_3Al precipitates in an alloy similar in composition to the one used in the present study, and the γ', $Ni_3(Al, Ti)$ in PE-16, were observed to break up during the irradiation and form a population of smaller precipitates. Solution-annealed material was observed to form precipitates of the same size following ion bombardment. This observation prompted Nelson et al [*2*] to propose a model in which an equilibrium-size precipitate formed as a consequence of a kinetic equilibrium between the dissolution of volumes of precipitate near the precipitate surface, when disordered by a displacement cascade, and the growth of the precipitates as a consequence of irradiation-enhanced diffusion. Hudson et al [*1*] observed a decrease in precipitate size after ion bombardment with 46.5 MeV Ni^{6+} ions at 525°C (977°F) and doses up to 60 dpa. These results [*1,2*] agree with our observations at 725°C (1337°F), where all the original precipitates decreased in size or were dissolved and reprecipitated. But they differ from our results at lower temperatures, where no small equilibrium size was observed even up to 125 dpa.

Potter and Hoff [*10*] irradiated an alloy near the composition of Ni-14Al in the solution-annealed condition with 3.2 MeV nickel ions at a damage rate of 2.7×10^{-3} dpa/s. Their unirradiated material, after the solution treatment, had a uniform and fine dispersion of very small precipitates (estimated to be under 50 Å in mean diameter). The morphology of the precipitates changed dramatically during ion bombardment at 550°C (1022°F). Whereas the small unirradiated precipitates were essentially spherical in shape, ion bombardment to 5.6 dpa produced a change to cuboidal shape, and by 19.4 dpa the precipitates had a decided look of fragmentation. The mean diameter increased with bombardment, passed through a maximum of about 120 Å at approximately 10 dpa, and then

approached a somewhat stabilized equilibrium size of about 85 Å at damage levels above 25 dpa. Dislocation loops nucleated in regions free of precipitate and appeared to sweep precipitates from adjacent areas. Ancillary experiments on the behavior of Ni_3Al during cold-working led Potter and Hoff to propose a model in which the precipitates were reduced in size by dislocation cutting and grew by irradiation-enhanced diffusion. The Potter and Hoff experiments differ from ours in that their solid-solution alloy matrix was highly supersaturated with aluminum at the irradiation temperature. In our aged material there were no precipitate-free zones in which dislocation loops could nucleate, and no areas free of precipitates were observed following irradiation. It thus appears that the irradiation response of a solution-annealed alloy differs from that of an aged alloy containing precipitates, which is contrary to the conclusions of Nelson et al [*2*].

Gelles [*11*] has investigated the stability of large γ'- precipitates in Inconel X-750 after both neutron and ion bombardment. The neutron irradiation resulted in growth of the precipitates by radiation-enhanced diffusion. Specimens bombarded with 5-MeV nickel ions at 525 °C (977 °F), however, showed unusual contrast markings and the appearance of fragmentation possibly due to dislocation structure in the original precipitates, or in the matrix between them. Rowcliffe et al [*12*] have documented the formation of dislocation loops and interfacial dislocations in ion-bombarded Inconel X-750 irradiated at these temperatures to similar doses. Contrast effects could partly explain the apparent fragmentation observed in our results below 725 °C (1337 °F) but cannot explain the results at 725 °C (1336 °F).

Korenko [*13*] has irradiated a similar alloy with 1-MeV electrons. Irradiations at 740 °C (1364 °F) produced only a growth in precipitate size and an astounding increase in volume fraction, sometimes approaching 100 percent. Korenko suggested that the increase in volume fraction of the Ni_3Al was due to incorporation of vacancies in the Ni_3Al lattice so as to shift the γ'-boundary to lower aluminum concentrations. This observation was dramatically different from the ion-bombardment results and suggests that the displacement cascade produced by the heavy ions is far more effective in disordering precipitates than the isolated Frenkel pairs produced by electrons.

Observations of the behavior of Ni_3Al precipitates subjected to ion irradiation, both in the present experiment and from other experiments reported in the literature, suggest that there are competing processes between dissolution of the precipitates and growth of the precipitates. All the proposed models recognize that growth of the precipitates will be accelerated over the growth rate in unirradiated material as a consequence of the increase in solute diffusion rates. There is less agreement on the processes which are important in breaking up or dissolving precipitates.

The low-temperature irradiation results of Nelson et al [2] show clearly that Ni_3Al precipitates are rapidly disordered by the displacement cascades. Above 300 to 325 °C (572 to 617 °F), however, the reordering process is apparently quite rapid because no marked change occurs in the volume fraction of the precipitates for doses 1000 times higher than those which produced complete disordering at low temperatures. The electron irradiation results of Korenko which showed growth of precipitates and a marked increase in volume fraction represent a uniquely different result from any seen in ion irradiations. The most obvious physical difference is, of course, the displacement cascade. The model originally proposed by Nelson et al [2] with the disorder dissolution mechanism for ordered precipitates thus satisfies the most obvious requirements of competing growth and shrinkage processes required to explain the effects of ion damage on ordered precipitates.

The Nelson model gives a reasonably good prediction of the final precipitate size for our experiment at 725 °C (1337 °F) for a suitable selection of parameters. Perhaps the least known variable is the dissolution parameter Ψ, defined as the product of the thickness of the layer which can be disordered by a cascade and the fraction of atoms which actually dissolve. Nelson et al used a value of 100 Å for the thickness of the shell of disordered precipitate and assumed all would dissolve, $f = 1$. It is difficult to understand how a region with high solute concentration in close proximity to a precipitate can diffuse away from the precipitate into the matrix, especially a matrix which is already supersaturated in aluminum, because irradiation is being performed at temperatures below the ageing temperature. Perhaps the fine-scale precipitation between large precipitates serves to reduce matrix supersaturation enough to permit the disorder dissolution mechanism to operate. A more serious difficulty with the model is the prediction that the equilibrium size of the precipitate should increase with irradiation temperature for a given precipitate density. This is clearly not the case in the lower-temperature (525 to 625 °C) (977 to 1157 °F) irradiations where large fragments of the original precipitates remained even after doses of 125 dpa. Likewise at 675 and 725 °C (1247 and 1337 °F) where the sizes are approaching those predicted by the model, the temperature dependence is still reversed. One of the deficiencies of the model is that it does not take into account the formation of new precipitates and the redistribution of solute to those precipitates. These factors would influence the final equilibrium size and the temperature dependence of the size, and would reflect in part the heat-treatment history. Nelson et al [2] acknowledged the occurrence of precipitation during the irradiation and the effect of precipitate density on final equilibrium size, but did not incorporate this consideration into a predictive model.

The mechanism of dislocation cutting suggested by Potter and Hoff

[*10*] provides an additional mechanism by which precipitate size could be reduced. The fragmented appearance of the precipitates irradiated at 525 to 675 °C (977 to 1247 °F) in the present study could have been produced by dislocation cutting, but no direct evidence for this mechanism was obtained from the present experiments.

The size or apparent size of precipitates in dark field can be strongly influenced by the interpretation of certain contrast features as pointed out by Gelles [*11*]. It is possible that a precipitate which appears to be fractured may in fact simply contain an antiphase boundary or a dislocation loop structure formed inside the precipitate, or interfacial dislocations on the precipitate surface. Calculations are not available at this time to predict the contrast effects these defect structures would produce. An attempt was made to image the 400 Å precipitates of the present investigation with different superlattice reflections to determine if the contrast features in dark field changed with the operative reflection, but the precipitates were too small to permit resolution of the internal features. Contrast effects cannot explain the 725 °C (1337 °F) observations where a uniform distribution of small precipitates formed.

Swelling in these alloys was completely suppressed except for a few scattered voids in the 56- and 125-dpa specimens. The general observation that swelling is reduced in γ'-bearing nickel-base alloys is now well established. The mechanism of swelling suppression is less well understood. Early hypotheses [*14*] suggested that precipitates suppressed swelling by either trapping vacancies at coherent precipitate interfaces, thereby enhancing recombination, or by pinning dislocations and restricting their climb. More recent studies demonstrate that the swelling resistance depends on the major alloy components [*15*] and the amount of minor solute elements in solution which may be influenced by the heat treatment of the alloy [*16*]. Solute atoms can influence swelling by point defect trapping with enhanced recombination, gettering of surface active agents which can lower the void surface energy, segregation to dislocations so as to alter the bias for interstitials, and changes in stacking fault energy. At the present time it is not evident which of these mechanisms are acting to suppress swelling.

Conclusions

An investigation of nickel ion damage in a nickel-aluminum alloy containing Ni_3Al precipitates has shown that:

1. Precipitates in specimens irradiated at 725 °C (1337 °F) to a dose of 20 dpa reached a narrow size distribution with an average size that was about 20 percent of their original size.

2. Precipitates in specimens irradiated at temperatures between 525 and 675 °C (977 and 1247 °F) had a ragged appearance and seemed to be frag-

mented or fractured. Fine-scale precipitation occurred in the matrix between the larger precipitates. Unusual contrast features of undetermined origin which were not present in the unirradiated precipitates were also observed.

3. There was essentially no swelling in any of the specimens that were irradiated to 20 dpa between 525 and 725 °C (977 and 1337 °F) or at 625 °C (1157 °F) to damage levels between 4 and 125 dpa, although a few inhomogeneously distributed voids were detected in the specimens irradiated to 56 and 125 dpa at 625 °C (1157 °F).

Acknowledgments

Financial support for the experimental portion of this work was provided by the Office of Naval Research. The authors wish to thank J. R. Reed for assistance with specimen preparation and ion bombardment of the specimens and one of the authors, L. G. K., wishes to thank the Naval Research Laboratory for permission to use their facilities during the course of this research, which is part of a Ph.D. thesis at the University of Wisconsin.

References

[1] Hudson, J. A., Francis, S., Mazey, D. J., and Nelson, R. S. in *Effects of Irradiation on Substructure and Mechanical Properties of Metals and Alloys, ASTM STP 529,* American Society for Testing and Materials, 1973, pp. 326–333.

[2] Nelson, R. S., Hudson, J. A., and Mazey, D. J., *Journal of Nuclear Materials,* Vol. 44, 1972, p. 318.

[3] Hudson, J. A., *Journal of the British Nuclear Energy Society,* Vol. 14, 1975, p. 127.

[4] Manning, I. and Mueller, G. P., *Computer Physics Communications,* Vol. 7, 1974, p. 85.

[5] Sprague, J. A., *Review of Scientific Instruments,* Vol. 46, 1975, p. 1171.

[6] Ardell, A. J. and Nicholson, R. B., *Acta Metallurgica,* Vol. 14, 1966, p. 1295.

[7] Phillips, V. A., *Acta Metallurgica,* Vol. 14, 1966, p. 1533.

[8] Chellman, D. J. and Ardell, A. J., *Acta Metallurgica,* Vol. 22, 1974, p. 577.

[9] Maniar, G. N. and Bridge, J. E., *Metallurgical Transactions* 2, Vol. 95, 1971.

[10] Potter, D. I. and Hoff, H. A., "Effects of Heavy-Ion Irradiation on the Morphology of γ/γ' Alloys," *Proceedings,* International Conference on Fundamental Aspects of Radiation Damage in Metals, Vol. II, 1976, pp. 1092–1099.

[11] Gelles, D. S., Hanford Engineering Development Laboratory, Richland, Wash., private communication.

[12] Rowcliffe, A. F., Diamond, S., Bleiberg, M. L., Spitznagel, J., and Choyke, J. in *Properties of Reactor Structural Alloys After Neutron or Particle Irradiation, ASTM STP 570,* American Society for Testing and Materials, 1975, pp. 565–583.

[13] Korenko, M. K., this conference, 1976.

[14] Nelson, R. S., Hudson, J. A., Mazey, D. J., Walters, G. P., and Williams, T. M., in *Radiation-Induced Voids in Metals,* J. W. Corbett and L. C. Ianniello, Eds., U.S. Atomic Energy Commission Symposium Series 26, 1972, p. 430.

[15] Johnston, W. G., Lauritzen, T., Rosolowski, J. H., and Turkalo, A. M. in *Properties Reactor Structural Alloys After Neutron or Particle Irradiation, ASTM STP 570,* American Society for Testing and Materials, 1975, p. 525–542.

[16] Johnston, W. G., Lauritzen, T., Rosolowski, J. H. and Turkalo, A. M., "The Effect of Metallurgical Variables on Void Swelling," *Proceedings,* American Society for Metals, Materials Science Seminar on Radiation Damage in Metals, Cincinnati, Ohio, 9–10 Nov. 1975 (to be published).

Radiation Embrittlement of Pressure Vessel Steels

T. R. Mager,[1] *J. Davidson,*[2] *and M. Galliani*[3]

Fracture Mechanics Characterization of the Trino Reactor Vessel Material

REFERENCE: Mager, T. R., Davidson, J., and Galliani, M., "**Fracture Mechanics Characterization of the Trino Reactor Vessel Material,**" *Irradiation Effects on the Microstructure and Properties of Metals, ASTM STP 611,* American Society for Testing and Materials, 1976, pp. 387–399.

ABSTRACT: During preirradiation testing it became known that the Trino reactor vessel material exhibited a Charpy-V upper-shelf impact energy level of approximately 36 ft·lb in a direction transverse to the plate rolling direction. Current U.S. practice is to require 75 ft·lb impact energy for materials in the beltline region of the reactor vessel. It was proposed that fracture toughness properties be obtained on Trino reactor vessel Plate W6306-1 in terms of both fracture mechanics parameters and conventional Charpy-V impact energy. Concurrent with preirradiation testing of Plate W6306-1 an accelerated irradiation program was initiated in a test reactor.

To generate the fracture toughness data, compact tension specimens were tested both statically (K_{Ic}) and dynamically (K_{Id}). The encapsulated specimens were irradiated at 550°F (288°C) to a fluence of 3×10^{19} neutrons (n)/cm^2 ($E > 1$ MeV).

The fracture toughness data obtained from the preirradiation testing indicated that Plate W6306-1 meets the intent of the ASME Appendix G, K_{IR} curve. Postirradiation fracture toughness data (static and dynamic) from the accelerated radiation program indicated that the fracture toughness for transverse specimens was approximately 100 ksi $(\text{in.})^{1/2}$. The upper-shelf impact energy of the Trino vessel Plate W6306-1 decreased a maximum of 7 ft·lb during the accelerated irradiation.

Based on the fracture toughness properties obtained during the evaluation, it was concluded that Plate W6306-1 exhibited adequate toughness to provide for continued safe operation of the Trino Vercellese Nuclear Power Plant.

KEY WORDS: radiation, fracture (materials), impact tests, fracture tests, dynamic tests, toughness, static hardness tests, equivalent energy, nuclear reactor materials

The Ente Nazionale per l'Energia Elettrica (ENEL) Trino Nuclear Power Plant went into operation in 1965. At the time of manufacturing and start-up of the Trino Nuclear Power Plant, there were no regulatory

[1] Manager, Materials Engineering, Westinghouse Nuclear Energy, Westinghouse Electric Corporation, Brussels, Belgium.

[2] Engineer, Nuclear Energy Systems, Westinghouse Electric Corporation, Pittsburgh, Pa. 15230.

[3] Chief, Reactor Service, Operating Branch, Ente Nazionale per l'Energia Elettrica, ENEL, Rome, Italy.

rules such as 10 CFR 50 Appendix G or Section III of the American Society of Mechanical Engineers (ASME) Boiler and Pressure Vessel Code to give guidance to allowable minimum fracture toughness properties. Because of changes made in the design of the Trino reactor vessel internals early in the life of the plant, the original reactor vessel material radiation surveillance program had to be discontinued. The original program, however, was replaced by placing new surveillance capsules in holders below the core.

During the preirradiation testing portion of the second program, it became known that the reactor vessel material Plate W6306-1 exhibited an upper-shelf impact energy level of approximately 36 ft·lb in a direction transverse (WR) to the rolling direction. Current U.S. practice is to require 75 ft·lb impact energy for materials in the beltline region of the reactor vessel.

In order to show that there can be no question about the integrity of the reactor pressure vessel at the Trino plant, which has been operating for three cycles, it was proposed that fracture toughness properties in terms of fracture mechanics parameters be obtained on Plate W6306-1. Concurrent with the preirradiation testing of Plate W6306-1, an accelerated irradiated program was initiated in a test reactor in the United States.

This paper presents the results of the fracture toughness testing program.

Experimental Program

Materials and Specimens

Plate W6306-1 was fabricated from a heat of Type A302 Grade B steel. The chemical composition and heat treatment for the plate are given in Table 1.

To generate the fracture toughness data, compact tension (CT) [1][4] specimens and standard Charpy-V (C_v) specimens were used. For the preirradiation testing, 0.394 T-CT, 2T-CT, and 4T-CT specimens were evaluated. In the postirradiated condition, only 0.394 T-CT specimens were evaluated. The configuration and dimensions of the CT specimens are shown in Fig. 1. The fracture mechanics specimens (CT) fabricated from Plate W6306-1 were oriented in the transverse (WR) or "weak" direction. The Charpy V-notch impact specimens represented both the longitudinal (RW) and transverse (WR) orientations. Use of specimens oriented in the transverse (WR) direction was consistent with the requirements of Appendix G, 10 CFR, Part 50 and Paragraph NB 2300 of the ASME Code.

[4] The italic numbers in brackets refer to the list of references appended to this paper.

TABLE 1—*Chemical analysis and heat treatment of Trino vessel plate W6306-1.*

Chemical Analysis—Composition, weight %							
C	Mn	P	S	Si	Mo	Cu	Ni
0.21	1.38	0.013	0.035	0.24	0.47	0.16	0.16

Heat Treatment
1600°F for 9½ h; water dip-quenched 1225°F for 9½ h; air-cooled 1150°F for 15½ h; furnace-cooled

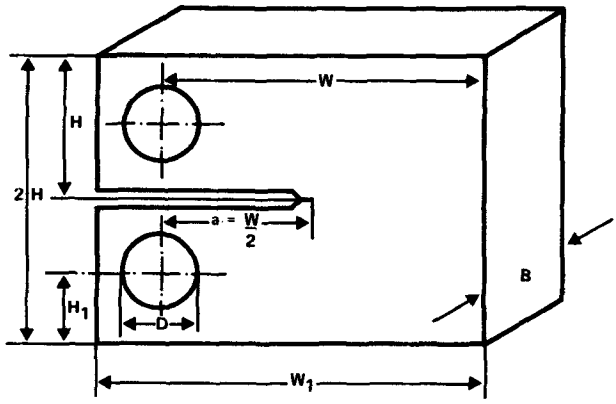

$W = 2.0B$ $D = 0.5B$

$a = 1.0B$ $W_1 = 2.5B$

$H = 1.2B$ $H_1 = 0.65B$

FIG. 1—*General configuration and proportions of compact tension specimens for* K_{Ic} *fracture toughness measurement.*

Testing of Compact Tension Specimens

The fracture mechanics approach provides quantitative data to assess the potential for fast or brittle failure and to develop criteria for designing or setting plant operating specifications, or both, to ensure the integrity of the nuclear system during the life of the plant. The basic principle is that a crack or crack-like material flaw will propagate when the crack tip stress intensity factor reaches a specific magnitude. Although this stress intensity factor is dependent on the state of stress and defect geometry, the critical stress intensity factor remains a distinct numerical quantity defining the material's fracture strength. The critical stress intensity factor

is designated K_{Ic} and is interchangeably called the "fracture toughness" when referring to the material. While K_{Ic} is a basic material parameter, it is also dependent upon mechanical and metallurgical variables. Strain rate (testing speed) and temperature are the most significant variables affecting the fracture toughness of a given material. Generally, toughness of medium-strength materials like A302 is highly temperature-sensitive, with a rapid increase in toughness at a temperature near the nil ductility transition temperature. At a given temperature, the fracture toughness generally decreases with increasing rate of strain.

Stated briefly, the testing method involved tension testing of the notched CT specimens which had been precracked in fatigue. The load versus the displacement occurring across the notch at the specimen edge was autographically recorded during the test. The specimen displacement was measured by using a clip gage spanning the front of the machined notch.

For static fracture toughness (K_{Ic}) testing, the techniques have been well-defined by ASTM Test for Plane-Strain Fracture Toughness of Metallic Materials (E-399-74). A maximum loading rate ($\dot{K}$) of 2.5 ksi $(\text{in.})^{1/2}/\text{s}$ is required for a standard static test. The static K_{Ic} ($K < 2.5$ ksi $\sqrt{\text{in.}/\text{s}}$) testing was performed using a Materials Testing System (MTS) machine. After the precracking operation, the specimens were tested at various preselected temperatures. The temperature of the specimen prior to testing was monitored using copper-constantan thermocouples until the temperature stabilized with ± 2°F. Liquid nitrogen was used to cool the specimens below ambient temperature, and elevated testing temperatures were achieved using an electrical furnace. A complete description of the test apparatus as well as the design of the grips and environmental chambers is given by Spewock and Ceschini [*1*]. Appendix G of the Summer 1972 Addenda to Section III of the ASME Code used a reference fracture toughness, K_{IR} versus temperature curve, to define safe operation of reactor vessels. The K_{IR} curve was based on dynamic fracture toughness, K_{Id} values. Unlike static K_{Ic} testing (ASTM Method E-399), dynamic fracture toughness validity criteria are not yet defined. The term K_{Id} is defined as the dynamic fracture toughness which is obtained from tests with a loading rate ($\dot{K}$) exceeding 2.5 ksi $\sqrt{\text{in.}}/\text{s}$. The dynamic testing performed in this program was consistent with the dynamic testing that generated the ASME Code K_{IR} curve found in Appendix G of Section III.

As in the static loading situation, the linear elastic stress field equations describe the dynamic stress field near the crack tip. Previous studies [*2*] conducted on the fracture toughness of mild steel plate indicate that high loading rates considerably decrease fracture toughness in the brittle/ductile transition region. As with the static tests, the dynamic tests were performed at various preselected temperatures after the precracking operation. The temperature of the specimens prior to testing was again moni-

tored using copper-constantan thermocouples until the temperature stabilized within ±2°F. Testing was performed using a specially designed apparatus with a loading system capable of producing ram velocities of 60 in./s and loads of 150 kip. Electrical strain-gage instrumentation and linear variable differential transformers (LVDT) were used to measure load and displacement, respectively. The outputs were recorded on a frequency-modulated magnetic tape recorder. A complete description of the testing apparatus and method of evaluation of the test results is given in Ref *3*.

Fatigue precracking procedures as recommended by ASTM Method E 399 were followed closely. Prior to irradiation, 0.394 T-CT specimens were fatigue precracked at room temperature, 75°F (24°C). The fact that neutron irradiation increases the yield strength of a steel complicates the advance prediction of the maximum allowable K_f level for fatigue precracking. In the present study, the maximum K_f level for the tension-zero-tension fatigue cycle was 15 000 psi $\sqrt{\text{in.}}$

Irradiation Experiment

Specimen irradiations were performed in the Union Carbide Research reactor (UCRR) A-4 fuel core position under the technical direction of the Naval Research Laboratory. Capsule design and fabrication, instrumentation and specimens loading was by the Naval Research Laboratory under the technical direction of H. Watson. The encapsulated specimens were irradiated at 550°F (288°C) to a fluence of 3×10^{19} neutrons (n)/cm^2 ($E > 1$ MeV).

Experimental Results

Compact Tension (CT) Specimens

Because of the limited material available, the CT specimen size was such that valid K_{Ic} data were not obtained using the recommended ASTM Method E 399 validity criteria. The validity of fracture toughness testing as set forth in ASTM E 399 is unusual in that it is necessary to compare posttest data with pretest dimensions to determine if the fracture toughness measured (K_Q) is the critical value for the material (K_{Ic}). In other words, the validity of the test can only be determined after testing. The ASTM Method E 399 recommendation as to the validity of CT specimen testing is based upon the specimen thickness B and the crack length a. ASTM Method E 399 recommends that both B and a be equal to or greater than 2.5 $(K_Q/\sigma_{ys})^2$. As the temperature increases, the yield strength of the material decreases and the fracture toughness increases; thus the

specimen thickness B and the crack length a must be increased to meet the recommended validity criteria.

Witt [*3*] proposed a method for using small CT specimens for obtaining lower-bound K_{Ic} data in the temperature range of interest (200 to 550°F) (93 to 288°C). The basis for the method of data analysis as set forth by Witt is the equivalent energy concept. In essence, equivalent energy concepts can be used to measure fracture toughness values, K_{Ic}, from small specimens where a much larger specimen would be required for a valid K_{Ic} value.

The procedure can be summarized as follows:

1. Select any point of the linear portion of the load-deflection curve (Point B). Measure the area under the load-deflection curve up to maximum load and divide this area by the area up to Point B. Call the ratio of areas B.

2. Using the load at point B(P_B), calculate K_{Bd} as follows

$$K_{Bd} = \frac{B^2 P_B}{bd(2bd)^{1/2}} f\left(\frac{a}{w}\right)$$

If the specimen does not meet the ASTM Method E 399 size requirements, K_{Bd} as just calculated represents the lower-bound fracture toughness of a specimen of that size. Experimental verification of the equivalent energy concept was reported by Mager and Buchalet [*4*].

The preirradiated fracture toughness properties of Plate W6306-1 are summarized in Table 2 and Figs. 2 (static) and 3 (dynamic). The postirradiated fracture toughness properties of Plate W6306-1 are summarized in Table 3 and Figs. 2 (static) and 3 (dynamic).

Charpy-V Properties

The postirradiation Charpy-V properties of Plate W6306-1 are summarized in Table 4 and Fig. 4. Also shown in Fig. 4 are the preirradiation Charpy-V properties and thus the extent of radiation-induced changes observed. The Charpy-V 30 ft·lb transition temperature was elevated by 100°F (37.7°C) and the upper-shelf level was lowered by 12 ft·lb (14.5 percent) for RW-oriented specimens and by 7 ft·lb (18 percent) for WR-oriented specimens.

Discussion

Mager and Buchalet [*4*] demonstrated that by utilizing the method as proposed by Witt [*3*], lower-bound fracture toughness data can be obtained from small compact specimens. As the specimen thickness is in-

TABLE 2—*Preirradiated fracture toughness properties of Torino Plate W6306-1.*

Specimen Number	Specimen Size, in.	Test Condition	Test Temperature, °F	K_{Icd}, ksi $\sqrt{in.}$
S-66	0.394 TCT	static	+50	144.5
S-67	0.394 TCT	static	+50	159.5
S-60	0.394 TCT	static	+75	125.2
S-65	0.394 TCT	static	+75	138.0
S-18	0.394 TCT	static	+85	121.0
S-70	0.394 TCT	static	+150	118.0
S-68	0.394 TCT	static	+150	131.0
S-19	0.394 TCT	static	+205	112.0
S-71	0.394 TCT	static	+250	103.2
S-72	0.394 TCT	static	+250	120.2
S-73	0.394 TCT	static	+550	102.5
S-75	0.394 TCT	static	+550	109.0
S-64	0.394 TCT	dynamic	+50	136.7
S-80	0.394 TCT	dynamic	+50	111.6
S-21	0.394 TCT	dynamic	+53	111.1
S-62	0.394 TCT	dynamic	+75	106.2
S-79	0.394 TCT	dynamic	+75	128.2
S-77	0.394 TCT	dynamic	+150	132.7
S-63	0.394 TCT	dynamic	+250	92.7
S-61	0.394 TCT	dynamic	+250	122.2
S-74	0.394 TCT	dynamic	+550	133.1
S-78	0.394 TCT	dynamic	+550	166.6
S-8[a]	2 TCT	static	±0	119.4
S-5[a]	2 TCT	static	+53	142.0
S-7[a]	2 TCT	static	+85	159.0
S-12[a]	2 TCT	static	+85	137.6
S-11[b]	2 TCT	static	+205	138.0
S-6[c]	2 TCT	dynamic	+93	187.1
S-9[a]	2 TCT	dynamic	+205	154.0
S-1	4 TCT	static	±0	96.0
S-3	4 TCT	static	+85	166.1
S-4	4 TCT	static	+205	153.0
S-2	4 TCT	dynamic	+205	205.5

[a] Surface.
[b] ¾ thickness.
[c] ¼ thickness.

creased, the lower-bound toughness approaches the plane-strain fracture toughness K_{Ic}. As the data shown in Figs. 2 and 3 for the unirradiated material demonstrates, as the specimen size is increased the lower-bound fracture toughness is increased. The data given in Figs. 2 and 3 would indicate that the 2T-CT and 4T-CT test results are approaching the plane-strain fracture toughness K_{Ic}. Hence, the plane-strain toughness K_{Ic} of Plate W6306-1 is approximately 160 ksi $\sqrt{in}$.

The dynamic fracture toughness K_{Id} is slightly higher than the static fracture toughness K_{Ic} on the upper shelf. This is characteristic of dynamic testing.

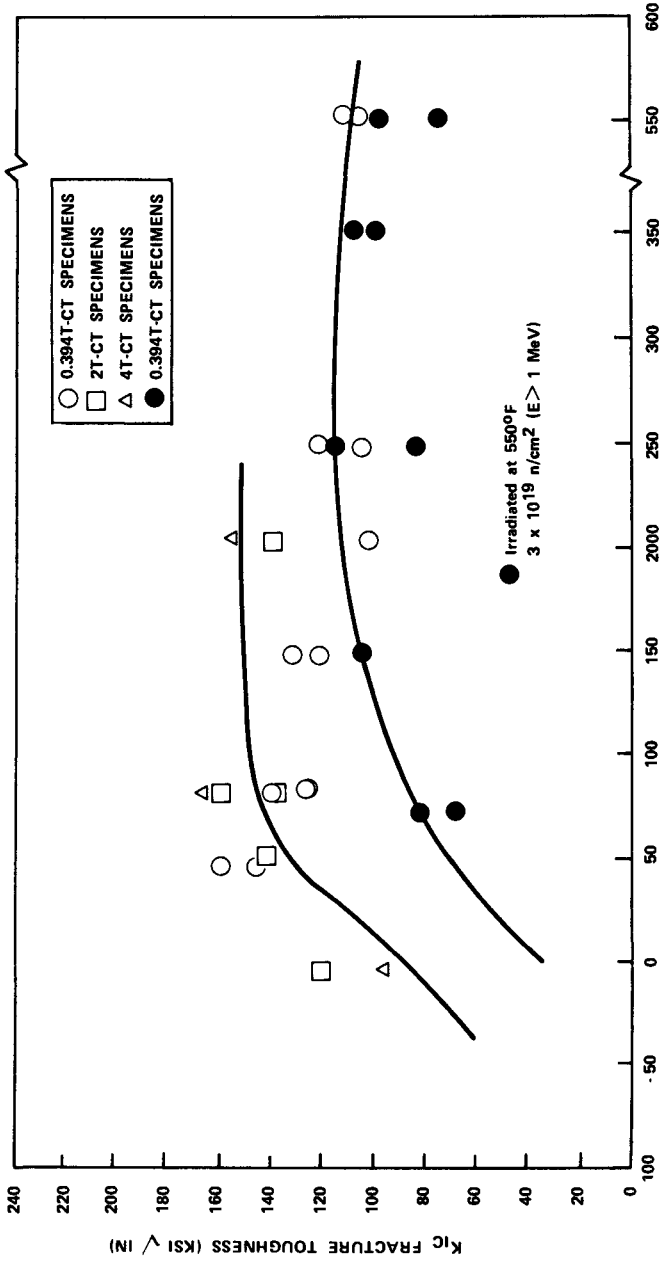

FIG. 2—K_{Ic} *fracture toughness values for Type A302 Grade B steel (Plate W6306-1) (equivalent energy method).*

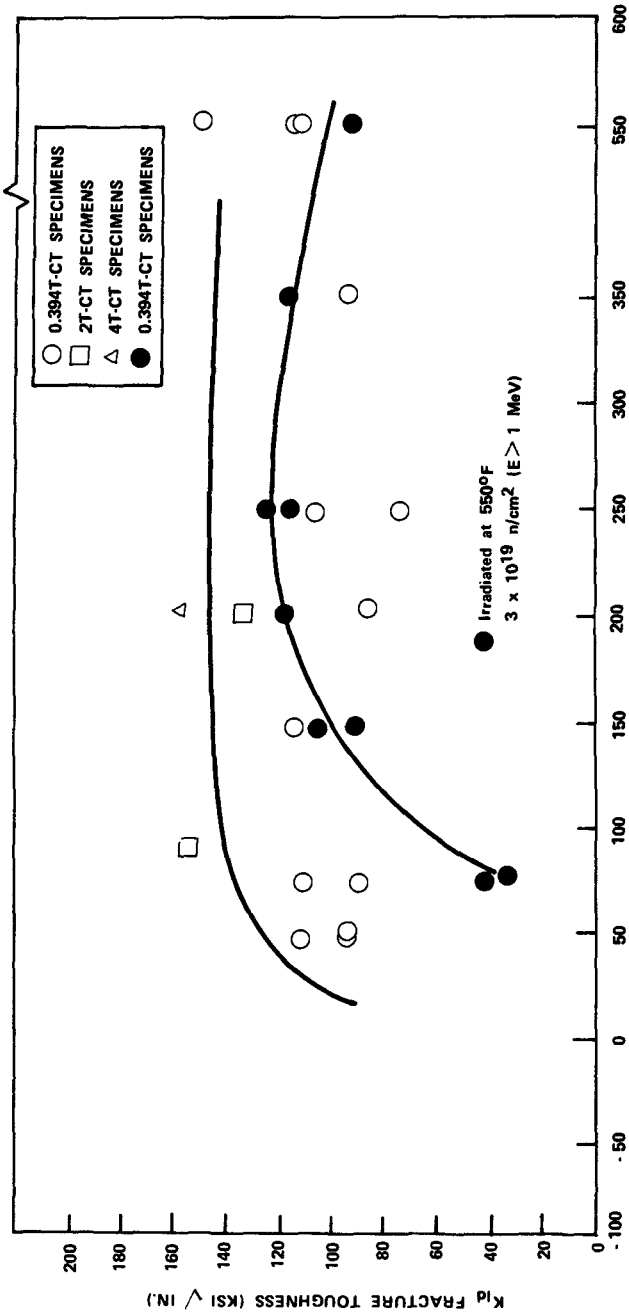

FIG. 3—K_{Id} *fracture toughness values for Type A302 Grade B steel (Plate W6306-1).*

TABLE 3—*Postirradiation fracture toughness properties of Trino Plate W-6306-1.*

Specimen Number	Specimen Size, in.	Test Condition	Test Temperature, °F	K_{Icd}, ksi $\sqrt{in.}$
E-19	0.394	static	+75	71.3
E-23	0.394	static	+75	81.8
E-15	0.394	static	+150	106.3
E-13	0.394	static	+250	114.2
E-16	0.394	static	+250	84
E-17	0.394	static	+350	107.5
E-22	0.394	static	+350	100
E-20	0.394	static	+550	74.6
E-25	0.394	static	+550	96
E-11	0.394	dynamic	+75	59.5
E-9	0.394	dynamic	+75	52.9
E-4	0.394	dynamic	+150	123.7
E-10	0.394	dynamic	+150	107.8
E-18	0.394	dynamic	+200	105.1
E-3	0.394	dynamic	+200	137.8
E-1	0.394	dynamic	+250	142.6
E-7	0.394	dynamic	+250	138.9
E-5	0.394	dynamic	+350	116.2
E-12	0.394	dynamic	+350	137.8
E-6	0.394	dynamic	+550	134.5
E-2	0.394	dynamic	+550	111.0

The postirradiation data summarized in Figs. 2 and 3 indicate that the neutron irradiation had little if any effect on the upper-shelf fracture toughness of Plate W6306-1. Without testing larger-size specimens in the postirradiation condition, one cannot conclude that the postirradiation fracture toughness is of the order of 160 ksi $\sqrt{in}$. One can conclude, however, that the minimum fracture toughness of Plate W6306-1 is of the order of 100 ksi $\sqrt{in}$. after exposure to a fluence of 3×10^{19} n/cm^2—recognizing, again, that the dynamic K_{Id} fracture toughness upper shelf is generally higher than the static K_{Ic} upper shelf.

Conclusions

The fracture toughness of Trino reactor vessel Plate W6306-1 was evaluated in both the unirradiated and postirradiated conditions. The following conclusions are drawn from the test data.

1. The preirradiation upper-shelf static K_{Ic} and dynamic K_{Id} fracture toughness based on the equivalent energy method are of the order of 160 ksi $\sqrt{in}$.

2. The postirradiation upper-shelf static K_{Ic} fracture toughness is of the order of 100 ksi $\sqrt{in}$.; the dynamic toughness is of the order of 135 ksi $\sqrt{in}$.

TABLE 4—*Postirradiation[a] Charpy V-notch impact data for Trino pressure vessel shell plate W-6306-1.*

Longitudinal Direction (RW)				Transverse Direction (WR)			
Test Temperature, °F	Energy, ft·lb	Shear, %	Lateral Expansion, mils	Test Temperature, °F	Energy, ft·lb	Shear, %	Lateral Expansion, mils
70	10	5	6	70	8	2	9
70	10	5	7	70	8	5	5
150	26	30	18	150	18	10	18
150	43.5	50	21	150	19	35	18
200	60	80	49	200	30.5	95	38
200	63.5	98	46	200	30	90	27
250	70	100	53	250	30	100	33
250	73.8	100	59	250	34	100	35
350	68.5	100	62	350	29	100	30
...	...	...	...	350	31	100	37
...	...	...	...	350	24.5	100	35
...	...	...	...	550	29	100	35
...	...	...	...	550	32.2	100	38

[a] 3×10^{19} n/cm^2 ($E > 1$ MeV).

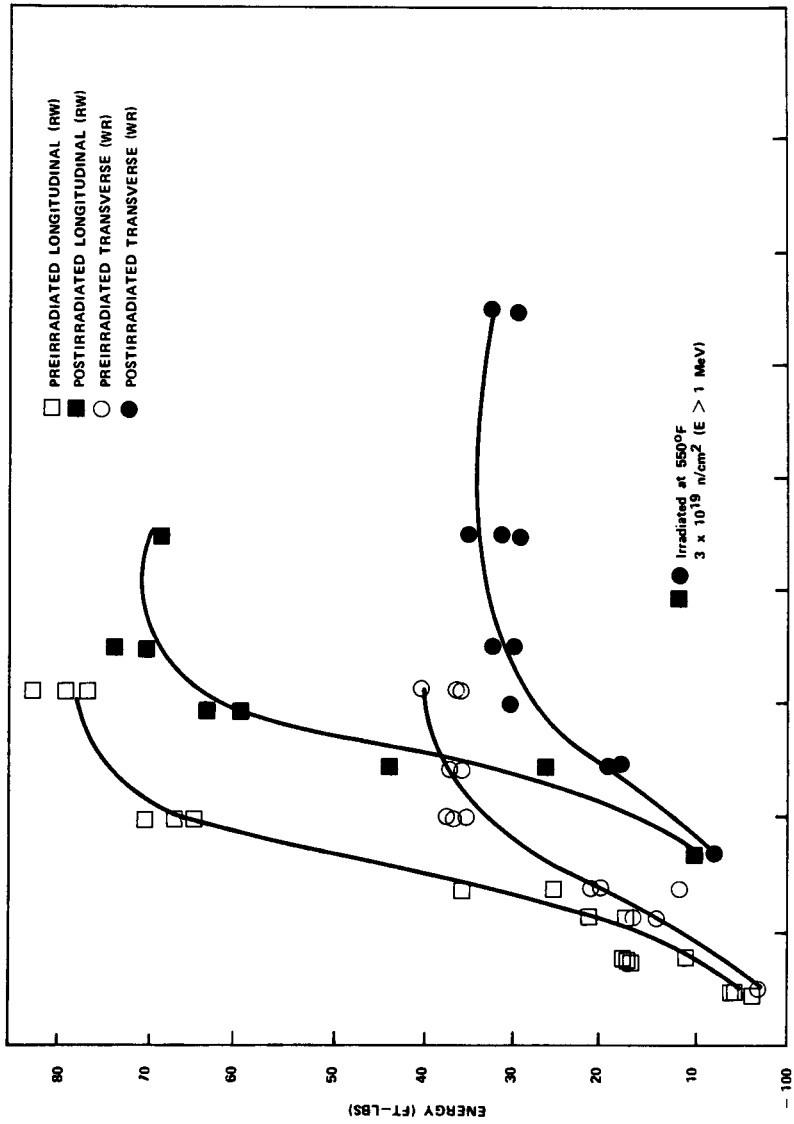

FIG. 4—Charpy V-notch impact data for Trino pressure vessel (Plate W6306-1).

3. The 30 ft·lb transition temperature shift after an exposure to a fluence of 3×10^{19} n/cm^2 ($E > 1$ MeV) is of the order of 100°F (38°C).

4. The postirradiation Charpy-V upper-shelf impact energy for WR-oriented specimens is approximately 30 ft·lb.

5. Although Trino reactor vessel Plate W6306-1 exhibits an upper-shelf impact energy of approximately 30 ft·lb, the upper-shelf fracture toughness is 100 ksi in. $\sqrt{\text{in.}}$ or greater.

Acknowledgments

We are deeply grateful to the Naval Research Laboratory and L. Steele for making the irradiation portion of this program possible. We would also like to thank H. Watson, Naval Research Laboratory, S. Yanichko, Westinghouse Nuclear Energy Division, and R. Shogan and L. Ceschini of Westinghouse R&D Laboratories for their contributions to the program.

References

[1] Spewock, M. and Ceschini, L., "Servo-Controlled Electro-Hydraulic System for Testing Fracture Toughness Specimens," Westinghouse Research Laboratories, Research Report 69-IP6-BTLFR-R3, Aug. 1969.

[2] Shabbits, W. O., "Dynamic Fracture Toughness Properties of Heavy Section A 533 Grade B Class 1 Steel Plate," HSST Report No. 13, Westinghouse Nuclear Energy System Division, WCAP-7623, Dec. 1970.

[3] Witt, F. J., "Equivalent Energy Method for Calculation of Elastic-Plastic Fracture, Oak Ridge National Laboratories, CONF 7/0342-11, Oak Ridge, Tenn., 1970.

[4] Buchalet, C. and Mager, T. R. in *Progress In Flaw Growth and Fracture Toughness Testing, ASTM STP 536,* American Society for Testing and Materials, pp. 281-296.

R. A. Wullaert,[1] *J. W. Sheckherd,*[1] *and R. W. Smith*[2]

Evaluation of the Maine Yankee Reactor Beltline Materials

REFERENCE: Wullaert, R. A., Sheckherd, J. W., and Smith, R. W., **"Evaluation of the Maine Yankee Reactor Beltline Materials,"** *Irradiation Effects on the Microstructure and Properties of Metals, ASTM STP 611,* American Society for Testing and Materials, 1976, pp. 400–417.

ABSTRACT: Tension and Charpy V-notch specimens of the base metal, heat-affected zone metal, and weld metal from the beltline region of the Maine Yankee pressure vessel (Type A533B-1 steel) were irradiated in an accelerated surveillance capsule. The specimens were exposed to a fluence of 1.3×10^{19} neutrons (n)/cm^2 (>1 MeV) at 550°F (288°C). Charpy V-notch specimens of a standard reference material (SRM) were also irradiated in the surveillance capsule as a correlation monitor for dosimetry. Irradiation increased the yield and ultimate strength and decreased the ductility of all of the Maine Yankee materials. The yield strength increased 50 percent for the weld metal and 35 percent for the base and heat-affected zone materials. Radiation-induced shifts in the Charpy V-notch curves at the 30 ft·lb, 50 ft·lb, and 35-mil levels were measured. The decrease in the Charpy upper shelf energy was also measured. The largest temperature shift occured at the 35-mil level for all materials, and this shift was used to determine the adjusted reference temperature. The increase in reference temperature ranged from 140°F (60°C) for the base metal to 345°F (174°C) for the weld metal. The weld metal also showed the largest drop in the Charpy upper-shelf energy (44 percent) versus 23 to 31 percent for the other materials.

The critical beltline material for determining the new operating limit curves for the reactor was the weld metal, with an adjusted reference temperature of 315°F (157°C) and a Charpy upper-shelf value of 57 ft·lb. The high copper and phosphorus content of the weld (0.36 percent copper, 0.015 percent phosphorus) caused the irradiated Charpy data to fall above the general trend curve for Type A533B steel. A trend curve for the weld metal was constructed using independently generated irradiation data on the same weld metal.

KEY WORDS: radiation, pressure vessels, nuclear reactors, irradiation, embrittlement, weld metal

Pressure-temperature limitations for heatup and cooldown of the reactor coolant system during operation and test conditions are provided in the technical specifications for each plant. These pressure-temperature

[1] President and manager, Testing Services, Fracture Control Corporation, Goleta, Calif. 93017.

[2] Metallurgical engineer, Yankee Atomic Electric Company, Westborough, Mass. 01581.

limits are imposed on the reactor coolant pressure boundary to provide adequate safety margins against nonductile or rapidly propagating failure of the ferritic pressure vessel materials. Appendixes G and H of 10 CFR 50[3] specify the requirements for the reactor vessel pressure-temperature limits. These limits are based on the ASME Code, Section III, Appendix G, which provides a fracture mechanics basis for determining allowable limits.

The operating limit curves in the plant technical specifications are based on the baseline mechanical properties of the reactor vessel adjusted by the anticipated embrittlement of the beltline region of the vessel due to neutron exposure. Trend curves of change in fracture toughness versus fluence are used to predict the embrittlement for the specific type of steel, residual element content, and operating temperature of the reactor. The functions of a reactor pressure vessel surveillance program are to continually monitor the neutron embrittlement of the ferritic materials and to use the data to verify the original operating limit curves.

The Maine Yankee nuclear reactor is a pressurized water reactor built by Combustion Engineering. The surveillance program design, selection of materials, specimen and capsule fabrication, and installation of the capsules were performed by Combustion Engineering as part of the Maine Yankee construction contract [*1*].[4] The unirradiated and irradiated mechanical properties of the Maine Yankee surveillance materials have recently been measured [*2,3*]. The surveillance examination determined that the specimens were irradiated at 550°F (288°C) to a fluence of 1.3×10^{19} neutron (n)/cm^2 (>1 MeV). Details of the surveillance material characterization, irradiation capsule configuration and location, capsule disassembly, and neutron dosimetry can be obtained from these reports and are not presented here. The purpose of this paper is to present the radiation-induced changes in mechanical properties and describe the determination of the adjusted reference temperature RT_{NDT}.

Mechanical Property Results

The various materials and mechanical property test specimens contained in the first accelerated capsule are given in Table 1, along with the chemical analysis of the materials. All tests were performed in accordance with appropriate ASTM standards [*4*] and internal procedures [*5*].

Tension Tests

Three irradiated tension specimens of the Maine Yankee base metal, weld metal, and heat-affected zone (HAZ) material were obtained from

[3] Amendments to Atomic Energy Commission (AEC) regulation Title 10, Part 50, published in *Federal Register*, 17 July 1973.

[4] The italic numbers in brackets refer to the list of references appended to this paper.

TABLE 1—*Materials, specimens, and chemistry for Maine Yankee Capsule Number 1.*

Specimen	A533B-1 Plate (D-8406-1)	Submerged-Arc Weld (D-8407-1, -3)	SRM[a] (HSST-01)	HAZ (D-8406-2)	Total
Charpy V-notch	12(L)[b]	12	12(L)	12	48
Tensile (0.252 in.)	3	3	...	3	9
Total	15	15	12	15	57
Chemistry					
Si	0.22	0.22	0.22	...	...
S	0.013	0.012	0.008	...	...
P	0.013	0.015	0.008	...	...
Mn	1.27	1.38	1.37	...	...
C	0.22	0.14	0.22	...	...
Cr	0.11	0.07	0.15	...	...
Ni	0.59	0.78	0.66	...	...
Mo	0.57	0.55	0.54	...	...
B	0.0004	0.0002	...	...	...
Cb	<0.01	<0.01	...	...	...
V	<0.001	0.003	0.02	...	...
Co	0.010	0.013	...	...	...
N	0.006	0.012	...	...	...
Cu	0.15	0.36	0.18	...	...
Al	0.021	0.004	...	...	...
Ti	<0.01	<0.01	...	...	...
W	0.01	0.01	...	...	...
As	0.01	<0.01	...	...	...
Sn	0.009	0.001	...	...	...
Zr	0.001	0.002	...	...	...

[a] Standard reference material, Type A533B-1 steel, plate 01 from the Heavy Section Steel Technology (HSST) program.
[b] Longitudinal orientation.

the surveillance capsule. The tension specimens were standard ASTM-type 0.252-in.-diameter specimens with a 1-in. gage length. One specimen of each material was tested at room temperature, the reactor operating temperature (566 °F (297 °C), and the reactor design temperature (650 °F (343 °C). The crosshead rate through 0.2 percent yield strength was 0.005 in./in./min. This crosshead rate was maintained after yielding. An extensometer was used to obtain load-elongation curves through yielding and a load-time (crosshead travel) curve was obtained past this load. The tensile properties measured were 0.2 percent yield strength, ultimate tensile strength, total elongation, and reduction in area. A summary of the irradiated tensile properties is given in Table 2 for comparison. An irradiation dose of 1.3×10^{19} n/cm^2 (>1 MeV) at 550 °F (288 °C) produced an increase in the yield strength of approximately 50 percent for the weld and 35 percent for the base and HAZ material.

It should be noted that irradiated tensile data play no direct role in deter-

TABLE 2—*Tensile properties of irradiated Maine Yankee beltline materials [550°F (288°C), 1.3 × 10¹⁹ n/cm² (>1 MeV)].*

Material	Specimen No.	Temperature, °F	0.2% Yield Strength, ksi	Ultimate Tensile Strength, ksi	Total Elongation, %	Reduction in Area, %
Base (L)	1JP	RT[a]	81.6	103.7	27.6	54.8
			(61.6)[b]	(84.4)	(29.0)	(71.3)
Weld	3JT	RT	102.2	116.9	24.2	52.1
			(71.1)	(87.2)	(28.5)	(70.4)
HAZ	4JU	RT	83.7	104.7	22.7	55.4
			(61.5)	(84.3)	(22.5)	(70.8)
Base (L)	1J4	566	73.9	95.3	22.5	45.8
			(54.8)	(83.6)	(23.8)	(66.2)
Weld	3J3	566	93.3	110.8	21.8	42.8
			(62.6)	(85.2)	(24.2)	(59.3)
HAZ	4KJ	566	78.6	97.8	20.2	47.6
			(55.7)	(83.2)	(20.2)	(63.0)
Base (L)	1JM	650	69.2	92.0	25.0	49.9
			(53.5)	(81.0)	(28.8)	(67.6)
Weld	3KJ[c]	650	...	~104.1	~18.2	~44.0
			(59.5)	(81.7)	(25.0)	(61.0)
HAZ	4K2	650	69.8	93.0	22.1	61.1
			(54.9)	(81.6)	(23.3)	(68.2)

[a] RT = room temperature.

[b] Parentheses enclose average value for three tests on unirradiated material.

[c] Accidental prestraining of specimen prior to testing resulted in unreliable yield strength measurement and questionable test results.

mining the adjusted reference temperature RT_{NDT}. However, the tensile results provide valuable backup information and are thus included in the paper.

Charpy Impact Tests

The surveillance capsule contained four Charpy impact compartments. Each compartment contained twelve Charpy V-notch specimens of a given material. All Charpy specimens were the standard 0.394-in. (10 mm) size. The Charpy V-notch tests were performed in accordance with ASTM Notched Bar Impact Testing of Metallic Materials (E 23-72). All tests were performed on a 220 ft·lb impact machine at an impact velocity of 16.7 ft/s. Army Materials and Mechanics Research Center (AMMRC) calibration specimens were tested prior to the irradiated specimens to ensure the calibration of the impact machine. The impact machine was instrumented to obtain additional test data. The instrumented Charpy results are not discussed here, but are presented in Ref *3*.

Twelve irradiated Charpy V-notch specimens of the base metal, weld, HAZ, and standard reference material (SRM) were tested over a range of temperatures to generate a full Charpy transition curve. Test temperature, dial energy, fracture appearance, and lateral expansion were recorded for each test, and the results for the various materials are plotted as a function of temperature in Figs. 1 through 4. The transition curves for the unirradiated materials [*2*] are included in the figures so that the various transition temperature shifts can be calculated. Shown in the figures is the shift in the energy curve at the 50 ft·lb level (T_{50}) and the shift in the lateral expansion curve at the 35-mil level (T_{35M}). Vertical arrows indicate the drop weight-nil ductility transition (NDT) temperature for the unirradiated materials and the reference temperature, RT_{NDT}, for the unirradiated and irradiated materials. Also shown in the figures is the upper-shelf energy value for the unirradiated and irradiated materials. Table 3 summarizes the radiation-induced changes in the Charpy energy curve for the four materials in terms of the shift at the 30 ft·lb level (T_{30}), the 50 ft·lb level (T_{50}), and the upper-shelf energy.

Discussion

Adjusted Reference Temperature

The fracture toughness tests required in surveillance programs are specified in Appendix H to 10 CFR 50, Section III. The adjusted reference temperature for the irradiated materials [$RT_{NDT}(i)$] is established by adding to the unirradiated reference temperature [$RT_{NDT}(u)$] the amount of the temperature shift in the Charpy V-notch test curves between the unirradiated material and the irradiated material, measured at the 50 ft·lb level (ΔT_{50}) or the 35-mil lateral expansion level (ΔT_{35M}), whichever temperature shift is greater. The shifts in the 50 ft·lb and 35-mil Charpy V-notch levels for the Maine Yankee surveillance materials are given in Table 4. Note that for every material $\Delta T_{35M} > \Delta T_{50}$.

Thus, the adjusted reference temperature for the irradiated materials is calculated by

$$RT_{NDT}(i) = RT_{NDT}(u) + \Delta T_{35M} \quad (1)$$

The unirradiated reference temperatures were reported in Ref *2* and were established according to Article NB 2300 of the ASME Code, Section III. Article NB 2300 requires that RT_{NDT} be based on test results from transverse specimens. For all of the unirradiated Maine Yankee surveillance materials, the transverse Charpy V-notch results exceeded 50 ft·lb and 35 mils at NDTT + 60°F (NDTT + 33°C). Thus, the reference temperature for the unirradiated materials was controlled by the NDT

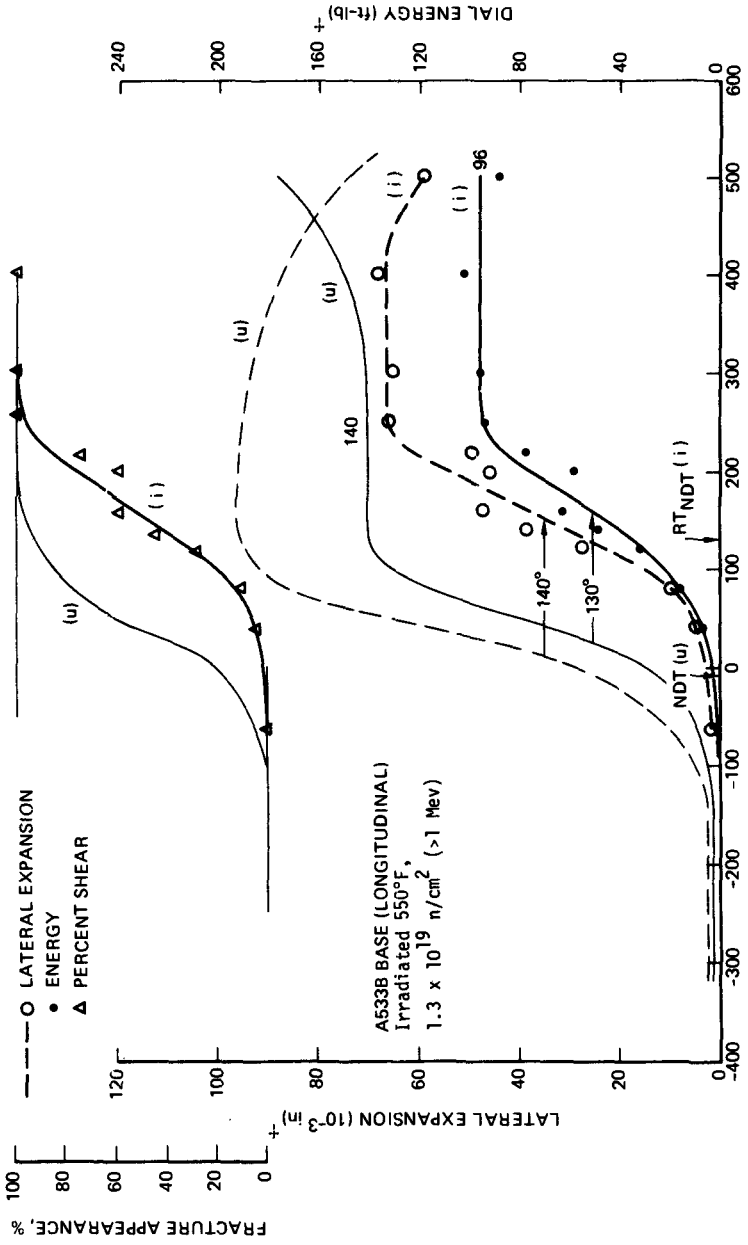

FIG. 1—*Charpy V-notch results for unirradiated* (u) *and irradiated* (i) *Maine Yankee base metal (longitudinal). Conversion to SI units: mils* × *2.54* × *10*$^{-2}$ = *mm; ft·lb* × *1.36* = *joules.*

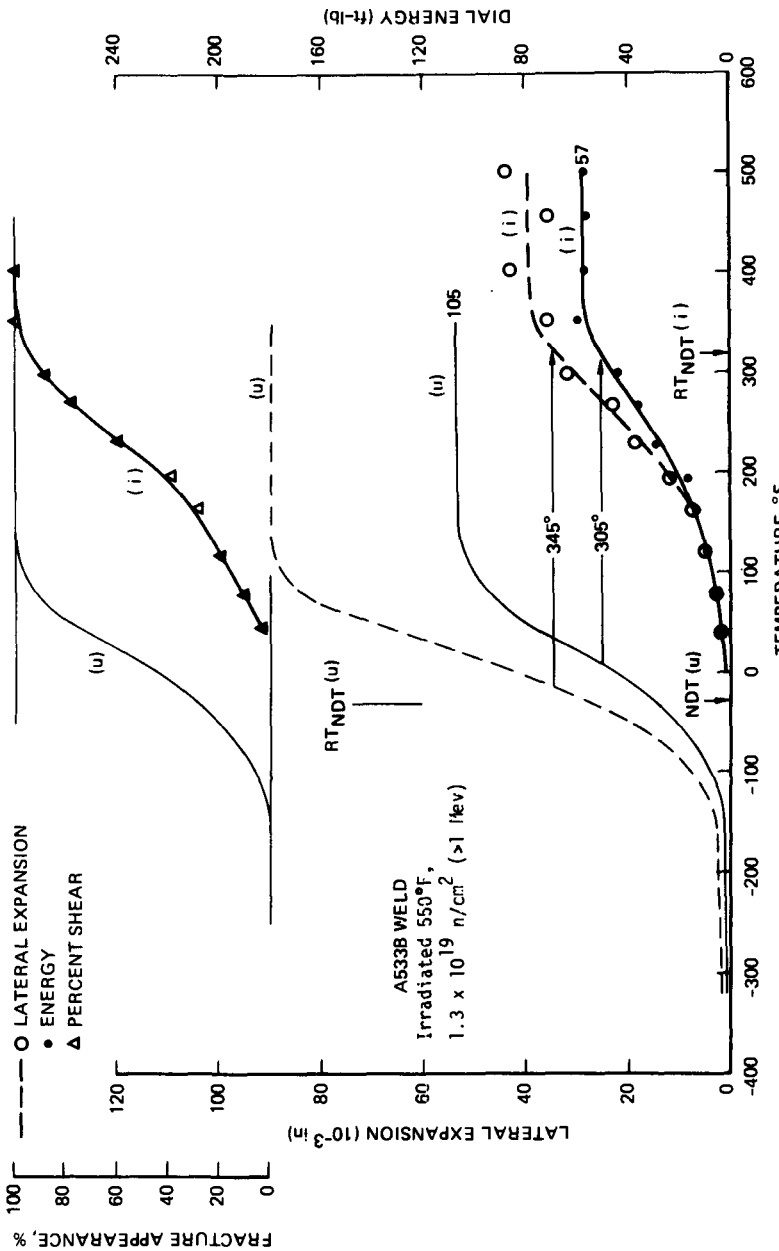

FIG. 2—*Charpy V-notch results for unirradiated* (u) *and irradiated* (i) *Maine Yankee weld metal.*

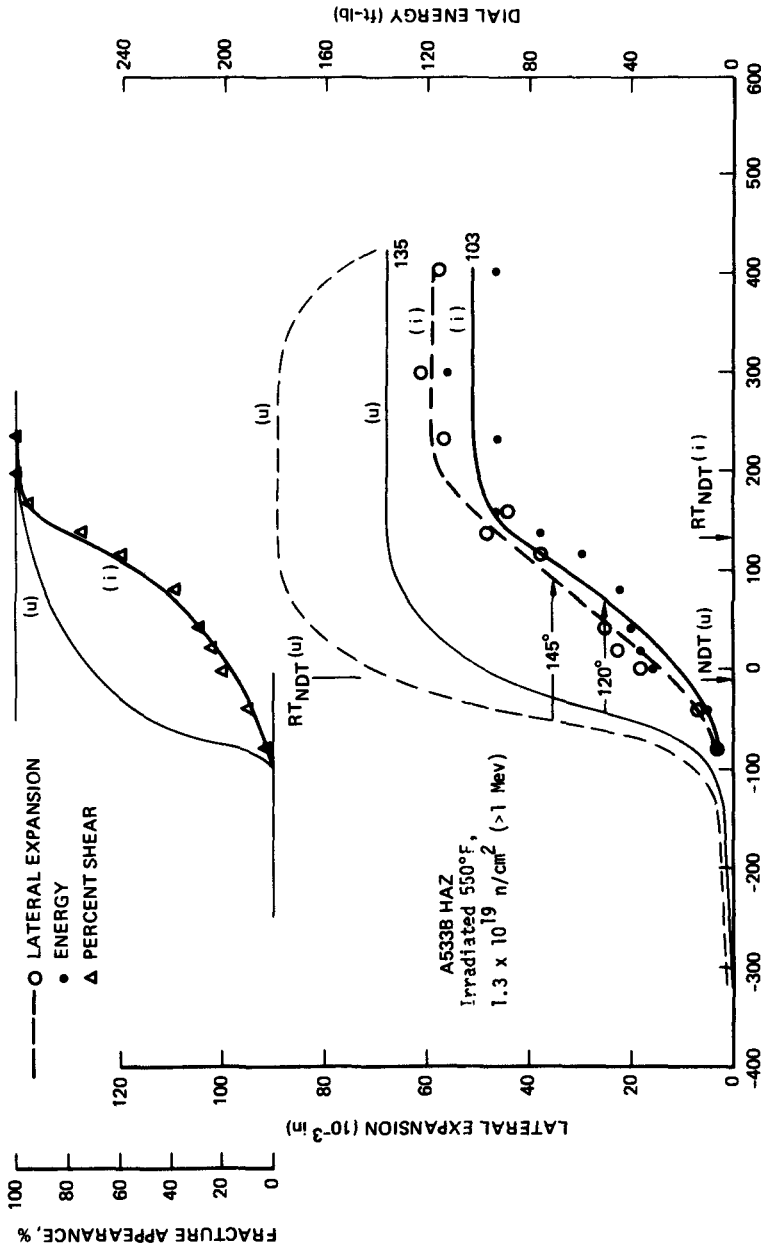

FIG. 3—*Charpy V-notch results for unirradiated* (u) *and irradiated* (i) *Maine Yankee HAZ metal.*

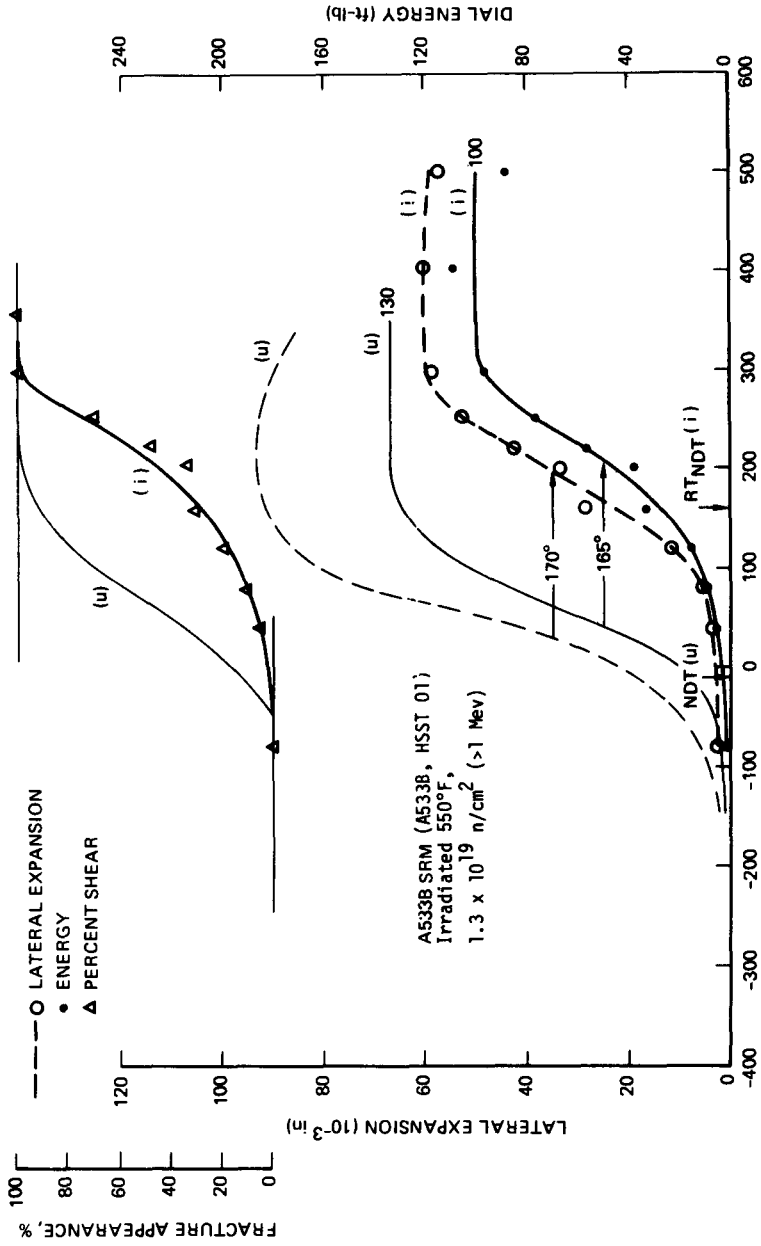

FIG. 4—*Charpy V-notch results for unirradiated* (u) *and irradiated* (i) *standard reference material (longitudinal).*

TABLE 3—*Summary of radiation-induced changes in Charpy V-notch toughness parameters [550°F (288°C), 1.3 × 10^{19} n/cm² (>1 MeV)]*

Material	T_{30}, °F	ΔT_{30}, °F	T_{50}, °F	ΔT_{50}, °F	Upper-Shelf C_v, ft·lb	ΔUpper-Shelf C_v, ft·lb	ΔUpper-Shelf Drop, %
Base (L)	120 (0)[a]	120	155 (25)	130	96 (140)	44	31
Weld	240 (−30)	270	315 (10)	305	57 (105)	48	45
HAZ	25 (−60)	85	75 (−45)	120	103 (135)	32	23
SRM(L)	165 (15)	150	205 (40)	165	100 (130)	30	23

[a] Parentheses enclose unirradiated values.

TABLE 4—*Tabulation of parameters used to establish RT_{NDT} for Maine Yankee materials irradiated at 550°F (288°C) to 1.3 × 10^{19} n/cm² (>1 MeV).*

Material	NDTT, °F	T_{50}, °F	ΔT_{50}, °F	T_{35M}, °F	ΔT_{35M}, °F	Basis for RT_{NDT}	RT_{NDT}, °F	ΔRT_{NDT}
Base (L)[b]	...	155	130	150	140	T_{35M}	130	140
	(−10)	(25)[a]		(10)		NDTT	(−10)	
Weld	...	315	305	330	345	T_{35M}	315	345
	(−30)	(10)		(−15)		NDTT	(−30)	
HAZ	...	75	120	90	145	T_{35M}	135	145
	(−10)	(−45)		(−55)		NDTT	(−10)	
SRM(L)[b]	...	205	165	195	170	T_{35M}	160	170
	(−10)	(40)		(25)		NDTT	(−10)	

[a] Parentheses enclose unirradiated values.

[b] The procedure for determining RT_{NDT} requires transverse specimens. However, since only longitudinal Charpy specimens of the base metal and SRM were irradiated, the irradiated RT_{NDT} was determined by the ΔT_{35M} from the longitudinal specimens.

temperature, and $RT_{NDT}(u)$ = NDTT(u). Only longitudinal Charpy specimens of the SRM were available for the unirradiated tests, so the 50 ft·lb and 35-mil criteria could not be determined. For the SRM, it was assumed that $RT_{NDT}(u)$ = NDTT(u).

The adjusted reference temperatures for the Maine Yankee surveillance materials were calculated using Eq 1, and the new RT_{NDT} values are listed in Table 4. The ΔT_{35M} values for the SRM and base material are based on shifts in longitudinal Charpy data, whereas the code specifies that the shift be based on transverse Charpy data. Although orientation influences the energy absorbed in a Charpy test, there are no published results that indicate that the radiation-induced *shift* in Charpy curves is orientation dependent.

In addition to establishing the radiation-induced shift in the RT_{NDT}, it is important to determine the influence of irradiation on the Charpy upper-shelf energy. Regulations in 10 CFR 50, Appendix G requires that the upper-shelf energy must be greater than 75 ft·lb before irradiation and cannot drop below 50 ft·lb during service (irradiation). Table 3 summarizes the upper-shelf behavior of the Maine Yankee materials due to irradiation. Note that the drop in the upper shelf ranged from 23 to 45 percent, with the weld metal showing the greatest sensitivity to radiation. For a fluence of 1.3×10^{19} n/cm^2 (>1 MeV), none of the materials exhibited a Charpy upper-shelf energy less than 50 ft·lb.

Standard Reference Material

The standard reference material used in the Maine Yankee surveillance program was A533B Class 1 plate from the Heavy Section Steel Technology Program (HSST plate 01). Berggren and Stelzman [*6*] have published a radiation embrittlement trend curve for this material. Figure 5 shows the radiation-induced shift in the 32 ft·lb Charpy level as a function of irradiation temperature. The shift has been normalized to 1×10^{19} n/cm^2 (>1 MeV). From Table 3, ΔT_{30} = 150°F (83°C) for the Maine Yankee SRM irradiated at 550°F (288°C). Figure 5 shows that the data point for the Maine Yankee SRM falls slightly above the trend band, indicating that the SRM experienced a fluence somewhat greater than 1×10^{19} n/cm^2 (>1 MeV).

The Maine Yankee SRM Charpy specimens were taken from the quarter thickness of HSST plate 01 and in the longitudinal direction (1/4T, RW). If only the 1/4T, RW data points in the trend curve at 550°F (288°C) are compared with the SRM data, there is an indication that the fluence obtained by the SRM was substantially greater than 1×10^{19} n/cm^2 (>1 MeV).

To resolve this question, a trend curve for HSST plate 01 irradiated at 550°F (288°C) has been constructed using the 1/4T, RW data just dis-

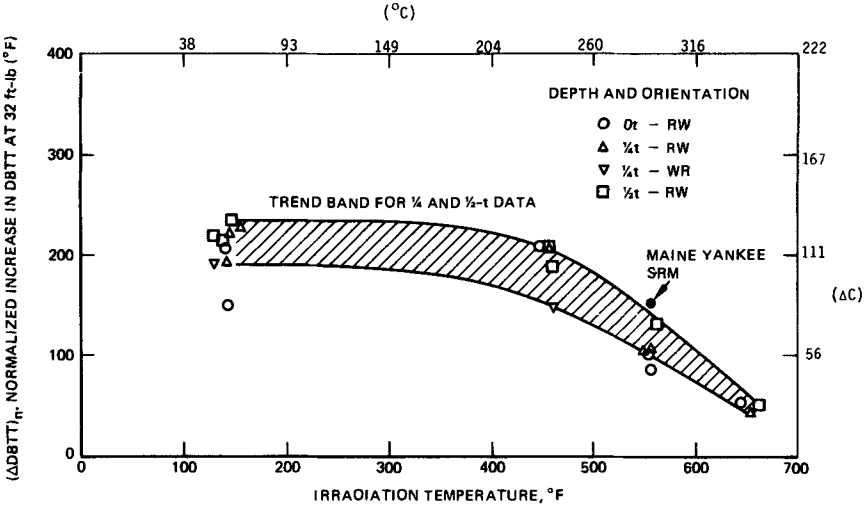

FIG. 5—*Effect of temperature of neutron irradiation on ductile-to-brittle transition temperature at 32 ft·lb of HSST plate 01 (normalized to 1 × 10^{19} n/cm² > 1 MeV)* [6].

cussed and recent data by Stelzman and Berggren [7] and Hawthorne [8]. This trend curve is shown in Fig. 6 and is based on radiation-induced shifts in Charpy curves at both the 30 ft·lb and 50 ft·lb levels. The values of

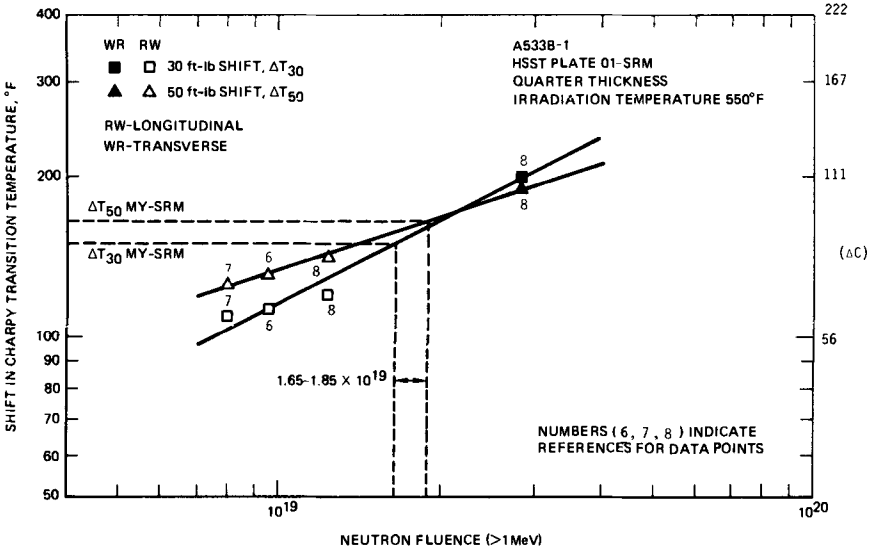

FIG. 6—*Trend curve for HSST plate 01, the standard reference material in the Maine Yankee surveillance capsules.*

ΔT_{30} = 150°F (83°C) and ΔT_{50} = 165°F (92°C) for the Maine Yankee SRM have been entered on the trend curve as horizontal dashed lines. Their intersection with the appropriate trend curve defines a fluence range for the SRM of 1.65 to 1.85 × 10^{19} n/cm² (>1 MeV). Thus, a fluence of 1.7 × 10^{19} n/cm² (>1 MeV) was used for the SRM in evaluating the fluence for the Maine Yankee accelerated surveillance capsule.

Fluence Estimates

The neutron dosimetry and neutron fluence calculations for the first Maine Yankee accelerated surveillance capsule are presented in detail in Ref *3* and will only be summarized here. Fluence calculations using current ASTM practices and the ANISN computer code[5] predicted a fluence of 9 × 10^{18} n/cm² (>1 MeV). Since the SRM indicated a fluence of 1.7 × 10^{19} n/cm² (>1 MeV), the initial dosimetry was ed and additional techniques for calculating fluence were tried. The nominal calculated fluence based on actual core operating history and rodded power distribution was estimated to be 1.33 × 10^{19} n/cm² (>1 MeV). This fluence value seems very acceptable when compared with the fluence of 1.27 × 10^{19} n/cm² (>1 MeV) obtained from the Mn-54 activity and the 1.7 × 10^{19} n/cm² (>1 MeV) fluence estimated from the SRM data. Also, the shifts in the Charpy curves for all of the irradiated Maine Yankee materials were more nearly in agreement with a fluence of 1.3 × 10^{19} n/cm² (>1 MeV) than for a fluence of 9 × 10^{18} n/cm² (>1 MeV). Thus, the best estimate of the fluence for the first Maine Yankee surveillance capsule is 1.3 × 10^{19} n/cm² (>1 MeV).

Trend Curves

Recently Bush [*9*] compiled a comprehensive data base on radiation damage in light-water reactor pressure vessel steels. Figure 7 shows the radiation-induced shift in the Charpy curves at the 30 ft·lb level for Types A533B and A508-2 steels. These steels had varying copper and phosphorus contents and were irradiated over a wide range of temperatures. The ΔT_{30} values from Table 3 for the Maine Yankee surveillance materials have been entered on this figure at a fluence level of 1.3 × 10^{19} n/cm² (>1 MeV). The Maine Yankee base metal (P) contained 0.15 percent copper and 0.013 percent phosphorus, whereas the Maine Yankee submerged arc weld contained 0.36 percent copper and 0.015 percent phosphorus. Points representing the same chemistry and irradiation temperature can be found in the near vicinity of the Maine Yankee base metal point (X-P).

[5] A one-dimensional discrete ordinate transport code with anisotropic scattering.

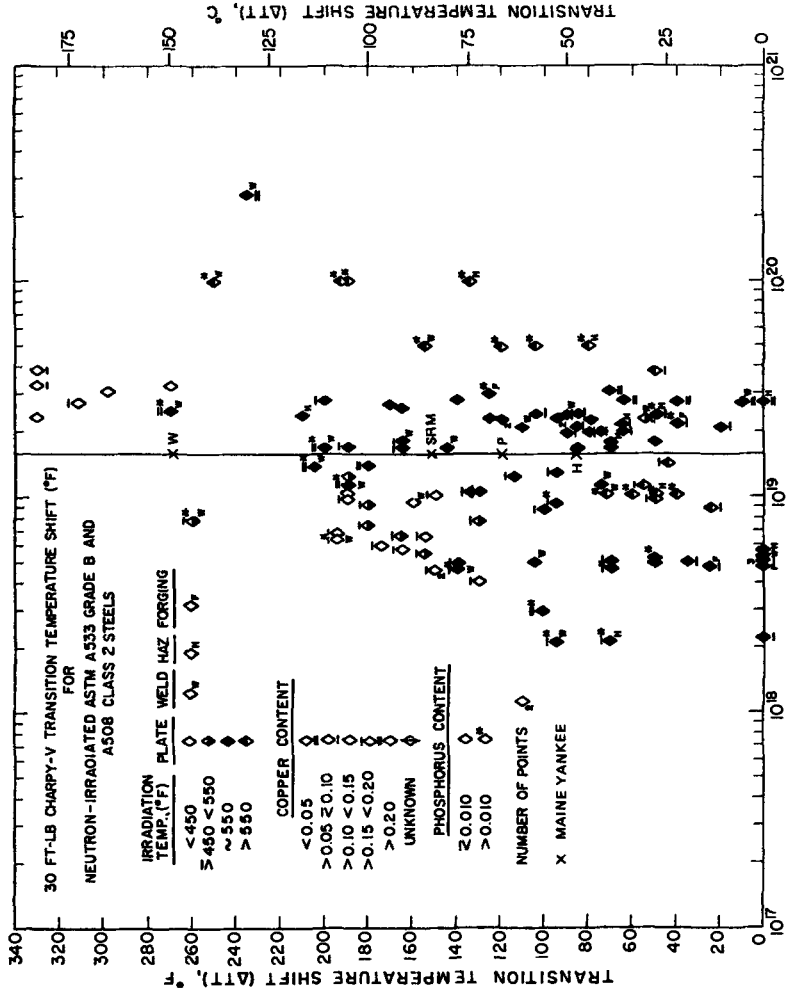

FIG. 7—*Comparison of Maine Yankee surveillance data with irradiation data compiled by Bush* [9].

The high copper and phosphorus content of the Maine Yankee weld metal resulted in a ΔT_{30} substantially higher than the general data base of points in Fig. 7. The only data point near the Maine Yankee value (X-W) that has the same irradiation temperature is just to the right of the Maine Yankee point. This point is for a weld with 0.23 percent copper and 0.011 percent phosphorus irradiated at 550°F (288°C) to a fluence of 2.5×10^{19} n/cm^2 (>1 MeV) [*8*]. This weld not only showed the same shift [ΔT_{30} = 270°F (150°C)] as the Maine Yankee weld, but also the same percent drop in the Charpy upper-shelf energy (44 percent, 125 to 70 ft·lb).

Critical Beltline Material

Current federal regulations (10 CFR 50 Appendix H, Section III) specify that the highest adjusted reference temperature and the lowest upper-shelf energy level of all the irradiated beltline materials shall be used to establish the new operating limit curves. Based on the Maine Yankee surveillance results, the weld metal is the limiting or critical beltline material.

By a rather fortunate coincidence, this same weld metal was studied as part of a radiation sensitivity study by the Naval Research Laboratory (NRL) and Combustion Engineering (CE) [*10*]. The NRL-CE Charpy curves for the unirradiated and irradiated Maine Yankee weld are shown in Fig. 8. Also included in the figure is the Charpy curve for the same

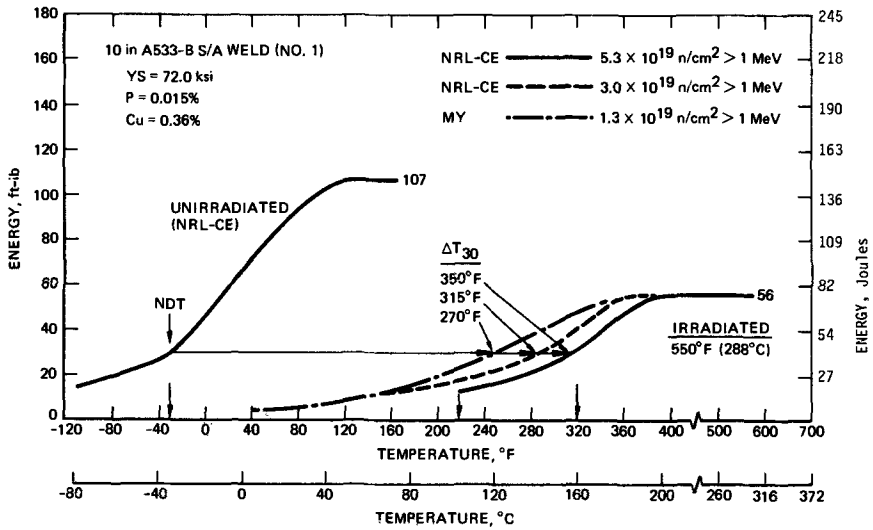

FIG. 8—*Charpy V-notch curves for Maine Yankee weld metal from surveillance program and NRL-CE study* [10].

weld obtained from the present surveillance program. Note that the unirradiated curves obtained by both laboratories are very similar [NDTT = −30°F (−34°C); Charpy upper shelf equals 105 ft·lb versus 107 ft·lb; see Fig. 2]. Also note that the upper-shelf values after irradiation are essentially identical. It is certainly encouraging that different laboratories can have such close agreement on Charpy curves from completely independent studies.

The shift in the Charpy curves at the 30 ft·lb level (ΔT_{30}) has been indicated in Fig. 8 for the three fluences involved. These ΔT_{30} values are plotted as a function of fluence in Fig. 9, which has been reproduced

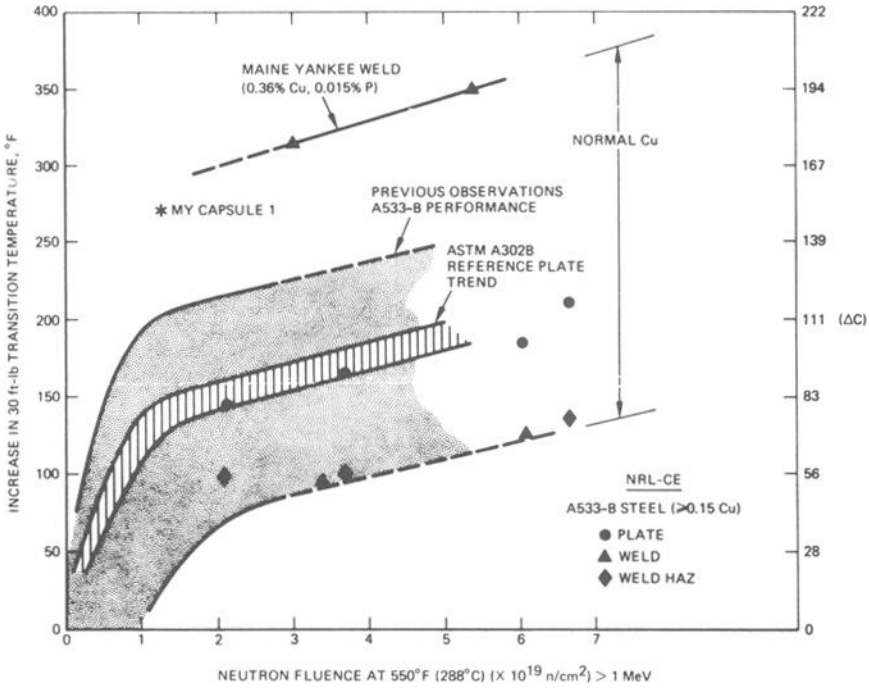

FIG. 9—*Radiation embrittlement trend curve reported by the NRL-CE with Maine Yankee surveillance data on weld added.*

from the NRL-CE study [*10*]. The data point for the weld irradiated in the first Maine Yankee surveillance capsule is indicated on the figure. The surveillance capsule fluence of 1.3×10^{19} n/cm² (>1 MeV) seems appropriate when compared with the NRL-CE data. It is obvious that the high copper content of the Maine Yankee weld causes the radiation-induced embrittlement to exceed the normal trend for Type A533B material.

Conclusions

The following conclusions were reached concerning the irradiation response of the Maine Yankee reactor beltline materials:

1. The base and heat-affected zone materials exhibited a radiation-induced embrittlement similar to the standard reference material and consistent with current embrittlement-fluence trend curves.

2. The enhanced radiation sensitivity of the weld metal is consistent with current theories concerning the detrimental effects of high copper content.

3. Radiation-induced shifts at the 35-mil level exceeded those measured at the 30 and 50 ft·lb levels for all materials. Thus, the 35-mil shift was used to determine the adjusted reference temperature.

4. The critical beltline material for determining the new operating limit curves for the Maine Yankee reactor was the weld metal, with an adjusted reference temperature of 315°F (157°C) and a Charpy upper-shelf value of 57 ft·lb.

References

[1] "Summary Report on Manufacture of Test Specimens and Assembly of Capsules for Irradiation Surveillance of Maine Yankee Reactor Vessel Materials," CENPD-37, Combustion Engineering, Windsor, Conn, 30 Dec. 1971.

[2] Sheckherd, J. W. and Wullaert, R. A., "Unirradiated Mechanical Properties of Maine Yankee Nuclear Pressure Vessel Materials," ETI CR 75-269, Effects Technology, Inc., Santa Barbara, Calif., 1 Feb. 1975.

[3] Wullaert, R. A. and Sheckherd, "Evaluation of the First Maine Yankee Accelerated Surveillance Capsule," ETI CR 75-317, Effects Technology, Inc., Santa Barbara, Calif., Aug. 1975.

[4] "Surveillance Tests for Nuclear Reactor Vessels," ASTM E 185-73, *Annual Book of ASTM Standards,* American Society for Testing and Materials, 1974.

[5] Sheckherd, J. W. and Prince, L. K., "Quality Assurance Program for Materials Testing of Unirradiated Baseline Specimens and Irradiated Surveillance Capsule Specimens," Effects Technology, Inc. Report to Maine Yankee Atomic Power Company, Sept. 1974.

[6] Berggren, R. G. and Stelzman, W. J., "Radiation Strengthening and Embrittlement in Heavy Section Plate and Welds," *Nuclear Engineering Design,* Vol. 17, 1971, pp. 103–115.

[7] Stelzman, W. J. and Berggren, R. G., "Radiation Strengthening and Embrittlement in Heavy Section Steel Plates and Welds," ORNL-4871, Oak Ridge National Laboratory, Oak Ridge, Tenn., June 1973.

[8] Hawthorne, J. R., "Postirradiation Dynamic Tear and Charpy-V Performance of 12-in. Thick A533B-1 Steel Plates and Weld Metal," *Nuclear Engineering Design,* Vol. 17, 1971, pp. 116–130.

[9] Bush, S. H., "Radiation Damage in Pressure Vessel Steels for Commercial Light Water Reactors," March 1974.

[10] Hawthorne, J. R., Koziol, J. J., and Groeschel, R. C., "Evaluation of Commercial Production A533B Plates and Weld Deposits Tailored for Improved Radiation Embrittlement Resistance," presented at ASTM Symposium on Effects of Radiation on Structural Materials, June 1974.

E. C. Biemiller,[1] *and S. T. Byrne*[1]

Evaluation of the Effect of Chemical Composition on the Irradiation Sensitivity of Reactor Vessel Weld Metal

REFERENCE: Biemiller, E. C. and Byrne, S. T., **"Evaluation of the Effect of Chemical Composition on the Irradiation Sensitivity of Reactor Vessel Weld Metal,"** *Irradiation Effects on the Microstructure and Properties of Metals, ASTM STP 611,* American Society for Testing and Materials, 1976, pp. 418–433.

ABSTRACT: The effects of weld metal alloying constituents on the irradiation response of reactor vessel weld metal have been evaluated to determine why vessel welds tend to be more sensitive to irradiation damage than parent plate material. Weld data, collected from published reports, were compared on the basis of neutron radiation exposure; subsequent nil-ductility transition temperature (NDTT) shift (measured at the Charpy 30 ft·lb energy fix); chemical composition; postweld heat treatment, and microstructure. The data comparison produced a correlation between NDTT shift with irradiation and a ratio of a weld's major alloying elements. The alloy ratio is designated A/B where the element content of the weld, by weight percent, is expressed: A/B = (Ni + Si)/(Mn + Cr + Mo). As the ratio increases for a weld, higher NDTT shifts with irradiation can be expected. Effects of postweld heat treatment and microstructure are also related to the NDTT shift-A/B correlation. The known effects of copper content on NDTT shift with irradiation have been found to be separate from the effects of the A/B ratio. Both copper and A/B effects, however, contribute to the total NDTT shift experienced by the weld with irradiation.

KEY WORDS: radiation, irradiation damage, neutron irradiation, pressure vessel weldments, vacancies, carbon, copper, nickel, ductility, transition temperature

Plate and weld materials used in the fabrication of nuclear reactor pressure vessels should be selected to optimize resistance to neutron irradiation-induced changes in mechanical properties. Early research programs [*1–4*][2] demonstrated that reduction of copper, present as a

[1]Development engineer and senior development engineer, respectively, Metallurgical Services, Nuclear Power Systems, C-E Power Systems, Combustion Engineering, Inc. Windsor, Conn. 06095.

[2]The italic numbers in brackets refer to the list of references appended to this paper.

residual element in the steel, improved resistance to irradiation-induced effects. Data from a joint Combustion Engineering (C-E)/Nuclear Regulatory Commission (NRC)/Naval Research Laboratory (NRL) program [5] supported previous research concerning the effect of copper; however, out of many specimens that were irradiated, only one heat of weld metal (Weld 1) exhibited an anomalous nil-ductility transition temperature (NDTT) shift, based on a Charpy 30 ft·lb energy fix. A subsequent review of published data [6] indicated results in which some heats of weld metal were more sensitive to neutron-irradiation effects than parent plate material. One such weld, whose chemistry and fabrication history were similar to welds from the C-E program, was Weld 50, evaluated in the Heavy Section Steel Technology Program (HSST) [7]. A comparison between Weld 1, another weld from the C-E/NRC/NRL program (Weld 2), and HSST Weld 50 demonstrated an effect of nickel on irradiation behavior. Weld 2 experienced a much lower NDTT shift than Weld 1 or HSST Weld 50, yet had a copper content similar to that of Weld 50. The nickel contents were

Weld 1	0.78 weight percent nickel
HSST Weld 50	0.68 weight percent nickel
Weld 2	0.04 weight percent nickel

As a result of this preliminary observation, a search for weld metal irradiation data was undertaken to determine if other trends based on nickel content and NDTT shift with irradiation could be ascertained.

The evaluation that followed established a correlation between alloy content and irradiation sensitivity for weld metal whose metallurgical structure was predominately ferrite. The correlation is based on the supposition that carbon atoms have the ability to pin irradiation-induced vacancies. The effects of copper on the irradiation sensitivity of weld metal were found to be separate from the effects of a weld's alloy content, but additive in terms of predicting NDTT shifts for irradiation weldments. This paper presents these findings.

Analysis

Work by Beeler and Beeler [8] concerning the stability of vacancies in neutron-irradiated metals showed that carbon atoms form bound complexes with vacancies in cubic transition metals. The configuration energy of such complexes is low and this makes it energetically favorable for carbon atoms, either free or those emitted from precipitates by thermal or neutron collision events, to attach themselves to vacancies. The presence of these vacancy complexes causes irradiation hardening and thus high NDTT shifts.

Indirect evidence for the carbon-vacancy complex hardening mechanism comes from several sources. Weld 1 from the C-E/NRC/NRL program experienced a large NDTT shift of 315°F (175°C) compared with a predicted shift of 250°F (138°C) based on copper content. Prior to irradiation, this weld contained numerous carbide precipitates which could act as sources of carbon for formation of carbon-vacancy complexes. Furthermore, Weld 1 contained high nickel, and Smith [*9*] had shown that nickel increases the thermodynamic activity of carbon in iron. With the activity of carbon so increased, the probability of vacancy complex and precipitate formation also increases.

Because the nickel content of Weld 1 and HSST Weld 50 were high, and because these factors seemed to be the cause of the unusually high NDTT shifts experienced by the welds, other elements affecting carbon activity (or the apparent effect of nickel) were evaluated. Smith [*10*] also had demonstrated that silicon raised carbon activity in iron, whereas manganese lowered it. Molybdenum has been found to counteract the effect of nickel in temper-embrittlement of steels [*11*] and has also been found to suppress irradiation hardening [*12*]. Finally, chromium was considered because it had been suggested that chromium might reduce the effects of nickel on radiation sensitivity [*13*]. Also, it is known that molybdenum and chromium are strong carbide formers and thus would tend to remove carbon from solid solution. The various elements mentioned were combined into two groups as follows:

A—Adverse effect	B—Beneficial (opposing A)
nickel, silicon	manganese, molybdenum, chromium

Ratios were formed for the weld chemistry data by summing the weight percent values of elements in the A-group and dividing by the summation of elements (weight percent) in the B-group. The weld data were also separated into two groups according to copper content to take into consideration the known effects of copper on irradiation damage.

Correlation of the formed A/B ratios with reported NDTT shift and irradiation fluence was accomplished by normalizing the NDTT shift values to a fluence of 3.0×10^{19} neutrons (n)/cm^2, >1 MeV. This was accomplished by plotting the weld NDTT shift data versus neutron fluence (log-log axes) and drawing straight lines through the data representing NDTT shift versus fluence trends. The slopes of the trend lines were taken and averaged, the average slope being 0.43. The normalization point of 3.0×10^{19} n/cm^2, >1 MeV was chosen because most of the data were grouped near this fluence, and, therefore, normalizing to this point reduces potential error.

The relation used for normalization is

$$\Delta\text{NDTT}_n = \Delta\text{NDTT}_i \left(\frac{\Phi_{t_n}}{\Phi_{t_i}}\right)^{0.43}$$

where

ΔNDTT = NDTT shift,
Φ_t = neutron fluence,
subscript i = initial values, and
subscript n = normalized values.

The weld chemistry data are reported in Tables 1 and 2 (high and low copper content groups, respectively). The weld heat treatments employed are listed in Table 3. The weld irradiation data, A/B ratios, and normalized NDTT shift values are reported in Table 4. These data represent all known 550°F (288°C) irradiation data for welds available at this time. The references given in the tables refer to the present paper.

Results

Figure 1 depicts the (normalized) ΔNDTT versus A/B ratio plot for weld data belonging to the high-copper group (>0.15 weight percent). The line drawn through the data of Fig. 1 represents the general rise in ΔNDTT_n experienced as the A/B ratio increases. Data Points PS3 and 64 lie below the trend line; this is attributed to rapid cooling from stress relief annealing or short time of anneal, or both (Table 3). Short annealing times hinder carbon diffusion in the weld metal. The importance of carbon diffusion is addressed in a later section, but is related with the need for carbon atoms to be in certain lattice positions in order to form vacancy complexes. Data Point CF48 demonstrates the effect of long heat treatments on NDTT shift. In addition to containing high nickel and copper, the material represented by CF48 was heat-treated for a total of 80 h. The A/B trend curve was drawn below CF48 because Point 3N5 (30-h heat treatment) was thought to be more representative of the general heat treatments given to weldments.

In Fig. 1 (Copper >0.15), the nickel-silicon effects cannot be ignored. Weld 2 had the lowest A/B ratio and the lowest ΔNDTT_n. Its copper level was 0.20 weight percent compared with Points 49 and N44, which contained less copper (0.19 and 0.16 weight percent, respectively) but experienced higher shifts commensurate with their A/B ratios. Data Point E, Weld 50, Weld 1, and W51 contained variable copper levels, yet when plotted as a function of A/B ratio the four points fall close together at a normalized shift around 300°F (166°C). The copper level for Points E and Weld 50 was 0.23 weight percent; for Weld 1, 0.36 weight percent; and W51 was reported as being between 0.15 to 0.33 weight percent copper. Data Point

TABLE 1—*High-copper weld data points.*

Data Point	Material Welded	Weld Method[a]	Reference	Chemical Composition, weight %										
				C	Mn	P	S	Si	Ni	Cr	Mo	Cu	V	Other
Weld-1	A533-B	S/A	[4]	0.14	1.38	0.015	0.012	0.22	0.78	0.07	0.55	0.36	0.003	0.004 Al, 0.012 N
CF24	A543	S/A	[3]	0.07	1.07	0.011	0.006	0.37	1.58	0.25	0.37	0.24	...	
CF48	A543	S/A	[3]	0.09	1.15	0.011	0.006	0.22	2.46	0.39	0.52	0.42	...	
3N5	3½ Ni-Cr-Mo	M	[18]	0.10	1.08	0.005	0.015	0.28	2.60	Nil	0.35	0.51	...	
Weld-50	A533-B	S/A	[7]	0.13	1.13	0.011	0.008	0.19	0.68	0.05	0.45	0.23	0.03	
64	A533-B	S/A	[19]	0.09	1.25	0.019	0.13	0.23	1.08	0.05	0.52	0.22	...	0.037 Al
E	A508-2	...	[20]	0.075	1.31	0.012	0.016	0.59	0.56	0.59	0.36	0.23	0.001	0.02 Al, 0.015 N
48	A533-B	S/A	[21]	0.17	1.25	0.015	0.011	0.32	0.11	0.16	0.53	0.22	0.03	
Weld-2	A533-B	S/A	[4]	0.13	1.11	0.016	0.013	0.17	0.04	0.05	0.53	0.20	0.01	<0.001 Al, 0.008 N
49	A533-B	E/S	[21]	0.22	1.28	0.008	0.014	0.10	0.40	0.14	0.48	0.19	0.03	
N43	HY-80	S/A	[14]	0.07	1.21	0.007	0.006	0.49	0.80	2.07	0.93	0.26	0.04	
N45	HY-80	S/A	[14]	0.08	0.79	0.007	0.004	0.43	1.20	2.01	0.93	0.27	0.05	
N44	HY-80	S/A	[14]	0.09	1.00	0.014	0.006	0.46	1.08	1.99	0.93	0.16	0.04	
N42	HY-80	S/A	[14]	0.07	0.82	0.007	0.005	0.45	0.82	2.04	0.93	0.21	0.05	
3C2	A533-C-2	S/A	[21]	0.13	1.68	0.016	0.015	0.33	0.14	0.05	0.48	0.27	0.02	
W51	A533-B	S/A	[22]	0.12–0.16	1.23–1.38	0.013–0.017	0.008–0.015	0.05–0.15	0.72–0.76	...	0.39–0.53	0.15–0.33	...	
PBV	A302-B	S/A	[23]	0.09	1.47	0.019	0.024	0.49	0.57	0.13	0.39	0.18	...	
PS3	Ni-Cr-Mo	S/A	[24]	0.06	1.85	0.012	0.003	0.21	1.30	0.08	0.56	0.29	0.02	0.015 Al, 0.011 N

[a]S/A = submerged arc; M = manual; E/S = electroslag.

TABLE 2—*Low-copper weld data points.*

Data Point	Material Welded	Weld Method[a]	Reference	Chemical Composition, weight %										
				C	Mn	P	S	Si	Ni	Cr	Mo	Cu	V	Other
52	A533-B	S/A	[25]	0.19	1.24	0.010	0.014	0.19	0.93	0.08	0.45	0.14	0.02	
53	A533-B	S/A	[25]	0.19	1.24	0.010	0.014	0.19	0.93	0.08	0.45	0.14	0.02	
54	A533-B	E/S	[26]	0.20	1.42	0.002	0.012	0.13	0.43	0.07	0.49	0.09	...	0.03 Al
C1938	A543	M	[3]	0.03	0.72	0.009	0.010	0.34	1.62	2.39	0.92	0.07	0.03	
C1948	A543	M	[3]	0.05	0.82	0.007	0.006	0.20	1.56	2.32	0.92	0.05	0.03	
C1934	A543	M	[3]	0.04	0.87	0.008	0.010	0.40	0.77	2.08	1.01	0.06	0.02	
C1936	A543	M	[3]	0.06	0.86	0.007	0.010	0.30	0.78	2.08	1.01	0.02	0.02	
PS2	Mn-Ni-Mo-V	S/A	[24]	0.07	1.20	0.016	0.006	0.25	1.53	0.09	0.41	0.05	0.03	0.025 Al, 0.008 N
Weld-3	A533-B	S/A	[4]	0.145	1.145	0.0095	0.0095	0.25	0.115	0.04	0.59	0.07	0.008	0.006 Al, 0.005 N
Weld-4	A533-B	S/A	[4]	0.15	1.25	0.004	0.010	0.19	0.09	0.06	0.62	0.05	0.007	0.001 Al, 0.004 N
B	A543	S/A	[16]	0.09	1.16	0.006	0.007	0.56	2.40	0.09	0.49	0.03	0.01	<0.01 Al
D	A543	S/A	[16]	0.10	0.84	0.006	0.008	0.35	0.83	2.40	1.10	0.01	0.02	
N23	Ni-Cr-Mo	S/A	[14]	0.06	0.90	0.006	0.005	0.49	0.55	1.95	0.87	0.03	...	
N40	HY-80	S/A	[14]	0.07	1.23	0.007	0.006	0.51	0.71	2.07	0.96	0.04	0.05	
N41	HY-80	S/A	[14]	0.07	0.84	0.007	0.004	0.46	1.10	2.06	1.01	0.01	0.05	
N39	HY-80	S/A	[14]	0.07	1.16	0.007	0.007	0.46	1.21	2.07	0.95	0.04	0.05	
PS1	A533-B	S/A	[24]	0.09	1.36	0.020	0.004	0.34	1.08	0.20	0.51	0.10	0.03	0.022 Al, 0.0105 N
PS4	Ni-Cr-Mo	S/A	[24]	0.06	2.29	0.014	0.007	0.27	0.09	0.95	0.45	0.09	0.01	0.002 Al, 0.008 N

[a] S/A = submerged arc; M = manual; E/S = electroslag.

TABLE 3—*Heat treatment.*

Data Point	Material Welded	Weld Method[a]	Reference	Postweld Heat Treatment Unless Specified Differently
52	A533-B	S/A	[25]	1150° ±25°F for 40 h; furnace cooled to below 600°F
53	A533-B	S/A	[25]	
Weld-1	A533-B	S/A	[4]	interstage stress relief—1100° to 1150°F for 15 min; final—1150°F for 40 h, furnace cooled to 600°F
Weld-2	A533-B	S/A	[4]	
Weld-3	A533-B	S/A	[4]	
Weld-4	A533-B	S/A	[4]	
C1934	A543	M	[3]	1125° to 1150°F for 30 h; furnace cooled to 600°F
C1936	A543	M	[3]	
C1938	A543	M	[3]	
C1948	A543	M	[3]	
CF24	A543	S/A	[3]	1050° to 1075°F for 65 h; furnace cooled to 600°F; 1075° for 15 h; furnace cooled to 700°F
CF48	A543	S/A	[3]	
N23	Ni-Cr-Mo	S/A	[14]	1150°F for 8 h; furnace cooled
N40	HY-80	S/A	[14]	
N41	HY-80	S/A	[14]	
N39	HY-80	S/A	[14]	
N43	HY-80	S/A	[14]	
N45	HY-80	S/A	[14]	
N42	HY-80	S/A	[14]	
3N5	3.5 Ni-Cr-Mo	M	[18]	1100° ±25°F for 30 h; furnace cooled to 600°F at 100°F/h max
Weld-50	A533-B	S/A	[7]	1150° ±25°F for 12 h; furnace cooled
64	A533-B	S/A	[19]	1148°F for 27 h; air cooled
49	A533-B	E/S	[21]	austenitized at 1675° to 1725°F for 6 h, brine quenched; reaustenitized at 1660° to 1650°F for 6 h, brine quenched; tempered at 1200° to 1225°F for 6 h, brine quenched; stress-relief annealed at 1115° to 1135°F for 30 h, furnace cooled at 40°F/h (max)
54	A533-B	E/S	[26]	same as Data Point 49 except quenching medium was water
48	A533-B	S/A	[21]	1125°F for 20 h; furnace cooled
3C2	A533-C	S/A	[21]	
E	A508-2	...	[20]	1100°F for 11¼ h; furnace cooled
B	A543	S/A	[16]	1135°F for 6.5 h; fan cooled 1135° to 600°F in 70 min
D	A543	S/A	[16]	1135°F for 6 h, still air cooled
PS2	Mn-Ni-Mo-V	S/A	[24]	1022°F for 5 h, furnace cooled; + 1022°F for 50 h, furnace cooled; + 1148°F for 15 h, furnace cooled
N44	HY-80	S/A	[14]	1150°F for 8 h as specimen blanks in a laboratory tube furnace. Rapidly cooled in an argon steam (1150° to 75°F in 30 min)

TABLE 3—*Continued.*

Data Point	Material Welded	Weld Method[a]	Reference	Postweld Heat Treatment Unless Specified Differently
W51	A533-B	S/A	[22]	1150° ±25°F for 37 h, furnace cooled to 600°F
PBV	A302	S/A	[23]	unknown
PS1	A533-B	S/A	[24]	1148°F for 15 min/air cooled + 1148°F for 12 h/furnace cooled to 600°F
PS3	Ni-Cr-Mo	S/A	[24]	1112°F for 3 h, furnace cooled
PS4	Ni-Cr-Mo	S/A	[24]	1022°F for 50 h, furnace cooled; + 1112°F for 15 h, furnace cooled

[a]S/A = submerged arc; M = manual; E/S = electroslag.

CF24 contained less copper (0.24 weight percent) than Weld 1, yet experienced a higher shift due to its higher A/B value. Thus, the use of the A/B ratio satisfactorily explains the irradiation behavior of welds which cannot be explained by copper content alone.

Figure 2 presents the weld data for the low-copper group containing 0.15 weight percent copper or less. As in Fig. 1, there are certain data points which do not lie on the trend curve of Fig. 2. The majority of these points represent weld metal whose structure is other than ferrite. The weld metal of Data Point N23, used initially in a study by Hawthorne, Fortner, and Grant, [*14*], was reported by Smidt and Sprague [*15*] to have a metallurgical structure of tempered martensite interspersed with a small amount of tempered bainite. Based on this information, it is assumed that other welds from the initial Hawthorne, Fortner, and Grant study (Data Points N40, N39, N41) also had structures other than ferrite. The largest anomaly of Fig. 2 is Data Point B. The weld metal of Point B contained 2.40 weight percent nickel, [*16*]. When nickel is present in steel in large amounts, it lowers the austenite to ferrite transformation temperature (nickel is an austenite stabilizer). As a result, the structure of the weld metal of Point B upon cooling probably contained martensite or bainite, or both, along with ferrite. The specific microstructure of Data Point B was not reported in Ref. *16*. Another difference with Point B is the method of cooling from the stress relief anneal and annealing time. This weld had a short annealing time of 6.5 h and was fan cooled from its stress-relief annealing temperature, 1135°F (613°C), to 600°F (316°C) in 70 min. Again, this hinders carbon diffusion during stress-relief anneal.

The effect of the stress-relief annealing treatment is demonstrated by referring back to Data Points CF24, CF48, and 3N5 (Fig. 1). These points also contained large amounts of nickel and could therefore have contained mixed structures. Their stress relief annealing times, however, were much

TABLE 4—*Irradiation data and A/B ratios.*

Data Point	Material Welded	Weld Method[a]	Reference	Copper Content, weight %	A/B, weight %	A/B, atomic weight %	Fluence, (10^{19} n/cm^2, >1 MeV), at 550°F	ΔNDTT at 30 ft·lb		ΔNDTT Normalized	
								°F	°C	°F	°C
Weld-1	A533-B	S/A	[4]	0.36	0.50	0.650	3.4	315	175	298	165.5
CF24	A543	S/A	[3]	0.24	1.15	1.408	3.5	415	230.5	388	215.5
CF48	A543	S/A	[3]	0.42	1.3009	1.455	3.5	530	294.4	496	275.5
3N5	3.5 Ni-Cr-Mo	M	[18]	0.51	2.01	2.310	2.9	390	216.6	396	220
Weld-50	A533-B	S/A	[9]	0.23	0.534	0.696	2.5	270	150	292	162.2
64	A533-B	S/A	[19]	0.22	0.720	0.9198	3.5	265	147.2	248	137.7
E[b]	A508-2	...	[20]	0.23	0.510	0.7820	0.49	140	77.7	305	169.4
48	A533-B	S/A	[21]	0.22	0.221	0.4196	1.7	200[c]	111.1	255	141.6
Weld-2	A533-B	S/A	[4]	0.20	0.124	0.2433	3.4	95	52.7	90	50
49	A533-B	E/S	[21]	0.19	0.290	0.3353	1.6	165	91.6	216	120
N43	HY-80	S/A	[14]	0.26	0.3064	0.4369	2.8	230	127.7	237	131.6
N45	HY-80	S/A	[14]	0.27	0.4369	0.5690	2.8	265	147.2	273	151.6
N42	HY-80	S/A	[14]	0.21	0.3350	0.5259	2.8	195	108.3	201	111.6
N44	HY-80	S/A	[14]	0.16	0.3928	0.4690	2.8	250	138.9	257	142.7
3C2	A533-C2	S/A	[21]	0.27	0.2126	0.3881	1.4	205	113.8	284	157.7
W51	A533-B	S/A	[27]	0.15–0.33	0.477	0.5733	1.16[d]	190	105.5	286	158.8
PBV	A302-B	S/A	[23]	0.18	0.532	0.8252	0.358	110	61.1	274	152.2
PS3	Ni-Cr-Mo	S/A	[24]	0.29	0.606	0.7206	5.0[e]	297	165	238	132.2
52	A533-B	S/A	[25]	0.14	0.633	0.786	0.5	105	58.3	227	126.1
53	A533-B	S/A	[25]	0.14	0.633	0.786	2.4	210	116.6	231	128.3
54	A533-B	E/S	[26]	0.09	0.283	0.3764	2.5	100	55.5	108	60.0
C1938	A543	M	[3]	0.07	0.486	0.5760	3.5	200	111.1	187	103.8
C1948	A543	M	[3]	0.05	0.434	0.4884	3.5	110	61.1	103	57.2
C1934	A543	M	[3]	0.06	0.295	0.4109	3.5	95	52.7	89	49.4
C1936	A543	M	[3]	0.02	0.2734	0.3632	3.5	45	25.0	42	23.3
PS2	Mn-Ni-Mo-V	S/A	[24]	0.05	1.07	1.258	5.0[e]	468	260	376	208.8
Weld-3	A533-B	S/A	[4]	0.07	0.206	0.3987	4.9	35	19.4	28	15.5

Weld-4	A533-B	S/A	[4]	0.05	0.145	0.2738	4.9	20	11.1	16	8.8
B	A543	S/A	[16]	0.03	0.70	2.188	3.6	110	61.1	102	56.6
D	A543	S/A	[16]	0.01	0.273	0.3655	3.6	45	25	42	23.3
N23	Ni-Cr-Mo	S/A	[14]	0.03	0.2795	0.4270	2.8	15	8.3	15.4	8.5
N40	HY-80	S/A	[14]	0.04	0.2863	0.4190	2.8	20	11.1	20.6	11.4
N41	HY-80	S/A	[14]	0.01	0.3989	0.5385	2.8	0	0	0	0
N39	HY-80	S/A	[14]	0.04	0.3995	0.5242	2.8	10	5.5	10.3	5.7
PS1	A533-B	S/A	[24]	0.05	0.6859	0.8990	5.0[e]	153	85	123	68.3
PS4	Ni-Cr-Mo	S/A	[24]	0.09	0.097	0.1727	5.0[e]	54	30	43	23.8

[a] S/A = submerged arc; M = manual; E/S = electroslag.
[b] Irradiation tempature unknown—irradiated in R. E. Ginna Unit 1 Reactor.
[c] C_v 40 ft·lb index.
[d] Irradiated at 563°F.
[e] Irradiated at 572°F.

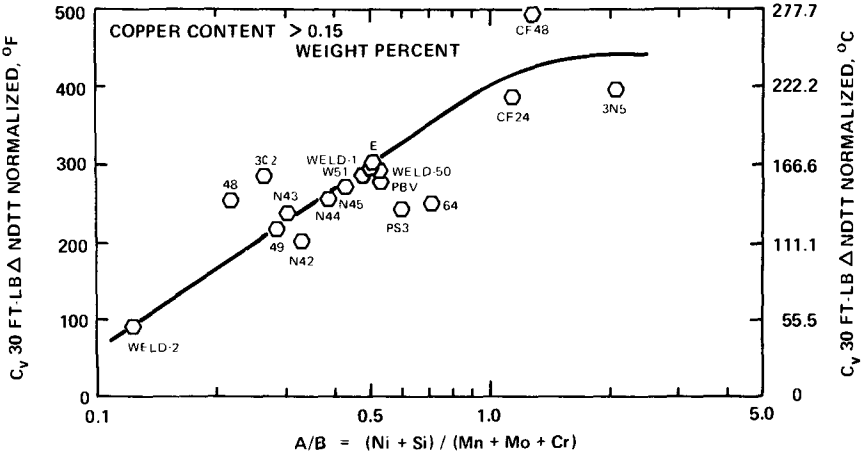

FIG. 1—*NDTT shift normalized to a fluence = 3.0 × 10¹⁹ n/cm², > 1 MeV versus the A/B ratio (weight percent values)—copper content* > 0.15 weight percent.

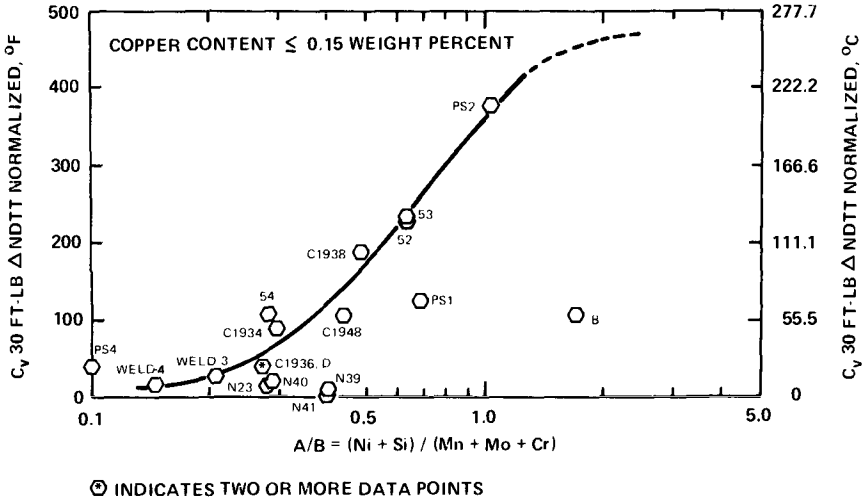

FIG. 2—*NDTT shift normalized to a fluence = 3.0 × 10¹⁹ n/cm², > 1 MeV versus the A/B ratio (weight percent values)—copper content* ≤ *0.15 weight percent.*

longer than for B. Points CF24 and CF48 were stress-relief annealed for 65 h, cooled, and then reannealed for 15 h; 3N5 was annealed for 30 h (Table 3). The differences in annealing times support evidence of the effects of carbon diffusion on subsequent irradiation sensitivity.

The nickel-silicon effects on irradiation sensitivity are again evident in Fig. 2. Data Point PS2 contained minimal copper (0.05 weight percent) and

had a normalized shift of 376°F (208.8°C). This shift is considerably higher than that exhibited by Points 52 and 53 containing 0.14 weight percent copper [$\Delta NDTT_n \cong 225°F$ (125°C)]. The shifts, however, are commensurate with the A/B ratios of the data points. The ratio for Point PS2 was 1.07 versus the 0.63 ratio of Points 52 and 53.

Discussion

The effects of nickel and silicon on the irradiation behavior of weld metal are clearly evident in Figs. 1 and 2. Regardless of copper content, as the weld A/B ratios increase, the ΔNDTT values increase.

Copper Effects

To demonstrate the separate, but additive effects of copper and the A/B ratio on NDTT shift, Fig. 3 was developed. Figure 3 depicts the ΔNDTT versus A/B weld data separated into three copper weight percent groups

$$\text{Copper} \leqslant 0.05$$

$$0.05 < \text{Copper} \leqslant 0.15$$

$$\text{Copper} > 0.15$$

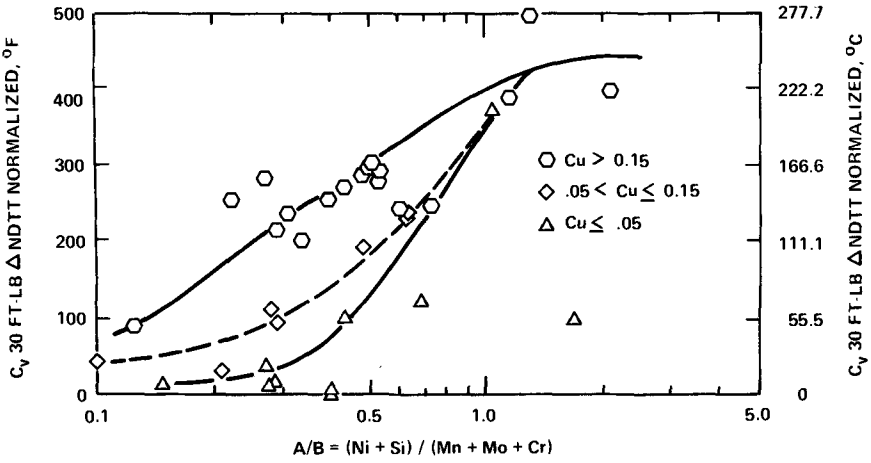

FIG. 3—*NDTT shift normalized to a fluence = 3.0 × 10^{19} n/cm², > 1 MeV versus A/B ratio (weight percent values)—trends relative to copper content.*

It can be seen that while the A/B ratio curves predict ΔNDTT trends, the trend curves start at and indicate higher shift values corresponding to in-

creases in residual copper content. Thus, copper and A/B effects on weld metal irradiation sensitivity are separate, but additive.

Effects of Heat Treatment

In most cases, when the postweld heat treatments consisted of short times at annealing temperatures, short cooling times from the annealing temperatures, or both, the welds experienced lower NDTT shifts than predicted by the trend lines of Figs. 1 and 2. These shorter times at temperature hinder the diffusion of carbon through the structure to preferred sites. Beeler and Beeler [*8*] have indicated that the carbon-vacancy complex in α-iron (ferrite) has a carbon atom positioned a finite distance from the vacancy along a <100> line. In order for the carbon atoms to arrive at these sites, diffusion of carbon through the structure, which is time and temperature dependent, must occur. Therefore, long postweld heat treatments and slow cooling rates aid the diffusion process. When irradiation events take place, the carbon atoms would be in position to pin the vacancies. The activity of the carbon atom would be affected by its nearest neighbor, that is, a silicon, nickel, manganese, etc. substitutional atom. The high carbon activity resulting from increased nickel and silicon promotes the formation of vacancy complexes which produce irradiation hardening and therefore higher NDTT shifts.

Effects of Metallurgical Structure

The metallurgical structure of the weld also affects the position of carbon atoms and it is for this reason that the nickel-silicon effects seem to apply only to ferrite-structured welds. Five data points in Fig. 2 (N23, N39, N40, N41, B), which lie below the trend line, were associated with weld metal whose structure was martensite or bainite, or both, or a combination of these with ferrite. In all cases, the data points exhibited lower NDTT shifts than that predicted by their respective A/B ratios. Martensite is a body-centered tetragonal (bct) structure, and carbon atoms are trapped in the structure by the martensitic transformation. The formation of bainite occurs by the nucleation of ferrite with carbide rejected. The resulting structure of carbides in ferrite has a very fine particle size. Before carbon-vacancy complexes can form in bainite, the carbon atoms must be knocked out of the carbides by an irradiation collision event, and the carbon atoms must diffuse into the ferrite. The effects of structure on the irradiation sensitivity of material were investigated earlier by Hawthorne and Steele [*17*]. In studies with HY-80 and A350-LF3 materials, they found that quenched-and-tempered structures, notably tempered martensite, had lower radiation sensitivity than that of higher-temperature transformation products such as ferrite. For both of the materials used in the study (HY-80 and A350-LF3),

when the heat treatment produced equiaxed ferrite, the irradiated ΔNDTT was highest.

Summary and Conclusions

The empirical evaluations of weld metal irradiation behavior conducted here have shown that definite trends exist among the weld metal alloy content (nickel plus silicon versus manganese plus molybdenum plus chromium), the postweld heat treatment, the weld microstructure, and subsequently the weld's NDTT shift with irradiation. Because these factors act collectively, it is suggested that carbon atoms and their known ability to pin irradiation defects (vacancies) play the dominant role in the irradiation sensitivity of a weld. It should be emphasized, however, that these effects are in addition to the known effects caused by residual element content, primarily copper. The following patterns and effects were noted.

1. Nickel and silicon act together to increase the sensitivity of welds containing ferrite to neutron-irradiation by affecting the activity of carbon in solid solution. It is suggested that the carbon atoms subsequently form carbon-vacancy complexes similar to those proposed by Beeler and Beeler [*8*].

2. Manganese, molybdenum, and chromium tend to counteract the effects of nickel and silicon in ferrite-structured welds.

3. The postweld heat treatment affects the irradiation behavior of welds. Those welds experiencing longer times at annealing temperature generally had higher NDTT shifts. This has been related to the longer heat treatments allowing carbon atoms to diffuse to preferred sites for the formation of carbon-vacancy complexes.

4. The metallurgical structure of the weld plays a dominant role, since the nickel-silicon effects appear to apply only to ferritic-structured welds. This again has been related to carbon positioning in the structure.

5. The effects of nickel and silicon on the irradiation sensitivity of ferrite-structured welds are separate from those effects produced by copper. This is shown by the nickel-silicon trends exhibited by low-copper-containing welds. When copper is present, however, the effects of nickel-silicon and copper are additive.

References

[*1*] Hawthorne, J. R. et al, "Irradiation Effects on Reactor Structural Materials," NRL Memorandum Report 1753, Naval Research Laboratory, Washington, D.C., 15 Feb. 1967.

[*2*] Potapovs, U. and Hawthorne, J. R., "The Effects of Residual Elements on 550 F Irradiation Response of Selected Pressure Vessel Steels and Weldments," NRL Report 6803, Naval Research Laboratory, Washington, D.C., 22 Nov. 1968.

[*3*] Steele, L. E. et al, "Irradiation Effects on Reactor Structural Materials," NRL Memorandum Report 1937, Naval Research Laboratory, Washington, D.C., 15 Nov. 1968.

[4] Hawthorne, J. R. in *Irradiation Effects on Structural Alloys for Nuclear Reactor Applications, ASTM STP 484,* American Society for Testing and Materials, 1970, pp. 96–127.

[5] Hawthorne, J. R., Koziol, J. J., and Groeschel, R. C. in *Properties of Reactor Structural Alloys After Neutron or Particle Irradiation, ASTM STP 570,* American Society for Testing and Materials, 1975, pp. 83–102; Combustion Engineering Publication TIS-4191.

[6] Steele, L. E., "Neutron Irradiation Embrittlement of Reactor Pressure Vessel Steels," International Atomic Energy Agency, Technical Report Series No. 163, 1975, pp. 117–119.

[7] Hawthorne, J. R., *Nuclear Engineering and Design,* Vol. 17, 1971, pp. 116–130.

[8] Beeler, J. R., Jr. and Beeler, M. F. in *Effects of Radiation on Substructure and Mechanical Properties of Metals and Alloys, ASTM STP 529,* American Society for Testing and Materials, 1973, pp. 289–302.

[9] Smith, R. P., *Transactions,* American Institute of Mining, Metallurgical, and Petroleum Engineers, 1960, Vol. 218, pp. 62–64.

[10] Smith, R. P., *Journal of the American Chemical Society,* Vol. 70, 1948, pp. 2724–2729.

[11] *Molybdenum for Nuclear Energy Applications, a Perspective,* Climax Molybdenum Company, New York, pp. 20–21.

[12] Igata, N. et al in *Effects of Radiation on Substructure and Mechanical Properties of Metals and Alloys, ASTM STP 529,* American Society for Testing and Materials, 1973, pp. 63–74.

[13] "Irradiation Effects on Reactor Structural Materials, 1 August 1973–31 January 1974," NRL Memorandum Report 2752, L. E. Steele, Ed., Naval Research Laboratory, Washington, D.C., March 1974, pp. 12, 20.

[14] Hawthorne, J. R. et al, *Welding Research Supplement,* Oct. 1970, pp. 453_s–458_s.

[15] Smidt, F. A., and Sprague, J. A. in *Effects of Radiation on Substructure and Mechanical Properties of Metals and Alloys, ASTM STP 529,* American Society for Testing and Materials, 1973, pp. 78–91.

[16] Hawthorne, J. R., "Radiation-Embrittlement Resistance of Advanced NiCrMo Steel Plates, Forgings, and Weldments," NRL Report 7573, Naval Research Laboratory, Washington, D.C., Sept. 1973.

[17] Hawthorne, J. R. and Steele, L. E., "Initial Evaluations of Metallurgical Variables as Possible Factors Controlling the Radiation Sensitivity of Structural Steels," NRL Report 6420, Naval Research Laboratory, Washington, D.C., Sept. 1966.

[18] Steele, L. E. et al, "Irradiation Effects on Reactor Structural Materials, Quarterly Progress Report, 1 August–31 October 1966," NRL Memorandum Report 1731, Naval Research Laboratory, Washington, D.C., Nov. 1966.

[19] Mager, T. R. and Thomas, F. O., "Evaluation by Linear Elastic Fracture Mechanics of Radiation Damage to Pressure Vessel Steels," WCAP-7328, Westinghouse Electric Corporation, Pittsburgh, Pa., Oct. 1969.

[20] Mager, T. R. et al, "Analysis of Capsule V from the Rochester Gas and Electric R. E. Ginna Unit No. 1 Reactor Vessel Radiation Surveillance Program," Westinghouse Electric Corporation, Pittsburgh, Pa., March 1973.

[21] Hawthorne, J. R. and Potapovs, U., "Initial Assessments of Notch Ductility Behavior of A533 Pressure Vessel Steel with Neutron Irradiation," NRL Report 6772, Naval Research Laboratory, Washington, D.C., Nov. 1968.

[22] Childress, C. E., "Fabrication Procedures and Acceptance Data for ASTM A-533 Welds and A 10-in.-thick ASTM A-543 Plate of the Heavy Section Steel Technology Program, Documentary Report 3," ORNL-4313-3, Oak Ridge National Laboratory, Oak Ridge, Tenn., Jan. 1971.

[23] Perrin, J. S. et al, "Point Beach Nuclear Plant Unit No. 1 Pressure Vessel Surveillance Program, Evaluation of Capsule V," Battelle Columbus Labs, Columbus, Ohio, 15 June 1973.

[24] Pachur, D. and Sievers, G. in *Properties of Reactor Structural Alloys After Neutron or Particle Irradiation, ASTM STP 570,* American Society for Testing and Materials, 1975, pp. 555–564.

[25] Steele, L. E. et al, "Irradiation Effects on Structural Materials, Quarterly Progress Report, 1 August 1968-31 October 1968," NRL Memorandum Report 1938, Naval Research Laboratory, Washington, D. C., Nov. 1968.

[26] Steele, L. E. et al, "Irradiation Effects on Reactor Structural Materials, Quarterly Progress Report, 1 May-31 July 1969," NRL Memorandum Report 2027, Naval Research Laboratory, Washington, D.C., Aug. 1969.

[27] Stelzman, W. J. and Berggren, R. G., "Radiation Strengthening and Embrittlement in Heavy-Section Steel Plates and Welds," ORNL-4871, Oak Ridge National Laboratory, Oak Ridge, Tenn., June 1973.

J. A. Spitznagel,[1] *R. P. Shogan,*[1] *and J. H. Phillips*[2]

Annealing of Irradiation Damage in High-Copper Ferritic Steels

REFERENCE: Spitznagel, J. A., Shogan, R. P., and Phillips, J. H., "**Annealing of Irradiation Damage in High-Copper Ferritic Steels,**" *Irradiation Effects on the Microstructure and Properties of Metals, ASTM STP 611,* American Society for Testing and Materials, 1976, pp. 434–448.

ABSTRACT: The postirradiation annealing response of one SA 302 Grade B plate material and two high-copper weld metals irradiated at 550°F (288°C) was measured for annealing temperatures in the range 600°F (316°C) to 850°F (454°C) and annealing times up to 1 week (168 h). Recovery of pre-irradiation microhardness was followed for all three steels. In addition, recovery of ductile-brittle transition temperature (DBTT) was measured for the SA 302 Grade B material. Optical and transmission electron microscopy (TEM) were utilized to characterize the microstructures of the irradiated and annealed SA 302 Grade B plate material. Small fracture specimens of all three steels were broken in an Auger spectrometer. Auger analyses were performed on the fracture surfaces, which were subsequently characterized with scanning electron microscopy (SEM). Microhardness measurements indicated that the weld metal with the highest copper content (0.31 weight percent) and lowest fluence (5.7×10^{18} neutrons (n)/cm^2) was the most resistant to softening under postirradiation annealing. The recovery of ductility as measured by the DBTT shift of the SA 302 Grade B material paralleled the recovery as measured by microhardness. All three steels showed increased recovery with higher annealing temperatures and longer annealing times. No visible microstructural changes accompanied irradiation or annealing. Some evidence for a 5 to 10 percent increase in copper concentration at the fracture surfaces of irradiated specimens was obtained. No significant segregation of any element to the fracture surfaces, however, was observed to result from irradiation or postirradiation annealing. The measured annealing response of these steels agreed well with the values predicted by a previously developed theoretical model based on the dissolution of copper-vacancy aggregates.

KEY WORDS: radiation, neutron irradiation, radiation effects, microhardness, ductility, microstructure, solute-vacancy clusters, ferritic steels, annealing, recovery, model, theory, Auger spectrometry, segregation, precipitation

Embrittlement of ferritic steels under neutron irradiation has been studied extensively for the past ten years. The mechanisms, however, are

[1] Senior engineers, Westinghouse Research Laboratories, Pittsburgh, Pa. 15235.
[2] Engineer, Westinghouse Pressurized Water Reactors, Systems Division, Pittsburgh, Pa. 15235.

not well understood. The loss of ductility of commercial steel such as ASTM Type A302 Grade B and Type A533 Grade B is usually manifested by a shift in the ductile-brittle transition temperature (DBTT), a drop in the "upper shelf" energy as measured in the conventional Charpy V-notch test, or a decreased fracture toughness (K_{Ic}). The magnitude of the change in toughness or ductility loss depends on the composition of the steel, the irradiation temperature, and the spectrum-averaged fast neutron fluence. Rapid embrittlement results from lowering the irradiation temperature, increasing the fluence, or increasing the concentration of certain solutes, especially copper. The ductility loss as measured by the DBTT shift is usually accompanied by increases in yield strength and hardness.

The possibility of restoration of preirradiation toughness and strength levels through postirradiation annealing treatments has not received much attention, however. Recovery of yield strength, hardness, notch ductility, and fracture toughness for Type A533 Grade B Class 1 steel have been measured by Smidt et al [*1*],[3] Hawthorne [*2*], Williams [*3*], and Mager and Hawthorne [*4*]. The data are as yet insufficient, however, to permit an accurate assessment of the combined effects of neutron fluence, neutron energy spectrum, irradiation temperature, and annealing conditions (time and temperature) on the recovery of preirradiation properties. Published data on earlier commercial steels (HY-80, A212B, A302B) as well as on weld and heat-affected zone (HAZ) material are scarce [*5–7*]. This study was undertaken to assess the postirradiation annealing response of high-copper SA 302 Grade B steel plate and weld metal and to permit a comparison of the measured recovery with that predicted by the vacancy-solute cluster dissolution model developed previously [*8,9*].

Experimental Procedure

Most of the specimens used in this investigation were prepared from irradiated and unirradiated 0.394 by 0.394 by 2.115 in. (1 by 1 by 5.375 cm) Charpy V-notch specimens and 0.394-in. (1 cm) compact tension specimens previously tested at temperatures below 200°F (93°C). Rectangular specimens 0.394 by 0.394 by 0.250 in. (1 by 1 by 0.635 cm) were cut with a diamond saw from broken specimens (¼ T locations) of one high-copper SA 302 Grade B plate and two high-copper welds for microhardness measurements. Chemical analyses of the steels are given in Table 1. Preirradiation heat treatments are given in Table 2. Irradiated and unirradiated microhardness specimens and several unbroken Charpy specimens were annealed in a muffle furnace at temperatures from 600°F (316°C) to 850°F (454°C) for times up to 168 h. Table 3 summarizes the

[3] The italic numbers in brackets refer to the list of references appended to this paper.

TABLE 1—*Chemical composition of plate and weld metal.*

Element	SA 302 Grade B Base Metal (Plate)	Weld Metal 1	Weld Metal 2
C	0.20	0.076	0.077
Mn	1.38	1.26	1.51
P	0.013	0.011	0.017
S	0.035	0.018	0.013
Si	0.24	0.66	0.47
Ni	0.14	0.57	0.55
Cr	0.11	0.14	0.064
V	0.003	0.002	0.39
Mo	0.47	0.42	0.003
Co	0.008	0.001[a]	0.001[a]
Cu	0.16	0.31	0.28
Sn	0.027	0.004	0.004
Zn	0.005	0.003	0.003
Al	0.056	0.015	0.030
N_2	0.006	0.012	0.014
Ti	0.016	0.001[a]	0.001[a]
Sb	0.008	0.001	0.001
As	0.008	0.005	0.003
B	0.003[a]	0.003[a]	0.003[a]
Zr	0.001[a]	0.001[a]	0.001[a]

[a] Not detected. The number indicates the minimum limit of detection.

TABLE 2—*Preirradiation heat treatment of plate and weld metal.*

Material Identification	Heat Treatment
SA 302 Grade B[a]	1600°F/9.5 h/water quenched
	1225°F/9.5 h/air cooled
	1150°F/15.5 h/furnace cooled[b]
Weld Metal 1[c]	1125°F/10.25 h/furnace cooled to 600°F
Weld Metal 2[c]	1125°F/25 h/furnace cooled to 600°F

[a] 9.5-in.-thick plate.
[b] Simulated stress-relief anneal.
[c] Submerged-arc weld.

irradiation history and postirradiation annealing times and temperatures used.

Small fracture specimens approximately 0.100 by 0.100 by 0.394 in. (0.25 by 0.25 by 1 cm) were cut from several as-irradiated specimens for analysis with an Auger spectrometer. Some of these specimens were also annealed and are listed in Table 3.

Following annealing, one surface on each microhardness specimen was metallographically polished through 6-μm diamond abrasive, and Vickers hardness (VHN) was determined at room temperature with a Leitz micro-

TABLE 3—*Irradiation history and postirradiation annealing conditions.*

Material	Specimen Type	Irradiation Temperature, °F (°C)	Neutron Fluence, n/cm² ($E > 1$ MeV)	Annealing Temperature, °F (°C)	Annealing Times, h
SA 302 B	microhardness	550 (288)	3.0×10^{19}	600 (316)	1, 16, 168
				660 (343)	1, 16, 168
				700 (371)	1, 16, 168
				750 (399)	1, 16, 168
				850 (454)	1, 16, 168
	Charpy V-notch longitudinal orientation[a]	550 (288)	3.0×10^{19}	700 (371)	168
				800 (427)	168
	transverse orientation[b]	550 (288)	3.0×10^{19}	700 (371)	1, 168
				800 (427)	1, 168
	Auger fracture specimens[c]	550 (288)	3.0×10^{19}	700 (371)	168
				800 (427)	16
Weld Metal 1	microhardness	550 (288)	5.7×10^{18}	600 (316)	1, 16, 168
				700 (371)	1, 16, 168
				800 (427)	1, 16, 168
	Auger fracture specimens[c]	550 (288)	5.7×10^{18}	700 (371)	168
				800 (427)	16
Weld Metal 2	microhardness	550 (288)	2.5×10^{19}	600 (316)	1, 16, 168
				700 (371)	1, 16, 168
				800 (427)	1, 16, 168
	Auger fracture specimens[c]	550 (288)	2.5×10^{19}	700 (371)	168
				800 (427)	16

[a] Long axis of Charpy specimen parallel to rolling direction of the plate (two specimens).
[b] Long axis of Charpy specimen perpendicular to rolling direction of the plate (nine specimens).
[c] Subsized, notched cantilever beam specimens for use with the fracture stage supplied with the Physical Electronics Industries Scanning Auger Microprobe.

hardness attachment to an Epivert microscope using a 400-g load. Charpy specimens of the SA 302B steel were tested at temperatures from 0°F (−17.8°C) to 200°F (93°C) following procedures outlined in ASTM Notched Bar Impact Testing of Metallic Materials (E 23-72). Optical microscopy and transmission electron microscopy (TEM) were conducted on metallographic cross sections and thin foils, respectively, prepared from SA 302B plate material. The Auger fracture specimens were clamped in specially designed stainless steel fixtures and notched on two adjacent faces with a small file. They were then placed in the Auger spectrometer, cooled below 0°F (−17.8°C), and fractured under a vacuum of approximately 10^{-9} torr (1.33×10^{-7} Pa). Auger analyses of the fracture surfaces were performed with a Physical Electronics Industries Scanning Auger Microprobe. The fracture surfaces were subsequently observed with a scanning electron microscope (SEM).

The experimentally determined recovery behavior for each material was compared with the theoretically predicted values using the RANEL computer code developed previously [*9*].

Experimental Results

Microhardness Measurements

The results of the microhardness measurements on unirradiated annealed control samples, as irradiated, and irradiated plus annealed specimens are shown in Figs. 1 through 3. An attempt was made to cut all irradiated specimens for any one annealing temperature from the same previously broken Charpy or compact tension specimen to minimize the

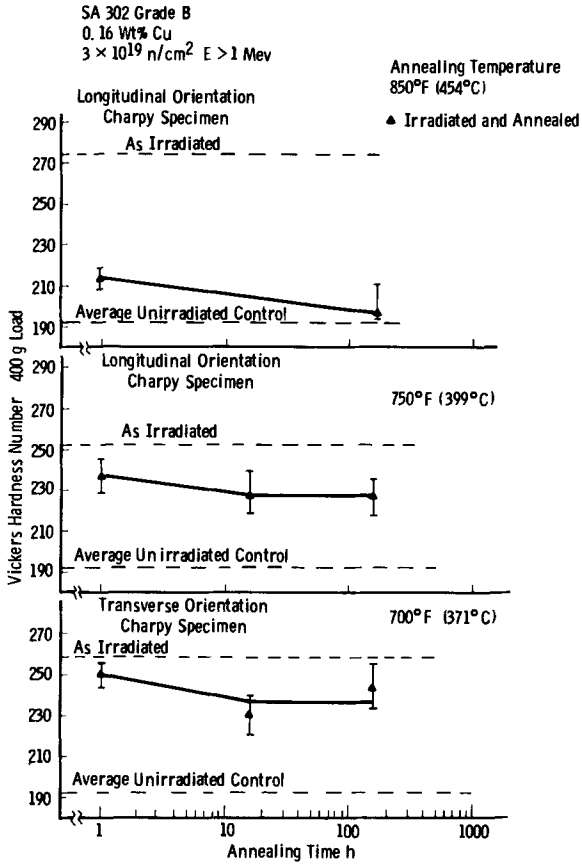

FIG. 1—*Microhardness changes at 68°F (20°C) resulting from postirradiation annealing of SA 302 Grade B plate material.*

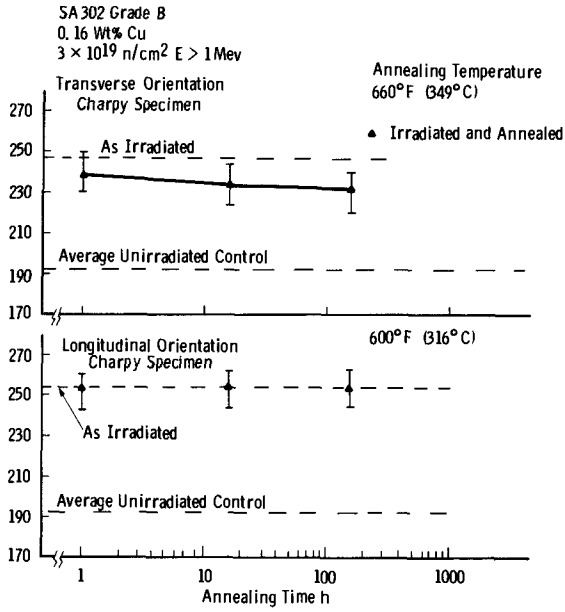

FIG. 1—*Continued*

experimental scatter. The points plotted represent the average of at least six measurements per specimen. Error bars reflect the range of hardness values determined for each specimen. Unirradiated control specimens were annealed with the irradiated specimens, and, since no statistically significant changes in microhardness resulted from their exposure to elevated temperatures, the average Vickers hardness value was plotted for every case.

The scatter in the data is large for all three steels and all annealing conditions. A definite trend toward increased recovery with higher annealing temperatures and longer annealing times, however, is seen for both the SA 302 Grade B plate and weld metals. Weld Metal 1 with the highest copper content and lowest fluence exposure exhibited the least recovery at all temperatures up to 800°F (427°C). Surprisingly, even 168 h at 700°F (371°C) failed to produce significant softening relative to the as-irradiated condition. Weld Metal 2 and the SA 302 Grade B, however, showed measurable recovery after one week (168 h) of annealing at temperatures as low as 600°F (316°C) and 660°F (349°C), respectively.

Charpy V-notch specimens of the SA 302 Grade B plate used in this investigation showed markedly different energy absorption characteristics for longitudinal or transverse orientations during previous tests. The initial orientations of the previously broken Charpy specimens from which the microhardness specimens were cut is shown in Fig. 1. There is

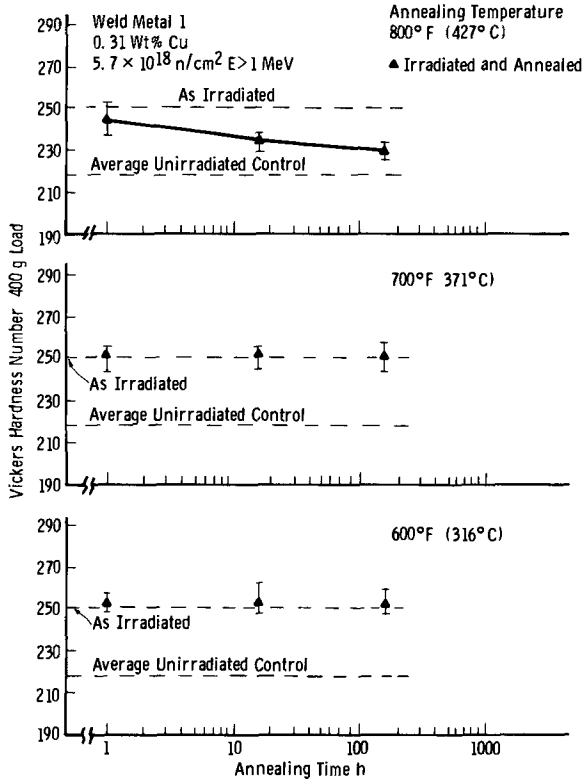

FIG. 2—*Microhardness changes at 68°F (20°C) resulting from postirradiation annealing of Weld Metal 1 material.*

some indication that postirradiation annealing response as measured by the shift in DBTT may vary slightly with specimen orientation, as discussed in the following section. It is unlikely that this difference would be detectable, considering the scatter in the microhardness data, but the orientation information is included for completeness.

Charpy V-Notch Measurements

Charpy test results for unirradiated, as-irradiated, and irradiated plus annealed ¼ T specimens of the SA 302 Grade B plate material are shown in Fig. 4. Specimens taken from the transverse orientation exhibited very low "upper shelf" values even in the unirradiated condition. Irradiation at 550°F (288°C) to a fluence of 3.0×10^{19} n/cm² ($E > 1$ MeV) produced estimated DBTT shifts of 112°F (44°C) and 142°F (61°C) for longitudinal and transverse specimens, respectively, at the 30 ft·lb (40.7 J) level. Very little recovery was obtained after 1 h at 700°F (371°C), which agrees well

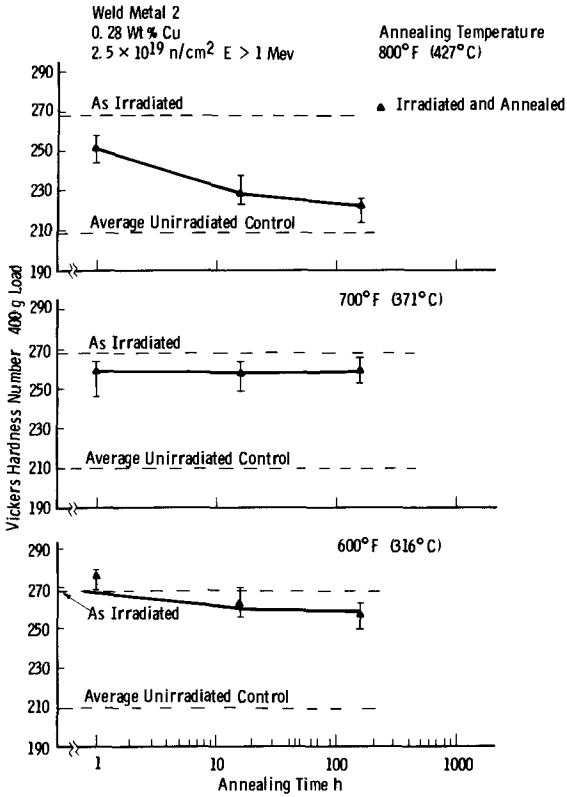

FIG. 3—*Microhardness changes at 68°F (20°C) resulting from postirradiation annealing of Weld Metal 2 material.*

with the microhardness results, Fig. 1. One week (168 h) anneals at 700°F (371°C), however, produced approximately 58 and 77 percent recovery in specimens of transverse and longitudinal orientations, respectively. Approximately 90 percent recovery was achieved for specimens of both orientations after annealing at 800°F (427°C) for 168 h. The results normalized in terms of percent recovery are shown in Table 4.

Optical and TEM Observations

Polished and etched cross sections of unirradiated SA 302 Grade B Charpy specimens annealed for 168 h at 600°F (316°C), 700°F (371°C), and 850°F (454°C) showed no significant microstructural changes from the annealing treatments. This was further confirmed by TEM. The microstructure remained essentially a tempered martensite with a dispersion of very fine precipitates, presumably Mo_2C.

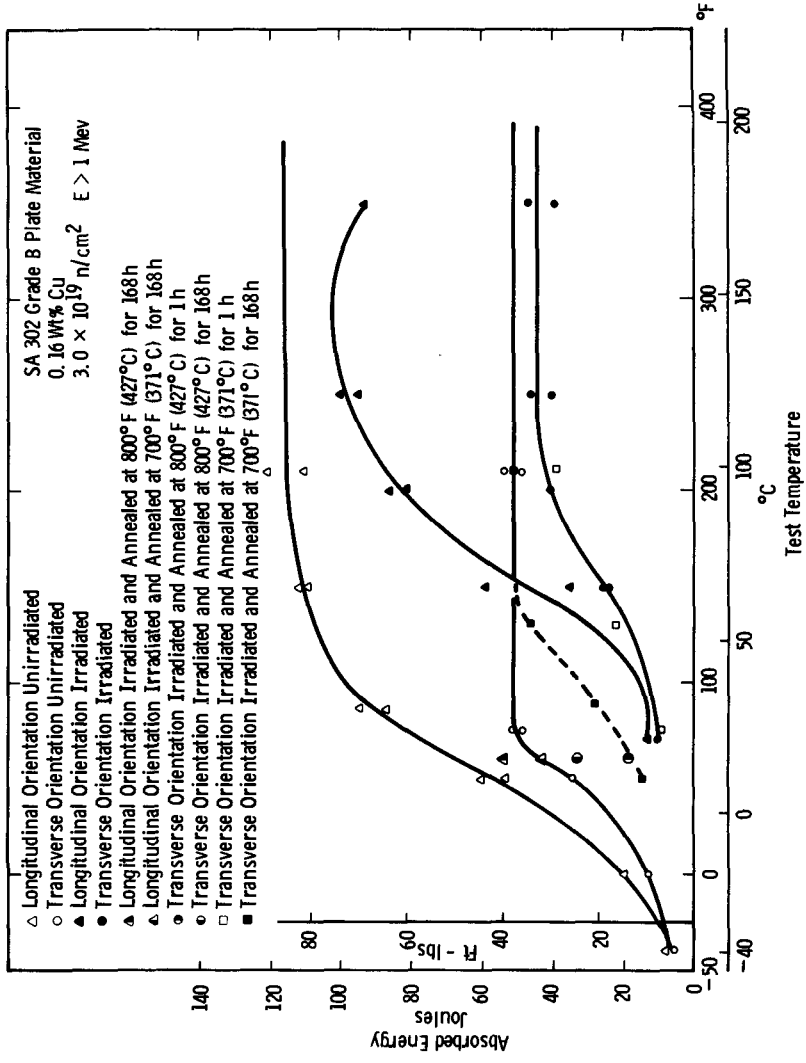

FIG. 4—*Charpy V-notch test results unirradiated, irradiated, and irradiated plus annealed SA 302 Grade B plate material.*

TABLE 4—*Comparison of experimental and theoretical annealing responses.*

Material	Specimen Type	Annealing Temperature, °F (°C)	Annealing Time, h	Percent Recovery	
				Experiment[a]	Theory[b]
SA 302 Grade B	microhardness	600 (316)	168	0	41
		660 (349)	168	27	58
		700 (371)	168	33	69
		750 (399)	168	42	84
		850 (454)	1	74	68
		850 (454)	168	95	99
	Charpy V-notch[c]				
	longitudinal	700 (371)	168	77	69
	orientation	800 (427)	168	89	94
	transverse	700 (371)	1	0	37
	orientation	700 (371)	168	58	69
	transverse	800 (427)	1	61	58
	orientation	800 (427)	168	90	94
Weld Metal 1	microhardness	600 (316)	168	0	13
		700 (371)	168	0	33
		800 (427)	1	21	19
		800 (427)	16	48	49
		800 (427)	168	64	63
Weld Metal 2	microhardness	600 (316)	168	17	18
		700 (371)	168	17	40
		800 (427)	1	27	34
		800 (427)	16	68	51
		800 (427)	168	78	74

[a] Calculated on the following basis: percent recovery =

$$\frac{\text{as-irradiated value} - \text{test point value}}{\text{as-irradiated value} - \text{unirradiated value}} \times 100\%$$

[b] Calculated with RANEL code (Ref *9*).

[c] Percent recovery calculated from DBTT shift at the 30 ft·lb (40.7 J) level when the annealing data were sufficient to generate a complete Charpy curve. For isolated data points, the percent recovery was calculated at the energy level of the datum point.

Auger Analyses and SEM Observations

Portions of the Auger spectra and corresponding SEM micrographs of the analyzed areas of several miniature fracture specimens of the SA 302 Grade B steel are shown in Figs. 5 and 6, respectively. At least four areas were randomly selected for analysis on each fracture surface. All fracture surfaces of the SA 302 Grade B material showed numerous sulfur-rich regions under scanning conditions. It is thought that these represent manganese sulfide inclusions in the steel. The areas corresponding to the Auger electron energy spectra of Fig. 5, however, encompassed very few sulfur-containing particles.

The approximate locations of the principal Auger peaks of interest in these steels are given by the chemical symbols in Fig. 5. Although care

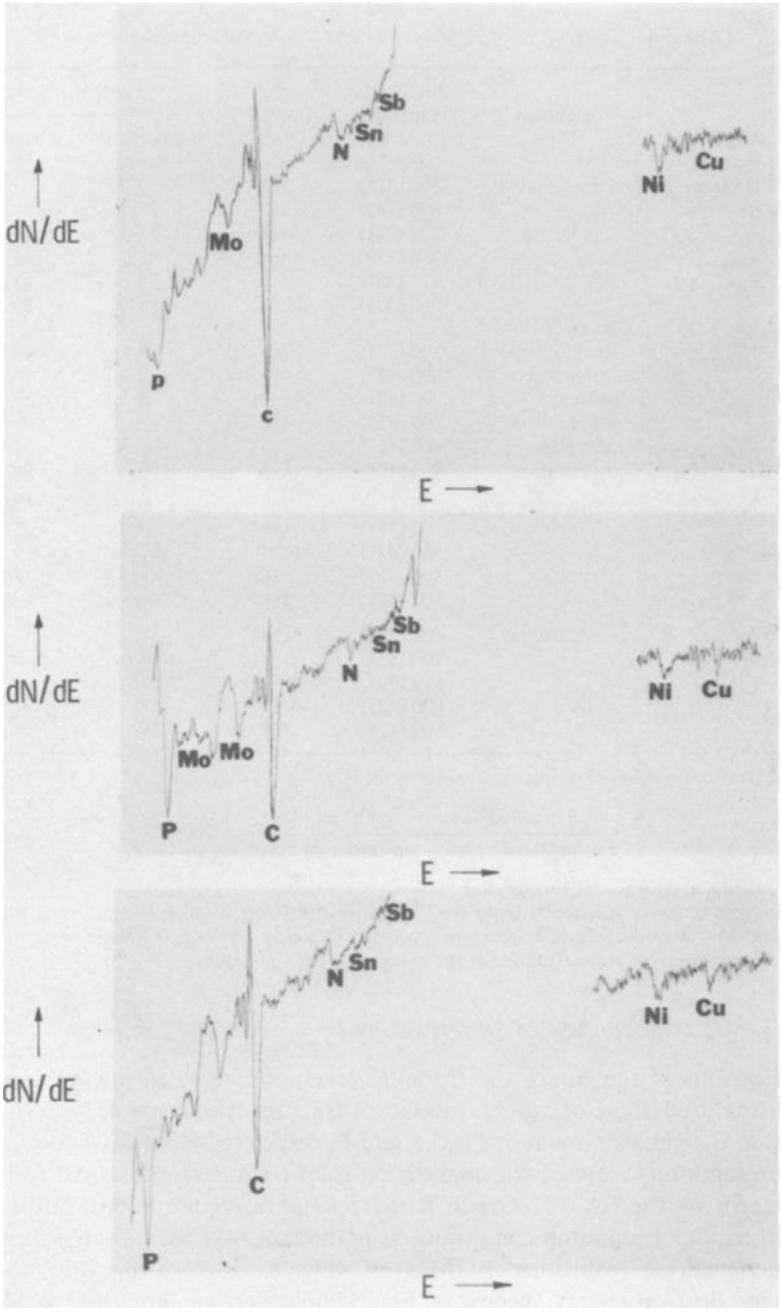

FIG. 5—*Auger spectra from fracture surfaces of small-fracture specimens of SA 302 Grade B plate material*: (top) *unirradiated control*; (center) *as-irradiated to* 3.0×10^{19} *n/cm*^{2} (E > *1 MeV*) *at 550°F (288°C)*; (bottom) *irradiated plus annealed at 800°F (427°C) for 16 h.*

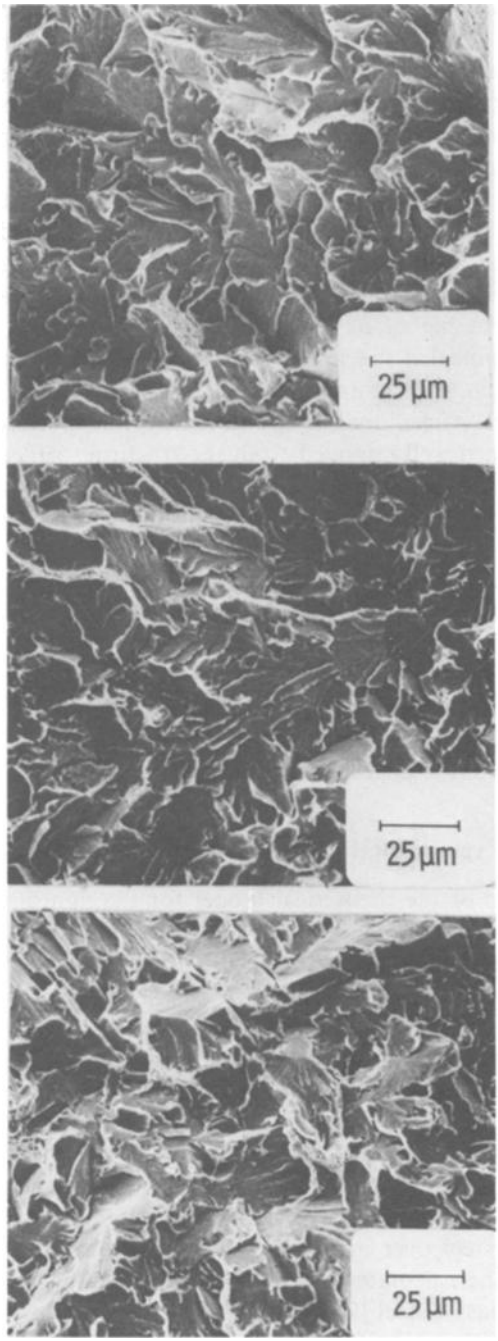

FIG. 6—*SEM's of fracture surfaces corresponding to the Auger analysis of Fig. 5*: (top) *unirradiated control*; (center) *as-irradiated to* 3.0×10^{19} *n/cm*^{2} (E > *1 MeV*) *at 550°F (288°C)*; (bottom) *irradiated plus annealed at 800°F (427°C) for 16 h.*

was taken to normalize the energy and current of the exciting electron beam, amplifier gain, etc. for each analysis, no appropriate standards were available, and any quantitative analysis utilizing these spectra would be unreliable. Some inferences as to relative concentrations, however, can be drawn from relative peak heights. For example, the copper concentration at the fracture surface of the unirradiated specimen was below the detectability limit. A definite copper signal was obtained, however, for the fracture surfaces of both the as-irradiated and irradiated plus annealed specimens. From a comparison of relative peak heights normalized to the 703 eV iron peak, it is estimated that the concentration of copper is 5 to 10 percent higher at the fracture surfaces of the irradiated and irradiated plus annealed specimens compared with the unirradiated specimen. This is much less than a monolayer and does not represent appreciable segregation. Auger analysis of a lightly ion-sputtered area of the irradiated specimen well removed from the fracture surface showed essentially the same spectrum as the unirradiated specimen fracture surface. No copper signal was observed. Similar results were obtained for the weld metals. No appreciable segregation of any element was observed for either the SA 302 Grade B steel or the weld metals following irradiation at 550°F (288°C) or postirradiation annealing at temperatures up to 800°F (427°C).

The SEM micrographs of Fig. 6 indicate that the failure mode of these small fracture specimens was primarily transgranular cleavage. This is similar to the fracture appearance of the 0.394-in. (1 cm) Charpy V-notch specimens tested in the ductile-brittle transition region.

Comparison of Experimental Results with Theoretical Model

A brief outline of the theoretical model for the annealing of radiation damage in ferritic pressure vessel steels has been given previously [*8*], and a more comprehensive description of the model and analysis of existing annealing data will be published elsewhere [*9*]. Briefly, the kinetic equations derived by Dollins [*10*] have been used to follow the dissolution of copper-vacancy aggregates detected and analyzed with an atom probe in a neutron-irradiated iron-copper binary alloy [*11*]. The only adjustable parameter in the model is the effective surface energy of the cluster or the binding energy of a vacancy to the solute-vacancy complex. In practice the model is fitted to one or two data points and then a digital computer is used to map out the predicted time-temperature-percent recovery response of the steel over any range. Excellent agreement has been obtained between the calculated and measured annealing response of Type A533 Grade B Class 1 steel [*9*].

Comparisons of the model calculations with the measured annealing response of the SA 302 Grade B steel and two high-copper weld metals

used in this investigation are given in Table 4. Considering the scatter in the microhardness data, the agreement between theory and experiment is very good for the weld metals. For the SA 302 Grade B plate material, good agreement was obtained for the Charpy V-notch and high-temperature microhardness data. The choice of vacancy binding energy required to get good agreement with the lower-temperature hardness data gave unacceptably small values for recovery in microhardness and DBTT at the higher temperatures. The reason for this discrepancy is not known at present.

Summary of Results and Discussion

Many possible mechanisms including solute segregation, radiation-enhanced precipitation, and the formation of complex solute-defect aggregates may contribute to the irradiation-induced hardening and embrittlement of commercial steels. The recovery of preirradiation strength and ductility levels by postirradiation annealing is thus expected to be a complex function of heat chemistry, welding practice, irradiation history, and annealing conditions. The different annealing responses observed for the SA 302 Grade B steel and two high-copper weld metals used in this investigation are consistent with this supposition. All three steels, however, showed increased recovery of preirradiation microhardness with higher annealing temperatures and longer annealing times. The Charpy V-notch results for the irradiated and annealed SA 302 Grade B material paralleled the recovery in microhardness in this respect. The lower apparent recovery for specimens of the low-shelf transverse orientation following the 700°F (371°C)–168 h anneal relative to that measured for the specimens of the longitudinal orientation will require additional testing for verification.

The optical microscopy, TEM, and Auger results suggest that no profound microstructural changes occurred in these steels from irradiation at 550°F (288°C) or postirradiation annealing at temperatures from 600°F (316°C) to 850°F (454°C) for times up to one week (168 h). Some evidence that a slight copper enrichment can occur at the fracture surfaces of irradiated specimens was obtained with the Auger spectrometer. However, no appreciable segregation of any element was observed to result from either irradiation or postirradiation annealing in these steels. The fact that the copper signal was still present in the 800°F (427°C) annealed specimens when microhardness and impact properties had recovered nearly 80 percent suggests that local copper enrichment contributed little to the increased hardness or loss of ductility resulting from irradiation.

The evidence suggests that most of the irradiation-induced mechanical property changes in these steels result from defects whose sizes or strain fields are smaller than the practical resolution limit of TEM. Previous atom-probe observations of copper-vacancy aggregates in neutron-irradi-

ated iron-copper alloys [*11*], and the good agreement between the measured annealing responses of these steels and those predicted by the cluster dissolution model, suggest that similar copper-vacancy aggregates may be responsible for most of the observed radiation-induced hardening and embrittlement.

Acknowledgments

We would like to acknowledge the assistance of the following people in connection with this work: T. R. Mager for assistance in procuring the samples; G. M. Burcin, K. J. Galbraith, and W. A. Orr for assistance with the irradiated specimen preparation and testing; F. J. Venskytis for assistance with the computer model, and J. N. Chirigos for helpful discussions.

References

[*1*] Smidt, F. A. and Steel, L. E., "Residual Elements and Irradiation Embrittlement," Report 7310, Naval Research Laboratory, Washington, D.C., Sept. 1971.

[*2*] Hawthorne, J. R., "Postirradiation Embrittlement Relief of Mn-Mo-Ni Reactor Vessel Steels by Low-Temperature Heat Treatment," in *Report of NRL Progress*, Naval Research Laboratory, Washington, D.C., March 1973.

[*3*] Williams, J. A., "The Irradiation and Temperature Dependence of Tensile and Fracture Properties of ASTM A533 Grade B, Class 1 Steel Plate and Weldment," Heavy Section Steel Technology Program Technical Report No. 31, Westinghouse Hanford Company, Hanford, Wash., Aug. 1973.

[*4*] Mager, T. R. and Hawthorne, J. R., in preparation.

[*5*] DeMeester, P. and Van Asbroeck, Ph. in *Radiation Damage in Reactor Materials*, Vol. 1, International Atomic Energy Agency, Vienna, 1969, p. 351.

[*6*] Seman, D. J. and Pasierb, E. J., *Transactions of the American Nuclear Society*, Vol. 8, 1965, p. 416.

[*7*] Carpenter, G. F., Knopf, N. R., and Bryon, E. S., *Nuclear Science* and *Engineering*, Vol. 19, 1964, p. 18.

[*8*] Spitznagel, J. A. and Venskytis, F. J., *Transactions of the American Nuclear Society*, Vol. 21, 1975, p. 161.

[*9*] Spitznagel, J. A. and Venksytis, F. J., in preparation.

[*10*] Dollins, C. C., *Radiation Effects*, Vol. 16, 1972, p. 271.

[*11*] Brenner, S. S., Wagner, R., and Spitznagel, J. A., "Field-Ion Microprobe Detection of Ultra-Fine Defects in Neutron-Irradiated Fe-0.34Cu Alloy," to be submitted.

J. R. Beeler, Jr.,[1] *and M. F. Beeler*[1]

Displacement Spike Annealing in Iron at Reactor Temperatures

REFERENCE: Beeler, J.R., Jr., and Beeler, M.F. **"Displacement Spike Annealing in Iron at Reactor Temperatures,"** *Irradiation Effects on the Microstructure and Properties of Metals, ASTM STP 611,* American Society for Testing and Materials, 1976, pp. 449–462.

ABSTRACT: Displacement spike annealing computer experiments were done for body-centered cubic (bcc) and face-centered cubic (fcc) iron using five different annealing models. Each model predicted a greater number of free interstitials than free vacancies. The number of annihilation events was increased by an increase in cluster migration and decreased by an increase in the clustering interaction radius. The largest number of surviving defects occurred when clusters of four or more defects were immobile and a small clustering interaction radius was assigned.

KEY WORDS: radiation, displacement spikes, defect annealing, computer experiments, irradiation, irradiation hardening, radiation effects, damage units, damage saturation, steel, nuclear reactor materials, precipitation

A displacement spike is a collection of interacting vacancies and interstitials produced directly by a collision cascade. Computer experiments indicate that it has two distinguishing features: (*a*) The concentration of vacancies and interstitials is saturated, and (*b*) the defect deployment consists of a vacancy-rich region partially surrounded by an interstitial-rich region. Dynamical-method computer experiments indicate that the number and the arrangement of defects in a displacement spike are nearly independent of the irradiation temperature. From an engineering standpoint, the most important aspects of irradiation-induced defect production in nuclear reactor structural components are those concerned with the production of and the thermal annealing of displacement spikes.[2] The prime measures of defect production in this context are the number of mobile

[1] Professor, Materials Engineering and Nuclear Engineering, and research assistant, respectively, North Carolina State University, Nuclear Engineering Department, Raleigh, N.C. 27607.

[2] Beeler, J. R., *Journal of Testing and Evaluation,* Vol. 3, No. 3, May 1975, pp. 230–237.

vacancies and mobile interstitials (free defects) produced per displacement spike and the number of vacancies and interstitials per spike that are contained in immobile clusters. The free defects provided by spikes are the source of "uniformly" distributed vacancies and interstitials used in diffusion model calculations and simulations of void growth, dislocation loop growth, and the growth of new precipitates (radiation-induced precipitation). The immobile defect clusters provided by spikes can serve as nucleation sites for voids, dislocation loops and new precipitates. In addition, an immobile vacancy or interstitial cluster can serve as a trap or sink for impurity atoms and develop into an impurity-defect complex which has a sufficiently large binding energy to act as a hardening agent, that is, a dislocation barrier.

A collision cascade produces a displacement spike in about 10^{-12} s. At temperatures in the range 500 to 600°C, (932 to 1112°F), short-term annealing of a displacement spike occurs within about 10^{-6} s in iron and nickel. In the displacement spike annealing simulation computer experiments we have performed, the number of vacancies (interstitials) present after short-term annealing of a displacement spike is 15 to 50 percent of the number initially present in the spike at the start of short-term annealing. The 15 percent survival fraction pertains to displacement spikes produced by cascades in the 100-keV range, and the 50 percent survival fraction pertains to spikes produced by cascades in the 1-keV range. Of those vacancies (interstitials) which survive short-term annealing, from 2 to 40 percent are free defects, depending upon the annealing parameters appropriate to the physical circumstances under which annealing proceeds.

This paper describes how the defect distribution changes as a 20-keV displacement spike is annealed at 560°C (1040°F) in iron. This is done for a wide range of annealing models. The results for each of these models support the appropriateness of the short-term annealing (STA) concept. These results also indicate that the populations of vacancies and interstitials, and their spatial distribution at the end of STA, are the basic defect production measures pertinent to irradiation effects assessments in reactor engineering design. Given these populations, a simple diffusion model calculation can be used to assess the pertinent irradiation effects in a reactor structural component. Annealing of a uniform, saturated distribution of vacancies and interstitials is described first, to characterize the particular influence of the initially saturated defect concentration on displacement spike annealing. Annealing of 20-keV displacement spikes in body-centered-cubic (bcc) iron and face-centered-cubic (fcc) iron is then described.

Computational Method

The RINGO Program[3] was used to perform the annealing computer ex-

[3] Beeler, J. R., U.S. Progress Report ORO-3912-19, Energy Research and Development Administration, Oct. 1972.

periments described in this paper. RINGO is a Monte Carlo program which simulates the simultaneous random walks of up to 1000 defects in cubic metals. At each time step in the simulation, each mobile defect is given the opportunity to jump to a different site. The jump probabilities are designated as VJUMP for vacancies and ZJUMP for interstitials. After each defect jump the distribution of defects is scanned to monitor defect clustering and annihilation events. The jump distance for a cluster of one, two, or three elemental defects is the interatomic distance (ID). A cluster containing a population (POP) of elemental defects greater than three can be assigned either a zero jump length or reduced jump length ID/POP. This particular reduced jump length recipe for clusters was suggested by the results of atomistic dynamical simulations of defect cluster migration. It cannot be simply related to continuum theory diffusion model results for cluster motion. The upper limit on the size of mobile clusters is an input variable. The time unit used in all of the computer experiments described here is the average time for an interstitial jump.

Annealing of Saturated Defect States

A 0 K saturated defect state containing equal numbers of vacancies and interstitials was set up by running the RINGO Program in the Frenkel pair production mode with VJUMP = ZJUMP = 0. This was done (Run NC-1806) using a 6750 atomic volume (av) cell for a bcc crystal and a 37-av vacancy-interstitial annihilation region. The cell was a cube with side L = 30 half-lattice constant (hlc). The number of elemental defects (179) and the defect state diameter (30 hlc) are comparable to their counterparts in a 15 to 20 keV displacement spike in bcc iron.

This defect state was annealed in two different environments. In one instance, the annealing simulation was done using L = 30 hlc cell with periodic boundary conditions. This type of computer experiment shows how a high-concentration defect state anneals when it is in contact with images of itself on all sides. This approximates the conditions under which the central part of a large displacement spike anneals. In the second instance, the annealing simulation was done using L = 300 hlc cell with periodic boundary conditions. This cell size so much exceeds the size of the initial defect state that the annealing simulation corresponds to annealing in an otherwise defect-free environment. The defect interaction radii used in the annealing runs were the same as those used in preparing the initial saturated defect state. They are defined in Table 1. All defects in the initial, saturated distribution were mobile and a common clustering radius was used for vacancies and interstitials to give equivalent defects with respect to clustering behavior.

Discussion is centered on the first run in the series of ten annealing simulations (NC-1873 Series) because the annealing time and the surviving defect fraction for this run were closer to the average for the series than

TABLE 1—*Annealing parameters used in the saturated-defect state annealing runs.*

Parameter	Assigned Value
Interstitial clustering radius	2.86 hlc[a]
Vacancy clustering radius	2.86 hlc
Annihilation interaction radius	3.29 hlc
Largest mobile cluster size[b]	3

[a] Half-lattice constant.
[b] Size means number of defects in a cluster.

were those for any other run. A plot of the number of vacancies (NVAC) versus annealing time (T) is given in Fig. 1. Table 2 lists the defect size

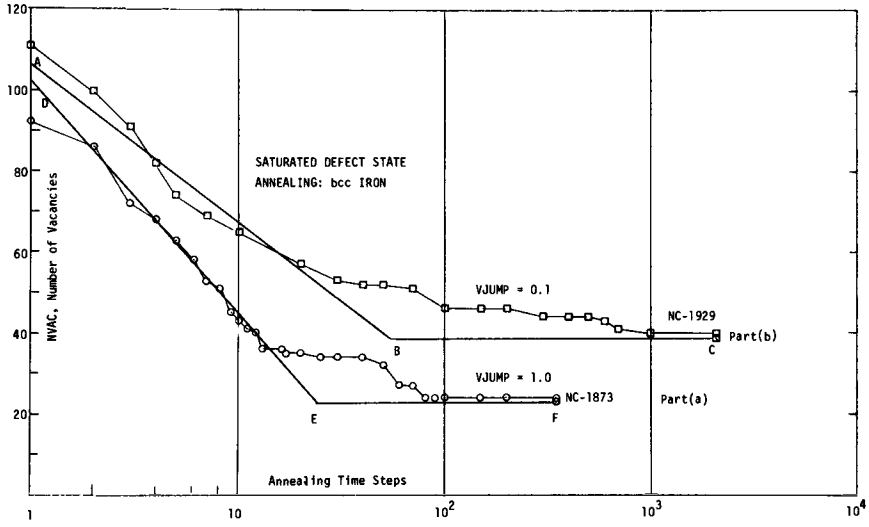

FIG. 1—*Number of vacancies during saturated-defect state annealing in bcc iron. The time unit is the average time between interstitial jumps. Part* (a) *VJUMP = 1.0; Part* (b) *VJUMP = 0.1.*

distributions at selected times during annealing. Defect annihilation took place in two clearly defined stages. The first stage occurred between $T = 0$ and $T = 15$, during which 80 percent of the defects initially present were annihilated. The defect population remained nearly stationary between $T = 15$ and $T = 40$. At $T = 40$, a second annihilation stage began and continued until $T = 80$. From $T = 80$ to $T = 350$, the only annealing activity consisted of defect clustering. At $T = 350$ all defects had collected into immobile

TABLE 2—*Defect size distributions at times* (a) T = *1,* (b) T = *15,* (c) T = *80, and* (d) T = *344, during annealing of the saturated-defect state.* L = *30 hlc and VJUMP = ZJUMP = 1.0 (Run NC-1873).*

(*a*) T = 1		NVAC = 92		(*b*) T = 15		NVAC = 36	
POPI No.		POPV No.		POPI No.		POPV No.	
1	50	1	32	1	8	1	4
2	9	2	14	2	1	2	4
3	4	3	6	3	2	3	0
4	3	6	1	4	1	4	2
...	...	8	1	5	2	5	2
				6	1	6	1
NID = 66		NVD = 54		NID = 15		NVD = 13	
PCMI[a] = 87		PCMV[b] = 85		PCMI = 44		PCMV = 33	
(*c*) T = 80		NVAC = 24		(*d*) T = 344		NVAC = 23	
POPI No.		POPV No.		POPI No.		POPV No.	
1	3	4	2	4	1	5	2
4	1	5	2	5	1	6	1
5	2	6	1	6	1	7	1
7	1	...	...	8	1	...	...
NID = 7		NVD = 5		NID = 4		NVD = 4	
PCMI = 12		PCMV = 0		PCMI = 0		PCMV = 0	

[a]Percent mobile interstitials: fraction of all interstitials contained in clusters with POPI $\leqslant 3$.
[b]Percent mobile vacancies: fraction of all vacancies contained in clusters with POPV $\leqslant 3$.

clusters and the annealing run terminated. There were 23 surviving vacancies (interstitials) of the 179 vacancies present at the beginning of annealing. This constitutes a 13 percent survival fraction. It is characteristic of annealing at the center of a large displacement spike.

Figure 2 describes the fraction of vacancies in immobile clusters and interstitials in immobile clusters during annealing. One sees that clustering activity occurs between $T = 0$ and $T = 22$. Between $T = 22$ and $T = 41$ there is a lull in clustering activity. Clustering begins anew at $T = 42$ and all vacancies become collected in immobile clusters at $T = 72$. All interstitials become collected in immobile clusters at $T = 350$.

In this particular run, vacancies collected themselves into a set of immobile clusters sooner than did the interstitials. This was purely accidental since each of the two defect types was assigned an identical clustering interaction radius, annihilation interaction radius, and jump rate. In another run it would be just as likely that interstitials would form the first set of immobile defect clusters. In the ten-run NC-1873 Series, there was an even split between vacancies and interstitials as the first species to form a set of immobile clusters. The equivalence of the two defect types shows up in the final defect size distribution given in Table 2. Note that the average cluster

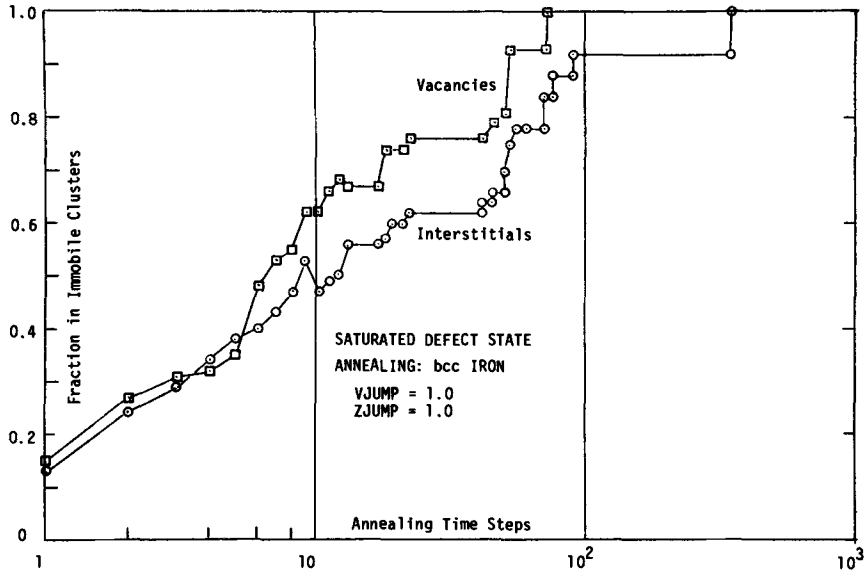

FIG. 2—*Fraction of vacancies and interstitials in immobile clusters during saturated-defect state annealing in bcc iron when VJUMP = 1.0. The time unit is the average time between interstitial jumps.*

size is 5.75 elemental defects for both vacancies and interstitials. A common average defect cluster size for vacancies and interstitials occurred in each of the ten runs.

A second series of ten runs (NC-1929 Series) was made to explore the effect of reducing the vacancy jump rate from VJUMP = 1.0 to VJUMP = 0.1 while retaining the interstitial jump rate at ZJUMP = 1.0. The number of vacancies versus annealing time is plotted in Part (b) of Fig. 1, and the fractions of vacancies and interstitials in immobile clusters are plotted in Fig. 3. Note that the slope of the initial trend line AB for the VJUMP = 0.1 data points in Fig. 1 is less than that for the VJUMP = 1.0 data points trend line DE. Examination of defect position maps shows that the intersection of the initial and final trend lines on an NVAC versus annealing time plot corresponds approximately to the time at which the initial annihilation stage sets up a locally segregated defect state. Reduction of the vacancy jump rate delays the onset of segregation, appears to extend the time required to complete the second annihilation stage, and increases the average number of surviving defects. The average number of surviving defects was 26 for VJUMP = 0.1 and 24 for VJUMP = 1.0.

The time required to collect all defects into immobile clusters increased from $T = 350$ to $T = 2264$. Clustering activity is described in Fig. 3. In this instance, the vacancy curve lags the interstitial curve by roughly a factor of

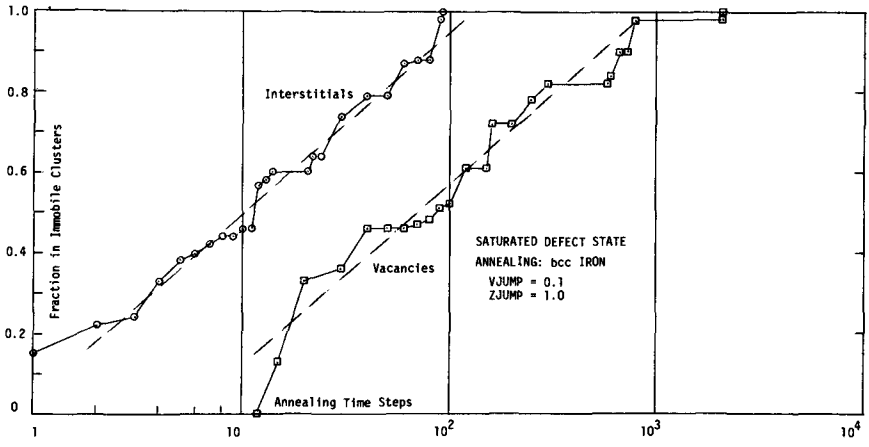

FIG. 3—*Fraction of vacancies and interstitials in immobile clusters during saturated-defect state annealing in bcc iron when VJUMP = 0.1.*

eight on the time scale. This separation occurred for each of the ten runs in the series and demonstrates that, given equal clustering and annihilation interaction radii, the defect with the largest jump rate exhibits the greatest clustering rate.

The nature of the NVAC versus annealing time curves and the fraction of defects in immobile clusters curves are not changed by annealing in a defect-free environment. The major effect of the defect-free environment is to enhance the number of surviving defects. This enhancement comes about by way of defect escape into the defect-free region. There appears to be an increase also in the fraction of the defects which are free defects. Table 3

TABLE 3—*Saturated-defect state annealing. Number of surviving vacancies (interstitials). Annealing parameters are given in Table 1.*

Environment	VJUMP = 1.0 ZJUMP = 1.0	VJUMP = 0.1 ZJUMP = 1.0
Saturated	24	26
Defect-free	36	42

describes the surviving defect populations for defect-free and saturated-environment runs.

Saturated-defect state annealing simulations also were done using VJUMP/ZJUMP ratios of 0.05 and 0.0. The principal effect of decreasing the VJUMP/ZJUMP ratio is to increase the fraction of free vacancies and the defect survival fraction. At 600°C (1112°F), for example, the thermal

equilibrium jump ratio would be about VJUMP/ZJUMP = 0.01. At this ratio, interpolation gives survival fractions of 0.19 and 0.23 for annealing in saturated and defect-free environments, respectively. Because the number of free defects is determined largely during the first 15 to 100 defect jumps, the free vacancy fraction does not change significantly as VJUMP/ZJUMP changes from 0.01 to 1.0. During the initial annihilation stage, defect interactions make the effective vacancy jump rate larger than that for an isolated vacancy in a thermal equilibrium environment, relative to the interstitial jump rate. This is shown in dynamical computer experiments on vacancy and interstitial movement in an initially *saturated* defect state. In view of these order of magnitude considerations, the use of the ratios VJUMP/ZJUMP = 0.1 and 1.0 was decided for the present discussion.

Displacement Spike Annealing (*A*)

Annealing computer experiments for 20-keV spikes C05 and C11 are considered in this section. These spikes were generated in bcc iron by the CASCADE-CLUSTER Program.[4] The annealing parameters used are identical to those used in the saturated-defect state annealing computer experiments. Each spike was annealed for 10^5 time steps with VJUMP = 0.1 and ZJUMP = 1.0. The initial defect cluster size distributions for spikes C05 and C11 are typical for 20-keV displacement spikes in bcc iron. At the onset, 41 percent of the vacancies in spike C05 were in immobile clusters and 28 percent of the vacancies in spike C11 were in immobile clusters. All interstitials in each spike were in mobile defect configurations.

The trend lines for the C05 spike NVAC plot intersect at about $T = 300$ in Fig. 4. Of the two spikes, C05 has the largest fraction of vacancies in immobile clusters at $T = 0$. Although not shown in this paper, the trend lines for the C11 spike intersect at $T = 1000$. The defect survival fractions at $T = 10^5$ are 25 percent and 22 percent, respectively, for spikes C05 and C11.

The defect type with the largest jump rate also had the largest fraction of elemental defects in immobile clusters in the defect-free environment annealing computer experiments for a saturated, random distribution of vacancies and interstitials. As a consequence, the curve for the fraction of vacancies in immobile clusters always fell below that for interstitials when VJUMP was less that ZJUMP. Equal clustering interaction radii were assigned to vacancies and interstitials in the C05 and C11 spike annealing simulations, and VJUMP = 0.1 and ZJUMP = 1.0 were assigned as well. As shown in Fig. 5, however, the curve for the fraction of vacancies in immobile clusters always exceeded that for interstitials in the C05 annealing runs. This relative standing is opposite to that which occurred in the

[4] Besco, D. G. and Baumbardt, N. R., General Electric Report GEMP-356, April 1965.

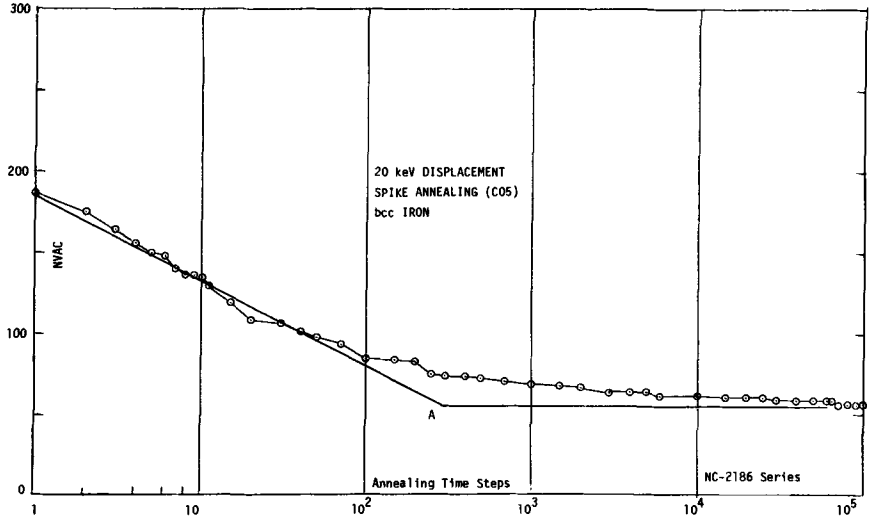

FIG. 4—*Number of vacancies during 20-keV displacement spike annealing in bcc iron when VJUMP = 0.1.*

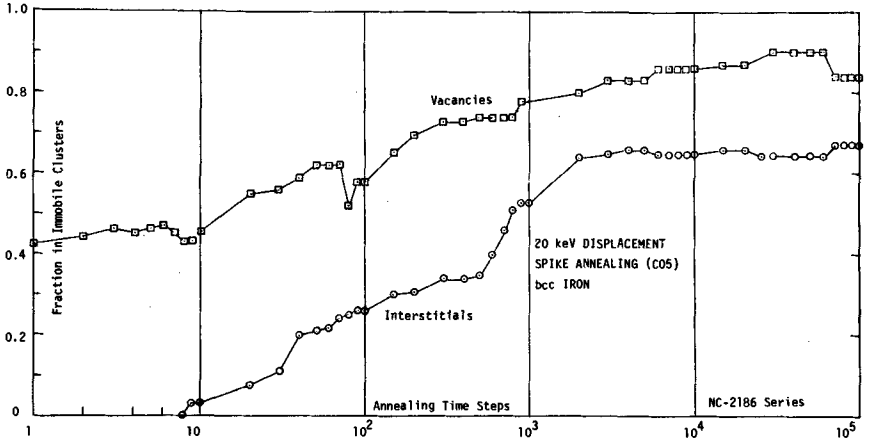

FIG. 5—*Fraction of vacancies and interstitials in immobile clusters during 20-keV displacement spike annealing in bcc iron when VJUMP = 0.1.*

saturated-defect state annealing runs. We conclude that this reversal occurs because the influence exerted by the initial centralized vacancy distribution and peripherally dispersed interstitial distribution in a displacement spike on the vacancy immobile cluster content overrides the influence of a slower vacancy jump rate for $0.1 \leqslant \text{VJUMP/ZJUMP} \leqslant 1.0$. Table 4 describes how

TABLE 4—*Defect size distributions at* (a) T = *1,* (b) T = *100,* (c) T = 10^4, *and* (d) T = 10^5, *during the annealing of Spike C05 in bcc iron in a defect-free environment. The annealing parameters are given in Table 1.*

(*a*) T = 1		NVAC = 186	
POPI No.		POPV No.	
1	150	1	40
2	15	2	26
3	2	3	5
NID = 167		4	3
PCMI = 100		5	4
		6	1
		7	3
		9	1
		11	1
		NVD = 84	
		PCMV = 58	

(*b*) T = 100		NVAC = 84	
POPI No.		POPV No.	
1	28	1	17
2	8	2	6
3	6	3	2
4	4	4	3
6	1	5	4
		7	1
NID = 47		10	1
PCMI = 74		NVD = 34	
		PCMV = 42	

(*c*) T = 10^4		NVAC = 62	
POPI No.		POPV No.	
1	7	1	1
2	6	2	1
3	1	3	2
4	4	4	3
5	1	5	2
6	2	6	2
7	1	7	1
—	—	12	1
NID = 22		NVD = 13	
PCMI = 35		PCMV = 14	

(*d*) T = 10^5		NVAC = 57	
POPI No.		POPV No.	
1	6	3	3
2	5	4	3
3	1	5	1
4	4	6	2
5	2	7	1
6	2	12	1
NID = 20		NVD = 11	
PCMI = 33		PCMV = 16	

the defect cluster size distributions change as annealing proceeds. The most durable portion of the vacancy cluster distribution is that for clusters of six or more vacancies.

Displacement Spike Annealing (*B*)

This section concerns the annealing of 20-keV displacement spikes in fcc iron generated by the COLLIDE Program.[5] Five spikes were annealed for 10^5 time steps for each of four different annealing parameter assignments in this study. The annealing parameter assignments for each case are defined in Table 5. The example selected for discussion is that from Case I in which the number of surviving defects was closest to the average of 38 out of 201.

[5] Beeler, J. R., U.S. Progress Report ORO-3912-21, Energy Research and Development Administration, April 1973.

TABLE 5—*Annealing parameters used in a four-case study on displacement spike annealing behavior in fcc iron.*

Parameter	Case I	Case II	Case III	Case IV
Interstial clustering radius	6 hlc	6 hlc	3 hlc	3 hlc
Vacancy clustering radius	2.8 hlc	2.8 hlc	2.8 hlc	2.8 hlc
Annihilation interaction radius	3 hlc	3 hlc	3 hlc	3 hlc
Largest mobile cluster size	20	3	20	3

Many of the conditions for this run are different from those in the bcc iron displacement spike study. There is an imporant difference in the initial cluster size distribution, the average cluster size in the fcc displacement spike instance being smaller than that for the bcc displacement spike instances. There are, in addition, three important differences in the annealing parameter assignments: (*a*) the interstitial clustering interaction radius exceeds the annihilation interaction radius in Case I; (*b*) defects with $3 > \text{POP} \leqslant 20$ can move in Case I, but with a very small jump length; and (*c*) VJUMP = ZJUMP.

NVAC versus the annealing time is plotted in Fig. 6 and the fraction of vacancies and interstitials in immobile clusters is plotted in Fig. 7. The average final trend line for Case I spikes is at NVAC = 38. The trend line

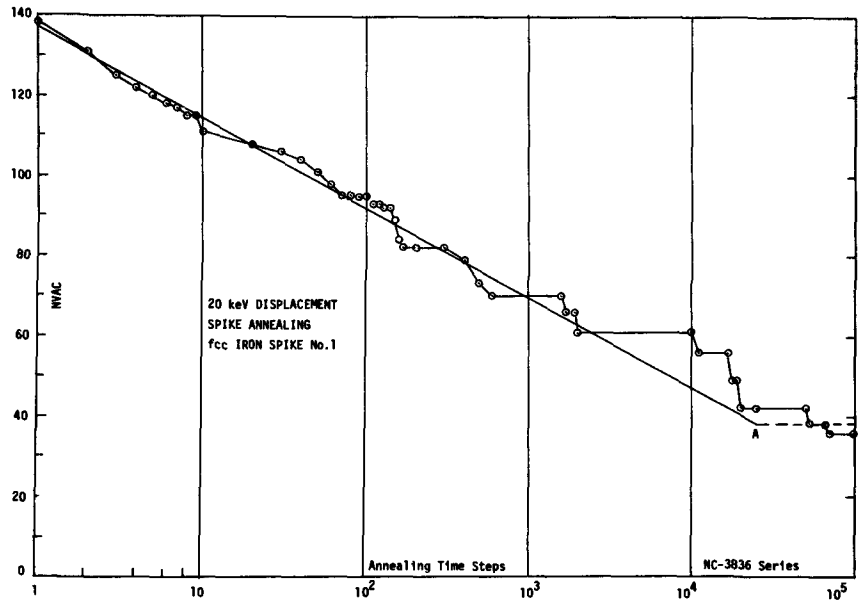

FIG. 6—*Number of vacancies during 20-keV displacement spike annealing in fcc iron when VJUMP = 1.0.*

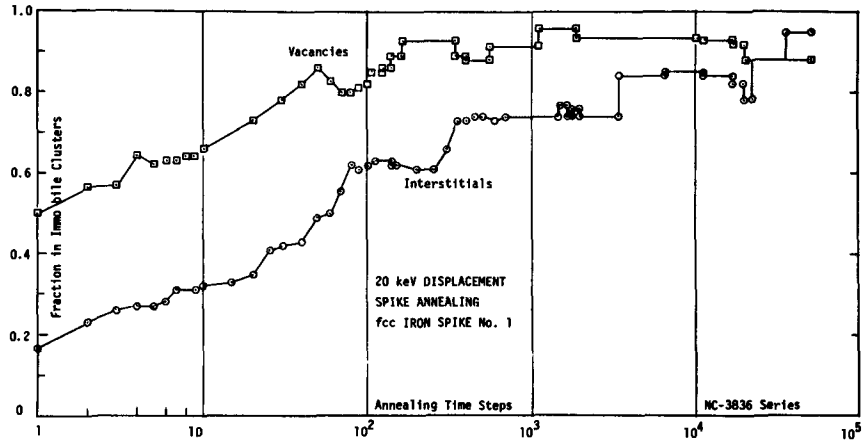

FIG. 7—*Fraction of vacancies and interstitials in immobile clusters during 20-keV displacement spike annealing in fcc iron when VJUMP = 1.0.*

intersection for the present spike is at 2.5×10^4, the maximum intersection time observed. This feature is pertinent because it appears to represent a tendency for the large cluster migration option (model) to delay the local segration of defects.

The fraction of vacancies and interstitials contained in various cluster sizes and the total elemental defect population after 30 000 jumps appear in Tables 6 and 7 for vacancies and interstitials, respectively, for all four cases. The results in these tables show the following:

1. Cluster mobility enhances defect annihilation. Note that the number of

TABLE 6—*Vacancy cluster size distribution and number of surviving vacancies after annealing for 30 000 time steps with VJUMP = ZJUMP = 1.0, for each of the four cases defined in Table 5.*

Cluster Size	Fraction of Vacancies			
	Case I	Case II	Case III	Case IV
1 to 3	0.107	0.023	0.122	0.088
4 to 10	0.274	0.913	0.554	0.754
11 to 20	0.358	0.063	0.221	0.158
> 20	0.260	0.0	0.103	0.0
	Number of Vacancies			
	Case I	Case II	Case III	Case IV
NVAC	43	85	38	52
FV	4.6	2.0	4.6	4.6
IMV	38.4	83.0	33.4	47.4

TABLE 7—*Interstitial cluster size distribution and number of surviving interstitials after annealing for 30 000 time steps with VJUMP = ZJUMP = 1.0 for each of the four cases defined in Table 5.*

Cluster Size	Fraction of Interstitials			
	Case I	Case II	Case III	Case IV
1 to 3	0.144	0.106	0.394	0.323
4 to 10	0.595	0.749	0.465	0.677
11 to 20	0.139	0.146	0.141	0.0
> 20	0.121	0.0	0.0	0.0
	Number of Interstitials			
	Case I	Case II	Case III	Case IV
NINT	43	85	38	52
FI	6.2	9.0	15.0	16.8
IMI	36.8	76.0	23.0	35.2

surviving vacancies (interstitials) is greatest for the two cases (II and IV) with the smallest upper bound on the mobile cluster size.

2. An increase in the interstitial clustering interaction radius enhances defect survival. Note that the number of surviving vacancies in Case I is 13 percent larger than that for Case III. These two cases differ only in that a larger interstitial cluster interaction radius is assigned in Case I.

3. An increase in the interstitial cluster interaction radius causes an increase in both the average interstitial cluster size and the average vacancy cluster size.

4. In each case there are more free interstitials than free vacancies.

5. Small clustering radii and cluster immobility enhance the number of free defects (Case IV).

6. Large clustering radii and cluster immobility enhance defect survival (Case II); hence, impurity atom trapping at clusters should enhance defect survival.

Summary and Conclusions

Displacement spike annealing is a cyclic process in which vacancies and interstitials alternately become mixed together and then experience localized segregation as a consequence of annihilation events that occur during the mixing stage. The result of annealing an infinite spike is a collection of immobile defect clusters. For this reason, annealing normally transforms the center region of a large displacement spike into a collection of immobile clusters. Free defects occur when a spike is annealed in a defect-free environment. Because the displacement spike vacancy population initially is

centralized and its interstitial population initially is peripherally dispersed, all annealing models explored thus far predict a greater number of free interstitials than free vacancies. Cluster migration increases the number of annihilation events as well as increasing the average cluster size. An increase in the clustering radius for any defect species lowers the number of annihilation events and increases the number of defects contained in immobile clusters.

All annealing models explored thus far indicate that displacement spike annealing divides naturally into two distinct regimes: (*a*) a short-term annealing regime, covering a span of 10^4 to 10^5 jumps per interstitial; (*b*) a long-term annealing regime. In short-term annealing, the migration of each defect is heavily influenced by interactions with neighboring defects in the parent spike. In long-term annealing, however, each defect migrates independently of other defects until its migration history ends at a sink. In somewhat less exact terms, a mobile defect loses its identity with its parent displacement spike during short-term annealing and becomes part of a general, uniformly distributed source of mobile defects. As a member of this general source, it diffuses isotropically during the long-term annealing regime until it is captured by a sink, usually a sink not related to its parent displacement spike.

Acknowledgments

This work was supported by U.S. ERDA Contract AT-(40-1)-3912 and by computer funds supplied by North Carolina State University.

D. G. Doran[1] *and N. J. Graves*[1]

Neutron Displacement Damage Cross Sections for Structural Metals

REFERENCE: Doran, D. G. and Graves, N. J., "**Neutron Displacement Damage Cross Sections for Structural Metals,**" *Irradiation Effects on the Microstructure and Properties of Metals, ASTM STP 611,* American Society for Testing and Materials, 1976, pp. 463–482.

ABSTRACT: Irradiation test data on reactor structural materials should include, in addition to fluence, the displacing dose expressed as displacements per atom (dpa) or damage energy per atom (depa). This provides a spectrum-dependent parameter that serves as a starting point for data correlations, as well as an exposure unit that is common to both neutron and charged-particle irradiations. To make this possible, displacement damage cross sections for neutrons have been calculated for aluminum, vanadium, chromium, iron, nickel, copper, zirconium, columbium, molybdenum, tantalum, tungsten, lead, and stainless steel using evaluated nuclear data files (ENDF/B-IV) data and the Lindhard energy partition model. These data extend to 20 MeV, hence cover the energy ranges of primary interest for both fission and fusion reactor applications. Tables are given in a standardized energy group structure. Figures are included to show the relative contributions of the various neutron scattering processes to both the primary knock-on atom spectra and the damage cross sections. A brief description of calculational procedures is given.

KEY WORDS: radiation, neutron irradiation, cross sections, radiation damage, structural metals, displacement damage

A major challenge in radiation damage studies of structural metals is the control of all the significant variables in the experimentation phase and the proper accounting for differences in these variables in the analysis phase. One of these variables is neutron spectrum. While some selection of spectra is possible, it is not generally feasible to match the test spectra to the spectra to which a material will be exposed. Important current examples are pressure vessel surveillance for thermal reactors and materials development for liquid metal fast breeder reactors (LMFBR's). In the former, accelerated surveillance specimens are exposed not only to a

[1] Fellow scientist and computer analyst, respectively, Hanford Engineering Development Laboratory, Westinghouse Hanford Company, Richland, Wash. 99352.

higher flux but also to a different neutron spectrum than seen by the vessel. In the latter case, many of the data are being obtained in the Experimental Breeder Reactor-II (EBR-II) spectra which are harder than the design spectra, due in part to the need for high-fluence data; high flux implies hard spectrum in EBR-II. Another example, of increasing importance, is the unavailability of high-flux neutron sources that are hard enough to simulate many of the spectra anticipated in fusion reactors.

The need to account for the neutron energy dependence of radiation damage has spawned two developments. One is the use of spectrum-dependent exposure units and the other is the development of semi-empirical effective damage functions (EDF) to describe the energy dependence of a particular damage state [*1*].[2] The former has evolved steadily from $\Phi t(E > 1 \text{ MeV})$ to $\Phi t(E > 0.1 \text{ MeV})$ to total displacements per atom (dpa). The energy dependence of an EDF is determined by experimental data if sufficient data exist; if not, the shape of the EDF is influenced by the *a priori* assumed energy dependence. Under conditions such that helium production is not considered a dominant damage mechanism, the assumed EDF shape is generally a displacement cross section. Thus both developments have in effect converged on the need for displacement cross sections for various materials and their application to define displacement rates in existing and proposed irradiation facilities.

Building on earlier work of Jenkins [*2*] and Sheely [*3*], displacement cross sections for several materials were developed [*4–7*]. These cross sections have been subsequently modified to include additional reactions and to reflect new cross-section evaluations. This paper includes results for a number of common metals based on the most recent version of the evaluated nuclear data files (ENDF/B-IV).

Calculational Procedures

General Approach

The approach used is generally as described previously [*4*] and will not be repeated in detail here. The general expression for the displacement cross section at neutron energy E due to a reaction of type i is

$$\sigma_d^i(E) = \sigma^i(E) \int_{-1}^{\mu_{\max}} p(E, \mu) \nu[T(E, \mu)] d\mu \qquad (1)$$

where T is the kinetic energy in the laboratory system of the primary knock-on atom (PKA) which is scattered at a center-of-mass angle $\phi = \cos^{-1} \mu$ with the probability $p(E, \mu)$. The value of $\mu_{\max}$ can be taken as $+1$ except for low-energy elastic scattering for which $\mu_{\max} = 1 - (2T_d/T_{\max})$;

[2] The italic numbers in brackets refer to the list of references appended to this paper.

$T_{max} = 4AE/(1 + A)^2$, the maximum knock-on energy in an elastic collision of a neutron with an atom of atomic weight A. T_d is an effective displacement energy. The function $\nu(T)$ describes the number of secondary displacements produced by the PKA in coming to rest. As in earlier work [*4*], the Lindhard energy partition model was used to define the fraction of energy not dissipated to electrons and hence available to cause displacements. Designating this energy by T_{DAM}, the conversion to displacements was by a simple proportionality factor [*8,9*]

$$\nu(T) = \frac{0.8}{2T_d} \cdot T_{DAM} \tag{2}$$

Because this assumption of proportionality is questionable and because there is not universal agreement on T_d values, a damage energy cross section (σ_{dam}) can be defined by replacing $\nu(T)$ in Eq 1 with $T_{DAM}(T)$. The tables included in this paper contain such cross sections. The advantage of this presentation is that the tabulated values are independent of T_d for sufficiently high E (namely, $2T_d/T_{max} \ll 1$). Since this independence is not complete, the values of T_d used in the computations are given in Table 1. Clearly, σ_{dam} can be converted to σ_d by multiplying by $0.8/2T_d$.

TABLE 1—*Effective displacement energies and estimated damage energies due to* (n, γ) *recoils.*

Metal	Mat[a]	T_d, eV	T_{DAM}^{γ}, eV
Al	1193	25	640
V	1196	40	380
Cr	1191	40	590
Fe	1192	40	420
Ni	1190	40	530
Cu	1295	30	380
Zr	1284	40	140
Nb	1189	60	97
Mo	1287	60	100
Ta	1285	90	3
W	1128-1131	90	13
Pb	1288	25	140

[a]ENDF/B material designation.

Both σ_d and σ_{dam}, when multiplied by a fluence, have been used as irradiation exposure indices. The former provides a useful physical model lacking in the latter and has become universally used in radiation damage studies with charged particles. When either index is used as a correlation parameter, the basic assumption is that the damage is indeed proportional to the so-called damage energy.

Treatment of Specific Reactions

1. (n, γ). This is the only reaction type omitted in the current work. Past experience has indicated this contribution to be negligible in various fast and thermal reactor spectra. However, an upper-bound estimate to the damage energy cross section can be easily obtained [4] by multiplying the energy-dependent (n, γ) cross section by $T_{\mathrm{DAM}}{}^{\gamma} = f \cdot T_{\gamma}$ where the recoil energy T_{γ} due to gamma ray emission is given by

$$T_{\gamma} = \overline{[E_{\gamma}(\mathrm{MeV})]^2}/(0.00186)(A + 1) \tag{3}$$

The numerator of Eq 3 is the mean square gamma energy determined from the gamma-ray energies and abundances tabulated by Orphan et al [10]. The damage energy fraction f ranges between 0.8 and 1. Values of $T_{\mathrm{DAM}}{}^{\gamma}$ are included in Table 1. The recoil energy is taken here to be independent of the neutron energy; when the neutron energy is high enough to invalidate this assumption, the (n, γ) contribution can be neglected relative to other reactions.

2. Elastic (n, n), and inelastic (n, n'). These were treated as described previously [4]. Anisotropy was included in all cases where appropriate data were given in the ENDF/B files.

3. $(n, 2n)$ and $(n, 3n)$. The secondary neutron emission spectra given in the ENDF/B file for $(n, 2n)$ and $(n, 3n)$ reactions do not distinguish between the emitted neutrons. An approximate treatment of the $(n, 2n)$ case was given previously [4]. An analogous treatment was used for $n, 3n$ reactions. It turns out that the results in both cases do not differ greatly from the simpler one-neutron treatment.

4. Charged-particle-out reactions (n, c). Some estimates of contributions of (n, c) reactions to displacement cross sections were made previously by simply approximating the number of displacements per reaction at a given neutron energy by the (n, n') value at that energy [5]. (This is quite reasonable so long as alpha particle emission is minor.) Subsequently, calculations were made using an evaporation model similar to that used for energetic (n, n') reactions [11]. The (n, c) reactions differ from (n, n') reactions in that first, the emitted particle must overcome a Coulomb barrier, and second, there is a reaction Q-value accounting for the difference in masses of the target and product nuclei. In particular, if $Q < 0$, there is an energy threshold for the reaction given by $E' = (A + 1)\, Q/A$. The presence of a Coulomb barrier effectively shifts the spectrum of emitted particles to the higher energies needed to overcome the barrier. It also causes the cross section to drop rapidly at lower energies, creating an apparent threshold even for exoergic reactions. Another distinction between (n, n') and (n, c) reactions is that the mass of the

charged particle may exceed that of a neutron and thereby enhance the recoil of the residual nucleus.

The model used here assumes compound nucleus formation with isotropic particle emission. The energy W available in the center-of-mass system (CM) for kinetic energy of the products is assumed to be distributed as

$$f(E, W) = We^{-W/\theta(E)}/I \tag{4}$$

where E is the energy of the incident neutron (laboratory system) and I is a normalization constant. The nuclear temperature θ can be expressed in terms of the excitation energy E^* of the residual nucleus

$$\theta(E) = (E^*/s)^{1/2} \tag{5}$$

Assume for the moment that E^* is large and that, for a particle to escape, its energy must exceed an effective Coulomb barrier given by

$$\varkappa E_b = \varkappa Z_{rn} Z_c e^2/(R + \varrho) \tag{6}$$

where

$Z_{rn}e$ and Z_ce = charges of the residual nucleus and emitted particle, respectively,
R = the nuclear radius ($= 1.5 \times 10^{-13} A^{1/3}$ cm), and
ϱ = a correction for the finite size of the emitted particle.

The constant $\varkappa$, which varies between 0.4 and 1 depending on Z_{rn} and Z_c, is evaluated empirically to fit cross-section data [*12*]. The mean energy (in CM), $\bar{E}_p$, of the emitted particle (atomic weight A_p) is then approximately $2\theta + \varkappa E_b$. Now

$$E^* = \frac{A}{A + 1} E + Q - E_p \tag{7}$$

Then, using $E_p \cong \bar{E}_p$ in Eqs 5 and 7 yields the high excitation energy approximation [*12*]

$$\theta(E) = \left[\frac{\dfrac{AE}{A + 1} + Q - \varkappa E_b}{s} \right]^{1/2} \tag{8}$$

From Eq 8, the effective neutron energy threshold is $E' = (A + 1) \times (\varkappa E_b - Q)/A$. The reaction cross section, however, generally vanishes at a lower energy than this. The reason is that a charged particle can escape at a lower energy than $\varkappa E_b$, although the barrier transmission probability decreases rapidly with decreasing energy. When E is low, the excitation of the compound nucleus is low, the energy spectrum of the charged particle becomes softer, and the approximation for $\bar{E}_p$ used in deriving Eq 8 is no longer appropriate. It is inconsistent with the evaporation model to permit the excitation energy of the residual nucleus to approach zero. Hence, as a rather arbitrary treatment at low neutron energies, the numerator of Eq 7 was not permitted to fall below 1 MeV. For these low-energy cases the energy spectrum of the emitted particle was extended to 0.

The values of s were calculated following Newton [*13*] as

$$s = 0.06204 \left[\frac{(2JZ + 1) + (2JN + 1)}{2}\right] A_{rn}^{2/3} \tag{9}$$

using effective spin values for the residual nucleus (atomic weight A_{rn}) tabulated by Pearlstein [*14*]. The normalization constant is

$$I = \theta^2 \left\{ \left(1 + \frac{W_{\min}}{\theta}\right) e^{-W_{\min}/\theta} - \left(1 + \frac{W_{\max}}{\theta}\right) e^{-W_{\max}/\theta} \right\} \tag{10}$$

The displacements are due predominantly to the recoil energy of the residual nucleus. Conservation of momentum leads to

$$T = \frac{A_p}{A_{rn}} E_p = \frac{A_{rn}}{(A + 1)^2} E - \frac{(4A_p E_p E)^{1/2}}{A + 1} \mu \tag{11}$$

Assuming isotropic emission, that is, $p(E, E_p, \mu) = \frac{1}{2}$, a generalized Eq 1 becomes

$$\sigma_d^{n,c}(E) = \sigma_{n,c}(E) \int_{W_{\min}}^{W_{\max}} f(E, W) \int_{-1}^{1} \nu[T(E, E_p, \mu)] d\mu dw \tag{12}$$

The foregoing treatment was used for reactions in which only one particle is emitted. The $(n, n'p)$ and $(n, n'\alpha)$ reactions were included by simply adding the cross sections to the (n, p) and (n, α) cross sections, respectively.

Results

PKA Spectra

The codes used in this work provide for specific calculation of PKA

spectra at a preselected set of neutron energies. A few spectra for iron are shown in Fig. 1 to illustrate their general energy dependence. As the

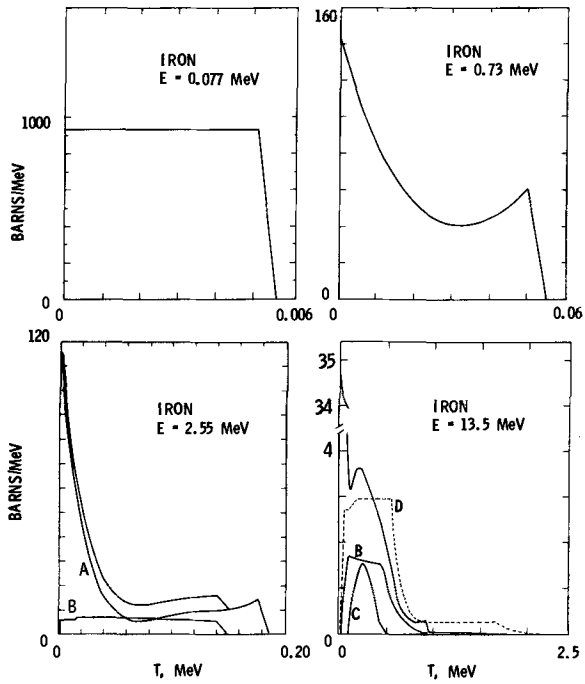

FIG. 1—*PKA spectra for iron at several neutron energies. Below ~0.1 MeV neutron scattering is elastic and isotropic, resulting in a flat PKA spectrum. The anisotropy increases with increasing energy and nonelastic scattering processes become important. The various contributions are designated by* A(n, n), B(n, n′), C(n, 2n), *and* D(n, c). *For clarity, the* (n, n) *contribution was omitted and the* (n, c) *contribution multiplied by 10 at 13.5 MeV.*

neutron energy is increased, the elastic scattering contribution to the PKA spectrum shifts strongly to low energies although still providing the highest-energy PKA's, while the intermediate PKA energy range becomes dominated by nonelastic scattering events. At still higher energies, the (*n, α*) reactions provide a high-energy tail to the PKA spectrum.

Dissected Displacement Cross Sections

The contributions of each reaction type to the displacement cross sections of several materials are shown in Fig. 2. At high *Z*, (*n, c*) reactions are absent (high Coulomb barriers) but (*n, xn*) thresholds are low. The situation is reversed at low *Z*.

Damage Energy Cross Sections

Damage energy cross sections (in eV-barns) are presented in Table 2

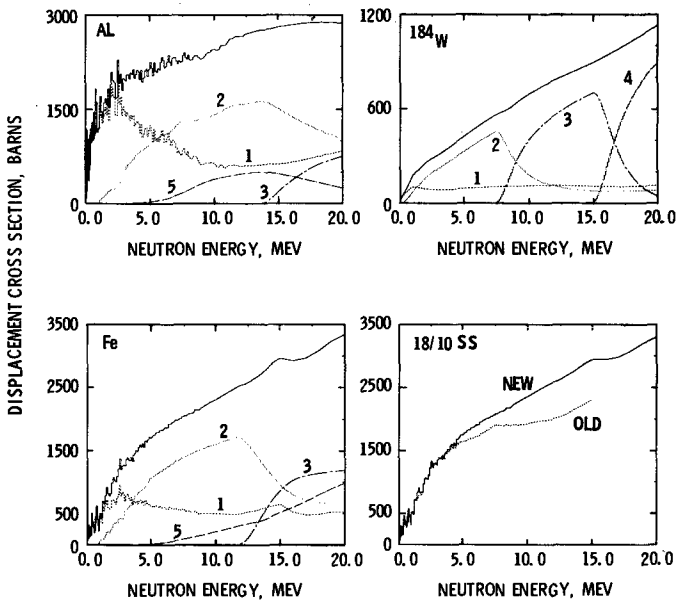

FIG. 2—*The composition of displacement cross sections for* (top left) *aluminum,* (bottom left) *iron, and* (top right) *tungsten. Contributions are designated by 1*(n, n), *2*(n, n′), *3*(n, 2n), *4*(n, 3n), *and 5*(n, c). (Bottom right) *A comparison of the present displacement cross section for 18/10 stainless steel with that of Ref* 4. *The latter has been multiplied by 0.66 to satisfy the recommendations of Refs* 8 *and* 9.

for the metals listed in Table 1 and for an 18Cr-10Ni stainless steel (applicable to Type 300 series steels). All cross-section data are from ENDF/B-IV. As indicated in the foregoing, the currently accepted procedure for converting a damage energy cross section to a displacement cross section is to multiply by the factor $0.8/2T_d$. Except for possible applications to soft spectra, the use of reasonable values of T_d other than those in Table 1 will have a negligible effect on relative magnitudes of spectral-averaged displacement cross sections for a given material. The group structure used in Table 2 was recommended by the Reactor Shielding Information Center at Oak Ridge. No spectrum weighting was used in collapsing the pointwise calculated data to this group structure.

Comparison With Previous Work

The Hanford Engineering Development Laboratory (HEDL) displacement cross section for 18Cr-10Ni stainless steel published earlier [*4,9*] has been used extensively in LMFBR program applications; hence, it is of interest to compare the earlier version with that given here. Such a comparison (see Fig. 2, bottom right) shows that the major differences

TABLE 2—*Damage energy cross sections based on ENDF/B-IV data and a Lindhard energy partition model.*

Group	Lower Energy, MeV	Al(1193) Sigma, eV-barns	V(1196) Sigma, eV-barns	Cr(1191) Sigma, eV-barns	Fe(1192) Sigma, eV-barns	Ni(1190) Sigma, eV-barns	Cu(1295) Sigma, eV-barns	Zr(1284) Sigma, eV-barns
	1.733E+01							
1	1.649E+01	1.791E+05	2.854E+05	2.903E+05	2.963E+05	3.261E+05	3.101E+05	2.554E+05
2	1.568E+01	1.777E+05	2.775E+05	2.893E+05	2.930E+05	3.187E+05	3.041E+05	2.470E+05
3	1.492E+01	1.761E+05	2.702E+05	2.848E+05	2.948E+05	3.113E+05	2.974E+05	2.425E+05
4	1.455E+01	1.745E+05	2.648E+05	2.790E+05	2.927E+05	3.068E+05	2.897E+05	2.383E+05
5	1.419E+01	1.736E+05	2.609E+05	2.780E+05	2.877E+05	3.047E+05	2.828E+05	2.346E+05
6	1.384E+01	1.730E+05	2.569E+05	2.767E+05	2.817E+05	3.025E+05	2.764E+05	2.305E+05
7	1.350E+01	1.726E+05	2.531E+05	2.754E+05	2.752E+05	2.996E+05	2.734E+05	2.269E+05
8	1.284E+01	1.711E+05	2.474E+05	2.736E+05	2.672E+05	2.950E+05	2.693E+05	2.218E+05
9	1.221E+01	1.686E+05	2.411E+05	2.677E+05	2.589E+05	2.895E+05	2.618E+05	2.146E+05
10	1.162E+01	1.663E+05	2.371E+05	2.617E+05	2.536E+05	2.849E+05	2.539E+05	2.090E+05
11	1.105E+01	1.638E+05	2.306E+05	2.547E+05	2.477E+05	2.803E+05	2.464E+05	2.037E+05
12	1.051E+01	1.579E+05	2.263E+05	2.476E+05	2.411E+05	2.755E+05	2.399E+05	1.987E+05
13	1.000E+01	1.532E+05	2.209E+05	2.405E+05	2.345E+05	2.691E+05	2.369E+05	1.943E+05
14	9.512E+00	1.515E+05	2.157E+05	2.337E+05	2.289E+05	2.622E+05	2.321E+05	1.899E+05
15	9.048E+00	1.468E+05	2.110E+05	2.281E+05	2.236E+05	2.549E+05	2.250E+05	1.857E+05
16	8.607E+00	1.445E+05	2.068E+05	2.236E+05	2.175E+05	2.429E+05	2.181E+05	1.815E+05
17	8.187E+00	1.451E+05	2.031E+05	2.197E+05	2.139E+05	2.292E+05	2.115E+05	1.769E+05
18	7.788E+00	1.438E+05	1.995E+05	2.160E+05	2.089E+05	2.263E+05	2.052E+05	1.725E+05
19	7.408E+00	1.456E+05	1.962E+05	2.132E+05	2.055E+05	2.176E+05	1.980E+05	1.675E+05
20	7.047E+00	1.402E+05	1.931E+05	2.094E+05	2.016E+05	2.140E+05	1.915E+05	1.626E+05
21	6.703E+00	1.441E+05	1.904E+05	2.057E+05	1.977E+05	2.107E+05	1.866E+05	1.576E+05
22	6.592E+00	1.376E+05	1.888E+05	2.031E+05	1.957E+05	2.059E+05	1.843E+05	1.534E+05
23	6.376E+00	1.436E+05	1.877E+05	2.017E+05	1.936E+05	2.031E+05	1.826E+05	1.505E+05
24	6.065E+00	1.376E+05	1.859E+05	1.988E+05	1.883E+05	2.017E+05	1.798E+05	1.457E+05
25	5.770E+00	1.417E+05	1.837E+05	1.951E+05	1.846E+05	1.991E+05	1.758E+05	1.403E+05
26	5.488E+00	1.323E+05	1.813E+05	1.916E+05	1.812E+05	1.939E+05	1.705E+05	1.354E+05
27	5.221E+00	1.334E+05	1.787E+05	1.888E+05	1.778E+05	1.859E+05	1.660E+05	1.307E+05
28	4.966E+00	1.359E+05	1.760E+05	1.867E+05	1.730E+05	1.799E+05	1.628E+05	1.262E+05
29	4.724E+00	1.304E+05	1.749E+05	1.836E+05	1.702E+05	1.717E+05	1.590E+05	1.214E+05

TABLE 2—*Continued.*

Group	Lower Energy, MeV	Al(1193) Sigma, eV-barns	V(1196) Sigma, eV-barns	Cr(1191) Sigma, eV-barns	Fe(1192) Sigma, eV-barns	Ni(1190) Sigma, eV-barns	Cu(1295) Sigma, eV-Barns	Zr(1284) Sigma, eV-barns
30	4.493E+00	1.287E+05	1.725E+05	1.793E+05	1.653E+05	1.656E+05	1.545E+05	1.165E+05
31	4.066E+00	1.273E+05	1.699E+05	1.666E+05	1.580E+05	1.585E+05	1.454E+05	1.094E+05
32	3.679E+00	1.291E+05	1.657E+05	1.599E+05	1.494E+05	1.473E+05	1.348E+05	1.009E+05
33	3.328E+00	1.274E+05	1.597E+05	1.525E+05	1.374E+05	1.376E+05	1.247E+05	9.609E+04
34	3.166E+00	1.268E+05	1.570E+05	1.517E+05	1.358E+05	1.267E+05	1.178E+05	9.308E+04
35	3.012E+00	1.227E+05	1.519E+05	1.435E+05	1.375E+05	1.176E+05	1.140E+05	8.967E+04
36	2.865E+00	1.212E+05	1.453E+05	1.395E+05	1.275E+05	1.198E+05	1.097E+05	8.881E+04
37	2.725E+00	1.209E+05	1.431E+05	1.450E+05	1.266E+05	1.184E+05	1.057E+05	8.799E+04
38	2.592E+00	1.228E+05	1.397E+05	1.436E+05	1.220E+05	1.087E+05	1.018E+05	8.729E+04
39	2.466E+00	1.328E+05	1.385E+05	1.329E+05	1.330E+05	1.081E+05	9.818E+04	8.658E+04
40	2.385E+00	1.054E+05	1.290E+05	1.371E+05	1.192E+05	1.030E+05	9.615E+04	8.512E+04
41	2.365E+00	1.047E+05	1.194E+05	1.154E+05	1.096E+05	1.004E+05	9.427E+04	8.284E+04
42	2.346E+00	1.047E+05	1.194E+05	1.154E+05	1.096E+05	1.004E+05	9.427E+04	8.284E+04
43	2.307E+00	1.047E+05	1.194E+05	1.154E+05	1.096E+05	1.004E+05	9.427E+04	8.284E+04
44	2.231E+00	1.188E+05	1.160E+05	1.233E+05	1.014E+05	9.327E+04	9.188E+04	7.949E+04
45	2.123E+00	1.216E+05	1.136E+05	1.225E+05	1.022E+05	9.192E+04	8.955E+04	7.724E+04
46	2.019E+00	1.286E+05	1.042E+05	1.142E+05	1.059E+05	9.062E+04	8.580E+04	7.521E+04
47	1.921E+00	1.210E+05	9.888E+04	9.933E+04	1.004E+05	8.242E+04	8.190E+04	7.336E+04
48	1.827E+00	1.003E+05	1.040E+05	9.361E+04	8.565E+04	7.659E+04	7.860E+04	7.157E+04
49	1.738E+00	1.084E+05	1.038E+05	1.037E+05	7.889E+04	7.481E+04	7.575E+04	6.988E+04
50	1.653E+00	1.054E+05	1.017E+05	9.781E+04	7.962E+04	7.317E+04	7.333E+04	6.855E+04
51	1.572E+00	1.005E+05	9.915E+04	9.205E+04	8.478E+04	7.144E+04	7.133E+04	6.656E+04
52	1.496E+00	1.040E+05	9.611E+04	9.757E+04	9.080E+04	7.044E+04	6.975E+04	6.388E+04
53	1.423E+00	1.002E+05	9.185E+04	1.047E+05	7.855E+04	7.477E+04	6.843E+04	6.311E+04
54	1.353E+00	9.075E+04	8.914E+04	9.108E+04	6.952E+04	7.549E+04	6.815E+04	6.211E+04
55	1.287E+00	8.706E+04	8.662E+04	8.353E+04	6.601E+04	7.550E+04	6.842E+04	6.218E+04
56	1.225E+00	9.081E+04	8.158E+04	7.964E+04	6.974E+04	7.405E+04	7.010E+04	6.450E+04
57	1.165E+00	1.001E+05	8.358E+04	6.635E+04	5.445E+04	6.842E+04	6.711E+04	6.362E+04
58	1.108E+00	1.066E+05	8.498E+04	5.707E+04	4.377E+04	6.449E+04	6.503E+04	6.300E+04
59	1.003E+00	7.706E+04	6.746E+04	5.997E+04	4.992E+04	5.378E+04	6.104E+04	6.172E+04

60	9.616E−01	7.113E+04	6.687E+04	6.568E+04	4.635E+04	5.416E+04	6.058E+04	6.730E+04
61	9.072E−01	7.306E+04	6.934E+04	4.945E+04	2.716E+04	5.397E+04	5.915E+04	7.227E+04
62	8.629E−01	8.256E+04	6.724E+04	6.421E+04	3.529E+04	5.571E+04	5.761E+04	7.244E+04
63	8.209E−01	9.838E+04	5.908E+04	5.715E+04	4.082E+04	4.897E+04	5.735E+04	6.816E+04
64	7.808E−01	1.046E+05	4.688E+04	4.858E+04	5.115E+04	4.955E+04	5.518E+04	6.773E+04
65	7.427E−01	9.350E+04	4.562E+04	4.817E+04	6.123E+04	4.110E+04	5.309E+04	6.848E+04
66	7.065E−01	6.819E+04	4.905E+04	4.928E+04	5.073E+04	3.603E+04	5.219E+04	6.709E+04
67	6.721E−01	6.544E+04	5.275E+04	3.136E+04	4.016E+04	4.031E+04	5.047E+04	6.387E+04
68	6.393E−01	8.100E+04	5.046E+04	5.370E+04	3.079E+04	4.519E+04	4.886E+04	6.061E+04
69	6.081E−01	7.081E+04	4.471E+04	5.355E+04	2.028E+04	4.850E+04	4.862E+04	6.018E+04
70	5.784E−01	6.800E+04	4.501E+04	3.956E+04	2.555E+04	3.870E+04	4.691E+04	6.151E+04
71	5.502E−01	7.525E+04	3.599E+04	4.523E+04	2.699E+04	3.164E+04	4.576E+04	6.143E+04
72	5.234E−01	7.975E+04	3.314E+04	4.129E+04	3.010E+04	3.790E+04	4.522E+04	5.932E+04
73	4.979E−01	6.050E+04	3.620E+04	3.489E+04	3.605E+04	3.978E+04	4.375E+04	5.629E+04
74	4.505E−01	6.556E+04	3.887E+04	4.117E+04	3.103E+04	3.995E+04	4.327E+04	5.427E+04
75	4.076E−01	7.144E+04	3.898E+04	4.246E+04	4.358E+04	3.738E+04	3.528E+04	5.203E+04
76	3.877E−01	4.900E+04	3.537E+04	2.752E+04	5.066E+04	2.760E+04	3.400E+04	4.650E+04
77	3.688E−01	5.576E+04	3.739E+04	2.128E+04	3.791E+04	3.257E+04	3.366E+04	4.302E+04
78	3.337E−01	4.366E+04	3.647E+04	2.357E+04	2.122E+04	3.942E+04	3.247E+04	3.937E+04
79	3.020E−01	4.969E+04	4.125E+04	2.023E+04	2.094E+04	3.553E+04	3.311E+04	3.679E+04
80	2.985E−01	5.983E+04	4.059E+04	1.671E+04	1.638E+04	3.834E+04	3.280E+04	3.582E+04
81	2.972E−01	6.450E+04	3.856E+04	1.749E+04	1.921E+04	4.434E+04	3.131E+04	3.495E+04
82	2.945E−01	6.450E+04	3.856E+04	1.749E+04	1.921E+04	4.434E+04	3.131E+04	3.495E+04
83	2.873E−01	6.450E+04	3.856E+04	1.749E+04	1.921E+04	4.434E+04	3.131E+04	3.495E+04
84	2.732E−01	4.708E+04	3.350E+04	1.698E+04	2.157E+04	4.245E+04	2.960E+04	3.411E+04
85	2.472E−01	2.400E+04	3.306E+04	2.854E+04	1.605E+04	3.002E+04	2.916E+04	3.141E+04
86	2.352E−01	2.847E+04	3.566E+04	3.000E+04	1.686E+04	4.041E+04	2.768E+04	2.942E+04
87	2.237E−01	3.722E+04	2.349E+04	1.775E+04	2.162E+04	3.078E+04	2.624E+04	2.791E+04
88	2.128E−01	4.640E+04	1.712E+04	2.304E+04	1.651E+04	3.547E+04	2.579E+04	2.677E+04
89	2.024E−01	5.173E+04	2.898E+04	2.159E+04	1.774E+04	3.865E+04	2.593E+04	2.576E+04
90	1.926E−01	3.673E+04	2.890E+04	2.243E+04	2.946E+04	3.196E+04	2.341E+04	2.476E+04
91	1.832E−01	2.813E+04	3.493E+04	2.271E+04	2.507E+04	2.096E+04	2.188E+04	2.375E+04
92	1.742E−01	3.020E+04	3.067E+04	2.320E+04	1.742E+04	2.110E+04	2.202E+04	2.278E+04
93	1.657E−01	4.033E+04	3.242E+04	2.553E+04	1.311E+04	3.144E+04	2.109E+04	2.188E+04
94	1.576E−01	5.538E+04	3.366E+04	2.922E+04	1.194E+04	3.345E+04	1.983E+04	2.105E+04
95	1.500E−01	7.200E+04	2.316E+04	3.352E+04	1.312E+04	1.830E+04	1.953E+04	2.031E+04

TABLE 2—*Continued.*

Group	Lower Energy, MeV	Al(1193) Sigma, eV-barns	V(1196) Sigma, eV-barns	Cr(1191) Sigma, eV-barns	Fe(1192) Sigma, eV-barns	Ni(1190) Sigma, eV-barns	Cu(1295) Sigma, eV-barns	Zr(1284) Sigma, eV-barns
96	1.426E−01	7.306E+04	1.403E+04	5.478E+04	2.531E+04	2.005E+04	2.187E+04	1.940E+04
97	1.357E−01	4.254E+04	2.913E+04	2.382E+04	2.207E+04	3.374E+04	2.008E+04	1.865E+04
98	1.291E−01	1.525E+04	1.987E+04	1.071E+04	1.389E+04	8.809E+03	1.769E+04	1.794E+04
99	1.228E−01	1.858E+04	2.931E+04	1.479E+04	8.532E+03	1.196E+04	1.544E+04	1.729E+04
100	1.168E−01	2.529E+04	3.365E+04	1.483E+04	7.244E+03	1.189E+04	1.514E+04	1.676E+04
101	1.111E−01	1.863E+04	2.737E+04	1.696E+04	8.511E+03	1.368E+04	1.644E+04	1.611E+04
102	9.804E−02	1.903E+04	7.213E+03	3.869E+04	1.007E+04	1.610E+04	1.478E+04	1.513E+04
103	8.652E−02	5.568E+04	1.305E+04	2.116E+04	1.446E+04	1.215E+04	1.377E+04	1.364E+04
104	8.250E−02	6.034E+04	1.918E+04	2.698E+03	2.348E+04	1.308E+04	1.523E+04	1.261E+04
105	7.950E−02	3.515E+04	1.582E+04	2.822E+03	1.478E+04	1.306E+04	1.648E+04	1.219E+04
106	7.200E−02	1.229E+04	9.950E+03	4.269E+03	1.431E+04	1.539E+04	1.589E+04	1.147E+04
107	6.738E−02	5.882E+03	3.489E+04	6.491E+03	4.285E+03	2.205E+04	1.007E+04	1.074E+04
108	5.656E−02	5.095E+03	2.000E+04	6.296E+03	5.893E+03	2.168E+04	1.094E+04	8.682E+03
109	5.248E−02	5.536E+03	1.201E+04	1.146E+04	7.908E+03	4.377E+03	1.373E+04	7.081E+03
110	4.631E−02	6.381E+03	8.254E+03	2.348E+04	6.770E+03	6.223E+03	5.753E+03	8.005E+03
111	4.087E−02	8.937E+03	4.451E+03	1.788E+03	6.089E+03	7.606E+03	8.835E+03	1.236E+04
112	3.431E−02	3.087E+04	6.649E+03	3.330E+03	7.108E+03	8.124E+03	7.665E+03	5.248E+03
113	3.183E−02	2.367E+04	6.009E+03	2.208E+03	1.025E+04	9.166E+03	8.048E+03	3.856E+03
114	2.850E−02	3.175E+03	9.913E+03	3.429E+03	2.800E+04	1.209E+04	8.123E+03	3.946E+03
115	2.700E−02	1.285E+03	9.533E+03	3.920E+03	4.331E+04	9.071E+03	8.677E+03	3.143E+03
116	2.606E−02	8.619E+02	9.339E+03	2.656E+03	6.068E+03	7.148E+03	1.386E+04	3.140E+03
117	2.479E−02	7.756E+02	1.068E+04	2.026E+03	2.884E+03	7.585E+03	1.066E+04	3.391E+03
118	2.418E−02	7.075E+02	1.173E+04	1.533E+03	3.894E+02	7.927E+03	8.153E+03	3.588E+03
119	2.358E−02	7.081E+02	1.463E+04	2.262E+03	3.680E+02	8.345E+03	6.207E+03	5.007E+03
120	2.188E−02	7.231E+02	2.111E+04	2.137E+03	4.501E+02	8.959E+03	7.451E+03	3.547E+03
121	1.931E−02	7.619E+02	1.061E+04	1.846E+03	6.512E+02	1.087E+04	7.538E+03	3.605E+03
122	1.503E−02	7.506E+02	2.242E+04	1.637E+03	8.850E+02	2.659E+04	5.994E+03	4.075E+03
123	1.171E−02	7.513E+02	3.007E+04	1.768E+03	1.077E+03	1.608E+04	4.496E+03	2.497E+03
124	9.119E−03	6.275E+02	2.321E+04	2.544E+03	1.335E+03	4.425E+03	7.212E+03	1.204E+03
125	7.102E−03	5.041E+02	8.010E+03	5.532E+03	3.134E+03	1.772E+03	3.188E+03	1.560E+03

126	5.531E−03	7.388E+02	2.264E+04	5.124E+03	1.407E+03	2.173E+03	1.160E+03	1.372E+03
127	4.307E−03	3.080E+02	1.622E+04	4.258E+03	6.653E+02	3.224E+03	1.982E+03	6.684E+02
128	3.707E−03	2.444E+02	2.481E+04	3.402E+03	6.709E+02	2.376E+03	7.823E+02	1.248E+03
129	3.355E−03	2.157E+02	4.784E+03	2.101E+03	5.061E+02	1.602E+03	3.287E+02	2.638E+02
130	3.035E−03	1.951E+02	1.869E+03	1.373E+03	4.587E+02	1.223E+03	3.587E+02	3.774E+02
131	2.747E−03	1.764E+02	1.100E+03	9.618E+02	4.225E+02	1.009E+03	4.261E+02	6.954E+02
132	2.613E−03	1.617E+02	7.971E+02	7.425E+02	3.945E+02	8.812E+02	1.713E+03	9.065E+02
133	2.485E−03	1.539E+02	6.933E+02	6.552E+02	3.790E+02	8.216E+02	1.609E+03	2.267E+02
134	2.249E−03	1.425E+02	5.700E+02	5.467E+02	3.554E+02	7.402E+02	6.012E+02	1.961E+02
135	2.035E−03	1.276E+02	4.480E+02	4.332E+02	3.222E+02	6.409E+02	2.783E+03	1.488E+02
136	1.585E−03	1.060E+02	3.321E+02	3.126E+02	2.695E+02	5.055E+02	6.483E+02	1.150E+02
137	1.234E−03	8.000E+01	2.377E+02	2.014E+02	1.969E+02	3.432E+02	8.692E+01	9.459E+01
138	9.611E−04	5.991E+01	1.278E+02	1.334E+02	1.320E+02	2.156E+02	6.856E+01	2.102E+01
139	7.485E−04	4.474E+01	6.624E+01	7.633E+01	7.127E+01	1.108E+02	4.688E+01	4.199E−01
140	5.830E−04	3.359E+01	2.766E+01	3.140E+01	2.643E+01	3.003E+01	4.180E+01	0.
141	4.540E−04	2.484E+01	8.509E+00	6.874E+00	1.066E+00	1.350E+00	1.346E+01	
142	3.536E−04	1.803E+01	1.071E+00	1.178E−02	0.	0.	5.891E−02	
143	2.754E−04	1.275E+01	0.	0.			0.	
144	2.145E−04	8.594E+00						
145	1.670E−04	5.386E+00						
146	1.301E−04	2.887E+00						
147	1.013E−04	9.388E−01						
148	7.889E−05	8.606E−03						
149	6.144E−05	0.						

TABLE 2—*Continued.*

Group	Lower Energy, MeV	Cb(1189) Sigma, eV-barns	Mo(1287) Sigma, eV-barns	Ta(1285) Sigma, eV-barns	W(1128-31) Sigma, eV-barns	Pb(1288) Sigma, eV-barns	18/10 SS Sigma, eV-barns
	1.733E+01						
1	1.649E+01	3.164E+05	2.774E+05	2.448E+05	2.201E+05	2.426E+05	2.980E+05
2	1.568E+01	3.041E+05	2.733E+05	2.376E+05	2.119E+05	2.325E+05	2.949E+05
3	1.492E+01	2.873E+05	2.687E+05	2.327E+05	2.041E+05	2.171E+05	2.945E+05
4	1.455E+01	2.732E+05	2.619E+05	2.313E+05	1.989E+05	2.079E+05	2.915E+05
5	1.419E+01	2.633E+05	2.570E+05	2.248E+05	1.959E+05	2.029E+05	2.875E+05
6	1.384E+01	2.535E+05	2.535E+05	2.199E+05	1.930E+05	2.027E+05	2.827E+05
7	1.350E+01	2.490E+05	2.502E+05	2.158E+05	1.902E+05	2.022E+05	2.776E+05
8	1.284E+01	2.432E+05	2.474E+05	2.097E+05	1.862E+05	1.983E+05	2.711E+05
9	1.221E+01	2.360E+05	2.420E+05	2.021E+05	1.811E+05	1.961E+05	2.636E+05
10	1.162E+01	2.279E+05	2.351E+05	1.945E+05	1.760E+05	1.931E+05	2.581E+05
11	1.105E+01	2.225E+05	2.247E+05	1.864E+05	1.708E+05	1.839E+05	2.522E+05
12	1.051E+01	2.163E+05	2.145E+05	1.798E+05	1.655E+05	1.749E+05	2.457E+05
13	1.000E+01	2.117E+05	2.108E+05	1.750E+05	1.598E+05	1.666E+05	2.390E+05
14	9.512E+00	2.072E+05	2.091E+05	1.668E+05	1.537E+05	1.598E+05	2.331E+05
15	9.048E+00	2.033E+05	2.034E+05	1.555E+05	1.476E+05	1.544E+05	2.275E+05
16	8.607E+00	2.006E+05	2.013E+05	1.480E+05	1.404E+05	1.487E+05	2.211E+05
17	8.187E+00	1.962E+05	2.001E+05	1.452E+05	1.335E+05	1.422E+05	2.166E+05
18	7.788E+00	1.922E+05	1.926E+05	1.413E+05	1.292E+05	1.365E+05	2.120E+05
19	7.408E+00	1.880E+05	1.860E+05	1.353E+05	1.260E+05	1.338E+05	2.082E+05
20	7.047E+00	1.832E+05	1.797E+05	1.299E+05	1.224E+05	1.303E+05	2.043E+05
21	6.703E+00	1.778E+05	1.737E+05	1.250E+05	1.183E+05	1.263E+05	2.005E+05
22	6.592E+00	1.734E+05	1.692E+05	1.219E+05	1.152E+05	1.238E+05	1.982E+05
23	6.376E+00	1.703E+05	1.661E+05	1.196E+05	1.131E+05	1.222E+05	1.961E+05
24	6.065E+00	1.653E+05	1.610E+05	1.161E+05	1.099E+05	1.198E+05	1.916E+05
25	5.770E+00	1.598E+05	1.553E+05	1.123E+05	1.064E+05	1.181E+05	1.880E+05
26	5.488E+00	1.548E+05	1.496E+05	1.094E+05	1.028E+05	1.188E+05	1.845E+05
27	5.221E+00	1.506E+05	1.443E+05	1.066E+05	9.909E+04	1.177E+05	1.807E+05
28	4.966E+00	1.472E+05	1.392E+05	1.039E+05	9.556E+04	1.150E+05	1.764E+05
29	4.724E+00	1.431E+05	1.347E+05	1.004E+05	9.230E+04	1.145E+05	1.730E+05

30	4.493E+00	1.386E+05	1.305E+05	9.632E+04	8.919E+04	1.131E+05	1.681E+05
31	4.066E+00	1.310E+05	1.256E+05	9.059E+04	8.480E+04	1.127E+05	1.598E+05
32	3.679E+00	1.217E+05	1.201E+05	8.449E+04	7.972E+04	1.111E+05	1.513E+05
33	3.328E+00	1.148E+05	1.148E+05	8.039E+04	7.522E+04	1.092E+05	1.404E+05
34	3.166E+00	1.112E+05	1.111E+05	7.758E+04	7.205E+04	1.113E+05	1.380E+05
35	3.012E+00	1.086E+05	1.089E+05	7.589E+04	7.009E+04	1.063E+05	1.368E+05
36	2.865E+00	1.056E+05	1.059E+05	7.394E+04	6.822E+04	1.038E+05	1.292E+05
37	2.725E+00	1.027E+05	1.026E+05	7.198E+04	6.678E+04	9.644E+04	1.294E+05
38	2.592E+00	1.004E+05	9.945E+04	7.007E+04	6.532E+04	9.531E+04	1.249E+05
39	2.466E+00	9.810E+04	9.620E+04	6.809E+04	6.374E+04	8.575E+04	1.307E+05
40	2.385E+00	9.657E+04	9.447E+04	6.669E+04	6.269E+04	8.519E+04	1.212E+05
41	2.365E+00	9.494E+04	9.318E+04	6.536E+04	6.167E+04	8.469E+04	1.099E+05
42	2.346E+00	9.494E+04	9.318E+04	6.536E+04	6.167E+04	8.469E+04	1.099E+05
43	2.307E+00	9.494E+04	9.318E+04	6.536E+04	6.167E+04	8.469E+04	1.099E+05
44	2.231E+00	9.286E+04	9.176E+04	6.390E+04	6.050E+04	7.719E+04	1.049E+05
45	2.123E+00	9.099E+04	9.051E+04	6.239E+04	5.942E+04	7.313E+04	1.051E+05
46	2.019E+00	8.824E+04	8.883E+04	6.019E+04	5.787E+04	6.863E+04	1.061E+05
47	1.921E+00	8.514E+04	8.703E+04	5.823E+04	5.627E+04	6.141E+04	9.852E+04
48	1.827E+00	8.184E+04	8.509E+04	5.661E+04	5.463E+04	5.306E+04	8.635E+04
49	1.738E+00	7.860E+04	8.319E+04	5.513E+04	5.303E+04	5.436E+04	8.329E+04
50	1.653E+00	7.542E+04	8.127E+04	5.366E+04	5.153E+04	5.254E+04	8.253E+04
51	1.572E+00	7.250E+04	7.943E+04	5.222E+04	5.015E+04	4.684E+04	8.495E+04
52	1.496E+00	6.999E+04	7.772E+04	5.081E+04	4.896E+04	4.080E+04	9.021E+04
53	1.423E+00	6.750E+04	7.523E+04	4.835E+04	4.734E+04	4.028E+04	8.324E+04
54	1.353E+00	6.626E+04	7.326E+04	4.640E+04	4.640E+04	3.794E+04	7.424E+04
55	1.287E+00	6.524E+04	7.176E+04	4.493E+04	4.570E+04	3.651E+04	7.028E+04
56	1.225E+00	6.348E+04	6.953E+04	4.275E+04	4.475E+04	3.521E+04	7.207E+04
57	1.165E+00	6.233E+04	6.852E+04	4.111E+04	4.352E+04	3.339E+04	5.807E+04
58	1.108E+00	6.153E+04	6.782E+04	3.996E+04	4.264E+04	3.212E+04	4.829E+04
59	1.003E+00	6.075E+04	6.639E+04	3.751E+04	4.039E+04	2.740E+04	5.223E+04
60	9.616E-01	6.044E+04	6.483E+04	3.524E+04	3.848E+04	2.723E+04	5.081E+04
61	9.072E-01	5.991E+04	6.291E+04	3.359E+04	3.688E+04	2.498E+04	3.398E+04
62	8.629E-01	5.945E+04	6.113E+04	3.206E+04	3.535E+04	2.518E+04	4.278E+04
63	8.209E-01	5.915E+04	5.951E+04	3.096E+04	3.382E+04	2.826E+04	4.473E+04
64	7.808E-01	5.868E+04	5.796E+04	3.002E+04	3.233E+04	2.657E+04	5.052E+04
65	7.427E-01	5.792E+04	5.652E+04	2.907E+04	3.092E+04	2.373E+04	5.685E+04

TABLE 2—*Continued.*

Group	Lower Energy, MeV	Cb(1189) Sigma, eV-barns	Mo(1287) Sigma, eV-barns	Ta(1285) Sigma, eV-barns	W(1128-31) Sigma, eV-barns	Pb(1288) Sigma, eV-barns	18/10 SS Sigma, eV-barns
66	7.065E−01	5.705E+04	5.537E+04	2.822E+04	2.963E+04	2.358E+04	4.908E+04
67	6.721E−01	5.589E+04	5.427E+04	2.723E+04	2.824E+04	2.149E+04	3.850E+04
68	6.393E−01	5.471E+04	5.330E+04	2.610E+04	2.698E+04	2.119E+04	3.656E+04
69	6.081E−01	5.355E+04	5.237E+04	2.500E+04	2.581E+04	2.075E+04	2.933E+04
70	5.784E−01	5.246E+04	5.153E+04	2.408E+04	2.475E+04	1.948E+04	2.948E+04
71	5.502E−01	5.121E+04	5.069E+04	2.311E+04	2.367E+04	1.927E+04	3.094E+04
72	5.234E−01	4.995E+04	4.983E+04	2.213E+04	2.261E+04	2.061E+04	3.299E+04
73	4.979E−01	4.884E+04	4.904E+04	2.128E+04	2.171E+04	1.326E+04	3.619E+04
74	4.505E−01	4.731E+04	4.680E+04	2.008E+04	2.042E+04	1.282E+04	3.383E+04
75	4.076E−01	4.520E+04	4.314E+04	1.857E+04	1.878E+04	1.451E+04	4.279E+04
76	3.877E−01	4.370E+04	4.089E+04	1.763E+04	1.778E+04	1.553E+04	4.406E+04
77	3.688E−01	4.241E+04	3.930E+04	1.695E+04	1.706E+04	1.671E+04	3.423E+04
78	3.337E−01	4.058E+04	3.723E+04	1.604E+04	1.613E+04	1.874E+04	2.340E+04
79	3.020E−01	3.827E+04	3.467E+04	1.495E+04	1.503E+04	1.569E+04	2.219E+04
80	2.985E−01	3.692E+04	3.332E+04	1.434E+04	1.445E+04	1.598E+04	1.852E+04
81	2.972E−01	3.596E+04	3.245E+04	1.392E+04	1.408E+04	1.601E+04	2.126E+04
82	2.945E−01	3.596E+04	3.245E+04	1.392E+04	1.408E+04	1.601E+04	2.126E+04
83	2.873E−01	3.596E+04	3.245E+04	1.392E+04	1.408E+04	1.601E+04	2.126E+04
84	2.732E−01	3.524E+04	3.188E+04	1.361E+04	1.383E+04	1.633E+04	2.267E+04
85	2.472E−01	3.296E+04	3.008E+04	1.264E+04	1.305E+04	1.601E+04	1.977E+04
86	2.352E−01	3.126E+04	2.877E+04	1.197E+04	1.248E+04	1.523E+04	2.161E+04
87	2.237E−01	2.997E+04	2.778E+04	1.152E+04	1.206E+04	1.494E+04	2.175E+04
88	2.128E−01	2.886E+04	2.694E+04	1.113E+04	1.171E+04	1.412E+04	1.956E+04
89	2.024E−01	2.781E+04	2.613E+04	1.076E+04	1.137E+04	1.293E+04	2.046E+04
90	1.926E−01	2.669E+04	2.520E+04	1.039E+04	1.102E+04	1.276E+04	2.835E+04
91	1.832E−01	2.552E+04	2.415E+04	1.003E+04	1.068E+04	1.236E+04	2.423E+04
92	1.742E−01	2.439E+04	2.309E+04	9.688E+03	1.035E+04	1.199E+04	1.888E+04
93	1.657E−01	2.334E+04	2.211E+04	9.369E+03	1.004E+04	1.173E+04	1.722E+04
94	1.576E−01	2.237E+04	2.121E+04	9.076E+03	9.763E+03	1.149E+04	1.729E+04
95	1.500E−01	2.150E+04	2.040E+04	8.816E+03	9.513E+03	1.128E+04	1.753E+04

96	1.426E−01	2.042E+04	1.940E+04	8.494E+03	9.198E+03	1.047E+04	3.048E+04
97	1.357E−01	1.952E+04	1.856E+04	8.210E+03	8.914E+03	1.003E+04	2.351E+04
98	1.291E−01	1.868E+04	1.776E+04	7.954E+03	8.651E+03	9.656E+03	1.281E+04
99	1.228E−01	1.790E+04	1.703E+04	7.717E+03	8.408E+03	9.944E+03	1.006E+04
100	1.168E−01	1.727E+04	1.643E+04	7.529E+03	8.210E+03	1.031E+04	9.140E+03
101	1.111E−01	1.650E+04	1.571E+04	7.297E+03	7.970E+03	9.356E+03	1.063E+04
102	9.804E−02	1.465E+04	1.451E+04	6.944E+03	7.618E+03	8.175E+03	1.614E+04
103	8.652E−02	9.413E+03	1.233E+04	6.327E+03	7.130E+03	7.556E+03	1.553E+04
104	8.250E−02	8.646E+03	1.128E+04	5.870E+03	6.685E+03	7.138E+03	1.852E+04
105	7.950E−02	8.334E+03	1.086E+04	5.681E+03	6.505E+03	7.494E+03	1.233E+04
106	7.200E−02	7.796E+03	1.013E+04	5.362E+03	6.185E+03	8.456E+03	1.248E+04
107	6.738E−02	7.164E+03	9.270E+03	4.982E+03	5.792E+03	6.438E+03	6.385E+03
108	5.656E−02	6.432E+03	8.274E+03	4.543E+03	5.328E+03	5.275E+03	7.461E+03
109	5.248E−02	5.712E+03	7.296E+03	4.113E+03	4.869E+03	4.676E+03	8.259E+03
110	4.631E−02	5.168E+03	6.561E+03	3.769E+03	4.516E+03	4.401E+03	9.928E+03
111	4.087E−02	4.596E+03	5.771E+03	3.326E+03	4.129E+03	4.867E+03	5.408E+03
112	3.431E−02	3.998E+03	4.940E+03	2.849E+03	3.375E+03	3.263E+03	6.480E+03
113	3.183E−02	3.539E+03	4.304E+03	2.486E+03	2.644E+03	2.509E+03	8.610E+03
114	2.850E−02	3.236E+03	3.882E+03	2.245E+03	2.206E+03	2.378E+03	2.179E+04
115	2.700E−02	3.023E+03	3.590E+03	2.077E+03	1.949E+03	2.235E+03	3.253E+04
116	2.606E−02	2.846E+03	3.345E+03	1.937E+03	1.716E+03	2.123E+03	5.517E+03
117	2.479E−02	2.760E+03	3.231E+03	1.868E+03	1.612E+03	2.202E+03	3.164E+03
118	2.418E−02	2.693E+03	3.141E+03	1.815E+03	1.531E+03	2.264E+03	1.320E+03
119	2.358E−02	2.603E+03	3.024E+03	1.737E+03	1.441E+03	2.015E+03	1.484E+03
120	2.188E−02	2.492E+03	2.877E+03	1.640E+03	1.320E+03	1.866E+03	1.577E+03
121	1.931E−02	2.268E+03	2.585E+03	1.446E+03	1.083E+03	1.743E+03	1.845E+03
122	1.503E−02	1.910E+03	2.133E+03	1.150E+03	7.592E+02	1.546E+03	3.460E+03
123	1.171E−02	1.491E+03	1.626E+03	8.147E+02	4.561E+02	1.224E+03	2.625E+03
124	9.119E−03	1.168E+03	1.240E+03	5.573E+02	2.639E+02	9.825E+02	1.859E+03
125	7.102E−03	9.612E+02	9.387E+02	3.607E+02	1.346E+02	7.581E+02	3.467E+03
126	5.531E−03	9.377E+02	7.040E+02	2.094E+02	5.778E+01	5.504E+02	2.193E+03
127	4.307E−03	5.799E+02	5.166E+02	9.279E+01	1.598E+01	3.967E+02	1.579E+03
128	3.707E−03	3.990E+02	3.927E+02	1.707E+01	4.500E−01	2.971E+02	1.356E+03
129	3.355E−03	3.639E+02	3.251E+02	0.	0.	2.468E+02	9.156E+02
130	3.035E−03	2.730E+02	2.763E+02			2.153E+02	7.065E+02

TABLE 2—*Continued.*

Group	Lower Energy, MeV	Cb(1189) Sigma, eV-barns	Mo(1287) Sigma, eV-barns	Ta(1285) Sigma, eV-barns	W(1128-31) Sigma, eV-barns	Pb(1288) Sigma, eV-barns	18/10 SS Sigma, eV-barns
131	2.747E−03	2.223E+02	2.331E+02			1.756E+02	5.815E+02
132	2.613E−03	3.600E+02	2.003E+02			1.503E+02	5.073E+02
133	2.485E−03	4.121E+02	1.823E+02			1.426E+02	4.739E+02
134	2.249E−03	2.193E+02	1.547E+02			1.218E+02	4.286E+02
135	2.035E−02	1.236E+02	1.172E+02			9.269E+01	3.737E+02
136	1.585E−03	6.522E+01	6.411E+01			5.803E+01	3.001E+02
137	1.234E−03	9.137E+00	8.571E+00			2.530E+01	2.117E+02
138	9.611E−04	0.	0.			6.363E+00	1.402E+02
139	7.485E−04					0.	7.599E+01
140	5.830E−04						2.773E+01
141	4.540E−04						2.209E+00
142	3.536E−04						2.262E−03
143	2.754E−04						0.

are at high energies, due both to changes in cross sections and to inclusion of more reactions in the new calculation. This was corroborated by finding that spectral-averaged values for a number of fast and thermal reactor spectra were unchanged. On the other hand, the value for a pure fission spectrum increased from 923 to 941 barns, and the value for a conceptual fusion reactor (UWMAK-1) [*15*] first wall spectrum increased from 855 to 1030 barns.

Summary

Damage energy cross sections, employing the Lindhard energy partition model, have been developed for a number of common metals based on ENDF/B-IV data. Tabulations of these cross sections are included in a relatively fine group structure. Examples of PKA spectra and displacement cross sections are given to illustrate the contributions of various nuclear reactions.

A more extensive compilation [*16*] will be available shortly that will include graphical presentations of all the displacement cross sections, a number of PKA spectra, EBR-II displacement rate maps for several metals, and other items omitted here due to space limitations.

Acknowledgment

This work was supported by the U.S. Energy Research and Development Administration under Contract E(45-1)-2170.

References

[*1*] McElroy, W. N., Simons, R. L., Doran, D. G., and Odette, G. R., *Journal of Testing and Evaluation*, Vol. 3, 1975, p. 220.

[*2*] Jenkins, J. D., *Nuclear Science and Engineering*, Vol. 41, 1970, p. 155.

[*3*] Sheely, W. F., *Nuclear Science and Engineering*, Vol. 29, 1967, p. 165.

[*4*] Doran, D. G., *Nuclear Science and Engineering*, Vol. 49, 1972, p. 130.

[*5*] Doran, D. G., *Nuclear Science and Engineering*, Vol. 52, 1973, p. 398.

[*6*] Doran, D. G. and Graves, N. J., "Displacement Cross Sections for Fe, Cr, Ni, 18/10 SS, Mo, V, Nb, and Ta," Technical Report HEDL-TME 73-59, Hanford Engineering Development Laboratory, Richland, Wash., July 1973.

[*7*] Kulcinski, G. L., Doran, D. G., and Abdou, M. A. in *Properties of Reactor Structural Alloys After Neutron on Particle Irradiation, ASTM STP 570*, American Society for Testing and Materials, 1975, pp. 329–351.

[*8*] "Recommendations for Displacement Calculations for Reactor/Accelerator Studies in Austenitic Steel" formulated by IAEA Specialists' Meeting on Radiation Damage Units, Seattle, Wash., Oct. 1972; *Nuclear Engineering and Design*, Vol. 33, 1975, p. 91.

[*9*] Doran, D. G., Beeler, J. R., Jr., Dudey, N. D., and Fluss, M. J., "Report of the Working Group on Displacement Models and Procedures for Damage Calculations," Technical Report HEDL-TME 73-76, Hanford Engineering Development Laboratory, Richland, Wash., Dec. 1973.

[*10*] Orphan, V. J., Rasmussen, N. C., and Harper, T. L., "Line and Continuum Gamma-Ray Yields from Thermal Neutron Capture in 74 Elements," Technical Report GA-10248, DASA-2500, Gulf General Atomic, 1970.

[11] "Controlled Thermonuclear Progress Report HEDL-TME 75-24," D. G. Doran and H. H. Yoshikawa, Compilers, Hanford Engineering Development Laboratory, Richland, Wash., Feb. 1975.
[12] Kikuchi, K. K. and Kawai, M., *Nuclear Matter and Nuclear Reactions,* American Elsevier Publishing Company, New York, 1968.
[13] Newton, T. D., *Canadian Journal of Physics,* Vol. 34, 1956, p. 804.
[14] Pearlstein, S., *Nuclear Data,* Vol. A3, 1967, p. 327.
[15] Fusion Feasibility Study Group, Kulcinski, G. L., Director, "UWMAK-I, A Wisconsin Toroidal Fusion Reactor Design," Technical Report UWFDM-68, University of Wisconsin, Madison, Wis., March 1974.
[16] Doran, D. G. and Graves, N. J., "Displacement Cross Sections and PKA Spectra: Tables and Applications," Technical Report HEDL-TME 76-70, Hanford Engineering Development Laboratory, Richland, Wash., Sept. 1976.

NOTE—A paper discussing more rigorous kinematic descriptions of several nonelastic reactions has been published recently by Odette and Dairon (*Nuclear Technology,* Vol. 29, 1976, p. 346). For slightly different approaches to the calculation of damage energy cross sections, see also the papers by Parkin and Goland (*Radiation Effects,* Vol. 28, 1976, p. 1) and Gabriel et al (*Nuclear Science Engineering,* Vol. 61, 1976, p. 21).

Index

A

Activation energy, 64
Aging, 77, 157, 166, 184, 308, 321, 355
Aluminum, 211, 331, 465
Anneal, 173, 443
Auger spectroscopy, 141, 150, 441
Austenitic alloys, 6, 33, 35, 37, 72, 92, 101, 120

B

Blue brittle, 54
Burst test, 103

C

Carbides, 82, 119, 228, 274
Carbon, 55, 67, 150, 197, 211, 301, 420
Cavities, 111
Channel fracture, 130, 133
Charpy-V notch test, 392, 397, 403, 435, 440
Chromium, 151, 270, 420, 465
Cladding, 6, 101, 107, 209, 220
Clusters, 242, 286, 375, 452
Cold working, 6, 35, 72, 84
Columbium, 211, 242, 465
Columbium alloys, 243
Compact tension, 389
Composition, effect of, 196, 199, 211
Control rod thimble, 120
Copper, 211, 415, 426, 465
Cottrell atmosphere, 260
Cracks, 389
Creep, 12, 23, 294
  Coefficients, 25, 35
  In-reactor, 10
  Irradiation, 10, 37, 285
  Model, 12
  Transient, 28

D

Damage energy cross section, 471, 480
Damage function, 187, 189, 470
Decarburized steel, 67
Defects, 451
Delta phase, 362, 365
Density, 73, 220, 273
Diffraction patterns, 359
Diffusion, 380
Dislocations, 82, 133, 143, 234, 245, 257, 285, 300, 302, 340, 375
  Climb-glide mechanism, 291
Displacement spikes, 449
DPA models, 230
  Kinchin and Pease, 230, 317, 339
Ductility, 94, 108, 129, 132, 160, 179

E

Electron diffraction, 359
Electron vacancy, 270, 278
Elongation
  Uniform, 165, 179, 182
  Total, 179, 182, 185

Eta phase, 367

F

Failure
  Strain, 104
  Stress, 104
  Temperature, 104
Fast Flux
  $E > 0.1$ MeV, 7, 20, 35, 55, 73, 93, 101, 120, 140
Ferritic alloys
  EM-12, 228
  HT-19, 228
Fluence effect, 127, 412
Foil, 73, 229, 243
Fracture
  Intergranular, 130
  Mode, 111, 128
  Strength, 1
  Toughness, 111, 388, 404
  Transgranular, 130
  Transition, 136
Fuel cladding transient tester, 102
Fuel column, 115
Fuel pin, 101, 130, 172, 220

G

Gamma heated, 271
Gamma prime, 143, 271, 315, 321, 355, 382
Grain boundaries, 156, 234

H

Hardening
  Percipitation, 143, 370
  Work, 59, 80
Hastelloy-X, 280
HAZ, 401
Heating rates, 109
Helium, 75, 95, 132, 154, 174, 190, 224, 317, 338

I

Impact testing, 389, 392, 397, 403, 435, 440
Impurities, 244, 259, 267
Incoloy 800, 280
Inconel 706, 354
Inconel 718, 156, 354
Interstitials, 244, 266, 292, 298, 449
Iron, 270, 450, 465
Iron-nickel chromium alloys, 315, 337
Irradiation
  Alpha particle, 285
  Deuteron, 285
  Electron, 213, 243
  Ion, 195, 229, 279, 300, 317, 338, 354, 371
  Neutron, 20, 35, 55, 73, 93, 101, 120, 140, 157, 176, 238, 391
  Temperature, 20, 35, 73, 92, 103, 120, 140, 156, 182, 295, 300

K

K_{Ic}, 390
Knoop hardness, 176, 178

L

Laves phase, 367
Luders band, 59, 64
Luders strain, 56, 64

M

$M_{23}C_6$, 82
Manganese, 420
McVetty relationship, 38
Mechanical properties, 12, 23, 75, 92, 95, 101, 120, 146, 160, 171, 185, 402
Metallography, 175
Microhardness, 174, 438

Microscopy
Optical, 441
SEM, 111, 129, 141, 149, 441
TEM, 78, 141, 231, 286, 317, 343, 354, 372, 441
Microstructure, 82, 141, 179, 233, 284, 288, 298, 340, 357
Mild steels, 55
Molybdenum, 420
Mu phase, 367

N

Nickel, 151, 285, 420, 465
Nickel alloys
PE16, 33, 140, 271, 354
GAB, 286, 271
Nickel-aluminum alloys, 372
Ni_3Al, 378
Nimonic alloys, 33, 140, 271, 354
Nitrogen, 150, 197, 203

O

Overaging, 362
Oxygen, 246, 301

P

Pauling's model, 278
Percipitates, 82, 143, 300, 305, 317, 321, 365, 373
Phosphorus, 151, 203, 415
Point beach nuclear, 172
Point defects, 258, 266, 349
Polygonization, 84
Pressure vessel, 389, 401

R

Reactors
CRBRP, 182, 195
CTR, 189
DFR, 35, 271
DMTR, 35
EBR-II, 20, 35, 73, 92, 103, 120, 140, 156, 182, 209, 225, 238, 464
ENEL, 387
FFTF, 91, 103, 195
FTR, 182, 209, 225
HFIAR, 55
HFIR, 182, 224
LAMPF, 188
LMFBR, 72, 91, 101, 156, 353, 463
Maine Yankee, 400
UCRR, 391
Recovery, 438, 441

S

Serrations, 59
Sigma phase, 276
Silicon, 211, 420
Simulation, of neutron irradiation, 195, 213, 229, 243
Stainless steels
316 SS, N-lot, 92, 209, 217, 271
M316, 33, 37, 271
316L SS, 271
316 SS, 6, 35, 72, 92, 101, 195, 209
321 SS, 271
FV548, 33, 37, 271
G 68, 271
Strain
Rate effects, 98, 126
Ratio, 105
Stress
Maximum fiber, 10
Relaxation, 8, 33
Structural steels
A302-B, 388, 422, 435
A508-2, 422
A533-B, 413, 422
A533-C-2, 422
A543, 422
HY80, 422

NiCrMo, 422
MnNiMoV, 423
Sulfur, 151, 203
Surveillance materials, 401
Swaged, 140, 271, 316
Swelling, 88, 142, 195, 200, 209, 231, 271, 273, 315, 317, 325, 345
Model, 210

T

Tantalum, 465
Tensile, 75, 92, 120, 156, 176, 401
Thermal transients, 104, 108
Thompson effect, 260
Titanium effects, 197, 211, 331
Transition temperature increase, DTT, 411, 419, 426
Tubing, 92, 271
Slit, 13
Tungsten, 465

U

Ultimate strength, 75, 95, 124, 125, 178, 182
Upper-shelf energy, 392, 411

V

Vacancies, 253, 257, 292, 449
Vanadium, 298
Vanadium alloys, 298
Voids, 73, 82, 111, 142, 220, 231, 256, 270, 300, 302, 322, 340, 347, 375

W

Welds, 157, 401, 416, 419, 436
Wisconsin Electric Company, 172
Wrought, 159

Y

Yield strength, 75, 95, 124, 164, 178, 182, 391

Z

Zircaloy, 171